A.I.M.P.A.

Commission internationale de physique des nuages

Communications à la VIII ème conférence internationale sur la physique des nuages

Volume I

Clermont-Ferrand - France - 15-19 juillet 1980

VIIIEME CONFERENCE INTERNATIONALE SUR LA PHYSIQUE DES NUAGES

CLERMONT-FERRAND, 15-19 juillet 1980

Sous le haut patronage de :

MADAME LE MINISTRE ALICE SAUNIER-SEITE, MINISTRE DES UNIVERSITES

Sous le patronage international de :

LA COMMISSION INTERNATIONALE DE PHYSIQUE DES NUAGES

LA COMMISSION INTERNATIONALE DU RAYONNEMENT

L'ASSOCIATION INTERNATIONALE DE METEOROLOGIE ET PHYSIQUE DE L'ATMOSPHERE

L'ORGANISATION METEOROLOGIQUE MONDIALE

Et les patronages nationaux des organismes suivants :

CENTRE NATIONAL DE LA RECHERCHE SCIENTIFIQUE

DELEGATION GENERALE A LA RECHERCHE SCIENTIFIQUE ET TECHNIQUE

UNIVERSITE DE CLERMONT II

COMITE NATIONAL FRANCAIS DE GEODESIE ET GEOPHYSIQUE

SOCIETE AMERICAINE DE METEOROLOGIE

SOCIETE FRANCAISE DE METEOROLOGIE

Subventions ou aides

ASSOCIATION INTERNATIONALE DE METEOROLOGIE
ET PHYSIQUE DE L'ATMOSPHERE (AIMPA)

CENTRE NATIONAL DE LA RECHERCHE SCIENTIFIQUE (CNRS)

INSTITUT NATIONAL D'ASTRONOMIE ET DE GEOPHYSIQUE (INAG)

DIRECTION DES RECHERCHES ET ETUDES TECHNIQUES (DRET)

ETUDES ET RECHERCHES DE L'ELECTRICITE DE FRANCE (EDF)

DEPARTEMENT DU PUY-DE-DOME

VILLE DE CLERMONT-FERRAND

AIR INTER, UTA, AIR FRANCE

UNIVERSITE DE CLERMONT II

UNITE D'ENSEIGNEMENT ET DE RECHERCHE "SCIENCES"

ASSOCIATION POUR LE DEVELOPPEMENT DE L'ENSEIGNEMENT
ET DE LA RECHERCHE EN AUVERGNE

MINISTERE DE L'AGRICULTURE

MINISTERE DES UNIVERSITES

Comité International des Programmes

Pr R.G. SOULAGE (France), Président

Pr W.F. HITSCHFELD (Canada), Président de
la Commission Internationale de Physique des Nuages (CIPN)

Dr H.K. WEICKMANN (U.S.A.), Président honoraire
de CIPN

Dr E. MESZAROS (Hongrie), Secrétaire de CIPN

Dr A. GAGIN (Israël)

Pr R. LIST (Canada), Président de la IIIème Conférence Scientifique
de l'O.M.M. sur la Modification du Temps

Dr I.P. MAZIN (U.R.S.S.)

Dr S. MOSSOP (Australie)

Pr H.D. ORVILLE (U.S.A.)

Pr H.R. PRUPPACHER (U.S.A.)

Dr. P. RYDER (Grande-Bretagne)

Comité d'Organisation

R.G. SOULAGE (Président), C. BOUTIN, J. DESSENS, M. FOURNIER D'ALBE,
H. ISAKA, Y. POINTIN, R. ROSSET, R. SERPOLAY.

Cet ouvrage a été imprimé et composé par :

L'UNITE D'ENSEIGNEMENT ET DE RECHERCHE "SCIENCES"

DE L'UNIVERSITE DE CLERMONT II

et le

LABORATOIRE ASSOCIE DE METEOROLOGIE PHYSIQUE
(L.A. CNRS n° 267)
B.P. 45
63170 AUBIERE (France)

Tel. (73) 26 42 87
Telex : 990 805 F

Il est disponible à la même adresse

LEGENDE DE LA COUVERTURE

Cumulonimbus tropical photographié depuis le DC 7 de la D.R.E.T. juste avant que l'avion ne pénètre dans la partie la plus active et n'y rencontre une teneur en eau condensée de 16 g/m^3 et une vitesse verticale de l'air de 20 m/s (cf. article de M. FODE et H. ISAKA) (cliché L.A.M.P.).

Tropical cumulonimbus photographed from the DC 7 of the D.R.E.T., just before the plane penetrated the most active part of this cloud, where it observed a liquid water content of 16 g/m^3 and an updraught velocity of 20 m/s (see paper by M. FODE and H. ISAKA) (Photo L.A.M.P.).

PREFACE

La Physique des Nuages est née avec la découverte, par Coulié en 1875 et Aïtken en 1880, des noyaux de condensation. Elle est devenue importante, entre 1933 et 1938, avec les travaux de T. Bergeron et W. Findeisen sur le rôle des cristaux de glace dans l'initiation des précipitations des régions tempérées. Elle s'est imposée au niveau de 1950, en tant que discipline à part entière dans la Météorologie, après la découverte par Langmuir, Schaefer et Vonnegut de possibilités d'action sur le temps par modification des nuages. De 1950 à 1964, elle a été, pour une grande part, la physique des changements de phase de l'eau dans l'atmosphère et la chimie physique des substances (noyaux divers) susceptibles de modifier ces changements de phase. Pendant tout ce temps-là, elle a été très liée à la modification du temps et victime d'expériences prématurées et incomplètes dans ce domaine, victime d'espoirs trop rapidement clamés, ainsi que d'un trop grand empirisme.

De 1964 à ce jour, une partie d'abord, la grande majorité ensuite des physiciens des nuages sont revenus à l'étude des bases de la discipline en considérant tous ses sous-domaines, c'est-à-dire la thermodynamique, la dynamique, le rayonnement des nuages aussi bien que leur microphysique. Ils se sont imposés le respect de trois étapes : connaissance, prévision, modification. Ils ont associé mesures in situ, interprétations physiques, modélisations numériques. Ils ont développé des techniques de mesures quantitatives des différents paramètres.

C'est ainsi qu'en 1980 la Physique des Nuages apparaît comme une discipline qui a consolidé ses bases, même si elle a encore beaucoup de progrès à faire, a redonné aux aspects thermodynamiques, dynamiques et radiatifs des phénomènes leur place, et est prête à des expériences scientifiques d'application.

Ces applications sont de nouveau la modification du temps pour laquelle les besoins sont encore plus grands que dans le passé, mais ce sont aussi l'influence des nuages sur les divers moyens de communication terrestres, le rôle des nuages dans le climat à travers leurs effets thermodynamiques et radiatifs, les effets des nuages artificiels que l'homme produit avec les rejets chauds et humides de ses parcs énergétiques.

Cette évolution de la Physique des Nuages que nous venons de décrire a été jalonnée, au cours des vingt-cinq dernières années, par sept Conférences, celle de Clermont-Ferrand étant la huitième.

La première Conférence Internationale sur la Physique des Nuages a eu lieu à Zurich (Suisse) en 1954, à l'initiative de Raymund Sänger qui avait lancé une des premières expériences scientifiques sur la grêle et dirigé une école sur les changements de phase de l'eau. C'est à cette Conférence que fut en quelque sorte consacrée la Physique des Nuages en tant que discipline à part entière.

La deuxième Conférence sur la Physique des Nuages s'est tenue à Vérone en Italie en 1959, sous la présidence d'Ottavio Vittori. Elle a été la première dominée par le problème de la grêle ; elle a

commencé à mettre en évidence aux yeux de certains la nécessité de retourner aux recherches fondamentales avant le passage aux applications

La troisième Conférence sur la Physique des Nuages a été organisée à Canberra et Sydney en 1961 par le très important groupe australien dirigé par Eugène "Taffy" Bowen. Les deux pôles de la Conférence ont été les noyaux glaçogènes et la pluie provoquée pour lesquels l'équipe australienne avait réalisé des travaux importants. Qui ne se souvient de la bataille sur les noyaux glaçogènes météoritiques !

La quatrième Conférence sur la Physique des Nuages s'est tenue à Tokyo en 1964 auprès de l'école japonaise, animée par Kenji Isono et Chôji Magono, et spécialisée depuis de longues années dans l'étude des cristaux de glace et des précipitations.

La cinquième Conférence sur la Physique des Nuages a été la première à se tenir sur le continent américain. Elle a été organisée par Roland List et Walter Hitschfeld. Elle a constaté le développement considérable de la discipline en Amérique du Nord, la possibilité de parvenir à des progrès rapides, la nécessité pour cela de confirmer le retour aux recherches fondamentales en renonçant pour un temps aux applications immédiates à la modification du temps, dans le double but d'économiser des efforts inutiles et de ne pas être victime du discrédit d'opérations prématurées ne conduisant à aucun résultat significatif.

C'est ainsi qu'à la sixième Conférence à Londres, présidée et organisée par B.J. Mason, la modification du temps a été pratiquement absente et seuls des problèmes fondamentaux ont été abordés.

Mais la modification du temps restait une potentialité pour le futur au niveau des applications, un problème scientifique pour le présent, qui ne pouvaient pas être négligés. Ceci conduisait la Commission de Physique des Nuages de l'Association Internationale de Météorologie Physique de l'Atmosphère et l'Organisation Météorologique Mondiale à s'entendre pour organiser à Boulder, en 1976, successivement la septième Conférence Internationale sur la Physique des Nuages, sous la présidence de Helmut Weickmann, et la deuxième Conférence Scientifique de l'O.M.M. sur la Modification du Temps, sous la présidence de Roland List. La Conférence sur la Physique des Nuages de Boulder vit les progrès de la discipline dans deux domaines, celui de la saisie des données quantitatives et précises principalement en Physique des Nuages, et celui de l'apparition d'outils mathématiques sous la forme de modèles numériques de développement de nuages et de croissance de leurs éléments.

La présente Conférence sur la Physique des Nuages se situe dans le prolongement direct de la Conférence de Boulder, étant suivie comme elle par une Conférence Scientifique de l'O.M.M. sur la Modification du Temps.

La Conférence de Clermont-Ferrand présentera cependant l'originalité de mettre l'accent sur l'importance des aspects thermodynamiques et dynamiques des nuages, sur l'interaction entre thermodynamique, dynamique, rayonnement et microphysique en leur sein, sur l'interaction entre les phénomènes à différentes échelles d'espace, depuis

l'échelle aérologique jusqu'à l'échelle synoptique. Enfin, sur chaque thème, donc dans chaque session, seront regroupés expérimentateurs et modélisateurs afin de jeter des ponts sur le fossé qui existe trop souvent entre théorie et expérience.

En réponse à la première et à la deuxième circulaires annonçant la Conférence de Clermont-Ferrand, nous avons reçu un nombre impressionnant de projets de communications : 251. Ce nombre montre la vitalité et l'expansion de notre discipline, mais il a posé un redoutable problème d'organisation.

Pour résoudre la difficulté, avec le Comité International des Programmes, nous avons décidé :

- de publier tous les résumés des projets de communications reçus dans le "Journal de Recherches Atmosphériques" (vol. 13, n° 4, 1979) et d'en faire une plaquette spéciale montrant l'activité générale de notre discipline en 1980, sans restriction ;

- d'organiser 14 sessions avec chacune six à huit courtes présentations orales suivies d'une table ronde animée par deux meneurs de jeux et portant sur les résultats les plus originaux et les problèmes les plus importants dans le domaine traité ;

- d'organiser trois sessions à "posters" (phénomènes microphysiques, phénomènes thermodynamiques et dynamiques, instrumentation) pour les communications non présentées oralement. Chaque "poster-session" comportera un temps pour l'examen des posters, un temps pour leur discussion plénière ;

- de ne pas traiter certains sujets malgré leur intérêt intrinsèque parce qu'ils ont été traités dans des Conférences récentes ou seront traités dans des Conférences prochaines (Conférence de Manchester sur l'Electricité Atmosphérique en août 1980 ou Conférence de Hambourg sur la Nucléation en août 1981).

Dans les pages qui suivent sont publiées toutes les communications acceptées, soit pour présentation orale, soit pour une session à "posters" soit en réserve. Ces communications sont regroupées suivant les sujets dans quatorze sessions normales ; dans chaque sujet, elles sont classées par ordre alphabétique.

Mon souhait, celui du Comité International des Programmes, sont que cette formule de conférence, sans doute encore très imparfaite, mais qui laisse une grande place aux discussions, permette à tous de faire connaître les progrès qu'ils ont accomplis, de s'informer des progrès des autres, de dégager les lignes directrices de rerecherches nouvelles pour hâter les progrès de tous dans la connaissance des nuages.

Il me reste l'agréable devoir d'exprimer ma reconnaissance la plus vive à toutes les personnalités et tous les organismes cités en page de garde, sans lesquels la présente Conférence n'aurait pu être mise sur pied.

R.G. SOULAGE

Président de la VIIIème Conférence Internationale sur la Physique des Nuages.

PREFACE

Cloud Physics, as a subject of scientific study, was born a hundred years ago, with the publication by Coulié (1875) and by Aitken (1880) of their discoveries of the existence of condensation nuclei. It came of age in the 1930's, through the work of Bergeron and Findeisen on the role of ice crystals in rain formation in temperate zones. It became a scientific discipline in its own right after the discovery by Langmuir, Schaefer and Vonnegut in 1950 of the possibility of weather modification by cloud seeding. During the following 15 years, research was directed mainly to the physics and chemistry of phase changes in atmospheric water substance. It benefited from, but was also the victim of the high hopes placed in weather modification, and suffered from hasty generalizations based on incomplete knowledge and insufficiently-controlled experimentation.

Since 1965, cloud physicists have gradually returned to the study of basic problems, seeking a deeper understanding of cloud processes, not only the microphysics but the dynamics and thermodynamics of clouds and the role played by them in the radiative budget of atmosphere. They have learnt not to jump fences before they come to them, but to proceed in the classical order of scientific progress : understanding - prediction - modification. Much effort has been devoted to the refinement of observational techniques, and the data acquired are the subject of close physical reasoning backed up by numerical modelling.

Thus, in 1980, one may say without fear of contradiction that Cloud Physics has been established on a sound experimental and theoretical basis, even though much still remains to be done to restore a proper balance between studies of the dynamical, thermodynamical, radiative and microphysical aspects of the subject. However, the basis for the scientific application of cloud physics now exists.

Chief among the possible applications is still weather modification, for which the need and the demand are steadily increasing. But there are many others : clouds interfere, in one way or another, with most terrestrial communication systems ; they play a key role in climate, through their influence on atmospheric thermodynamics and radiation ; and this is true not only of natural clouds, but of those produced by human activities such as the release of heat and water vapour to the atmosphere by large power stations.

This evolution of Cloud Physics has been marked, in the course of the past 25 years, by seven international cloud physics conferences. This, at Clermont-Ferrand, is the eighth.

The first International Conference on Cloud Physics was held in Zürich, Switzerland, in 1954, on the initiative of Raymund Sänger, who had launched one of the first scientific experiments on hail and who was a leader of research on phase changes in water. It was this Conference which confirmed the emergence of Cloud Physics as a scientific discipline.

The second Cloud Physics Conference took place in Verona, Italy, in 1959 under the chairmanship of Ottavio Vittori. Here, for the first time, the hail problem took pride of place, and the discussions on this subject revealed to some workers the need for a return to basic research before attempting to apply a science which was still in its infancy.

The third Cloud Physics Conference was organized in 1961, in Canberra and Sydney, by the strong Australian research group led by Eugene "Taffy" Bowen. Here, the limelight focussed on freezing nuclei and rainmaking, subjects to which the Australians had devoted considerable scientific effort. None of those present at this Conference will have forgotten the epic battle over the question of the meteoric origin of freezing nuclei !

The fourth Conference was held in Tokyo in 1964, under the wing of the Japanese group headed by Kenji Isono and Choji Magono, which had devoted many years of research to the study of ice crystals and their formation.

The fifth Cloud Physics Conference was the first to be held on American soil. It was organized by Roland List and Walter Hitschfeld, and revealed the rapid development of the subject in North America. Here again, despite good progress in observational techniques, it became clear that no useful results could be expected from the premature application of incomplete knowledge, and in the lack of the understanding which could only come from the systematic study of the basic physical problems.

Thus it was that at the sixth Conference, organized in London by B.J. Mason, weather modification was scarcely mentioned, all the emphasis being given to fundamental research.

The prospects or hopes of weather modification nevertheless remained in the background as a potential application whose immense practical importance could not be neglected. This led the Cloud Physics Commission of IAMAP and the World Meteorological Organization to arrange for the seventh Cloud Physics Conference, held in Boulder (Colorado) in 1971 under the chairmanship of Helmut Weickmann, to be followed immediately by the second WMO Scientific Conference on Weather Modification, presided over by Roland List. The Boulder Cloud Physics Conference revealed considerable progress in two fields : observational techniques, and the mathematical modelling of cloud processes.

The present Conference follows the one established in Boulder : it will be followed by the third WMO Scientific Conference on Weather Modification.

This Clermont-Ferrand Conference will differ slightly from its predecessors in placing greater emphasis on cloud dynamics and thermodynamics, on the interaction between dynamical, thermodynamical, radiative and microphysical processes in clouds, and on the interaction between processes taking place on different scales, from the aerological to the synoptic. Furthermore, under each theme, and therefore at each session, experimentalists and modellers will be brought together in the hope of bridging the gap which too often exists between experiment and theory.

In response to the first two circulars announcing the Conference, an impressive number (251) of draft papers have been submitted. This shows how vigorous is the subject, but it also poses a formidable problem of organization. It has therefore been decided, on the advice of the International Programme Committee :

- to publish all the abstracts received, in the "Journal de Recherches Atmosphériques" (Vol. 13, No. 4, 1979), in the form of a special reprint which will thus give a broad picture of the state of the subject in 1980.

- to organize 14 conference sessions, each beginning with 6-8 short oral presentations, followed by a round-table discussion with two question-masters, during which attention will be concentrated on the outstanding problems in each particular field and on important new results ;

- to organize three "poster sessions" (microphysics, dynamics and thermodynamics, and instrumentation) for papers not presented orally. Each poster session will include a period for the study of the posters and a period for their discussion.

- not to discuss certain subjects, despite their intrinsic interest, on the grounds that they have been dealt with in other recent conferences, or will be dealt with at forthcoming conferences (e.g., the Manchester Conference on Atmospheric Electricity, August 1980 ; or the Hamburg Conference on Nucleation, August 1981).

The following pages contain the texts of all the papers accepted either for oral presentation, or for poster sessions, or for retention in reserve. They are grouped by subject matter under the headings of the 14 conference sessions ; within each group, they appear in the alphabetical order of the author's names.

My feeling, which is shared by the International Programme Committee, is that this mode of organization of the Conference is still far from being perfect ; however, it has the merit of providing ample time for discussion, of allowing each participant to learn of progress in fields bordering on his own, and, we hope, of bringing out more clearly the important problems to which future research in cloud physics may be directed.

It only remains to me to express, with pleasure and gratitude, my deep appreciation to all those, persons and organizations, who took part in this Conference and especially to those whose names appear on the opening pages of this volume and without whose devoted efforts this Conference could never have been held.

R.G. SOULAGE

Chairman of the VIIIth International Conference on Cloud Physics.

TABLE DES MATIERES

TABLE OF CONTENTS

* Manuscript appears in the back of the book.
** See erratum in the back of the book.

*Manuscript appears in the back of the book.

*Manuscript appears in the back of the book.

*Manuscript appears in the back of the book.

VOLUME 1

SESSION I : NOYAUX ATMOSPHERIQUES
ATMOSPHERIC NUCLEI

SESSION II : PROCESSUS MICROPHYSIQUES
MICROPHYSICAL PROCESSES

SESSION I - NOYAUX ATMOSPHERIQUES

Atmospheric Nuclei

I.1 - Noyaux de Condensation

Condensation Nuclei

LA LOI CARACTERISTIQUE DES NOYAUX DE CONDENSATION NUAGEUSE ET SON EVOLUTION EN MILIEU INTERTROPICAL HUMIDE

F. Désalmand et J. Baudet
Département de Physique Générale, Abidjan, COTE D'IVOIRE

R. Serpolay
I.O.P.G. du Puy de Dôme, LAMP, Clermont-Fd, FRANCE

I - INTRODUCTION

La région d'Abidjan (Côte d'Ivoire) jouit, en zone intertropicale humide, d'une situation remarquable non seulement à cause d'une pollution anthropogène encore faible, mais surtout en raison de l'abondance des poussières continentales - en relation avec l'arrivée du Front Intertropical (F.I.T.) - et de la richesse de la végétation qui croit et se décompose en toute saison pour participer à la constitution de l'aérosol naturel, ainsi que de récents travaux l'ont montré (1) (2).

Profitant de ces conditions privilégiées, nous nous sommes proposés :
1°/ de montrer que les spectres des noyaux de condensation nuageuse (n.c.n.) établis en fonction de la sursaturation satisfont bien à une relation puissance ;
2°/ de suivre l'évolution quotidienne et saisonnière de cette loi caractéristique ;
3°/ d'interpréter les résultats obtenus en tenant compte des deux principales sources d'aérosol : la source continentale et la source végétale.

2 - METHODE DE MESURE DES n.c.n. ET LOI CARACTERISTIQUE

Le dispositif utilisé pour déterminer la concentration d'un échantillon d'air en n.c.n. est la chambre à diffusion thermique à plaques parallèles et horizontales du modèle décrit par TWOMEY (4). La plaque supérieure est chauffée, tandis que la plaque inférieure reste à la température ambiante. On photographie les gouttelettes contenues dans un volume de 0,027 cm3 éclairé par un faisceau laser.

Les mesures sont effectuées à proximité de la ville d'Abidjan, en un lieu non situé sous le vent de la cité.

Les spectres de n.c.n. sont réalisés pour les 5 valeurs suivantes de la sursaturation S : 0,15%, 0,25%, 0,50%, 0,75% et 1,0%.

Pour chaque valeur de S, on effectue successivement 4 déterminations de la concentration à partir de 4 échantillons d'air. C'est la moyenne arithmétique de ces 4 déterminations qui est donnée à N dans la relation :

$$[1] \qquad N = C\,S^{k}$$

qui relie S et N et où C et k sont des paramètres différant pour chaque spectre.

On a ainsi réalisé 20 spectres à différentes dates entre janvier et juin 1978 et on a montré, à partir des résultats obtenus, que la loi de la relation [1] leur était applicable avec un rapport de corrélation r voisin de l'unité.

A Abidjan, dans le domaine des sursaturations étudié, la population des n.c.n. suit donc bien la relation puissance : c'est leur loi caractéristique.

Il est évident que C mesure la concentration des n.c.n. activés à la sursaturation S = 1,0% et que k varie dans le même sens que le rapport de la concentration des noyaux les moins actifs - qui sont en général les plus petits - à celle des noyaux les plus actifs - qui sont aussi les plus gros. On a, par exemple :

$$[2] \qquad k = \left[\log \frac{N_{0,50}}{N_{0,25}}\right] \Big/ \log 2$$

où $N_{0,50}$ = concentration des n.c.n. activés à S = 0,50%
$N_{0,25}$ = concentration des n.c.n. activés à S = 0,25%

Mais on a sussi :

$$[3] \qquad C = (N_{0,50})^2 \,/\, N_{0,25}$$

3 - ETUDE EXPERIMENTALE DES VARIATIONS DE N, C et k

Au cours de 11 journées réparties le long de l'année entre décembre et juin et à chaque heure de la journée, les valeurs de $N_{0,50}$ et $N_{0,25}$ ont été déterminées expérimentalement de la manière ci-dessus indiquée. On en a déduit, par le calcul (relation [2]), les valeurs de k et on s'est servi de l'ensemble de ces données pour construire le tableau I.

Si l'on remplace la valeur du paramètre X (= $N_{0,50}$, $N_{0,25}$, C, k) par sa valeur $\overline{X}$ moyennée sur l'ensemble de la journée, on constate que

DATE	$N_{0,50}$max	$N_{0,50}$min	k max	k min	$\frac{N_{0,50}\text{max}}{N_{0,50}\text{min}}$	$\frac{\text{k max}}{\text{k min}}$
2 au 03.06.77	2400 8h	150 3h	3,71 1h	0,45 0 & 5h	16,0	8,2
11 au 12.06.77	2890 19h	260 5h	2,54 18h	0,22 5h	11,1	11,5
28.12.77	3590 19h	1150 24h	1,44 4h	0,45 2h	3,1	3,2
01.01.78	3370 0h	1110 10h	1,28 18h	0,32 0h	3,0	4,0
03.01.78	2780 21h	960 16h30	1,62 8h	0,60 7h	2,9	2,7
15.01.78	2810 8h	590 4h	1,73 13h	0,42 4h	4,7	4,1
26.01.78	3920 20h30	1220 13 & 16h	1,47 18h	0,65 16h	3,2	2,2
14.02.78	4070 19h	520 14h	1,95 17h	0,80 14h	7,8	2,4
15.04.78	4140 8h	330 12h	2,03 16h	0,85 5h	12,5	2,3
07.05.78	1480 9 & 10h	260 0,2 & 12	2,42 18h30	0,70 16h30	5,7	3,4
15.05.78	2780 9h	440 20h	2,33 21h	0,42 20h	6,3	5,5

TABLEAU I - VALEURS EXTREMES DES CONCENTRATIONS Nmax et Nmin DES NOYAUX ACTIFS A LA SURSATURATION S = 0,50% ET VALEURS EXTREMES DU PARAMETRE k DECOULANT DES SPECTRES HORAIRES ETABLIS A PARTIR DE 11 JOURNEES DE MESURE. L'HEURE OU L'EXTREMUM A ETE TROUVE EST INDIQUEE SOUS LE RESULTAT DE LA MESURE

la loi caractéristique [1] ainsi que les relations [2] et [3] sont encore applicables.

Dans le tableau II, un mois est représenté par une ligne sur laquelle figurent les valeurs $\bar{N}_{0,25}$, ..., $1/\bar{k}$ ainsi que la valeur H (en mètres) de la hauteur mensuelle de pluie. Lorsque, dans ce mois, les mesures horaires ont été effectuées sur plusieurs journées, on a pris pour $\bar{X}$ la moyenne arithmétique des valeurs moyennées relatives à chaque journée.

MOIS	$\bar{N}_{0,25}$	$\bar{N}_{0,50}$	$\bar{C}$	$\bar{k}$	$\frac{1}{k}$	H(m)
juin 1977	365	890	2 200	1,30	0,77	0,339
décembre 1977	1 130	2 040	3 680	0,85	1,18	0,047
janvier 1978	855	1 670	3 290	0,98	1,02	0,0075
février 1978	590	1 410	3 390	1,27	0,79	0,099
mars 1978						0,150
avril 1978	470	1 220	3 200	1,39	0,72	0,278
mai 1978	400	1 030	2 685	1,42	0,70	0,548

TABLEAU II - MOYENNES DES DIFFERENTES VARIABLES ETABLIES A PARTIR DES 11 JOURNEES DE MESURE ET ORDONNEES SELON LE MOIS CORRESPONDANT A CES JOURNEES

Il est ainsi aisé de constater que les paramètres $\bar{N}_{0,25}$, ... $1/\bar{k}$ affectent une variation saisonnière se manifestant par une décroissance régulière de décembre à juin - c'est-à-dire de la saison sèche (mi-décembre à avril) à la saison des pluies (mai à mi-juillet) - alors que H varie en sens inverse. La concentration $N_{0,25}$ en "gros noyaux" et $1/\bar{k}$ peuvent de plus être corrélés par la relation : $N_{0,25} = -670 + 1510(\frac{1}{\bar{k}})$ avec un coefficient de corrélation linéaire r = 0,97.

Le tableau III, déduit du tableau II, présente les valeurs des rapports $\bar{X}$max/$\bar{X}$min. En comparant les valeurs des cases 2 et 4 à celles des rapports correspondant qui figurent dans les deux dernières colonnes du tableau I, on constate que les variations saisonnières de la concentration $\bar{N}_{0,50}$ et du paramètre $\bar{k}$ sont inférieurs aux variations diurnes de $N_{0,50}$ et k.

$\frac{\bar{N}_{0,25}\ \text{max}}{\bar{N}_{0,25}\ \text{min}} = 3,1$	$\frac{\bar{N}_{0,50}\text{max}}{\bar{N}_{0,50}\text{min}} = 2,3$	$\frac{\bar{C}\ \text{max}}{\bar{C}\ \text{min}} = 1,7$	$\frac{\bar{k}\ \text{max}}{\bar{k}\ \text{min}} = 1,7$

TABLEAU III

On constate également que les variations saisonnières de la concentration des noyaux actifs à sursaturation S s'atténuent quand S augmente. Ce fait est mis en évidence par la courbe de variation, en fonction de S, du rapport Nmax/Nmin tiré du tableau II (fig. 1, trait plein). Par extrapolation (partie en tiretés), il semble que ce rapport tende vers 1 aux environs de S = 2,0%, valeur pour laquelle la moyenne journalière $\bar{N}$ serait alors indépendante de la saison.

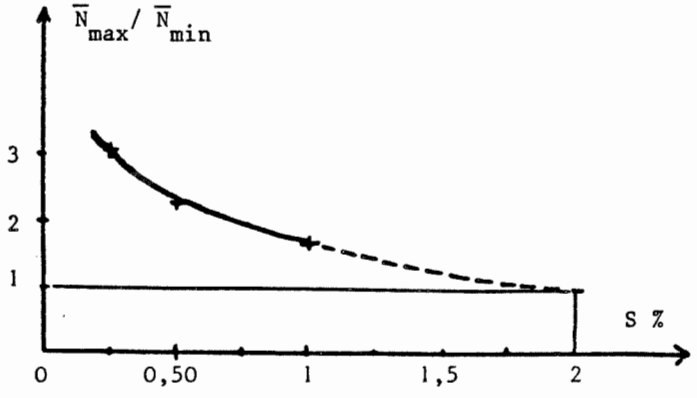

FIGURE 1 - VARIATION, EN FONCTION DE S, DU RAPPORT DES VALEURS EXTREMALES DES MOYENNES DES CONCENTRATIONS DES NOYAUX ACTIFS A LA SURSATURATIONS S

4 - COMPARAISON DES MESURES DE N AVEC CELLES EFFECTUEES EN D'AUTRES LIEUX

Pour l'ensemble des mesures réalisées à Abidjan, les valeurs de N varient entre 40 et 8700 noyaux/cm3, tandis que les valeurs de k oscillent entre 0,3 et 3,7.

Les concentrations maximales sont anormalement élevées et les concentrations habituelles sont comparables à celles des régions industrielles d'Europe ou d'Amérique (3). Or, dans notre cas, la pollution anthropogénique est faible.

D'après TWOMEY et WOJCIECHOWSKI (5), l'air maritime présente des valeurs de C et k à peu près constantes et faibles (C ≃ 100noyaux/cm3) sur l'ensemble des océans. On voit, par conséquent, que nos mesures ne traduisent pas une influence maritime sur la région d'Abidjan. Il reste donc à examiner l'intervention d'autres sources de production des n.c.n.

5 - PROFIL DES VARIATIONS DIURNES ET INTERPRETATION

La figure 2 présente le graphique de variation diurne des concentrations mesurées les 2 et 3 juin 1977, au cours de l'une des onze périodes de 24 heures précitées.

Il est clair que nous sommes en présence d'une distribution bimodale typique avec des valeurs maximales de N vers 8-9 h et 18-19 h et minimales vers 4-5 h et 13-14 h. Avec prudence et en attendant confirmation de résultats obtenus par le groupe de recherche sur les aérosols de l'Université d'Abidjan, on peut tenter l'analyse suivante de nos mesures :

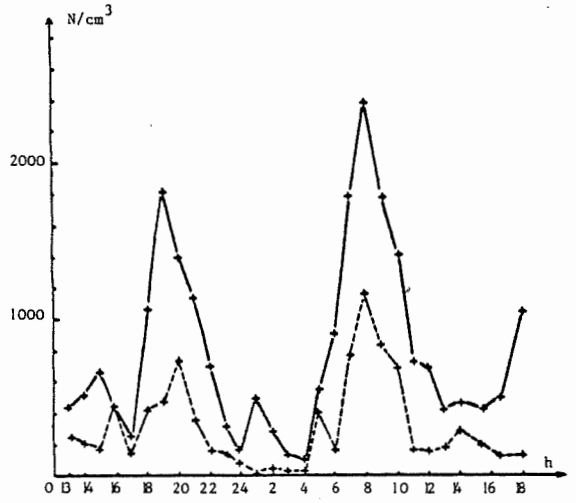

FIGURE 2 - VARIATIONS DES CONCENTRATIONS $N_{0,25}$ (en tiretets) ET $N_{0,50}$ (en trait plein) DES NOYAUX DE CONDENSATION NUAGEUSE ENTRE LE 2 JUIN 1977 A 13h ET LE 3 JUIN A 18h

5-1 Valeurs maximales de N et k après le lever du soleil

Différentes sources sont susceptibles de produire un grand nombre de petits noyaux (N et k élevés), à savoir : source terrigène locale, sources anthropogéniques et source végétale. Cette dernière mérite une explication. En effet, la grande stabilité qui s'est établie au-dessus de la forêt à la faveur de la nuit est détruite vers 8-9 h et l'aérosol forestier commence à se disperser dans l'atmosphère. Il est riche en petites particules de potassium (1). Par ailleurs, des réactions photochimiques se développent à partir des produits de décomposition bactérienne de la lagune et de la forêt (oxydation en sulfites et sulfates des gaz sulfureux et des mercaptans) et donnent lieu à la formation de petits noyaux (2). La station de mesure étant située à proximité des arbres et sous le vent de la lagune, il y a lieu de penser que la production de noyaux d'origine végétale est importante devant les deux autres sources ainsi qu'il peut en découler d'une critique plus approfondie de l'intervention de ces dernières.

5-2 Occurrence des autres valeurs extrêmales de N et k

. Vers 13-14h, l'activité thermoconvective passe par un maximum : la couche de surface est dilatée ou disparaît et les valeurs de N passent par un minimum, tandis que, par coagulation, les petits noyaux peuvent en former de plus gros (k minimal).

. En fin de nuit, la stabilité des basses couches atmosphériques est à son maximum et favorise la sédimentation des noyaux, rendant N minimal. Cette évolution est accentuée par les pluies (110/cm3 le 3 juin à 4h) ; mais lorsque le FIT se trouve au niveau d'Abidjan, les valeurs de N peuvent rester élevées dans l'air chargé de poussières continentales et de particules provenant de feux de brousse (1700/cm3 le 28.12.77 à 4h).

. Au contraire, en fin d'après-midi, l'affaissement de la couche de surface entraîne une augmentation des valeurs de N.

5-3 En conclusion, la production végétale consécutive au lever du soleil et les mouvements de l'atmosphère liés aux échanges thermiques paraissent responsables des variations journalières de N et k. L'amplitude de ces variations est plus grande en saison des pluies qu'en saison sèche ainsi qu'un examen attentif des deux dernières colonnes du tableau 1 nous le montre.

6 - VARIATIONS SAISONNIERES ET INTERPRETATION

Le tableau II indique que la richesse relative de l'aérosol en petits noyaux augmente en même temps que la hauteur de pluie. Ce résultat peut être interprété en considérant que la pluie a, sur les concentrations en n.c.n., des effets concourant à accroître k en activant la production des petits noyaux selon les processus indiqués en 5-1.

De plus, par intervention du processus naturel de condensation, les noyaux les plus actifs, qui sont généralement les plus gros, ont tendance à s'éliminer plus rapidement de l'atmosphère. Ce sont aussi les noyaux les plus gros qui sont captés par les gouttes de pluie dans leur chute. On peut, par conséquent, proposer le schéma suivant pour expliquer les variations saisonnières des n.c.n. :

En toute saison, l'aérosol végétal produit des noyaux dont certains sont actifs à S < 1%, plus précisément vers 8-9h et davantage en sai-

son des pluies.

En décembre, la source continentales apporte de grandes quantités de gros noyaux (le 28. 12.77, $\bar{C}$ = 3680 noyaux/cm3 et $\bar{k}$ = 0,85).

Dès février, les orages amorcent le lessivage de l'atmosphère : il y a élimination des plus gros noyaux, qu'ils soient d'origine continentale ou végétale.

La production par la végétation de particules plus petites consécutivement aux pluies est telle qu'elle compense largement l'effet de lessivage pour l'ensemble des noyaux actifs à S = 2,0%.

7 - CONCLUSION GENERALE

Les mesures horaires au cours des 11 journées considérées dans le tableau I ont mis en évidence les variations diurnes et saisonnières des paramètres C et k de la loi caractéristique des n.c.n. Par ailleurs, la richesse de l'aérosol naturel en milieu équatorial a été confirmée. Pour expliquer les valeurs élevées des concentrations, nous avons éliminé la source océanique et retenu la source continentale et la source végétale.

Par sa variation journalière et saisonnière, la source végétale apparaît particulièrement importante.

REFERENCES

(1) G. CROZAT, 1978, *L'aérosol atmosphérique en milieu naturel. Etude des différentes sources de potassium en Afrique de l'Ouest (côte d'Ivoire)*, thèse, Université Paul Sabatier de Toulouse

(2) R. DELMAS, J. BAUDET et J. SERVANT, 1978, *Mise en évidence des sources naturelles de sulfate en milieu tropical humide*, Tellus, 30, pp. 158-168

(3) W.C. KOCMOND, 1965, *Investigation of warm fog properties and fog modification concepts* Cornell Aeronautical Laboratory, rept. n° RM-1788-P 9, pp. 36-47

(4) S. TWOMEY, 1963, *Measurements of natural cloud nuclei*, J. Rech. Atmos., 1, pp. 101-105

(5) S. TWOMEY and J.A. WOJCIECHOWSKI 1969, *Observations of the geographical variations of cloud nuclei*, J. Atmos. Sci., 26, pp. 684-688

REMERCIEMENTS

Au cours de ce travail, nous avons utilisé une chambre à diffusion thermique prêtée par le Graduate Center for C. P. Research (Laboratoire du Prof. J.L. KASSNER) de l'Université de Missouri-Rolla. Cette recherche a aussi bénéficié d'un financement octroyé au titre du Fond d'Aide à la Coopération.

A PRELIMINARY STUDY OF CLOUD CHEMISTRY

Dean A. Hegg, Peter V. Hobbs and Lawrence F. Radke

Atmospheric Sciences Department, University of Washington
Seattle, Washington, 98195 USA

1. INTRODUCTION

Progress in several areas of atmospheric science (e.g. planetary albedo; global sulfur cycle; gas-to-particle conversion; acid rain) is being retarded by a lack of understanding of the chemical processes that occur in clouds and of the interactions of clouds with the atmospheric aerosol. In this paper we present some preliminary measurements on the ionic composition of cloud water and we examine the related question of particle production in clouds.

2. INSTRUMENTATION AND ANALYSIS TECHNIQUES

All of the data presented were taken aboard the University of Washington's B-23 research aircraft which is well equipped for cloud chemistry and aerosol studies (Hobbs et al., 1979; Hegg and Hobbs, 1980).

Cloud water samples were analyzed for pH and total dissolved sulfur. Selected samples were also analyzed for sulfate and nitrate content.

Four different techniques were used to detect sulfate production in the clouds. Changes in CCN activation spectra downwind of clouds can be attributed to sulfate production, as discussed quantitatively by Easter and Hobbs (1974). Changes in total particle volume due to cloud passage can also provide information on sulfate production. Measurements of sulfate concentration by filter sampling upwind and downwind of clouds can provide direct evidence of sulfate production in clouds. Finally, sulfate production can be detected by measuring the cloud water sulfate concentrations at the leading and trailing edges of wave clouds--the trailing edge concentration being higher if sulfate production has occurred.

3. RESULTS AND DISCUSSION

(a) *Cloud water composition*

The bulk cloud water pH values ranged from 3.7 to 6.5 with a mean of 4.8 ± 0.9 (Table 1). The cloud water sulfur concentrations (expressed as sulfate concentrations) ranged from 2.5 to 19.7 mg ℓ^{-1} with a mean of 10.3 ± 5.3 m ℓ^{-1} (Table 1). The data in Table 1 do not show the strong negative correlation between pH and sulfate concentration found in some rainwater samples (Likens, et al., 1977). Also, the data in Table 1 are not entirely in agreement with Petrenchuk and Drozdova's (1966) hypothesis that the higher concentrations of ions found in water from stratus and stratocumulus clouds compared to water from nimbostratus cloud are due to the larger droplet sizes in the rain clouds and consequent greater dilution of ionic species. Our simultaneous measurements of cloud water sulfur and mean cloud droplet radius show the correlation coefficient between these parameters to be a modest 0.56 (significant at the 95% level). Clearly, other factors must be taken into account to explain the sources of variation in cloud water sulfate concentrations.

To explore the extent to which the sulfur in cloud water is in the form of sulfate, a limited number of cloud water samples were analyzed for $SO_4^=$ and NO_3^- (Table 2). The results suggest that not all of the sulfur is sulfate. This should be kept in mind when comparing total sulfur with sulfate concentrations. The nitrate concentrations shown in Table 2 are somewhat lower than those reported for rainwater (Dawson, 1978; March, 1978), which may indicate the importance of below-cloud scavenging.

Our data also provide insights into the extent to which nucleation scavenging alone can explain the sulfate concentrations observed in cloud water. It can be seen from Table 3 that in two out of four cases the sulfate concentrations measured directly in the ambient air were lower than those derived from measurements of amount of sulfate in cloud water. This suggests that, on occasions, processes other than nucleation scavenging are responsible for the sulfate in cloud water. In the two cases for which the cloud-water-derived sulfate was higher than the ambient, the clouds were relatively low altitude, long-lived stratiform. Petrenchuk and Drozdova also found relatively high sulfate levels in such clouds.

(b) *Gas-to-particle conversion in clouds*

We have found evidence of gas-to-particle conversion in about one-third of the clouds we have studied. We describe below just three case studies.

On May 3, 1979, data were gathered in wave clouds over Mt. Rainier, Washington. Cloud condensation nucleus (CCN) spectra taken upwind and downwind of one of these clouds are shown in Fig. 1. The results suggest production of some soluble CCN component. Particle size spectra measurements upwind and downwind of

Table 1: Summary of Bulk Cloud Water pH and Sulfur Measurements

	Location	Cloud type	Mean cloud droplet radius (μm)	pH	Mass concentration of sulfuric cloud water (expressed as $SO_4^=$)(mg/liter)
April 24, 1979	18 km north of Mt. Rainier, Wa.	Wave	5.4	4.4	7.3
"	"	"	6.1	4.4	5.5
April 27, 1979	Washington Cascades	"	10.0	4.2	13.2
April 30, 1979	54 km south of Tacoma, Wa.	Stratus	243	3.7	17.8
"	"	"	105	3.9	12.0
"	"	"	16	3.9	16.0
"	"	"	—	3.8	17.9
May 3, 1979	Over Mt. Rainier, Wa.	Wave	3.1	4.8	9.4
"	"	"	—	4.6	5.8
May 10, 1979	Over Orcas Is., Wa.	"	—	6.2	15.7
"	"	"	—	6.5	14.7
May 15, 1979	9 km northwest of Olympia, Wa.	"	34	5.9	6.3
"	"	"	—	6.0	2.5
"	"	"	—	5.9	4.8
"	"	"	—	5.9	10.0
July 12, 1979	Washington Cascades	Stratus	—	4.1	19.7
"	"	"	—	4.8	14.9
"	"	"	12	5.6	10.9
"	"	"	20	5.2	13.0
July 13, 1979	Over Mt. Rainier, Wa.	Wave	3.7	4.3	4.4
"	"	"	3.6	4.5	3.0
August 3, 1979	West of Cascades, just south of Seattle	Stratus	32	3.9	6.4
"	"	"	32	3.9	4.8

Table 2: Comparison of Cloud Water Species Concentrations Derived from Ion Exchange Chromatography (IEC) with those Derived from Flash Vaporization (FV). Samples Taken in Stratus Clouds over the Washington Cascades on July 12, 1979.

Sample No.	IEC[NO_3^-] (mg ℓ^{-1})	IEC[$SO_4^=$] (mg ℓ^{-1})	FV[$SO_4^=$]* (mg ℓ^{-1})
3	2.5 (±10%)	7.3 (±10%)	10.9 (±25%)
4A	0.75 (±10%)	2.9 (±10%)	5.6 (±25%)
4B	0.53 (±10%)	1.8 (±10%)	3.1 (±25%)
6	0.28 (±10%)	0.67 (±10%)	1.1 (±25%)

* Total sulfur expressed as [$SO_4^=$]

Table 3: Comparisons of Directly Measured Ambient Particulate Sulfate Concentrations with those Derived from Cloud Water Sulfate Measurements

Date	Directly measured [$SO_4^=$] (μg m^{-3})	[$SO_4^=$] derived from cloud water (μg m^{-3})
30 April 1979	1.02	6.20
3 May 1979	0.93	0.53
12 July 1979	0.97	30.7
13 July 1979	0.34	0.19

this cloud (Fig. 2) corroborated the particle production within the cloud. The particle production seems most pronounced at a particle diameter of ∿1 μm. This 1 μm "peak" is typical of cases in which enhanced CCN concentrations downwind of clouds are observed.

On May 10, 1979, measurements were obtained in a wave cloud over Orcas Island, Washington. The only evidence for sulfate production in this case were slightly elevated CCN concentrations downwind of the cloud (Fig. 3). Particle size spectra showed no discernible effects attributable to cloud passage (Fig. 4).

On July 13, 1979, particle size spectra, particulate sulfate, and cloud water sulfate data were obtained for a wave cloud situated over Mt. Rainier, Washington. The most direct and conclusive evidence of sulfate production was provided by the measurements of sulfate upwind and downwind of the cloud. The upwind sulfate concentration was below the detection limit (0 ± 0.40 μg m^{-3}) while the downwind concentration was 0.68 ± 0.46 μg m^{-3}. This yields a sulfate production of 0.68 μg m^{-3}. These measurements, together with a cloud transit time of 5.8 min and a rather high ambient SO_2 level of 4 ppb, yield an SO_2-to-$SO_4^=$ conversion rate of 104% hr^{-1}. Ambient sulfate concentrations derived from

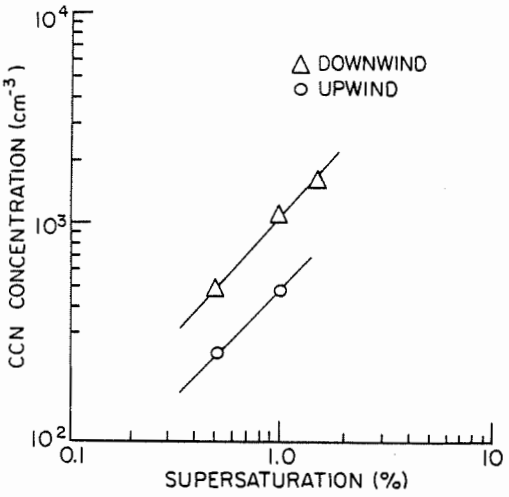

Fig. 1 Cloud condensation nucleus spectra measured upwind and downwind of a wave cloud on May 3, 1979.

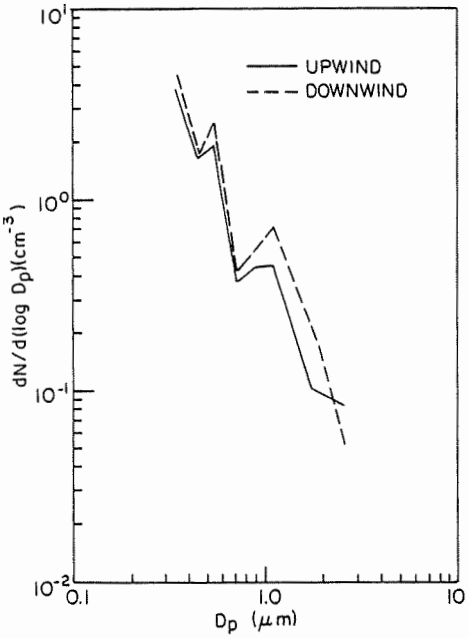

Fig. 2 Particle size spectra measured upwind and downwind of a wave cloud on May 3, 1979.

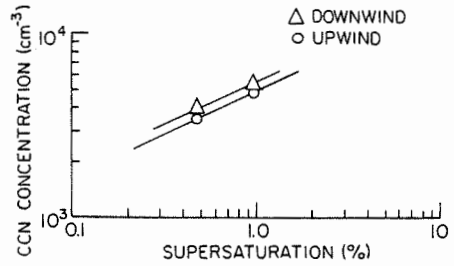

Fig. 3 CCN spectra measured upwind and downwind of a wave cloud on May 10, 1979.

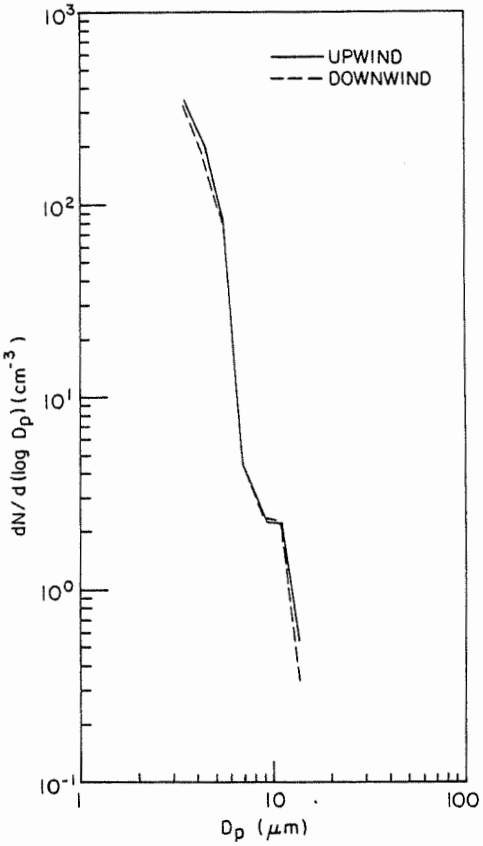

Fig. 4 Particle size spectra measured upwind and downwind of a wave cloud on May 3, 1979.

measurements of sulfate in cloud water samples were found to be 0.041 and 0.285 μg m^{-3} on the upwind and downwind edges of the clouds, respectively. Based on these measurements, the amount of sulfate produced in the cloud was ∿0.24 μg m^{-3}. While these concentrations do not differ significantly from those obtained from direct measurements in the ambient air upwind and downwind of the cloud, they yield a considerably lower oxidation rate of 37% hr^{-1}. The particle size spectra measurements taken upwind and downwind of the cloud (Fig. 5) show definite evidence of particle production in certain size ranges. Total particle volumes derived from the spectra of Fig. 5 are 3.5 ± 2.6 μm^3 cm^{-3} downwind and 3.1 + 1.7 μm^3 cm^{-3} upwind. If the excess volume is assumed to be $(NH_4)_2SO_4$, these measurements yield a sulfate production in the cloud of ∿0.52 ± 7.7 μg m^{-3}. Clearly, the total particle volume method is a very inaccurate technique for determining sulfate production in clouds. But the three estimates of sulfate production given above are not inconsistent.

Recent modeling work (Hegg and Hobbs, 1979) suggests that oxidation of SO_2 in solution by O_2 or O_3 can produce gas-to-particle conversion rates in clouds similar to those described above. An alternative mechanism is oxidation by H_2O_2 as proposed by Penkett et al. (1979).

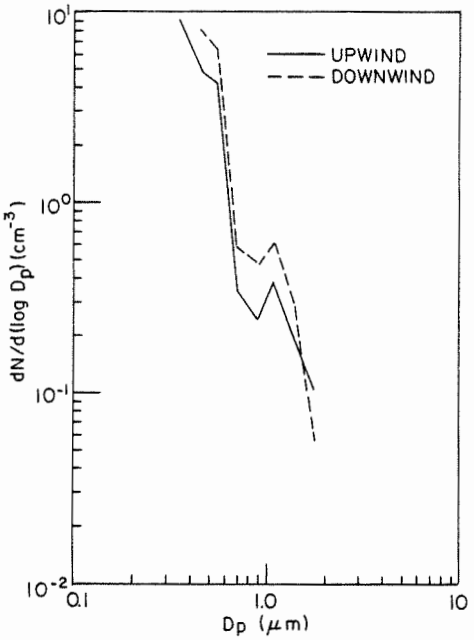

Fig. 5 Particle size spectra measured upwind and downwind of a wave cloud over Mt. Rainier on July 13, 1979.

4. SUMMARY AND CONCLUSIONS

Measurements have been presented on cloud water composition and gas-to-particle conversion in clouds. Sulfur levels in clouds correlate rather poorly with both cloud water pH and cloud droplet mean radius. The results suggest that not all cloud water sulfur is in the form of sulfate and that mechanisms other than nucleation scavenging must be invoked to explain cloud water sulfur levels. Evidence of gas-to-particle conversion has been found in roughly one-third of the clouds studied. The particles produced in clouds tend to "peak" in number concentration near particles of diameter 1 μm. Data from one case study yielded an SO_2-to-SO_4 conversion rate in the cloud of between 37 to 104% hr^{-1}.

Acknowledgments. Work supported by EPA Grant R80 52 63010.

REFERENCES

Dawson, G. A., 1978: Ionic composition of rain during sixteen convective showers. Atmos. Envir., 12, 1991-1999.

Easter, R. C. and P. V. Hobbs, 1974: The formation of sulfates and the enhancement of cloud condensation nuclei in clouds. J. Atmos. Sci., 31, 1584-1594.

Hegg, D. A. and P. V. Hobbs, 1979: The homogeneous oxidation of sulfur dioxide in cloud droplets. Atmos. Envir., 13, 981-987.

Hegg, D. A. and P. V. Hobbs, 1980: Measurements of gas-to-particle conversion in the plumes from five coal-fired electric power plants. Atmos. Envir., 14, 99-117.

Hobbs, P. V., D. A. Hegg, M. W. Eltgroth and L. F. Radke, 1979: Evolution of particles in the plumes of coal-fired power plants - I. Deductions from field measurements. Atmos. Envir., 12, 935-951

Likens, G. E., T. H. Bormann, R. S. Pierce, J. S. Eaton and N. M. Johnson, 1977: Biogeochemistry of a Forested Ecosystem. Springer-Verlag, New York.

Marsh, A. R. W., 1978: Sulphur and nitrogen contributions to the acidity of rain. Atmos. Envir., 12, 401-406.

Penkett, G. A., B. M. Jones, K. A. Brice and A. E. Eggleton, 1979: The importance of atmospheric ozone and hydrogen peroxide in oxidising sulphur dioxide in cloud and rainwater. Atmos. Envir., 13, 132-137.

Pentrenchuk, O. P. and V. M. Drozdova, 1966: On the chemical composition of cloud water. Tellus, 18, 280-286.

ON THE PROPERTIES OF THE CONDENSATION NUCLEI IN RURAL UTAH AND NEW-MEXICO.

Y. Mamane[1] and R.F. Pueschel

NOAA/ERL/APCL, Boulder, Colorado, U.S.A.
1. NRC Postdoctoral Associate, Affiliation : Technion, Haifa, ISRAEL.

1. INTRODUCTION . In this paper the properties of atmospheric particles in rural regions of the western United States, in which energy developments are taking place, are described. The locations east-central Utah and north-west New Mexico are the subject of two different research investigations: The Utah Visibility Study in which baseline values for horizontal visibilities are being established, and the Four Corners Power Plant Study whose purpose is to determine the effect of an isolated coal-fired power plant on the atmosphere (Mamane and Pueschel, 1979, and references therein).

2. EXPERIMENTAL. The data were mostly collected on board a light twin engine aircraft equipped to measure aerosol, gas and meteorological parameters. In Utah, surface measurements complement the airborne set of data. Detailed description is given in the above references.

Aerosol samples were also collected on 0.1 µm Nuclepore filters and on electron microcospe screens using a cascade impactor. The filters were later analysed in a scanning electron microscope (SEM) interfaced with an x-ray energy dispersive analyzer (XEDA) for the elemental content of individual particles down to 0.05 µm dia. (Pueschel. 1976); and the screens were chemically treated to detect individual sulfate (Mamane and de Pena, 1978) and nitrate particles (Mamane and Pueschel, 1980).

3. RESULTS AND DISCUSSION . In-situ measurements of the aerosol size spectra show that in both rural locations, the number size distribution is trimodal with modes around 0.01, 0.07 to 0.08 and 2 µm radius. The first mode was obtained with the Aitken Nuclei (AN) counter which was assumed to represent the 0.01 µm mode. Figure 1 shows the size distribution of particles collected within the boundary layer at about 2000 m MSL, and above it at 3800 to 4200 m MSL for both locations. The Utah and New Mexico samples were collected on May 18 and June 6, 1978, respectively. In the lower elevations the nucleation mode at 0.01 µm is significantly higher in east central Utah than in northwest New Mexico. However, the accumulation mode at 0.07 to 0.08 µm is lower in Utah.This may be in part caused by different aerosol sources in these regions.

According to Whitby (1978), in a typical trimodal size distribution when all particles are considered to be lumped at one mean size for each mode, the rate of change of the number concentration in the three modes can be described by the following equations:

Nucleation Mode:

$$\frac{dN_N}{dt} = Q_N - K_{NN}N_N^2 - K_{NA}N_N N_A - K_{NC}N_N N_C$$

Accumulation mode:

$$\frac{dN_A}{dt} = Q_A - K_{AA}N_A^2 - K_{AC}N_A N_C \qquad \text{where}$$

N is the average number concentration,
Q the average rate insertion of new particles,
K the coagulation constant.

The subscripts N,A,and C denotes nucleation, accumulation and coarse particle modes respectively.

For the background aerosols one may assume that dN/dt is equal to zero during midday, when meteorological conditions are uniform.

This also follows from figure 2, the normalized hourly AN counts for four different months in 1978 measured at the top of Cedar Mountain, which shows clearly that dN/dt is equal to zero during the morning and noon hours in July, during the noon hours only in May and October, and during the afternoon in January and February. Similar results have been obtained by Went(1964) and Lopez et al.(1976), both studying rural locations. Figure 2 clearly indicates that the production of AN in the different seasons is related to the ambient temperature and solar radiation, and therefore could be through photochemical processes.

Another important information could be obtained from the above equations when solved to determine the atmospheric residence time, $\tau = N/Q$. Thus the τ obtained in Utah and New Mexico is respectively 0.6 and 2 days for the nucleation mode, and 65 and 36 days for the accumulation mode. The shorter residence times of the nucleus mode suggest that the AN are formed locally, especially in Utah, and are not transported over long distances as in the case for the accumulation mode. Long residence times for the warm season in the western United States are to be expected since the removal processes when the precipitation is low and the mixing layer is deep are not efficient.

Table 1. Parameters used to calculate particle transfer rate into each mode.

Locale	Modal radii (µm)			Concentrations (cm^{-3})		
	R_N	R_A	R_C	N_N	N_A	N_C
Rural Utah	0.01	0.07	2.0	7800	140	0.8
Rural New Mexico	0.01	0.08	2.0	1000	260	0.8

Table 2. Summary of aerosol physical and chemical properties in background aerosol.

	Percentage	UTAH		NEW MEXICO	
		d < 0.5 μm	d > 0.5 μm	d < 0.5 μm	d > 0.5 μm
1.	Scanning electron microscopy and x-ray analysis				
	Spherical Particles	88	17	93	29
	Emitting Particles	33	100	67	86
	Emitting Particles containing only S.	65	17	78	17
	Non emitting spherical particles.	66	<1	29	25
2.	Nitrate and sulfate spot test technique.				
	Particles containing sulfate	70	<1	86	30
	Particles containing nitrates	<1	8	<1	11

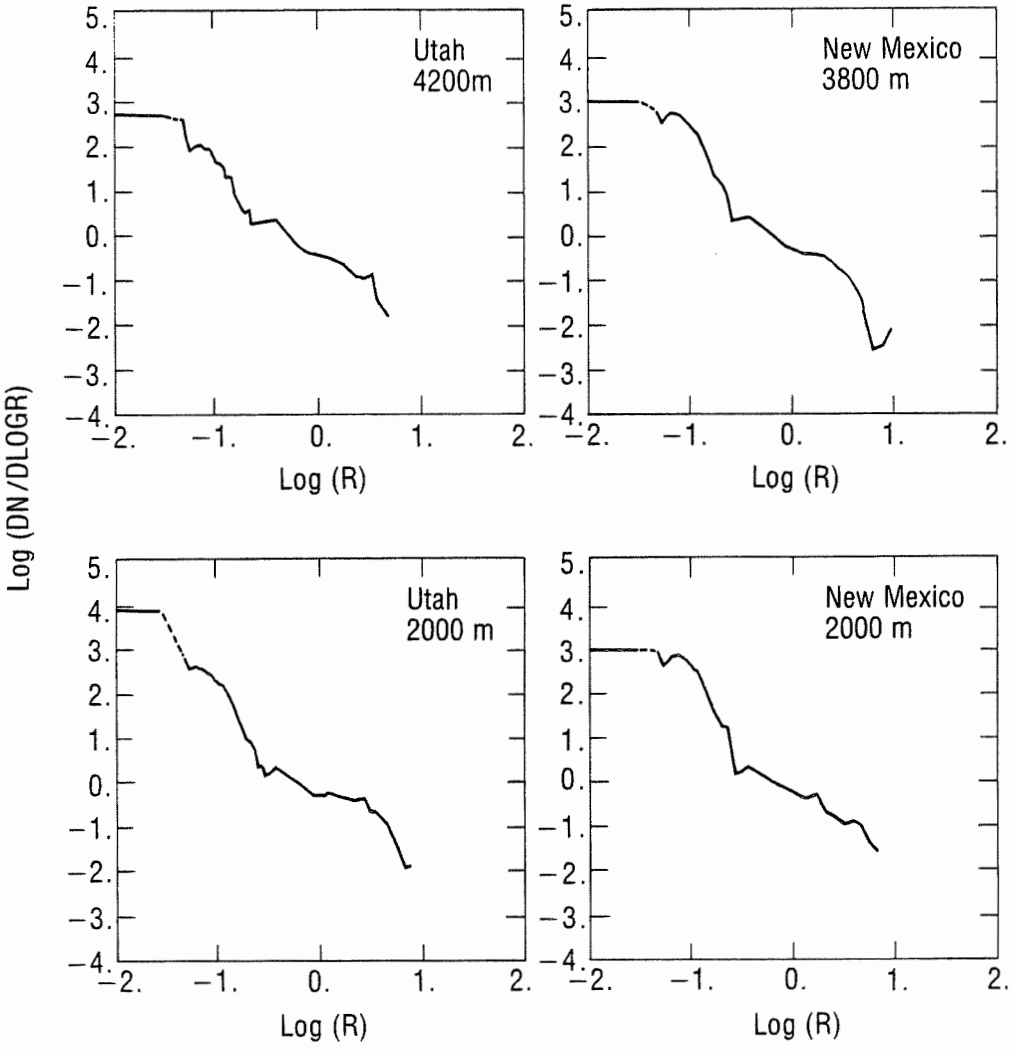

Figure 1. Size distribution of particles collected within the boundary layer at 2000 m MSL and above it at 3800 and 4200 m MSL. dN/dlogR is in cm^{-3} and R in μm.

Results of the application of the SEM-XEDA system and the spot test techniques for nitra- and sulfates to individual particlès are given in Table 2. The data were derived from individual particles and were grouped into two size ranges: smaller and larger than 0.5μm. In Utah, about two-thirds of the particles below 0.5μm areidentified as "non emitting particles", i.e. they are composed of elements lighter than sodium such as C,O,H,and N. Since nitrates (Table 2) and inorganic carbon were not found in these samples, we concluded that the Utah aerosol in this range was dominated by organic spheres probably formed by photochemical reaction of terpenes (Went,1964; Rasmussen and Went, 1965) and other organic vapors.

In Utah the"emitting particles", consist mainly of two groups: The sulfur type and the mineral type aerosol. In the former group particles emit only sulfur and are made up of S in combination with cations such as H^+ and NH_4^+ ions. The second group is composed of the Al, Si, Fe, Ca and Mg elements.

In New Mexico sulfur is found in about 50 percent of the particles of diameter below 0.5μm while the mineral type particles occupy less than 5 percent of the emitting particles. The major difference however is in the percentage of non-emitting particles: 66 in Utah versus, 29 in New Mexico - thus the organic particles in Utah dominate particle of this size range. This is probably due to the lack of forests in desert like northwest New-Mexico, and the presence of large power plants there.

The production of AN from a forest canopy as function of time can be expressed as (Lopez et al., 1976):

$$\frac{dN}{dt} = \frac{\phi_N}{h} - K_{NN} N_N^2(t), \quad \text{where}$$

$N_N(t)$ is the AN counts at time t.

ϕ_N is the nucleus flux

h is the height of the mixing layer, and

K_{NN} is the coagulation constant for AN.

In Utah where dN/dt is equal to zero during midday as is suggested from Fig. 2; h~1500 m, K~$2.4 \times 10^{-9} cm^3 . S^{-1}$, $N_N \sim 5100 cm^{-3}$;then the flux of AN is approximately $10^4 cm^{-2} S^{-1}$ a value which is close to estimates obtained by Lopez et al.(1976) in southwest France.

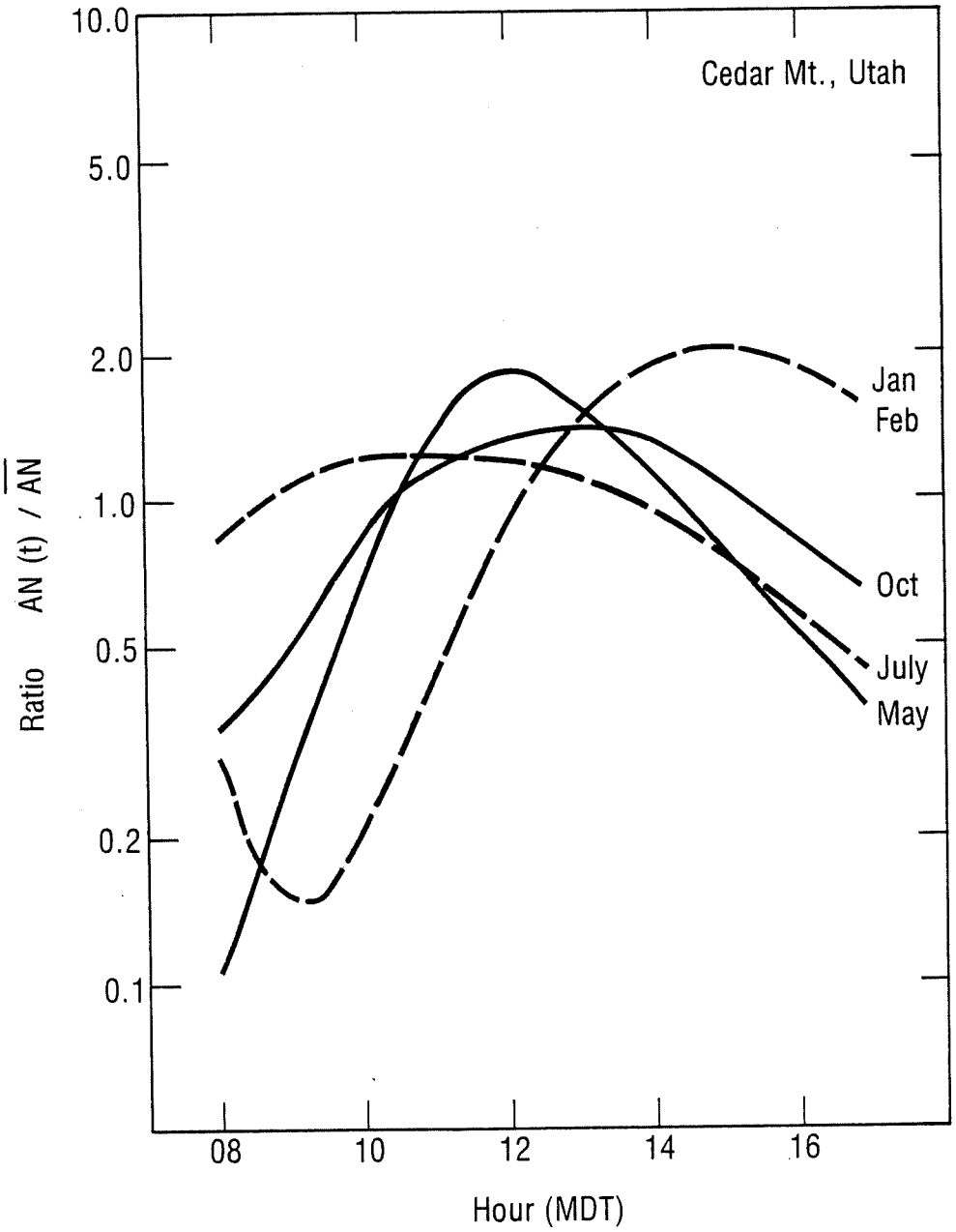

Figure 2. The diurnal variation of the normalized Aitken nuclei counts for different seasons of the year. Measurements were taken at the top of Cedar Mountain during 1978.

In Northwest New Mexico where AN (organic) is only 290 cm^{-3} (29% of 1000 cm^{-3}), and h is about 1700 m, the organic nuclei flux is over two orders of magnitude smaller than that of Utah.

4. CONCLUSIONS. The conclusions from this paper are that at present the aerosol in some parts of the western United States is still dominated by particles originating from natural sources. There are indications however, that the sulfur content of the aerosol in the vicinity of a power generating station is enhanced. This can lead to an increase in haziness at high relative humidities because of the hygroscopic nature of sulfate particles. Due to long residence times of the sulfur aerosol in the western United States, long range transport is a distinct possibility and effects are to be expected in the regional, eventually the mesoscale.

REFERENCES

Lopez, A., J. Fontan and J. Servant, 1976, "Mesoscale Determination of Aitken Nuclei Flux Near the Ground - Use of Radioactive Tracers (Radon and ^{212}Pb)." ERDA Symposium Series 38, pp. 171-191, ERDA Technical Information Center, Oak Ridge, Tennessee. (Available as CONF-740921 from NTIS).

Mamane, Y. and R.G. de Pena, 1978, "A Quantitative Method for the Detection of Individual Submicrometer Size Sulfate Particles." Atmos. Environ., 12, 69-82.

Mamane, Y. and R.F. Pueschel, 1979, "Oxidation of SO_2 on the Surface of Fly Ash Particles under Low Relative Humidity Conditions." Geophys. Res. Letters, 6, 109-112.

Mamane, Y. and R.F. Pueschel, 1980, "A Method for the Detection of Nitrate Particles." Accepted for publications in Atmos. Environ.

Pueschel, R.F., 1976, "Aerosol Formation During Coal Combustion: Condensation of Sulfates and Chlorides on Fly Ash." Geophys. Res. Letters, 3, 651-653.

Rasmussen, R. and F.W. Went, 1965, "Volatile Organic Matter of Plant Origin in the Atmosphere." Proc. National Academy of Sciences, 53, 215-220.

Went, F.W., 1964, "The Nature of Aitken Condensation Nuclei in the Atmosphere," Proc. National Academy of Sciences, 51, 1259-1267.

Whitby, K.T., 1978, " The Physical Characteristics of Sulfur Aerosols." Atmos. Environ., 12, 135-159.

ACKNOWLEDGMENTS

This research was supported in part by the U.S. EPA, BLM and the National Research Council which provided a postdoctoral associateship to Yaacov Mamane.

ON THE CAPABILITY OF ATMOSPHERIC SULFATE PARTICLES AS CCN

A. Ono and T. Ohtani

Water Research Institute, Nagoya University
Nagoya, JAPAN

1. Introduction

The most important particles in the atmosphere for their effects upon weather and climate are the cloud active particles serving as the nuclei for cloud droplet formation (CCN) and ice formation (IFN).

The cloud condensation nuclei (CCN) are hygroscopic compounds and a study of their sensitivity to heat has suggested that sulfate particles (sulfuric acid and/or its neutralization products with ammonia) formed in the atmosphere by gas-to-particle conversion are the most likely inorganic component of CCN (Twomey, 1971; Dinger et al., 1974).

However, the volatility measurements of atmospheric CCN, though useful, are indirect and may not provide a unique identification. More direct evidences are needed to prove the capability of atmospheric sulfate particles as CCN and their cloud physical importance.

Since atmospheric CCN occure as a minority fraction of a population of atmospheric particles exhibiting a great variety of size and composition, they cannot be separated without actually nucleating them as CCN at low, cloud-like supersaturations of 1% or less.

To study directly the capability of atmospheric sulfate particles as CCN, we carried out a series of experiments using a vertical flow-type thermal diffusion cloud chamber (Sinnarwalla et al., 1973) in conjunction with the application of $BaCl_2$ thin film technique for the detection of soluble sulfate in individual particles described by Bigg et al. (1974).

2 Experimental procedures

Figure 1 shows the schematic diagram of the experimental system used in the present studies.

Outside air was drawn into the cloud chamber operated at slight supersaturations less than 1% and then passed through a impactor collecting 2μm radius droplets with 50% collection efficiency to separate the active particles as CCN from the atmospheric particles. The active particles as CCN were expected to be removed from the air by the impactor as a result of small water droplets forming on them in the cloud chamber at slight supersaturations less than 1%, while the inactive particles emerging from the impactor were collected on EM grids by electrostatic precipitation. For comparison, particles in the original air were also collected simultaneously at the inlet of the cloud chamber on EM grids by electrostatic precipitation.

To measure the sulfate particle concentration, the sulfate test described by Bigg et al. (1974) was applied to a set of particles collected from the original air and that emerging from the cloud chamber-impactor system. The presence of soluble sulfate in individual particles is indicated by the growth of a characteristic $BaSO_4$ reaction product around the particle after exposed to alcoholic atmosphere. This method is specific to soluble sulfate with the detection limit of about 10^{-17}g.

3. Results

From the comparisons of a set of measurements of the sulfate particle concentration in the original air and that emerging from the cloud chamber-impactor system, it will be possible to see what proportion of atmospheric sulfate particles is activated as CCN at a given supersaturation.

Figure 2 shows the comparisons of a set of sulfate particle concentrations (3 hrs average) in the original air (left) and that emerging from the cloud chamber-impactor system operated at a slight supersaturation less than 1% (right). In the figure, similar comparisons using a average of the sulfate particle concentration obtained from two long-period samplings (July 10-12 and August 6-11, 1979) are also shown.

It can be seen that when the air was passed through the cloud chamber-impactor system operated at a slight supersaturation less than 1%, virtually almost all sulfate particles were disappeared.

The losses of sulfate particles could be due to the processes where sulfate particles in the original air were activated as CCN and removed from the air by the impactor as a result of small water droplets forming on them in the cloud chamber with long availabe growth time. However, some diffusional loss of particles in the experimental system are inevitable. Therefore, in order to make certain that the losses of sulfate particles is mainly due to the activation as CCN, we examined the losses of sulfate particles in the air emerging from the cloud chamber-impactor system operated at water saturation.

As shown in Fig. 3, when the air was passed through the cloud chamber-impactor system operated at water saturation, no significant losses of sulfate particles were observed.

These experimental results, considered together, suggest that observed losses of sulfate particles in the air emerging form the cloud chamber-impactor operated at a slight supersaturation less than 1% are due to the activation of sulfate particles as CCN and they are removed from the air as a result of small water droplets forming on them.

4. Conclusion

From our direct experimental evidences discussed above, we conclude that atmospheric sulfate particles with mass larger than 10^{-17}g are in fact served as very efficient CCN at low, cloud-like supersaturations of 1% or less.

Aknowledgements

This work forming part of "Special Research Project on Environmental Science" was supported financially by Ministry of Education, Culture and Science. The authors express their sincere appreciation to this agency for their support.

References

Bigg, E. K., A. Ono and J. Williams, (1974): Chemical tests for individual submicron aerosol particles. Atmospheric Environment 8, 1-13.

Dinger, J. E., H. B. Howell and T. A. Wojciechowski, (1970): On the sources and composition of cloud nuclei in a subsident air mass over the North Atlantic. J. Atmos. Sci., 27, 791-797.

Sinnarwalla, A. M. and D. J. Alofs, (1973): A cloud nucleus counter with long available growth time. J. Appl. Meteor., 12, 831-835.

Twomey, S., (1971): The composition of cloud nuclei. J. Atmos., Sci., 28, 377-381.

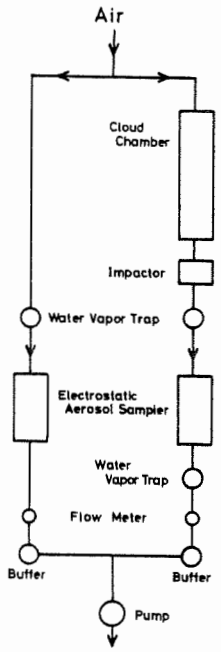

Fig.1. Schematic diagram of experimental system.

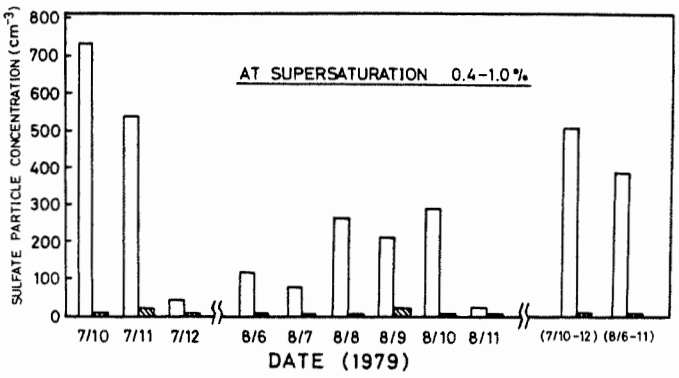

Fig.2. Comparisons of a set of sulfate particles concentrations(3 hrs average) in the original air (left) and that emerging from the cloud chamber-impactor system operated at slight supersaturations less than 1%(right). In the figure,similar comparisons using a average of the sulfate particle concentrations obtained from two long-period samplings(July10-12 and August 6-11,1979) are also shown.

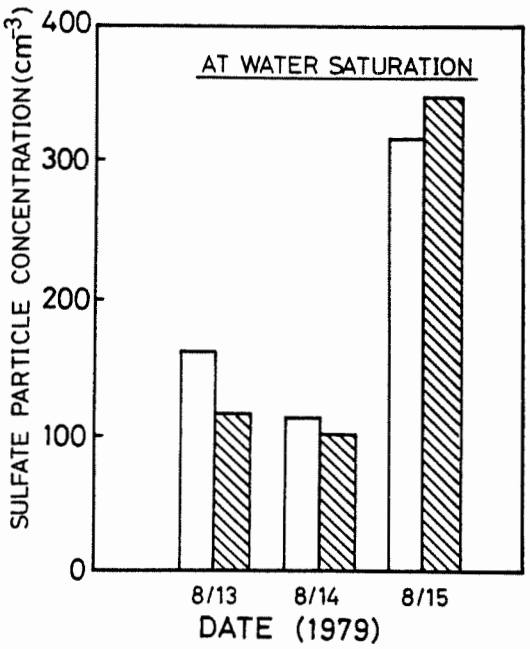

Fig.3. Comparisons of a set of sulfate particle concentrations (3 hrs average) in the original air(left) and that emerging from the cloud chamber-impactor system operated at water saturation(right).

THE INFLUENCE OF AEROSOL INHOMOGENEITY ON CLOUD FORMATION IN COASTAL REGION

Josef Podzimek

Graduate Center for Cloud Physics Research
University of Missouri-Rolla
Rolla, Missouri USA

1. INTRODUCTION

Coastal regions are a natural and unique laboratory for investigating the impact of atmospheric aerosol on the cloud evolution, propagation of optical signals and potential degradation of materials and soil. The interaction, space and time variability of marine and continental aerosol over coastal regions promises further to check some of the existing theories on aerosol size evolution at a specific meteorological situation.

Bearing in mind the aforementioned aspects of an aerosol study in a coastal region, a research program supported by the National Science Foundation was established in 1978. It included theoretical and laboratory work, ground and aircraft measurements in January 1979 on the seashore of South Padre Island and over the Gulf of Mexico and South Texas. This report summarizes the main findings stemming from aircraft sampling, which was performed in an instrumented Beechcraft Queen Air aircraft of the National Center for Atmospheric Research (NCAR), Boulder.

2. AIRCRAFT MEASUREMENT AND METEOROLOGICAL CONDITIONS

The main parameters measured in the two engine aircraft were the following: Aitken nuclei ($r < 0.1$ μm) concentration (Environment One Counter); Aerosol ($0.18 < d < 3.0$ μm) concentration and size distribution (Knollenberg laser cavity aerosol spectrometer); Giant and ultra-giant nuclei of chlorides and sulfates (UNICO cascade impactor) - sample processing is described in the article by Podzimek (1959); Air temperature, pressure and humidity - the description of instruments and installation can be found in the bulletin of NCAR Atmospheric Technology (1973) and in Lenschow and Pennell's article (1974); Mean wind velocity and gust components of the wind vector; Time lapse camera pictures of cloud evolution.

All data (including aircraft position) were recorded on the multi-track recording system ARIS-IV (NCAR, RAF Bulletin No. 9, Nov. 1976) except laser cavity spectrometer counts (all points of the size spectrum were printed every 4 sec.) and the evaluation of impactor samples. Particle counters were calibrated shortly before the field measurements by latex particles. Aerosol was sampled from a sampling tube of 2.54 cm ID in which the permanent flow of outside air was maintained by a venturi tube pressure difference. Negligible particle losses in the sampling tubes were assumed.

The scheme of aircraft sampling and geographical location of the sampling site is depicted in Fig. 1. The main sampling profile was oriented approximately NW-SE direction referred to the ground station at South Padre Island close to Port Isabel. Samplings over the Gulf of Mexico have been performed 50 to 70 km from the seashore outside of the main cell of sea breeze. Most of the samplings over the mainland happened around Lake Lasara. This site represented a typical continental environment not directly polluted from the nearby heavily populated and industrialized areas around Brownsville and Harlingen. However, at S and SE winds the influence of highly polluted atmosphere on the aerosol measurements was apparent.

The seven series of aircraft measurements were performed during the time period between January 12 and January 18, 1979 mostly in the afternoon hours. First days of this time period were characterized by a low pressure over the northern part of the Gulf of Mexico and the low pressure over northern Colorado which gradually moved southwards. The change in pressure configuration caused northwest (NW) winds in the ground layer over the sampling area to change into SW and S wind with a strong W wind advection above 2.0 km altitude. High relative humidity up to 0.3 km and very dry air (R.H. < 20%) above the inversion at 0.6 km prevailed till January 14 (Fig. 2). Since January 15 the air circulation over southern Texas was governed by the low pressure over the Pacific Ocean off shore of

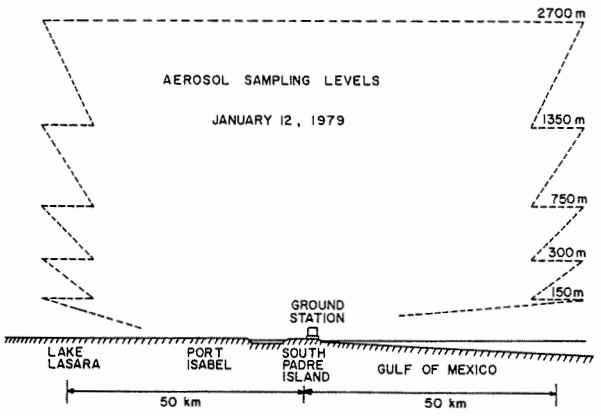

Fig. 1

California and by the mighty high pressure system over the central parts of the United States which gradually moved eastwards. At the same time a ridge of high pressure evolved over Arizona. During the whole remaining time period secondary low pressure was over the Colorado Rocky Mountains and over northern Mexico. The pattern of aerological charts

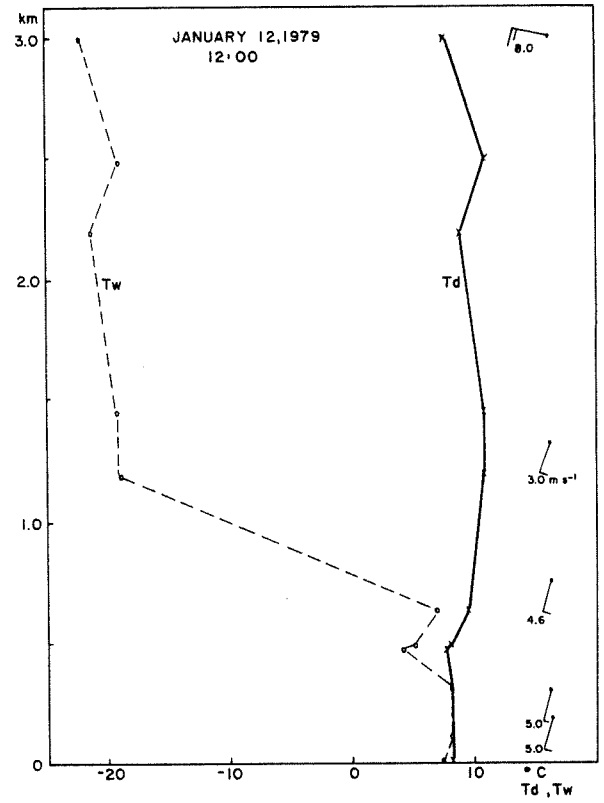

Fig. 2

remained almost unchanged from January 16 to January 19: very high relative humidity in the planetary boundary layer up to 2.0 km altitude with a shallow but very strong inversion above it. At altitudes above 2.0 km a very dry air prevailed with a strong south wind component which, by the end of the time period changed to SW and W wind.

In Fig. 3 are plotted the air mass trajectories based on the ground weather chart analysis and circulation pattern at 850 mb and 700 mb level. The example indicates that the aerosol of the January 12 sample over the ocean was of continental origin with a short dwelling time over the ocean. Also, there is a high probability of finding the heavily polluted air from the industrial areas in South Texas in the boundary layer over the ocean. The same analysis for the time period of January 15 to January 19 supports the idea that the aerosol sampled over the Gulf of Mexico resided for at least one day in the boundary layer over the ocean. During this time it might change its original continental character (descending apparently from northern Mexico). However, in the lowest sampling levels one might anticipate pure maritime aerosol generated over the sea surface.

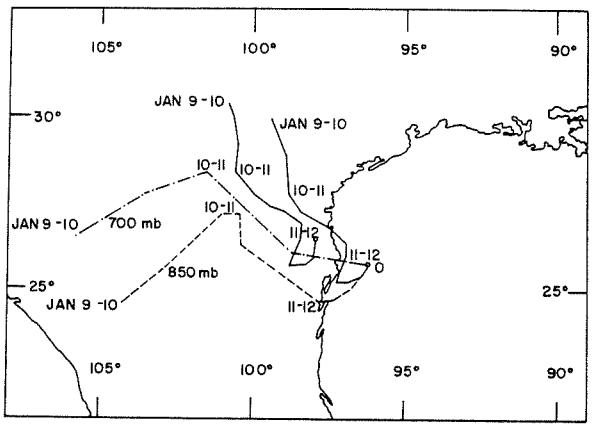

Fig. 3

3. ANALYSIS OF AEROSOL SIZE SPECTRA

All data from the Knollenberg laser spectrometer were divided into four groups corresponding to the four particle size ranges: 0.181 µm - 0.369 µm; 0.315 µm - 0.864 µm; 0.359 - 1.488 µm; 0.467 µm 3.000 µm in diameter. In each sampling level the four ranges were automatically switched on so that a record at least for one minute for each range was obtained. In particularly interesting levels records of approximately 5 minutes in duration were made and the concentrations (printed every four seconds) analyzed. The number of evaluated four second printings are indicated in parenthesis (in Figs. 4-6) at each specific level so that the reliability of the plotted mean particle concentration (in percent of the total concentration - ΣN cm^{-3} can be estimated.

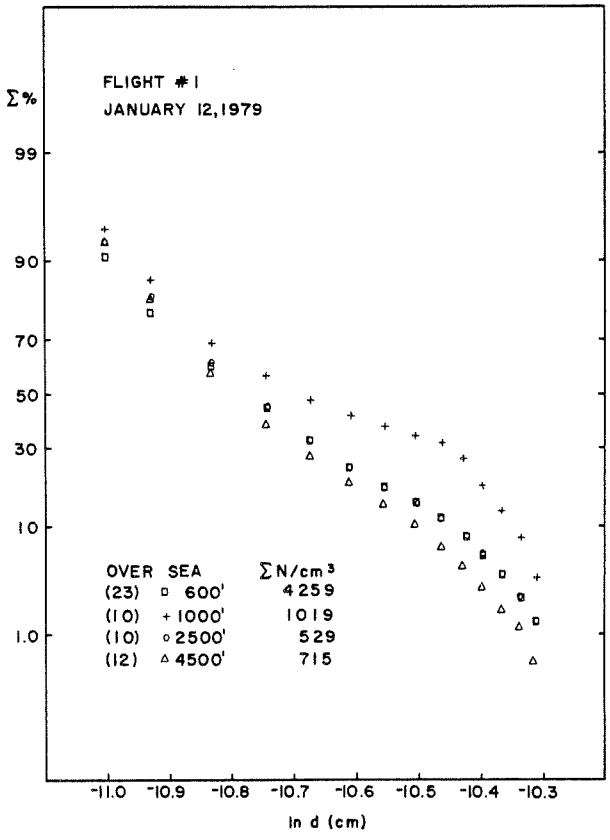

Fig. 4

Three examples of the plottings (Figs. 4-5) were selected out of more than 50 diagrams of size distributions of particles collected over the Gulf of Mexico and over the mainland. The curves do not follow exactly the log-normal distribution law. There is an apparent tendency to form a plateau in case of sampling close to the cloud boundary or temperature inversion. This conclusion is supported by sampling on January 12 at an altitude of 300 m above the sea (in Fig. 4 marked by crosses) where a hazy layer of high humidity persisted (Fig. 2). Another example is presented in Fig. 5 which shows how the aerosol size distribution measured at an altitude of 220 m above the ground was distorted when the aircraft approached the layer with patches of clouds (which later gave origin to drizzle drops). Apparently the most active particles of this marine aerosol are confined to the domain of mean diameters between 0.226 μm and 0.337 μm. Basically different are the particle size distribution curves from the flights at fair weather (Fig. 5) which were performed on the same day (January 16) shortly before the sampling over the mainland. Similar observations were also made during January 15 and 18 flights when the relative humidity was not high enough (R.H. < 88%) to cause the shifting in particle size distribution curves.

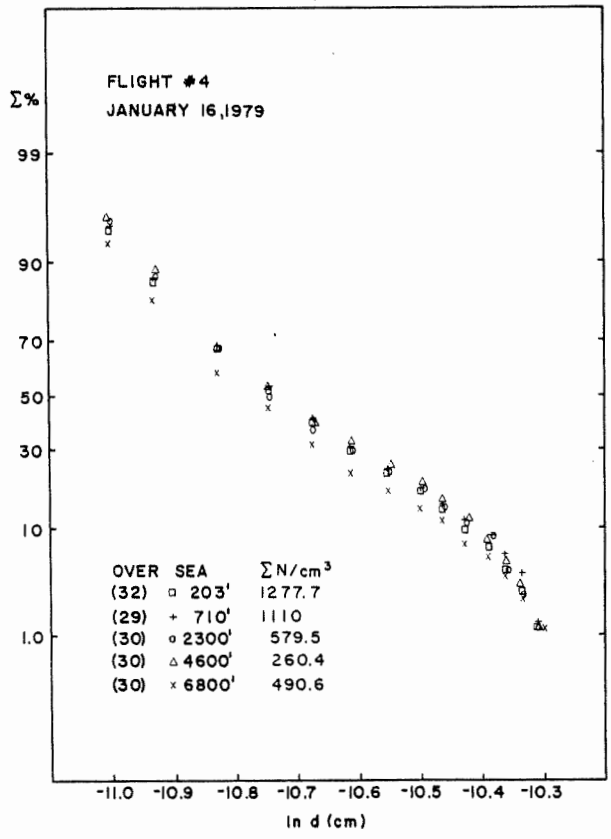

Fig. 5

Simultaneous measurements of the Aitken nuclei (AN) concentration and of the larger particulates classified by Knollenberg aerosol spectrometer offer a unique opportunity of estimating how many aerosol particles are smaller than the critical size detected by aerosol spectrometer. As an example AN concentrations measured at a specific level (in parenthesis) during the morning flight of January 16 can be mentioned: 850 cm^{-3} (120 m); 1500 cm^{-3} (230 m); 980 cm^{-3} (720 m); 780 cm^{-3} (1370 m) and 6500 cm^{-3} (2370 m) over the sea. Over the mainland AN concentrations were a little higher but their course was almost parallel to that over the sea. An exception is high AN counts above the ground: 12000 cm^{-3} (120 m) and 10000 cm^{-3}. If one compares these numbers to the total particle concentration in the smallest size range of the Knollenberg aerosol spectrometer (Fig. 5 and 6), the conclusion can be made that marine aerosol in the planetary boundary layer is almost exclusively composed of particles detectable by the Knollenberg spectrometer. However, the majority of AN emitted from ground sources and transported in altitudes above 2.0 km over mainland between January 16 and 19 cannot be detected by Knollenberg spectrometer. This hypothesis is also supported by the comparison of data from the remaining flights.

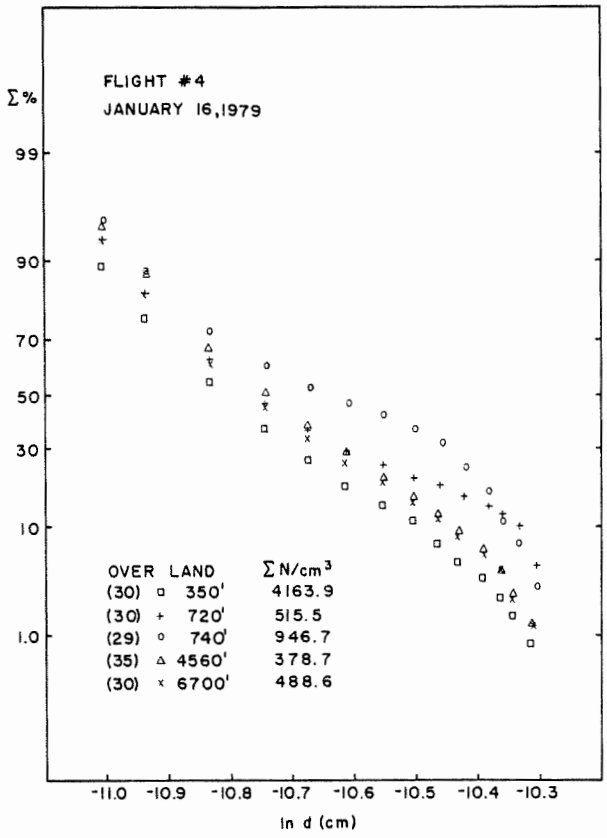

Fig. 6

4. TIME VARIABILITY OF AEROSOL CONCENTRATIONS

An attempt was made to investigate the characteristics of the fluctuating aerosol concentration. This was the continuation of the previous study (Podzimek, 1978) when Fourrier coefficients of the fluctuating particle concentration were plotted in dependence of frequency for different altitudes. This time the work was completed in order to characterize the aerosol concentration fluctuation $\sqrt{\overline{N'^2}}/N$ expressed in percent and to estimate the wavelength of fluctuating concentration if any. The calculated parameters have, however, a very limited statistical weight mainly for counting less numerous large particles (d > 0.4 μm). This might partly explain the finding of much larger mean factor $\sqrt{\overline{N'^2}}/N$ for

particle size interval 0.315 μm - 0.864 μm (51.6%) than for the smaller particles with diameters between 0.181 μm and 0.369 μm (19.9%).

Rough estimates of the mean wavelength of the aerosol concentration fluctuation were found for the mentioned group of layer particulates around 1,300 m and for smaller particulates around 1,000 m. These were the most important peaks on the concentration curves which significantly overshadowed the small amplitude concentration fluctuations due to statistical errors. In general, smallest amplitudes of aerosol concentrations were found in layers of stable thermal stratification (in the samples of e.g., January 12 around 9.0%) if compared to instable temperature stratification (42.9%).

Comparison of the aerosol concentration fluctuation with the change of the vertical component of the wind vector for finding a correlation between the supersaturation and particle growth (based on a simple assumption of a linear relationship between updraft and supersaturation) did not lead to any conclusive result.

5. SIGNIFICANCE OF AEROSOL INHOMOGENEITY FOR CLOUD FORMATION

A very interesting experience was made while analyzing the time lapse camera cloud pictures which accompanied the aerosol measurement. The camera was mounted in the aircraft's nose section and the pictures document the sampling conditions, cloud shape and the very important sampling just below the cloud base and above its top. During each flight differences in cloud base altitude were found even over a very uniform terrain. From the flight records of January 13 and 15 one concludes that the altitude of the bases of Cu hum and med might vary more than 50 m from cloud to cloud. There is of course a dramatic change in the height of cloud base above the sea and the mainland. On one specific day (January 15) the cloud base of Cu type clouds was 875 m above the sea and 480 m close to Lake Lasara. Similar observation was made on January 16 during the afternoon sampling. 50 m above cloud tops e.g., on January 15 was found a strong fluctuation of aerosol concentration with a wavelength roughly corresponding to the cloud distribution in this specific area (1.2 to 1.5 km).

The study which is still in a rudimentary stage proved qualitatively that aerosol nature might influence - together with the important thermodynamic field - the initial cloud evolution and vice versa that the cloud formation can modify the aerosol characteristics. It was demonstrated that at R.H. around 95% happens an activation of marine aerosol and that this threshold is confined to particle size between 0.2 to 0.4 μm depending upon the aerosol nature (origin).

Finally, the analysis of aerosol size distribution curves for the most important size range for cloud physics ($0.18 < d < 3.0$ μm leads to the conclusion that particles smaller than 1.0 μm survive and are transported on longer distances. Their character changes gradually after passing over the shoreline due to the small particle diffusion, gravitational coagulation with eventual settling and condensational growth. However, in mean there seems to be a tendency towards establishing a quasistable size distribution. In this sense these findings from the coastal region do not contradict the findings, e.g., by Whitby (1971) or Blifford and Gillette (1971), made over different locations if one excludes from the particle size distribution the influence of local sources of pollutants and layers with high relative humidity. Then the combination of two or three log-normal distributions seems to reflect well the aerosol state.

ACKNOWLEDGEMENT

The author appreciates very much the financial support by NSF (Grant ATM 77-22173), the help of Mr. G. Frick during aerosol sampling and the assistance of NCAR's staff, mainly the pilot Mr. T. McQuade, Project Engineer E. N. Brown and instrumentation technician L. Abbot. The staff of the NOAA National Weather Service at the Brownsville airport supplied the author with all synoptical and aerological data and advice important for the flight preparation. Mrs. Vickie Maples ably helped the author with the technical preparation of this paper.

REFERENCES

Blifford, I. H., Jr. and D. A. Gillette, 1971: Applications of the log-normal frequency distribution to the chemical composition and size distribution of naturally occurring atmospheric aerosols, Water, Air and Soil Pollution, 1, 106-114.

Burris, R. H., J. C. Covington, and M. N. Zrubek, 1973: Beechcraft Queen Air aircraft, Atmospheric Technology, NCAR, 1, 25-27.

Lenshow, D. H., and W. T. Pennell, 1974: On the measurement of in-cloud and wet-bulb temperatures from an aircraft, Monthly Weather Rev., 102, 447-454.

Podzimek, J., 1959: Determination of size spectrum of chloride giant condensation nuclei, Studia Geophys. et Geod. 3, 393-402.

Podzimek, J., 1978: Concentration fluctuation of marine aerosol in the planetary boundary layer, Preprint Vol. Conf. Cloud Physics and Atm. Electricity, Issaquah, AMS, Boston, 20-24.

Whitby, K. T., 1971: New data on urban aerosols and formation mechanisms. Proc. of the First Aerosol Modelling Sympos., NCAR, Res. Tech. Note TN-68, Oct.

SOME WINTERTIME CLOUD-AEROSOL INTERACTIONS OVER LAKE MICHIGAN

V. K. Saxena

North Carolina State University
Raleigh, NC U.S.A.

1. INTRODUCTION

Cloud-aerosol interactions are of consequential importance in understanding the thermodynamics and energy balance of the environment, extent of the cloud cover, scavenging mechanisms operative in clouds, and the chemical nature of precipitation received on the ground. In urban-industrial regions where the acidity of precipitation has been a cause of concern, it is imperative to investigate these interactions if the precipitation acidity is desired to be controlled through regulatory emission standards. Aerosols are removed from the atmosphere by being deposited or transported to the ground. The aerosol particles which are so received at the ground often differ greatly in their physico-chemical characteristics from the ones they had at the location of their formation or emission. Between emission and deposition, condensation and evaporation of water, growth and evaporation of particles themselves, chemical and photochemical reactions, coagulation of particles, diffusion of particles to cloud droplets and hydrometeors, and inertial collection by larger particles affect their physico-chemical characteristics. Obviously, there are a large number of steps and a great variety of combinations of such steps which may occur between emission and deposition. Precipitation processes originating in warm and cold clouds constitute an important sink for aerosols.

In urban-industrial areas, the precipitation acidity is largely controlled by sulfur which is one of the most dominant pollutants. It gets involved in essentially all of the scavenging interactions that are typically important as removal mechanisms. Sulfur dioxide can be scavenged as a gas, leading to the presence of dissolved SO_2 in precipitation and sulfate can be scavenged directly as an aerosol or it can be formed in precipitation by acqueous-phase SO_2 oxidation, eventually leading to the precipitation-borne sulfate. Recent estimates (MAP3S, 1979) show that roughly one-third of the MAP3S-area (i.e., the region including the upper Midwest and the Northeast U.S., often referred to as Greater Northeast) sulfur emissions are removed within the region by precipitation scavenging, with an average of about ninety percent of the sulfur occurring in rain as sulfate, the remainder being in the form of dissolved SO_2. Investigations of the lake effect snowstorms reveal (Scott, 1978) that between 50-90% of the subcloud sulfate gets activated as CCN.

The cloud nucleation activity of aerosols was investigated by us over Lake Michigan during November 1978-January 1979 under MAP3S (Multi-State Atmospheric Power Production Pollution Study). The field experiment was carried out in cooperation with the Battelle, Pacific Northwest Laboratory (PNL) with an aim to delineate cloud-aerosol interactions. The PNL DC3 aircraft was used as an observational platform and a network of ground stations collected precipitation samples. Our cloud condensation nucleus (CCN) spectrometer (Fukuta and Saxena, 1973; Fukuta et.al., 1974; Saxena and Fukuta, 1976; Saxena and Dytch, 1978; Fukuta and Saxena, 1979a; 1979b) was installed in the aircraft which was also equipped for measuring the Aitken nuclei concentration, cloud droplet size distribution, liquid water content of clouds, SO_2 concentration in the subcloud layer, and sulfate concentration in the cloud water collected through direct aircraft penetrations. This paper describes preliminary findings of our one year field study.

2. EXPERIMENTAL PROCEDURE

In order to examine the cloud-aerosol interactions over Lake Michigan, airborne observations were made near Muskegon, Michigan (see Fig. 1) during November, 1978 and January, 1979. It was planned to investigate the lake-effect snowstorms primarily, although all precipitation events were sampled whenever possible logistically. The CCN Spectrometer, as displayed in Fig. 2, was installed in the DC3 aircraft for sampling purposes. Choice of the Muskegon site was made because of relatively high frequency of occurrence of wintertime, lake-effect snow squalls which are accurately predictable thus enabling a better coordination of airborne and ground crews. Such storms afford unique and unusual opportunity for sampling since they are of low intensity and are slow moving thus enabling frequent cloud penetrations and providing sufficient sampling time in the clear air at cloud boundaries.

Experimental flights were made on 17 Nov., 29 Nov., 1978 and on 22, 23, 24, 25 and 27 Jan., 1979. One flight was made each day except on 23 Jan. when two flights were made as indicated in Table 1. On 22 Jan., a flight was conducted in clear air (cloudless sky) in order to test the equipment and provide calibration cross-checks. In Table 1, the duration of each flight, and the type of precipitation received at the ground from each storm are listed. During each flight, measurements were made in the sublcoud layer at one or two levels below the cloud base and in a layer about 2000 m thick both upwind and downwind of the lake-effect snowstorms. In addition to the measurements of CCN activity spectrum, the aircraft was

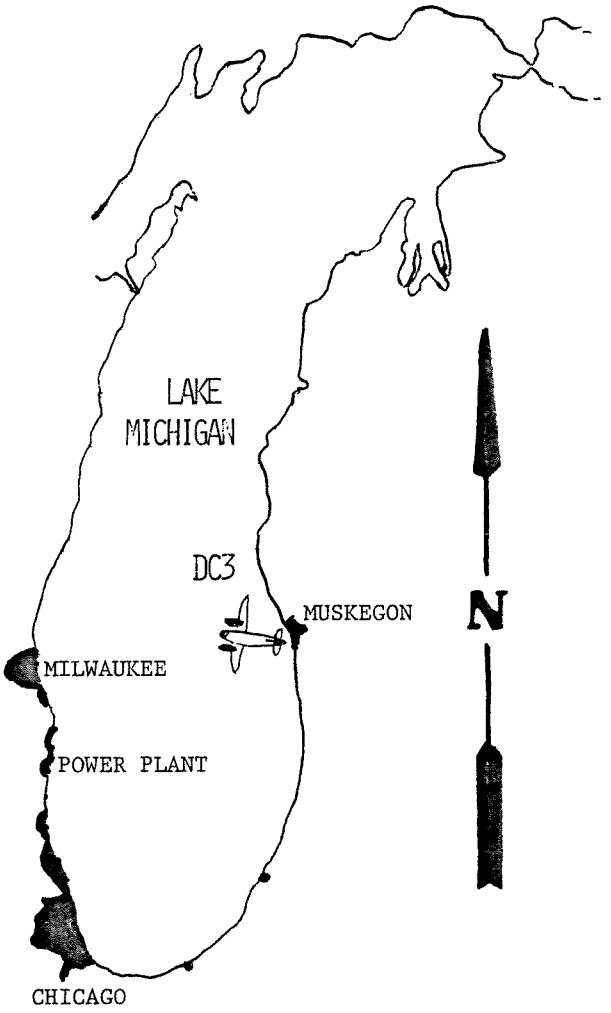

Fig. 1: Location of Muskegon which was used as a base for airborne observations.

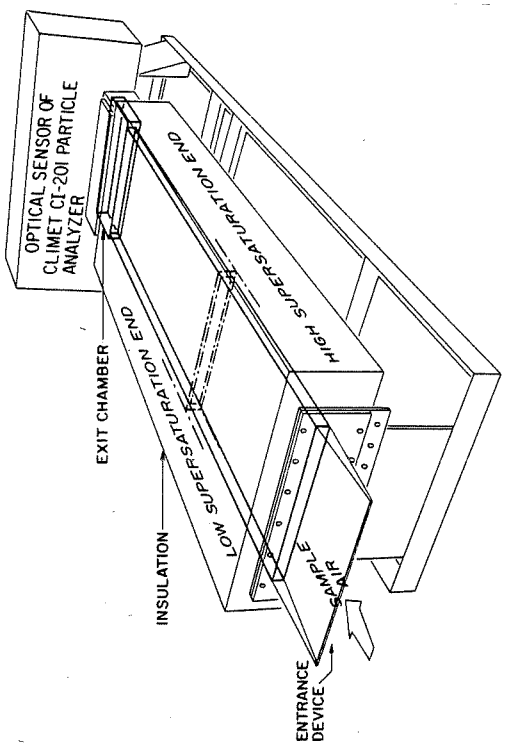

Fig. 2: Perspective view of the aerosol sampling section of the CCN spectrometer (Fukuta and Saxena, 1979a, b) installed in the DC3 aircraft for the MAP3S observations.

Table 1

Summary of DC3 flights conducted for studying the cloud-aerosol interactions during November 1978-January 1979

Flight No.	Date	Take Off EST hr.	Landing EST hr.	Duration hr.	Duration min.	Type of Precipitation from the Storm
1	17 Nov. 1978	1305	1630	3	25	Rain
2	29 Nov. 1978	1035	1400	3	25	Freezing Rain
3	22 Jan. 1979	1122	1325	2	05	Clear Air
4	23 Jan. 1979	1140	1340	2	00	Light Snow
5	23 Jan. 1979	1440	1722	2	44	Snow
6	24 Jan. 1979	1058	1342	2	44	Graupel
7	25 Jan. 1979	1243	1507	2	24	Very Light Snow
8	27 Jan. 1979	1157	1446	2	49	Snow stopped before take off

equipped to measure $SO_4^=$ aerosol mass, SO_x and total NH_3 volume concentrations, and aerosol size distribution in the range from 0.01 μm to 7 μm. Once these observations were completed, the aircraft was directed to penetrate the clouds at locations upwind of the ground

sampling sites which provided sequential samples of surface precipitation, meteorological data, and replicas of falling ice crystals for determination of growth histories of the precipitation particles. During cloud penetrations, the aircraft obtained measurements of cloud liquid water content and droplet size distribution. Samples of supercooled cloud water were collected for chemical analysis in the laboratory. Except for the CCN Spectrometer, all other equipment was manned by the scientists from the Battelle, Pacific Northwest Laboratory. The former was operated by us and real-time records of the cloud nucleation activity of the aerosol in the subcloud layer and at cloud boundaries were obtained.

3. RESULTS AND DISCUSSION

For the sake of brevity, results from only three flights are reported in Table 2 at selected times in order to point out some salient features. The measured CCN activity spectrum was fitted to the usual functional form, $n=CS^k$, where n is the number concentration of CCN per unit volume with critical supersaturations less than S, and C and k are concentration and slope parameters respectively. Primary cloud-aerosol interaction takes place in evolving the cloud droplet size spectrum. The concentration, N, of cloud droplets (in cm^{-3}) resulting from an updraft U (cms^{-1}), may be expressed (Twomey, 1959; Braham, 1974) as

$$N=C^{2/(2+k)}\left[\frac{68.8\times10^{-3}U^{3/2}}{k\,\beta(3/2,k/2)}\right]^{k/(2+k)}, \qquad (1)$$

which is only an approximation and in reality, the cloud-aerosol interactions leading to N are very complex in nature. From Eq. (1) the dependency of N upon C and U can be easily understood. For values of $k \leq 0.5$, N varies almost linearly with C. For $k > 1.0$, the dependency of N upon U is stronger. Thus, in the former case, the cloud droplet concentration is primarily determined by the CCN concentration while in the latter, it is strongly influenced by the rate of ascent or the rate of supersaturation generation (i.e. dS/dt).

From Table 2, it seems that values of k >1.0 are almost as frequent as the ones around 0.5. In the air masses that we investigated over Lake Michigan, the dynamics of cloud formation seems to be as important as the microphysics in evolving the cloud droplet size spectra. It may be noted that larger values of k may also indicate the presence of a CCN source since freshly generated nuclei are finer in size and consequently activate at larger supersaturations resulting in the steeper slope of the spectrum.

On 29 Nov. 1978, a warm front was passing through Muskegon. The cloud base was about 900 m MSL. Measurements were made at 365 m (11:37:03 EST) and 760 m MSL in the subcloud layer. The data (see Table 2) reveal that the air at 760 m was, in general, twice or three times richer in CCN and represented aged aerosol (low values of k) when compared with the air at 365 m. In terms of the vertical concentration gradient, this seems contrary to expectations if the nuclei source is assumed to be at the surface. Either dry or aqueous phase conversion of SO_2 into sulfate particles may explain this finding. To this end, further investigations are in progress. One striking feature of the data, as shown by examples of Jan. 24, and 25 is that the measured CCN Spectrum does not always conform to $n=CS^k$ form although the measurements may be fitted to this form in small supersaturation intervals. This finding resulting from our real-time, in situ measurements with the help of the CCN Spectrometer, may have several interesting implications, especially in dealing with the polluted air masses.

More than one value of k parameter for the same air sample indicates that either the measurements do not conform to $n=CS^k$, or the sample is derived from two air masses which are not homogeneously mixed. It may be recalled that if the air sample is not represented by singular values of C and k, Eq. (1) cannot be adequately used to estimate the total cloud droplet concentration. The data recorded on Jan. 25, 1979 show that for a considerable number of samples taken at different times during the flight, two sets of C and k values may be found. Table 2 lists only a very few selected measurements and the evidence from the comprehensive data sets that we obtained, supports this conclusion. There exist a few instances where within a supersaturation interval of 0.12-1.0%, three sets of C and k values may be found. For this particular day, it may be noted that the cloud base was not well defined and the cloud tops were at about 914 m MSL. The vertical cloud development ranged from 152-243 m. The wind direction at the surface was 310-320° with speeds of 10-15 ms^{-1}.

Based on the above data sets and other cloud physical parameters measured during the field study, we are in the process of assessing the effectiveness of the cloud nucleation process for removing pollutants such as SO_2 and sulfates originating from urban-industrial areas, e.g. Chicago or Milwaukee (Fig. 1). For the formation of each cloud droplet, a cloud condensation nucleus (CCN) is required and a cloud droplet has to grow a million times in size in order to become a raindrop. Evidently, an enormous range of dimensions is spanned by these processes. The efficiency of in-cloud removal processes for particles in most size ranges is high when compared with the processes for dry removal and removal by precipitation below cloud levels. This is due to the fact that very large surface area is provided by the cloud droplets and cloud nucleation is capable of transferring aerosol particles from a small size into a much larger size range quite abruptly. The latter indeed is most effective when particles are soluble. For example, a sulfate particle with an initial radius of 0.02 μm will grow through cloud nucleation one hundred times and thereby advance some two decades through the size spectrum within a short time interval of ten seconds or so.

TABLE 2

Measured values of slope (k) and concentration (C) parameters at selected times during three flights

Date: Nov. 29, 1978 S(%): 0.2-1.2			Jan. 24, 1979				Jan. 25, 1979			
Time EST	C cm^{-3}	k	Time EST	C cm^{-3}	k	S (%)	Time EST	C cm^{-3}	k	S (%)
11:37:03	3245	1.70	11:20:20	10825	0.36	0.11-0.75	13:11:18	4640	1.04	0.11-0.62
12:01:04	7283	0.68	11:30:46	10335	0.30	0.11-0.75	13:11:48	3870	1.22	0.11-0.62
12:05:34	11470	0.86	11:34:16	4247	0.91	0.19-0.39	14:09:17	4140	0.17	0.11-0.37
				16323	1.94	0.39-0.75		6825	0.68	0.37-0.62
12:06:04	9726	1.23	11:40:10	2457	0.58	0.11-0.40	14:10:47	4060	0.19	0.11-0.37
				11480	2.70	0.40-0.75		9430	0.94	0.37-0.62
12:09:16	10668	0.79	11:41:40	5423	1.31	0.20-0.75	14:14:17	1227	0.40	0.11-0.37
								2833	1.23	0.37-0.62
12:20:33	11316	1.10	11:45:23	7955	1.58	0.20-0.75	14:16:17	1426	0.31	0.11-0.26
								3504	1.02	0.26-0.62

Acknowledgments

The author is indebted to Drs. J.M. Hales, B.C. Scott, N.S. Laulainen, and the crew of the PNL DC3 for their excellent cooperation. Professor N. Fukuta provided valuable help through stimulating discussions. Mr. Walter Klinger assisted in the field phase of the experiment. The research was supported by the Department of Energy under Contract No. DE-AS02-78EV04965.

References

Braham, R. R. Jr., 1974: Information content of CCN spectra vs. measurements at a single supersaturation. Preprints Conference on Cloud Physics, Tucson, Arizona, 21-24 October, 9-12.

Fukuta, N., and V. K. Saxena, 1973: Cloud condensation nucleus spectrometer. Bull. Amer. Meteor. Soc., 54, 1105.

Fukuta, N., V. K. Saxena, and A. Gorove, 1974: Cloud condensation nuclei spectrometer II: Measurements on the natural aerosol. Preprints Conference on Cloud Physics, Tucson, Arizona, 21-24 October, 361-367.

Fukuta, N., and V. K. Saxena, 1979a: The principle of a new horizontal thermal gradient cloud condensation nucleus spectrometer. J. Rech. Atmos., 13, 169-188.

Fukuta, N., and V. K. Saxena, 1979b: A horizontal thermal gradient cloud condensation nucleus spectrometer. J. Appl. Meteor., 18, 1352-1362.

MAP3S, 1979: The multistate atmospheric power production pollution study: Progress report for FY1977 and FY1978, DOE/EV-0040. Available from the National Technical Information Service (NITS), Springfield, VA, 404 pp.

Saxena, V. K., and N. Fukuta, 1976: Field applications of a new cloud condensation nucleus spectrometer: Investigations of continental and maritime aerosols. Preprints Intl. Conf. on Cloud Physics, July 26-30, Boulder, Colorado, 607-612.

Saxena, V. K., and H. E. Dytch, 1978: Comparison of an airborne CCN Spectrometer with a conventional CCN counter. Preprints from the Symposium on Meteorological Observations and Instrumentation, 10-14 April 1978, Denver, Colorado, 308-313.

Scott, B. C., 1978: Parameterization of sulfate removal by precipitation. J. Appl. Meteor., 17, 1375-1389.

Twomey, S., 1959: The nuclei of natural cloud formation, Part I and II. Geofis. Pura. Appl., 43, 227-249.

ETUDE DE L'INFLUENCE DE SUBSTANCES TENSIOACTIVES SUR LA CINETIQUE DE LA CONDENSATION SUR DES NOYAUX GEANTS DE NaCl

B. Thaveau, R. Serpolay
I.O.P.G. du Puy de Dôme, L.A.M.P.
Clermont-Ferrand, FRANCE

S. Piekarski
Laboratoire de chimie Organique B
Limoges, FRANCE

I - INTRODUCTION

L'idée que les substances tensioactives puissent modifier la cinétique des processus de condensation et d'évaporation a été utilisée par différents auteurs : DERJAGUIN, 1957 (2), JIUSTO, 1964 (3). D'autres, comme KOCMOND et coll., 1972 (4), ont comparé au laboratoire l'évolution d'un brouillard traité à l'hexadecanol-1 à celle d'un brouillard non traité. BAKHANOVA et SILAYEV (1) s'intéressèrent à la croissance de particules hygroscopiques recouvertes d'une couche d'alcool cétylique. D'une façon générale, le principe de la mesure des vitesses de croissance fait intervenir soit la diffusion de la lumière - le coefficient d'extinction étant en relation avec le rayon de la particule, soit la cinématographie de la chute des particules - la vitesse de ces dernières étant directement liée à leur rayon.

La méthode que nous proposons diffère des précédentes dans le sens où il est possible de suivre, dans son ensemble, la croissance d'une particule isolée. La croissance est initiée à partir de cristaux de NaCl et les substances tensioactives ont été choisies parmi celles qui sont susceptibles de se retrouver à la surface des eaux et dans l'atmosphère du fait de l'activité industrielle et des rejets des eaux ménagères.

Nous nous intéressons ainsi aux substances tensioactives en tant que facteurs susceptibles de modifier l'activité des noyaux de condensation dans un cycle naturel où intervient l'activité humaine.

Cette étude a été orientée, d'une part, en considérant la structure des divers tensioactifs (anionique, cationique, non ionique), d'autre part, en tenant compte de quantités croissantes de ces substances à l'interface particule-air.

II - DESCRIPTION DE LA METHODE EXPERIMENTALE

Dans une cuve thermostatée où règne une humidité relative proche de 100%, la croissance des gouttes à partir de noyaux salins est cinématographiée sous microscope. Le film, une fois développé, est projeté sur papier millimétré. On peut ainsi mesurer le diamètre avec une précision de ±1µm.

Les cristaux de NaCl sont obtenus par pulvérisation d'une solution de NaCl au moyen d'un aérosoleur médical. On recueille les particules pulvérisées sur un réseau de fils d'araignée. Pour une concentration de la solution saline de 3% en poids, on obtient des cristaux se situant dans la classe des noyaux géants avec des dimensions qui varient entre 10µm et 40µm. Avec des cristaux plus petits, les conditions d'observation qui sont alors imposées donnent lieu à des phénomènes de diffraction qui rendent les mesures difficiles à effectuer.

La cuve thermostatée (figure 1) permet de réaliser deux régimes de condensation :

a) régime statique : au moyen d'une seringue, on introduit de l'eau dans le fond de la cuve après avoir rendu celle-ci hermétique.

b) régime dynamique : on fait barboter un courant d'air dans un récipient d'eau à la température de la cuve et on dirige cet air sur la particule. Cette méthode permet également de faire évaporer les gouttelettes en envoyant de l'air sec dans la cuve.

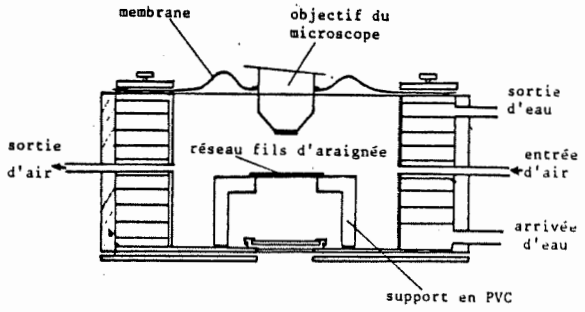

Schéma de la cuve

FIGURE 1

Toutefois, pour la majorité des expériences, le régime statique a été préféré au régime dynamique, ce dernier imprimant parfois à la particule en voie de croissance des vibrations préjudiciables à la qualité des images sur le plan cinématographique.

Les tensioactifs sont choisis parmi les corps solubles des 3 classes suivantes :
- anionique : la longue chaîne est portée par l' anion. Exemple : le dodecylsulfate de sodium : $C_{12}H_{25} - SO_4^{\ominus}\ Na^{\oplus}$

- cationique : la longue chaîne est portée par le cation. Exemple : l'amine tertiaire qui, avec l'eau, donne l'équilibre suivant :

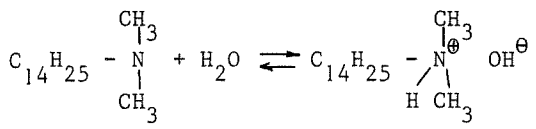

- non ionique : la longue chaîne est reliée à des groupes polaires non ionisés. Exemple : le tween 20 ou monodecanoate de polyethoxy-sorbitol.

Pour pouvoir établir une comparaison entre les courbes de croissance des cristaux de NaCl purs et des cristaux de NaCl pollués avec ces différents tensioactifs, il importe d'opérer dans des conditions de propreté superficielle draconiennes pour éviter une éventuelle contamination du cristal.

Deux méthodes de pollution du cristal ont été utilisées. L'une consiste à ajouter le tensioactif (0,1 à 0,6% en poids) à la solution de NaCl qui sera pulvérisée. On obtient alors des gouttelettes salines polluées et, par la suite, des cristaux pollués après évaporation de l'eau. L'autre méthode consiste à polluer directement un cristal de NaCl pur, dont on a filmé la croissance auparavant, par contact avec une gouttelette de solution de tensioactif. Dans ce but, on utilise un micromanipulateur qui permet de superposer un cristal de NaCl porté par un réseau de fils d'araignée à la gouttelette polluée, portée par un second réseau. L'avantage de cette méthode est de pouvoir utiliser le même cristal, donc la même masse de sel, et ainsi rendre plus significatives les comparaisons des courbes de croissances. C'est pourquoi nous l'avons employée dans la plupart de nos expériences.

III - RESULTATS

1°) Courbe de croissance et reproductibilité (diamètre en fonction du temps)

La courbe de croissance comprend deux parties :

- la première, assimilable à une droite, correspond à la phase de dissolution du cristal jusqu'au moment où il disparaît complètement;
- la seconde, qui tend asymptotiquement vers une valeur limite.

Pour un même cristal et dans les mêmes conditions de température, la pente de la droite est reproductible à 10% près et varie en sens inverse de la masse du cristal. Cette masse peut d'ailleurs être calculée à partir du diamètre de la goutte à l'instant de la disparition du cristal.

Le film étant réalisé à une cadence de 2 images/s., cet instant peut être situé à une image près. On considère que la gouttelette est alors une solution saturée. A une température de 20°C, la formule utilisée est la suivante : $m = 1{,}655 \times 10^{-13}\ \phi^3$ (ϕ : diamètre en µm ; m : masse en gramme).

Compte tenu de la précision de la mesure sur le diamètre, la masse peut être calculée à 10% près.

Pour des cristaux de même masse, et dans les mêmes conditions expérimentales, la deuxième partie de la courbe de croissance est reproductible dans un domaine d'erreur de ±2µm.

La différence entre les deux régimes de croissance se manifeste surtout dans la première partie de la courbe, la vitesse étant plus rapide en régime dynamique. Dans la seconde phase de croissance, les courbes correspondant à ces différents régimes finissent par se rejoindre.

2°) Comparaison des courbes de croissance pour des cristaux purs et des cristaux pollués

a) Tensioactif non ionique : le tween 20

D'après la figure 2 qui représente les courbes de croissance d'un cristal pur et du même cristal soumis successivement à trois pollutions, on constate que la pente de la droite diminue quand on augmente la quantité du tensio-

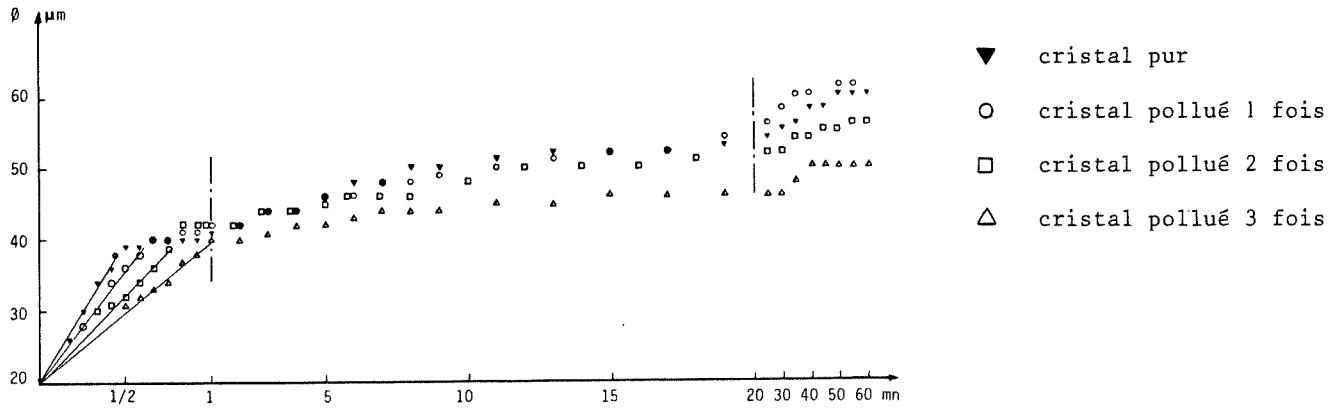

FIGURE 2 - Tensioactif non ionique. Croissance en statique à 20°C

actif apportée sur la particule de sel. La seconde partie de la courbe est relativement proche de celle correspondant au cristal pur pour une première pollution, mais s'en écarte d'une façon significative pour les pollutions suivantes. Il apparaît donc que la présence de ce tensioactif diminue la vitesse de croissance des gouttes. D'autres expériences avec ce tensioactif ont confirmé ce résultat.

b) tensioactif cationique : l'amine tertiaire

En statique, à une température de 20°C (figure 3), la vitesse de croissance est diminuée, surtout après que deux pollutions successives aient été cumulées sur le cristal. Des essais effectués avec un autre tensioactif cationique (le chlorure de dimethyl-ethyl-tetradecyl ammonium) ont abouti au même résultat : une diminution de la vitesse de croissance.

Exposé à une humidité relative de 76%, le cristal de NaCl pollué avec ce tensioactif voit diminuer sa vitesse de croissance sans toutefois que son seuil d'hydratation ne soit altéré. La même constatation a été faite avec le tensioactif non ionique.

c) Tensioactif anionique : le dodecylsulfate de sodium

La figure 4 représente les courbes de croissance de deux cristaux : le premier, de diamètre initial 22µm, a été pollué une fois ; il affecte une vitesse de croissance supérieure à celle du cristal pur. On retrouve cette dif-

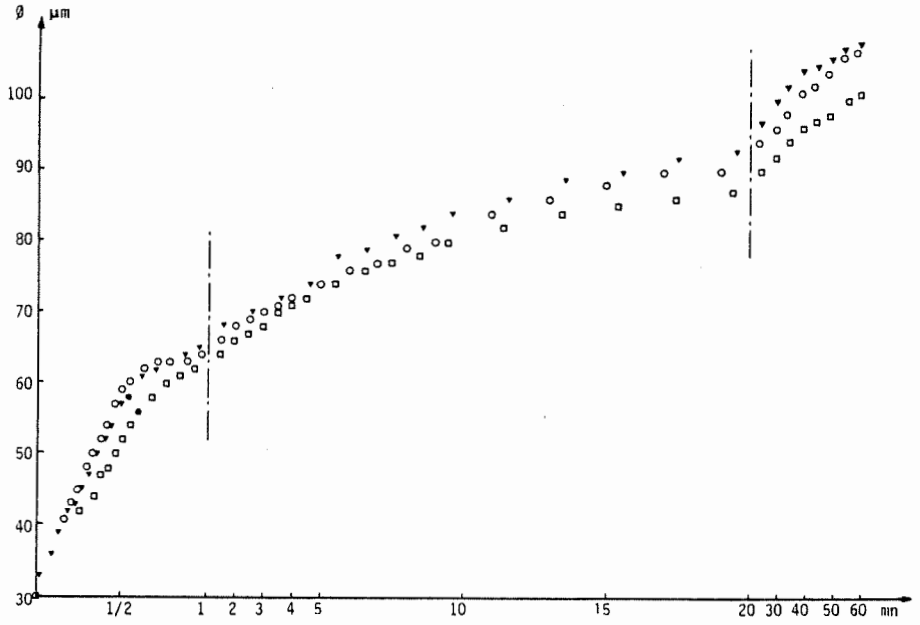

FIGURE 3 - Tensioactif cationique, croissance en statique à 20°C

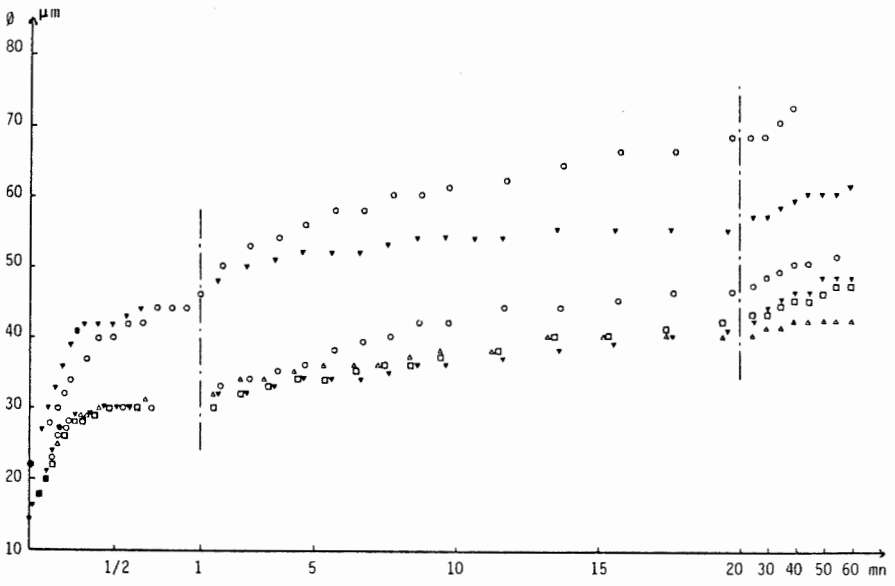

FIGURE 4 - Tensioactif anionique, croissance de 2 cristaux en statique à 20°C

férence avec le cristal de diamètre initial 14 µm. Après une deuxième pollution, la courbe de croissance est à peu près confondue avec celle du cristal pur. Après une troisième pollution, la croissance subit un net ralentissement entre 20 et 60 minutes.

Nous avons réalisé les mêmes expériences avec deux autres tensioactifs anioniques très purs : le dodecylbenzenesulfonate de sodium et le décanoate de potassium. Ces deux tensioactifs contribuent également à augmenter la vitesse de croissance. Il semble, par conséquent, que l'augmentation de la vitesse de croissance lorsque le cristal est faiblement pollué soit due à une propriété particulière de ces tensioactifs anioniques qui pourrait être leur hygroscopicité. Nous avons en effet constaté qu'au voisinage de 100% d'humidité relative, ces substances condensaient l'eau. Une étude systématique de leur hygroscopicité devrait pouvoir vérifier cette hypothèse.

IV - CONCLUSION

Ce travail essentiellement expérimental, a mis en évidence une cinétique de croissance différente selon le type et la quantité de tensioactif utilisés. Le résultat le plus net est que, pour une quantité importante de tensioactif sur le noyau salin, la vitesse de croissance est diminuée.

Ce résultat est sensible dans la première phase de la croissance, surtout avec le tensioactif non ionique. Mais il est également très apparent dans la seconde phase de croissance à la fois pour les tensioactifs non ionique et cationique. L'examen attentif de la figure 2 nous montre par exemple que la gouttelette formée sur un cristal de NaCl met environ 1 heure pour atteindre, en régime statique, la dimension de 60 µm, tandis qu'au bout du même temps, la gouttelette formée sur le même cristal, après que celui-ci ait été soumis à 3 pollutions, a seulement atteint la dimension de 50µm.

Ce ralentissement de la vitesse de croissance par les tensioactifs peut avoir une incidence sur l'évolution du spectre de distribution de taille des gouttelettes de nuage dans la mesure où les noyaux géants de l'atmosphère sont susceptibles de modifier ce spectre. Il convient toutefois de considérer qu'en atmosphère libre, les conditions de croissance des particules hygroscopiques sont plus proches du régime dynamique que du régime statique.

Avant de conclure sur la modification significative des propriétés des noyaux salins atmosphériques par les tensioactifs, il serait nécessaire d'étudier l'influence de ceux-ci sur les particules appartenant à la fraction la plus fine de l'aérosol en utilisant une méthode apte à traduire l'aspect statistique des phénomènes qui ont été observés sur des cristaux isolés.

REFERENCES

(1) BAKHANOVA R.A. et SILAYEV A.V. (1974) - *On a method of fog modification by passivation of condensation nuclei* - Proceeding of the WMO/IAMAP scientific conference on weather modification, Tashkent, oct. 1973, p. 13

(2) IZMAILOVA G.L., PROKHOROV I.S., DERJAGUIN B.V. (1957) - Kolloidny Zhurnal, 19, n°5

(3) JIUSTO J.E. (1964) - *Project fog drops, investigation of warm fog properties and fog modification concepts* - Cornell Aeronautical labs, Buffalo, New-York, Report CR-72.

(4) KOCMOND W.C., GARETT W.D. et MACK E.J. (1972) - *Modification of laboratory fog with organic surface films* - J. Geoph. Res., 77, pp. 3221-3231.

REMERCIEMENTS

Ce travail a bénéficié d'un crédit attribué par la Délégation Générale à la Recherche Scientifique et Technique dans le cadre de l'aide à la recherche n°78.7.0093.

I.2 - Noyaux Glaçogènes

Ice Forming Nuclei

EFFECT OF INDUSTRIAL POLLUTANTS ON THE ACTIVITY OF ICE NUCLEI OF NATURAL ORIGIN

F.Anýž

Institute of the Physics of the Atmosphere, Czechosl.Acad.Sci.
Prague CZECHOSLOVAKIA

The effect of common pollutants emitted into the atmosphere and water on the ice-forming activity of various substances was studied.The combined effect of a number of chemicals at -15° C resulted in a change in the yield of ice nuclei in the range greater than 1:200.Sulphur dioxide at a concentration of 10 mg.m^{-3} caused a decrease in the yield of ice nuclei produced by the most effective nucleation on agents by as much as one order. The yield for medium effective materials fell to one half or even to one third of the original value.Study of the drop freezing temperature of powder suspensions exposed to sulphur dioxide demonstrated a shift in the drop freezing temperature to lower values by up to several °C. Thus the activity of the ice nuclei decreased.Oil vapours on the other hand, increased the yield of ice nuclei for less effective nucleants by up to 7 times.A similar effect was also demonstrated in the freezing of a powder suspension exposed to the effect of oil vapours, where the freezing temperature shifted to higher values, i.e. the ice nuclei were activated. This effect was strongest for nucleants of low activity The results demonstrated that it will also be necessary in the future to consider the effect of increased pollution of the biosphere from the point of view of changes in the concentration of ice nuclei and of the formation of cloud systems. A similar effect must also be considered in the evaluation of the possibility of artificial intervention into the weather by dispersion of various nucleants in areas with intense industrial and agricultural production.

The variations of the ice-power of air mentioned many years ago (Soulage, Admirat 1962) and the activity of freezing nuclei from decaying vegetation (Schnell, Vali, 1972) must be considered from this point of view. The results of a 16 years long series of measurement of freezing nuclei concentrations (Schmidt, 1975) showed that the variations greater by as much as one order are very rare. Such variations are comparable with the results of the influence of chemical gaseous pollutants mentioned in this paper. That means the activity and the concentration of ice nuclei is dependent on the level of pollution of the air as well.

Table I.

Sample	Method of sample chemical treatment	Yield of ice nuclei per gram at -15°C and saturation to water
Montmorillonite V fine fraction	untreated sample	4.6 x 10^6
"	5 % $CuSO_4$	2.7 x 10^6
"	5 % $CuSO_4$ + H_2S vap.	2.5 x 10^8
Montmorillonite N coarse fraction	untreated sample	2.1 x 10^7
"	1 % KI	4.3 x 10^6
"	1 % $AgNO_3$	2.0 x 10^6
Montmorillonite BV 16 activated with CuS	untreated sample	1.1 x 10^8
"	10 mg SO_2.m^{-3}	1.2 x 10^7
Montmorillonite BV 22 activated with CuS	untreated sample	2.3 x 10^8
"	10 mg SO_2. m^{-3}	3.3 x 10^7
Rotten oak tree trunk	untreated sample	2.1 x 10^7
"	10 mg SO_2.m^{-3}	6.6 x 10^6
Rotten pine tree trunk	untreated sample	4.7 x 10^4
"	oil vapours	3.5 x 10^5

REFERENCES

Schmidt M.,1975:Periodicities in freezing nuclei concentrations from 16 years of continuous records.Arch.Met. Biokl.,Ser.A,24,281-294.

Schnell R.C.,Vali G.,1972:Atmospheric Ice Nuclei from decomposing vegetation. Nature,Vol.236,No 5343,163-165.

Soulage G.,Admirat P.,1962:Description d'anomalies estivales du pouvoir glaçogène de l'air en France.Bull.Obs. Puy de Dome., 10,No 4, 155-171.

Table II.

Sample	Drop freezing temperature ($0^{o}C$) of 1 % suspensions of substances
Coal dust	-13.3
Ground limestone	-13.3
Power plant ashes	-9.6
Montmorillonite N	-1.6
Montmorillonite V	-1.5
Copper sulphide	-1.6
Aerosol freed by burning a mixture containing sulphides	-1.1

THE EFFECT OF OIL VAPOURS AND SULPHUR DIOXIDE ON THE DROP FREEZING TEMPERATURE OF 1 % AQUEOUS SUSPENSIONS OF SUBSTANCES

Relative frequency of frozen drops at a cooling rate of 10-15^{o}C per minute.

CURVE DESIGNATION : 0-distilled water, 1.untreated sample, 2-effect of oil vapours, 3-effect of sulphur dioxide. The vertical lines designate the median of the average freezing temperature of the suspensions.

Drops with 3.3 mm diameter.

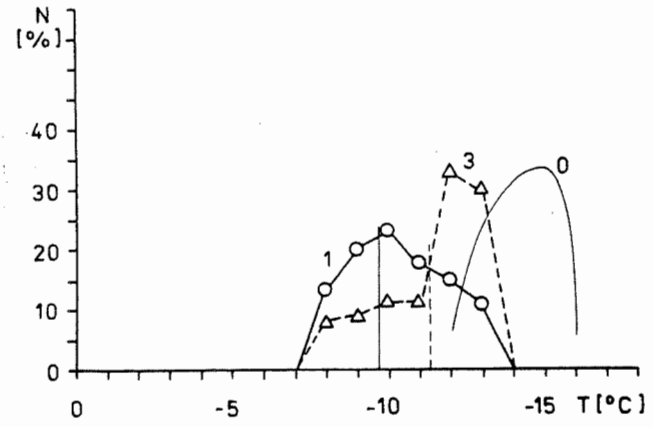

Power plant ashes CH

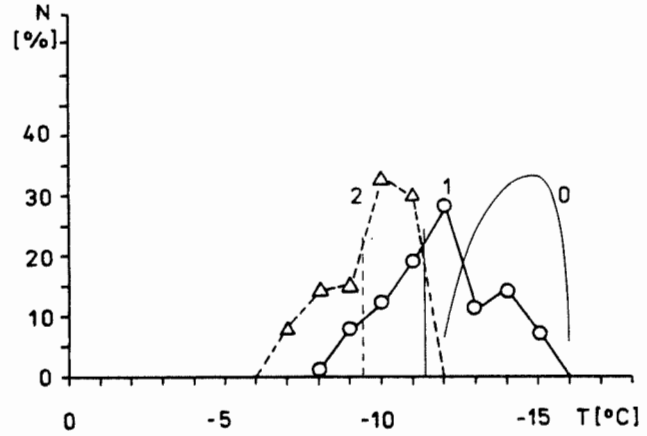

Zeolite KC 36

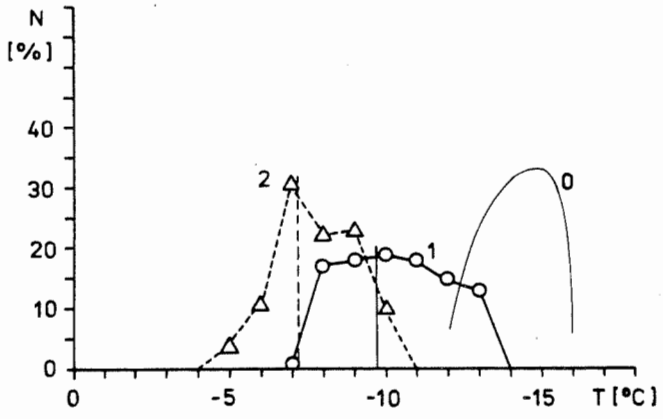

Rotten pine tree trunk

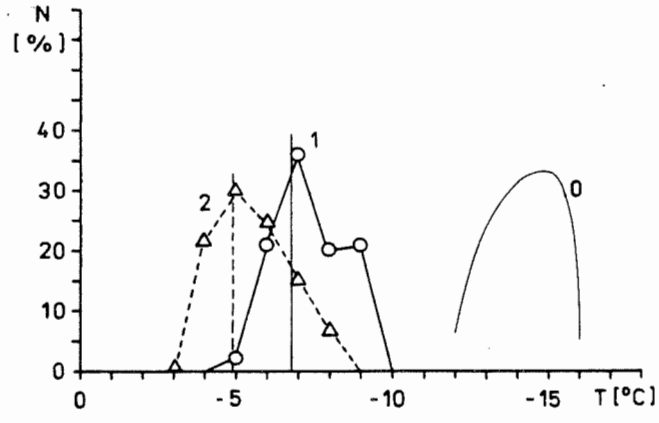

Zeolite BG

ON THE TEMPERATURE DEPENDENCE OF THE RELATIVE FREQUENCY OF ICE NUCLEATION BY CONTACT AND VAPOR DEPOSITION

Ulrich Katz* and Eugene J. Mack

Calspan Corporation
Buffalo, New York, U.S.A.

1. INTRODUCTION

This study is an expansion of an earlier experimental investigation carried out by Katz and Pilié (1974) which indicated that only a small fraction of ice crystals were formed through contact nucleation when a supercooled laboratory cloud was seeded with submicron AgI particles at about -16°C. The aim of the present work was to determine the relative frequency of contact nucleation over an extended temperature range relevant to glaciating conditions in natural clouds.

Among several possible mechanisms of ice crystal initiation in clouds, nucleation by contact of a nucleus with a supercooled droplet occupies a special position. On one hand, a number of early experimental studies (reviewed by Katz and Pilié, 1974) showed contact nucleation to be highly effective and, in particular, active at higher temperatures than immersion-freezing and possibly even the deposition nucleation process. On the other hand, by its very nature, contact nucleation should depend, in its rate, on the variables governing collision processes in contrast to the deposition mechanism which is mainly vapor pressure and temperature dependent.

For the case of an ice nucleus inside a supercooled cloud one has to consider only two competing nucleation mechanisms: contact and deposition (the latter including what is sometimes called sorption nucleation), since immersion-freezing was found to be much less effective (see, e.g., Gokhale and Spengler, 1972).

In recent years, several workers attempted to determine which of the two mechanisms in question was responsible for the glaciation observed in clouds. Theoretical studies by Cooper (1974) and by Young (1974) suggested that contact nucleation was predominant. Similar conclusions were reached on the basis of experimental work by Kumai (1974), Garvey and Davis (1975) and Parungo, et al. (1976), while, e.g., Langer (1974) and Langer and Rodgers (1975) estimated the contact mechanism to be inefficient. While discrepancies in previous studies clearly point to the need for further investigation of the contact vs. deposition problem, a recent investigation by Lamb, et al. (1980) concerning the glaciation of cumuli re-emphasizes the requirement for knowing the primary nucleating mechanism despite the fact that (in their model) most ice particles are formed by a secondary process.

*Present Affiliation: Desert Research Institute Reno, Nevada, U.S.A.

2. EXPERIMENTAL PROCEDURE

The pivotal element of this experiment is the scheme for detecting events of contact nucleation. Insoluble tracer particles incorporated into cloud droplets remain there when the droplets freeze (Katz and Pilié, 1974) and can thus be found at the center of ice crystals that formed from frozen drops (i.e., by contact nucleation in this case). Conversely, if an ice crystal develops from water vapor deposition on an ice nucleus, the tracer particles remain inside the evaporating drops relatively remote from the growing crystal which, therefore, will not contain a tracer particle in its center. The advantage of this method is its decisiveness as compared to the technique where one locates a presumed nucleus in an ice crystal and attempts to draw conclusions regarding its nucleation history depending on the exact nucleus position.

The basic experimental procedure was to fill a 2 m^3 cold chamber with a cloud of tagged droplets, seed the cloud with ice nuclei, and subsequently collect ice crystals for microscopic examination and detection of tracer particle presence in the crystal centers. Since the present experiments were carried out in essentially the same manner as described by Katz and Pilié (1974), only a few key items will be mentioned here.

The clouds were generated by atomizing a hydrosol of fluorescent zinc-cadmium particles (fp) resulting in droplet size spectra shown in Figure 1 as determined with an impactor-replicator. It has been established previously that the insoluble fp with a median diameter of 2 μm did not influence the glaciation behavior of the droplets. Thermally (on hot wire) produced submicron AgI particles in nitrogen as carrier served as ice nuclei; the particle size distributions as measured with an electrical aerosol analyzer are depicted in Figure 2. Particle number concentrations were not determined since only the ratio of contact and deposition nuclei was of interest.

Large numbers of precipitating ice crystals were collected on microscope slides and replicated with Krylon (Clear Spray No. 1302, which is not as fluorescent as formvar) for later evaluation through microscopic examination with combined UV and visible illumination. However, numerous microscopic observations were carried

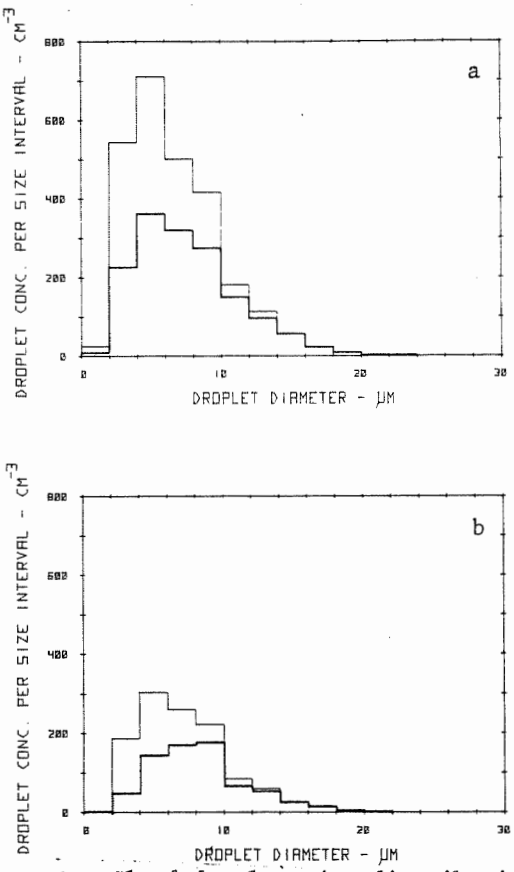

Figure 1. Cloud droplet size distributions, (a) at time of ice nuclei injection, (b) 100 s later. Thin lines represent total drop concentration; heavy lines indicate concentration of droplets containing fluorescent tracer particles.

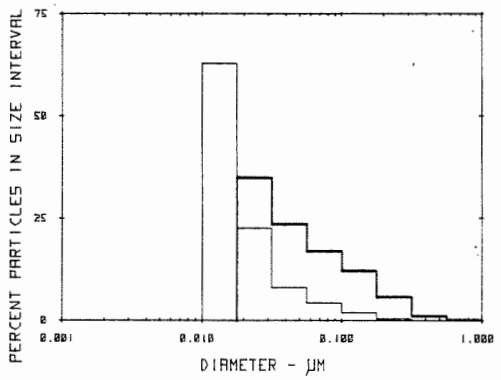

Figure 2. Size distribution of AgI aerosols used to seed laboratory cloud. Thin line represents histogram for fresh AgI smoke; heavy line refers to coagulated aerosol.

out in the coldroom while the replicating solution was drying and the ice crystals were evaporating. Thereby, it was found that particles not adhering to the plastic replica shell may migrate with the receding crystal surface towards the center of symmetry. This was particularly evident with the "vapor method" of replication in which the replicas often are incomplete, thus promoting the migration of particles that may have attached themselves to the crystal during or after sedimentation. An example of this type of particle migration is shown in Figure 3 in the sequence of an evaporation double plate where an fp on the upper plate is gradually drawn into the center. It is, therefore, particularly important to attempt complete encapsulation in the replicating process. Obviously, particles totally embedded anywhere inside ice crystals would still tend to migrate towards the center - a fact that points to the danger of interpreting particle position in terms of mode of nucleation as performed, e.g., by Kumai (1974) and Parungo, et al. (1976).

In order to determine experimentally to what extent such particle migration or any other effect leading to centrally located fp not associated with contact nucleation would affect the results of the present study, fp-doped clouds were nucleated homogeneously by adiabatic expansion of a small volume of compressed air. This procedure of cloud glaciation generates ice crystals from the water vapor, as shown by Hicks (1976) and, therefore, any fp appearing in the central area of the grown ice crystals had to be attributed to processes other than contact nucleation. The low frequency of these events is indicated in Table I.

While Katz and Pilié (1974) had shown for the case of dendrites and plates that fp involved in the initial stage of crystal formation (as in contact nucleation) could indeed be found in the center of the crystals as well as their replicas, the same was now found to be true in the case of columnar ice crystals as demonstrated in Figure 4 where fp are clearly visible in the centers of crystals which were grown from frozen droplets.

The measurements were carried out in one-degree temperature ranges centered at -8, -10, -13, -16 and -19°C. Typical examples of ice

Table I. Percentage of Ice Crystals with Centrally Located fp for Indicated Temperatures and Seeding Agent. *Adjusted Total Percentage of Ice Crystals Attributable to Contact Nucleation.*

Temperature	-8°C	-10°C	-13°C	-16°C	-19°C
Nucleation by Compressed Air	1.5%	1.3%	2.3%	1.8%	1.6%
Seeding with AgI Smoke, Fresh	3.2%	2.5%	4.0%	3.1%	4.0%
Adjusted Value for Contact Nucleation	*2.6%*	*2.8%*	*2.6%*	*2.0%*	*3.6%*
Seeding with AgI Smoke, Coagulated	2.8%	2.7%	5.2%	3.6%	3.5%
Adjusted Value for Contact Nucleation	*2.0%*	*2.1%*	*4.3%*	*2.7%*	*2.8%*

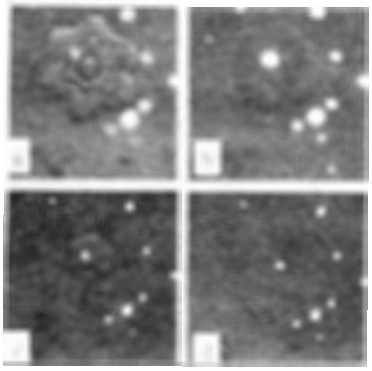

Figure 3. Evaporating double-plate ice cyrstal on Formvar substrate after application of chloroform vapor replication technique. Sequence shows fluorescent particle on top plate gradually migrating to center.

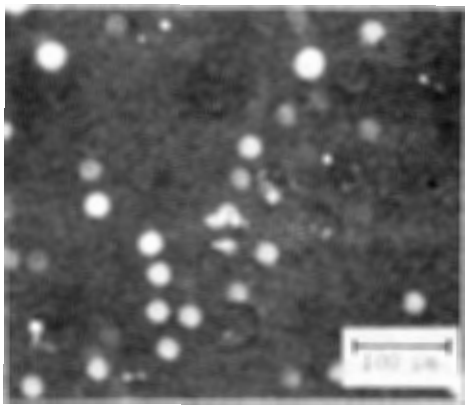

Figure 6. Sample of thick plates collected at -10°C in fp-doped cloud.

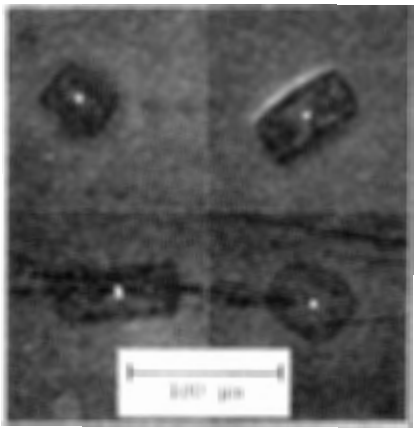

Figure 4. Columnar ice crystals (replicas on right side) obtained at -8°C from supercooled cloud with droplets containing both AgI and fluorescent particles.

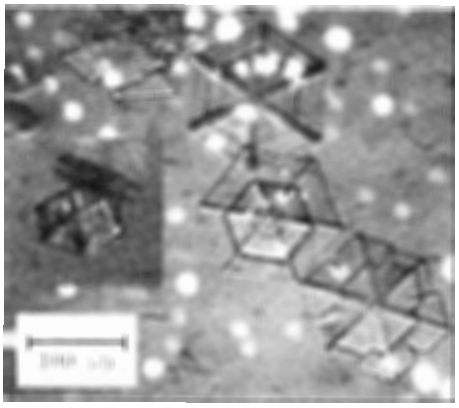

Figure 7. Double-plate ice crystals collected at -13°C in fp-doped cloud. Note inset with side view of double-plate.

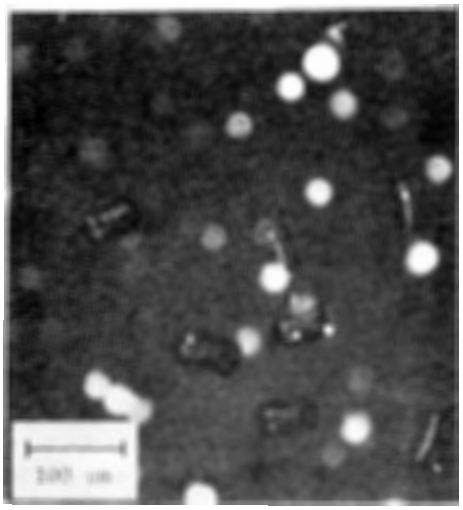

Figure 5. Example of ice crystals collected at -8°C in fp-doped cloud. No fp in crystal centers.

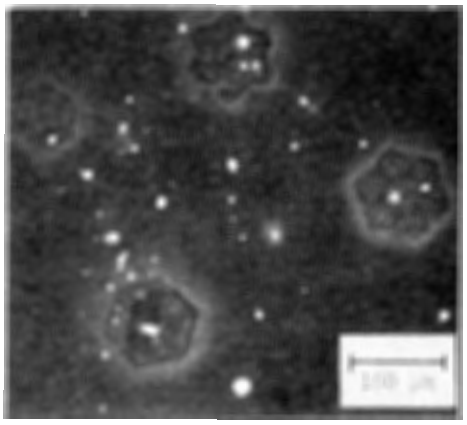

Figure 8. Ice crystal sample collected at -19°C in fp-doped cloud.

crystals obtained at these temperatures are presented in the photomicrographs of Figures 5 through 8. Illumination and focus were chosen such that fp in or on the ice crystals could be seen. Actual analysis for fp required, of course, inspection of each crystal while varying the focus in order to determine the fp location. Multiple reflection and refraction of fp-emitted light within the actual ice crystals made it generally preferable to conduct most of the analysis on replicas.

3. RESULTS AND DISCUSSION

Based on the examination of nearly 20,000 ice crystals and replicas, evaluation of the data proceeded as follows. For each combination of temperature and seeding mode (see Table I) the percentage of crystals with a centrally located fp was established. Since the compressed air seeding cases represent all those events which generate center fp by means other than contact nucleation, their respective percentages have to be subtracted from the values obtained for the AgI seeding experiments which comprise both contact nucleated crystals and all other ice crystals. The resulting numbers indicate the percentage of crystals which contain fp in the center presumably due to contact nucleation. However, since only about 2/3 of the cloud droplets contained fp, the final adjusted result (italics in Table I) is arrived at by multiplying the previous figures by 3/2. (The end result would be affected insignificantly by taking into account the fact that larger cloud drops have a higher probability for both containing fp and colliding with AgI nuclei). It should be noted that the average percentage appearing in Table I do not reflect the considerable scatter in the raw data within individual test series at a given set of conditions; typically, values would range from near zero to 7%. Thus, no significance can be attributed to any of the variations shown in Table I, and one has to conclude that contact nucleation contributes at most only a few percent (2-5%) of the ice crystals formed regardless of temperature within the investigated range of -8°C to -20°C. Similarly, Table I indicates that the difference in size of the AgI aerosols (i.e., fresh and aged) had no influence on the frequency of contact nucleation, possibly because of the opposite size dependence of collision efficiency and nucleating activity.

Although these results confirm the limited earlier findings of Katz and Pilié (1974), they are rather unexpected in view of some of the previous studies mentioned in the Introduction. The obvious question arises whether the relatively short experiment duration did prevent a large portion of potential contact nuclei from becoming active. However, periodic replenishment of the cloud was designed to reveal such prolonged ice crystal formation but only in cases of initial overseeding did more ice crystals appear (in a short burst) after reformation of the cloud - thus indicating that a prolonged gradual increase in ice crystal number was unlikely. The rapid formation of ice crystals (evidently by deposition nucleation) in the present experiments conforms quite well to the time lag of deposition nucleation reported by Anderson and Hallett (1976).

The widely held assumption that the frequently observed ice crystals with a circular center (-13°C to -20°C) develop from frozen droplets (and are indicators of contact nucleation) is incompatible with the findings of the present experiments. However, in a recent investigation Yamashita (1976) has demonstrated how double plates with circular centers grow from simple hexagonal plates, thus providing a satisfactory explanation for the occurrence of that crystal type without having to resort to the concept of contact nucleation.

4. SUMMARY

The relative frequency of contact and deposition nucleation in AgI-seeded, supercooled laboratory clouds was investigated in the temperature range of -8°C to -20°C. Doping cloud droplets with insoluble fluorescent tracer particles provided the distinction between differently nucleated ice crystals. With a frozen drop at their center, contact nucleated ice crystals contained a centrally located fluorescent particle in contrast to the crystals formed by vapor deposition. Based on the microscopic search for fluorescent particles in the centers of a large number of ice crystal replicas, it was concluded that contact nucleation contributed at most only 2-5% of the ice crystals under conditions where both nucleation mechanisms were competing with each other.

5. ACKNOWLEDGEMENTS

This research was supported by the Atmospheric Sciences Section, National Science Foundation under Grant No. ATM 75-14474. We are indebted to Mr. James R. Hicks and Dr. Motoi Kumai of CRREL for the use of their facilities and their assistance with equipment. We are grateful to Mr. Roland J. Pilié for his continued interest and helpful suggestions.

6. REFERENCES

Anderson, B.J. and J. Hallett, 1976: Supersaturation and Time Dependence of Ice Nucleation from the Vapor on Single Crystal Substrates, J. Atmos. Sci., 33, 822-832.

Cooper, W.A., 1974: A Possible Mechanism for Contact Nucleation, J. Atmos. Sci., 31, 1832-1837.

Garvey, D.M. and C.I. Davis, 1975: Ice Nucleation Characteristics of AgI Aerosols in an Isothermal Cloud Chamber, Proc. 8th International Conf. on Nucleation, Leningrad, 1973, 166-173.

Gokhale, N.R. and J.D. Spengler, 1972: Freezing of Freely Suspended, Supercooled Water Drops by Contact Nucleation, J. App. Meteor., 11, 157-160.

Hicks, J.R., 1976: Compressed Air Seeding of Supercooled Fog. Special Report 76-9, U.S. Army Cold Regions Research and Engineering Laboratory, Hanover, New Hampshire.

Katz, U. and R.J. Pilié, 1974: An Investigation of the Relative Importance of Vapor Deposition and Contact Nucleation in Cloud Seeding with AgI. J. Appl. Meteor., 13, 658-665.

Kumai, M., 1974: Investigations of Ice Nucleation Processes, Preprints, Conf. Cloud Physics, Tucson, Ariz., Amer. Meteor.Soc.,57-60.

Lamb, D., Sax, R.I., Hallett, J., 1980: Limitations on the Rates and Magnitudes of Latent Heat Released in Seeded Cumuli. Proc. Third WMO Scientific Conference on Weather Modification (Clermont-Ferrand, France, 21-25 July, 1980).

Langer, G., 1974: Contact vs Condensation-Freezing Nucleation for AgI Particles Below 0.1 m. Preprints, Conf. Cloud Physics, Tucson, Arizona, Amer. Meteor. Soc., 38-40.

Langer, G., and J. Rodgers, 1975: An Experimental Study of the Detection of Ice Nuclei on Membrane Filters and Other Substrata, J. Appl. Meteor., 14, 560-570.

Parungo, F.P., E. Ackerman and H. Proulx, 1976: Natural Ice Nuclei, J. Rech. Atmos., X, 45-60.

Yamashita, A., 1976: Growth Processes of Ice Crystals and a Law which is Related to the Symmetric Growth of Plate-like Snow Crystals, Preprints, International Conf. Cloud Physics, Boulder, CO, 136-141.

Young, K.C., 1974: The Role of Contact Nucleation in Ice Phase Initiation in Clouds, J. Atmos. Sci., 31, 768-776.

ON THE ROLE OF NATURAL ICE-FORMING NUCLEI IN HAILSTONE EMBRYO FORMATION

V.G.KHORGUANI

HIGH MOUNTAIN GEOPHYSICAL INSTITUTE

NALCHIK USSR

The subject of this paper is the microstructural features and ice-forming properties of aerosol particles present in hailstone embryos, rain shower and snow samples. The comparison of atmospheric ice-forming nuclei (IN) with these data is made and the mechanism of hailstone embryo formation is discussed.

1. PROCEDURE

A sterile dissecting knife and blade were used to separate the hailstone embryo (usually 2-4 mm). Study of a hailstone center by a long-focus microscope was made. Then embryo was plased on a special plate and the drop, produced by melting, evaporated or the embryo evaporated escaping liquid phase. As a result of this there was a deposition on the plate, containing aerosol particles of different sizes. For complete representation of particle size distribution the photograph of samples was taken by optical and electron microscope. The reading of particles from the film was made by famous method. And from these samples the microstructural features of aerosols were studied and then these samples were plased in a thermodiffusion cold chamber, where the ice-forming activity was examined under control temperatures and supersaturation, according to described tegnology(1). Samples were studied in temperature interval -8°C to -20°C. In addition, the temperature on the sample surface and chamber walls were chosen in such a way that the supersaturation practically was constant and samples of rain shower and snow were examined in quite a similar method.

2. EXPERIMENTAL RESULTS

The aerosol structure of 150 hail stones of different sizes collected on North Caucasis during 7 hailfalls was observed. Analysis of experimental data showed that in embryo hailstones the particle concentration is 10^5-10^6 cm^{-3} (in some embryos 10^4-10^7) besides, any hailfall character dependence can not be found. However, we noted that in hailstone embryos of intensive hailfalls large unsoluble particles can be met more often and their size was about 200-300 m. In this connection, the mean size and supergiant (d>30 μm) aerosol particle concentrations were considered individually. The results of four hailfalls, rain shower and snow are shown in Table 1. These hailfalls were quite different in their character and put in the Table 1 according to intensity and hailstone size. The first hailfall was catastrophic; the size of some hail stones reached 8 cm. And the last one had small hailstones and slight intensity. Analysis of this Table shows that with the increase of hailfall intensity the concentration of supergiant (d>30 μm) particles increases; at this time difference between the first and the fourth is about two orders. The lowest concentration is observed in rain shower and in snow samples the particles with d >30 μm were not observed practically.

Different concentrations of giant aerosol particles in precipitation of different types were also noted in paper / 2 /.

Fig.1 shows size distribution of aerosol particles in hail embryos, rain drops and snowflakes in atmosphere according to measurements made by aircraft impactor in hailfall regions up to 3 km altitude.

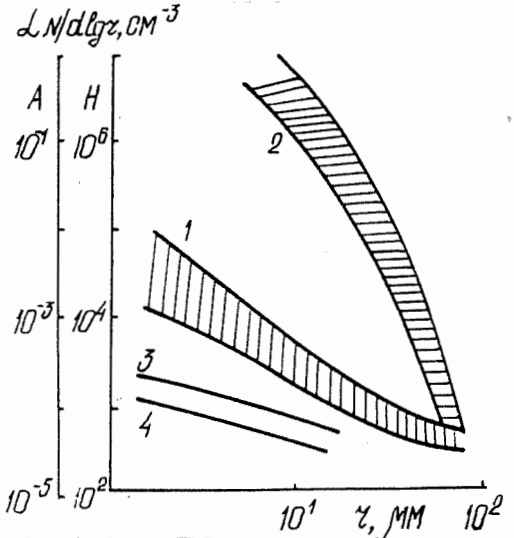

Fig.1 Aerosol particle size distribution in atmosphere/A/, in hailstone embryos and precipitation/H/. 1-hailstone embryos, 2-in atmosphere at heights of 1-3 km, 3- rain shower, 4-snow shower.

Table 1

N°	Data and hailfall location	mean cubic diametero of hailstone D_3, cm	number of studied hail stones, samples	mean cubic diameter and concentration of particles d > 30 μm	
				d_3, μm	n, $cm^{-3} 10^4$
1	15.06.74 Krasnodar	3,8	19	50,2	1,11
2	21.05.75 Kabardino-Balkar.	2,2	14	46,1	0,79
3	31.07.75 -"-	1,2	15	43,9	0,15
4	14.04.76 Nalchik	0,7	16	41,2	0,06
5	31.05.77 rain shower	-	14	34,5	0,02
6	3.03.77 snow shower	-	7	-	-

The curves were drawn according to particle size distribution of Junge

$$dN/d\log r = a r^{-\alpha}$$

Data analysis of Fig.1 shows that in hailstone embryos a portion of larger particle concentration more than in atmosphere. The exponent in Junge distribution for hailstone embryos ava rages α=1,5 and for atmosphere α=4,4. Thus, it seems that in hailstone embryos the accumulation of giant aerosol particles occurs. Fig.2 shows IN concentration in embryo ice, rain and snow as a function of temperature. Concentration of active IN at -20°C is 10^2 - 10^3 cm^{-3} and sharply decreases with temperature increase.

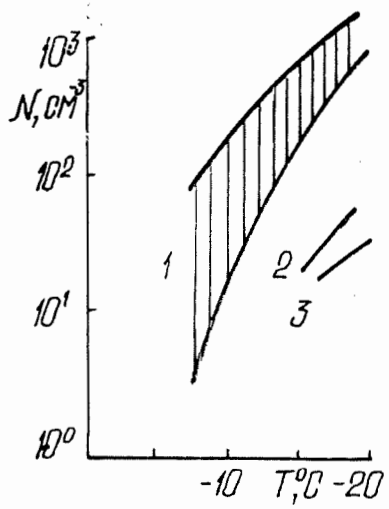

Fig.2 IN concentration in hailstone embryos(1), rain shower(2), snow shower(3) as a function of temperature.

In addition, in all cases the first crystalls formed on the giant and supergiant aerosol particles at -8°C to -10°C. With temperature increase the spread of concentration magnitude increases; at -10°C its mean value is about 10 cm^{-3}. Thus, in temperature interval from -8°C to -20°C the ratio of aerosol particle concentration of IN_5 in hailstone embryo changes from 10^5 to 10^3. The concentration of IN in raindrops and snowflakes is one or two orders less than in hailstone embryos (Fig.2) and in these samples first crystalls formed at -15°C to -17°C.

3. DISCUSSION

The most significant point in these investigations is the influence of secondary ice-forming on temperature activity of aerosol particles. Besides this, at sampling the coagulation of submicron particles and the activity loss are of necessity. The physical and chemical properties of particles play the main role in this process, however, these particles are expected to be deactivated/3/.

The concentration of hailstones usually is about 10^{-1} to 10^2 m^{-3} /4/ and it is closed to IN concentration at -10°C and above. At lower temperatures the IN concentration is one or two orders more than hail concentration. At the same time the initial crystalls usually form on giant particles present in hailstone embryos at -10°C and above. On the other hand the concentration of giant aerosol particles in embryo ice is very high. The calculations /5/ show that for such accumulation it is necessary for particle concentration in atmosphere to be one order more compared to observed one at heights of 1,5-2,0 km and above. Aircraft observations showed that over the developing thunderstorm cloud the increase of giant aerosol particle concentration by one or two orders is observed. Thus, in hail cloud formation processes from the surface layer a large amount of giant aerosol particles rises and only those particles which initiate the formation of ice phase at relatively high temperatures (above -8°Cto -10°C) can transform into hail embryos, graupel and frozen drops. Particles,

which show ice forming activity at lower temperatures, have no time to grow into hailstones or they are caried out of cloud at all.

REFERENCES

1. Myakonki G.B., Khorguani V.G.1973, Technique and equipment for measurement of ice forming niclei with millipore filters. Tr. VGI, 24, 107-117.
2. Rosinski J., Kerrigan T.,1969, The role of particles in the formation of raindrops and hailstones in several thunderstorms. J. Atm. Sci., No.4, p. 695-715.
3. Plaude N.O., Solovev A.D., 1978, Contact ice nucleation. Trudy Cent. Aerol. Obser., issue 132, p.3-31.
4. Khorguani V.G., Tlisov M.I.,1976, On nature and concentration of hailstones in clouds. Academy of Sciences Reports of the USSR., vol.227 No.5, p. 1108-1111.
5. Khorguani V.G., 1979, On the role of giant aerosol particles and ice forming nuclei in hailstone embryo formation. Prec. of Academy of Sci. of the USSR, Atm. and ocean Phys., vol. XV, No. 9, p. 920-927.

Table 1

N°	Data and hailfall location	mean cubic diametero of hailstone D_3, cm	number of studied hail stones, samples	mean cubic diameter and concentration of particles $d > 30\,\mu m$	
				d_3, μm	$n, cm^{-3} 10^4$
1	15.06.74 Krasnodar	3,8	19	50,2	1,11
2	21.05.75 Kabardino-Balkar.	2,2	14	46,1	0,79
3	31.07.75 -"-	1,2	15	43,9	0,15
4	14.04.76 Nalchik	0,7	16	41,2	0,06
5	31.05.77 rain shower	-	14	34,5	0,02
6	3.03.77 snow shower	-	7	-	-

ICE NUCLEATION AND ANTIFREEZE ACTIVITY BY SIMONSIDA CHENISIS LINK

R.G. Layton and G. Caple
Northern Arizona University - U.S.A.

I. Introduction

Since Schnell and Vali (1974,1976) found a source of ice nuclei in decomposing vegetation much study has been directed at understanding the source and character of biogenic ice nuclei. This study has mainly been devoted, however, to decaying leaves and the associated bacteria. The present study involves ice nucleation by the seed of simonsida chenisis link (the Joioba bean), the changes which occure as the seeds oil is extracted using common organic solvents, and some possible implications of the results for cloud physics.

II. Proceedure and results

The jojoba beans were crushed in a mortor and pestle until no particles larger than 1.0 mm remained. The crushed beans were extracted by palcing the solvent (50.0 ml) in a flask and adding 2 grams of bean material. The mixture was stirred with a magnetic stirrer four times varying from 5 to 50 hrs. After extraction, the solid material was removed by filtration, rinsed with 5 ml of the solvent and air dried.

The nucleation properties of the residue were determined using the freezing drop method (Vali, 1971) by placing the solid material on a mylar film in contact with a cold plate. Distilled, deionized water was then placed in contact with the solid material and the temperature decreased as the freezing of the drops was noted. Frequent runs were also made using only water to check for contamination.

The drops were three millimeters in diameter and were in contact with particles which we estimate in no case exceeded 10 mg of residue. We have not determined the soluble fraction of the seed, but comparison with other seeds (Diem and Lenther, 1971) suggests that any soluble component must have been present in rather minute quantities. Indeed, if the estimated total inorganic or soluble inorganic content were dissolved in the drop, the molality would be less than 10^{-3}. During the course of the freezing experiments there was little observed change in the bean fragments suggesting a far lower concentration of dissolved substance.

The nuclei spectra which we present are calculated using a method based on that of Vali (1971), however we have normalized our results such that the cumulative spectrum is presented in terms of the precentage of drops which contain an ice nucleus active in the 0.5 C temperauture interval immediatly below the temperature indicated on the graph. No correction was made for the fact that not all drops used was sufficient that this did not seem to be a problem. All results whcih we report in this paper except the 48 hr. extraction data have been duplicated in two or more independant runs.

Figure 1 contains the first data which we obtained. The ice nuclei spectrum obtained when the oil is extracted with hexane is noticably different from that obtained when the oil is extracted using either. The fact that the curves cross suggest that more than one substance is involved in the ice nucleation, with the substances being extracted at different rates by the different solvents. This data encouraged us to evaluate the ice nucleation characteristics vs. extraction time. (Fig. 2). During these experiments we temporaraly experienced some difficulty with the pruity of our water. Looking back, is is fortunate that this occured as we may have missed the freezing point depression exhibited by the seven hour residue if we had been using our usual quality of water. The water plotted in Figure 3 represents the worst water used in these experiments. Note that the addition of the seven hour jojoba residue depresses the freezing temperatures at the warm end of the spectrum while raising them at the coolder end. Figure 4 compares the spectra for the residue from a 22 hour extration with that from of 7 hour extraction.

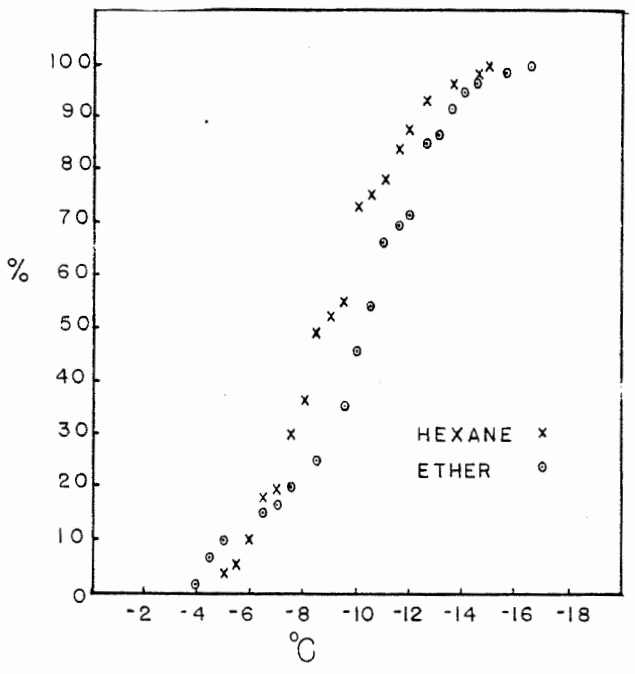

Figure 1 Nucleus spectra of jojoba bean when extracted with hexane and diethylether. Crossing strongly suggest two or more components being extracted at differing rates.

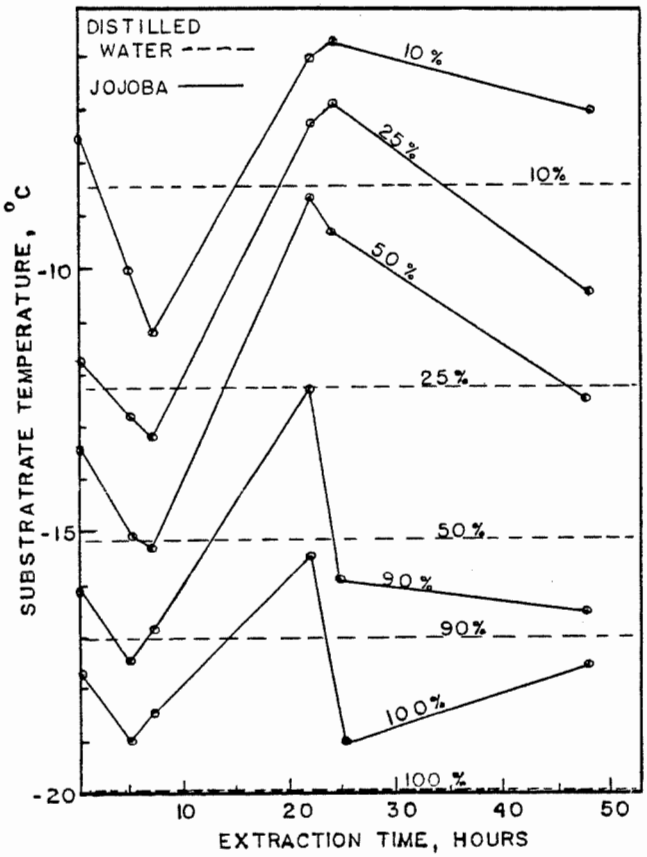

Figure 2 Nucleas spectrum of hexane extracted jojoba bean with T 10, 25, 50, 90, and 100 percent nucleation plotted against extration time. The dashed lines give the T 10°,25,50,90,100 nucleation spectrum of the water sample used in this study. The sample sizes were (in order of time) 115,235,291,71,115,86 drops with 169 drops used for the illustrated water sample.

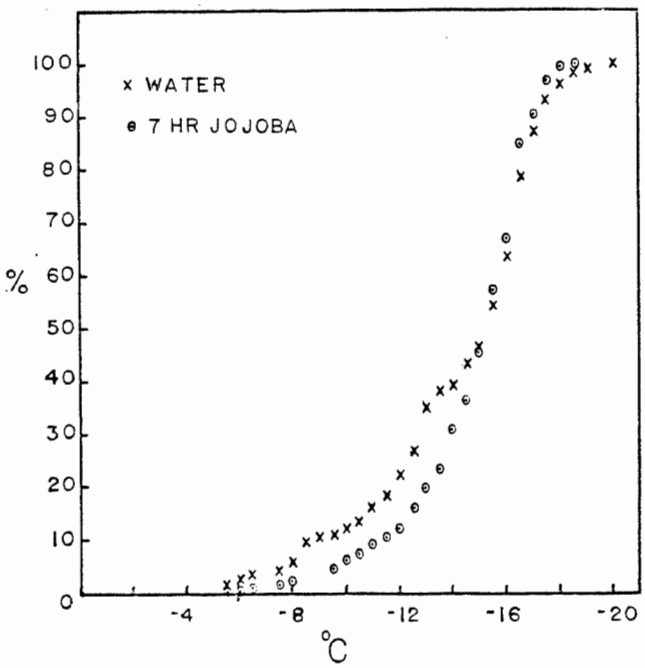

Figure 3 Nucleus spectra of jojoba bean extracted for seven hours with hexane. This spectrum shows inhibition at warmer temperatures and slight enhancement at colder temperatures.

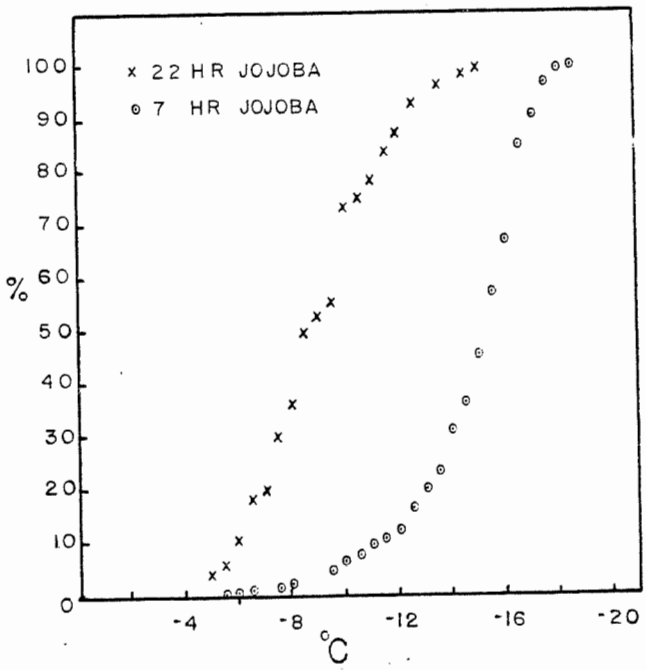

Figure 4 Nucleas spectra of jojoba bean material extracted for 7 and 22 hours with hexane.

III. Discussion

Extraction of the jojoba bean with solvents removes unsaturated long chain esters with an average molecualr spacing which in a situation where the mismatch is large should not have a great effect on the ice nucleation (Mondolfo, 1972), and a change of the ratio of hydrophyllic to hydrophobic sites which should have a pronounced effect on the ice nucleation. Indeed, a change in such sites has been shown to result in an ice nucleation size effect in silver iodide which involves neither curveture nor shape (Layton, 1973).

The surpression of freezing at the warmer temperatures indicates that the activity of the existing nuclei is being changed. Reischel and Vali (1975) report similar changes, but only wtih concentrations far in excess of that which we report.

Schnell (1974) has related the ice nucleating character of biogenic material to the climate zone of the biogenic source. In general the better warmer temperature nucleators originate in colder climiate zones. We suggest perhaps the property of noncolligitive freezing inhibition may be involved in ice nculeation processes. Yey and Fenny (1978) have investigated the properties of anti freeze glyco protiens and anti-freeze protiens openly suggest that noncolligative anti freeze materials may in fact at slightly colder temperatures be efficient ice nucleators. There data indicate that noncolligitive ice nucleation inhibition involves the formation of embryonic ice nuclei; and the inhibition is preventing crystal growth. They discuss hydrophobic group and hydrophilic group spacings as described by Zettlemoyer (1968) as a possible explanation for the observed results.

In our experiment, clearly the unique change is removal of a very hydorphobic oil from the bean matrix. This would change the overall hydorphobic material to the particle surface and in turn to the water surface. Since inhibition was observed even in the presence of other nucleators, possibly, a water solvable material was exposed such that it could easily be dissolved.

Although exteraction by a slovent such as hexane is not possible in the atmosphere, the atmosphere can be regarede as a gaseous solvent system, with varying hydrophobic-hydrophillic character depending ypon water content and temperature. It is well known that vapor-pressure rises on the surface of small pariticles and relatively large organic molecules have been reported in the gaseous state in the atmosphere.

Like wise, chemical processes could be continually modifing the surface or small biogenic particles. This modification could be by direct chemical modification or chemical cmodification followed by enchanced physical change (sublimation of condensation). Some possible chemical changes that might be expected to occur on particle surfaces have been studies by organic chemists March (1977).

The changes we observe are tantilizingly similar to those observed by Schnell (1974) as he observed the ice nucleating activity of decaying leaves as a function of time. It seems logical to assume that the jojoba is not an isolated case, but is representative of plants subjected to freezing stress. This result is consistant with the geographical distributions found by Schnell (1974) and Schnell and Vali (1976). Although solvent extraction is not a process which is active in the atmosphere, there are reactions which should produce similar results. A glance at Figure 4 indicates the type of changes that could result. Such changes suggest that more attention should be paid to the dynamic character of the nuclei population and to the possibility of negative interaction amoung them.

Bibliography

Diem, K., and Lenther, G. (Ed), 1971: Scientific tables 7th ed. Ciba-Geigy Ltd., Basle, Switzerland, 809 pp.

Layton, R.G., 1973: Ice nucleation by silver iodide: a new size effect. J. Coll. interface sci. 45:215-216.

March, J., 1977: Advanced organic chemistry 2nd ed. McGraw-Hill Book Co. New York, 1328 pp.

Miwa, T.K., 1971: Jojoba oil wax esters and derived fatty acids and alcohols, gas chromatographic annlysis. J. Amer. oil chem. soc. 39 (7): 259-264.

Mondolfo, L.F., 1972: Nucleation and lattice disregistry science 176:695.

Reischel, M.T., and Vali, G., 1975: Freezing nucleation in aqueous electrolytes. Tellus, 27: 414-427.

Schnell, R.C., 1974: Biogenic sources of atmospheric ice nuclei. Report ARIII, Dept. of Atmos. Resources, Univ. of Wyo., Laramie, Wyo. 45pp.

____, and Vali, G., 1972: Atmopsheric ice nuclei from decomposing vegetation. Nature 236, 163-165.

____, and ____, 1976: Biogenic ice nuclei: part I. Terrestrial and Marine Sources. J. Atmos. Sci. 33 (8) : 1554-1564.

Vali, G., 1971: Quantitative evaluation of experimental results on the heterogeneous freezing nucleation of super cooled liquids. J. Atmos. Sci., 28, 402-409.

Yeh, Yin, and Feeney, R.E., 1978: Anomalous depression of the freezing temperature in a biological system. Acc. Chem. Res. 129-135.

Zettlemoyer, A.C., 1968: Hydrophobic surfaces. J. Colloid Interface Sci., 28, 343-369.

CITRUS DERIVED BACTERIA ACTIVE AS FREEZING NUCLEI AT -2.5 C

Z. Levin*, N. Sandlerman*, A. Moshe**
T. Bertold**, and S.A. Yankofsky**

Tel Aviv University, Ramat Aviv, ISRAEL

A. Isolation of INA Bacteria

The existence of a few bacteria active as ice nuclei at relatively high temperatures (-2^0C to -5^0C) has recently been demonstrated (Schnell and Vali, 1976, Vali et al, 1976, and Maki and Willoughby, 1978). Moreover, based on the work of Lindow et al (1978), these so-called INA (ice nuclei active) bacteria are almost certainly causative agents of frost damage in various plants. We have now found that citrus leaves in Israel also carry INA bacteria, and that the sensitivity of citrus crops to frost damage is probably due to these bacteria.

The bacterium was isolated from frost-damaged leaf fragments by techniques similar to those described by Maki and Willoughby (1978) and its freezing nucleus spectrum assayed in a drop-freezing spectrometer of a modified version to the one designed by Vali (1971). A typical cell from a stationary-phase culture of the active isolate obtained is shown in Fig.1. As can be seen, the organism, called M1, is a typical, rod-shaped bacterium with a single polar flagellum. It should,however, be noted that actively dividing cells actually possess many flagella distributed across all cell surfaces. Thus, in spite of its yellow pigment and fermentative ability, M1 is different from all INA bacteria yet described. (Maki et al, 1974, and Lindow et al, 1978).

B. Freezing Nucleus Activity of Whole Cells

The freezing spectrum of 100 drops of a dense ($1-2\times10^9$ cells/ml) culture of M1 is compared in Fig.2 to that of drops from cultures of non-INA yellow bacteria of citrus origin, and to water drops exposed to AgI smoke. While the inactive bacteria obviously contain no freezing nuclei active at higher temperatures than the aqueous medium they were suspended in for testing, drops from M1 culture froze over the range -2.5^0C to -3.5^0C. On the other hand, no drop containing AgI particles froze at a temperature above -6^0C.

* Dept. of Geophysics and Planetary Sciences.

** Dept. of Microbiology

The effect of bacteria number concentration on drop-freezing temperatures is given in Fig.3. As can be seen, a sharp dependence on number of bacteria per 5 µl drop (1 mm radius) can be seen. Specifically, nuclei active at temperatures above -5^0C are present only where the number of cells examined exceeds $4\times10^6/cm^3$. Indeed, careful Poisson statistics have established that the frequency of -4^0C (or higher) nuclei is on the order of 1 per 50,000 cells in stationary cultures and 1 per 5000 cells in dividing cultures. Equally evident is a second class of nuclei active over the temperature range -6^0C to -10^0C. Others have also shown the presence of these less efficient nuclei in INA bacteria (Maki and Willoughby, 1978).

Fig. 1. Scanning electron photomicrograph (20000x) of the citrus INA bacterium, M1. The horizontal line in the lower right hand corner represents 1 µm and the average pore diameter of the support membrane is 0.6 µm.

Three alternative interpretations of the above data can be entertained: (1) That efficient freezing nucleus activity demands some cooperative interactions among all the cells (e.g. excretions from cells or other far field interactions); (2) that efficient freezing nuclei are produced by aggregation of a few cells; and (3) that only rare single cells within the population act as

nuclei.

The first two interpretations imply that the freezing temperature will be lowered as cell concentration decreases. On the other hand, the third alternative can be likened to a queen bee in a hive which suggests that in each family of cells there is only one which causes freezing at the higher temperature range. The last possibility turns out to be the correct one.

Evidence for this latter conclusion was obtained by the following experiments. A volume 0.5 ml containing 10^5 cells was equally distributed into 10 test tubes containing 0.45 ml each of buffer. The derivative tubes which froze after 30 min at -4^0C were then subjected to further rounds of distribution and dilution as above. In this way it was a simple matter to purify freezing nuclei to the point where they represented one in fewer than 20 cells. Unless one wishes to claim that each so-called cell is itself a multicellular aggregate, the above experiments rule out the cooperative mode of nucleus origination. In a second experiment, culture containing freezing nuclei passed through filters which trapped multicellular clumps (i.e. 1.2 µm pore size). Since the filtered culture still possessed the freezing capability, the idea of aggregation as a required criterion for efficient INA was ruled out.

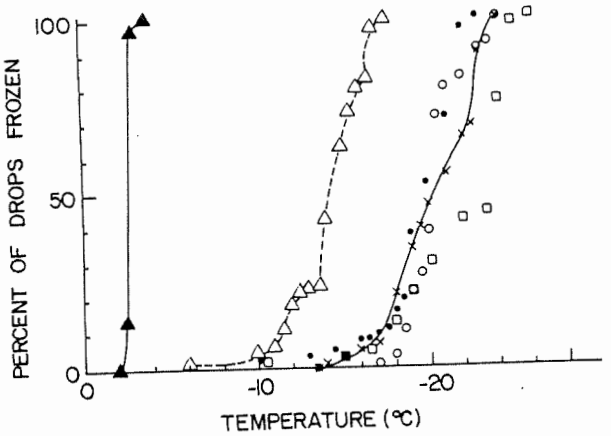

Fig. 2. Freezing temperature spectra of drops containing various ice nuclei, - M1 bacteria; , and - other yellow bacteria (named L1, L2 and L3 respectively) also isolated from citrus leaves. L1 cannot be distinguished from M1 by either colony morphology or substrate range; L2 differs from M1 with respect to substrate range; and L3 is distinguished from M1 by the fact that it forms rough colonies. x - saline (NaCl) solution. - drops exposed to AgI aerosol particles.

It was further established by plating all of the individual cells in an enrichment, freezers and non-freezers alike, on nutrient agar that the number of freezing nuclei per unit cell number in resulting colonies was always the same. In other words, the factors which determine whether a given cell will generate or not generate freezing nuclei at any given moment are physiological in nature, and not genetic. Once again, the queen-bee analogy would seem to be pertinent.

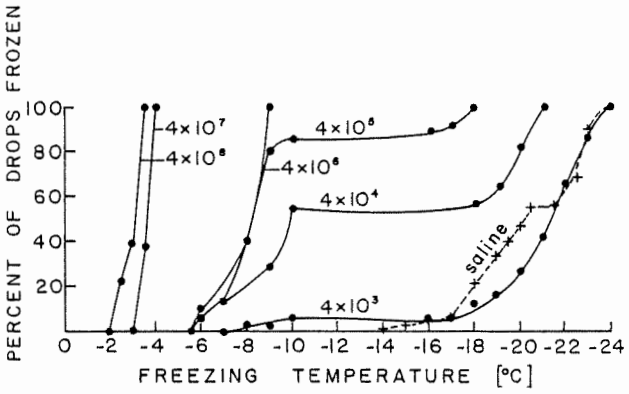

Fig. 3. Freezing temperature spectra of drops containing M1 at different concentrations. The few good INA bacteria among M1 population are responsible for the freezing of drops down to -4^0C. The grouping of curves between -6^0 to -10^0C is a result of the freezing due to the rest of M1. The lowest freezing temperatures (< -16 C) are caused by the very inactive bacteria and the saline itself.

C. Freezing Nucleus Activity of Subcellular Fractions.

In contrast to what has been found with other INA bacteria (Maki and Willoughby, 1978), fragments derived from whole cells by sonic vibration retained activity at temperatures warmer than -5^0C. It was possible to pass such sonicates through 0.45 µm pores without loss of activity, whereas 0.1 µm pores did not allow nuclei to pass through. Moreover, the number of nuclei in sonicates approximately equalled that originally present in the starting cells. Thus, there would appear to be about 1 nucleus per cell incorporated into some sort of very large subcellular structure. An obvious candidate would, of course, be the surface wall of the organisms.

D. Mode of Nucleation.

Preliminary tests in which anhydrous bacterial colonies on membrane filters were placed in a standard ice nuclei counter (Gagin and Aroyo, 1969) suggest that

bacterium M1 is not active as a deposition nucleus at temperatures higher than -8^0C when tested under conditions of water subsaturation. On the other hand, when the atmosphere in the chamber reached supersaturation with respect to water, ice crystals grew. This latter finding suggests that M1 acts as a condensation-freezing nucleus. Conclusive results must, however, await further testing. Also in progress are parallel studies on the mode of action of subcellular nuclei.

E. Concentration of INA Bacteria in the Atmosphere.

The leaf origin of M1 and other INA micro-organisms suggest their easy dissemination through the atmosphere. Such organisms can be incorporated into clouds acting as ice or condensation nuclei (Soulage, 1957 and Dingel, 1966) or be swept out by rain or snow. (Mandrioli et al, 1973). Since the number of INA bacteria per unit area of citrus leaf surface suggests some variation with season (i.e. is maximal in winter), it might also follow that the number density concentration of INA bacteria in the atmosphere may vary similarly. The possibility is under current investigation. Air samples of 5000 l are periodically collected onto 0.45 μm filters and deposited bacteria allowed to grow out into colonies at 4^0C on nutrient agar. After 2-4 weeks of growth, each visible colony on a filter is tested for its freezing nucleus function. Thus far we have obtained various sorts of bacteria active at temperatures ranging from -4^0 to -8^0C. However, not one of these isolates retains the INA trait on further cultivation in the laboratory, and not one single isolation of M1 has yet been made. The study is continuing.

F. Possible Application to Cloud Physics and Weather Modification.

If bacterially-derived ice nuclei can effectively grow ice crystals to sizes large enough to initiate riming in clouds at temperatures around -5^0C, their advantage over currently used nuclei in rain enhancement operations becomes obvious. One way to evaluate the effect of ice formation at such a warm temperature on the formation of precipitation is through simulation in a numerical cloud model. Another would be experiments in laboratory cloud chambers and, eventually, by actual seeding trials in the field. In this latter regard, the number of nuclei needed can be calculated. For example, in typical cloud seeding operations, about 10-30 artificial nuclei per liter are released. For a cloud updraft of 2 km diameter and 4 km height, the number of nuclei needed to give a density of 10 per liter would be $1x10^{14}$. Assuming 1 nucleus per 5000 M1 cells, the corresponding cell number is some $5x10^{17}$. Standard cell yields are approximately $5x10^{12}$/l of culture. Therefore, as things now stand, we would require 10^5 l of culture per experiment. Clearly then, even if modeling suggests feasibility, some way to increase the nucleus to cell ratio in cultures must be found. Search for ways to do so is now underway.

References

Dingel, A.N. 1966: Pollens as condensation nuclei. J. Rech. Atmos. 2, 231-237.

Gagin, A. and M. Aroyo, 1969: A thermal diffusion chamber for the measurement of ice nuclei concentration. J. Rech. Atmos. IV, 115-122.

Lindow, S.E., D.C. Arny, C.D. Upper and W.R. Barchet, 1978: The role of bacterial ice nuclei in frost injury to sensitive plants. p. 244-263. P. Li and A. Sakai Editors, Plant cold-hardiness and freezing stress mechanisms and crop implications. Acad. Press, Inc. N.Y.

Maki, L.R., E.L. Galyan, M.M. Chang-Chien and D.R. Caldwell, 1974: Ice nucleation induced by "Pseudomonas Syringae". Appl. Microbiology, 28, 456-459.

Maki, L.R and K.J. Willoughby, 1978: Bacteria as biogenic sources of freezing nuclei. J. Appl. Meteor. 17, 1049-1053.

Mandrioli, P., G.K. Pappi, N. Bagni and F. Prodi, 1973: Distribution of microorganisms in hailstone. Nature, 246, 416-417.

Schnell, R.C. and G. Vali, 1976: Biogenic ice nuclei. Part I: Terrestrial and Marine sources. J. Atmos. Sci. 33, 1554-1564.

Soulage, G., 1957: Les noyaux de congelation de l'atmosphere. Ann. Geophys. 13, 103-134.

Vali, G., 1971: Quantitative evaluation of experimental results on the heterogeneous freezing nucleation of supercooled liquids. J. Atmos. Sci. 28, 402-409.

Vali, G., M. Christensen, R.W. Fresh, E.L. Galyan, L.R. Maki and R.C. Schnell, 1976: Biogenic ice nuclei, Part II: Bacterial sources. J. Atmos. Sci. 33, 1554-1564.

Size Distribution of Inorganic and Organic Ice-forming Nuclei Present in Downdrafts of Convective Storms

J. Rosinski, G. Morgan, C.T. Nagamoto, and G. Langer
National Center for Atmospheric Research
Boulder, Colorado U.S.A.

and

G. Yamate
Illinois Institute of Technology
Research Institute

and

F. Parungo
National Oceanic and Atmospheric Administration
Boulder, Colorado, U.S.A.

Introduction

Large increases in the concentration of ice-forming nuclei (IFN) were observed at ground level in thunderstorm downdrafts for the first time by Georgii [3]. This has been substantiated by others, most recently by Langer, et al. [6].

The questions posted by these observations are: what are these aerosol particles which acted as ice-forming nuclei and where did they come from? Why did the concentration of aerosol particles active as ice-forming nuclei increase up to three orders of magnitude while the general population of aerosol particles showed hardly any change? Experiments were performed in an attempt to answer some of these questions.

Experimental procedures

An NCAR ice nucleus counter equipped with a special low-velocity circular or slit impactor was used during the summer of 1978 in N.E. Colorado to collect single ice crystals grown on ice-forming nuclei [5]. Ice crystals (d_{ice}>20 μm) separated from cloud droplets (d_{water} ~6 μm) were deposited on the surface of either a vitreous carbon black or a nuclepore filter. The separated ice crystals were allowed to sublime at temperatures below 0°C. Lithium chloride particles used as condensation nuclei were not detected in the residues; the detection limit for Li is 10^{-7} atomic percentage due to a lack of interference with other elements. This indicates that droplets and aerosol particles scavenged by droplets did not contaminate separated IFN under the experimental conditions.

Particle size distributions of X-ray emitting (inorganic) and non-emitting (organic) particles which acted as ice-forming nuclei were determined from the screens of the scanning electron microscopes.

An ion microprobe analyzer (W.C. McCrone Associates, Inc., Chicago, Illinois, U.S.A.) used lithium detection as a means of evaluating the scavenging of cloud droplets by growing ice crystals [8].

Results

Size distributions of ice-forming nuclei, inorganic and organic, separated under different meteorological conditions are given in Fig. 1 and 2.

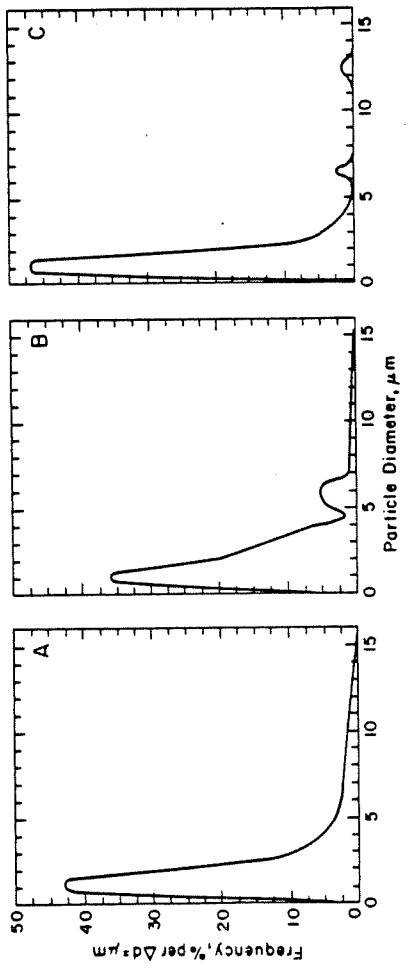

Fig. 1. Size distribution of ice-forming nuclei active at -20°C. (A-all particles, B-inorganic particles, C-organic particles; 278 particles sized; exp. 1, 2, 7, and 8). [Background during convective storm activity].

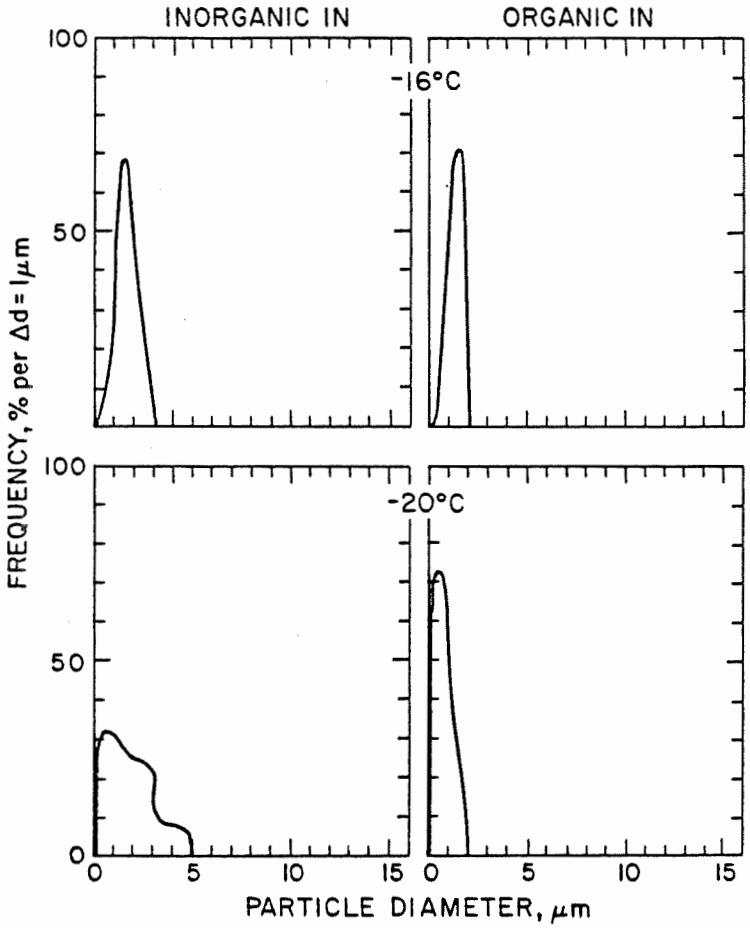

Fig. 2. Size distribution of ice-forming nuclei separated at -16°C and -20°C. (exp. 3 and 4; 9-10 July; 175 and 250 particles sized). [Downdraft]

Discussion

A large percentage of the air in the thunderstorm outflow has its origin in the dry, low θ_e air typically found in the middle troposphere (altitudes of 4 to 7 km). It can be speculated that this wind-level air mass is the source, or one of the sources (e.g., part of air in the updraft mixing with the down-draft air), of these aerosol particles, and perhaps of IFN. Examination of thermodynamic soundings in the near-storm environment shows an ample (1 km thick or more) subfreezing layer to be generally available for the downdraft.

The descent of the low θ_e air is believed to be due to the chilling effect of evaporating rain and cloud particles. Aerosol particles present in the initially dry air are brought, therefore, into the proximity of evaporating cloud particles. A fraction of these aerosol particles colliding with supercooled droplets in the downdraft will nucleate ice by contact.

Concentrations of aerosol particles in the 0.3 to 2 μm diameter size range over N.E. Colorado are approximately 10^7, 10^6, and $10^5 m^{-3}$ at altitudes of 2, 3, and 6 km, respectively; these concentrations are of course variable in time and space [1].
The updraft air frequently contains particles in the 0.1 to 2 μm diameter size range in concentrations of up to 10^9 particles m^{-3}; concentrations of $10^8 m^{-3}$ are quite common. These particles survive in-cloud scavenging and are transferred into the downdraft when part of the updraft mixes with downdraft air. It was shown by Greenfield [4] that aerosol particles in this size range are too large to be removed by Brownian scavenging and too small to be scavenged by aerodynamic interaction between cloud and aerosol particles. The net balance of the phoretic forces in a downdraft favors capture of the aerosol particles smaller than 1 μm diameter by evaporating cloud droplets through thermophoretically induced drift [9,10]. The same drift but of opposite direction in the updraft prevents capture of aerosol particles by growing droplets through condensation, thus providing additional force to protect aerosol particles in the "Greenfield gap" from being scavenged.

Not every collision between an aerosol particle and a droplet results in the freezing of a droplet because only a fraction of the aerosol particles can nucleate ice at any particular cloud temperature. In-cloud conditions favorable for ice nucleation by contact are present in downdrafts or in the presence of ice particles; both conditions induce collisions between evaporating cloud droplets and aerosol particles.

The experimentally determined thermal velocity [7] diminishes at approximately 2 μm diameter aerosol particles, indicating that there is a cut-off at about 2 μm diameter for aerosol particles during aerosol-cloud particle interactions; this seems to have been confirmed by our observations.

Aerosol particles which acted as contact ice-forming nuclei should become IFN active at some warmer temperatures after the ice they produced at the temperature of their ice nucleation in the downdraft is evaporated [2]. Laboratory experiments with particles from different soils from N.E. Colorado have indeed shown the formation of IFN through this process. The temperature at which these IFN became active were up to 9°C warmer than the temperatures at which the original aerosol particles nucleated ice. If this explanation of the origin of IFN in the 0.1 to 2 μm diameter size range is correct, then the entire population of IFN present in the outflows of convective storms most likely was never involved directly in the formation of precipitation produced by that storm. Only some of these IFN could be a source of IFN for a parent storm through mixing of the downdraft air with the updraft; most of them can supply IFN to an adjacent storm in the area.

It should be emphasized that the narrow size distributions observed for separated inorganic and organic IFN indicate that a physical process and not the chemical composition was responsible for the classification of aerosol particles. Activation of organic particles into IFN has never been reported in the literature.

Conclusions

Both inorganic and organic aerosol particles were found to be ice-forming nuclei in the convective storm environment. Inorganic IFN were

usually more abundant than organic IFN, but on few occasions both were present in equal concentrations. Organic spherical particles in the 0.01-0.1 μm diameter size range were separated as ice-forming nuclei on one occasion.

Size distributions of separated IFN indicate the presence of particles predominantly in the 0.1-2 μm diameter size range. If they are activated through the evaporation of the ice they produced in storm downdrafts, they may then constitute a source of IFN for the parent storm or some other storm in the area through recycling. The presence of both inorganic and organic particles as IFN indicate that a physical process is the basis for size classification. Measuring the population of IFN in order to understand and model their role in ice formation within clouds must therefore include not only separation of IFN for the purpose of determining their size distribution and nature but also analysis of the trajectories of IFN-rich air parcels.

The lack of knowledge of the trajectories of air masses makes measurements of the "background" IFN population during convective storm activity meaningless.

Results of this study pertain to the population of ice-forming nuclei present during convective activity over N.E. Colorado.

References

[1] Blifford, I.H., Jr. and Ringer, L.D., 1969. J. Atmos. Sci., 26, 716.
[2] Fournier d'Albe, E.M., 1949. Quart. J. Roy. Meteor. Soc., 75, 1.
[3] Georgii, H.W., Geofisica Pura e Applicata, 1959, 42, 62.
[4] Greenfield, S.M., 1957, J. Meteor., 14, 115.
[5] Langer, G., Rosinski, J. and Edwards, C.P., 1967, J. Appl. Meteor., 6, 114.
[6] Langer, G., Morgan, G., Nagamoto, C.T., Solak, M. and Rosinski, J., 1979, J. Atmos. Sci., 36, 2484.
[7] Prodi, F., Santachiara, G. and Prodi, 1979, J. Aerosol Sci., 10, 421.
[8] Rosinski, J., Langer, G., Nagamoto, C.T. and Bayard, M.C., J. Rech. Atmos., 10, 243.
[9] Rosinski, J. and Kerrigan, T.C., 1977, J. Rech. Atmos., 11, 77.
[10] Slinn, W.G.N. and Hales, J.M., 1971, J. Atmos. Sci., 28, 1465.

SEASONAL CHANGES AND TERRESTRIAL SOURCES OF ATMOSPHERIC ICE NUCLEI AT BOULDER, COLORADO

R. C. SCHNELL
CIRES Associate, NOAA/ERL/ARL, Boulder, Colorado, 80303, U.S.A.

B. WROBEL
Institut Fur Meteorologie, Johannes Gutenberg Universitat
Mainz 6500, Federal Republic of Germany

S. W. MILLER
NOAA/ERL/ARL, Boulder, Colorado, U.S.A.

I. INTRODUCTION

Atmospheric ice nucleus (IN) concentrations have been measured at 20 m AGL at Boulder, Colorado on a regular basis since July of 1978 and at irregular intervals at ground level over various terrestrial surfaces, using a combination membrane filter-drop freezing technique in which the freezing temperatures of clean distilled water drops placed on exposed membrane filters are taken to be a measure of the IN in the air (Schnell, 1979). The data in that report (ibid.) suggested that atmospheric IN concentrations decreased immediately following the passage of snow producing cold fronts with recovery to pre-snow levels over the space of a few weeks, as the snow cover melted. In this present report, the results from 3 months of IN measurements in a summertime period are presented along with data from tests on aging and exposure of IN to vacuum treatments.

The IN measurement technique used in these studies has not undergone the rigors of extensive intercomparison with more established methods of IN detection, thus the data presented herein are best regarded as being internally comparable and consistent but not absolute values until the results of intercomparison studies are published. It may be observed though, that in the data presented below, the relative concentrations and changes in observed IN activity can be related to meteorological and physical factors with precision and, on some occasions, with a degree of predictability.

II. ATMOSPHERIC ICE NUCLEUS CONCENTRATIONS

The temperature at which threshold IN activity and concentrations of 500 nuclei m^{-3} were observed over the period of June 18 through August 15, 1979 are shown in Figure 1. From this Figure it may be seen that the passage of cold fronts which introduced new air masses of northern origins to the Boulder area were coincident with decreases in IN threshold temperatures and in IN concentrations. The IN concentrations are seen to recover within a few days following frontal passage as is well illustrated by the measurements associated with the frontal passage of July 24, 1979. Another interesting feature of the summer's IN record is the persistent period of low IN concentrations from August 2 through 6, 1979. This period was coincident with a heat wave and dry period over the Western USA resulting in part from a large zone of persistent subsiding air of upper level origins. Relative hu-

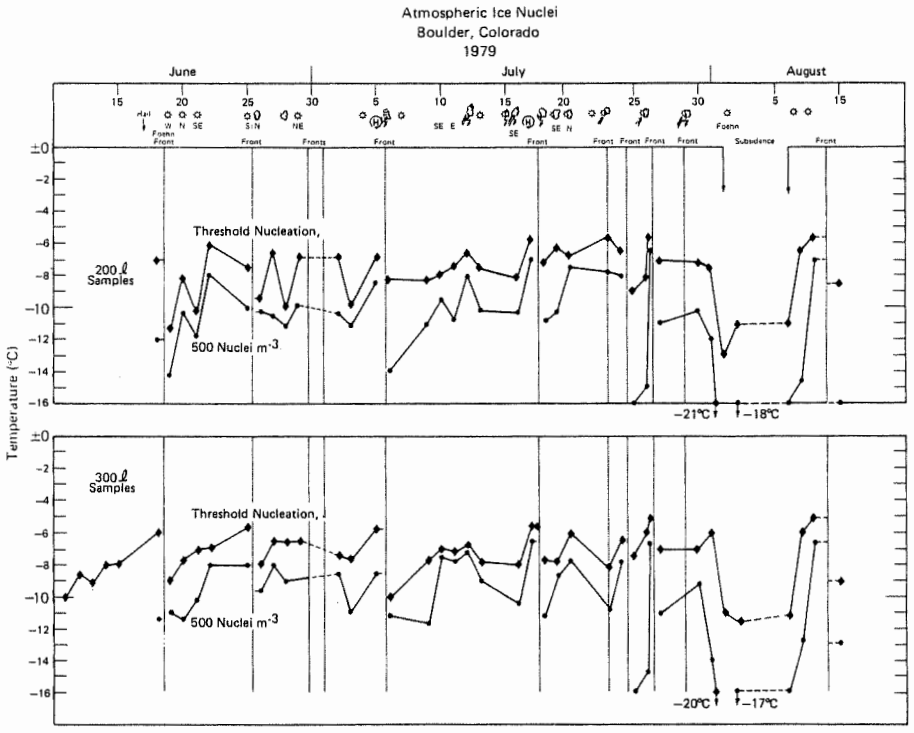

Figure 1. Atmospheric ice nuclei measured at 60 m AGL at Boulder, Colorado in the summer of 1979 showing threshold activity and the temperatures at which 500 nuclei m^{-3} were observed for 200 ℓ and 300 ℓ air samples. The decrease in atmospheric ice nucleus concentrations following frontal passages and the persistent low concentrations measured during a period of large scale subsidence (August 1-6) are worthy of note.

midities in Boulder during this period were occasionally as low as 17%. Along with a change in the air mass on August 6 and 7, IN concentrations returned to previous levels. This pattern has been observed on two subsequent occasions.

III. RELEASE OF ICE NUCLEI FROM TERRESTRIAL SURFACES

It has been shown by Schnell and Vali (1976), that naturally decayed plant litter contains numerous freezing nuclei active within the temperature range from -4°C and -8°C. In experiments designed to measure the release rates of these IN from terrestrial surfaces, filters were exposed at 5 cm above a variety of vegetated and cultivated soils in and near Boulder. The results from one set of tests are shown in Fig. 2 where it may be observed that on July 13, 1979, under calm wind conditions, (left-hand graph) the ambient air above the grass contained IN active at -6.5°C and -7.8°C in 50 ℓ and 25 ℓ samples in concentrations in the region of 1 nucleus ℓ^{-1} active at -8°C. At 20 m vertical and 400 m horizontal from the grass plot, an air sample of 250 ℓ exhibited threshold nucleation at -8.1°C in concentrations of 1 nucleus ℓ^{-1} active at -11.5°C. Disturbing the surface by agitation of the grass with a 20 cm long piece of coiled rope released greater numbers of nuclei than were in the ambient air. The freezing nuclei in a bulk sample of the surface leaf litter tested with the drop freezing technique (Schnell and Vali, ibid.) is also shown. It is interesting to note that the threshold activity of the IN from the larger (50 ℓ) sample of air above the agitated surface is equal to that in the bulk sample of the leaf litter suggesting that the IN on the filter were the same as the IN in the leaf litter.

A somewhat different picture was observed over the same grass plot on September 14, 1979 following a 3-day period of rain (right-hand portion of Fig. 2). There it may be seen that there were few IN in the ambient air above the wet grass. By disturbing the surface, appreciably greater numbers of IN were released to the air although their numbers and activity were lower than when the same grass was dry. The IN spectra for the bulk leaf litter and for ambient air at 20 m AGL for this day are also presented.

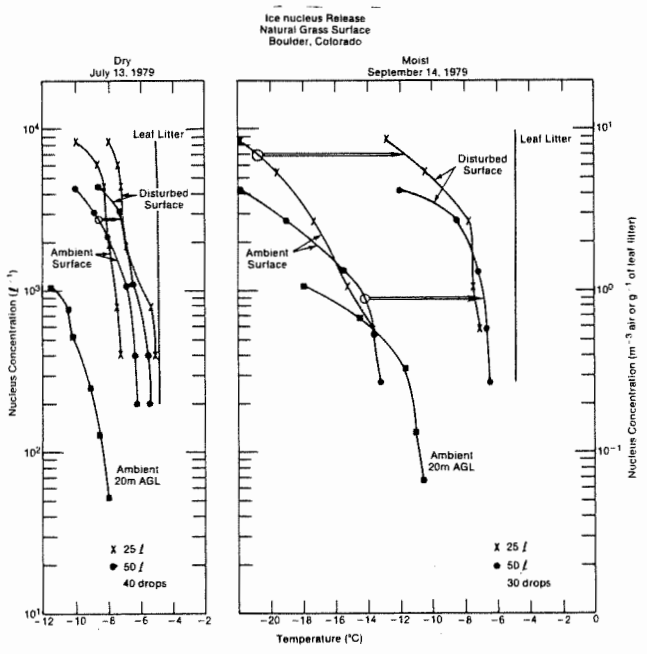

Figure 2. Ice nucleus concentrations measured in air at 5 cm above a dry grass surface (left-hand graph) and above the same grass surface (right-hand graph) following a 3-day period of rain. The open circles indicate the number of freezing nuclei measured in samples of decayed leaf litter from the surface of the soil.

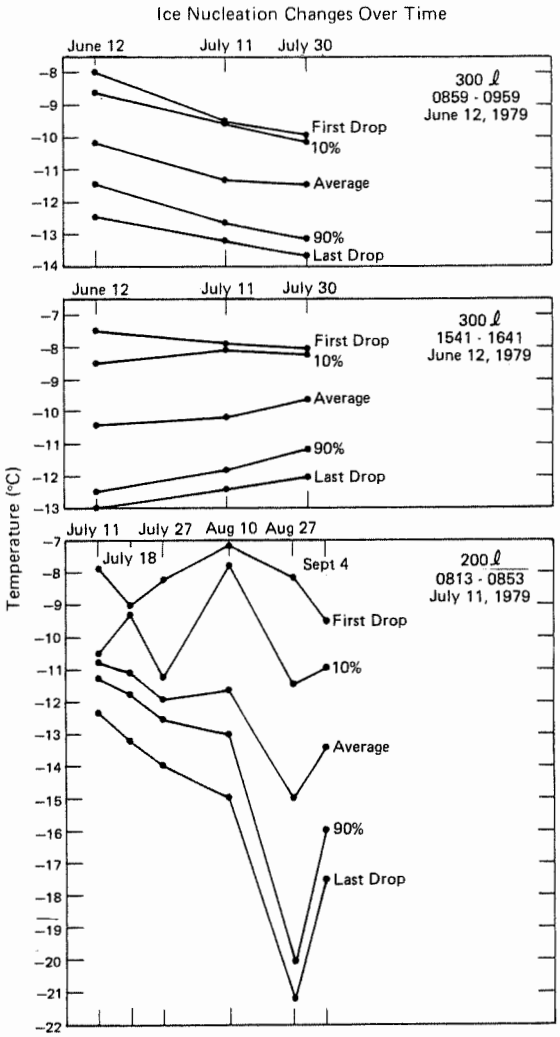

Figure 3. The freezing ranges of 20 drops of distilled water placed on membrane filters which were exposed in sets and stored for various periods of time prior to testing. The general decrease in the nucleation characteristics of the aerosols on the filters collected July 11, 1979 are of interest.

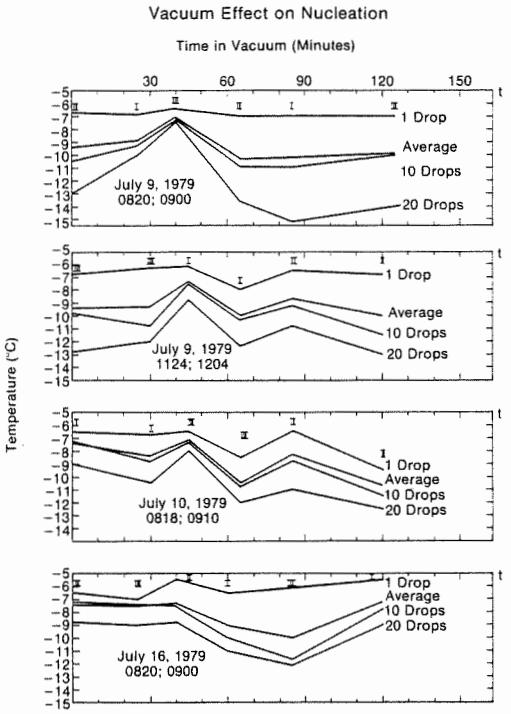

Figure 4. The freezing range of 20 drops of distilled water placed on membrane filters which were exposed in triplicate, halved, then placed in a 10^{-6} Torr vacuum for various periods of time prior to testing. Halves from the same filters are indicated by Roman numerals. A general increase in ice nucleation activity after a vacuum treatment of about 40 minutes is predominate on filters exposed on July 9 and 10, but not on July 16.

IV. ICE NUCLEUS ACTIVITY CHANGES WITH TIME

During the early stages of this research project, it was noted that separate halves of a filter occasionally produced different IN spectra when processed at times separated by a few days. To quantify these observations, a series of triplicate and sextuplicate filters were exposed to natural air, stored at room temperature in sealed petri dishes, and then processed singly over time intervals varying from a few hours to a month. The range of changes observed in the IN activity are shown in Fig. 3 where the freezing temperatures of 20 drop samples are plotted. From Fig. 3 it may be seen that there was a slight but steady decrease in IN activity on the filters collected on the afternoon of the same day. The filters exposed on July 11, 1979 exhibited a notable spreading of the freezing range after 1 month of storage, followed by a slight recovery of activity. In other tests, little change in IN activity was observed to occur on filters stored less than 2 days. These results suggest that the IN on the filters are either changing in themselves over time, or are reacting with the filters in some as yet unexplained and apparently random manner. If the nuclei are indeed changing, this suggests that they may contain unstable organic materials or adsorbed gases which can change or be removed over time. These changes also raise questions about the validity of data obtained from filters stored more than a few days.

V. EFFECT OF VACUUM ON NATURAL ICE NUCLEI

In an experiment to test the volatility of natural IN, triplicate filters were exposed to natural air, halved, and then all but one portion subjected to a vacuum of 10^{-6} Torr for time periods ranging from 20 minutes to 125 minutes prior to testing for IN activity. The results from 4 such tests are shown in Fig. 4 when it may be seen that in 3 out of 4 cases the IN activity was significantly increased at around 40 minutes of treatment, to be followed by deactivation at from 60 minutes to 80 minute of treatment. At 80 minutes to 120 minutes, 2 filter sets exhibited further deactivation and 2 sets exhibited reactivation. In other tests, 36 out of 48 filters collected between June 2 and July 16, 1979 exhibited an activation of IN at and around 40 minutes of treatment, to be generally followed by some deactivation between 80 and 120 minutes. These results suggest that the vacuum may have removed some gaseous or liquid component of/on the IN which was suppressing nucleation or that removal of some component of the nuclei produced a new structure which was more active. Continued exposure to the vacuum further changes the nature of the nuclei such that either deactivation and/or further reactivation occurs over time. Again, the possibility that the filter material and the deposited aerosols may somehow be reacting to produce the observed results must not be discounted at this point.

VI. DISCUSSION

The changes in atmospheric IN concentrations which were observed during this study (using a combination membrane filter-drop freezing technique) can be related to large scale meteorological effects, thereby suggesting a cause and effect relationship controlled by the meteorological characteristics /life history/ source region of a particular air mass. These results are similar to those embodied in the data collected in an ice nucleus benchmark as reported by Allee (1974). Also, Rogers and Vali (1978) and Langer et al.,(1979)have presented data which suggests that atmospheric IN concentrations fluctuate on the mesoscale in response to gust fronts and local wind patterns, and that these effects are measurable from ground level up to cloud base. The present results differ from these earlier results mainly in that the threshold nucleation temperatures we detect are generally 6 to 10°C warmer than reported in the other studies, and in that the concentrations of IN we measured were appreciably greater at temperatures warmer than -10°C. The initial increase in IN activity resulting from the outgassing treatment on the filters is similar to that noted by Parungo et al., (1978) for filter samples collected in powerplant plumes, although in the present study the samples were collected in relatively clean

air. In the powerplant studies, removal of adsorbed IN suppressing pollutant gasses from the surface of the IN was suggested as being a factor in the enhanced nucleation affects observed.

Based on the results from the surface measurements of IN, and the results from the ambient temperature and pressure tests, we suggest that the IN observed on filters both at the surface and at 60 m AGL were surface derived, and that the nuclei probably contained an appreciable component of biogenic material.

ACKNOWLEDGMENTS

This research was supported by Dr. H. K. Weickmann, then Director, NOAA/ERL/APCL with support from Dr. R. F. Pueschel, NOAA/ERL/ARL. Funds were provided by the National Research Council Research Associate Program, the Cooperative Institute for Research in Environmental Sciences, and, in part, by the Environmental Protection Agency through Interagency Agreement 78 REGEHE-625/D5-E693.

REFERENCES

Allee, P.A., 1974: Ice nuclei concentration measured by a benchmark network. Preprints, 4th Conf. on Weather Modification, Ft. Lauderdale, Florida. American Meteorological Society, pp. 242-245.

Langer, G., G. Morgan, C. T. Nagamoto, M.Solak and J. Rosinski, 1979: Generation of ice nuclei in the surface outflow of thunderstorms in northeast Colorado. Jr. Atmos. Sci., 36, pp. 2484-2494.

Parungo, F., E. A. Ackerman, H. Proulx, and R. Pueschel, 1978: Nucleation properties of fly ash in a coal-fired powerplant plume. Atmos. Environ., 12, pp. 929-935.

Rogers, D. C. and G. Vali, 1978: Summer climatology of aerosols and nuclei in the central high plains of the U. S. Preprints, Conf. on Cloud Physics and Atmospheric Electricity, Issaquah, Washington. American Meteorological Socity, pp. 25-30.

Schnell, R. C., 1979: A new technique for measuring atmospheric ice nuclei active at temperatures from -20°C to approaching 0°C, with results. Preprints, 7th Conf. on Inadvertant and Planned Weather Modification. Banff, Canada. American Meteorological Society, pp. 110-111.

Schnell, R. C. and G. Vali, 1976: Biogenic ice nuclei; part I. terrestrial and marine sources. Jr. Atmos. Sci., 33, pp 1554-1564.

SESSION II - PROCESSUS MICROPHYSIQUES
Microphysical Processes

II.1 - Gouttes de Nuage
Cloud Droplets

THE NON-ZERO CLOUD DROPLET KERNEL FUNCTION

Fausto C. de Almeida

Fundação Centro Tecnológico, CETEC
Belo Horizonte, BRASIL

1. Introduction

In studying the growth behavior of a cloud droplet population, the kernel function of the stochastic collection growth equation(Mason,1971) is a defining factor(Almeida,1979.a).

This function has been dealt in general as a consequence of the collision efficiency function, and in reality little has been done to analize it as a function in itself accessing its representativeness of the physical phenomena being simulated. In this respect, more has been done about its pure mathematical aspects than what it really represents even on the light of more recent theoretical and laboratory results.

2. The non-zero kernel

Recently, Almeida(1976,1979.b) treating the problem of cloud drop interactions in a turbulent environment has offered a more general definition of the kernel function, that allows the investigator to analyze deterministic as well as probabilistic cloud drop interactions.

Using this more general definition it became clear that the usual definition of the kernel function,- as the product of the collision efficiency times the terminal velocities difference, not only neglects the interactional behavior of the collisional problem, by using terminal velocities calculated, as the drops were falling in isolation, instead of the actual collisional velocities (Almeida,1978) but also attaches a zero value to the kernel function, for equal size drops, regardless of the value calculated for the collision efficiency. In other words, even if a collision between equal size drops is observed as possible, this widely used definition negates this very outcome.

Evidence has been piling up in the literature (e.g., Telford and Thorndike, 1961; Woods and Mason, 1965; Almeida, 1978 among others) that equal size drops can and do actually collide, resulting in calculated values for the collision efficiencies that are different than zero for all size ratios. Indeed, all published gravitational collision efficiencies have indicated (assumed or calculated) a different than zero value for nearly equal or equal size drops (Hocking and Jonas, 1970; Davis and Sartor, 1967; Klett and Davis, 1973; Almeida, 1979.b, and others).

Note then, that in actual numerical simulations, although the values for the collision efficiencies entered in the model would assure possible collisions between two equal size drops, the use of the 'usual' definition for the kernel function negates this very possibility.

Although it is easier to calculate from an analytical formula the values of the terminal velocities than it is to interpolate a table of mean collisional velocities in order to define the kernel function in actual cloud models calculations, the same look-up procedure used to find the collision efficiencies can be used to find the mean collisional velocities from another table. For calculating the mean collisional velocities (Almeida, 1978), this extra book-keeping in terms of parameter calculations, means only a very small increase in computer time, when compared to a simple collision efficiency instead of a collision efficiency plus a collisional velocity calculation.

What this written presentation wants to emphasize is the need - "not-to-deny" this possibility in cloud models or any other calculation; to investigate this non-zero behavior of the kernel function in the growth of a cloud droplet population; and to review its effect on mathematical schemes developed to solve the stochastic collection equation.

3. Remarks

Responding to the organizers of the conference, and to make the central point of the paper stronger it was decided to limit the scope of this written presentation, leaving the other discussion topics to the oral and round table discussions.

4. References

Almeida, F. C. de, 1976: The collisional problem of cloud droplets moving in a turbulent environment-Part I: A method of solution. J. Atmos. Sci., 33, 1571-1578.

_____, 1978: Height dependence and volume definition of the collision kernel function for cloud droplets. AMS Conf. Cloud Physics, July 31-August 4, Issaquah, Washington.

_____, 1979.a:The effects of small scale turbulent motions on the growth of a cloud droplet spectrum. J. Atmos. Sci., 36, 1557-1563.

_____, 1979.b: The collisional problem of cloud droplets moving in a turbulent environment-Part II:Turbulent collision efficiencies. J. Atmos. Sci., 36, 1564-1576.

Davis,M. H., and J. D. Sartor, 1967: Theoretical collision efficiencies for small cloud droplets in Stokes flow. Nature, 215, 1371-1372.

Hocking,L.M.,and P.R. Jonas,1970: The collision efficiency of small drops. Quart.J.Roy.Meteor.Soc.,96,722-729.

Klett,J.D.,and M.H.Davis,1973:Theoretical collision efficiencies of cloud droplets at small Reynolds numbers. J.Atmos.Sci.,30, 107-117.

Mason,B.J., 1971: The Physics of Clouds. Claredon Press, 671 pp.

Telford, J. W., and N.S.C. Thorndike, 1961: Observations of small drop collisions. J. Meteor., 18, 382-387.

Woods, J. D., and B. J. Mason, 1965: The wake capture of water drops in air. Quart. J. Roy. Meteor. Soc., 91, 35-43.

PHORETIC SCAVENGING OF MICRON SIZE PARTICLES BY CLOUD DROPS

K. V. Beard*, K. H. Leong, and H. T. Ochs
Illinois State Water Survey
Urbana, Illinois, USA

1. Introduction

Since thermal and vapor density gradients are usually encountered in the vicinity of cloud drops and ice crystals, aerosol particles are subjected to thermophoretic and diffusiophoretic forces. Phoretic forces have only been studied recently as scavenging mechanisms and are not as well understood as other mechanisms such as nucleation and Brownian capture. Facy's (1955) experiments indicated that thermophoresis was relatively unimportant for growing and evaporating drops. However, later work (Deryagin and Dukhin, 1957; Slinn and Hales, 1971; Styra and Tarasyuk, 1974) indicated that the temperatures of the drops in Facy's experiment were not well controlled and thermophoresis could be larger or comparable to diffusiophoresis. Slinn and Hales recognized the dominance of thermophoresis over diffusiophoresis for particles less than 1 μm radius in their evaluation of scavenging mechanisms. They showed that phoretic forces were the major scavenging mechanism in the 0.1-1 μm particle range. A primary mechanism for precipitation initiation, the contact nucleation of supercooled droplets, is thought to be significantly enhanced by phoresis (Young, 1974). Hogan (1976) suggested that phoresis may account for scavenging rates measured in Hawaiian trade wind cumulus, and that phoresis may provide a major sink of particles at cloud level and an important source of large particles aloft.

Several capture efficiency experiments have been conducted in subsaturated air, but the effects of phoresis have usually been disregarded. Wang and Pruppacher (1977) have produced the only available experimental data on the phoretic scavenging efficiency of evaporating drizzle and rain size drops (100-2500 μm radius). The values obtained were believed to show good agreement with the efficiency calculations of Grover *et al.* (1977). In this paper we discuss the preliminary results from measurements of scavenging by falling cloud drops (i.e., <100 μm radius).

2. Method

The design of the experiment is illustrated by the schematic diagram in Fig. 1. The basic technique is to produce a stream of widely spaced drops of uniform size which fall at terminal velocity through a cloud of monodisperse particles at a known temperature and humidity. The drops are collected at the bottom of the cloud and analyzed for the mass of particles collected by atomic absorption/emission (AAE) analysis. The major features of the experiment are the cloud drop generator, aerosol generator, neutralizer, humidifier and aerosol chamber.

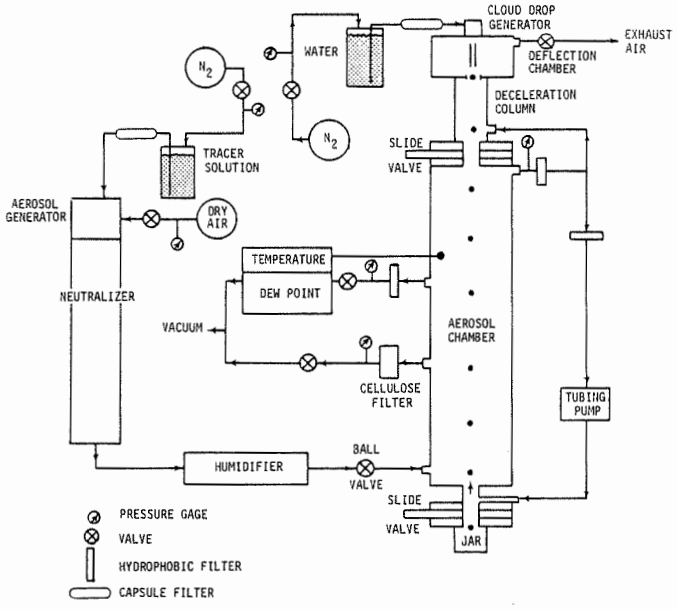

Figure 1. Diagram of experimental apparatus used to measure capture efficiencies.

Drop Generation. The method of drop formation has been described by Adam *et al.* (1971). Water is forced through a pinhole and a jet instability is excited at a chosen frequency by a piezoelectric crystal producing a stream of uniform size drops. A pulse controlled charging ring and deflection plants are used to separate charged drops from the uncharged ones. The residual charge on the drops falling into the chamber can be computed from the horizontal displacement of a decelerating drop by using the drag, electric force and initial conditions. For drop sizes of 60 to 90 μm the residual charges are less than 2×10^{-15} and 5×10^{-14} coulombus respectively. The drops achieve terminal velocity in the deceleration chamber before entering the aerosol chamber. Thermal equilibrium is also attained by the drops according to Davies (1978).

Aerosol Generation. A monodisperse cloud of droplets is generated by a Berglund-Liu generator (TSI Inc. 3050). A pressure reservoir is used instead of a syringe pump to produce a wider range of constant feed rates. The aerosol substances were disolved in dionized water. A 0.2 μm capsule filter is used between the reservoir and generator to eliminate plugging of the pinhole. Dry air is used for the dispersion and dilution flow to promote rapid evaporation of the solution drops. The charge on the particles is reduced to Boltzman equilibrium by ion capture as they pass through the neutralizer (TSI, Inc. 3054). The particle mass is obtained accurately from a measure of the solution feed rate, the generation frequency and solute concentration.

Humidity Control. The relative humidity within the aerosol chamber is dependent on the water evaporated from the solution drops and the

* Also affiliated with the Laboratory for Atmospheric Research, University of Illinois.

temperature of the room. With a value of 40 psi in the tracer reservoir and pinhole sizes of less than 10 μm, relative humidities of less than 50% are produced. Higher humidities are attained by wetting the absorbent paper wall of the 2.3 m long pipe between the neutralizer and aerosol chamber.

The Aerosol Chamber. The aerosol chamber consists of a 1 m long plexiglass cylinder with an inside diameter of 15 cm. Before an experimental run, both slide valves are closed and a continuous flow of aerosol is introduced into the chamber through a ball valve for over 8 min. The aerosol particles are removed by a large hydrophobic filter on exiting the camber and fed back into the base of the deceleration column. Clean air is introduced continuously above the bottom slide valve at a rate of 4.3 mL s^{-1} to prevent aerosol particles from entering the collector jar. Before the ball valve is closed the dewpoint is measured through a port located halfway up the chamber by an EG&G 911 digital humidity analyzer (±0.2C) which is also used to monitor the temperature (±0.1C). A 1L volume of the aerosol is passed through 0.2 μm cellulose filter for a later determination of the mass concentration of the aerosol by AAE analysis. After the ball valve and the top chamber are closed, both slide valves are open and 6-10 thousand drops fall through the chamber into the collection jar. The separation between the drop range from 600 radii for the 65 μm drops to 1400 radii for 100 μm drops. After all the drops have fallen through the aerosol chamber, the dewpoint and the filter measurements are taken again.

3. Results

Measurements of the scavenging efficiencies were made for cloud drops in the range 54 to 93 μm near 24°C and 1 atm. Two solutes were used to produce monodisperse clouds of aerosol particles. The first one, lithium carbonate, yielded hollow spheres of 2 μm radius at 90% relative humidity with an effective density of 0.26 g cm^{-3} and an effective thermal conductivity of 18 mW cm^{-1} K^{-1}. The second solute, manganese hypophosphite, yielded solid spheroids at 30% relative humidity with a density of 2.2 g cm^{-3} and a thermal conductivity of 50 mW cm^{-1} K^{-1}. The capture efficiency for 7 different particle sizes (0.58-3.2 μm) was measured. Results of 4 to 8 experimental runs were averaged for each combination of drop, particle size and particle type.

The measured capture efficiencies for the smaller manganese particles were found not to decrease as rapidly with particle size as phoretic theory predicts. Therefore, a much larger efficiency was measured in the Greenfield gap region than expected. The discrepancy between the measured results and theory may be due to higher order effects neglected by theory (e.g., curvature in the thermal field). Measured efficiencies for manganese particles larger than 1.5 μm radius increase strongly and are consistent with numerical efficiencies based on the theory of inertial impaction. The results for the two particle types are consistent with the prediction by theory that the thermophoretic force is larger on a particle of lower thermal conductivity. A graphical display of the comparison of the experimental results with theory will be available at the conference.

Acknowledgments

This material is based upon work supported by the Atmospheric Research Section of the National Science Foundation under Grant ATM78-05740.

REFERENCES

Adam, J.R., R. Cataneo, and R.G. Semonin, 1971: The production of equal and unequal size droplet pairs. Rev. Sci. Instr., 42, 1847-49.

Davies, C.N., 1978: Evaporation of airborne droplets In Fundamentals of Aerosol Science, Wiley Interscience, New York, D.T. Shaw, Ed., 372 pp.

Deryagin, B.V., and S.S.Dukhin, 1957: The influence of thermophoresis on the coagulation of droplets in clouds. Izv. Akad. Nauk SSSR, ser Geofiz., 6, 779-84.

Facy, L., 1955: La capture des noyaux de condensation par chocs moleculaires au cours des processus de condensation. Arch. Meteor. Geophys. Bioklimatol., Ser. A, 8, 229.

Grover, S.N., H.R. Pruppacher, and A.E. Hamielec, 1977: A numerical determination of the efficiency with which spherical aerosol particles collide with spherical water drops due to inertial impaction and phoretic and electrical forces. J. Atmos. Sci., 34, 1655-63.

Hogan, A.W., 1976: Aerosol of the trade wind region. J. Appl. Meteor., 15, 611-19.

Slinn, W.G.N., and J.M. Hales, 1971: A reevaluation of the role of thermophoresis as a mechanism of in- and below cloud scavenging. J. Atmos. Sci., 28, 1465-71.

Styra, B.I., and N.V. Tarasyuk, 1974: Influence of the temperature of a free-falling droplet on aerosol capture. Prec. Scav. ERDA Symp. Series, No.41, 167.

Wang, P.K., and H.R. Pruppacher, 1977: An experimental determination of the efficiency with which aerosol particles are collected by water drops in subsaturated air. J. Atmos. Sci., 34, 1664-69.

Young, K.C., 1974: The role of contact nucleation in ice phase initiation in clouds. J. Atmos. Sci., 31, 768-76.

CLOUD FORMATION STUDIES BY THERMAL WAVE PROPAGATION

James M. Carter

University of Tennessee Space Institute
Tullahoma, Tennessee, USA

B. Jeffrey Anderson

Marshall Space Flight Center
Huntsville, Alabama, USA

Introduction

Laboratory investigation in space, in a gravity-free environment, makes experiments possible which are not feasible for earth-based studies. In this paper we discuss the example of cloud formation in a cold thermal wave carried by conduction from a surface. In the terrestrial laboratory this process is accompanied by convection in all but one geometry (cold plate below the gas) and by sedimentation of the cloud drops with a velocity comparable to the propagation velocity of the thermal wave. These factors restrict the usefulness of the method to very short-duration experiments only -- the study of aerosol activation in a static diffusion chamber, for example. The case we will discuss is an experiment which was prepared for possible flight in the laboratory environment provided by the European Space Agency's (ESA) Spacelab and the Space Transportation System (Shuttle) currently being developed by NASA. It is a long-duration experiment to study cloud growth and thermal conductivity by a new method which utilizes the convection-free and sedimentation-free low gravity environment in space.

The experiment configuration to be considered is as follows: a gas laden with a monodisperse hygroscopic aerosol is at rest in a cloud chamber. The system is isothermal, at or near saturation. The temperature of a surface in contact with the gas is driven to a predefined function of time. As a cloud forms or dissipates in response to the temperature changes on the surface, the location and movement of the cloud/clear air interface is recorded photographically. The cloud drop number density can be obtained from the photographs. The detection threshold (minimum radius) for the system is known, but no other drop size information is obtainable. A numerical model of this situation was used to develop the experimental protocol described later. The experiment provides a determination of the condensation coefficient, β , for water vapor on cloud drops and the thermal conductivity of cloud air.

The Model

The numerical model used in this study was the "Non-adiabatic Expansion" model, which is one of a set developed by Dr. Myron Plooster and the General Electric Space Division, Huntsville Operations, as part of NASA's Atmospheric Cloud Physics Laboratory (ACPL) analytic simulator. The model was designed to simulate wall effects in the ACPL expansion chamber. It is a time-dependent, one-dimensional description of the microphysics in a spherical gas parcel bounded by a wall. Expansions and sealed chamber operations can be simulated with various initial aerosols, initial conditions, and boundary conditions on the walls. The model accounts for both heat and vapor diffusion toward or away from the walls as well as gas motions caused by temperature changes and composition gradients. The droplet growth formulation uses the well-known Kohler theory, and it incorporates the treatment of surface kinetic effects as described by Carstens and Kassner (1968), Fukuta and Walter (1970), and subsequent publications by Carstens and his colleagues.

Thermal Conductivity

The simplest experimental procedure which will generate a well-characterized wave is to produce a rapid pressure drop in an expansion chamber. The chamber with uniform wall temperature is first allowed to come to equilibrium at a temperature just above the dew point. An expansion of -1.5 mb/s for approximately 20 s is usually adequate to produce a cloud of detectable drops, 10 μm diameter. (The detection threshold for the system is expected to be less than 4 μm.) The wall temperature may either be held constant during and after the expansion or it may be changed to a new value during the expansion and then held constant. This procedure forms the cloud and closely approximates the application of a temperature step function to the boundary. Then, with the chamber sealed, heat from the wall is conducted into the cloud and evaporates the drops. The location of the cloud/clear air interface marks the progress of the wave. Its passage is recorded photographically as it enters the central portion of the 18 cm diameter chamber. The numerical model verifies the common laboratory experience that the interface remains sharp until all but the last vestige of cloud remains (Figure 1).

Numerical simulation of this expansion and heat conduction process has shown that the method will allow measurement of the thermal conductivity of moist air at a precision of 5 percent or better. This is comparable to the best ground laboratory method. Final determination of the experiment accuracy must await completion and calibration of the hardware. A change in conductivity by some percentage is reflected as a shift by the same percentage in

the time of passage of the cloud interface. The experiment requires precise knowledge of the initial temperature difference between the wall and the chamber dew point before expansion and the depth of the expansion. Typically, shifting the wall temperature from 0.05° to 0.1°C above the dew point yields a 9 percent shift in the movement of the wave (wall temperature held constant during and after expansion). Relative temperature measurements approximately 0.01°C are feasible; thus the resulting uncertainty should be 2 to 4 percent. All other sources of error are small compared to this. The experiment is sensitive to the pressure change, a half-millibar shift will produce a 1 percent error, but this contribution can be kept small because high-accuracy pressure measurements are relatively easy. Cumulative errors contributed by uncertainties in the water vapor diffusion coefficient, aerosol particle size and number concentration, and the mass accommodation coefficient in the droplet growth rate were found to be less than 0.4 percent in the cases considered.

There are other possible contributions to the error that cannot be evaluated numerically; they must await the actual experiment. The prime concern is residual air motion in the chamber caused by vehicle motions or the residual "g" forces, primarily drag, on the vehicle. These factors are dependent upon the orbital altitude, experiment duration, concurrent activities by the crew and other experiments, and other factors that must be evaluated postflight. However, analysis based on expected flight profiles indicates that the errors contributed by all of these potential concerns should be insignificant.

Droplet Growth

When a step function is applied to the temperature -- as discussed previously -- the thermal conductivity is the limiting microphysical parameter that determines the rate of penetration of the thermal wave. This condition can be changed by applying a short-period sinusoidal thermal boundary condition of low amplitude. In this case the wave takes the form of a strongly damped sine wave (Carslaw and Jaeger, pp. 64-69, 1976), and the growth and evaporation rate of the cloud drops becomes the limiting factor. A typical example, and the baseline for our numerical study, is a wave with a 0.4°C amplitude at the source and a 10 second period. This wave is attenuated approximately 94 percent at 2.5 cm from the source. If the mean temperature is equal to or just below the dew point of the air, 4 to 6 μm diameter drops will alternately form and evaporate near the wave source. The maximum drop size at a specified location is a strong function of the mass condensation coefficient. (Figure 2). Thus, when one knows the wave source amplitude, period, phase, and the detection threshold for the camera system, it is possible to determine this parameter by matching the results from the numerical model with measured values of the cloud boundary location. The method circumvents the problem of measuring the drop size as a function of time.

The experiment as currently visualized makes use of a thermal wave probe-- the device that generates the sinusoidal temperature boundary condition-- in the center of an expansion chamber with adiabatic walls. Other variations using a static diffusion chamber can easily be conceived, but these will not be discussed here. Beginning with an isothermal chamber and probe, a short expansion is used to grow a cloud of 10 μm diameter drops on a monodisperse salt aerosol of known size. During the expansion, the mean chamber wall and probe temperatures are set as close as possible to the post-expansion dew point. With the chamber remaining sealed and isothermal, a

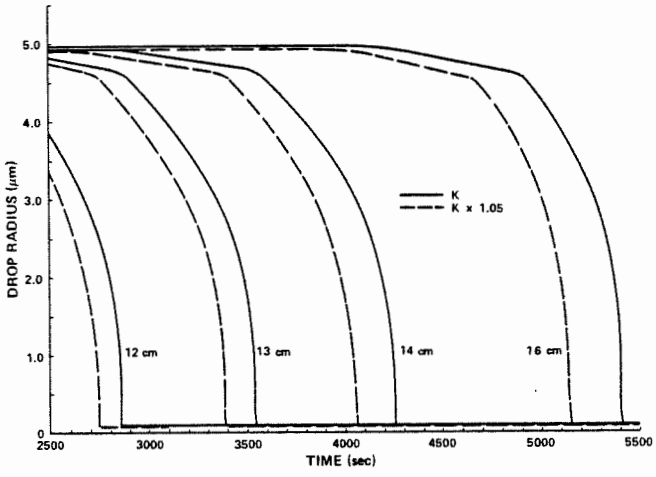

Figure 1. Drop radius versus time at various distances from wall of chamber. This shows that the propagation of the heat wave gives rise to a sharp cloud/no-cloud boundary. A change in thermal conductivity, K, shifts the time dependence a measurable amount.

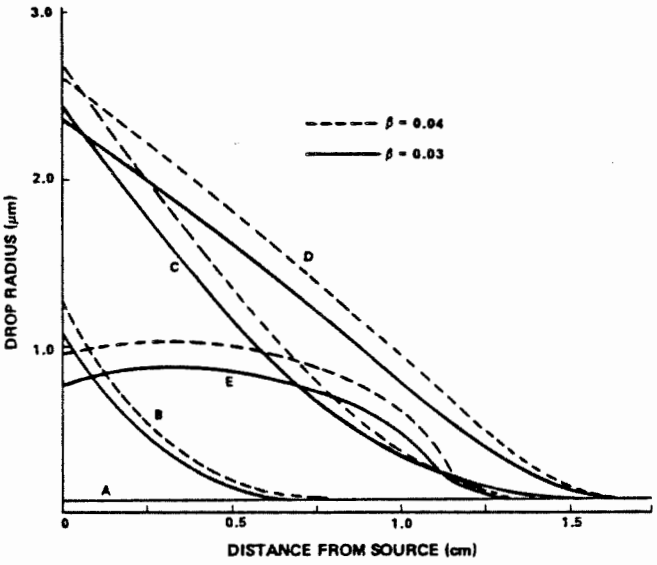

Figure 2. Drop radius versus distance from a surface whose temperature is driven sinusoidally with period τ (10s) for two values of condensation coefficient. Curve A: time = t_o, B: $t_o + 0.2\tau$, C: $t_o + 0.4\tau$, D: $t_o + 0.6\tau$, E: $t_o + 0.8\tau$. Wave amplitude was 0.4°C at source.

thermal wave is generated from the probe. Various amplitudes and periods are stepped through in sequence. The appearance of cloud drops larger than the detection threshold is recorded photographically in the first 1.5 cm space above the surface of the probe. Final data reduction from the photographs will be facilitated by use of a microdensitometer and automatic image processing as required.

The sample experiment developed in this study used the following initial conditions:

Grid	0.25 cm spacing
Initial temp.	291.20°K
Initial dewpoint	291.15°K
Initial pressure	1000 mb.
Expansion	-1.5 mb/s for 17 s
Mean probe temp.	290.70°K
Wave amplitude	0.4°K
Wave period	10.0 s.
Aerosol critical sat. ratio	0.005
Aerosol no. den.	500 cm^{-3}

These conditions yield drop sizes near the detection threshold (< 2 μm radius) if one assumes the thermal accommodation coefficient is unity and the condensation coefficient is between 0.03 and 0.04. By looking at variations of the parameters about this baseline we have obtained the following results:

1. The condensation coefficient can be measured to the first significant figure, assuming the thermal accommodation coefficient is taken as unity.

2. The results are not sensitive to uncertainties in the values of the thermal conductivity of air and the diffusivity of water vapor in air. A 5 percent shift in the value of the conductivity alters the drop size by approximately 0.05 μm, which is not detectable. The results are even less sensitive to the diffusivity.

3. The experiment is only moderately sensitive to the properties of the aerosol. Changing the number density from 500 to 300 cm^{-3} produced no detectable change near the probe. Narrowing the size distribution by reducing the standard deviation from 0.2 $\bar{r}$ to 0.1 $\bar{r}$ only sharpens the cloud/clear air interface. A change in the mean aerosol size will alter the measured value of the condensation coefficient. The measurement is altered by one significant figure if the critical saturation ratio is shifted from 0.0044 to 0.0074.

4. The precision in temperature measurement required for this experiment is well within the state of the art. The most critical temperature measurement is the amplitude of the thermal wave source. A 10 percent change in amplitude changes the drop size by 10 percent. Deviations of the wave form from a perfect sine wave are not important since high-frequency changes are very strongly damped and the measured wave form can be put into the model in the post-flight analysis. A simulated 0.05°C error in the dewpoint changed the drop sizes by undetectable amounts, less than 0.1 μm.

Conclusions

The growth of small cloud drops and the associated problem of measuring the condensation coefficient has a long history in cloud physics. This is a result of both the theoretical and experimental difficulty of the problem and its great importance in the development of cloud drop size distributions and instrumentation design. Many of the experimental difficulties are discussed by Chodes et. al. (1974), who arrive at a value of 0.033 for the condensation coefficient. This is near the classical value of 0.036 reported by Alty and Mackay (1935). They looked at the potential worst case errors from their measurements and reported that the value could range from 0.022 to 0.073. They concluded that the value should be less than 0.1 for atmospheric conditions. However, a complete search of the literature yields values from near zero to at least 0.5, Johnson et. al. (1979), or even to unity. Thus the experimental method discussed in this paper is significant because it allows determination of the condensation coefficient by a completely new method which does not require the direct measurement of the growth rate or fall speed of small drops.

This method also has the advantage that the conditions closely duplicate the atmospheric environment. For example, measurements can be made at various temperatures and pressures; the maximum saturation ratios in the wave are not large, near 0.023 in the baseline case. The experiment exploits the low-gravity space environment and, at the same time, is based on a numerical model of the basic cloud formation process. Thus it provides a new opportunity to confirm our understanding of this segment of cloud physics.

References:

Alty, T., and C. A. Mackay, 1935: The accommodation coefficient and the evaporation coefficient of water. Proc. Roy. Soc. London, 149, Series A, 104-116.

Carslaw, H. S., and J. C. Jaeger, 1976, "Conduction of Heat in Solids," Oxford Univ. Press, 510 pp.

Carstens, J. C., and J. L. Kassner, Jr., 1968: Some aspects of droplet growth theory applicable to nuclei measurements. J. Rech. Atmos., 3, 33-39.

Chodes, N., J. Warner and A. Gagin, 1974: A determination of the condensation coefficient of water from the growth rate of small cloud droplets. J. Atmos. Sci., 31, 1351-1357.

Fukuta, N., and L. A. Walter, 1970: Kinetics of hydrometeor growth from a vapor-spherical model. J. Atmos. Sci., 27, No. 8, 1160-1172

Johnson, R. A., R. Dumont and M. A. Vietti, 1979: Water droplet growth in the presence of highly soluble gases. J. Rech. Atmos., 13, No. 1, 21-36.

COMPARISON OF LABORATORY AND NUMERICAL MODEL STUDIES OF THE INITIAL PHASE OF CLOUD DROPLET GROWTH BY CONDENSATION

J.W. Fitzgerald and S.G. Gathman
Naval Research Laboratory
Washington, DC, USA

and

E.J. Mack and U. Katz[1]
Calspan Corporation
Buffalo, NY, USA

1. INTRODUCTION

The theory of droplet growth by condensation in a fixed parcel of air which is cooled by adiabatic expansion has been used to describe the initial development of the droplet distribution in cumulus clouds (Howell, 1949; Mordy, 1959; Fitzgerald, 1972). This model has been able to account for some observations of droplet spectra made in the first two hundred meters above cloud base if values of the 0.04 are used (Warner, 1969; Fitzgerald, 1972). However, the adiabatic parcel model predicts that the droplet spectrum narrows with further ascent above cloud base. This behavior is in conflict with observations (Warner, 1969) which show that the dispersion of the droplet distribution increases with height in the first 2 km.

Various mechanisms have been proposed to explain the broadening of the droplet spectrum in the region of the cloud where condensation dominates over collision-coalescence. These include turbulent fluctuations in the updraft velocity (Warner, 1969; Bartlett and Jonas, 1972), mixing between cloud and environment (Warner, 1973; Lee and Pruppacher, 1977) and turbulent mixing between different parcels of air (Manton, 1979). Of these mechanisms, only entrainment of nuclei-laden air and in-cloud turbulent mixing appear to broaden the droplet spectrum to any significant extent.

The purpose of the present study was to conduct a test of the theory of droplet growth by condensation in an adiabatically cooled parcel, without the complicating effects of entrainment and turbulence. To accomplish this, clouds were formed by adiabatic expansion in a large atmospheric simulation chamber. The observed cloud properties were then compared with those predicted by the adiabatic parcel model given the expansion rate and cloud condensation nucleus (CCN) spectrum of the aerosol.

2. LABORATORY EXPERIMENTS

The cloud experiments were performed in Calspan's 600 m^3 atmospheric simulation chamber. This chamber is approximately 9.2 m high and 9.1 m in diameter. Clouds were generated by humidifying the chamber to 95% relative humidity and then expanding the air at a nearly constant rate of from 2.5 to 5.5 mb min^{-1}.

Natural (rural continental) nuclei as well as artificially produced sodium chloride and ammonium sulfate nuclei were used as the cloud-forming aerosol. When artificial nuclei were used, the chamber was first filtered for a period of several hours to remove the natural nuclei. The artificial aerosol was not introduced until the background count fell below 15 cm^{-3}. Artificial nuclei were produced by pneumatically nebulizing aqueous solutions of the desired salt and rapidly diluting the mist to prevent coagulation. A large stirring fan was used to distribute the aerosol uniformly.

The CCN supersaturation spectrum of the aerosol was measured with the NRL thermal gradient diffusion cloud chamber, which was located outside the simulation chamber. CCN concentrations were measured at five supersaturations between 0.15% and 1.0%. Following completion of the CCN measurements, the chamber was humidified by wetting the floor and the lower half of the walls. At this point, a quick check of the CCN concentrations was made to determine if there had been any significant change. The stirring fan was used to achieve a uniform distribution of humidity. When the relative humidity reached 95%, the air in the chamber was expanded at a preselected rate. A maximum expansion of about 40 mb could be achieved.

By varying the expansion rate and the concentration of nuclei available for condensation, it was possible to produce clouds exhibiting a fairly wide range of microphysical characteristics. The cloud properties measured were the visibility and the number concentration and size distribution of the droplets.

Visibility was measured with the two 18.3-m path length transmissometers, positioned at the 1.5 and 4.5-m levels of the chamber. A reflecting mirror was used to obtain a path length of twice the chamber diameter.

Droplet samples were obtained with Calspan's gelatin-coated slide impactor. This device has proven to be a reliable droplet sampler. The collection efficiency of the sampler coupled with the difficulty of resolving very small

[1]Present Address: Desert Research Institute, University of Nevada, Reno, NV, USA.

droplets limits the range of operation to drops larger than about 3μm diameter. Raw size distributions were obtained by manually sizing drop replicas on 150X microphotographs. The sample size generally exceeded 400 drops per distribution. A collection efficiency correction based on the work of Langmuir and Blodgett was applied.

Droplet number concentrations were determined by two methods. First, concentrations were obtained directly by photographing the light scattered by individual droplets in an intensely illuminated volume of 0.1 cm^3. Droplet concentrations were also determined from the measured visibilities and the corrected, normalized size spectra, by means of the Koschmieder visibility formula.

3. DROPLET GROWTH MODEL

The growth, by condensation, of a population of droplets contained in a parcel which is cooled uniformly by adiabatic expansion is governed by the following set of equations describing the time rate of change of temperature, pressure, water vapor mixing ratio and droplet radius (Fitzgerald, 1974).

$$\frac{dT}{dt} = \frac{(1+x)\,R_m \frac{T}{p}\frac{dp}{dt} - L\frac{dx}{dt}}{c_{pd} + xc_{pv} + wc_w} \qquad (1)$$

$$\frac{dp}{dt} = \text{given rate of expansion} \qquad (2)$$

$$\frac{dx}{dt} = -4\pi \sum_i \rho_w N_i r_i^2 \frac{dr_i}{dt} \qquad (3)$$

and

$$r\frac{dr}{dt} = \frac{\frac{D'e_s}{\rho_w R_v T}\left[\frac{xp}{f_w e_s (x+\xi)} - B\exp\left(\frac{a}{r}\right)\right]}{1 + \frac{D'e_s L^2}{K'R_v^2 T^3} B\exp\left(\frac{a}{r}\right)}. \qquad (4)$$

The terms a, B, D' and K' in Eq. (4) are defined by

$$a = \frac{2\sigma'}{\rho_w R_v T}$$

$$B = \left[1 + \frac{i\epsilon M_w \rho_d r_d^3}{M_s\{\rho'[r^3 - r_d^3(1-\epsilon)] - \epsilon\rho_d r_d^3\}}\right]^{-1}$$

$$D' = D\left[\frac{r}{r+\Delta_D} + \frac{D}{r\alpha}\left(\frac{2\pi\xi}{R_d T}\right)^{1/2}\right]^{-1}$$

$$K' = K\left[\frac{r}{r+\Delta_T} + \frac{4K}{r\rho_a \beta c_{pd}}\left(\frac{\pi}{8R_d T}\right)^{1/2}\right]^{-1}$$

Table 1. Data for selected cloud experiments.

Cloud experiment no.	Aerosol type	Expansion rate (mb/min)	Equivalent updraft velocity (ms^{-1})	Initial temp. (°K)	Initial R.H. (%)
7	NaCl	5.0	0.73	295.10	95.2
15	Natural	5.0	0.75	296.15	95.2
19	$(NH_4)_2SO_4$	3.75	0.54	298.88	95.8

To conserve space, we will define only a few of the less obvious symbols. Here ε is the mass fraction of soluble material in a nucleus; α is the condensation coefficient of water; β is the thermal accommodation coefficient of water; Δ_D is the vapor jump distance at the droplet surface; Δ_T is the temperature jump distance; ξ is the ratio R_d/R_v and f_w is a correction factor for the departure of the air-water vapor mixture from ideal behavior.

The model was used to predict the microphysical properties of the clouds formed in the chamber. The equations were integrated by means of the standard fourth-order Runge-Kutta scheme. The input parameters to the numerical simulations were the initial temperature and relative humidity, the expansion rate and an aerosol size distribution which was inferred from the CCN spectrum. Based on the measurements of Sinnarwalla et al. (1975), a value of α of 0.035 was used. In the case of the natural aerosols, the value of ε was taken to be 0.3. Ammonium sulfate was assumed to be the soluble constituent of the natural nuclei.

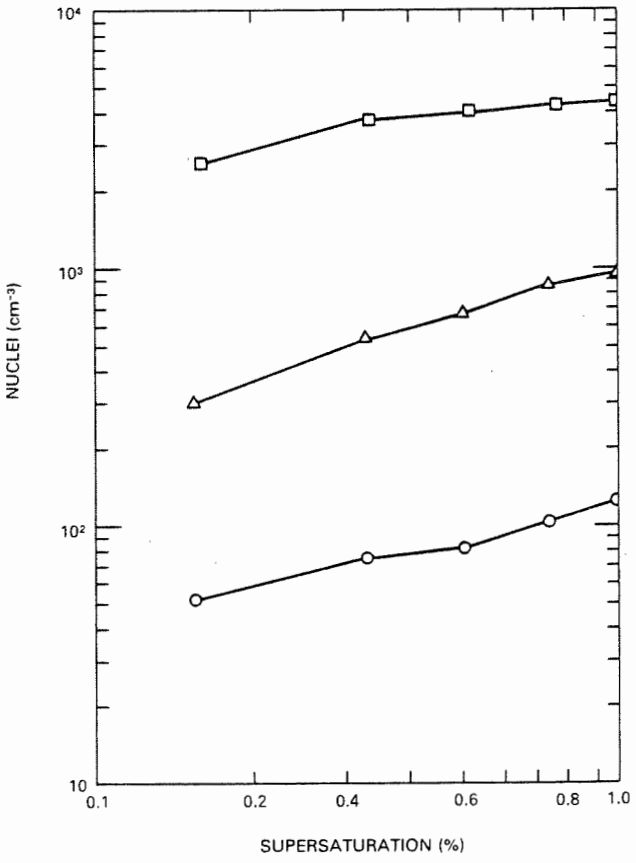

Fig. 1. CCN supersaturation spectra for three of the cloud experiments. Upper curve: cloud 15; middle curve: cloud 7; lower: cloud 19.

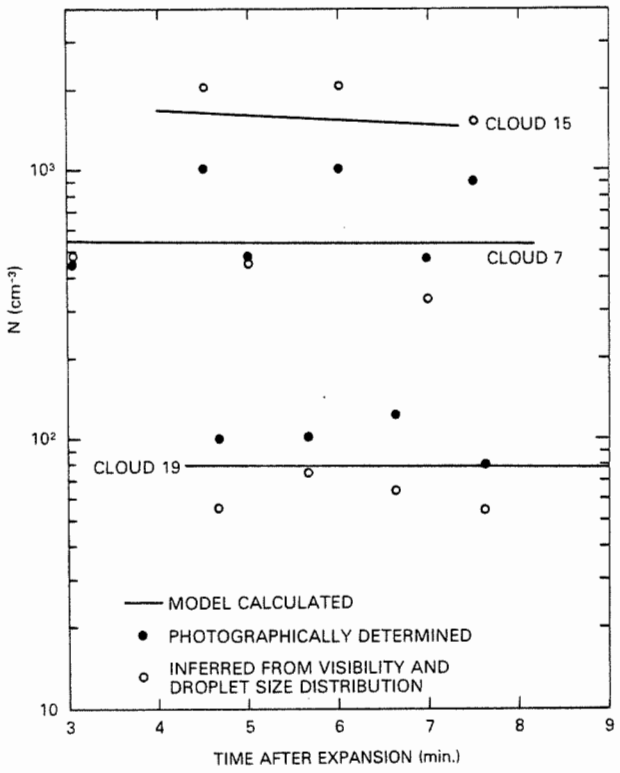

Fig. 2. Comparison of observed and model-calculated droplet number concentrations.

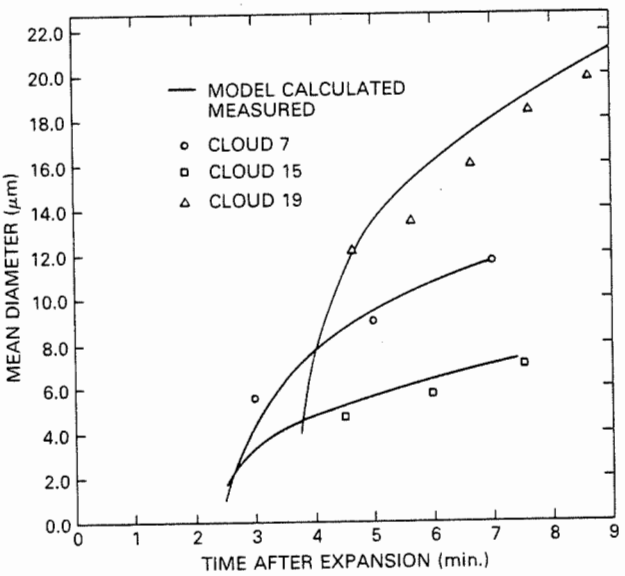

Fig. 3. Comparison of observed and model-calculated values of the mean droplet diameter.

4. COMPARISON OF OBSERVED AND CALCULATED CLOUD PROPERTIES

A detailed comparison of the observed and model-predicted cloud microphysical properties is presented for three of the cloud experiments. These cases involve a range of aerosol characteristics and expansion rates. Table 1 gives some pertinent data for these experiments. The CCN supersaturation spectra for these cases are shown in Fig. 1. Figs. 2-8 present comparisons of the observed and predicted droplet number concentrations, mean droplet diameter, visibilities and droplet size distributions.

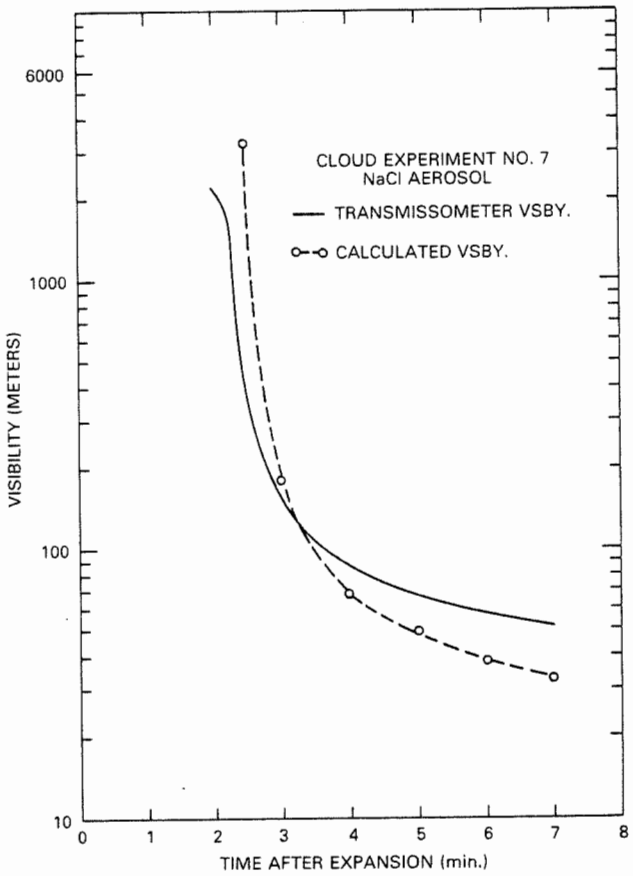

Fig. 4. Comparison of observed and model-calculated visibilities in the case of cloud experiment 7.

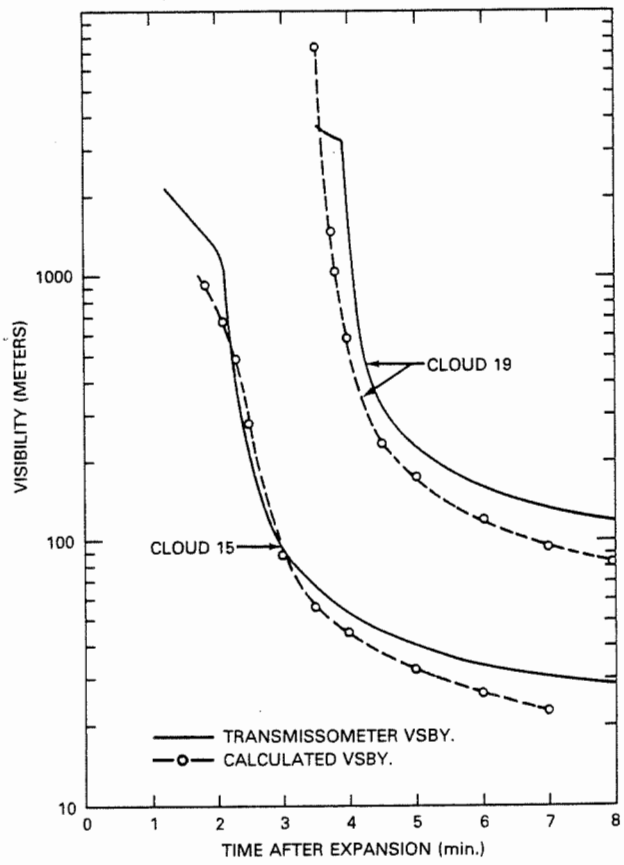

Fig. 5. As in Fig. 4 except for cloud experiments 15 and 19.

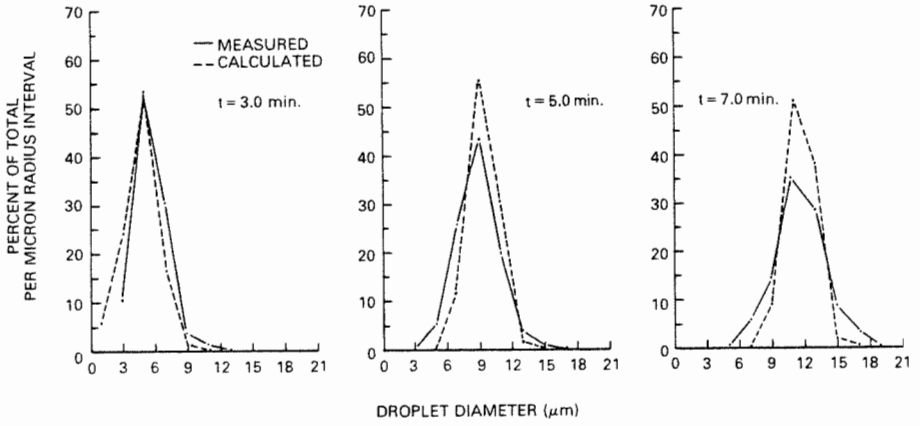

Fig. 6. Comparison of model-calculated and observed droplet size spectra for cloud experiment 7 at 3 min, 5 min and 7 min after start of expansion.

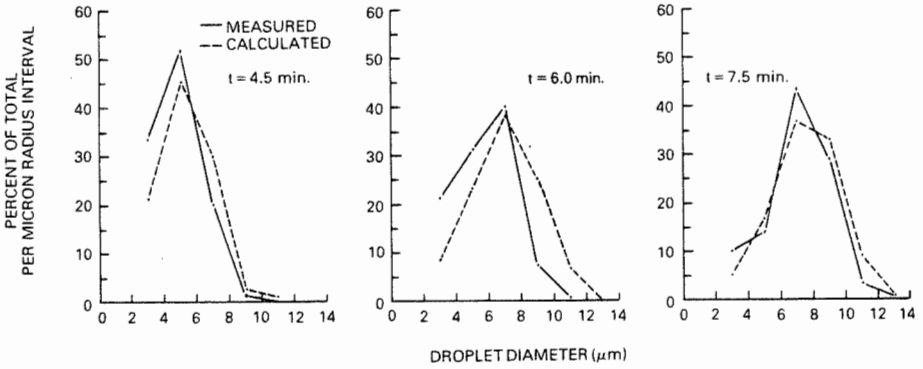

Fig. 7. As in Fig. 6 except for cloud experiment 15 at 4.5 min, 6 min and 7.5 min after start of expansion.

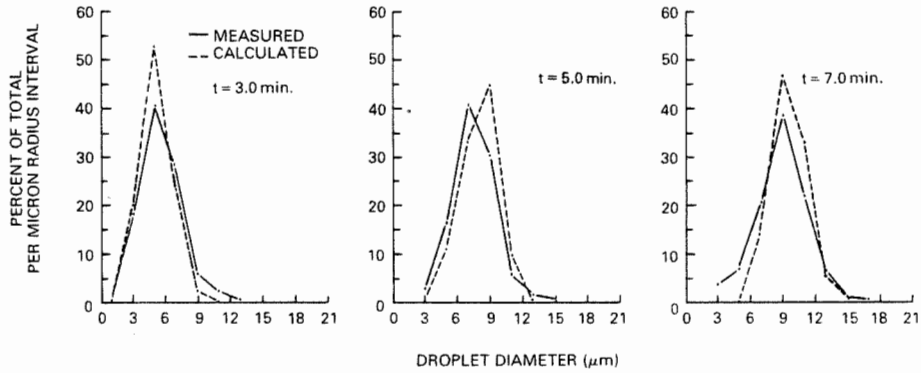

Fig. 8. As in Fig. 6 except for cloud experiment 10 at 3 min, 5 min and 7 min after start of expansion.

5. REFERENCES

Bartlett, J. T., and P. R. Jonas, 1972: On the dispersion of the sizes of droplets growing by condensation in turbulent clouds. Quart. J. Roy. Meteor. Soc., 98, 150-164.

Fitzgerald, J. W., 1972: A study of the initial phase of cloud droplet growth by condensation: A comparison between theory and observation. Ph.D. Thesis, Dept. of Geoph. Sci., Univ. of Chicago, Chicago, Ill.

_____, 1974: Effect of aerosol composition on cloud droplet size distribution: A numerical study. J. Atmos. Sci., 31, 1358-1367.

Howell, W. E., 1949: The growth of cloud drops in uniformly cooled air. J. Meteor., 6, 134-149.

Lee, I. Y., and H. R. Pruppacher, 1977: A comparative study on the growth of cloud drops by condensation using an air parcel model with and without entrainment. Pure Appl. Geophys., 115, 523-545.

Manton, M. J., 1979: On the broadening of a droplet distribution by turbulence near cloud base. Quart. J. Roy. Meteor. Soc., 105, 899-914.

Mordy, W. A., 1959: Computations of the growth by condensation of a population of cloud droplets. Tellus, 11, 16-44.

Sinnarwalla, A. M., D. J. Alofs and J. C. Carstens, 1975: Measurements on growth rate to determine condensation coefficients for water drops grown on natural cloud nuclei. J. Atmos. Sci., 32, 592-599.

Warner, J., 1969: The microstructure of cumulus cloud: Part II. The effect on droplet size distribution of the cloud nucleus spectrum and updraft velocity. J. Atmos. Sci., 26, 1272-1282.

_____, 1973: The microstructure of cumulus cloud: Part IV. The effect on the droplet spectrum of mixing between cloud and environment. J. Atmos. Sci., 30, 256-261.

A SPECTRAL APPROACH TO CLOUD DROPLET GROWTH BY CONDENSATION

Hsiao-ming Hsu

Department of Atmospheric and Oceanic Science
The University of Michigan
Ann Arbor, Michigan, U.S.A.

I. Introduction

Traditionally , the detailed calculations of cloud microphysical processes are achieved by numerically integrating a set of governing equations for each discrete size class. Recent research efforts have been reviewed by Ochs and Yao (1978), Cotton (1979), etc. The numerical techniques used in previous calculations are finite-difference methods. These methods are popular and easy because of their simplicities in application. The general drawback to them is their low accuracy caused by the low-order truncation of the Taylor series expansion when the finite-difference methods are formulated. Clark has used gamma distributions (1974) and log-normal distributions (1976) to represent the droplet spectra. He calculates the parameters of the distributions to determine the shapes of the droplet spectra. The representations are limited by the assumption that the spectra of the droplets for all time and space are described by the gamma or log-normal distributions. The detailed microphysical processes should be simulated to a more satisfactory degree. A more accurate numerical algorithm is very crucial to the outcome of microphysical calculations. The main purpose of this paper is to describe a new methodology for calculating the spectra of cloud droplets and raindrops by using spectral methods. The superior accuracy of the spectral method and its applications to other fluid problems are discussed in Orszag and Israeli (1974), Gottlieb and Orszag (1977), and Boyd (1978).

The application of the spectral method to microphysical calculations will now be illustrated. A Lagrangian parcel model will be used to show the basic relationship between a cloud model in the condensation/evaporation stage and the droplet spectrum.

II. The Cloud Model

A Lagrangian cloud model, which is similar to Clark (1976), may be summarized as follows. The tendency equations for pressure (p), temperature (T), mixing ratio of water vapor (q_v), and mixing ratio of liquid water (q_w) may be expressed in the following forms

$$\frac{dp}{dt} = -\rho_a g w, \tag{1}$$

$$\frac{dT}{dt} = -\frac{g}{C_p} w - \frac{L}{C_p}\frac{dq_w}{dt}, \tag{2}$$

$$\frac{dq_v}{dt} = -\frac{dq_w}{dt}, \tag{3}$$

and

$$\frac{dq_w}{dt} = 4\pi\frac{\rho_w}{\rho_a}\int_b^a r^2 \frac{dr}{dt} n(r)\,dr, \tag{4}$$

where ρ_a is the air density, g the gravitational acceleration, w the vertical velocity, C_p the specific heat of constant pressure, L the latent heat, ρ_w the water density, r the droplet radius, n the number density of droplets, a and b the lower and upper bounds of the spectrum respectively. The tendency equation for super-saturation (S) and the equation of the diffusional growth for a droplet have the forms of

$$\frac{dS}{dt} = H_1 w - H_2\frac{dq_w}{dt}, \tag{5}$$

$$r\frac{dr}{dt} = G\left(S - \frac{a_*}{r} + \frac{b_*}{r^3}\right)F, \tag{6}$$

respectively, where H_1, H_2, and G are the thermodynamic parameters, a_* relates to the effects of surface tension, b_* relates to the presence of solute, F is the ventilation factor, and the details can be found in Fletcher (1969). Finally, the kinematic equation for the number density of droplet spectrum is

$$\frac{dn}{dt} + \frac{\partial}{\partial r}\left(\frac{dr}{dt} n\right) = 0. \tag{7}$$

With the aid of (6) and the following definitions

$$f(r) \equiv \frac{dr}{dt} = GF\left(\frac{S}{r} - \frac{a_*}{r^2} + \frac{b_*}{r^4}\right), \tag{8}$$

and

$$g(r) \equiv \frac{\partial}{\partial r}\left(\frac{dr}{dt}\right) = GF\left(-\frac{S}{r^2} + \frac{2a_*}{r^3} - \frac{4b_*}{r^5}\right), \tag{9}$$

equations (7) and (4) can be re-written

$$\frac{\partial}{\partial t} n(r,t) + f(r)\frac{\partial}{\partial r} n(r,t) + g(r) n(r,t) = 0, \tag{10}$$

and $$\frac{dq_w}{dt} = -4\pi\frac{\rho_w}{\rho_a}\int_a^b r^2 f(r)n(r)dr, \quad (11)$$

respectively. The last two equations are explicitly involved in formulating the spectral algorithm for the cloud model. In the next section, the famous Galerkin approximation will be given. The spectral method is only one special case of the Galerkin approximation.

III. The Galerkin Approximation

A Galerkin approximation to (10) is constructed as follows. The approximation of the droplet spectrum $n_N(r,t)$ is sought in the form of the truncated series,

$$n_N(r,t) = \sum_{n=0}^{N-1} a_n(t)\phi_n(r), \quad (12)$$

where the time-independent basis functions ϕ_n of degree n are assumed linearly independent. After substituting (12) into (10), the inner products of (10) and the basis functions ϕ_m of degree m give

$$\sum_{n=0}^{N-1}\{<\phi_m|\phi_n>\frac{da_n}{dt} + <\phi_m|(f\frac{d\phi_n}{dr})>a_n + <\phi_m|(g\phi_n)>a_n\} = 0,$$

$$m = 0, 1, \cdots, N-1, \quad (13)$$

where

$$<p|q> = \int_a^b p(x)q(x)h(x)dx, \quad (14)$$

and h(x) is a weighting function. The matrix form of (13) is

$$A\frac{d\vec{a}}{dt} + (B+C)\vec{a} = 0, \quad (15)$$

where the matrices

$$A = \{<\phi_m|\phi_n>\},$$

$$B = \{<\phi_m|(f\frac{d\phi_n}{dr})>\},$$

$$C = \{<\phi_m|(g\phi_n)>\},$$

and $\vec{a}$ is a vector which consists of $a_n(t)$. The partial differential equation (10) is now a set of ordinary differential equations (15). Equation (11) may also be expressed in the Galerkin form,

$$\frac{dq_w}{dt} = 4\pi GF\frac{\rho_w}{\rho_a}\sum_{n=0}^{N-1}(\int_a^b r^2 f\phi_n dr)\, a_n. \quad (16)$$

The procedure for approximation is quite general. The choice of the basis functions ϕ_n of degree n determines the complexity of the matrices in (15). A wise choice leads to sparse matrices which are easily manipulated.

IV. Discussion

The general algorithm described in the previous section may provide different practical algorithms based on the selections of the basis functions. In the spectral method, global continuous functions which are usually a subset of a complete system of orthogonal functions are chosen. The set of expansion coefficients of a certain variable are actually calculated with the truncated orthogonal functions.

In the calculations of the droplet spectrum within a radius bound (a,b), the shifted Chebyshev polynominals may be chosen as the basis functions providing the independent variable r is transformed to x = (r-a)/(b-a). The bound for the integration in (14) becomes (0,1) for x. The property of orthogonality of the shifted Chebyshev polynominal gives a diagonal matrix A in (15). Matrices B and C may be obtained with the known properties of the shifted Chebyshev polynominals (e.g. Abramowitz and Stegun, 1965; Luke, 1969, etc).

If only the derivatives in (10) are evaluated by the selected basis functions and the rest of calculations are still performed on the grids, the approximation is called the pseudo-spectral method. Obviously, the spectral calculations for the non-linear terms are eased, but the accuracy of the pseudo-spectral method is relatively less than that of the spectral method.

One may choose locally continuous piece-wise polynominals as the basis functions, i.e. functions each of which are different from zero only in a limited part of the integration domain. This choice of the Galerkin approximation gives the finite-element method. In the simplest cases, the finite-element method obtained coincides with simple finite-difference methods (Strang and Fix, 1973).

Numerical calculations and comparisons are currently under way.

Acknowledgements

The author wishes to acknowledge the helpful discussions with F. Baer, J.P. Boyd, A.N. Dingle, B.G. Heikes, G.L. Pellett, J.J. Tribbia, and their encouragements. The research has been supported by the National Aeronautics and Space Administration under Grant NSG 1243.

References

Abramowitz, M., and I.A. Stegun, Eds., 1965: Handbook of Mathematical Functions. Dover. 1046pp.

Boyd, J.P., 1978: Spectral and pseudo-spectral methods for eigenvalue and nonseparable boundary value problems. Mon. Wea. Rev., 106, 1192-1203.

Clark, T.L., 1974: A study in cloud phase parameterization using the gamma distribution. J. Atmos. Sci., 31, 142-155.

Clark, T.L., 1976: Use of log-normal distributions for numerical calculations of condensation and collection. J. Atmos. Sci., 33, 810-821.

Cotton, W.R., 1979: A review for 1975-1978 IUGG quadrennial report. Rev. of Geophysics and Space Physics, 17, 1840-1851.

Fletcher, N.H., 1969: The Physics of Rainclouds. Cambridge. 390pp.

Gottlieb, D., and S.A. Orszag, 1977: Numerical Analysis of Spectral Methods: Theory and Application. NSF-CBMS Monograph No. 26, SIAM. 172pp.

Luke, Y.L., 1969: The Special Functions and Their Approximations. V. I. Academic. 349pp.

Ochs, H.T., III, and C.S. Yao, 1978: Moment-conserving thchniques for warm-cloud microphysical computations. Part. I: Numerical techniques. J. Atmos. Sci., 35, 1947-1958.

Orszag, S.A., and M. Israeli, 1974: Numerical simulation of viscous incompressible flows. Ann. Rev. Fluid Mech., 5, 281-318.

Strang, G., and G.J. Fix, 1973: An Analysis of the Finite Element Method. Prentice-Hall. 306pp.

A SPECTRAL APPROACH TO CLOUD DROPLET GROWTH BY CONDENSATION

Hsiao-ming Hsu

Department of Atmospheric and Oceanic Science
The University of Michigan
Ann Arbor, Michigan, U.S.A.

I. Introduction

Traditionally , the detailed calculations of cloud microphysical processes are achieved by numerically integrating a set of governing equations for each discrete size class. Recent research efforts have been reviewed by Ochs and Yao (1978), Cotton (1979), etc. The numerical techniques used in previous calculations are finite-difference methods. These methods are popular and easy because of their simplicities in application. The general drawback to them is their low accuracy caused by the low-order truncation of the Taylor series expansion when the finite-difference methods are formulated. Clark has used gamma distributions (1974) and log-normal distributions (1976) to represent the droplet spectra. He calculates the parameters of the distributions to determine the shapes of the droplet spectra. The representations are limited by the assumption that the spectra of the droplets for all time and space are described by the gamma or log-normal distributions. The detailed microphysical processes should be simulated to a more satisfactory degree. A more accurate numerical algorithm is very crucial to the outcome of microphysical calculations. The main purpose of this paper is to describe a new methodology for calculating the spectra of cloud droplets and raindrops by using spectral methods. The superior accuracy of the spectral method and its applications to other fluid problems are discussed in Orszag and Israeli (1974), Gottlieb and Orszag (1977), and Boyd (1978).

The application of the spectral method to microphysical calculations will now be illustrated. A Lagrangian parcel model will be used to show the basic relationship between a cloud model in the condensation/evaporation stage and the droplet spectrum.

II. The Cloud Model

A Lagrangian cloud model, which is similar to Clark (1976), may be summarized as follows. The tendency equations for pressure (p), temperature (T), mixing ratio of water vapor (q_v), and mixing ratio of liquid water (q_w) may be expressed in the following forms

$$\frac{dp}{dt} = -\rho_a g w, \tag{1}$$

$$\frac{dT}{dt} = -\frac{g}{C_p} w - \frac{L}{C_p}\frac{dq_w}{dt}, \tag{2}$$

$$\frac{dq_v}{dt} = -\frac{dq_w}{dt}, \tag{3}$$

and

$$\frac{dq_w}{dt} = 4\pi\frac{\rho_w}{\rho_a}\int_b^a r^2 \frac{dr}{dt} n(r)\,dr, \tag{4}$$

where ρ_a is the air density, g the gravitational acceleration, w the vertical velocity, C_p the specific heat of constant pressure, L the latent heat, ρ_w the water density, r the droplet radius, n the number density of droplets, a and b the lower and upper bounds of the spectrum respectively. The tendency equation for super-saturation (S) and the equation of the diffusional growth for a droplet have the forms of

$$\frac{dS}{dt} = H_1 w - H_2\frac{dq_w}{dt}, \tag{5}$$

$$r\frac{dr}{dt} = G\left(S - \frac{a_*}{r} + \frac{b_*}{r^3}\right)F, \tag{6}$$

respectively, where H_1, H_2, and G are the thermodynamic parameters, a_* relates to the effects of surface tension, b_* relates to the presence of solute, F is the ventilation factor, and the details can be found in Fletcher (1969). Finally, the kinematic equation for the number density of droplet spectrum is

$$\frac{dn}{dt} + \frac{\partial}{\partial r}\left(\frac{dr}{dt} n\right) = 0. \tag{7}$$

With the aid of (6) and the following definitions

$$f(r) \equiv \frac{dr}{dt} = GF\left(\frac{S}{r} - \frac{a_*}{r^2} + \frac{b_*}{r^4}\right), \tag{8}$$

and

$$g(r) \equiv \frac{\partial}{\partial r}\left(\frac{dr}{dt}\right) = GF\left(-\frac{S}{r^2} + \frac{2a_*}{r^3} - \frac{4b_*}{r^5}\right), \tag{9}$$

equations (7) and (4) can be re-written

$$\frac{\partial}{\partial t} n(r,t) + f(r)\frac{\partial}{\partial r} n(r,t) + g(r) n(r,t) = 0, \tag{10}$$

and $$\frac{dq_w}{dt} = -4\pi\frac{\rho_w}{\rho_a}\int_a^b r^2 f(r)n(r)dr, \quad (11)$$

respectively. The last two equations are explicitly involved in formulating the spectral algorithm for the cloud model. In the next section, the famous Galerkin approximation will be given. The spectral method is only one special case of the Galerkin approximation.

III. The Galerkin Approximation

A Galerkin approximation to (10) is constructed as follows. The approximation of the droplet spectrum $n_N(r,t)$ is sought in the form of the truncated series,

$$n_N(r,t) = \sum_{n=0}^{N-1} a_n(t)\phi_n(r), \quad (12)$$

where the time-independent basis functions ϕ_n of degree n are assumed linearly independent. After substituting (12) into (10), the inner products of (10) and the basis functions ϕ_m of degree m give

$$\sum_{n=0}^{N-1} \{<\phi_m|\phi_n>\frac{da_n}{dt} + <\phi_m|(f\frac{d\phi_n}{dr})>a_n + <\phi_m|(g\phi_n)>a_n\} = 0,$$

$$m = 0, 1, \cdots, N-1, \quad (13)$$

where

$$<p|q> = \int_a^b p(x)q(x)h(x)dx, \quad (14)$$

and h(x) is a weighting function. The matrix form of (13) is

$$A\frac{d\vec{a}}{dt} + (B+C)\vec{a} = 0, \quad (15)$$

where the matrices

$$A = \{<\phi_m|\phi_n>\},$$

$$B = \{<\phi_m|(f\frac{d\phi_n}{dr})>\},$$

$$C = \{<\phi_m|(g\phi_n)>\},$$

and $\vec{a}$ is a vector which consists of $a_n(t)$. The partial differential equation (10) is now a set of ordinary differential equations (15). Equation (11) may also be expressed in the Galerkin form,

$$\frac{dq_w}{dt} = 4\pi GF\frac{\rho_w}{\rho_a}\sum_{n=0}^{N-1}\left(\int_a^b r^2 f\phi_n dr\right) a_n. \quad (16)$$

The procedure for approximation is quite general. The choice of the basis functions ϕ_n of degree n determines the complexity of the matrices in (15). A wise choice leads to sparse matrices which are easily manipulated.

IV. Discussion

The general algorithm described in the previous section may provide different practical algorithms based on the selections of the basis functions. In the spectral method, global continuous functions which are usually a subset of a complete system of orthogonal functions are chosen. The set of expansion coefficients of a certain variable are actually calculated with the truncated orthogonal functions.

In the calculations of the droplet spectrum within a radius bound (a,b), the shifted Chebyshev polynominals may be chosen as the basis functions providing the independent variable r is transformed to x = (r-a)/(b-a). The bound for the integration in (14) becomes (0,1) for x. The property of orthogonality of the shifted Chebyshev polynominal gives a diagonal matrix A in (15). Matrices B and C may be obtained with the known properties of the shifted Chebyshev polynominals (e.g. Abramowitz and Stegun, 1965; Luke, 1969, etc).

If only the derivatives in (10) are evaluated by the selected basis functions and the rest of calculations are still performed on the grids, the approximation is called the pseudo-spectral method. Obviously, the spectral calculations for the non-linear terms are eased, but the accuracy of the pseudo-spectral method is relatively less than that of the spectral method.

One may choose locally continuous piece-wise polynominals as the basis functions, i.e. functions each of which are different from zero only in a limited part of the integration domain. This choice of the Galerkin approximation gives the finite-element method. In the simplest cases, the finite-element method obtained coincides with simple finite-difference methods (Strang and Fix, 1973).

Numerical calculations and comparisons are currently under way.

Acknowledgements

The author wishes to acknowledge the helpful discussions with F. Baer, J.P. Boyd, A.N. Dingle, B.G. Heikes, G.L. Pellett, J.J. Tribbia, and their encouragements. The research has been supported by the National Aeronautics and Space Administration under Grant NSG 1243.

References

Abramowitz, M., and I.A. Stegun, Eds., 1965: Handbook of Mathematical Functions. Dover. 1046pp.

Boyd, J.P., 1978: Spectral and pseudo-spectral methods for eigenvalue and nonseparable boundary value problems. Mon. Wea. Rev., 106, 1192-1203.

Clark, T.L., 1974: A study in cloud phase parameterization using the gamma distribution. J. Atmos. Sci., 31, 142-155.

Clark, T.L., 1976: Use of log-normal distributions for numerical calculations of condensation and collection. J. Atmos. Sci., 33, 810-821.

Cotton, W.R., 1979: A review for 1975-1978 IUGG quadrennial report. Rev. of Geophysics and Space Physics, 17, 1840-1851.

Fletcher, N.H., 1969: The Physics of Rainclouds. Cambridge. 390pp.

Gottlieb, D., and S.A. Orszag, 1977: Numerical Analysis of Spectral Methods: Theory and Application. NSF-CBMS Monograph No. 26, SIAM. 172pp.

Luke, Y.L., 1969: The Special Functions and Their Approximations. V. I. Academic. 349pp.

Ochs, H.T., III, and C.S. Yao, 1978: Moment-conserving thchniques for warm-cloud microphysical computations. Part. I: Numerical techniques. J. Atmos. Sci., 35, 1947-1958.

Orszag, S.A., and M. Israeli, 1974: Numerical simulation of viscous incompressible flows. Ann. Rev. Fluid Mech., 5, 281-318.

Strang, G., and G.J. Fix, 1973: An Analysis of the Finite Element Method. Prentice-Hall. 306pp.

ROLE OF COAGULATION PROCESSES IN CLOUD AND RAIN FORMATION

A.A.Lushnikov
Karpov Institute of Physical Chemistry
Moscow USSR

Two kinds of coagulation processes are considered responsible for different stages of atmospheric condensational aerosol formation: i. source enhanced coagulation in free molecular regime and ii.gravitational kinematic coagulation.

Source enhanced coagulation in free molecular regime is responsible for formation of size spectra of high dispersed condensational aerosols within the size interval 10 - 100nm. Such aerosols serve then as condensational nuclei affecting considerably on early stages of cloud droplet formation.These aerosols form usually as a result of influence of the sun ultraviolet radiation on trace organic impurities which yield nonvolatile combinations raising due to different atmospheric chemical and photochemical reactions.These processes provide condensing substances forming the high dispersed particles.The kinetics of their growth is governed by the well known equation (see e.g. [1]):

$$\partial_t c(g,t)=I(g,t)+\int_{\ell_1,\ell_2} \mathcal{K}(g|\ell_1,\ell_2)c(\ell_1,t)c(\ell_2,t) \qquad (1)$$

where

$$\mathcal{K}(g|\ell_1,\ell_2)=\frac{1}{2}K(\ell_1,\ell_2)[\delta(g-\ell_1-\ell_2)-\delta(g-\ell_1)-\delta(g-\ell_2)]$$

$c(g,t)$ is the concentration of particles containing g monomers, $I(g,t)$ is the rate of supplying the system with fresh particles, $K(l_1,l_2)$ is the coagulation kernel and $\delta(x)$ stands for the Dirac delta function.All values are dimensionless.

In what follows the steady state external source is considered: $I(g,t)=I(g)$.The coagulation kernel is assumed to be of the form (the free molecular regime):

$$K(\ell_1,\ell_2)\propto(\ell_1^{1/3}+\ell_2^{1/3})\sqrt{\frac{1}{\ell_1}+\frac{1}{\ell_2}} \qquad (2)$$

Source enhanced coagulation processes had been studied by several authors [2 - 5].The main attention had been paid to the cases when at $t\to\infty$ the asymptotically steady state regime of coagulation was settled.The conditions for this were found to be $\lambda<1, \mu<1, \lambda=\alpha+\beta, \mu=|\alpha-\beta|$ where λ is the homogeneity parameter of the kernel and α, β are the exponents of the asymptotic expansion of the coagulation kernel: $K\propto \ell_1^{\alpha}\ell_2^{\beta}$ at $\ell_1>>\ell_2$ .For the kernel (2) $\lambda=1/6$ $\alpha=2/3$, $\beta=-1/2$ and $\mu=7/6$,i.e.the steady state asymptotic regime is never achieved.Instead of this the coagulation process proceeds as follows.At the initial stage the mass spectrum is smooth (the case $c(g,0)=0$ and $I(g)=0$ at $g>g_0$ is considered) and spreads to the right along the g-axis in increasing t.In some time at $g>>g_0$ there appears a peak containing almost all mass of the system,while the total particle number in it remains small.Particles inside this peak grow for two reasons:due to coalescence with each other and as a result of joining small particles,providing by the external source.The latter process leads to decrease of the total particle number of the high dispersed part of the spectrum.According to the above consideration the spectrum c is divided into two parts:

$$c=c_A+c_I \qquad (3)$$

where subscripts A and I are prescribed to the coarse and high dispersed fractions respectively.The coarse fraction is expected to "forget" the form of the external source $I(g)$ and therefore can be found in the self-preserving form[5]:

$$c_A=\mathcal{J}tB^2\psi(gB) \qquad (4)$$

where $\mathcal{J}=\int g I\,dg$ .Substituting eqs. (3) and (4) into eq.(1) yields:

$$-x\psi'-2\psi=\varkappa^2\int\mathcal{K}(x|y,z)\psi(y)\psi(z)\,dy\,dz \qquad (5)$$

$$B(t)\propto t^{-\frac{2}{1-\lambda}} \qquad (6)$$

where $\varkappa$ is a separation constant. Remaining part of the equation define c_I .At large t two factors are shown to affect c_I :the form of the external source and the coalescence of small and large particles:

$$\partial_t c_I=I(g)-c_I g^{\beta}\mathcal{S}_{A\alpha} \qquad (7)$$

where $\mathcal{S}_{A\alpha}=\int g^{\alpha}c_A\,dg$ .The asymptotic solution to eq.(7) is:

$$c_I(g,t)\approx I(g)\Big/g^{\beta}\mathcal{S}_{A\alpha}(t) \qquad (8)$$

Using eqs.(4) and (8) one gets:

$$N_A = \int c_A dg \propto t^{-\frac{1+\lambda}{1-\lambda}}, \quad M_A = \int g c_A dg \propto t$$

$$N_I = \int c_I dg \propto t^{-\frac{\mu-1}{1-\lambda}}, \quad M_I = \int g c_I dg \propto N_I \qquad (9)$$

For the coagulation kernel (2) eq.(9) gives:

$$N_A \propto t^{-7/5}, \quad N_I \propto t^{-1/5}$$

It is seen that $N_A \ll N_I$ at $t \to \infty$ in accordance with the assumptions made.

Thus we see that the asymptotic mass spectrum in the case of the source enhanced coagulation in free molecular regime consists of two parts one of which (c_A) is independent of the form of the external source, while the other one (c_I) depends essentially on it.

The rain formation from warm clouds is related to coagulation of comparatively large droplets ($\gtrsim 10 - 20\mu$). The simplest version of the coagulation kernel in this case (gravitational kinematic coagulation) is:

$$K(\ell_1, \ell_2) \propto (\ell_1^{1/3} + \ell_2^{1/3})^2 \left| \ell_1^{2/3} - \ell_2^{2/3} \right| \qquad (10)$$

Some attempts had been undertaken to study the kinetics of gravitational kinematic coagulation. However, recently [6,7] a very nontrivial fact had been elicited. The Smoluchowski equation had been shown to give nonadequate description of some coagulation processes (the gravitational kinematic coagulation is in that number). The reason for this is the formation of giant superparticles the concentration of which is vanishingly small in the thermodynamic limit. Nevertheless the appearance of the superparticles affects appreciably the coagulation kinetics. This fact led to the necessity to consider coagulation processes in finite systems and to learn to diagnose situations in which the formation of superparticles is possible. Attempts to make this had been done in [8]. There an assumption had been suggested and confirmed by a numerical experiment that superparticles form in cases when coagulation kernels grow too fast with increase of the size of coagulating particles. The exact condition for this was supposed to be $\lambda > 1$. The coagulation kernel (10) has the homogeneity exponent $\lambda = 4/3 > 1$, so the superparticle is expected to form.

The kinetics of the coagulation process with the kernel (10) was studied with the aid of the Monte Carlo method according to receipt of ref. 9 . The simulation was performed of the coagulation process for a finite system containing M particles (M=100 ÷ 800). The dependence on M of the time $\tau_{1/2}$ of formation of a particle with the mass equal to M/2 served as a criterion of the superparticle formation. Once $\tau_{1/2} \to const$ in increasing the total mass M the superparticle is considered to appear. The time dependence of the second moment of the mass spectrum was followed as well. It was shown that $\gamma_2(t)$ increases sharply at the moment of the superparticle appearance (see also [6 - 8]). The result of the numerical experiment showed that the time of formation of the superparticle was

$$t_c = 158 / L r_0 \ (\text{min}) \qquad (11)$$

where L is the water content of the cloud (gramm/m^3) and r_0 is the initial radius (in microns) of coagulating droplets. This time is of the order of several minutes and even less for values L and r_0 typical for tropic warm clouds. So the appearance of superparticles should be accounted for in constructing theoretical models of tropic shower formation.

References

1. Hidy, J.M., Brock, J.R., (1970) "The Dynamics of Aerocolloidal Systems", Pergamon Press, N.Y.
2. Lushnikov, A.A., Smirnov, V.I., (1975) "Steady-state coagulation and size distribution of atmospheric aerosols", Atmos. Ocean Phys., v.9, No2, 139 - 151.
3. Klett, J.D., (1975) "A class of solutions to the steady-state, source-enhanced, kinetic coagulation equation", J. Atmos. Sci., v.32, No2, 380.
4. Lushnikov, A.A., Piskunov, V.N., (1976) "Coagulation in presense of external sources of particles", Dokl. Akad. Nauk SSSR, v.231, No6, 1403 - 1406.
5. Lushnikov, A.A., Piskunov, V.N., (1977) "Asymptotic regimes of coagulation in systems with external source of particles", Kolloid. Zh., v.39, No6, 1076 - 1081.
6. Lushnikov, A.A., (1978), "Coagulation in finite systems", J. Colloid Interface Sci., v.65, No2, 276 -285.
7. Lushnikov, A.A., (1978), "Some new aspects of the coagulation theory", Atmos. Ocean Phys., v.14, No10, 1046 - 1055.
8. Domilovski, E.R., Lushnikov, A.A., Piskunov, V.N., (1979), "A Monte Carlo simulation of coagulation processes" Atmos. Ocean Phys., v.15, No2, 194-201.
9. Gillespie, D.T., (1975), "An exact method for numerically simulating the stochastic coalescence process in a cloud", J. Atmos. Sci., v.32, No10, 1977 - 1989.

EXPERIMENTAL DETERMINATION OF COEFFICIENT OF GRAVITATIONAL COAGULATION FOR WATER DROPLETS IN WIDE RANGE OF SIZES ($10^{-3} \leq Re \leq 10$)

A.I. Neizvestny and A.G. Kobzunenko

The Central Aerological Observatory, Moscow, USSR

I. Introduction

The determination of the growth rate of cloud drops due to their collision and coalescence is an important problem of cloud microphysics. This rate is determined definitely if collision efficiency K* of drops is known.

In theory the collision efficiency (CE) is determined by integrating the equations of relative motion for interactive drops using various expressions for the velocity field of the flow around the drops. Different approaches to solving the problem of cloud drop CE determination arise considerable discrepancy in final results /1-4/. The experimental data about CE are obtained only in cases $P=r_2/r_1 \leq 0.2$ /5-8/, or $P \geq 0.95$ /9,10/, therefore in fact these data** make it impossible to determine the limits of applicability for different methods to calculate K.

In this work we experimentally determine CE for drops with radius $10 \leq r_1 \leq 100$ μm and for droplets with radius $5 \leq r_2 \leq 19$ μm, at $0.15 \leq P \leq 0.64$. The idea of the experiment is as follows. The chamber with height h is filled with monodisperse droplets of known r_2, charges q_2 and concentration N. Then the known number of drops n_0 ($n_0 \approx 1000$) being introduced into the chamber, pass through the droplet column and collide with some of the droplets with probability $F=n_c/n_0$, where n_c is the number of drops which captured the droplets. If the droplets are distributed in the chamber at random applying to Poisson's distribution and their concentration is so small that the probability of two-multiple and three-multiple captures is significantly less than the probability of one-multiple capture, we determine K from equation /5/:

$$K = -\ln(1-F)\cdot\left[\pi\cdot(r_1 + r_2)^2 Nh\right]^{-1}.$$

*) $K=\rho^2/(r_1+r_2)^2$, where ρ is linear parameter of collision; r_1, r_2 - drop and droplets radii, respectively.

**) With the exception of works /11-13/, where P changes from 0.2 to 0.6.

In order to determine CE in so wide range of r_1 and r_2 two different techniques and experimental apparatuses are used. One of them allows determining drop CE with $38 \leq r_1 \leq 100$μm, and another one - with $12 \leq r_1 \leq 38$ μm. Let us discuss every technique.

2. The technique for determining CE of drops with $38 \leq r_1 \leq 100$ μm

The chamber represents the cylinder 260 cm high with inner diameter 11 cm. The height of the chamber is divided into three parts: 1. The input zone, 50 cm long, where generation and dissipation of monodisperse droplets take place. 2. The interaction zone, 100 cm long, where drop-droplet interactions take place. 3. The separation zone, 110 cm long, where drops overtake droplets and separate from them due to the difference in the sedimentation rate.

The droplets are produced from 10% water solution of NaCl in the generator of monodisperse drops with productivity $2\cdot10^5\ s^{-1}$ /14/. The degree of monodispersion of the obtained droplets does not exceed 1-2%, and the number of coagulated droplets during dissipation does not exceed 3-4%.

The drops are obtained in the generator with a vibrating needle /14/, with productivity 120-140 s^{-1}. They are produced from 0.5% water solution of fluorescent material. To prevent scavenging, the generator is provided with the scanning device dissipating drops at area 2x2 cm^2.

Drop and droplet sizes are determined with sedimentation rates found from pictures of their tracks in pulsed light /14/. The droplet specific concentration ($Nh\ cm^{-2}$) is determined with photoelectric method /14/. The drop (q_1) and droplet (q_2) charges do not exceed values $q_1 \leq 2\cdot10^{-16}$ C, $q_2 \leq 1\cdot10^{-15}$ C.

3. The technique for determining CE of drops* with $12 \leq r_1 \leq 38$ μm

The chamber represents the cylinder 175 cm high with inner diameter 3 cm. It consists of three parts - the imput zone, 35 cm long, interaction zone, 140 cm long and zone of separation, i.e. the horizontal channel with cross-section 6x9 cm , where the laminar airflow moves 1.5-2 cm/s. In this flow drops separate from droplets.

The drops and droplets are obtained in the generator of monodisperse drops with a vibrating needle /14/. The productivity of the generator is 1200 s^{-1} and that of the droplet one is 120-140 s^{-1} . The drops are produced from 10% water solution of NaCl and the droplets - from the same solution and 0.5% of fluorescent material.

The methods of determining drop and droplet sizes and the specific droplet concentration are the same as in the above technique. When r_2 and r_1 change from 5 to 38 μm, drop or droplet charges vary from $1 \cdot 10^{-18}$ C to $1 \cdot 10^{-16}$ C, respectively.

4. Results and discussion

The results of experiments are given in Table 1. The intercomparison of obtained data and calculated values of CE shows that if $40 \leq r_1 \leq 100$ μm, the best agreement is observed with the data of Lin and Lee /4/. The calculations of Shlamp et al. /15/ are also in good agreement with the experiment when $P \geq 0.25$, but when P is less, they show somewhat underestimated results. The calculations of Klett and Davis /3/ with the above said values of r_1 show underestimated results for all studied P.

In the range of values $25 \leq r_1 \leq 40$ μm for all P we observe good agreement with calculations /3/. But if $r_1 < 25$ μm, calculations /3/ are significantly overestimated. It is particularly seen for experimental points $18.8 \leq r_1 \leq 21.8$ μm, which well coincide with curve K=f(P) when $r_1 = 20$ μm, calculated by Jonas /2/, and almost 100% lower the values obtained in /3/.

*) This technique and obtained results are being published in "Izvestia Academii Nauk SSSR", Physika Atmospheri i Oceana", 1980.

The experimental data for droplets with $11 \leq r_1 \leq 25$ μm and $0.2 \leq P \leq 0.65$ are in good agreement with calculations of Jonas /1/ and Davis /2/.

The evaluation of the effect of residual electrical charges of droplets upon the values of K showed /14/, that, on the one hand, they are small enough not to influence the values of K and, on the other hand, great enough for the coefficient of droplet coalescence to be equal to unity. The evaluation of the influence of microturbulence on the value of CE showed that this effect may be negligible.

For $10 \leq r_1 \leq 300$ μm and $0.05 \leq P \leq 1$ we have chosen approximate formulas* in a form:

$$K = A(r_1)\sin\frac{\pi}{2}z(r_1,P) + B(r_1)\cdot [1+(1953.0/r_1+9.0/r_1^2\cdot P^3-6.2)\cdot (P-108.0/r_1^2-0.5)^5] + 1.14/r_1^1\cdot P^6; \quad (1)$$

where $A(r_1) = 0.050\exp[-0.0142(r_1-15)^2] + 0.31\exp[-0.019(r_1-30)^2]$,

$$B(r_1) = \exp[-(32.2/r_1)^5];$$

$$z(r_1,P) = P^{1.0+0.034r_1-5\cdot10^{-7}r_1^4}.$$

In calculations according to (1) we must introduce two limitations in the program: 1. If $K < 0$, $K = 0$. 2. If $r_1 \geq 50$ μm, $A(r_1) = 0$ and the whole first term in (1) equals 0. The first limitation allows to exclude negative values of K. The second one allows to shorten the time of computations as well as to avoid infinitely great values of $z(r_1,P)$ at $r_1 \geq 80$ μm. The comparison of calculations (1) with numerical calculations /1-4,15,16/ showed, that for $10 \leq r_1 \leq 300$ μm and $0.1 \leq P \leq 0.95$ the formulas (1) error does not exceed 3-6%. On the limit of applicability for formulas (1) with parameter P their error depending on r_1 may reach 15-30%.

*) In formulas (1) r_1 in micrometres.

Table 1

Numerical values of experimental data about CE of drops. n - number of measurements in a series; εr_1, εK - confidence intervals in determining r_1, r_2, K, respectively, with confidence probability 0.68

Series	n	$r_1 \pm \varepsilon r_1$, μm	$r_2 \pm \varepsilon r_2$, μm	$K \pm \varepsilon K$
1	8	100.0 ± 0.6	14.7 ± 0.9	0.93 ± 0.02
2	10	96.2 ± 3.0	19.2 ± 0.2	0.92 ± 0.02
3	9	82.9 ± 1.1	19.2 ± 0.2	0.93 ± 0.02
4	12	79.4 ± 0.6	14.7 ± 0.9	0.92 ± 0.03
5	12	63.0 ± 1.4	13.5 ± 0.1	0.86 ± 0.04
6	4	61.2 ± 2.2	19.2 ± 0.2	0.88 ± 0.02
7	10	55.5 ± 1.3	12.9 ± 0.1	0.81 ± 0.03
8	4	48.2 ± 0.8	12.9 ± 0.1	0.82 ± 0.08
9	8	47.0 ± 1.2	14.1 ± 0.2	0.82 ± 0.04
10	6	42.1 ± 0.3	14.1 ± 0.5	0.76 ± 0.03
11	10	38.2 ± 0.5	14.1 ± 0.5	0.73 ± 0.03
12	4	35.3 ± 0.6	19.2 ± 0.2	0.66 ± 0.05
13	10	38.3 ± 0.4	17.5 ± 0.2	0.69 ± 0.03
14	12	31.9 ± 0.3	7.9 ± 0.1	0.24 ± 0.02
15	12	31.1 ± 0.2	10.0 ± 0.1	0.45 ± 0.02
16	10	30.4 ± 0.3	17.5 ± 0.2	0.59 ± 0.01
17	12	29.6 ± 0.3	9.0 ± 0.2	0.25 ± 0.01
18	10	28.2 ± 0.3	4.9 ± 0.3	0.015± 0.002
19	8	24.7 ± 0.5	13.0 ± 0.1	0.22 ± 0.03
20	5	22.9 ± 0.6	4.9 ± 0.1	0.016± 0.001
21	12	21.8 ± 0.2	10.0 ± 0.1	0.072± 0.004
22	8	20.4 ± 0.2	13.0 ± 0.1	0.088± 0.006
23	12	19.2 ± 0.1	7.9 ± 0.1	0.051± 0.003
24	6	18.8 ± 0.3	11.0 ± 0.1	0.083± 0.015
25	8	15.0 ± 0.2	6.6 ± 0.1	0.034± 0.004
26	12	12.0 ± 0.2	6.9 ± 0.1	0.041± 0.006

5. Conclusion

Thus, the description of all the obtained and early known experimental data needs the assumption of at least three theories, corresponding to different approaches to the problem of the collision of two spheres. 1. In the range of values of $40 \leq r_1 \leq 100$ μm - the theory of Lin and Lee /4/. 2. In the range of values of $10 \leq r_1 \leq 25$ μm - the theory of Davis /1/ or Jonas /2/. 3. In the range of values of $25 \leq r_1 \leq 40$ μm - the theory of Klett and Davis /3/.

In conclusion the authors express their gratitude to Dr. I.P. Masin for the discussion of the obtained data and to G.B. Kotov for assistance in the experiment.

Reference

1. Davis M.H. 1972 "J. Atmos. Sci.", v.29, N5, 911-915.
2. Jonas P.R. 1972 "Quart. J.Roy. Met. Soc.", v.98, N417, 681-683.
3. Klett J.D., Davis M.H. 1973 "J. Atmos.Sci.", v.30, N1, 107-117.
4. Lin C.L., Lee S.C. 1975 "J. Atmos. Sci." , v.32, N7, 1412-1418.
5. Picknett K.G. 1960 "Intern. J. Air Pollut.", N3, 160-167.
6. Woods J.D., Mason B.J. 1964 "Quart. J. Roy. Met. Soc.", v.90, N386, 373-381.
7. Beard K.V., Pruppacher H.R. 1971 "Quart. J. Roy. Met. Soc.", v.97, 242-248.
8. Kinzer G.D., Cobb W.E. 1958 "J. Met.", v.15, 138-148.
9. Woods J.D., Mason B.J. 1965 "Quart. J.Roy. Met. Soc.", v.91, N387, 35-43.
10. Beard K.V., Pruppacher H.R. 1968 "J. Geoph. Res.", v.73, N20, 6407-6414.
11. Krasnogorskaya N.V., Neizvestny A.I. 1971, XV Generalnaya Assamblea mezdunarodnogo geophizicheskogo i geodezicheskogo soiuza. Tezisi docladov. Moskva.
12. Neizvestny A.I. Avtoreferat dissertacii. Dolgoprudny, CAO, 21p., 1974.
13. Krasnogorskaya N.V., Neizvestny A.I. 1973, "Meteorologia i Gydrologia", N12.
14. Neizvestny A.I., Kobzunenko A.G. 1980, "Izvestia Academii Nauk SSSR", PAO, N4.
15. Schlamp R.J., Grover S.N., Pruppacher H.R. 1976, "J. Atmos. Sci.", v.33, N9, 1747-1755.
16. Shafrir U., Gal-Chen T. "J. Atmos. Sci." 1971, v.28, 741-751.

MEASUREMENTS OF THE COLLECTION EFFICIENCY FOR CLOUD DROPS

H. T. Ochs, K. V. Beard, and T. S. Tung
Illinois State Water Survey
Urbana, Illinois, USA

1. Introduction

In evaluating the collision-coalescence process for cloud drops the collection efficiency is usually assumed to be equivalent to the computed collision efficiency for rigid spheres. Davis (1972) and Jonas (1972) have calculated the collision efficiencies for rigid spheres including viscous and slip effects. Klett and Davis (1973) and de Almeida (1977) have included viscous and inertial effects. For a stronger inertial influence the method of superposition has been used (e.g., Shafrir and Neiburger, 1963). The validity of the assumption that rigid sphere results are applicable to deformable drops is not firmly established because of a lack of experimental data.

Differences between the theory for rigid spheres and experimental work with drops have been interpreted as a coalescence problem, e.g., the rebound effect (Foote, 1971). Levin *et al.* (1973) concluded from wind tunnel measurements that the coalescence efficiencies were quite low for collector drops of 50-110 μm radius for a size ratio of $p \simeq 0.2$. On the other hand high coalescence efficiencies can be inferred from the measurements of Picknett (1960) and also Woods and Mason (1964) for collector drops of 30-50 μm radius and $p \simeq 0.2$ since these empirical findings were comparable to theoretical collision efficiencies. High coalescence efficiencies can also be inferred from the collection efficiency measurements of cloud drops for similar sizes, $0.7 \leq p \leq 1$ (Woods and Mason, 1965; Beard and Pruppacher, 1968; Abbott, 1974) and for greatly dissimilar sizes, $p < 0.1$ (Beard and Pruppacher, 1971).

This unresolved question concerning the coalescence of cloud drops was singled out in a review of cloud physics (Simpson *et al.*, 1974) as an area in "urgent need for further testing." The purpose of our research is to help resolve this question. New findings are presented for collector drops between 63 and 84 μm radius and cloud drops between 14 and 22 μm radius.

2. Experimental Design and Procedure

The experimental apparatus which is explained in more detail in Beard *et al.* (1979) is shown in Fig. 1. A tracer solution of lithium sulfate in deionized water (0.1% Li^+) was used to form a highly monodisperse cloud of droplets using a vibrating orifice device. The cloud was passed through an ion discharge device and the cloud chamber. A second vibrating orifice device was used to produce uniform collector drops which were free of lithium. Widely spaced collector drops that were injected into the top of the cloud chamber were collected in polypropylene bottles at the bottom. The cloud drops were prevented from entering the sample bottle by a sheath of horizontally flowing air at the bottom of the cloud chamber.

Two improvements in the experiment of Beard *et al.* (1979) were adopted. First, by using longer electrical deflection plates in the collector drop generator (see Adam *et al.* 1971) better charge minimization was achieved. Computations of the collector drop trajectory through the deflecting electrodes established upper air limits on the drop charge. These calculations included effects of gravity, drag and electrical forces as well as the initial horizontal and vertical drop velocities and alignment uncertainties. These computations yielded a typical upper charge limit of 10^{-14} coulombs. The second improvement was the use of polypropylene sample bottles to minimize any loss of lithium ions to the container walls.

The collection efficiency was determined from experimental parameters using the equation

$$E = M/[\pi A^2(1 + p)^2 \Delta V \, nmXtN],$$

where M is the amount of lithium measured for an experimental run and the term in brackets is the amount of lithium expected from capture of all cloud droplets in the geometric path of the collector drops (i.e., unity collection efficiency). The term $\pi A^2(1 + p)^2$ is the geometric cross section for a collector drop of radius A and a smaller drop (size ratio p). Multiplication of this cross section by the relative terminal velocity (ΔV) and the number concentration of drops (n) results in the number of cloud droplets encountered geometrically per unit time by a single collector drop. Further

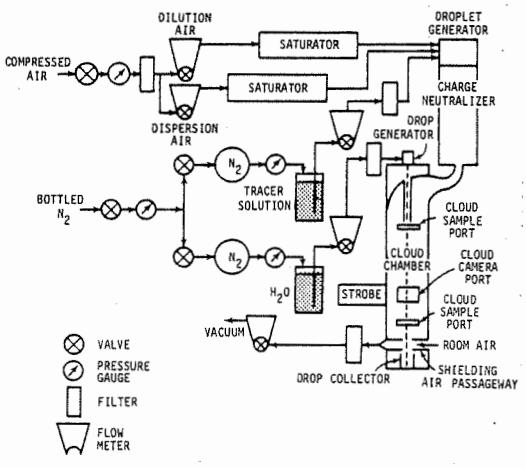

Figure 1. Diagram of experimental apparatus used to measure collection efficiencies.

multiplication by the mass of one cloud drop (m) and mass fraction of lithium in one cloud drop (X) results in the amount of lithium encountered geometrically per unit time by a single collector drop. Finally, the lithium encountered by all collector drops is found from multiplication by the interaction time for one collector drop (t) and the total number of collector drops for one experimental run (N).

The amount of lithium for each run (M) was determined by atomic absorption analysis. The size of the collector drop and cloud drop was used to obtain the size ratio (p) and the relative terminal velocity (ΔV) using the equations in Beard (1976). The collector drop size was calculated from a measurement of the water flow rate, and the size of cloud drop in the chamber was determined using a calibrated stain method similar to that used by Liddell and Wootten (1957). The initial cloud drop mass (m) was obtained from a flow rate measurement, whereas the initial lithium was fixed by the concentration of the tracer in the cloud water solution (X=0.001). The cloud drop concentration (n) was determined photographically. The interaction time (t) was determined from the fall-speed of the collector drop, the downward air velocity in the cloud chamber and the cloud chamber height. Accurate knowledge of the air velocity was unnecessary because its magnitude was only about 5% of the collector drop velocity.

3. Results

To date we have obtained seven points for collector drop radii between 63 and 84 μm and for radius ratios between 0.21 and 0.32. These data all indicate collection efficiencies below accepted values of computed collision efficiencies. Based on our data and computed collision efficiencies the coalescence efficiency is between 0.36 and 0.67.

The collection of cloud droplets by the few larger cloud drops present has been shown to be an important factor in the initiation of warm rain (Ochs and Semonin, 1979; Johnson, 1979). Thus the efficiency with which these collector drops sweep out cloud water is important to the rate at which precipitation is formed. The data presented here indicates that the collection efficiencies for these drops are significantly lower than computed collision efficiencies.

From a comparison with a summary by Takahashi (1972) on measurements of charges in warm rain, we have concluded that our cloud droplet charges were considerably below those occurring naturally, but our collector drop charges were compaable to observed mean values. Thus, we are continuing to make measurements with reduced collector drop charge. We are also extending the size range of the cloud and collector drops. These additional results will be presented at the conference.

Acknowledgments. The authors appreciate the guidance of Richard G. Semonin during the early stages of this research and the chemical analysis performed by Mark R. Peden and Loretta Skowron. This work was supported by the National Science Foundation under Grant ATM79-14170.

REFERENCES

Abbott, C. E., 1974: Experimental cloud droplet collection efficiencies. *J. Geophys. Res., 79.*

Adam, J. R., R. Cataneo, and R. G. Semonin, 1971: The production of equal and unequal size droplet pairs. *Rev. Sci. Instrum., 42.*

de Almeida, F. C., 1977: Collision efficiency, collision angle and impact velocity of hydrodynamically interacting cloud drops: A numerical study. *J. Atmos. Sci., 34.*

Beard, K. V., and H. R. Pruppacher, 1968: An experimental test of theoretically calculated collision efficiencies of cloud drops. *J. Geophys. Res., 73.*

_____, and _____, 1971: A wind tunnel investigation of collection kernels in small water drops in the air. *Quart. J. Roy. Meteor. Soc., 97.*

_____, H. T. Ochs, and T. S. Tung, 1979: A measurement of the efficiency for collection of cloud drops. *J. Atmos. Sci., 36.*

Davis, M. H., 1972: Collision of small cloud droplets: Gas kinetic effects. *J. Atmos. Sci., 29.*

Foote, G. E., 1971: *A theoretical investigation of the dynamics of liquid drops.* PhD Thesis, Univ. of Arizona, 206 pp.

Johnson, D. B., 1979: *The Role of Coalescence Nuclei in Warm Rain Initiation.* PhD Thesis, The Univ. of Chicago, 119 pp.

Jonas, P. R., 1972: The collision efficiency of small drops. *Quart. J. Roy. Meteor. Soc., 98.*

Klett, J. D., and M. H. Davis, 1973: Theoretical collision efficiencies of cloud droplets at small Reynolds numbers. *J. Atmos. Sci., 30.*

Levin, Z., M. Neiburger, and L. Rodriguez, 1973: Experimental evaluation of collection and coalescence efficiencies of cloud drops. *J. Atmos. Sci., 30.*

Liddell, H. F., and N. W. Wootten, 1957: The detection and measurements of water droplets. *Quart. J. Roy. Meteor. Soc., 83.*

Ochs, H. T., and R. G. Semonin, 1979: Sensitivity of a cloud microphysical model to an urban environment. *J. Appl. Meteor., 18.*

Picknett, R. G., 1960: Collection efficiencies for water drops in air. *J. Air Water Poll., 3.*

Shafrir, U., and M. Neiburger, 1963: Collision efficiencies of two spheres falling in a viscous medium. *J. Geophys. Res., 68.*

Simpson, J., B. Ackerman, A. Bett, J. McCarthy, H. Orville, R. Ruskin, R. Sax, J. Warner, and H. Weickmann, 1974: Achievements and expectations in cloud physics. *Bull. Amer. Meteor. Soc., 55.*

Takahashi, T., 1972: Electric charge of cloud droplets and drizzle drops in warm clouds along the Mauna Lao-Mauna Kea Saddle Road of Hawaii Island. *J. Geophys. Res., 77.*

Woods, J. D., and B. J. Mason, 1964: Experimental determination of collection efficiences for small water drops in air. *Quart. J. Roy. Meteor. Soc., 90.*

_____, and _____, 1965: The wake capture of water drops in air. *Quart. J. Roy. Meteor. Soc., 91.*

A NUMERICAL SOLUTION OF THE KINETIC COALESCENCE EQUATION

SH.I. Tzivion (Tzitzvashvili)

Israel Meteorological Service, Dept. for Research and Development
Bet Dagan, ISRAEL

INTRODUCTION

Numerical methods of solving the coalescence equation for cloud droplets, as a rule, involve restrictions with recpect to the shape of the unknown distribution function. Piecewise power and exponential distribution functions are used by Bleck (1970) and Soong (1974), respectively. Interpolation methods for the distribution function are used by Berry and Reihardt (1974). One may assume that the above restrictions must lead to certain inaccuracies in solving the coalescence equation. In the present study a different approach is followed. Only the known function, describing the probability of collision between cloud particles, is approximated.

EQUATION OF THE MOMENTS

The kinetic equation of coalescence of cloud droplets may be written in the form:

$$\frac{\partial f(x,t)}{\partial t} = -f(x,t)\int_0^\infty \sigma(x,y) f(y,t)dy + 0.5\int_0^x \sigma(x-y) f(x-y,t) f(y,t)dy \qquad (1)$$

where $f(x,t)$- the distribution denisity function of cloud droplets by their mass x, at a time instant t, $\sigma(x,y)$-the probability of coalescence betveen cloud particles with mass x and y, respeqtively,at unit of time and a unit of cloud air volume. In case of gravitational coalescence mechanism the $\sigma(x,y)$ function may be expressed:

$$\sigma(x,y) = (9/16\pi)^{1/3}\,(x^{1/3}+y^{1/3})^2\, E(x,y)\,|V_x - V_y| \qquad (2)$$

where: $E(x,y)$- is a capture coefficient which was approximated by a method suggested by Long (1974) and V_x, V_y - are gravitational fall velocities of particles with mass x and y, respeqtively. They are approximated by the use of experimental data of Gunn and Kinzer (1949), and Beard (1976).

The overall spectrum is subdivided into separate spectral intervals acording to the expression:

$$x_{k+1} = p x_k \qquad (3)$$

where: k- number of the spectral interval, x_k, x_{k+1} - the lower and upper mass limits of the spectral class k respectively, p - a parameter, designating the width of the spectral interval and it may take values of 2, $\sqrt{2}$, or $\sqrt[3]{2}$.

A moment of the order j of the distribution function $f(x,t)$, in the spectral interval k, is now introduced in the form:

$$M_k^j(t) = \int_{x_k}^{x_{k+1}} x^j f_k(x,t)dx \qquad (4)$$

Using expression (4) a system of equations can now be derived from (1) with respect to the moments in each class:

$$\frac{dM_k^j(t)}{dt} = -\sum_{i=1}^{k}\int_{x_k}^{x_{k+1}} x^j f_k(x,t)dx \int_{x_k}^{x_{i+1}} \sigma_{k,i}(x,y) f(y,t)dy + 0.5\int_{x_k}^{x_{k+1}} x^j dx \int_{x_i}^{x} \sigma(x-y) f(x-y,t) f(y,t)dy \qquad (5)$$

where k is the number of spectral classes considered. Defining the second integral in (5) in accordance with Bleck's approach (1970), and after some transformations, the following equations were obtained:

$$\frac{dM_k^j(t)}{dt} = \sum_{i=1}^{k}\int_{x_k}^{x_{k+1}-y} (x+y)^j \sigma_{k,i}(x,y) f(x,t)dx + \sum_{i=1}^{k-2}\int_{x_i}^{x_{i+1}} f_i(y,t)dy \int_{x_k-y}^{x_k} (x+y)^j \sigma_{i,k-1}(x,y) f_{k-1}(x,y)dx +$$

$$+0.5\int_{x_{k-1}}^{x_k} f_{k-1}(y,t)dy \int_{x_{k-1}}^{x_k} (x+y)^j \sigma_{k-1,k-1}(x,y) f_{k-1}(x,t)dx - \sum_{i=1}^{k}\int_{x_k}^{x_{k+1}} x^j f_k(x,t)dx \int_{x_i}^{x_{i+1}} \sigma_{i,k}(x,y) f_i(y,t)dy +$$

$$+0.5\int_{x_k}^{x_{k+1}} f_k(y,t)dy \int_{x_k}^{x_{k+1}} (x+y)^j \sigma_{k,k}(x,y) f_k(x,t)dx - 0.5 \int_{x_{k-1}}^{x_k - x_{k-1}} f_{k-1}(y,t)dy \int_{x_{k-1}}^{x_k - y} (x+y)^j \sigma_{k-1,k-1}(x,y) \times$$

$$\times f_{k-1}(x,t)dx \qquad (6)$$

Given j=1 and assuming specific shape of the distribution function, the algorithm of Bleck-Soong is obtained as a particular case of (6).

METHOD OF SOLUTION

For the closure and solution of the system of equations (6), the integrate entering these equations were expresed through moments of the order not exceding j. This can be accomplished if the probability functions $\sigma_{k,i}(x,y)$ are approximate by x and y polinomials of integer orders. High order moments which may occur in this process must then be expressed by moments, the order of which does not exceed j.

The $\sigma_{k,i}(x,y)$ function can be approximated in each spectral interval by power polinomials with any given accuracy. The closure problem of the system of equations (6) can be solved in principle by finding the interrelationships between the various moments in the given spectral intervals. To accomplish this a non-dimensional relationship between the various neighbouring moments of the distribution function isintroduced in each k interval, as following:

$$\xi_p = \int_{x_k}^{x_{k+1}} x^{j-1} f_k(x,t)dx \int_{x_k}^{x_{k+1}} x^{j+1} f_k(x,t)dx \Big/ \Big\{ \int_{x_k}^{x_{k+1}} x^j f_k(x,t)dx \Big\}^2 \qquad (7)$$

Using the known rules of inequalities, the following expression can be written with respect to ξ_p:

$$1 < \xi_p < (p+1)^2/4p \qquad (8)$$

where $p=x_{k+1}/x_k$, and it varies within the limits $1<p<2$. The extreme values of ξ_p deviate from the mean values between 0.0- 6.0%, depending on the value of p. Using the mean ξ_ρ, the relationship between three neighbouring moments of the distribution function can be expressed in the form:

$$M_k^{j+1} = \xi_\rho (M_K^j)^2 / M_K^j \qquad (9)$$

By decreasing the parameter p, i.e. the width of spectral intervals, it is possible in principle to approximate any of the moments by means of two lower order neighbouring moments, with any given accuracy. Th above procedure does not depend appreciably on the shape of the distribution function.

To solve the system of equations (6) it is necessary also to determine the integrals of the type:

$$I_k = \int_{x_k}^{x_{k+1} - y} F_K(x,t)dx \qquad (10)$$

where $F_k(x,t) = x^\beta f_k(x,t)$, $y<x_k$ and $\beta=1,2,3,...$ Introducing a new variable $x=\{1-y/(p-1)x_k\}z+y/(p-1)$ and expanding the integral function into a MacLaurin series around the point y=0, the following expression has been obtained after some transformations:

$$I_K = \int_{x_k}^{x_{k+1}} F_K(x,t)dx - F_K(x_{k+1},t) + \sum_{n=1}^{\infty} [(-1)^{n+1}/(n+1)!] \Big[\frac{\partial^n F_K(x,t)}{\partial x^n}\Big]_{x=x_{k+1}} \times y^{n+1} \qquad (11)$$

The above series is an infinitive, monotonously converging one, and the accuracy of approximation of the integral (10) will depend thus on the number of series members which will be considered. The derivatives occuring in equation (11) were calculated by applying a finite difference scheme. To find the values of $F_k(x,t)$ at the various points the conditions of normalizing the distribution function by its moments are used. An approximate schem of integration is then used.

NUMERICAL EXPERIMENTS WITH A TWO-MOMENT APPROXIMATION

The system of equations (6) can be used for the calculation of any of the physical moments of interest. However, in applying the relationship (9) it is necessary to consider at least two moments, In th numericl experiments which were carried out the zero-order and first moment of the distribution function were used, i.e. concentration-$N_K(t)$ and water content $M_k(t)$ in spectral intervals k. To calculate the above moments from (6) the following system of equation is obtained:

$$dN_k(t)/dt = \Phi_K[N_i(t), M_j(t)] \qquad dM_K(t)/dt = \Psi_K[N_i(t), M_j(t)] \qquad (12)$$

where Φ_K and Ψ_K are known analitical functions of concentration and water content in spectral classes, and $i,j=1,2,3,...K$.

The numerical experiment is carried out by assuming an initial exponential distribution function. The total initial concentration of droplets is assumed to by 3.0×10^6 particles per gr of

air, and the total water content - 1gr per Kg of air. The number of spectral classes is choosen K=36, the minimum drop-radius is R_1=1.5625μm, and p=2.0. The coagulation probability function σ(x,y) is approximated by a first-order polinomial in the form:

$$\sigma_{\kappa,i}(x,y)=A_{k,i}(x+y) \quad \text{where} \quad A_{k,i}=[1.0/(x_{k+1}-x_k)(x_{i+1}-x_i)]\int_{x_k}^{x_{i+1}}[\sigma_{k,i}(x,y)/(x+y)]dx \qquad (13)$$

For the sake of comparison the obtained results were compared with other known solutions. The analitical solution of Scott (1968) for a constant Kernel, as well as Golovin's solution (1963) for a kernel proportional to the total mass of colliding particles were applied. In addition, the results obtained in this study are also compared with the numerical solution of Bleck (1970) for the case when the distribution function within a spectral class is assumed constant with respect to droplet masses.

The distributions of specific water content by spectral intervals and time, are plotted in figure 1A, the three curves represent a precise analytical solution, the proposed method and Bleck's method, respectively, for a value of $\sigma(x,y)=1.0\times10^{-4}cm^{-3}sec^{-1}$. Analyzing figure 1A can see that the distribution obtained with the present method is considerably closer to the analytical solution, as compared with Bleck's method. A similar comparison between the distribution curves in case of Golovin's kernel which equals $1,5\times10^{3}(x+y)$ is shown in figure 1B. It is seen clearly that the distribution obtained by using Bleck's method, 30 minutes after the beginning of the coagulation process, deviates considerably from the analytical solution, whereas the present method yields results close to the analytical solution. It is reasonable to conclude therefore that also in case of a real kernel the proposed method may provide results closer to reality than Bleck's method. Distribution curves in case of a real hydrodynamic kernel are plotted in figure 1C. Analyzing figure 1C one may reveal that the coagulation processes calculated by using Bleck's method is faster by about a factor of two, as compared to the present method.

The accelration of the coagulation process, obtained by applying Bleck's method, for any coagulation kernel, seems to stem from averaging the distribution function in each spectral class. By assuming a given shape of the distribution function valid for the whole spectral interval, as is done by Bleck (1970) and Soong (1974), the solution is approximated to a given analitical solution for a specific case. However, one can not deduce that the above approximation will be valid also for a real hydrodynamic kernel. It is worth to mentionalso that the proposed method allows to investigate the dependence of the coagulation process on the initial distribution by spectral classes of concentration, water contant, radar reflectivity, average mass of droplets and other characteristics. This is not case with the algorithm of Bleck and Soong, as the solution is determined by the initial distribution of water content by spectral classes, only. Due to above merit of the proposed method it was possible to apply it for numerical simulation of the effects of cloud seeding by hygroscopic particles (Tzivion et al, 1980).

CONCLUSIONS

Applying Bleck's approach (1970) for the calculation of the double integrals, a system of ordinary differential equations with respect to the moments of the distribution function was derived. By finding the interrelationships between the various moments, and representing the partial interval moments by the whole interval moments, the closure of the system of equations with respect to the moments of the distribution function, was achieved.

The proposed numerical method of solving the coalescence equation preserves the balance with respect to the distribution function moments. The only requirement is that the distribution function must be continuous and positive, and no other restrictions as to the shape of the unknown function are required. The accuracy of the algorithm is determined primarily be the value of the parameter $p=x_{k+1}/x_k$. In the examples considered a value of p=2.0 was selected. The results of the numerical computations are very close to the precise analytical solutions in case of a constant and Golovin's kernel, respectively. No other values of p were therefore tested. However, one may assume that by decreasing the value of p, even a higher accuracy of the numerical solution may be reached. This will however increase considerably the required computer time. It should be noted that the computer time, required for the computation of each of the moments with the proposed algorithm, is about the same required by Bleck's (1970) algorithm. The proposed algorithm may be used to investigate the dependence of the coagulation process on the initial distribution of the distribution function moments by spectral intervals. Due to the above merit of the proposed algorithm it can be applied successfully for numerical smulation of the effects of cloud seeding by hygroscopic particles on coagulation processes (Tzivion et al., 1980). Worthwhilile mentioning is also that the basic approach used in the present algorithm may be applied easily to elaborate numerical schemes for the computation of other microphysical processes in clouds.

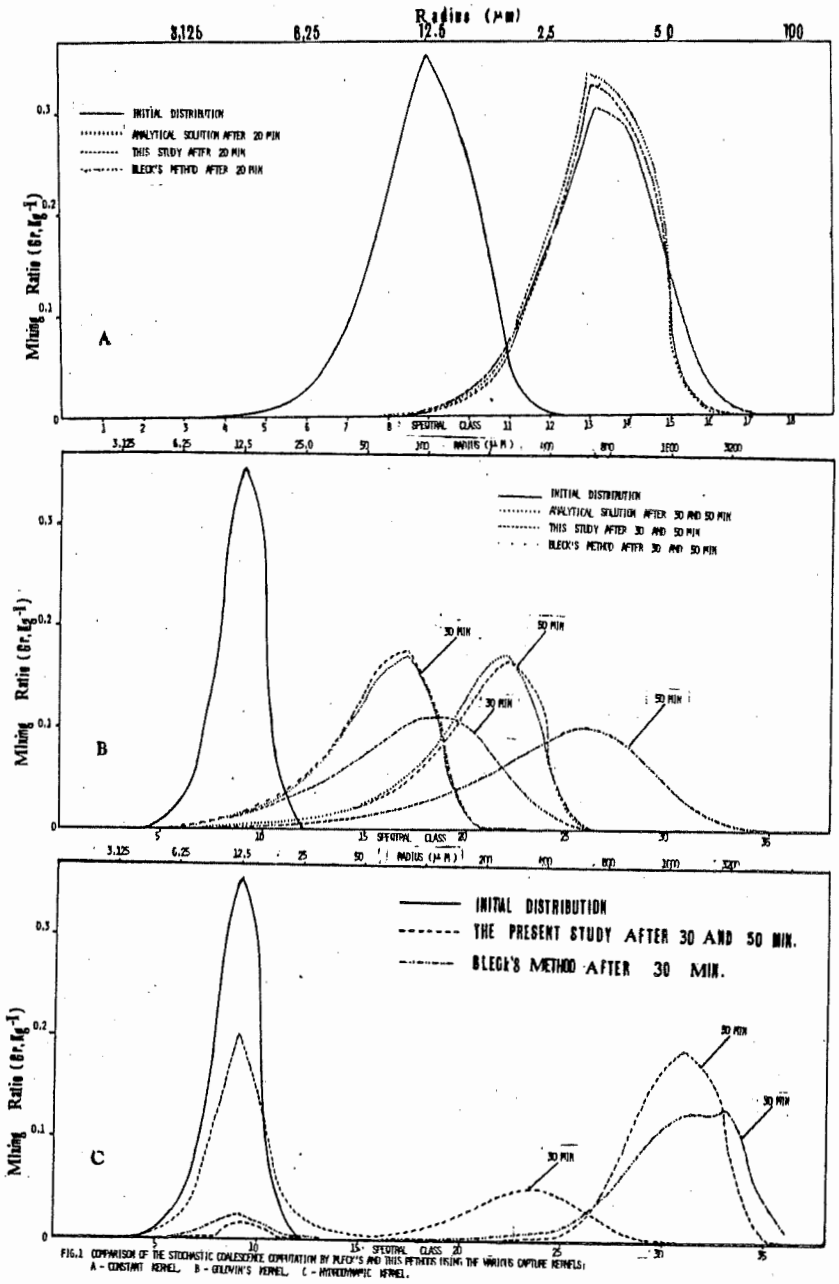

FIG.1 COMPARISON OF THE STOCHASTIC COALESCENCE COMPUTATION BY BLECK'S AND THIS METHODS USING THE VARIOUS CAPTURE KERNELS:
A - CONSTANT KERNEL, B - GOLOVIN'S KERNEL, C - HYDRODYNAMIC KERNEL.

REFERENCES

Beard, K.,V., 1976: Terminal velocity and shape of cloud and precipitation drops aloft. J. Atm. Sci., 33, 851-864.

Berry, E.,X. and Reinhardt, R.,L., 1974: An analysis of cloud drop growth by collection. J. Atm. Sci., 31, 1814.

Bleck, R., 1870: A fast approximative method for integrating the stochastic coalescence equation. J. Geophys. Res., 75, 5165-5171.

Golovin, A.,M., 1963: The solution of the coagulation equation for cloud droplets in arising air currents. Izv. Akad. Nauk. SSSR, Ser. Geofiz., 5, 783-791.

Gunn, R. and Kinzer, G.,D., 1949: The terminal velocity of fall for water droplets in stagnat air. J. Meteor., 6, 243-248.

Long A.,B., 1974: Solutions to the droplet collection equation for polynomial kernels. J. Atmos. Sci., 31, 4, 1040.

Scott, W.,T., 1968: Analytic studies of cloud droplet coalescence. J. Atmos., Sci., 25, 54.

Soong, S., 1974: Numerical simulation of warm rain development in an axisymmetric cloud model. J. Atmos. Sci., 31, 1262-1285.

Tzivion, SH.,I., Yanetz, A. and Manes, A., 1980: Numerical simulation of cloud seeding by hygroscopic particles on coalescence processes in clouds. Third WMO Scientific Conference on Weather Modification, Clermont- Ferrand, France.

II.2 - Cristaux de Glace

Ice Crystals

LABORATORY STUDIES OF ICE SPLINTER PRODUCTION DURING RIMING

T W Choularton, D J Griggs, B Y Humood and J Latham

Physics Department, UMIST
Manchester, ENGLAND

In some slightly supercooled clouds the concentration of ice particles is known to exceed the number of effective ice nuclei by a factor of up to 10^4.

Various experiments (eg, Hallett & Mossop, 1974) and calculations (eg, Chisnell & Latham, 1976) have indicated that ice splinter production during riming is responsible for this effect.

Choularton et al (1978) suggested a possible explanation of this effect when they observed spikes on frozen accreted droplets of radius around 10μm. These protuberances form when an ice shell surrounding the liquid interior of a drop freezing fairly symmetrically is ruptured at a single weak point. It was suggested that the alternative to this is the occasional explosion of such a shell,producing many splinters.

This paper describes experiments in which the frozen products produced by the accretion of small numbers of supercooled drops on to an ice surface were examined.

The Experiment

A frost coated needle was rotated, at a known speed, in a supercooled cloud of liquid water content around 0.1 to 1 g m^{-3} contained in a chest-type freezer. The cloud was produced either using steam from a boiler (a typical drop size distribution is shown in Figure 1) or a spinning-top droplet generator (for larger droplets). In some experiments both methods were used together to obtain a broad drop size distribution. Care was taken to ensure that the needle, droplets and surrounding air were at the same temperature.

Riming was allowed to proceed for around 30 seconds. Warming of the needle due to the release of latent heat of fusion was negligible. The rimer was then removed to the coldest part of the freezer for examination, during which time it was protected from any further drops.

Results

i) Riming with smaller droplets

The experiments with the boiler were conducted over a temperature range -1 to -15C, with collection speeds around 2m s^{-1}. In the temperature range -2 to -9C some droplets exhibited protuberances, as shown in Fig.2(a,b).

On some of the photographs it was possible to estimate the relative rates of heat loss from freezing drops to the surrounding air and the substrate. In each case, where a protuberance formed, the restriction of heat flow to the rimer was sufficient that the two losses were at least comparable.

Figure 3 shows the rate of protuberance production as a function of temperature. The error bars were calculated using the expression $(N \pm \sqrt{N})/A$ where N is the number of protuberances observed at a particular temperature and A is the total number of droplets examined at this temperature.

These results closely parallel the findings of Hallett & Mossop in the high and low temperature cut-offs and the temperature of peak production rate for ice splinters.

The need for a restriction in the heat flow from the freezing drop to the rimer is consistent with the findings of Mossop (1977) that a wide size distribution of droplets is required for splinter production. However, most of the droplets on which protuberances were observed were below the diameter (24μm) which Mossop reports as being required for splinter production.

ii) Riming with larger droplets

The droplet spectrum from the spinning top had a mean diameter of around 40μm. With these drops no protuberances were observed at temperatures higher than -7C,when the droplets were observed to have spread substantially. In this circumstance the thermal contact between the droplet and the rimer would be increased, and the resultant dominance of heat flow to the needle would eliminate the possibility of near symmetric freezing.

The low temperature cut-off appeared unaffected by the size increase. However, the rate of protuberance production between -7C and -9C was much smaller than over the same temperature range for the droplets in (i) and was about 1 protuberance for every 120 drops accreted. Insufficient data were obtained to assess how the rate varied as a function of temperature.

(iii) Riming with a mixture of smaller and larger droplets

In the majority of these experiments

the needle was first rimed in the cloud produced by the boiler and then the drops from the spinning top were introduced. The rate of protuberance production on the larger (spinning top) drops was higher than in (ii), about 1 for every 80 drops observed. Further, the high temperature cut-off was raised to -4.5C, but again the low temperature cut-off appeared unaffected. The results of this experiment were complicated by the fact that the larger droplets were on average smaller than in (ii), with a mean diameter around 25μm. It was observed that some of the larger drops showing protuberances had landed on smaller droplets, (Fig.2c), thus restricting the heat loss to the substrate.

Discussion

The observation that the temperature range for protuberance production on accreted drops of all sizes corresponded closely with that established by other workers for splinter production during riming is suggestive of a strong link between the two effects.

This work is not consistent with the suggestion of Choularton et al. that protuberance production is indicative of symmetric freezing which results, for other droplets, in explosion and the ejection of splinters. It is suggestive of a much closer link between the protuberances themselves and the splinter production. In this connection we point out that the photograph in Fig.2d appears to show a disrupted region on a frozen drop surface, where a protuberance may have shattered.

A possible mechanism for this is suggested by the results of Visagie (1969) who noted that after a protuberance formed on a freezing drop is sealed a rapid rise in pressure occurs as freezing continues. As the ice shell around the protuberance will be thinner at this time than elsewhere, it may be prone to disrupt explosively.

It is clear from these results that the sensitivity of the high-temperature cut-off in protuberance production to droplet size is due to the increasing spreading of larger drops on impact, thus causing heat loss to the substrate to become increasingly dominant.

The low-temperature cut-off remains unexplained.

References

Chisnell R G & Latham J 1976 "Ice Particle Multiplication in Cumulus Clouds". Quart.J.Roy.Met.Soc., 102, 133-156

Choularton T W, Latham J & Mason B J 1978 "A Possible Mechanism of Ice Splinter Production During Riming" Nature, 274, 791-792

Hallett J & Mossop S C 1974 "Production of Secondary Ice Particles During the Riming Process" Nature, 249, 26-28

Mossop S C 1978 "The Influence of Drop Size Distribution on the Production of Secondary Ice Particles During Graupel Growth" Quart.J.Roy.Met.Soc., 104, 323-330

Visagie P J 1969 "Pressures Inside Freezing Water Drops" J.Glaciol., 8, 301-309

ACKNOWLEDGEMENT The research described herein was supported by the Natural Environment Research Council.

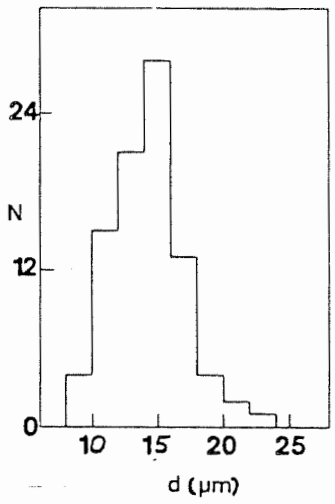

Figure 1. Relative drop concentration n against diameters d for boiler produced cloud.

Figure 2. The frozen products of droplets accreted on the frost coated needle

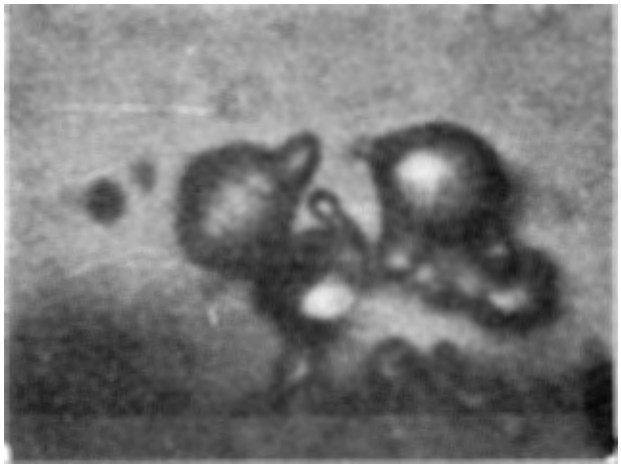

A. Droplets of around 20μm in diameter showing protuberances, collected at a speed of 2m s^{-1} and temperature $-3^{o}C$

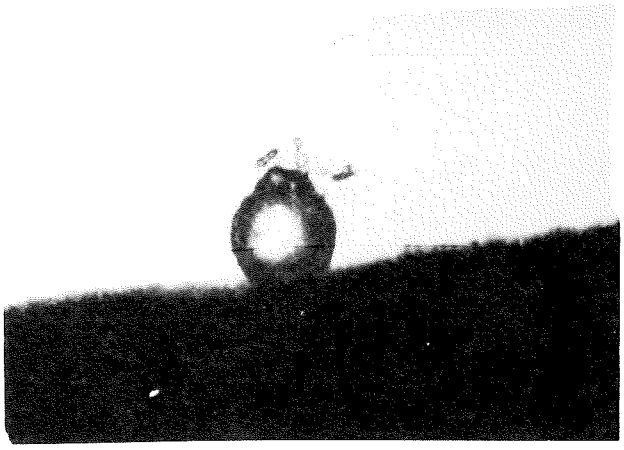

D. A droplet of 35μm diameter showing evidence for the disruption of a protuberance, collected at a speed of 1.5m s^{-1} and temperature $-7^{o}C$

B. A droplet showing a protuberance collected at a speed of 1.75m s^{-1} and temperature $-5^{o}C$

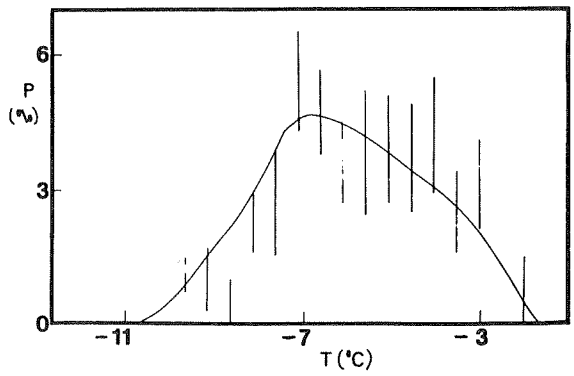

Figure 3. Percentage P of drops showing protuberance against temperature T.

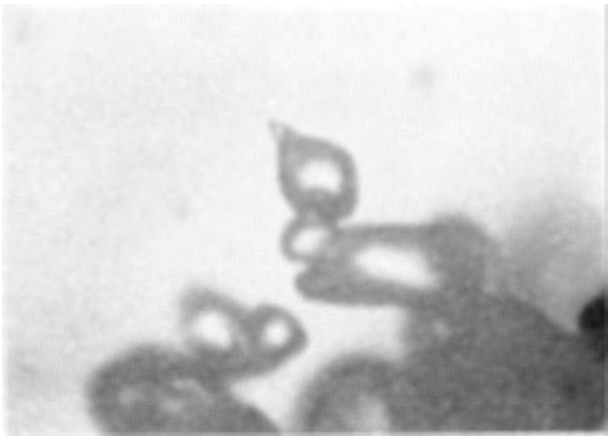

C. A droplet of about 25μm diameter showing a protuberance collected at a speed of 1.75m s^{-1} and temperature $-7\frac{1}{2}^{o}C$

DEVELOPMENT OF FAST FALLING ICE CRYSTALS IN CLOUDS AT -10°C AND ITS CONSEQUENCE IN ICE PHASE PROCESSES

N. Fukuta

Department of Meteorology, University of Utah
Salt Lake City, Utah, U.S.A.

1. INTRODUCTION

When growing in natural supercooled clouds, ice crystals undergo complex microphysical changes such as habit and dendrite developments while falling relative to the cloudy air. Under the existing cloud conditions, the shape, size and mass of an ice crystal provide sufficient information to describe the fall behavior, but as the fall continues, those ice crystal features change. This, in turn, affects the fall behavior. In order to understand the behaviors of dynamically changing ice crystals, it is desirable to simultaneously determine all the relevant growth parameters under simulated conditions of natural clouds as a function of time. The first of such attempts was made in our laboratory about a decade ago (Fukuta, 1969). Since then, other researchers extended the measurements into longer periods of time (Ryan, et al., 1974 and 1976; Gallily and Michaeli, 1976). However, lack of fall velocity determination made their data difficult to apply to natural clouds. For this reason, we recently extended the time periods of our original work including the fall velocity measurement in a new, simple supercooled cloud tunnel (Fukuta, et al., 1979). This paper reports the result and its possible consequence in ice phase cloud processes.

2. SIMULTANEOUS DETERMINATION OF ICE CRYSTAL GROWTH PARAMETERS IN A NEW SUPERCOOLED CLOUD TUNNEL

2.1 Measurements and Results

Ice crystal growth measurements were carried out in a supercooled cloud tunnel operated in a walk-in cold room. Air in the walk-in cold room was introduced into the tunnel via an air filter and steam was injected into it to form supercooled fog. After passing through honeycombs to suppress the turbulence, the fog entered into the vertical section. Ice crystals first generated in a preseeding chamber were taken in a controlled number and injected into the lower portion of the vertical section of the tunnel. The vertical velocity of the fog was adjusted to the fall velocity of the growing crystals by means of suction at the top. The average liquid water content of the fog was adjusted to be between 0.5 and 1.0 g m^{-3}. Terminal velocity measurements were carried out by allowing some of the ice crystals to fall out of the main flow through a glass chamber which was illuminated with a chopped light beam. Photographs of the crystals were then taken as they fell through the chamber for the velocity analysis.

The ice crystals thus grown in the supercooled cloud tunnel were received and held at the interface of two water-immiscible and mutually-immiscible viscous liquids, one lighter than ice (motor oil) and the other heavier than water (silicone oil, DC-550). The density of DC-550 is 1.07 g cm^{-3} and the viscosity 125 centistokes. Ice crystal preservation was excellent at the interface without undesirable motions and aggregation, and they could be rotated for observation from different angles by applying a horizontal shear. Photomicrographs of the crystals with and without melting provided necessary data for the size, shape and mass.

Fig. 2 shows the result of ice crystal mass measurements using ice crystals nucleated by vapor activation of metaldehyde. There was no difference in growth behaviors of ice crystals nucleated by expansion of compressed air and by metaldehyde vapor activation at temperatures above -13°C. Below this temperature, however, ice crystals by metaldehyde vapor activation become mostly double plates. The primary peak of the growth rate at -15°C for plate crystals and the secondary peak at -7°C for column crystals with a minimum at -10°C are all in agreement with the previous observations. However, the fall velocity measurements resulted in

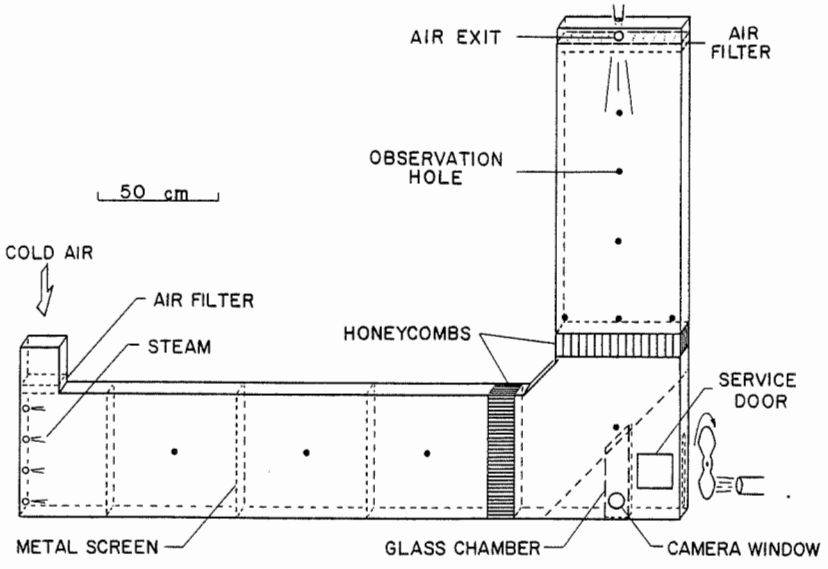

Fig. 1. The L-shaped supercooled cloud tunnel.

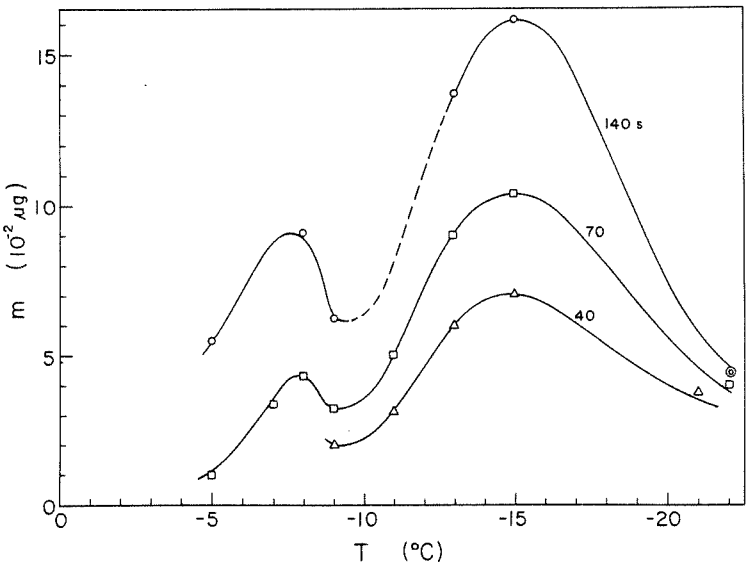

Fig. 2. The ice crystal mass m plotted as a function of temperature T at different time intervals.

discovery of a new peak at -10°C, which corresponds to the growth rate minimum rather than a maximum. Fig. 3 presents the fall velocity data for ice crystals nucleated by vapor activation of metaldehyde and grown at water saturation. Data below -13°C are not representing for single plate ice crystals but for double plates. Nevertheless, new data are again in good agreement with those of our previous measurement (Fukuta, 1969) for the entire temperature zone of measurement within the first 60 s of growth. Ice crystals growing at -10°C have the c/2a ratio near unity and the density almost as high as solid ice. Considering the fact that -15°C is the temperature at which the environmental condition is most advantageous for ice crystal growth even without development of spatial dendrite forms, and the fact that the shape of small crystals shortly after nucleation is close to spherical, being dominated by the effects of surface free energy and vapor flux, not by the surface diffusion; spatial forms of ice crystals are yet to be developed later. Then, small crystals before the shape and dendrite developments are expected to fall fastest at around -15°C. The fall velocity data after 20 s of growth apparently shows such an effect. As the ice crystals develop different shapes, the diffusional rates of growth and the fall velocities change due to varying electrostatic capacities and aerodynamic resistances respectively. Therefore, we examine next the combined effect of shape and size on the fall velocity development of ice crystals under different temperatures at water saturation.

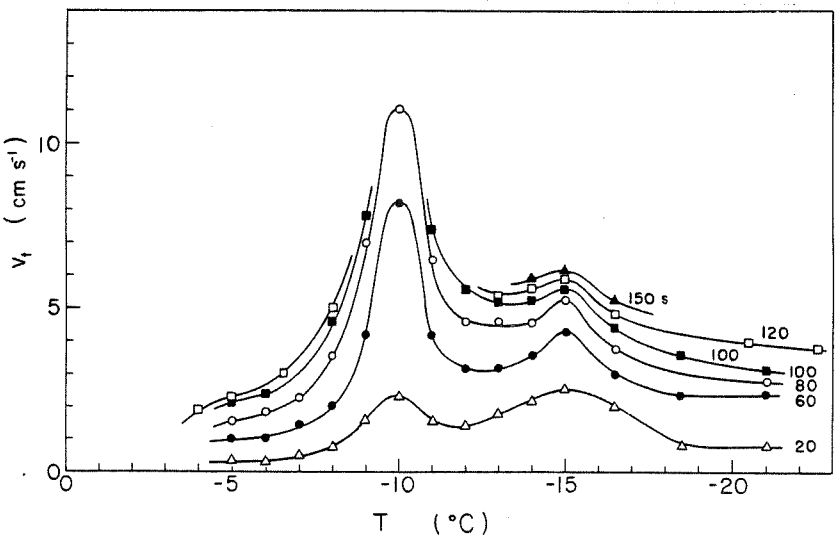

Fig. 3. The fall velocity of ice crystal v_t plotted as a function of temperature T at different time intervals after the onset of growth

2.2 Interpretation of Fall Velocity Peak Development at -10°C

Since both the growth rate by vapor diffusion and the fall velocity are functions of the shape and size of the ice crystal, let us examine the fall velocity development while the crystal is growing by vapor diffusion assuming the shape is held unchanged. For convenience, we employ spheroidal shapes.

For prolate spheroids of rotation representing columnar crystals at temperatures above -10°C, the gravitational force acting on the crystal balances the viscous resistance force in the Stokes regime, so that the fall velocity of a small crystal is given as (Fuchs, 1964)

$$v = \frac{2}{9}\frac{gb^2}{\eta}\cdot\frac{(1-e^2)^{\frac{1}{2}}}{\kappa}, \qquad (1)$$

where η, g, b, e and κ are, respectively, the dynamic viscosity of air, the gravitational acceleration, the polar semi-axis, $e = (1 - a^2/b^2)^{\frac{1}{2}}$, where a is the equatorial semi-axis, and

$$\frac{1}{\kappa} = \frac{3}{8}\frac{(1-e^2)^{\frac{1}{2}}}{e^3}\left[\frac{3e^2-1}{2}\ln\left(\frac{1+e}{1-e}\right)+e\right]. \qquad (2)$$

By ignoring corrections due to fog, ventilation, and thermal accommodation and deposition coefficients (Fukuta et al., 1974), the growth rate may be described as

$$\frac{dm}{dt} = 4\pi b^2(1-e^2)\rho\frac{db}{dt} = 4\pi C(S_\infty - 1)\left[\frac{L_d^2}{KRT_\infty^2}+\frac{1}{\rho_{i,sat,\infty}D}\right]^{-1}, \qquad (3)$$

where m, t, ρ, S_∞, L_d, K, R, T_∞, $\rho_{i,sat,\infty}$, D, and C are, respectively, the mass, the time, the density of ice crystal, the supersaturation with respect to ice, the latent heat of deposition of 1 g water, the thermal conductivity of air, the specific gas constant of water vapor, the temperature in the environment, the saturation vapor density of ice at T_∞, the diffusivity of water vapor in air, and the electrostatic capacity of ice crystal.

$$C = 2be\left[\ell n\left(\frac{1+e}{1-e}\right)\right]^{-1} \qquad (4)$$

Integrating (3) under a given shape, i.e., e = const., and inserting it with (2) and (4) into (1), we have

$$v = \frac{g(S-1)t}{3\eta}\left[\frac{L_d^2}{KRT_\infty^2} + \frac{1}{\rho_{i,sat,\infty}\cdot D}\right]^{-1} \times\left\{\frac{3e^2-1}{2e^2} + \left[e\ell n\left(\frac{1+e}{1-e}\right)\right]^{-1}\right\}. \quad (5)$$

In this equation, the term in { } converges to unity when $e \to 1$ (long needle). Whereas, when $e \to 0$ (sphere), the term converges to 7/6. Since the nearly spherical shape happens at -10°C, and the rest of (5) becomes largest at -10°C within the temperature range between 0 and -10°C, -10°C is clearly the most favorable temperature for rapid increase of v.

An identical treatment for oblate spheroids of rotation using

$$\frac{1}{\kappa} = \frac{3}{4}\left[\frac{2e^2-1}{e^3}\cdot\sin^{-1}e + \frac{(1-e^2)^{\frac{1}{2}}}{e^2}\right], \quad (6)$$

and

$$C = a\,e\,(\sin^{-1}e)^{-1}, \quad (7)$$

results in

$$v = \frac{g(S-1)t}{3\eta}[\quad]^{-1}\cdot\left\{\frac{2e^2-1}{e^2} + \frac{(1-e^2)^{\frac{1}{2}}}{e\sin^{-1}e}\right\}. \quad (8)$$

The { } term in (8) converges into unity when $e \to 1$ (flat plate). Whereas, the term converges into 4/3 when $e \to \infty$ (sphere). In this case, although the nearly spherical shape at -10°C is advantageous for v - development, other terms, particularly (S-1), may very likely give adverse effects. Indeed, as can be seen in Fig. 3, v at -15°C appears to be larger at 20 s after the start of growth. However, thereafter, v - development at -15°C slows down compared with that at -10°C, suggesting a hindrance due to spatial, aerodynamically high resistance dendrite growth at -15°C. We did confirm dendrite development at -15°C under water saturation after the initial 20 s period. This implies that in the regime of vapor diffusion growth, the mass increase and the fall velocity development are in dichotomy. This further suggests a consequence in phenomena involving the subsequent riming growth of ice crystals.

3. FALL VELOCITY DEVELOPMENT OF ICE CRYSTALS AT -10°C AND ITS CONSEQUENCE IN ICE PHASE CLOUD PROCESSES

When an ice crystal falls fast through a supercooled cloud, it collides with cloud droplets and riming growth proceeds. In the riming growth,

$$\frac{dm}{dt} = 4\pi r^2\rho\frac{dr}{dt} = \pi r^2\cdot\bar{E}\cdot L_w\cdot v, \quad (9)$$

where r, $\bar{E}$, and L_w are respectively the radius of ice crystal, the average riming efficiency, and the liquid water content of cloud. Eq.(9) under the regime of $v \propto r^{\frac{1}{2}}$ with constant $\bar{E}$, results in

$$m \propto (L_w t)^6 \quad \text{or} \quad m \propto v^6. \quad (10)$$

(10) may be compared with

$$m \propto t^{\frac{1}{2}} \quad \text{or} \quad m \propto v^{1\frac{1}{2}}$$

of vapor diffusion growth (Fukuta, 1969) in the Stokes regime ($v \propto r^2$) under constant temperature at water saturation. Fig. 4 gives comparison of these processes.

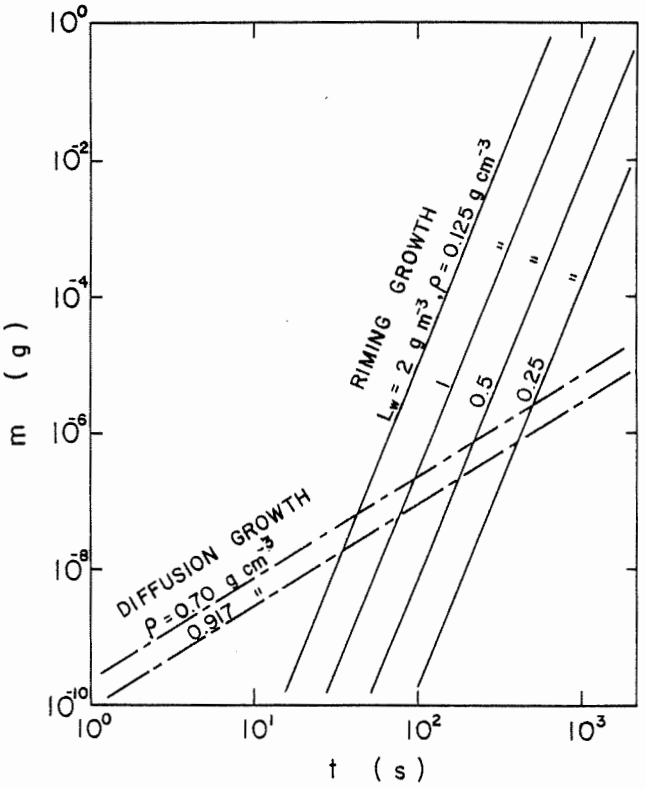

Fig. 4. Relationship between the ice crystal mass m and the time t for vapor diffusion and riming growths. For conditions assumed, see text.

Graupel formation. From (10) and (11), it is apparent that high L_w and fast v favor the riming process. In this regard, unless frozen rain drops exist, the best temperature for riming crystal development and therefore graupel formation following the normal diffusional growth is -10°C, since it is the zone where fastest falling ice crystals were observed to develop. It should be interesting to point out that if this riming growth starts at -10°C, the ice crystals previously at the minimum of mass growth rate by vapor diffusion will become fastest growing. Hence, the -10°C zone may be considered as "the window of graupel formation".

Examination of vapor diffusion and riming mechanisms for ice crystal growth reveals their incompatibility. The vapor diffusion mechanism depends highly on the temperature, whereas the riming mechanism hardly does. Fast growing ice crystals by the former are of spatial forms of high aerodynamic resistance and those by the latter are vice versa. Furthermore, once either mechanism has fully developed, mechanism change automatically ceases, for it is not common to observe a dendrite at the center of a snow pellet nor is it usual for a grauped with dend-

ritic development on it.

Ice crystal multiplication. Hallett and Mossop (1974) reported a possible mechanism of ice crystal multiplication in the temperature range between -3 and -8°C. There are two major requirements for the process to take place. One is the existence of large droplets exceeding 24 μm in diameter and the other ice crystals falling faster than 140 cm s^{-1} (Mossop and Wishart, 1976). How are these fast falling crystals provided in nature ? Ice crystals nucleated do not normally stay in the original temperature zone. The fast falling crystals required for the multiplication process must come from above and the -10°C zone is likely to supply these crystals.

Hail embryo formation. Hail often contains snow pellets in their centers (Mason, 1971). As already discussed above, the easiest zone for the graupel growth seems to be at around -10°C. The graupel formed or ice crystals grown for some time in this temperature zone should subsequently become hail if all other conditions necessary for hail growth are satisfied. Once the fall velocity exceeds a critical value, which is yet to be determined, the habit not only stops developing but is destroyed, and growth of graupel and hail becomes possible regardless of the temperature of the cloud environment. Thus, for hail embryo formation without involving frozen rain drops, the -10°C zone may be considered as the most favorable region.

The above findings may have possible implications in weather modification and they will be discussed elsewhere.

ACKNOWLEDGMENTS

A part of this work was supported by National Foundation under Grant ENV77-15346. Measurements were carried out by L. R. Neubauer and D. D. Erickson and their contributions are acknowledged.

REFERENCES

Fuchs, N. A., 1964: The Mechanics of Aerosols. MacMillan Co., New York, 408 pp.

Fukuta, N., 1969: Experimental studies on the growth of small ice crystals. J. Atmos. Sci., 26, 522 - 531.

Fukuta, N., W. Guo and T. Guo, 1974: Kinetics of hydrometeor growth - spheroidal model. Preprints, Conf. on Cloud Physics, Tucson, Arizona, 21 - 24 October 1974, 67 - 72.

Fukuta, N., L. R. Neubauer and D. D. Erickson, 1979: Laboratory studies of organic ice nuclei smoke under simulated seeding conditions. Final Report to National Science Foundation under Grant NSF ENV77-15346.

Gallily, I., and G. Michaeli, 1976: Growth rate of freely falling ice crystals. Nature, 259, 110.

Hallett, J. and S. C. Mossop, 1974: Production of secondary ice particles during the riming process. Nature, 249, 26 - 28.

Mason, B. J., 1971: The Physics of Clouds, 2nd Ed., Oxford Univ. Press (London), 671 pp.

Mossop, S. C., and E. R. Wishart, 1976: Ice crystal concentration in cumulus clouds: influence of the droplet spectrum. Science, 186, 632 - 634.

Ryan, B. F., E. R. Wishart and E. W. Holroyd, III, 1974: The densities and growth rates of ice crystals between -5°C and -9°C. J. Atmos. Sci., 31, 2136 - 2141.

Ryan, B. F., E. R. Wishart and D. E. Shaw, 1976: The growth rate and densities of ice crystals between -3°C and -21°C. J. Atmos. Sci., 33, 842 - 850.

ICE CRYSTAL GROWTH FROM LIQUID IN LOW-GRAVITY

Vernon W. Keller and Otha H. Vaughan, Jr.
NASA
Marshall Space Flight Center, Alabama, USA

and

John Hallett
Desert Research Institute
Reno, Nevada, USA

I. BACKGROUND

Ice crystals are grown from the liquid in the low-gravity environment available on the NASA KC-135 aircraft parabolic flights. Since natural convection, associated with latent heat induced density gradients surrounding a growing crystal, is reduced in such an environment, the flights provide the opportunity to perform experiments which give useful insights into the effects of reduced convection on growing crystals. These insights are valuable to the development of a better understanding of basic crystal growth mechanisms and to the assessment of future cloud physics experiment concepts for low-gravity space flight. The low-gravity time available in a single flight parabola, about 20 seconds, is too short for most experiments involving growth from the vapor, but it covers a useful range for applicable liquid-growth experiments.

2. PROCEDURE

Ice crystals are grown in an optical glass cell, having dimensions 20 mm x 20 mm x 80 mm high, which is contained in a temperature controlled growth chamber. The growth chamber is a 15 cm diameter by 16 cm high cylindrical block of aluminum with a 4.5 cm diameter by 10 cm deep well machined along the centerline of the cylinder. A hole machined through the block, perpendicular to this well, facilitates 2.2 cm diameter windows on either side of the block. This allows observation of the crystals using backlight illumination while minimizing thermal effects due to the windows. For the experiments described here, the aluminum block was cooled by circulating a cold fluid through copper tubing coiled around the block. A cell filled with distilled water and capped with a teflon lid is pre-cooled to $0^{o}C$ in an ice water bath before being placed into the water-ethylene glycol filled cavity of the chamber. This reduces the time necessary for the temperature within the cell to approach by conduction the temperature of the growth chamber which is normally chosen in the range $-0.5^{o}C$ to $-1.5^{o}C$. Even so, the time necessary to insure that the temperature of the water in the cell is uniform and has come to equilibrium with that of the chamber, i.e. within $0.1^{o}C$, is still on the order of 30 minutes. This limits the number of low-gravity experimental runs to about four on each flight. To maximize the number of runs per flight and to eliminate the possibility that solidification-melt cycling might have an influence on these experiments, a different cell is used for each run.

When temperature equilibrium is achieved for a cell, a nucleation probe, pre-cooled to dry ice temperature, is inserted into a capillary tube which extends into the bulk of the distilled water. Ice crystals then grow from the end of the capillary into the supercooled water and are photographed at 24 frames per second using a 16 mm movie camera. Observation of the growth of a crystal throughout an entire flight parabola, i.e. low-gravity to high-gravity to low-gravity, enhances the likelihood of observing effects due to reduced convection because other parameters can be maintained constant. At supercoolings near $-1.0^{o}C$ growth rates along the 'a'-axis are about 100 times greater than those along the 'c'-axis (Hallett, 1964) but are still sufficiently slow ($\sim$.01 cm s^{-1}) such that a crystal can be observed throughout an entire parabola before growing to the opposite wall of the cell.

Our experiments have shown that it is also possible to nucleate and observe the growth of ice crystals freely suspended in the supercooled water. In this case, the crystals remain freely suspended and stationary so long as the aircraft is in the low-gravity portion of the flight parabola. Further along in the parabola, as gravity increases, the unsupported ice crystals float toward the top of the cell. As they float upward, heat transfer from the crystals is enhanced at the leading edges and the growth rate increases.

3. RESULTS

At this time, ice crystal growth from liquid experiments have been performed on only two aircraft flights. Some problems, which have since been corrected, were encountered in these flights with the thermal control of the growth chamber. The chamber temperature slowly flucuated several tenths of a degree during the course of the experiments. Nonetheless, preliminary results indicate, as anticipated, that ice crystals have slower growth rates in low-gravity where convection is reduced. Figure 1 is a photograph of crystals growing from a capillary support at a supercooling of $-0.8^{o}C$. Growth rates for these crystals ranged from 30 $\mu m\ s^{-1}$ in low-gravity to 40 $\mu m\ s^{-1}$ in one gravity. Figure 2 is a photograph of freely suspended ice crystals growing at a supercooling of $-0.5^{o}C$.

Unfortunately, there were air bubbles on the inner surface of the observation window which appear as black spots on the photograph. On this run featureless thin circular discs grew and then changed shape as they became larger.

Although the growth of ice discs from the liquid has been studied previously in one gravity (Arakawa and Higuchi, 1952; Kumai and Itagaki, 1953; and Arakawa, 1954, 1955) most studies involved the nucleation and growth of crystals on the surface of supercooled water. In those instances in which unsupported crystals were nucleated in the free liquid they rapidly floated to the surface. Under either of these growth conditions heat transfer from the crystal was asymmetrical. Our preliminary experiments indicate that the study of the transition of ice discs to dendrites under symmetrical heat transfer conditions is possible in low-gravity. With the incorporation of a revised thermal control for the growth chamber and improved optical resolution, future low-gravity experiments scheduled on the KC-135 will investigate this phenomena in more detail as well as other changes in crystal shape and linear growth rate which result from a reduction in natural convection.

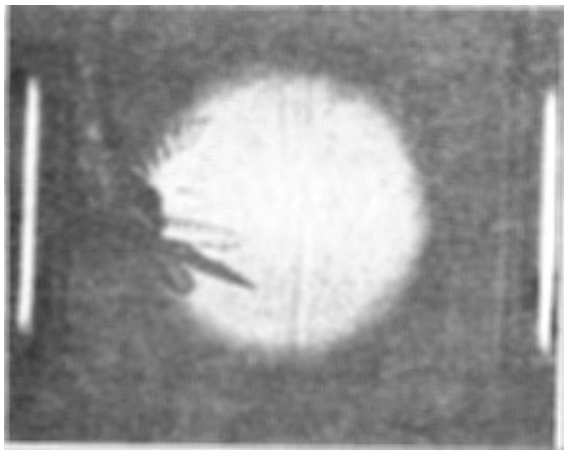

FIGURE 1. Ice crystals growing from the liquid in low-gravity at a supercooling of -0.8°C.

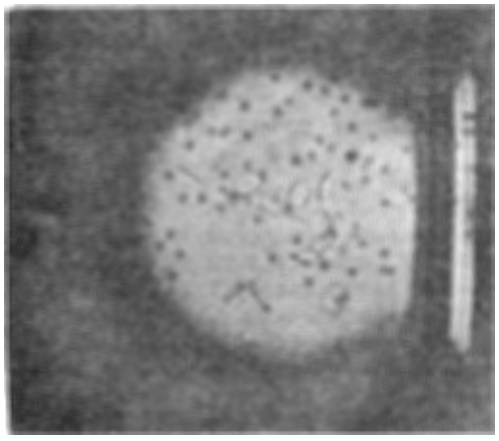

FIGURE 2. Freely suspended ice crystals growing in low-gravity at a supercooling of -0.5°C.

4. REFERENCES

Arakawa, K., and K. Higuchi, 1952: Studies on the freezing of water, J. Fac. Sci., Hokkaido Univ., Ser. II, 4, 201-208

Arakawa, K., 1954: Studies on the freezing of water, J. Fac. Sci., Hokkaido Univ., Ser. II, 4, 311-339.

Arakawa, K., 1955: The growth of ice crystals in water. J. Glaciol., 2, 463-468.

Hallett, J., 1964: Experimental studies of the crystallization of supercooled water, J. Atmos. Sci., 21, 671-682.

Kumai, M., and K. Itagaki, 1953: Cinematographic study of ice crystal formation in water, J. Fac. Sci., Hokkaido Univ., Ser. II, 4, 235-246.

THE PLATE-DENDRITE TRANSITION OF GROWING SNOW CRYSTALS

V. Keller

Marshall Space Flight Center
Huntsville, Alabama, U.S.A.

J. Hallett

Desert Research Institute
Reno, Nevada, U.S.A.

A laboratory simulation of snow crystal growth from the vapor varies temperature, supersaturation and velocity independently. This is achieved by a dynamic thermal diffusion chamber which consists of two horizontal ice covered plates, 1 m long and 3 cm separation.

A temperature difference between the plates establishes both a thermal and a moisture gradient; an external closed circuit air circulation system establishes velocity. With the uppermost plate at higher temperature and flow Reynolds' Number < 10^4 a stable laminar, flow results. Ice supersaturation maximum occurs near the mid point between the plates and reaches equilibrium, in the geometry used, for velocities up to 10 cm s^{-1}, equivalent to crystals of a few hundred μm diameter in terminal velocity. All nuclei are removed from the chamber air by filtration so supersaturation in excess of water saturation may be attained. Crystals are grown on a vertical fine glass fiber at the downstream end of the chamber; crystal growth is recorded by time lapse camera.

At temperatures near -15°C, laboratory studies under static conditions Nakaya (1954), Kobayashi (1957), Hallett & Mason (1958), have shown that ice crystals grow in the form of plates or dendrites depending on the supersaturation. Under static conditions with velocities $\lesssim$ mm s^{-1} resulting from crystal and chamber temperature irregularities, crystals transformed from plates to sector plates to dorites ("a" axis growth without branches), and dendrites as supersaturation was increased from water saturation ($\sim$ 15% over ice) to about double this value. It was found that with increasing air velocity, this transition occurred at successively lower ice supersaturation. At the same time increasing air velocity gave enhanced "a" axis growth rate.

Fig. 1 shows dendrites changing to dorites, sector plates or plates as the velocity is removed, and resuming dendrite growth as the velocity is reestablished. The air flows from left to right of the photographs. Temperatures and excess vapor density (g m^{-3}) are shown.

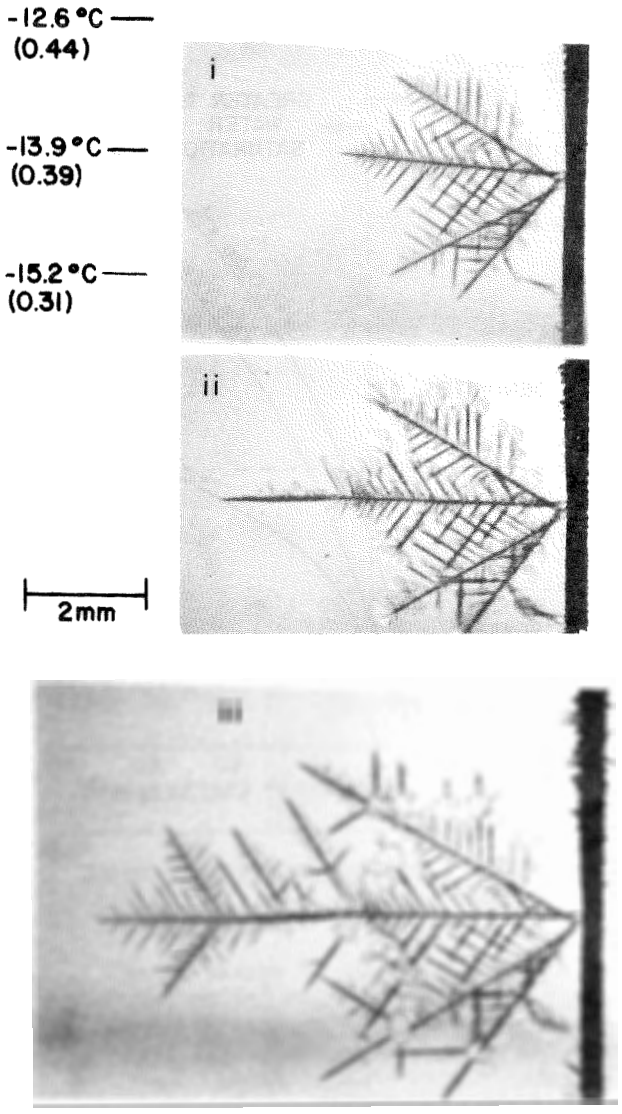

Figure 1. (i) Shows dendrites which have been growing at wind speed of 7 cm s^{-1}. The wind tunnel was shut off, and the crystals in (ii) grew after 19 minutes. These show a sector plate at the top, a dorite center and a plate lower; each was originally a branching dendrite. In (iii) the velocity has been returned to 7 cm s^{-1} for 12 minutes and dendrites are again growing similar to (i).

Observations from a series of sequences similar to Fig. 1 enable the different forms to be related to ice supersaturation and wind speed (Fig. 2). This diagram shows that near water saturation the growth rate in the "a" axis direction increases from 0.5 μm s^{-1} for plate growth to near 2 μm s^{-1} for dendrite growth at a ventilation of 10 cm s^{-1}.

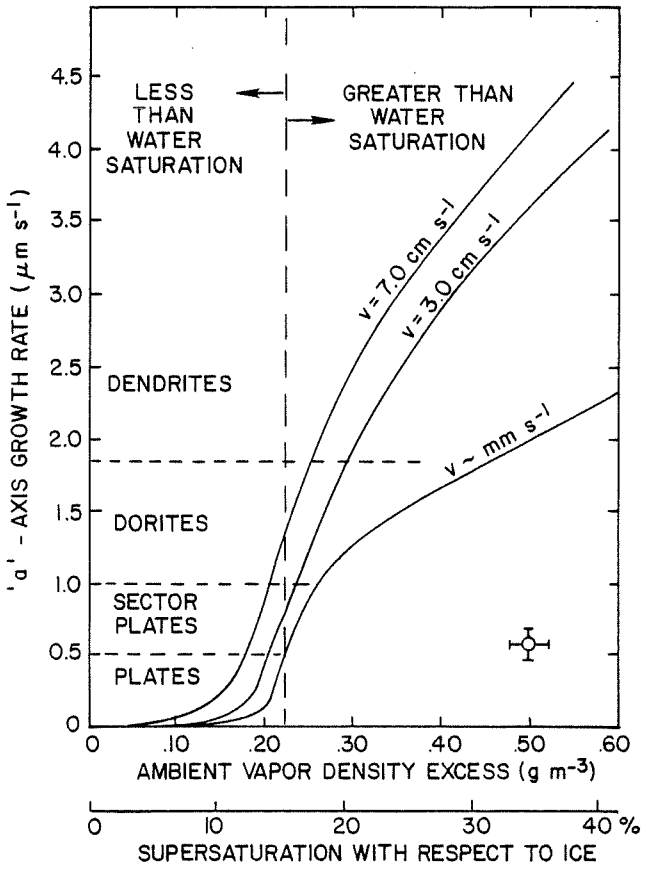

Figure 2. The influence of excess vapor density, ice supersaturation (s) on the "a" axis growth rate at -14½°C under different ventilation velocities. Horizontal lines delineate different crystal forms. Zero velocity is in practice ∿ mm s^{-1}, caused by residual chamber convection. In the complete absence of convection, (low "g" case) the V=0 line would lie below V ∿ mm s^{-1}.

DISCUSSION

The growth rate of an ice crystal in a supersaturated environment is, in the absence of kinetic barriers, limited by the rate of moisture diffusion to the crystal and the rate of heat removal of latent heat by conduction away from the crystal into the environment. Each of these processes is enhanced by ventilation (F) when the boundary layer through which this transport takes place is reduced in thickness as $(\frac{D, \kappa}{U})^{\frac{1}{2}}$ where U is the ventilation velocity and κ, D are the molecular diffusivities for vapor or heat. The classical mass growth rate equation of the form

$$\frac{dm}{dt} \alpha \frac{sF}{\frac{a}{D} + \frac{b}{K}}$$

where K is the environment thermal conductivity and a, b, constants gives a relation which enhances the growth velocity with $U^{\frac{1}{2}}$. An increase of diffusion coefficient and thermal conductivity of the gaseous environment both lead to a growth rate increase. The results presented here show that the tendency for skeletal growth increases with supersaturation and ventilation. Gonda (1976) found that increase of thermal conductivity alone enhanced skeletal growth whereas increase of diffusion coefficient made skeletal growth less likely.

This latter case leads to a reduction of vapor gradients along the periphery of the dendrite, in contrast to enhancement in the other cases of increased ventilation and carrier gas conductivity. This observation is consistent with an interpretation that the thermal gradients in a growing plate are small because of heat conduction in the plate itself, whereas gradients of adsorbed molecule concentrations cannot be smoothed out over distances $\gtrsim$ 5 μm, the order of magnitude of the distance which molecules can migrate on the basal plane of ice (Hallett 1961).

ACKNOWLEDGEMENT

This work reported here was supported in part by a Grant from the National Science Foundation, Washington D.C., Grant No. (ATM 77-07995).

REFERENCES

Gonda,T. 1976. The growth of small ice crystals in gases of high and low pressures. J.Met.Soc.Japan, 54, 233-239.

Hallett,J. & Mason,B.J. 1958. The influence of temperature & supersaturation on the habit of ice crystals grown from the vapor. Proc.Roy.Soc.A., 247, 440-451.

Hallett,J. 1961. The growth of ice crystals on freshly cleared covellite surfaces. Phil.Mag., 6, 1073-1087.

Kobayashi,T. 1957. Experimental researches on the snow crystal habit and growth by means of a diffusion cloud chamber. J.Met.Soc.Japan, 75th Anniv.Vol., 38-47.

PECULIAR SHAPES OF NATURAL SNOW CRYSTALS

K. Kikuchi

Department of Geophysics, Faculty of Science
Hokkaido University, Sapporo, JAPAN

1. Introduction

There appears to be considerable interest in the origin of polycrystalline and peculiar shapes of natural snow crystals. However, regarding polycrystalline snow crystals, namely, spatial dendrites, radiating assemblages of dendrite and combination of bullets, some crystallographic properties of these crystals have been clarified to date (Lee, 1972; Uyeda and Kikuchi, 1976, 1979; Kobayashi et al. 1976).

On the other hand, regarding the peculiar shapes of natural snow crystals discovered and reported mainly by the author at Syowa Station, Antarctica, and later at Hokkaido, Japan (Kikuchi, 1969, 1970, 1971, 1974; Kikuchi and Yanai, 1971; Iwai, 1972) microphotographs of these snow crystals were taken by ordinary transmitted light at the beginning of examination. For this reason, the principal axis and growth mechanisms were considered based on typical and common shapes of the snow crystals. Kikuchi and Hogan (1976, 1979) firstly carried out a polarization microscope study of these peculiar snow crystals in the austral summer season at Amundsen-Scott South Pole Station, Antarctica during January 1975. As a result, it might be laid down as a general rule that the former considerations were correct, however, several new questions arose from the study. Therefore, a more careful series of observations to obtain increasingly exact information and new discovery regarding peculiar shapes were required. In this paper, peculiar shapes of natural snow crystals observed at the arctic and antarctica till the present, and their falling frequency will be described.

2. Data acquisition

The main observation locations and durations are as follows: Syowa Station, Antarctica (69°00'S, 39°35'E); from February 1968 to January 1969, Amundsen-Scott South Pole Station, Antarctica (90°S); January 1975 and November 1978, Inuvik, Northwest Territories, Canada (68°22'N, 133°42'W); from January to February, 1977 and from November 1979 to January 1980. Surface weather observations were made hourly at all stations and upper air observations were made once daily at Syowa Station and twice at South Pole and Inuvik, routinely.

A polarization microscope with double cameras was used to take photographs of snow crystals, and to determine the principal axis of the crystals at 10 min. interval approximately; one of the cameras was for color and the other was for monochrome films. Falling snow crystals simultaneously were collected and replicated on 25 X 75 mm glass slides coated with a 0.5 % Formvar solution at 5 or 10 min. interval. These replicas were used to estimate the precipitation intensity and the rate of peculiar shapes to common shapes of snow crystals.

3. Results

Fig.1 shows a time cross section of air temperature and relative humidity from the surface up to 400 mb level from January 11 to February 5, 1977 at Inuvik, Canadian North as an example of the typical ones. The isotherms are drawn at an interval of -5 °C by solid lines and the isopleths of relative humidity are drawn by 80 %, thin dashed and by 100 %, thick dashed lines, respectively. Short horizontal bars with spikes at both ends above the time cross section, show the observation period of snow crystals. Typical shapes of snow crystals observed during the period were sketched by graphic symbols and additional characteristics based on the classification of solid precipitation agreeded upon by the International Commission on Snow and Ice in 1949 (Mason, 1971). As may be clearly seen, the classification does not include "side planes" type snow crystals (Nakaya, 1954; Magono and Lee, 1966), at present "crossed plates" (Kikuchi, 1969) which is a typical shape growing in relatively cold temperature regions. Thus we added this shape to the classification depicted by a graphic symbol (). Furthermore, the discovery and frequency of the peculiar shapes are the most interesting objective, and we added these shapes to the classification depicted by a graphic symbol (). This graphic symbol indicates a tetragonal shape which is formed by two prism planes growing from two columns or bullets. Therefore, the diagonal line in general shows the grain boundary between both prism planes. On January 19 and 29, 1977, "Seagull" shaped crystals similar to "V-shaped crystals" introduced on the basis of

cold temperature experiments (Yamashita, 1971) were discovered, thus we added them as a graphic symbol (⌄) (Kikuchi and Kajikawa, 1979).

As seen in Fig.1, there were water saturation layers aloft consistently throughout the observation period. Especially, the height of water saturation layers on January 21 and February 2 reached approximately 500 mb and the height of over 80 % of relative humidity reached 400 mb or more. As considered in general, the shapes of snow crystals vary widely in accordance with the thickness of the saturation layer, in other words, the wider the temperature region is the greater the variation of the crystal shapes becomes. As pointed out by graphic symbols in Fig.1, the peculiar shapes were observed for eight days. Especially, however, it showed high frequency on the January 27, 29 and 30 and February 1 and 2, 1977. The temperature profiles of these days differed widely, however, three cases of January 30 and February 1 and 2 showed nearly the same profiles from the surface to 800 mb level. The temperature differences on the surface and 800 mb level each were within 5 ^{o}C, and the average temperatures on the surface and 800 mb were -32 ^{o}C and -28 ^{o}C, respectively. Therefore, it is estimated in approximation that the temperature regions of the peculiar shapes of natural snow crystals were -30 ^{o}C for their growth.

Typical examples of the peculiar shapes observed at three observation stations described previously are shown in Fig.2. As these photographs are taken by a polarization microscope except (a) to (d) taken at Syowa Station, their principal axes could easily detect under a sensitive color plate. As a result, almost peculiar shapes were consisted of prism planes extended abnormally. Recently, Kobayashi et al (1976) explained the grow of linear development of the crystals of (c) and (d) as a preferred nucleation at a re-entrant twin edge and (a) and (e) as ones of a very early stage of them. Therefore, the crystals of a square part of (b), (g), (h), (m) and (n) may be similar to them. The crystals of (f) and (o) are clearly some kind of combination of bullets, however, they are single crystal frequently. The crystals of (k) and (l) are a seagull type from their external shape, (i) is a different type of polycrystalline and (j) is a quite new type of natural snow crystals.

Falling frequencies of these peculiar shapes against other common shapes in Inuvik are shown in Figs.3 and 4. In these figures, upper and lower parts show the total flux of snow crystals and the falling frequency of peculiar shapes against other shapes. The flux of snow crystals is an index of snowfall intensity. In the case of January 30, 1977, the main shapes of snow crystals were side planes, column and combination of bullets. Peculiar shapes were observed a little time variation in 3 to 5 %, but did not exceed 10 %. This result coincided with that of the observations at Hokkaido (Kikuchi, 1974). The greater part of peculiar shapes was "multiple extended prism planes of tetragonal form with bullets" as represented by (c), (d) and (g) in Fig.2. Its rate accounted for 25 % of all peculiar shapes. In the case of February 2, the main shapes of snow crystals were bullets, combination of bullets, side planes and plate around 0900. At that time, the peculiar shapes accounted for 9 % of other shapes. After 1100, however, the rate of peculiar shapes decreased, and radiating types, plate and dendrite increased instead of them.

4. Conclusion

A number of peculiar shapes of natural snow crystals observed mainly at the arctic region and antarctic continent were introduced. They were mainly consisted of prism planes extended abnormally from prism planes of combination of bullets. Temperature conditions for their growth were estimated -30 ^{o}C approximately. Their falling frequencies to the common crystals falling in the same time were 3 to 4 % in average, and less than 10 % in the maximum. A theoretical treatment for growth mechanisms of multiple extended prism planes of tetragonal form with bullets which is the most typical one of peculiar shapes was attempted by Kobayashi et al (1976) on the basis of a "twinned structure model". On the other hand, Magono and Sasaki (1970) attempted a reproduction of these peculiar shapes using a convection type cloud chamber artificially. Their growth mechanisms, however, have not been clarified to date. As a matter of course, they do not give exact names, neither do they classified yet.

References

Iwai, K., 1972: Uncommon and peculiar shapes of snow crystals observed at Shiga Heights, Nagano Prefecture. Bull. Inst. Natural Educ., Shiga Height, Shinshu Univ., 11, 81-91.

Kikuchi, K., 1969: Unknown and peculiar shapes of snow crystals observed at Syowa Station, Antarctica. J. Fac. Sci., Hokkaido Univ., Ser.VII, 3, 99-116.

Kikuchi, K., 1970: Peculiar shapes of solid precipitation observed at Syowa Station, Antarctica. J. Meteor. Soc. Japan, 48, 343-349.

Kikuchi, K., 1971: Peculiar shapes of snow crystals of antarctic type observed at Hokkaido. Geophys. Bull. Hokkaido Univ., 25, 167-180.

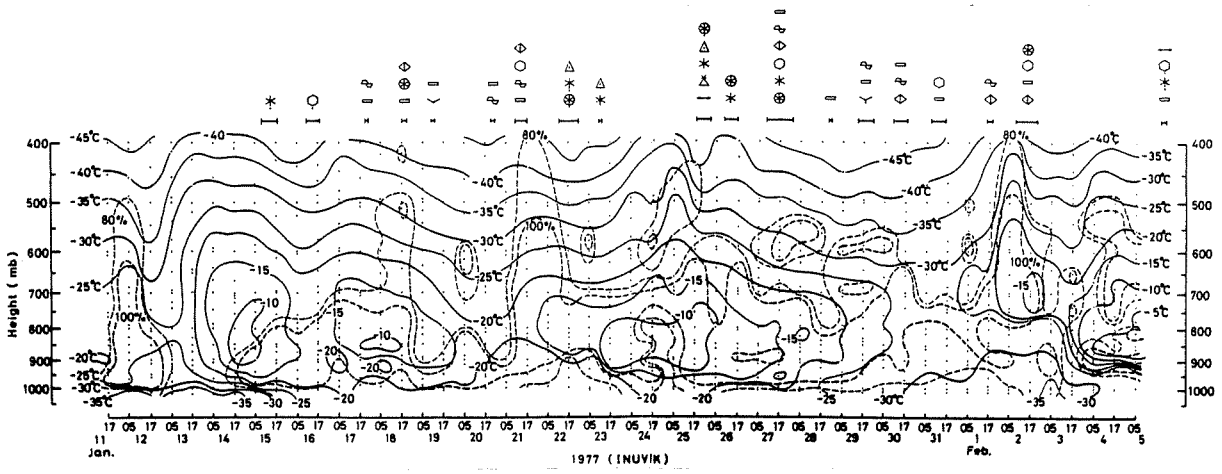

Fig.1 Time cross section of air temp. and relative humidity at Inuvik, 1977.

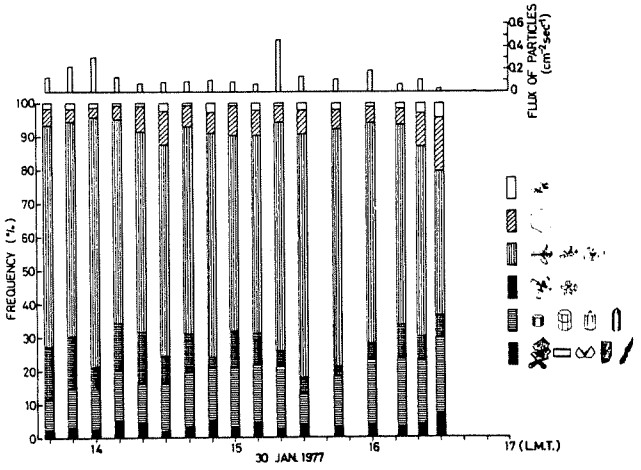

Fig.3 Time variation of snow crystals on Jan. 30, 1977.

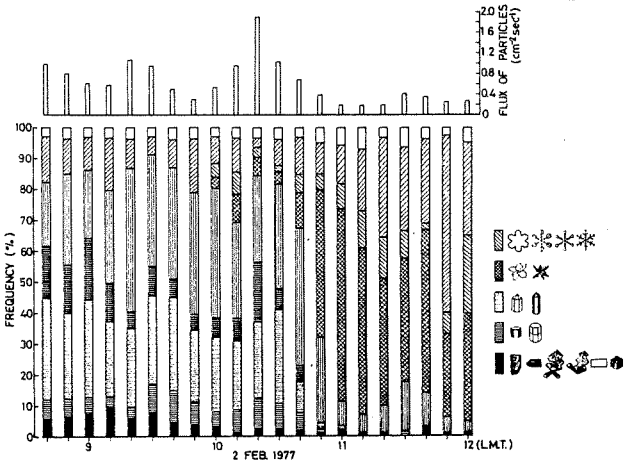

Fig.4 Time variation of snow crystals on Feb. 2, 1977.

Kikuchi, K., 1974: Researches on cloud physics at Syowa Station, Antarctica. Tenki, 21, 496-506.

Kikuchi, K. and A.W. Hogan, 1976: Snow crystal observations in summer season at Amundsen-Scott South Pole Station, Antarctica. J. Fac. Sci., Hokkaido Univ., Ser.VII, 5, 1-20.

Kikuchi, K. and A.W. Hogan, 1979: Properties of diamond dust type ice crystals observed in summer season at Amundsen-Scott South Pole Station, Antarctica. J. Meteor. Soc. Japan, 57, 180-190.

Kikuchi, K. and M. Kajikawa, 1979: Comments on V-shaped snow crystals observed in Arctic Canada. J. Meteor. Soc. Japan, 57. 484-487.

Kikuchi, K. and K. Yanai, 1971: Observation on the shapes of snow crystals in the south pole region in the summer. Antarctic Record, Polar Res. Center, Tokyo, 41, 34-41.

Kobayashi, T., Y. Furukawa, K. Kikuchi and H. Uyeda, 1976: On twinned structures in snow crystals. J. Crystal Growth, 32, 233-249.

Lee, C.W., 1972: On the crystallographic orientation of spatial branches in natural polycrystalline snow crystals. J. Meteor. Soc. Japan, 50, 171-180.

Magono, C. and C.W. Lee, 1966: Meteorological classification of natural snow crystals. J. Fac. Sci., Hokkaido Univ., Ser.VII, 2, 321-335.

Magono, C. and H. Sasaki, 1970: On the optical axes of snow crystals of the side plane types. J. Fac. Sci., Hokkaido Univ., Ser.VII, 3, 267-275.

Mason, B.J., 1971: The Physics of clouds. Clarendon Press, 671 pp.

Nakaya, U., 1954: Snow Crystals, natural and artificial. Harvard Univ. Press, 510 pp.

Uyeda, H. and K. Kikuchi, 1976: Remeasurement of the axial angle between spatial branches of natural polycrystalline snow crystals. J. Fac. Sci., Hokkaido Univ., Ser.VII, 5, 21-28.

Uyeda, H. and K. Kikuchi, 1979: Observations of the three dimensional configuration of snow crystals of combination of bullet type. J. Meteor. Soc. Japan, 57, 488-492.

Yamashita, A., 1971: Skeleton ice crystals of non-hexagonal shape grown in free fall. J. Meteor. Soc. Japan, 49, 215-231.

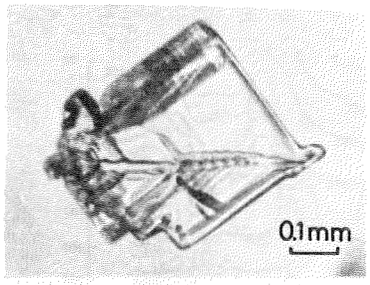

(a) Syowa Station, 1968.

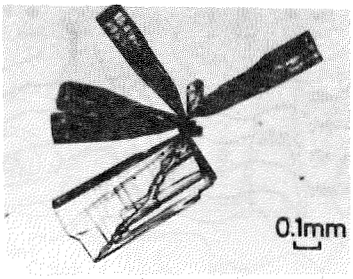

(b) Syowa Station, 1968.

(c) Syowa Station, 1968.

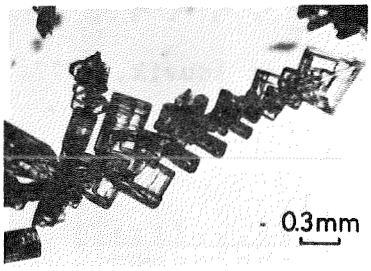

(d) Syowa Station, 1968.

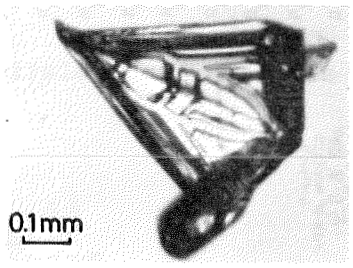

(e) South Pole, 1975.

(f) South Pole, 1975.

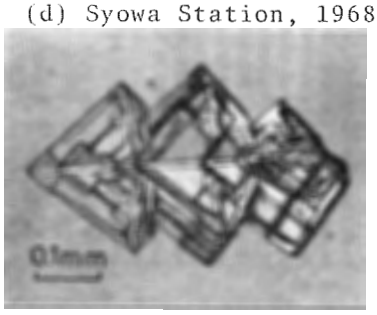

(g) South Pole, 1978.

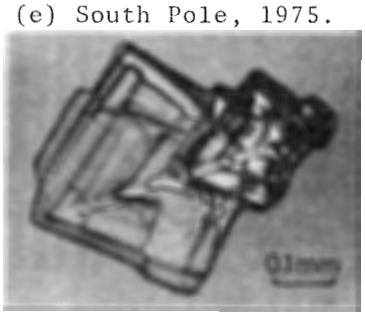

(h) Inuvik, 1977.

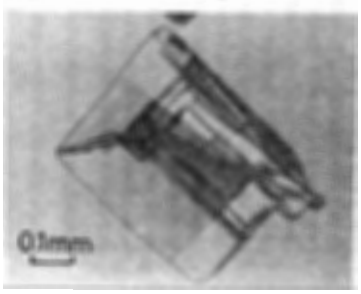

(i) Inuvik, 1977.

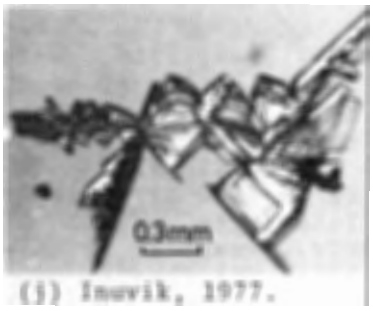

(j) Inuvik, 1977.

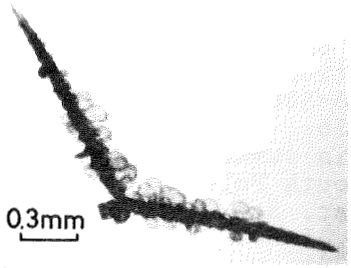

(k) Inuvik, 1977.

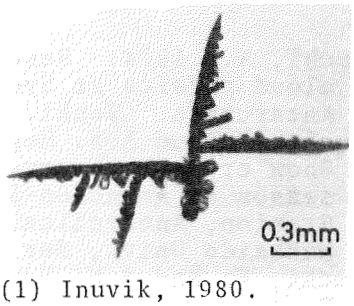

(l) Inuvik, 1980.

(m) Inuvik, 1979.

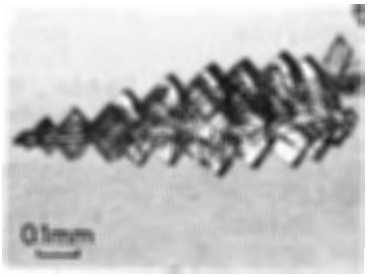

(n) Inuvik, 1979.

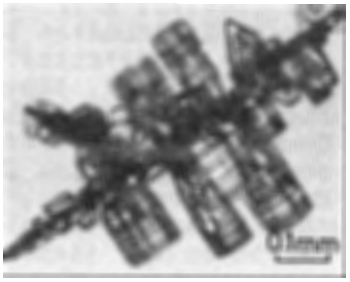

(o) Inuvik, 1979.

Fig.2 Typical examples of peculiar shapes of natural snow crystals observed at three stations.

GROWTH KINETICS OF ICE FROM VAPOUR PHASE AND ITS GROWTH FORMS

T.KURODA* AND R.LACMANN

Lehrstuhl A und Institut für Physikalische Chemie der Technischen Universität
Braunschweig GERMANY

Introduction.

Fig.1 shows the observed growth forms of vapour-grown ice-crystals in the $\Delta p/p$-T diagram by Kobayashi (1961). In this paper we will give a new interpretation of the polyhedrical growth form. There are 4 primary habits of ice depending on the growth temperature (T):

A: Plates : $0^{\circ}C > T > -4^{\circ}C$ (T_{AB})
B: Columns: $-4^{\circ}C > T > -10^{\circ}C$ (T_{BC})
C: Plates : $-10^{\circ}C > T > -20^{\circ}C$ to $-35^{\circ}C$ (T_{CD})
D: Columns: $T_{CD} > T$

T_{CD} depends on the supersaturation of the vapour phase, it decreases with decreasing supersaturation.

Fig.2 and 3 show the influence of H_2O-diffusion coefficient (in He(○) and Ar(●)) on the c/a-relation of ice crystals (after Gonda (1976)) (c,a = length of crystals in the c- or a-direction). With increasing diffusion coefficient the c/a-relation nears 1. In fig.4 you can see the different lenght of crystals in a- and c-direction in dependence on the temperature after a growth time of 200 s, observed by Yamashita (1974).

The growth of snow crystals from the vapour phase was interpreted by Lacmann and Stranski (1972) by the aid of a quasi-liquid-layer and the unwettability of edges and corners. A first very incomplete interpretation of polyhedral growth forms of ice in the region of -10° to 0°C with the Vapour → Quasi-liquid-layer → Solid-mechanism was given by Lacmann (1977).

Growth mechanism.

The theory is based on a viewpoint that the surface of ice just below 0°C is covered with a quasi-liquid-layer, whose thickness (δ) or coverage (θ) decreases with falling temperature, and therefore there are 3 growth-mechanism:

I. Vapour → Quasi-liquid-layer → Solid-(V-Qll-S)-mechanism; (δ>3 Å, θ>1):
$0^{\circ}C > T > T_{I/II}$.
II. Adhesive mechanism (δ<3 Å, θ<1):
$T_{I/II} > T > T_{II/III}$.
III. Two-dimensional-nucleation-mechanism (θ<0.01) $T_{II/III} > T$.

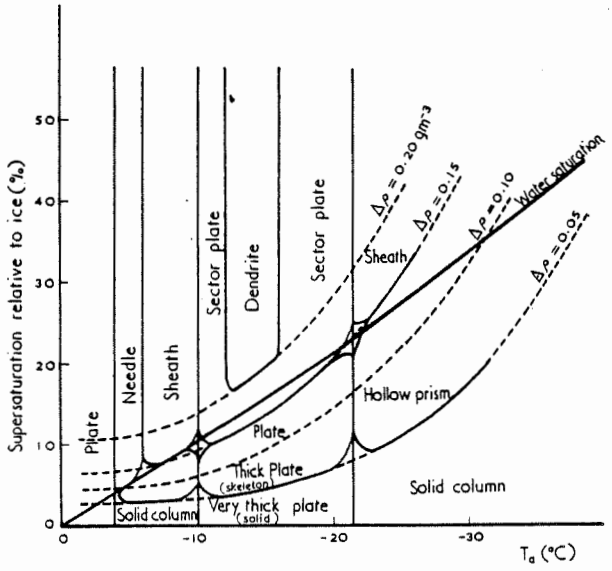

Fig. 1

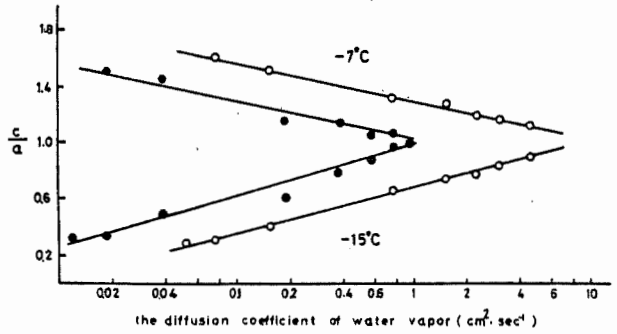

Fig. 2

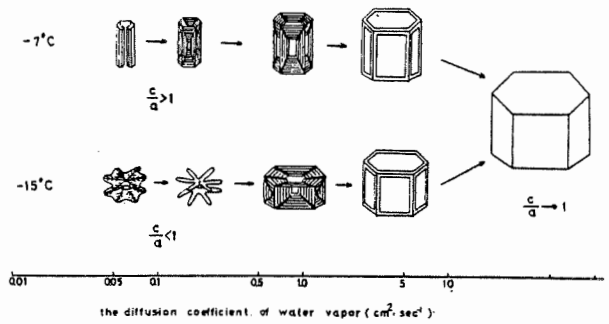

Fig. 3

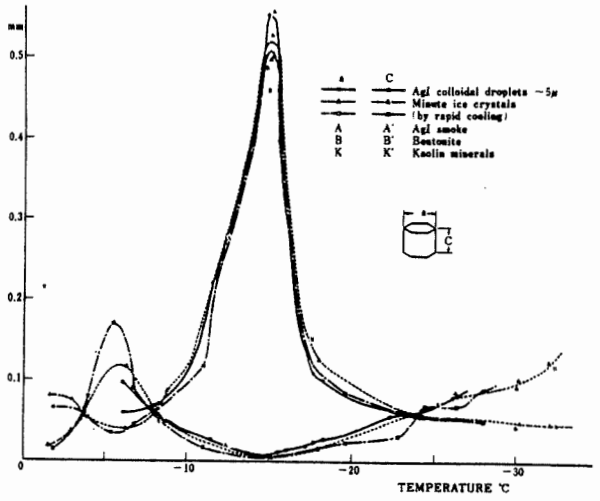

Fig. 4

As the change in surface structure as well as growth mechanism depend on surface orientation, the complicated habit change is caused mainly by the combination of growth mechanism of each face, i.e. {0001} and {10$\bar{1}$0}.

V-Qll-S-mechanism (I): According to the Lacmann-Stranski-model (1972) the quasi-liquid-layer just below 0°C can exist in a stable way, so as to lower the surface free energy of the system. The thickness of the quasi-liquid-layer on the surface with larger wettability-defined by

$$\Delta\sigma_\infty = \sigma_I - (\sigma_W + \sigma_{I/W}) > 0 -$$

is larger than that with lower one (σ_I = surface tension of ice without quasi-liquid-layer, σ_W = surface tension of water, $\sigma_{I/W}$ = interfacial tension between water and ice). Using broken bond model (cp. Kuroda (1979), Kuroda and Lacmann (1980)), it is shown that

$$\Delta\sigma_\infty(10\bar{1}0) > \Delta\sigma_\infty(0001)$$

is valid. Therefore the quasi-liquid-layer on {10$\bar{1}$0}-faces is thicker than on {0001}-faces at the same temperature and it remains thicker than about 3 Å ($\delta \approx 3$ Å $\triangleq \theta \approx 1$) until lower temperature, i.e. $T_{I/II}(0001) \approx -4$°C; $T_{I/II}(10\bar{1}0) \approx -10$°C. Fig. 5 shows the surface free energy (Δf) as a function of the thickness (δ) of the quasi-liquid-layer. There is equilibrium between ice and quasi-liquid-layer at the minimum of Δf ($\delta = \delta_{eq}$). Fig. 6 shows the equilibrium-vapour-pressure of the quasi-liquid-layer ($p(\delta)$) as a function of δ for 3 different temperatures. The thermodynamic potential of the quasi-liquid-layer referred to that of ice is given by $\Delta\mu_{Qll/I} = kT \ln(p(\delta)/p_I)$ for an ideal vapour-phase. δ_{eq} decreases with decreasing temperature.

The growth rate by this mechanism is given by the rate of condensation of the vapour-phase to the quasi-liquid-layer (R_{Ia}) and that of crystallization from the quasi-liquid-layer (R_{Ib}). R_{Ia} is given by the Hertz-Knudsen-equation ($R_{Ia} = V_m(p - p(\delta))/(2\pi mkT)^{1/2}$) and decreases with increasing thickness, because $p(\delta)$ increases with increasing δ (cp.fig.6). R_{Ib} is given by the growth rate from the melt with two-dimensional nucleation, but the $\Delta\mu$-value is given by $\Delta\mu_{Qll/I}$, which is less than $\Delta\mu_{W/I}$ at the same temperature and $\delta < \infty$ (cp.fig.6). It increases with increasing δ. In steady state $R_{Ia} = R_{Ib}$ is valid. Fig.7 shows R as a function of δ with $R_{Ia} = R_{Ib} = R_{st}$.

Adhesive mechanism (II): At $T_{I/II}$ the thickness δ_{eq} is equal to about 3 Å. The model of the quasi-liquid-layer is not valid for $T < T_{I/II}$. It is better to name it a strong eigen-adsorption with coverage ($\theta < 1$) of adsorbed H_2O-molecules on the ice surface. In this case a direct crystallization from the vapour phase without two-dimensional nucleation is possible (adhesive growth) (cp.fig.8). The growth rate (R_{II}) is given by the Hertz-Knudsen-equation with $p_{eq} = p_I$, that means the faces are growing with maximum growth rate (the condensation coefficient α is equal to 1).

Two-dimensional-nucleation mechanism (III): If θ is very small ($\theta < 0.01$) the adhesive growth mechanism is not possible and the growth rate is given by the two dimensional nucleation rate. The nucleation rate depends on the

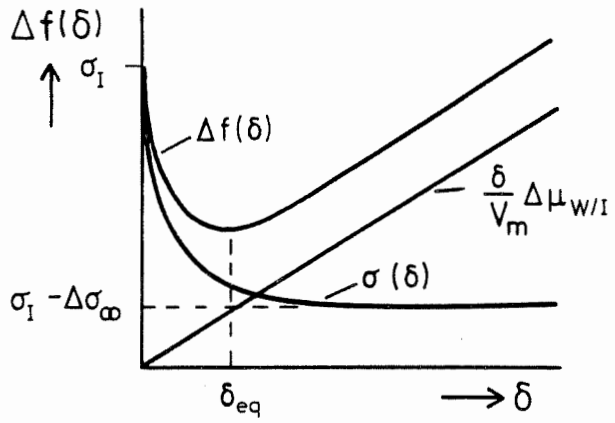

Fig. 5

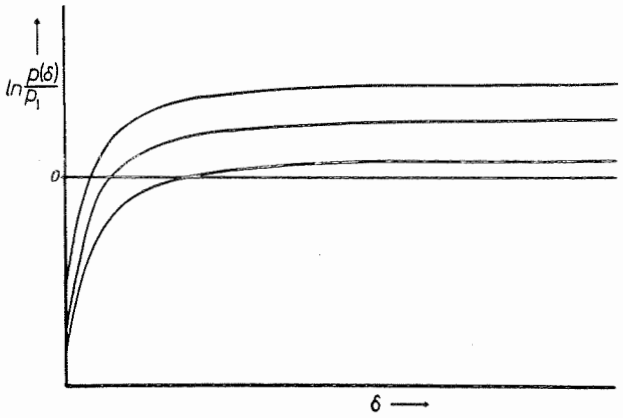

Fig. 6

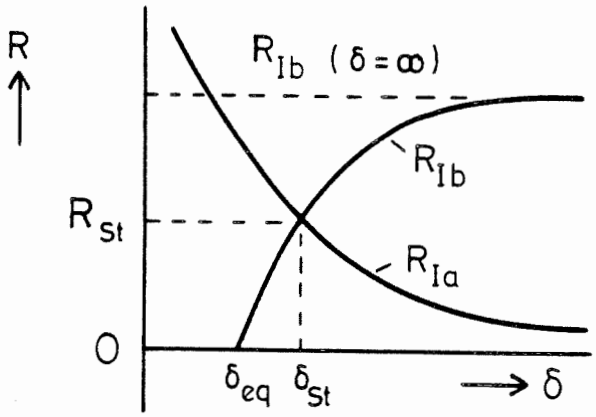

Fig. 7

relative supersaturation $\Delta p/p_I$ and increases very much with increasing $\Delta p/p_I$. Fig.9 shows $p_W - p_I$, $\Delta p/p_I$ for $\Delta p = p_W - p_I$ and $\Delta p/p_I$ for Δp = 0.01, 0.05, 0.1, 0.15 and 0.2 torr as a function of the temperature. Using broken bond model (cp.Kuroda(1979)), we get

$$\Delta G_2^*(0001) > \Delta G_2^*(10\bar{1}0)$$

for the growth from the quasi-liquid-layer (I: $\Delta G_2^* \sim 1/\Delta\mu_{Qll/I}$) and the vapour phase (III:

$\Delta G_2^* \sim 1/\Delta\mu_{V/I}$). ΔG_2^* is the free energy of nucleation.

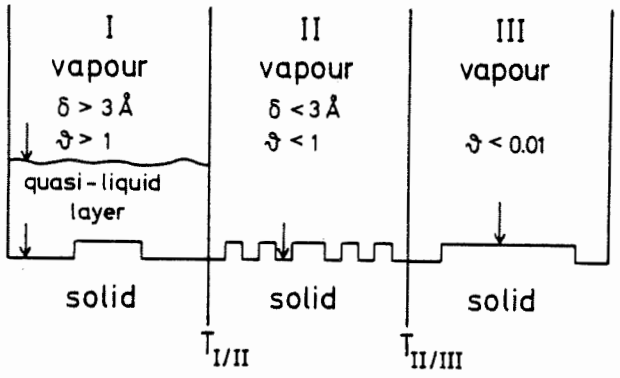

Fig. 8

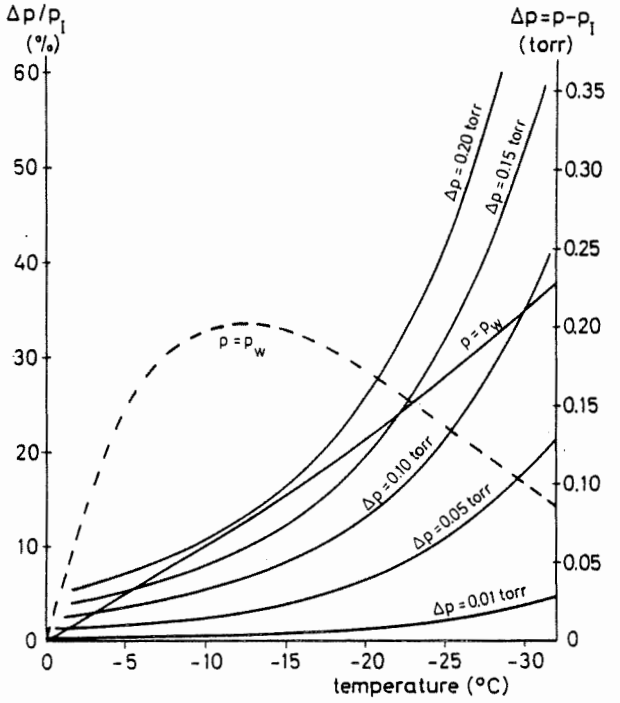

Fig. 9

Diffusion rate.

If an ice crystal is growing in air or in an other gas the growth rate is determined by diffusion decreasing with increasing gas pressure. Fig.2 shows the c/a-relation increases in the case of columns (B,D) or decreases in the case of plates (A,C), with increasing influence of diffusion on the growth rate.

For a spherical crystal with a radius of r_{cr} in a spherical vessel (r_{ve}) the growth rate by diffusion is given by

$$R_D = V_m \cdot D \cdot \Delta c / r_{cr} \cdot f_{sp} \qquad (1)$$

with $f_{sp} = (1 - r_{cr}/r_{ve})$; f_{sp} is normally ≈ 1. (V_m = mole volume, D = diffusion coefficient, Δc is the concentration difference between the wall of the vessel and the surface of the crystal).

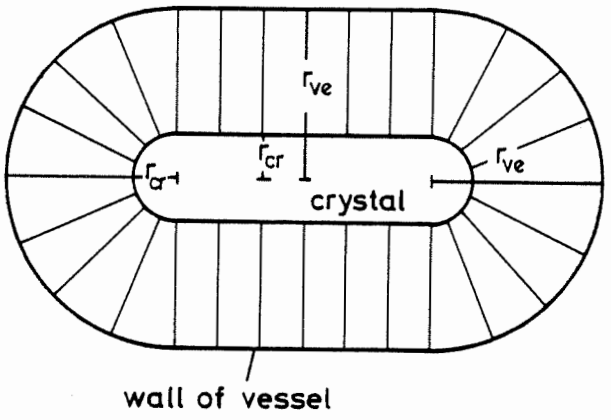

Fig. 10

In the case of a cylindrical crystal in a cylindrical vessel eq.(1) is also valid with $f_{cy} = \ln(r_{ve}/r_{cr})$. It means $R_{D/cy}$ depends on the dimension of the diffusion field and $R_{D/cy} < R_{D/sp}$ is valid.

For plane crystal face eq.(1) is also valid setting $f_{pl} = (r_{ve}/r_{cr} - 1)$ and no convection beeing effective. From this we get

$$R_{D/sp} >> R_{D/cy} > R_{D/pl}.$$

Fig.10 shows the model for an ice crystal in a diffusion field. In the case A and C (plates) 2 r_{cr} in fig.10 is equal to the thickness of the plate. The horizontal extent of the crystal in the figure is equal to the diameter of the (0001)-face. The diffusion field on the $(000\bar{1})$-face is a plane field and that on the $(10\bar{1}0)$ a cylindrical one. The relation

$$R_D(0001) < R_D(10\bar{1}0) \qquad (\alpha)$$

is valid.

In the other case (B,D ≙columns) 2 r_{cr} in fig.10 is equal to the diameter of the column and the length of the column is given by the horizontal extent in the figure. The growth rate of (0001) is given by $R_{D/sp}$ (spherical field around the tip of the column) and that of $(10\bar{1}0)$ by $R_{D/cy}$ (cylindrical field around the side-faces of the column). So we get

$$R_D(10\bar{1}0) < R_D(0001) \qquad (\beta)$$

Growth forms.

The interpretation of the growth forms is given by combination of the rate of surface mechanism and diffusion. Fig.11 shows the growth rates and growth forms in dependence on the temperature for $p = p_w$.

A. Both faces are growing by V-Ql1-S-mechanism. The free energy of nucleation for {0001} is larger than that for $\{10\bar{1}0\}$, and $R(0001) < R(10\bar{1}0)$ is valid. From this we get a c/a-value only some smaller than 1. Taking also into account the diffusion, (α) is also valid and the growth form is a typical plate (cp.fig.4).

B. The growth rate of {0001} increases at T_{AB}, because the adhesive mechanism gets effective on this face ($T_{AB} = T_{I/II}(0001)$). So the growth form given by the surface mechanism is a column with c/a near to 1. As shown in fig.2 and 3 (cp.fig.4) the c/a-relation increases with increasing retardation by diffusion and (β) is valid.

C. At T_{BC} the growth rate of {0001}

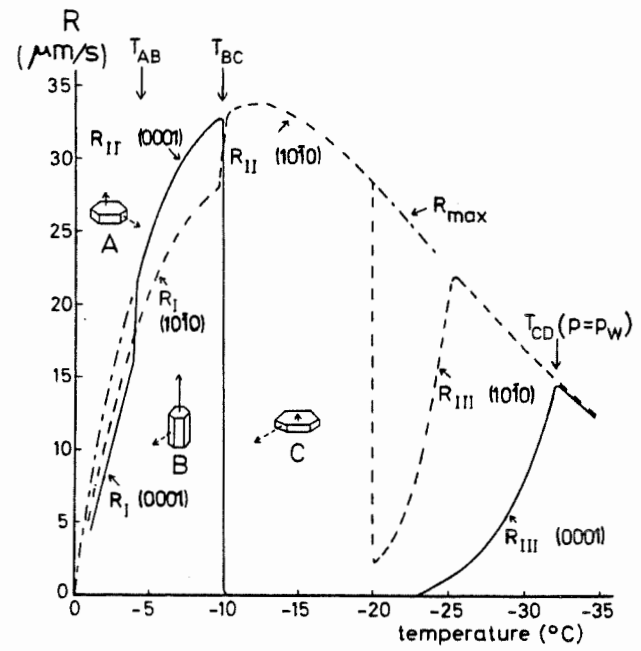

Fig. 11

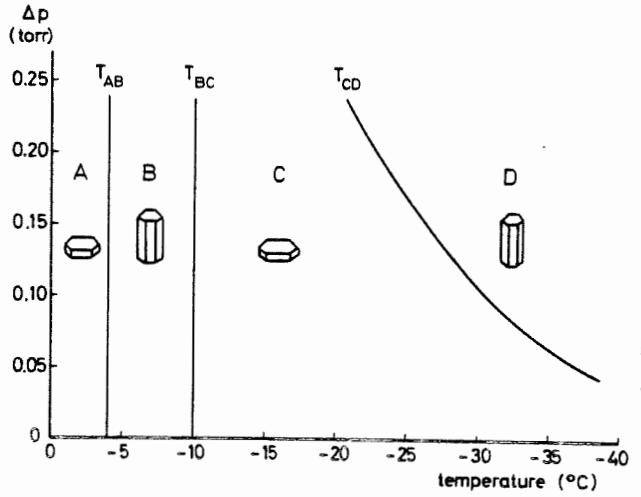

Fig. 12

decreases and that of {10$\bar{1}$0} increases supposing $T_{BC} \approx T_{II/III}(0001) \approx T_{I/II}(10\bar{1}0)$. In this case {0001} is growing very slowly, because the twodimensional nucleation rate is near to zero. Because this the {10$\bar{1}$0}-face is growing not only by direct condensation from the vapour-phase but also by surface diffusion from the {0001}-face. Beside this gas-phase volume diffusion is also effective as shown in fig.2 and 3.

D. The second change of growth mechanism of {10$\bar{1}$0} ($T_{II/III}(10\bar{1}0)$) may be at -20°C. but no habit change occurs at this temperature because like A the two dimensional nucleation rate on {0001} is much smaller than that on {1010}. With increasing $\Delta p/p_I$ the nucleation rate drastically increases and the growth rate increases until R_{max} (given by Hertz-Knudsen-equation). At given Δp the growth rate of {10$\bar{1}$0} reaches R_{max} at higher temperature than that of {0001}. T_{CD}^{max} is given by this temperature for {0001} depending on Δp. This is right for the interpretation of an isometric habit. The observed columns are explainable taking into account the gas phase diffusion with relation β. Fig.12 shows the regions A, B, C and D in a Δp-T-diagram (cp.Kuroda (1979), Kuroda and Lacmann (1980).

The given theoretical results are also in agreement with new experimental results by Anderson et al.(1976), Gonda(1977), Kikuchi and Hogan(1978). Anderson et al.(1976) reported that the column is the dominant habit of ice crystal only at higher supersaturation (e.g. $\Delta p/p_I$ > 25% at -30°C). These results are consistent with our theoretical prediction about $T_{CD}(\Delta p)$. The measurement of the $T_{CD}(\Delta p)$-curve is expected. If ice crystals grow in pure water vapour without air or other gases, the rate of growth is not determind by the diffusion process but only by surface kinetics. Thus columnar crystals would never appear below -20°C, even if Δp is very large under this conditions.

The dependence on Δp of growth rate determined by each growth mechanism proposed here at constant temperature is also discussed.

Literature.

1. Anderson,B.J., V.Keller, C.McKnight and J. Hallet(1976):Internat.Conf.on Cloud Physics, ed.by H.K.Weickmann,Amer.Meteor.Soc.,Boston,Mass., 97.
2. Gonda,T.(1976):J.Meteor.Soc. Japan,54,233.
3. Gonda,T.(1977):J.Meteor.Soc. Japan,55,142.
4. Kikuchi,K. and A.W.Hogan(1978):J.Meteor.Soc. Japan, 57, 180.
5. Kobayashi,T.(1961):Phil.Mag. 6, 1363.
6. Kuroda,T.(1979):Diss.,Techn.Univ.Braunschweig.
7. Kuroda,T. and R.Lacmann(1980):J.Crystal Growth, in preparation.
8. Lacmann,R. and I.N.Stranski(1972):J.Crystal Growth, 13/14, 235.
9. Lacmann,R.(1977):Z.physik.Chem.(N.F.),104,1.
10. Yamashita,A.(1974):Kisho Kenkyu Note,Meteor. Soc. Japan, No.123, 813.

* Present address:Gakushuin University,Faculty of Science, Mejiro, Toshima-ku,Tokyo,171 Japan

METEOROLOGICAL CONDITIONS OF SNOWFALL IN ARCTIC CANADA

C. Magono and K. Kikuchi

Department of Geophysics, Faculty of Science, Hokkaido University
Sapporo, Japan

1. Introduction

Since the investigation by Nakaya (1954), the study on natural and artificial snow crystals was mostly limited to snow crystals of relatively regular shapes which were formed in temperature regions warmer than -25 °C. The classification of natural snow crystals made by Magono and Lee (1966) likewise was insufficient to describe snow crystals in cold temperature regions. With this background, the Cloud Physics Group, Hokkaido University made an expedition to observe snow crystals in mid-winter from Jan. 12 to Feb. 6, 1977 at Inuvik, N.W.T., Canada.

From a meteorological point of view, the following factors are generally considered in order to understand snowfall phenomena.

1) The mechanism, in which the air is cooled to produce snow crystals in the air.
2) The origin of the water vapor which is supplied to produce the snow crystals.
3) The supplement of ice nuclei sufficient to produce the snow crystals.
4) Cloud height, in other words, cloud temperature range where the snow crystals are formed.

Our efforts were mainly concentrated on the observation of snow crystals, the analysis of synoptic conditions during snowfall, and the vertical structure of clouds in which snowfall occurred. The weather maps and the data of vertical structure of clouds were offered from the Surface Weather Office and the Upper Air Station at Inuvik.

2. Results

2.1 Heaviest snowfall during the observation period

Almost every day, snowfall was observed during the observation period from Jan. 15 to Feb. 6, 1977, but its amount was very light, that is, 1 or 2 cm/day. The snowfall in the afternoon of Feb. 2 was exceptionally heavy for this area, amounting to 5.1 cm/day. Firstly the meteorological conditions on this day were analyzed for the purpose of finding the original source of vapor supply for the formation of snow crystals.

Snow crystals of radiating assemblage of dendrites or sectors were predominant in the afternoon, as illustrated in Fig.1. According to Nakaya (1954) or Magono and Lee (1966) it was expected that these types of snow crystals are born as ice crystals of polycrystalline type in a cloud layer with a temperature somewhat colder than -20 °C, and then dendritic branches (extensions) would develop when the crystals fall into warmer cloud layers in a temperature range of -12 to -18 °C.

The vertical structure of air four hours after the snow crystal observation is shown in Fig.2. The vertical distribution of wind, temperature and humidity with respect to water surface (Hw) are shown from the

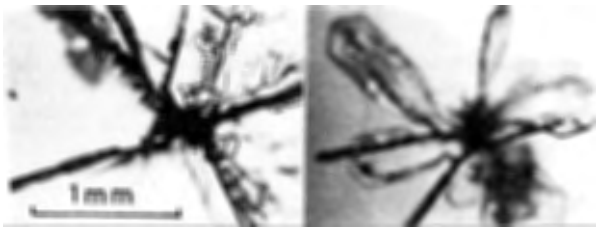

Fig.1 Snow crystals of radiating assemblage of dendrites or sectors, 1420-1430 2 Feb.

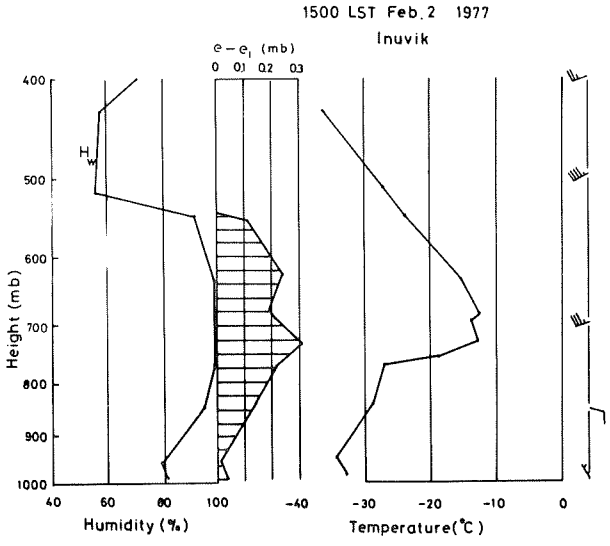

Fig.2 Vertical structure of atmosphere, 1500 2 Feb.

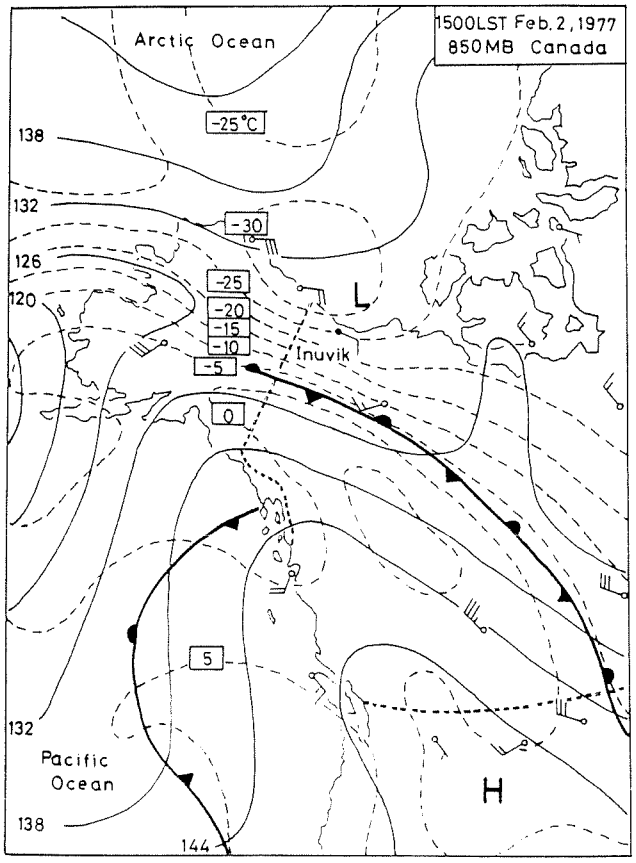

Fig.3 850 mb weather map, 1500 2 Feb.

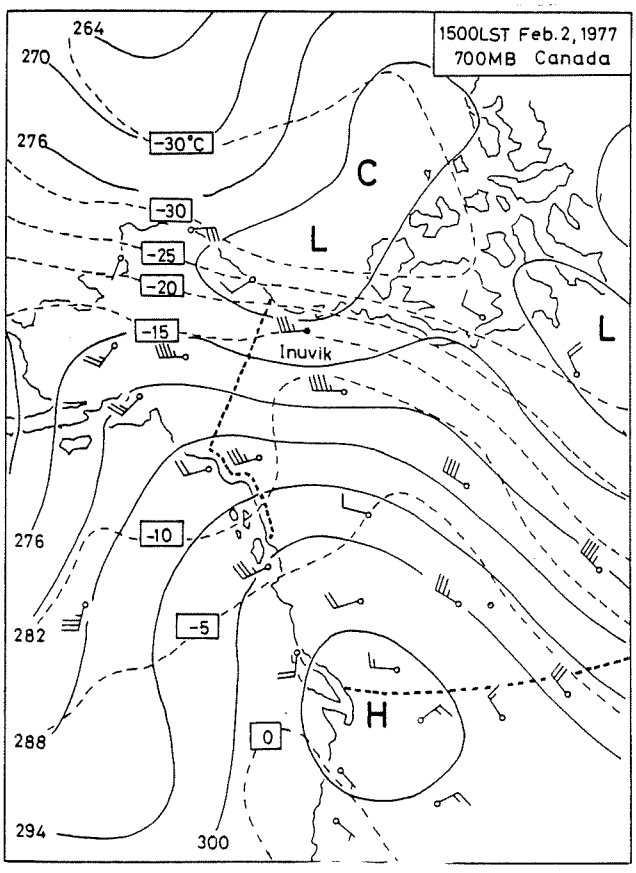

Fig.4 700 mb weather map, 1500 2 Feb.

right to left in the figure. The excess of water vapor pressure over the ice saturation ($e - e_i$) is indicated by shaded area.

In Fig.2, following points are noted:

1) The wind of in the layers below 800 mb level was very light and entirely different from those of higher layers than the level.
2) The temperature of air layers lower than 750 mb level were about 20 °C colder than those above the level.

These facts suggest that there was a frontal surface at about the 750 mb level below which a cold airmass existed, while a fairly warm airmass existed over the cold airmass.

Figure 3 shows a weather map at 850 mb level at the time nearest to the observation time of snow crystals in Fig.1. It may be seen that a stationary front existed to the south of Inuvik and it extended in a southeasterly direction. This front corresponds to that which was expected from Fig.2. The isotherms of the map in Fig.3 show that an airmass as warm as 0 °C existed to the southwest side of the front.

Figure 4 shows a 700 mb weather map at the same time. On this map, no front is described, but the distribution of wind clearly indicates that air was flowing from over the warm Eastern Pacific Ocean to the northeast, and when it arrived at Inuvik area, it turned to the southeast toward Middle Canada.

From the synoptic and cloud-physical analysis described above, it is considered that warm, moist air was supplied from the sea surface of the Eastern Pacific Ocean, from where it was transported northeastward, and then it proceeded along the upslope of the frontal surface to be cooled there.

Thus clouds are formed in air layers higher than the 750 mb level above Inuvik area. Depending on the temperature range of the layers, snow crystals rapidly grew to the type of radiating assemblage of dendrites or sectors. Below the frontal surface, snow crystals did not show detectable growth, because the temperature was too low and the vapor pressure was not high. Thus, it may be said that the heavy snowfall on Feb. 2 could be explained as to be a frontal snowfall from both synoptic and cloud-physical points of view.

Snow crystals of plane dendritic as illustrated in Fig.5 fell throughout the daytime on Jan. 26. Both the cloud-physical and synoptic situations were entirely similar to those on Feb. 2.

2.2 Diamond dust particles or ice fog particles

Minute ice crystals as illustrated

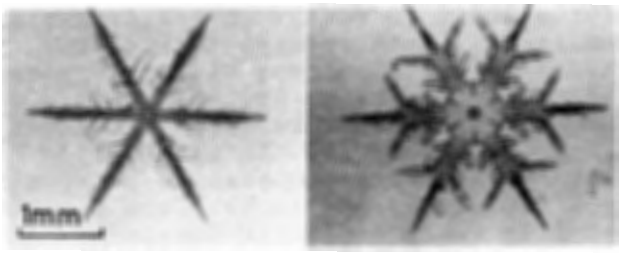

Fig.5 Plane dendritic snow crystals, 1528-1600 26 Jan.

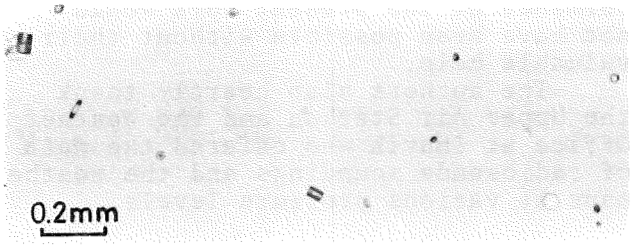

Fig.6 Diamond dust particles, 0843-0913 31 Jan.

in Fig.6 were observed in the morning of Jan. 31. It is considered that these ice crystals were formed close to the observation site, because their sizes were very small, although radiosonde data showed a thin moist layer between 750 and 950 mb levels. The surface air temperature was as cold as -38 °C. This was 6 °C colder than that at a 100 m height level. It was also very calm. Therefore, these diamond dust particles were considered to be ice fog particles.

2.3 Supercooled raindrops

Snow crystals of needle type fell in the evening of Jan. 25. This type of snow crystals are formed in a cloud of -5 °C or thereabouts (Magono and Lee, 1966). Therefore, the fall of needle snow crystals indicates that a fairly warm cloud covered Inuvik at this time. Around 22:00 LST supercooled small raindrops and graupel began to fall, as illustrated in Fig.7. This condition continued for about one hour. Circular dots in the figure show the trace of raindrops which were not yet frozen when they fell on the recipient glass plate.

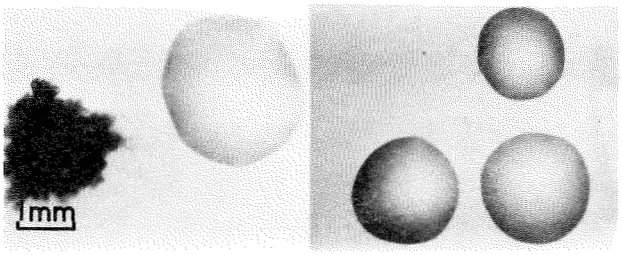

Fig.7 Supercooled raindrops and graupel, 2155-2211 25 Jan.

Around 23:00 LST, instead of raindrops, snow crystals of plane dendritic type began to fall. Such a rapid change in the type of precipitation suggests that a warm airmass sufficiently warm to melt snow crystals, passed over the observation site only for a short time. According to radiosonde data, however, there were no cloud layers warmer than -6 °C, and the weather map at 850 mb level showed no temperature region warmer than melting point near Inuvik.

3. Discussion

In the extra-tropical region, it is usual that visual clouds are formed when the relative humidity with respect to water surface exceeds 85 %, or when the vapor pressure exceeds the ice saturation vapor pressure. If that is the case for clouds over Inuvik, it would be considered that the cloud top in Fig.2 was at the 530 mb level, and that snow crystals originated near at the level, and grew at a rate proportional to the value of $e - e_i$. This shows that the snow crystals were born at about -23 °C temperature layer, as polycrystalline ice crystals, and then dendritic or sector-form branches extended from the ice crystals in a temperature range -13 to -18 °C. This temperature range exactly coincided with that predicted by Nakaya's diagram (1954). Accordingly it may be said that Nakaya's diagram is applicable to the snow crystals on this day.

Theoretical calculations made by Koenig (1970) and Jayaweera (1971) show that the growth rate of snow crystals is highest around a -15 °C temperature but it is extremely low around -5 °C and -25 °C. It is, therefore, considered that snow crystals hardly grew at air layers below 900 mb level, because the temperature was too cold and the vapor pressure was not sufficiently high at extremely cold temperature. With due regard to these facts, it is considered that snow crystals mostly grew in the cloud layer higher than 750 mb level, in other words, in the warm air layer on Feb. 2.

The vertical extension of snow clouds in the Arctic region is not generally as high as that of congestus clouds in the lower latitude region. Accordingly it is of course that the type of snow crystals is similar to that of in the extra-tropical region, if the snow clouds include a temperature range around -15 °C disregarding the cold temperature near the ground. However when the cloud temperature was extremely low, that is, -30 to -40 °C throughout of a cloud, irregular snow crystals of cold temperature type were actually observed at Inuvik, although in a low frequency of a few percents, as reported by Kikuchi and Kajikawa

(1979).

It is generally accepted that the majority of raindrops observed in the extra-tropical regions are the result of melting graupel or snowflakes. In the present rainfall case the upper half of the cloud layer was in a condition to form snow crystals and the lower half was in a condition to form graupel or snowflakes. It was actually observed that graupel fell together with the raindrops. The mass of graupel was nearly equivalent to the raindrops, assuming that the density of graupel was 0.1 or 0.2 g/cm. Accordingly it is very likely that those raindrops were the result of melted graupel, although no clouds warm enough to melt the graupel were recognized by the routine observations.

4. Conclusion

At first the authors predicted that snow crystals at Inuvik would be formed in cloud air of very cold temperature, that is, -30 to -50 °C. However, according to the results of analysis of synoptic conditions, the cloud temperature and snow crystals were in general nearly the same as over Hokkaido, Japan except rare cases. This was because the extremely cold temperature and low vapor pressure near the ground surface did not affect the growth and shape of snow crystals. When the air near the surface was moist, an ice fog was formed.

Occasionally a rainfall was observed, together with the fall of graupel, even if the air temperature at the observation site was about -12 °C. It was considered that the raindrops were formed by the melting of graupel in a warm air layer above the lower cold air layer, although the existence of such an air warm sufficient to melt the graupel was not detected in the cloud air around Inuvik.

The moisture for the growth of snow crystals at Inuvik was mostly transported from the eastern or northern Pacific Ocean.

The study on the formation mechanism of rainfall in such cold climate will be an important theme in the future.

Acknowledgements

This work was carried out as a part of the scientific expedition entitled "The Scientific Research on the Snow Crystals of Cold Temperature Type in Canada" under the Program of Overseas Field Researches, Ministry of Education, Japan.

It was considered that the success of fail in this kind of observation depended upon the occurrence of expected snowfall and the finding of observation site where the participants could reside to make their observations over a month in such a severe climatic condition. With special regard to this point, the authors wish to express their best thanks to Dr. Stanley R. Shewchuk, Saskatchewan Research Council, Canada, who arranged the observation site and made the cooperative observation at Inuvik, and to Mr. John D. Ostrick, manager, Inuvik Research Laboratories, who permitted to use a house in the laboratory for the present work and gave every facility in carrying out the observation. The performance of the present work would not have been possible without their valuable help.

The authors also heartly thank the Upper Air Station and the Weather Office at Inuvik who offered the data of radiosonde soundings and the weather maps at various pressure levels.

References

Jayaweera, H., 1971: Calculations of ice crystal growth. Jour. Atmos. Sci., 28, 728-736.

Kikuchi, K. and A.W. Hogan, 1976: Snow crystal observation in summer season at Amundsen-Scott South Pole Station, Antarctica. Jour. Fac. Sci., Hokkaido Univ., Ser.VII, 5, 1-20.

Kikuchi, K. and M. Kajikawa, 1979: Comments on V-shaped snow crystals observed in Arctic Canada. Jour. Met. Soc. Japan, 57, 484-487.

Koenig, I.R., 1970: Numerical modelling of ice deposition. Jour. Atmos. Sci., 27, 226-237.

Magono, C. and C.W. Lee, 1966: Meteorological classification of natural snow crystals. Jour. Fac. Sci., Hokkaido Univ., Ser.VII, 2, 321-335.

Nakaya, U., 1954: Snow Crystals. Harvard Univ. Press, 510 pp.

THE MECHANISM OF SECONDARY ICE PARTICLE PRODUCTION DURING THE GROWTH OF RIME

S.C. Mossop

Division of Cloud Physics, CSIRO
Sydney, Australia

It is now generally accepted that the apparent "multiplication" of ice crystals at temperatures near -5°C in maritime cumuli is due to the ejection of secondary ice particles when drops $\gtrsim$25 μm diameter are swept up by graupel particles and subsequently freeze. The physical mechanism by which ice "splinters" are ejected is still uncertain. However, Choularton et al. (1978) have revived the hypothesis that some of the large drops freeze in such a way that a peripheral shell of ice is formed. The internal pressure builds up as the water freezes and expands. This may be relieved by cracking of the shell and outflow of water which produces a spike on the frozen drop. In some cases the release of pressure may be violent enough to eject small ice splinters. It is not clear at this stage whether splinter ejection is directly related to spike formation or whether the two phenomena merely have a common cause.

This hypothesis could be tested by artificially introducing impurities which are known to weaken the ice structure. The ice shell round the freezing drop would then give way at a lower pressure, with less likelihood of either spike formation or the ejection of ice fragments.

Nakamura and Jones (1973) have shown that single crystals of ice made from water containing HF, HCℓ or NH_4OH are "softer" (i.e. the creep rate under applied stress is higher) at -11°C than crystals made from pure water. We have therefore carried out two sets of experiments to test the effect of added NH_3 or HCℓ on both spike formation and splintering of freezing water drops.

In the first series of experiments, drops of diameter 1-2 mm were suspended at the interface between layers of carbon tetrachloride and liquid paraffin in three petri dishes. One dish contained approximately 100 drops of distilled water. The other two contained similar numbers of drops made from the same water with the addition of measured quantities of either HCℓ or NH_4OH. (To assist freezing, a small quantity of freshly ground metaldehyde was added to the basic stock of distilled water.) The dishes were placed in an isothermal chamber at -8±0.5°C until most of the drops had frozen.

About half the drops of distilled water formed a spike on freezing. Addition of NH_4OH or HCℓ reduced the proportion of frozen drops that had spikes. The reduction was significant for concentrations of the solutes (HCℓ or NH_3) greater than about 3 p.p.m. by weight. Concentrations greater than about 100 p.p.m. suppressed spike formation entirely (Fig. 1).

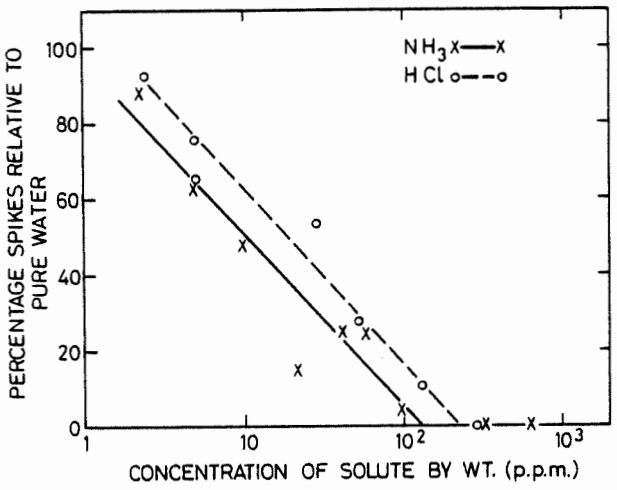

Fig. 1 - The effect of various concentrations of solute on the formation of spikes on frozen drops. The ordinate shows the percentage of spikes which form on "doped" drops relative to those on drops of pure water, considering the same total number of frozen drops in each case.

This series of experiments supports the idea that the pressures which build up within freezing drops can be relieved without spike formation if the ice structure is weakened by the incorporation of NH_3 or HCℓ.

In the second series of experiments we studied the freezing and splintering of much smaller drops, accreted upon an ice surface.

A cloud was continuously generated by injecting steam into a chamber of volume 18 m^3 held at a temperature of about -5°C. Cloud air could be drawn downwards from this chamber through a small wind tunnel in which a metal rod of length 4 cm and diameter 0.2 cm was exposed normal to the airstream. Air velocity was 2 m s^{-1}. Supercooled drops striking the rod froze as rime and in doing so ejected secondary ice particles. These could be counted as they traversed a beam of light downstream of the riming rod. Successive 1-min counts of ice particles established the production rate. A measured quantity of NH_3 gas was then injected into the cloud chamber and the new production rate of splinters was found.

The cloud temperature was -5.5±0.5°C and liquid water content about 0.8 g m^{-3}. The drop concentration was typically 500 cm^{-3} with median diameter 13 μm. Injection of NH_3 produced no measurable change in the cloud-drop spectrum. The background concentration of NH_3 in the cloud chamber at the start of an experiment was <1 μg m^{-3}.

In a typical experiment the injection of 10 cm^3 of NH_3, giving a calculated concentration of 420 μg m^{-3}, reduced the counting rate of splinters from 28.3 to 2.6 min^{-1} - i.e. to 9% of the value for an uncontaminated cloud.

We see from Figure 2 that the rate of splinter production decreases steadily as the concentration of ammonia in the cloud is increased. Only 3 μg m^{-3} of NH_3 is needed to halve the splinter production rate.

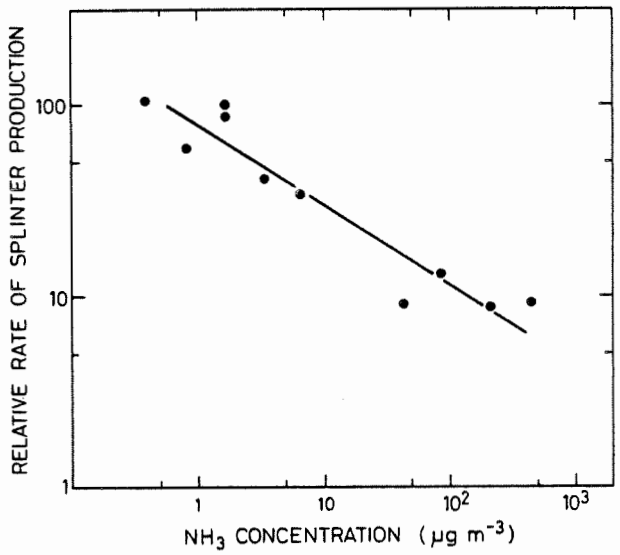

Fig. 2 - The effect of added NH_3 on the number of ice splinters observed per minute during rime growth in a cloud at -5°C. The ordinate shows the number of splinters per minute after introduction of NH_3 as a percentage of the number before.

These two sets of experiments show that the formation of spikes on frozen drops and the ejection of secondary ice particles can be reduced by adding impurities which weaken the ice structure. This provides strong support for the suggestion of Choularton et al. (1978) that the ejection of ice splinters is associated with the sudden release of pressure built up within freezing drops. This is the only known mechanism consistent with a reduction of splintering when the ice is weakened.

The ice shell hypothesis accounts for most of the known features of the Hallett-Mossop splintering process as follows.

(a) Splinter production is dependent upon the concentration of large drops (≳25 μm diameter) and small drops (≲13 μm) in the cloud (Mossop, 1978). This is consistent with the idea that shell formation is most likely when a large drop alights upon an already frozen small drop so that it is joined to the ice substrate by only a narrow bridge.

(b) The formation of this type of structure is less likely at high impact velocities - hence the lower efficiency of splinter production as the velocity increases (Mossop and Wishart, 1978). On the other hand, the velocity effect is not a dramatic one, since higher velocities favour shell formation by improving the ventilation of the freezing drop.

(c) The rate of formation of secondary ice crystals reaches a maximum value at a cloud temperature of about -5°C, falling to zero at about -3 and -8°C (Hallett and Mossop, 1974).

The peak at -5°C is probably not due to any property of ice characteristic of this temperature alone but rather to different combinations of conditions which render shell formations less likely at temperatures above and below -5°C.

The cut-off at -3°C can be readily explained. At temperatures approaching 0°C the rime becomes much denser as accreted drops spread more easily over the substrate (Macklin and Payne, 1968). The type of structure described in (a) is then no longer possible.

The cut-off on the low-temperature side is probably governed by three factors which change rapidly as the temperature is reduced:

(i) a higher proportion of the mass of the accreted drop freezes immediately on impact;
(ii) the velocity of propagation of ice dendrites through the freezing drop is much more rapid;
(iii) the structure of these dendrites becomes more elaborate below -5°C.

Though all these factors will strongly influence the internal structure of the freezing drop it is not yet clear how the shell-fracture mechanism is thereby rendered inoperative.

REFERENCES

Choularton, T.W., J. Latham and B.J. Mason, 1978. A possible mechanism of ice splinter production during riming, Nature, 274, 791-792.

Hallett, J. and S.C. Mossop, 1974. Production of secondary ice particles during the riming process. Nature, 249, 26-28.

Macklin, W.C. and G.S. Payne, 1968. Some aspects of the accretion process. Q. J. R. Meteorol. Soc., 94, 167-175.

Mossop, S.C., 1978. The influence of drop size distribution on the production of secondary ice particles during graupel growth, Q. J. R. Meteorol. Soc., 104, 323-330.

Mossop, S.C., and E.R. Wishart, 1978. The mechanism of splintering during rime growth, Geophys. Res. Lett., 5, 1083-1086.

Nakamura, T., and S.J. Jones, 1973. In Physics and Chemistry of Ice (Eds. E. Whalley et al.), p. 365, R. Soc. Canada, Ottawa.

CONVECTIVE DIFFUSION AND ICE CRYSTAL HABIT

R.L.Pitter
University of Maryland
College Park U.S.A.

1. INTRODUCTION

The initial determination of whether an ice crystal will grow in a plate-like form or in a columnar form is a fascinating and important phenomenon. Magono et al. (1976) showed how 10 um diameter frozen drops evolve first into polyhedrons with 20 faces and then into plates or columns, depending on the environmental temperature. Several studies have indicated that ice crystal habit may be caused by the migration of water molecules on the crystal surface prior to orienting in place in the molecular ice crystal lattice (Hobbs and Scott, 1970; Lamb and Hobbs, 1971). The result of these studies is the propagation of steps across the surface of the ice crystal. The growth conditions of these experiments were not controlled by the rate of supply of water vapor to the crystal surface.

The present study examines another mechanism, convective diffusion, to see whether it acts to preserve or to modify the habit of thin ice plates, and to see whether that mechanism contributes significantly to the evolution of a regular polyhedron into a thin ice plate during its diffusion growth.

2. THEORY

a. Ice Crystal Model

The thin ice plate is modeled as a thin oblate spheroid of axis ratio 0.05. List and Schemenauer (1971) showed that simple ice plates can be modeled by a thin circular disk, and Pitter et al. (1973) showed that thin oblate spheroids are dynamically similar to thin disks. The axis ratio chosen is typical of those for thin ice plates.

b. Measure of Habit Change

An overall measure of the rate of habit change is the rate of change of the axis ratio, AR=b/a, with change in the logarithm of ice crystal mass, log M. The relation is derived from expressions of the linear growth rate of the ice crystal surface at the equator and the two poles. The rate of growth of the semi-major axis length, a, is

$$\frac{da}{dt} = \frac{\mathcal{D}\Delta\rho_v}{\rho_I}\left(h\,\frac{\partial \rho^*}{\partial \xi}\right)_{\xi_0,\pi/2} \qquad (1)$$

The rate of growth of the semi-minor axis length, b, is

$$\frac{db}{dt} = \frac{\mathcal{D}\Delta\rho_v}{\rho_I}\left[\left(h\,\frac{\partial \rho^*}{\partial \xi}\right)_{\xi_0,0} + \left(h\,\frac{\partial \rho^*}{\partial \xi}\right)_{\xi_0,\pi}\right]. \qquad (2)$$

The mass growth rate is

$$\frac{dM}{dt} = \frac{4}{3}\pi\rho_I a^2\left(\frac{db}{dt} + 2\,AR\,\frac{da}{dt}\right). \qquad (3)$$

It is easily shown that the metric coefficient $h = h_\xi = h_\eta$ has the value of 1/a at the crystal surface on the equator, and 1/b at the crystal surface at either pole. Thus, one finds

$$\frac{d\,AR}{d\,\log M} = AR\left[\frac{\frac{\partial \rho^*(0)}{\partial \xi} + \frac{\partial \rho^*(\pi)}{\partial \xi} - 2\,\frac{\partial \rho^*(\pi/2)}{\partial \xi}}{\frac{\partial \rho^*(0)}{\partial \xi} + \frac{\partial \rho^*(\pi)}{\partial \xi} + 4\,\frac{\partial \rho^*(\pi/2)}{\partial \xi}}\right]. \qquad (4)$$

The sign of d AR/ d log M determines the tendency of habit change. If the value is zero it implies equilibrium: the habit does not change during growth. If the sign is positive, the axis ratio is increasing during growth, leading to a non-maintenance of initial ice crystal habit. If the sign is negative, the axis ratio is decreasing with growth and the ice crystal becomes more plate-like as it grows larger.

If sublimation does not occur from any part of the ice crystal surface during growth, the limits of d AR / d log M are $-\frac{1}{2}$ and +1, which correspond to db/dt = 0 and da/dt = 0, respectively.

c. Vapor Density Field

At Reynolds number zero, the vapor density field about the ice crystal is laplacian:

$$\nabla^2 \rho^* = 0 . \qquad (5)$$

When the appropriate boundary conditions are applied, the vapor density field is determined, from which the surface derivative is found:

$$\left.\frac{\partial \rho^*}{\partial \xi}\right|_{\xi=\xi_0} = \frac{-\operatorname{sech}\xi_0}{\pi/2 - \sin^{-1}(\tanh \xi_0)} . \qquad (6)$$

When the ice crystal obtains a significant fall velocity, the vapor density field is determined by the convective diffusion equation

$$V\cdot\nabla\rho^* = \mathcal{D}\nabla^2\rho^* . \qquad (7)$$

Solution of ρ^* here requires knowledge of the velocity field about the falling body.

3. EVALUATION OF HABIT CHANGE

Evaluation of ice crystal habit change, as expressed in Eq. (4), was undertaken using Eq. (6) for the unventilated case and solutions of Eq. (7) for the ventilated case.

In the unventilated case, the derivative of S^* normal to the ice crystal surface is independent of position on the surface, so d AR/d log M = 0. This simple result is rather important, since it shows that stationary vapor diffusion to an ellipsoid of revolution proceeds in such a manner as to exactly preserve the body's initial shape.

For the ventilated case, numerical solutions of the velocity field by Pitter et al. (1973) were used by Pitter et al. (1974) to numerically solve the vapor density field about oblate spheroids of axis ratio 0.05 and Reynolds numbers from 0.1 to 20. Table 1 presents the results in terms of the surface derivative $-\partial S^*/\partial \xi$ at meridional angles 0, π and $\pi/2$.

TABLE 1

$-(\partial S^*/\partial \xi)_{\xi_0}$

Reynolds Number	Meridional Angle 0	π	$\pi/2$
0.1	.699	.684	.692
0.5	.753	.705	.732
1	.795	.718	.761
2	.857	.732	.801
5	.987	.754	.879
10	1.146	.774	.959
20	1.886	.802	1.050

Evaluation of ice crystal habit change during convective diffusion growth was then performed using Eq. (4). The results are presented in Table 2.

TABLE 2

Rate of Habit Change

Reynolds Number	$\frac{d\ AR}{d\ \log M}$
0.1	-1.2×10^{-5}
0.5	-6.8×10^{-5}
1	-9.9×10^{-5}
2	-1.4×10^{-4}
5	-1.6×10^{-4}
10	1.7×10^{-5}
20	4.3×10^{-3}

4. DISCUSSION

Inspection of Table 2 reveals two characteristics. First, the sign of habit change reverses from negative to positive between Reynolds numbers 5 and 10. This is the result of the formation of reverse flow in the lee of the ice crystal, providing a more direct advection of air with higher vapor density to the back side of the ice crystal.

More importantly, the absolute values of d AR/d log M are very small compared with the limiting values. A simple illustration shows that these are too low to significantly alter ice crystal shape during diffusion growth. Suppose that an initial 10 μm radius spherical frozen drop evolves to an ice crystal of axis ratio 0.05 when it achieves a Reynolds number of 5 (a = 300 μm). To do so requires a mean d AR/d log M of -0.35 during evolution. The present results (for AR=0.05) are plotted in Figure 1 with the mean (Line 1) and the limiting value (Line 2) of d AR/d log M. The present results are three orders of magnitude less than Line 1, and they diminish as Reynolds number approaches zero. Thus, they indicate that convective diffusion is not a mechanism for ice crystal habit change. Another mechanism is required.

FIGURE 1

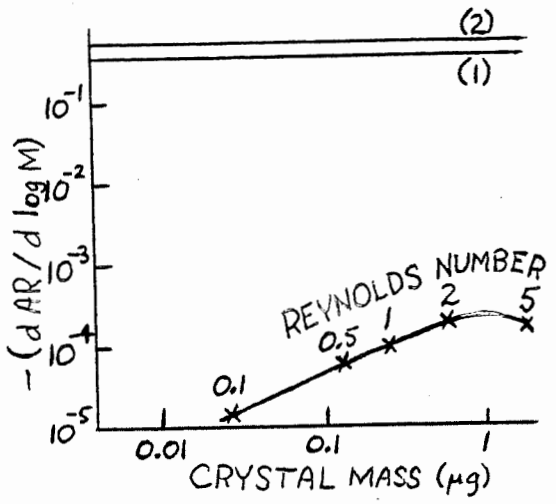

5. CONCLUSION

Convective diffusion exhibits an extremely weak ability to modify the initial habit of an ice crystal of Reynolds number less than 20. It therefore acts to preserve ice crystal habit by supplying water vapor to surface sites in the proportion needed to preserve crystal shape during growth. Other mechanisms are responsible for habit change during diffusion growth.

6. REFERENCES

Hobbs, P.V., and W.D.Scott, 1970: A theoretical study of the variation of ice crystal habits with temperature. J.Geophys.Res., 70(20), 5020-5034.

Lamb, D., and P.V.Hobbs, 1971: Growth rates and habits of ice crystals grown from the vapor phase. J.Atmos.Sci., 28(8), 1506-1509.

List, R., and R.S.Schemenauer, 1971: Free fall behavior of planar snow crystals, conical graupel and small hail. J.Atmos.Sci., 28(1), 110-115.

Magono, C., S.Fujita and T.Taniguchi, 1976: Shapes of single crystals originated from frozen cloud droplets. Preprints, Intern. Conf. on Cloud Physics, Boulder, CO, 103-106.

Pitter, R.L., H.R.Pruppacher and A.E.Hamielec, 1973: A numerical study of viscous flow past a thin oblate spheroid at low and intermediate Reynolds numbers. J.Atmos.Sci., 30(1), 125-134.

_____, _____, and _____, 1974: A numerical study of the effect of forced convection on mass transport from a thin oblate spheroid of ice in air. J.Atmos.Sci., 31(4), 1058-1066.

A WIND TUNNEL INVESTIGATION ON THE MELTING OF ICE PARTICLES

R. Rasmussen and H. R. Pruppacher

Department of Atmospheric Sciences, University of California
Los Angeles, California, USA

1. Introduction

The melting of ice particles is a microphysical process which is relatively poorly understood. Yet, this process is of fundamental importance in determining whether or not an ice particle, falling on its way from the cloud to the ground, through the 0°C-level, will arrive at the ground as a hard ice particle or as a raindrop. Inside clouds, the melting process plays an important role in the formation of what is known as the "bright band" in radar-meteorology.

Thus far, only two studies have been reported in literature on the melting process of ice particles (Mason, 1956; Drake and Mason (1966)). In these studies, an attempt has been made to determine the time an ice particle requires to melt while falling through an atmosphere of given temperature, pressure and humidity. For a melting ice particle falling in air the heat balance can be expressed by the relation

$$4\pi L_m r^2 \rho_i (dr/dt) = 4\pi a k_w [T_o - T_a(r)]/(a-r)$$
$$= -4\pi a \bar{f}_h k_a [T_\infty - T_a(r)] + 4\pi a \bar{f}_v L_e D_v [\rho_{v,\infty} - \rho_{v,a}], \quad (1)$$

where the first term expresses the latent heat consumed during melting, the second term expresses the heat transferred through the melted portion of the falling ice particle, the third term representes the heat transferred through the air, and the fourth term represents the heat acquired (consumed) on the particle surface due to condensation (evaporation). From Eq. (1) Mason found that the time t_m for the ice particle to completely melt is given by

$$t_m = \frac{L_m \rho_i}{k_w a} \int_{r=a}^{r=0} \frac{r(a-r)dr}{T_o - T_a(r)} \quad (2)$$

In the above equations r is the radius of the ice core surrounded by a water layer of radius a-r, a being the overall radius of the melting particle, T_o = 273.15°K, T_∞ and $\rho_{v,\infty}$ are the temperature and vapor density of the particle's environment, $T_a(r)$ is the surface temperature of the particle k_w and k_a are the heat conductivity of water and air, respectively, ρ_i is the density of ice, t is time, D_v is the diffusivity of water vapor in air, $\bar{f}_v$ and $\bar{f}_h$ are the ventillation coefficients for water vapor diffusion and heat diffusion in air, and L_m and L_e are the latent heat of melting and evaporation, respectively.

For the derivation of Eq. (2) it was assumed: (1) that the overall radius of the melting particle remains constant, (2) that the melting ice particle is spherical, (3) that the ice core is spherical, being at all times concentric with the outer boundary of the melting particle, (4) that heat dissipation inside the melting particle takes place by molecular heat conduction only, and (5) that the melting proceeds under steady state conditions.

All these assumptions are highly suspect since: (1) a melting ice particle, especially a delicate dendrite or a graupel particle with fine surface feature, may lose mass on melting; (2) the shape of a frozen drop, graupel, hailstone, snowflake or single ice crystal cannot be represented by an exact sphere or cone, although some frozen drops, graupel or hailstones may be spherical or conical; (3) one may not a priori assume that the ice core of a melting particle is spherical or concentric with the outer boundary of the melting particle; and (4) one must suspect that the heat dissipation through the water in the melting ice particle is affected by convection currents of the type present inside a falling water drop (LeClair et al. 1972).

The only experimental test of Mason's theory was carried out by Drake and Mason (1966) in a simple wind tunnel in which smooth, small ice spheres and cones were artifically supported in the tunnel air stream by means of a nylon supporting-grid. The ice spheres studied had radii between 5 to 20 mm, and the cones had maximum diameter of 3.6 mm. The relative humidity of the tunnel air stream was varied between 20 and 100%. The tunnel air stream temperature and humidity were held constant during melting. The experimentally found melting times appeared to be in fair agreement with those theoretically predicted, except when the air temperature was warmer than 5°C.

The experimental study of Drake and Mason is unrealistic in that: (1) the ice particle is held fixed in the air stream and is therefore not allowed to hydrodynamically behave as it does when it freely falls, (2) atmospheric ice particles are not smooth but have rough surfaces and have a variety of shapes other than spherical, (3) ice particles rarely melt while the environmental temperature remains constant, (4) the sizes of ice particles investigated were of hailstone size and did not reflect the sizes of the large

number of smaller ice particles found in atmospheric clouds.

2. Experimental Set-up

Our experimental study on the melting of ice particles involved the UCLA Cloud Tunnel which allows us to freely suspend in the tunnel air stream, water drops of 20 μm to 8 mm in diameter and ice particles from 50 μm to 2 mm in diameter. The experimental set-up was essentially that of Pitter and Pruppacher (1973), and of Pflaum et al. (1978). During a particular experiment a supercooled water drop, freely floating in the air stream of the tunnel, was converted to a frozen drop by contact with clay particles. In the present experiment drops of radii between 300 to 350 μm were considered. The temperature of the air was then raised at a constant rate of 2°C/min from about -10°C to about +10°C. Temperature and humidity of the air were closely monitored. The melting ice particle was observed and photographically studied between crossed polarizers by color motion picture. From our photographic records it was possible to observe the hydrodynamic motion of the ice particle and to determine the rate of melting and the total melting time of the ice particle. The actual surface temperature of the melting ice particle was computed from the air temperature and air humidity in the ambient air surrounding the ice particle using the method given by Beard and Pruppacher (1971) and Hall and Pruppacher (1976).

3. Results

A colored motion picture film is presented which demonstrates the melting behavior of frozen drops. Our observations allow the following conclusions:

(1) Melting has a profound effect on the hydrodynamic behavior of the falling ice particle. Thus, while a frozen drop at temperatures below 0°C exhibits a helical motion of the type described by Pitter and Pruppacher (1973), melting induces an erratic sailing motion which stops when the thickness of the water layer is about 1/10 of the overall particle radius.

(2) Melting always begins on the upstream side of the ice particle and also progresses more efficiently on this side, causing the ice core to recede as a spherically or oblate-spheroidally shaped ice particle. Also, this ice core is not concentric with the outer boundary of the drop, due to the non-uniform melting over the ice surface and because the ice core "floats" to the top of the drop.

(3) Internal circulation and convection currents are suppressed as long as the layer of melt water is thin, but becomes increasingly pronounced if the thickness of the melted layer becomes larger than the ice particle radius.

(4) Initially, melting proceeds quite slowly but progesses at an ever increasing rate once internal circulation inside the melt-water has begun.

(5) The rate of melting is strongly affected by the relative humiditiy of the surrounding air. For a 305 μm radius frozen drop, no melting occurred if the relative humidity of the surrounding air was less than about 65 to 70% caused by cooling due to continuous evaporation of the melt water.

(6) Equation (1) was evaluated numerically and the theoretically determined size of the ice core observed inside the melting, frozen drop was compared with the size of the ice core observed during our wind-tunnel experiments. Fair agreement between our experiment and Mason's theory was found during the initial stages of melting. During the final stages of melting the experimentally observed melting rate was somewhat faster than that theoretically predicted.

(7) Equation (2) was evaluated numerically and the theoretically determined overall melting time compared with the overall melting time observed during our wind tunnel experiments. The melting times observed where somewhat shorter than those theoretically predicted by Mason's theory although considerably uncertainty existed in our experiments regarding the exact time at which melting began.

References

Beard, K. V., and Pruppacher, H. R., 1971: A wind tunnel investigation of the rate of evaporation of small water drops falling at terminal velocity in air. J. Atmos. Sci., 28, 1455-1464.

Drake, J. C., and Mason, B. J., 1966: The melting of small ice spheres and cones. Quart. J. Roy. Meteor. Soc., 92, 500-509.

Hall, W. D., and Pruppacher, H. R., 1976: The survival of ice particles falling from cirrus clouds in sub-saturated air. J. Atmos. Sci., 33, 1995-2006.

LeClair, B. P., Hamielec, A. E, Pruppacher, H. R., ed. Hall, W. D., 1972: A thoretical and experimental study of the internal circulation in water drops falling at terminal velocity in air. J. Atmos. Sci., 29, 728-740.

Mason, B. J., 1956: On the melting of hailstones. Quart. J. Roy. Meteor. Soc., 82, 209-216.

Pitter, R. L., and Pruppacher, H. R., 1973: A wind tunnel investigation of freezing of small water drops falling at terminal velocity in air. Quant. J. Roy. Meteor. Soc., 99, 540-550.

Pflaum, J. C., Martin, J. J., and Pruppacher, H. R., 1978: A wind tunnel investigation of the hydrodynamic behavior of growing, freely falling graupel. Quart. J. Roy. Meteor. Soc., 104, 179-187.

Pflaum, J. C., and Pruppacher, H. R., 1979: A wind tunnel investigation of the growth of graupel initiated from frozen drops. J. Atmos. Sci., 36, 680-689.

THE MICROPHYSICAL STRUCTURE OF STRATIFORM COLD CLOUDS IN SPRING OVER JILIN

by

You Lai-guang

Academy of Meteorological Science, Central Meteorological Bureau, China

Lu Yu-jun and Wang Xue-lin

Meteorological Research Institute of Jilin Province, China

1. Introduction

The rainmaking experiment in China started in Jilin province in 1958. From 1963, in spring the microstructure of stratiform clouds in "Northeastern Cyclones" were observed from aircraft while cloud seedings were conducted. Most of the cyclones moved in from the west or the north rather than formed in Jilin. The aircraft observations were carried out over the rain belt on surface. The precipitation rate ranges from 0.1 to 3.0 $mmhr^{-1}$ while cloud top temperature is between -15 °c and -25 °c. In this paper, main results from 55 flights are reported, also the formation and growth of snow crystals are discussed.

2. Ice crystal concentration (ICC) and snow crystal concentration (SCC) in clouds

From 357 aluminum -- foil samples obtained in 15 flights from April to June in 1963, the mean value of ICC is 26.2 L^{-1}, the maximum being 222 L^{-1}[1] The mean concentration of ice and snow crystals in different ranges of temperature are given in table 1 a-b. It is shown that ICC increases with temperature, i.e. ICC increases downwards from the cloud top.

The presence of Ci has an important effect on ICC. High values of ICC were generally observed in the upper parts of As when Ci was seen over As. The observed ICC is given in table 2 and the positions of measurement are shown in Fig. 1. [2]

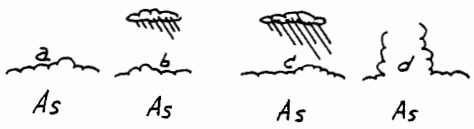

Fig.1 The sampling positions of ice crystal observation.

We take the diameter of 300μm as criterion to differentiate ice crystals from snow crystals. The relation between ICC and SCC is shown in Fig.2.[2] It is noted that SCC increases with ICC. The ratio of SCC to ICC decreases with the increase in ICC and approaches a constant value of 5.2×10^{-3} when ICC $1.5 \times 10^{4} m^{-3}$.

The snow crystal spectra may be classified into several types: the exponential distribution for plate and column crystals, the normal distribution for needle and dendritic crystals, etc.

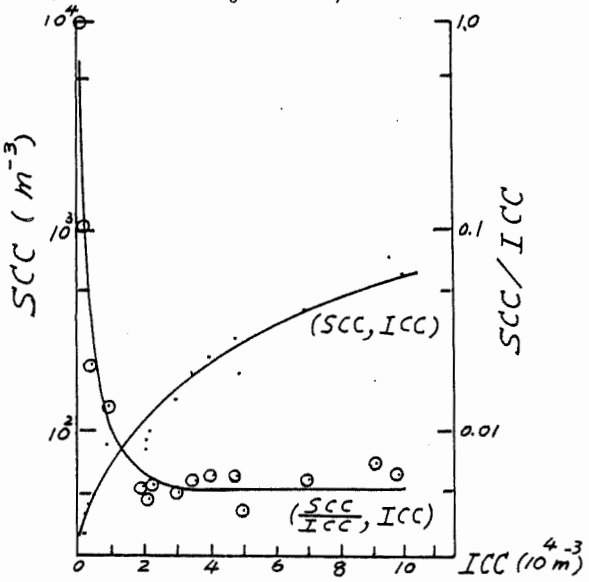

Fig. 2 The relation between ICC and SCC.

3. The formation of ice crystals in clouds

Observations of mean ice nuclei concentration in certain areas in the Northern part of China are shown in Fig.3. It can be seen that the mean ice nuclei concentration is 1-2 order of magnitude smaller than ICC. From observed SCC, droplet spectra and supercooled water content, the

importance of ice multiplication is studied, employing the results of Mossop's experiments (1978) [6]. Take a multiplication layer of 1 km depth in a cloud, the calculated rate of ice crystal multiplication is 3.2×10^3 $m^{-2}s^{-1}$. When the cloud top temperature is -15 °c and the updraft velocity is 10 cm sec^{-1}, the generation rate of ice crystals on ice nuclei within the cloud is calculated to be 2.1×10^3 $m^{-2}sec^{-1}$. Hence, it seems that the high values of ICC in clouds over Jilin is related not only to the high ice nuclei concentration but also to the ice multiplication processes.

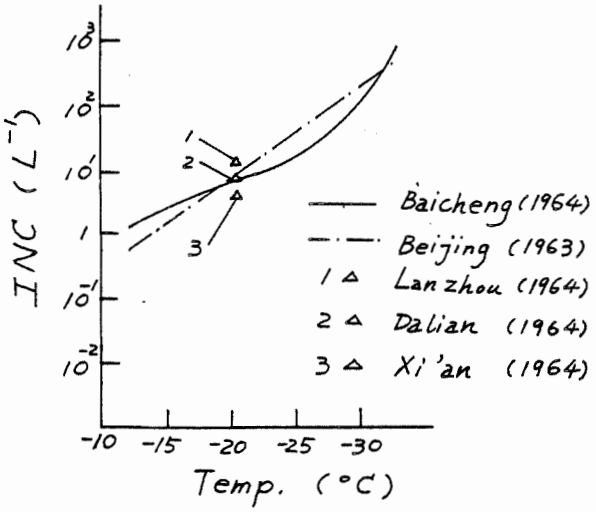

Fig. 3 The concentration of ice nuclei at various temperatures in certain areas in China [3][4][5].

4. The microphysical processes of precipitation

Observed data from 12 flights are analysed to study the microphysical processes of precipitation growth. Calculations indicate that the contribution of sublimation to total mass of precipitation elements predominates only in a few cases. The mean contribution of sublimation growth to total precipitation elements mass amounts to 25%, while the contribution of riming growth is 55% and the coalescence growth in warm region is 20%. Fig. 4 shows the mean percentage of precipitation growth in various height intervals. The mass of precipitation which increases within a layer of 1 km depth above the 0 °c isotherm accounts for 40% of the total mass.

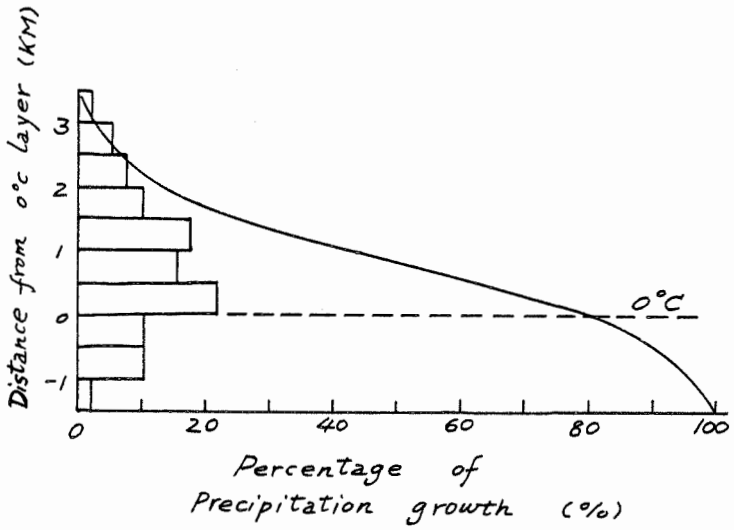

Fig.4 Mean percentage of precipitation growth in various height intervals.

From theoretical investigation of precipitation enhancement, ICC of 125 L^{-1} will be required to attain the highest precipitation efficiency, when the updraft velocity w is equal to 10 cm sec^{-1} [7]. In view of the observed values of ICC which do not exceed 125 L^{-1}, it suggests that the clouds in spring over Jilin may be seeded with nucleating agents to enhance precipitation.

References

[1] Sun ke-fu and You Lai-guang, 1965. Ice and snow crystals observations in cold layer clouds in Jilin province during April-June 1963. Acta Meteorologica Sinica, vol.35, 265-272.

[2] You Lai-guang et.al., 1965. The formation and growth of snow crystals in cold stratiform clouds over Jilin in spring. Acta Meteorologica Sinica, vol. 35, 423-438.

[3] Wang Xue-ling et.al., 1965. Ice nuclei over Baicheng area in spring. Acta Meteorologica Sinica, vol. 35, 273-279.

[4] You Lai-guang and Shi Au-ying, 1964. The measurement and analysis of ice nuclei concentration in Beijing during the period from March 18th to April 30th in 1963. Acta Meteorologica Sinica, vol.34, 548-553.

[5] Zhao Jian-ping, et.al., 1965. An observational analysis of ice nuclei over North area of China. Acta Meteorologica Sinica, vol.35, 416-422.

[6] Mossop, s.c., 1978. The influence of drop size distribution on the production of secondary ice particles during graupel growth. Quart. J. Roy. Met. Soc., vol.104, 323-330.

[7] Zhao Bo-ling and Ding Rong-liang, 1963. The possibility of precipitation enhancement of Nimbostratus. Acta Meteorologica Sinica, vol.33, 382-391.

Table 1 The observed ICC in different temperature ranges (a 1963, b 1974-1978)

a.

Temperature range (°c)	cloud top temp. -15°c		Cloud top temp. -15°c	
	ICC(L^{-1})	SCC(L^{-1})	ICC (L^{-1})	SCC(L^{-1})
-15.0- 12.1	6.5	0.10	15.9	0.22
-12.0- 9.1	2.3	0.07	29.8	0.28
-9.0- 6.1	22.9	0.12	31.4	0.15
-6.0- 3.1	16.9	0.12	41.3	0.25
-3.0- 0.1	10.7	0.07	44.2	0.24
Mean	11.9	0.10	32.5	0.23

b.

Temperature range (°c)	-12.0 - 9.1	-9.0 - 6.1	-6.0 - 3.1	-3.0 - 0.1	Mean
ICC (L^{-1})	8.8	11.5	16.2	15.4	13.0

Table 2. The effect of Ci on ICC in As.

Observation position*	No. of Observations	Ice crystal concentration (L^{-1})	
		Mean	Max.
a	10	0.19	0.96
b	6	1.3	9.7
c	10	6.2	14
d	7	16.0	42

* See Fig.2

II.3 - Population de Gouttes de Nuage et Gouttes de Pluie

Cloud Droplet Population and Raindrops

BIMODAL DROPLET SIZE DISTRIBUTIONS WITHIN CUMULUS CLOUDS

D A Bennetts and J Gloster

Meteorological Office Bracknell UK

Introduction

In an observational study Warner (1969a) concluded that the droplet size distribution of a non-precipitating, non-freezing cumulus cloud was usually positively skewed having a single mode. However in a substantial minority of cases it assumed a bimodal form. This occurred more frequently in clouds which grew in relatively unstable environments and there was evidence to suggest that the frequency increased towards the top of the clouds.

Many papers have been written in an attempt to explain these observations. Mason and Chien (1962) and Warner (1969b) concluded that the condensation on a realistic spectrum of soluble nuclei in an ascending air parcel cooling adiabatically, without mixing with its surroundings, produces much narrower cloud droplet distributions than are observed, and could not account for the high concentrations of small droplets ($< 5\ \mu m$ radius) which occur at all levels. However if a parcel is allowed to mix with the surrounding air, good agreement is obtained with the observed single mode distributions. Provided the parcel remains within a saturated environment, the final form of the drop size distribution depends mainly on the height risen, and is only very slightly affected by the route taken. Mason and Jonas (1974) showed that the maintenance of a saturated environment was crucial to this result. Using a double thermal, with mixing, they produced bimodal distributions whenever a parcel of air became unsaturated and the droplets partially evaporated before being mixed with the second thermal.

These papers explain in a general way mostof the features observed by Warner. In particular bimodal distributions are expected near the tops of clouds where dry environmental air can easily mix with the cloudy air, allowing evaporation before the droplets re-enter the growing cloud. However they do not explain the occurrence of bimodal distributions within the main body of the cloud. Warner's papers contain insufficient detail to analyse these cases.

It is to be expected that the occurrence of such distributions is determined in some way by the dynamical structure of the cloud and its environment; the rather simplistic dynamics of Mason and Jonas' model being only one of a range of possibilities. To date there is little information available on the internal circulations of convective cloud, although the recent study by Caughey and Kitchen (1980) provides hope of progress in this direction. In this paper data from a recent observational study both confirm Warner's results and provide new evidence of the spatial distribution of bimodal drop size spectra. As a result, the possibility is explored that a 'P' type of circulation (Ludlam 1978) might create bimodal drop size distributions. Following Kimura (1976), the range of conditions under which such circulations may develop is investigated.

Observational study

All the measurements were made from the Hercules aircraft operated by the Meteorological Research Flight. The aircraft is fully equipped to measure quantities of meteorological interest and additionally on these flights two PMS Axially Scattering Spectrometer Probes (ASSP-100), modified as described in Roach 1977, were fitted; one was mounted on a port window blank just forward of the leading edge of the wing and the other on the starboard external wing pod.

ASSP droplet spectra were obtained once per second during cloud transit. Thus the data are means over distances of the order of 100 m.

It was found that in general three penetrations could be made through an active non-precipitating cumulus cloud but occasionally as many as six were possible. The passes were usually arranged to minimize the effect on later measurements; early penetrations were at the top or sides of the cloud and later ones in the bottom or middle regions. All the penetrations were completed within 4 to 10 minutes.

A total of 45 clouds were sampled on 3 different days. The results can be classified into three groups.

Changes to the spectrum with cloud age I

For this experiment the clouds were penetrated three times at a given height. In general the results confirm Warner's hypothesis that the shape of the droplet size distribution is a function of age/height. For brevity the detailed results are not presented here.

Changes to the spectrum with cloud age II

Clouds were penetrated approximately on their centre line at different heights. Again the observed drop size distribution is a function of age/height, the drops being small and nearly monodispersed at the base with both the size and the distribution increasing towards cloud top.

Incidence of bimodal spectra

Warner found that 25% of his samples had a bimodal structure. These occurred mainly near the top of the clouds, the frequency varying with the static stability of the atmosphere. The present study confirms that bimodal spectra occur more frequently near the top of the clouds. However nothing can be said about this in relation to the static stability as the observations were not made in such a variety of conditions as those

of Warner.

In the top 1/5 of all the clouds 30% of 47 spectra were bimodal, while in the bottom 1/5 there were 12% of 85 spectra. (Most of the data were collected from the centre regions of the clouds).

However there were certain clouds which did not fit into Warner's simple hypothesis. These clouds all contained regions within the main body of the cloud, in which a high percentage of the spectra were bimodal. These were comparatively few in number and, of those clouds sampled in a manner that would detect this, 2 showed it well, a further 4 had regions which, although well above the background values, could not alone be considered convincing, and 12 were of the type discussed earlier, which were relatively uniform, in a horizontal cross-section.

An example of bimodal spectra in the central region of a cloud is shown in Figure 1.

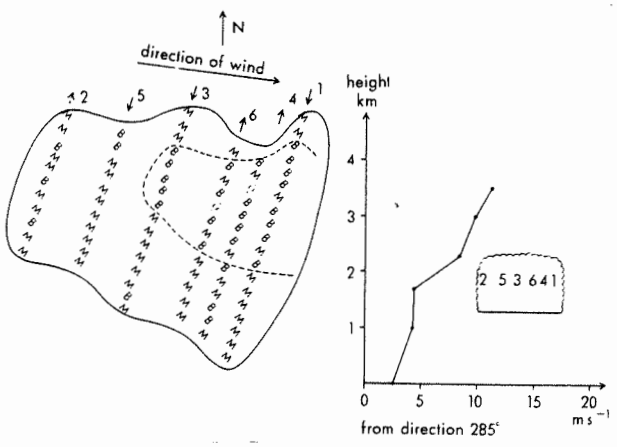

Fig 1. Plan view of a region of bimodal spectra which occurred in one of the clouds sampled. B indicates bimodal, M mono-dispersed and ∅ indicates samples with no cloud droplets. The wind profile is shown alongside.

This cloud was remarkably resilient and six passes were obtained before any visible changes occurred. The cloud was penetrated at right angles to the wind and the spectra obtained classified as bimodal (B), mono-dispersed (M) or drop free (∅). Figure 1 shows their distribution throughout a horizontal cross-section of the cloud. The definition of bimodal was taken to be that the peaks were distinct and at least 5% higher than the minimum between them. This is well above the error of the measurements. It will be noted that the bimodal region is on the downshear side of the cloud; a common feature of all the clouds observed.

Theoretical model

The growth of the visible cumulus cloud is preceded by the creation of a cold moist region just below the condensation level. This is built up by the cumulative effect of dry thermals from the boundary layer. Eventually these break throughand the visibile cloud is formed. This sub-condensation-level region may be considered as the reservoir from which the cloud grows. Provided it is large in comparison to the cloud the situation may be likened to convection generated from a heat island.

A suitable formulation of the problem that illustrates this idea was given by Kimura (1976). He considered a Boussinesq fluid in which the controlling influences were bouyancy, vorticity and diffusion. When small perturbations are considered the problem reduces to the solution of linearized equations containing two parameters; the Prandtl number (Pr) and F where

$$F = E^{-1/3}\frac{U}{l\sqrt{\alpha g l}}, \quad E = \frac{\nu}{l^2\sqrt{\alpha g \Gamma}}$$

where U is a typical value of the velocity, ie the mean cloud speed relative to the condensation level, l is a length scale, α is the coefficient of cubical expansion of air, Γ is the lapse rate (reduced for saturated ascent) and ν is the diffusion. For a full derivation of the equations see Kimura. To gain an understanding of the types of flow that are possible the problem is reduced to steady state, two dimensional flow which allows an analytic solution and permits a full exploration of parametric space.

When U is small the familiar symmetric vortex solution develops and this is called solution 1 (symmetric). As U is increased the flow can change in one of two ways depending on the relative magnitude of the bouyancy, vorticity and diffusion. The streamlines of solution 3 are shown in Figure 2. Superimposed on the streamlines is one contour of the temperature perturbation. Its shape naturally suggests the nomenclature right leaning solution. (The wind is from left to right in the diagram). Solution 2 (left leaning) is also shown in Figure 2. The temperature perturbation in this case leans to the left (into the wind) but for clarity the contour is omitted. The distribution of these solutions within parametric space is shown in figure 3. The significance of the dashed line will be discussed later.

Bimodal spectra have been associated with parcels of air in which drops partially evaporate. Therefore interest centres on streamlines, such as depicted in figure 2, on which this could occur. A full treatment of this problem requires that a range of microphysical processes be represented in the model. This in fact has been attempted, however it transpires that a simpler approach gives a better intuitive understanding of the basic idea.

Consider the circulation of a cloud for example that of solution 2 in figure 2. The regions of interest are the sides of the clouds where parcels may exit and re-enter, for example trajectory AB. As a first approximation the cloud boundaries are put at the

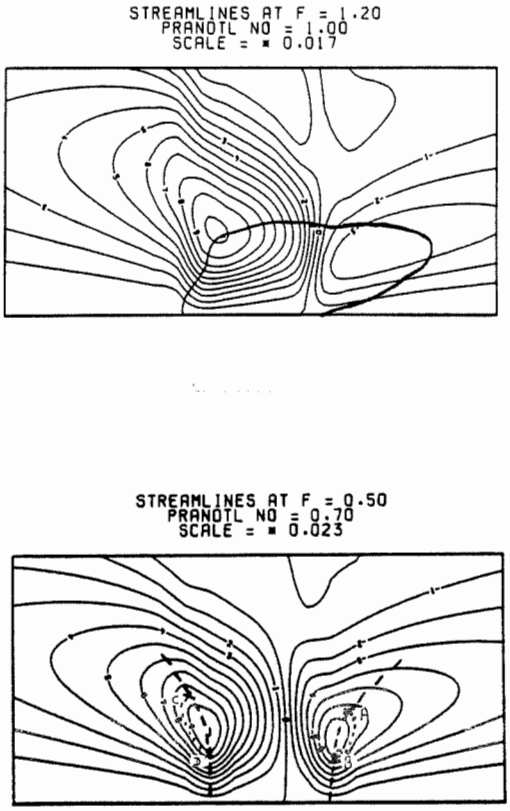

Fig 2. A typical solution of solution 3 (right leaning) is shown in the upper part of the figure and solution 2 (left leaning) in the lower. The contour scale and position in parametric space is indicated at the top of each. One temperature contour is superimposed onto solution 3 and interesting trajectories (see text) indicated on solution 2 (lower). The plot is in scaled co-ordinates.

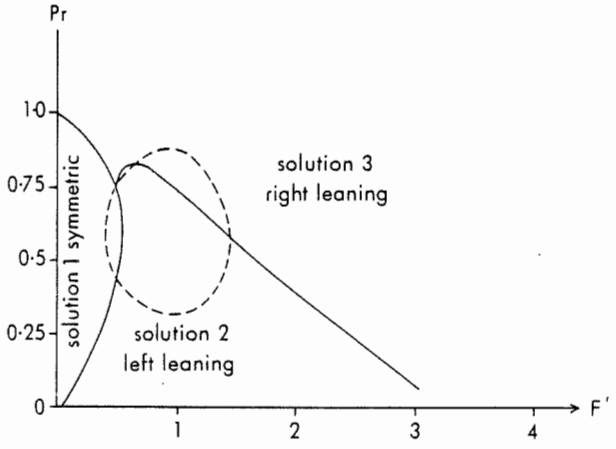

Fig 3. Distribution of solution 1, 2 and 3 in (F, Pr) space. The dashed region very approximately outlines the region where 'P' type circulations can occur.

interface of the upward and downward motion, illustrated by the dashed lines. Solutions are then sought such that a parcel of air can traverse AB within 10–100 s depending on the ambient conditions and the initial droplet size distribution. Clearly the cloud boundaries will be modified but the microphysical model shows this to be of secondary importance as is the exact position of the cloud boundaries.

In figure 3 the dashed line shows, very approximately, the regime where recirculation is possible. The initial state of the atmosphere eg temperature, humidity, cloud condensation nuclei, will be important, however these effects only alter the size of the region not its location.

Realistic atmospheric values of the parameters are $\alpha \sim 1/300\ ^{\circ}C^{-1}$, $\vartheta \sim 3\ m\,s^{-1}$, $\ell \sim 1000$ H giving $F = U/(450\,\Gamma)^{1/3}$. Using the modified lapse rate Γ the model predicts 'P' type circulations for U (measured relative to the condensation level) in the region of 0.5 to 2.5 m s^{-1}. With clouds having an aspect ratio of one this would correspond to a shear of 1 to 5 x 10^{-3} s^{-1}; light to moderate. If the shear is too light the circulation is symmetric and the trajectory lengths outside cloud are too long; if the shear is too strong the cloud leans well over and again trajectories are prohibitively long. The optimum region is when the cloud is in transition from solution 2 to solution 3 ie left to right leaning, and then the recirculation appears in the right hand cell (AB rather than CD). In relation to the condensation level this is the down wind side.

Figure 3 shows that the regime also depends on the Prandtl number. The normal atmospheric assumption is for Pr to be unity ie the turbulent diffusion acts equally on temperature and velocity. When dealing with cumulus convection, where vertical motion is equally important, this is no longer necessarily so. If the lapse rate is large, temperature gradients can become larger than velocity gradients and Pr < 1. Bimodal spectra can occur by means of 'P' type circulations only if $0.3 \lesssim Pr \lesssim 0.8$. Turbulent diffusion of temperature must be stronger than turbulent diffusion of velocity.

Conclusions

Evidence has been presented that a few (10%) of the cumulus clouds observed had regions of bimodal spectra within the main body of the cloud. This can be explained in terms of a 'P' type of circulation as illustrated by a simple dynamical model after Kimura (1976). Atmospheric conditions favourable to the development of such circulations are that the shear is light to moderate (0.001 to 0.005 s^{-1}) and that the turbulent diffusion of temperature is stronger than the turbulent diffusion of velocity, $Pr \sim 0.5$. The 'P' circulation then favours the down wind side (in relation to the condensation level).

The model is two dimensional and steady state. Clearly in the evolution of natural cumulus, young clouds will not have sufficient time to establish the circulation described and old clouds will be in a state of decay. Therefore

well developed but active clouds are most likely to have regions of bimodal spectra. This would suggest that more than the observed 10% of clouds develop 'P' type circulations subject to favourable environmental conditions: in the present study there was no selection of clouds by age.

References

Caughey, S J and Kitchen, M, 1980, Multilevel turbulence probe studies of the structure of small cumulus clouds. Proc 8th Int Cloud Physics Conf, Clermont Ferrand.

Kimura, R, 1976, Effects of general flows on heat island convection. Part 1: linear theory for the uniform flow. J Meteor Soc Japan Vol 54 pp 308-320.

Ludlam, F H, 1978, The forms and patterns of cumulus. Weather Vol 33 pp 54-63.

Mason, B J and Chien, C W, 1962, Cloud droplet growth by condensation in cumulus Vol 88 pp 136-142. Quart J Roy Meteor Soc.

Mason, B J and Jonas, P R, 1974, The evolution of droplet spectra and large droplets by condensation in cumulus clouds, Ibid Vol 100 pp 23-38.

Roach, W T, 1977, An assessment of the performance of the ASSP-100 Met O 15 Internal Report No 8. Met Office, Bracknell, Berks.

Warner, J, 1969a, The microstructure of cumulus clouds Part I General features of the droplet spectrum. J Atmos Sci Vol 26 pp 1049-1059.

Warner, J, 1969b, The microstructure of cumulus clouds Part II The effect of droplet size distributions of the cloud nucleus spectrum and up draught velocity, Ibid Vol 26 pp 1272-1282.

Jean-Pierre Chalon, Anne Van Thournout et Jean-Louis Champeaux

Etablissement d'Etudes et de Recherches Météorologiques

78470 Magny-les-Hameaux FRANCE

1 - INTRODUCTION

Dans les zones arides ou semi-arides des régions intertropicales, l'initialisation des précipitations se produit souvent dans des cumulus dont le sommet n'atteint pas une altitude suffisamment élevée pour avoir une température négative (cumulus chauds). L'étude de leurs caractéristiques microphysiques devrait permettre de mieux comprendre les processus qui favorisent ou inhibent la formation des précipitations. Des mesures in-situ du spectre dimensionnel des gouttelettes contenues dans les nuages ont pu être effectuées grâce au développement de l'instrumentation aéroportée. Les gouttes furent d'abord mesurées et comptées grâce à des méthodes d'impaction ou de prélèvement (voir par exemple Squires et Gillespie - 1952). L'utilisation de moyens de mesure optique (Knollenberg - 1970) permet de limiter les perturbations introduites par l'instrument (effets aérodynamiques) et souvent d'automatiser les procédures de comptage des gouttes. Pour obtenir des informations sur la répartition verticale du spectre dimensionnel des gouttelettes dans des nuages chauds, l'Etablissement d'Etudes et de Recherches Météorologiques (EERM) de la Direction de la Météorologie a mis au point un instrument largable muni d'un capteur optique : l'Aquasonde. Cette sonde est larguée depuis un avion dans le nuage étudié et transmet le résultat de ses mesures (dimension des gouttes rencontrées et pression du milieu ambiant) par l'intermédiaire d'un émetteur d'ondes radioélectriques. Les signaux de plusieurs Aquasondes peuvent être enregistrés simultanément. Les caractéristiques techniques de cette sonde ont été décrites par Klaus et Champeaux (1977) et sont présentées par Champeaux au cours de cette conférence.

Une expérience préliminaire d'étude des nuages chauds s'est déroulée en Septembre 1978 dans le Sud-Ouest de la France (à Captieux dans les Landes) avec la collaboration de l'Institut et Observatoire de Physique du Globe du Puy de Dôme (IOPG). Elle mettait en oeuvre le radar millimétrique (8,6 mm de longueur d'onde) de l'IOPG, l'avion instrumenté Cessna 206 de l'EERM et huit prototypes de l'Aquasonde. Cette expérience a été décrite de façon détaillée par Chalon et al. (1979). Nous présentons ici les principaux résultats d'une étude des nuages qui se sont développés au-dessus du site d'expérimentation le 6 Septembre 1978.

2 - DESCRIPTION DE LA SITUATION METEOROLOGIQUE

Un front froid axé Nord-Sud est passé au-dessus des Landes le 6 Septembre à 02 TU et se déplace rapidement vers l'Est. A l'arrière l'air d'origine polaire maritime (θ'_W = 12°C) arrivant sur le sol chaud est en instabilité sélective et convective. La traîne associée est affaiblie par le passage d'une dorsale qui précède l'arrivée d'un front chaud actif. Ce front passera sur la région dans la nuit du 6 au 7.

Les nuages étudiés se sont développés entre 12.00 et 13.00 TU dans la masse d'air qui suivait le front froid. Les sondages (voir Figure 1) montrent la présence, du sol à 1500 mètres, d'une couche en instabilité convective et sélective surmontée jusqu'à 2700 mètres d'une couche légèrement plus stable. Au-dessus, l'air est stable jusqu'à 4500 mètres et limite la convection. A 12.15 TU, la hauteur au-dessus du sol de la base des nuages observés à partir de l'avion Cessna est évaluée à 500 mètres, les sommets ne dépassent pas 2100 mètres. A 13.00 TU, les bases seront observées à 1000 mètres et certains sommets pourront atteindre 4000 mètres. L'isotherme 0°C se trouve à 2900 mètres.

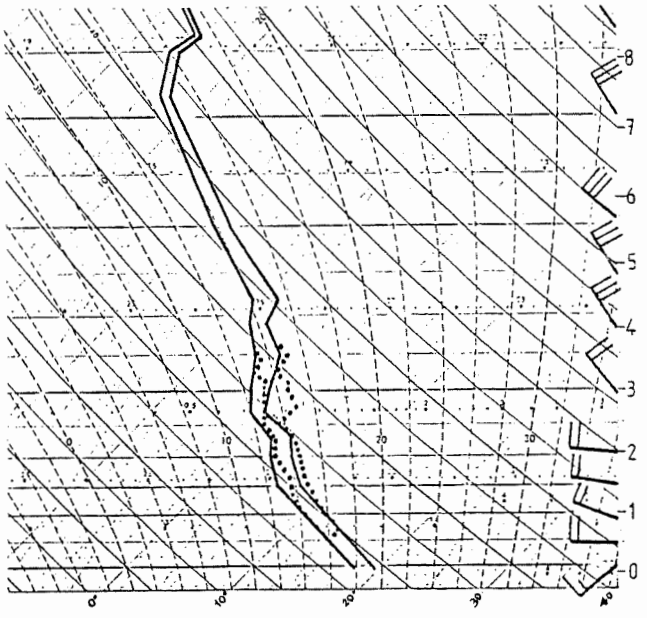

Figure 1 - Radiosondage de Bordeaux à 12.00 TU (traits pleins) et sondage effectué par l'avion Cessna au voisinage des nuages étudiés (traits pointillés)

3 - STRUCTURE ET EVOLUTION DES NUAGES OBSERVES

Les nuages observés ont l'aspect de strato-cumulus de 1000 mètres d'épaisseur surmontés de tours espacées d'environ deux kilomètres et pouvant atteindre 3000 mètres d'altitude. Les tours correspondent à des cellules actives et prennent

naissance successivement au Nord des cellules plus anciennes qui se dissipent dans la partie Sud. Ces cellules ont une durée de vie assez courte. Elles se déplacent sensiblement dans la direction (110 degrés) et à la vitesse (11 m/s) des vents de la couche (500 à 3000 mètres) dans laquelle elles évoluent (voir Figure 2).

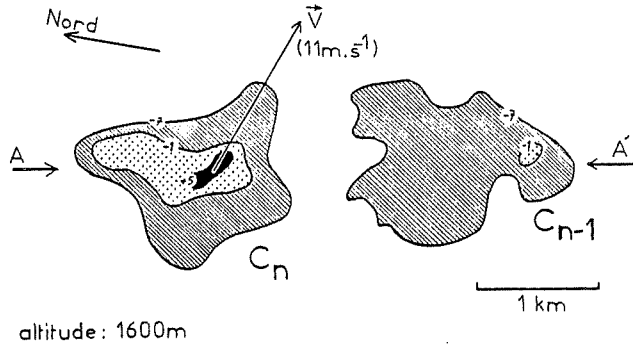

Figure 2 - Coupe horizontale de réflectivité radar (en dBZ) mesurée à 12.30 TU à 1600 m d'altitude. Le vecteur $\vec{V}$ indique la direction et la vitesse de déplacement.

La Figure 3 montre une coupe verticale effectuée suivant l'axe AA' de la Figure 2 à 12.30 TU. La base des échos enregistrés par le radar se trouve à une altitude inférieure à celle de la base des nuages estimée avec les mesures des Aquasondes et les observations effectuées depuis l'avion instrumenté. Cette différence peut être attribuée à la présence sous la base des nuages de particules difficilement détectables par l'Aquasonde ou par les méthodes visuelles (gouttes éparses de précipitation, aérosols ou insectes accompagnant l'ascendance). Au moment de sa représentation, le nuage est constitué de deux cellules. La cellule C_n qui se développe est pratiquement verticale, son sommet se trouve à 2500 mètres. Les réflectivités atteignent 8 dBZ au centre de la cellule ce qui correspond probablement à des précipitations n'atteignant pas le sol ou trop faibles et trop localisées pour avoir été détectées. La cellule la plus ancienne C_{n-1} a atteint son stade de dissipation, elle s'affaisse en s'inclinant suivant l'axe de la coupe. Son sommet se trouve à 2100 mètres et sa réflectivité maximale ne dépasse pas 0 dBZ. Deux ou trois cellules sont présentes simultanément dans les nuages étudiés. La durée de vie de ces nuages est nettement supérieure à celle des cellules qui les constituent. Elle dépend essentiellement de la formation latérale de nouvelles cellules qui assurent le maintien du système et contribuent à son déplacement. Bien que d'amplitude plus modeste, ce système nuageux a une évolution comparable à celle des systèmes multicellulaires décrits par Marwitz (1972) ou par Chalon et al. (1976).

4 - STRUCTURE MICROPHYSIQUE

Deux Aquasondes ont été larguées dans la cellule C_n. La première à 12.35 TU, soit 5 minutes après la coupe de la Figure 3, au moment du développement maximum de la cellule (sommet atteignant 2800 mètres). Le deuxième sondage a été effectué 4 minutes plus tard alors que la cellule s'affaissait. La localisation de la trajectoire des sondes est délicate. Nous ne possédons pas d'information précise sur leur position pendant la chute. Nous avons essayé d'estimer les trajectoires en comparant le profil de réflectivité calculé avec les données d'Aquasonde à des profils verticaux de réflectivité radar. La trajectoire obtenue pour la première sonde est indiquée par TT' Figure 3.

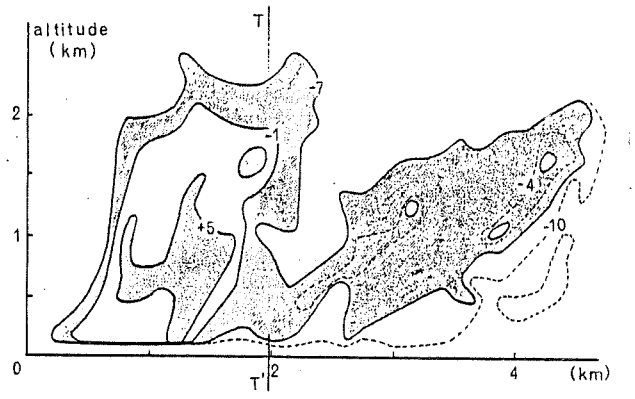

Figure 3 - Coupe verticale de réflectivité radar (en dBZ) à 12.30 TU effectuée suivant l'axe AA' indiqué sur la Figure 2.

Il existe toutefois entre l'instant de la coupe et ce sondage un délai de 5 minutes pendant lequel le nuage va poursuivre son développement pour atteindre son altitude maximale et s'incliner légèrement vers la droite de la Figure. Lorsque la deuxième sonde est larguée, la cellule C_n a commencé à s'affaisser (sommet à 2600 mètres) et se trouve très inclinée. Sa structure ressemble alors à celle de la cellule C_{n-1} à l'instant de la Figure 3.

Les spectres observés ont une forme unimodale montrant une forte concentration en gouttes de rayon compris entre 15 et 20 microns (voir Figure 4). La courbe décroît ensuite de façon exponentielle vers les rayons plus importants (25 à 50 microns). La dispersion des rayons augmente de la base du nuage vers le sommet, à proximité duquel se trouvent les gouttes les plus grosses. Ces distributions sont représentées avec une bonne approximation par une loi du type $n(r) = Ar^k \exp(-Br)$
où $n(r)dr$ est la concentration des gouttes dont le rayon est compris entre r et r+dr. B a été obtenu à partir de la valeur mode de la distribution (r_m), A peut être déduit du calcul d'un de ses moments.

$B = \frac{k}{r_m}$ et par exemple : $A = \frac{NB^{k+1}}{k!}$ où N est la concentration totale. L'expression de B a été choisie pour ajuster la courbe sur la valeur maximale de la fonction de distribution. Les valeurs obtenues pour k sont comprises entre 8 et 10 et diffèrent de la valeur (k = 2) utilisée dans la distribution de Khrgian-Mazin (Borovikov et al, 1963).

Dans la cellule C_n, les valeurs moyennées, sur chaque sondage, du contenu en eau liquide sont comprises entre 0.5 et 1.8 g.m^{-3}, celles de la concentration restent inférieures à 100 cm^{-3}. Ces données sont compatibles avec les observations effectuées dans le passé (Squires et Gillespie, 1952) et sont très proches des valeurs généralement obtenues dans le cas de petits cumulus d'origine maritime. Pour ces

nuages qui ont pris naissance à 80 km à l'intérieur des terres, les particules d'origine océanique jouent vraisemblablement un rôle prépondérant dans la nucléation des gouttelettes.

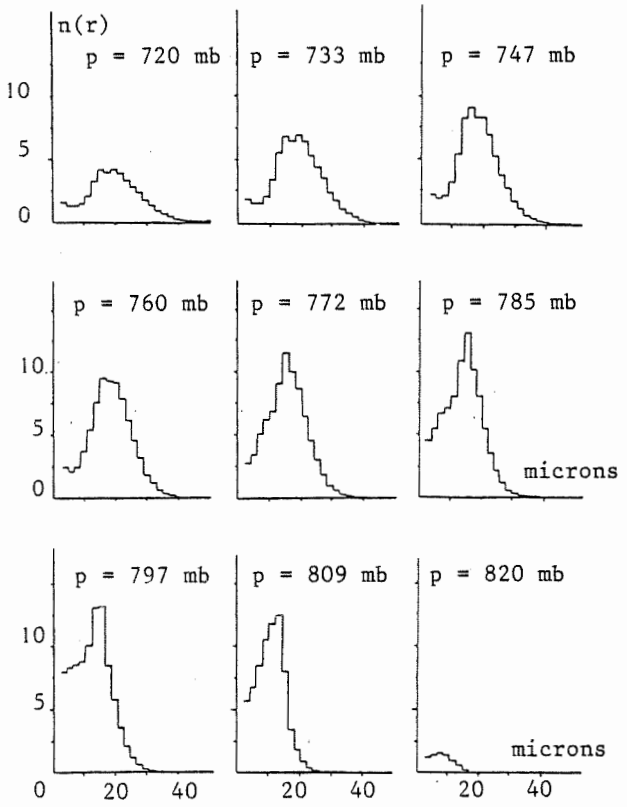

Figure 4 - Spectres dimensionnels des gouttes rencontrées pendant la traversée de la cellule C_n. Les rayons sont exprimés en microns et les distributions en $cm^{-3} \times (2\ microns)^{-1}$.

La Figure 5 montre la concentration totale N et le rayon moyen $\bar{r}$ des gouttes rencontrées par la première sonde au cours de sa chute. Elle met en évidence la présence de deux couches distinctes correspondant, de 700 à 1600 mètres, au stratocumulus formé par la cellule C_{n-1} en voie de dissipation et, de 1800 à 2800 mètres, au cumulus associé à la cellule active C_n. Dans cette cellule, les plus grosses gouttes (enregistrées par la première sonde) ont un diamètre de 50 microns et la concentration dépasse 90 cm^{-3}. Lorsque C_n commence à s'affaisser, les gouttes deviennent moins grosses et moins nombreuses (données du deuxième sondage). Dans le stratocumulus qui correspond à un état encore plus avancé de la vie des cellules, le rayon des plus grosses gouttes ne dépasse pas 20 microns et la concentration 65 cm^{-3}.

La structure de la cellule C_n obtenue à partir de la première sonde étant représentative du nuage en cours de développement, nous allons maintenant limiter notre étude à l'analyse des données correspondantes. Dans la partie inférieure du cumulus (voir Figure 5), la concentration augmente avec l'altitude pour atteindre sa valeur maximale (92 cm^{-3}) et décroît ensuite lentement. Le rayon moyen des gouttes croît de façon régulière jusqu'au voisinage du sommet. Ce type de répartition peut être associé à trois modes d'évolution principaux :

- une région où la condensation est le processus dominant (N est constant pendant que $\bar{r}$ augmente)
- une région où la coalescence est le processus de croissance le plus efficace (N décroît, $\bar{r}$ est sensiblement constant
- des régions de mélange avec l'environnement où l'évaporation est le processus d'évolution dominant (parties inférieure et supérieure où l'on enregistre de fortes diminutions de N et de $\bar{r}$ en allant de l'intérieur vers le bord du nuage).

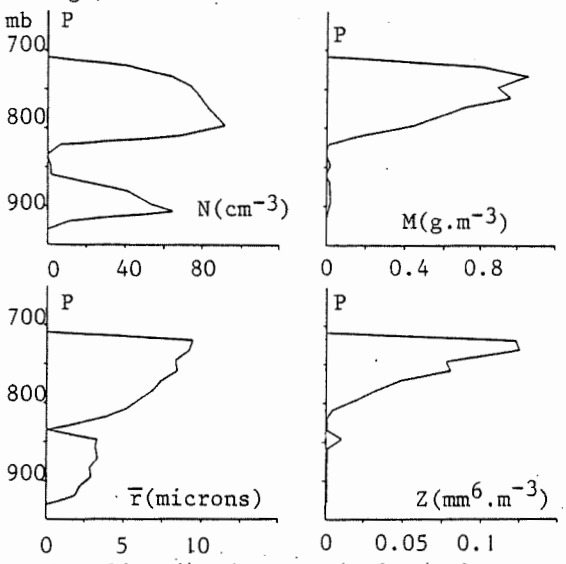

Figure 5 - Distribution verticale de la concentration N, du contenu en eau liquide M, du rayon moyen $\bar{r}$ et de la réflectivité Z.

La Figure 5 montre la répartition verticale du contenu en eau liquide M et de la réflectivité Z calculés à partir des données de l'Aquasonde. Ces deux quantités augmentent progressivement avec la hauteur au-dessus de la base puis elles amorcent une brusque décroissance à l'approche du sommet.

L'utilisation quantitative des données radar dans l'étude des nuages observés nécessite la connaissance de relations entre la réflectivité et des paramètres représentatifs de la structure microphysique. Atlas (1954) propose des relations avec le contenu en eau liquide et avec le diamètre du volume médian (D_o). Appliquées à la cellule C_n, ces équations donnent à M constant, des réflectivités 2.5 fois trop faibles et à D_o constant des réflectivités 3 fois trop fortes. Nous avons recherché des ajustements du type $Z = aX^b$ par la méthode des moindres carrés. De bonnes corrélations (coefficient de détermination $r^2 > 0.97$) sont obtenues pour les ajustements avec le contenu en eau liquide M, le rayon moyen $\bar{r}$, le rayon du volume moyen $\bar{r}_v$ ou le rayon du volume médian r_o. La réflectivité et la concentration ne sont pas associées par une loi de ce type.
La relation obtenue entre Z et M est :

$Z = 13 \times 10^{-2} M^{1,95}$ où M est exprimé en gm^{-3} et Z en $mm^6 m^{-3}$. L'approximation à la valeur 2 du coefficient b nous conduit à :

$Z = 12,3 \times 10^{-2}\ M^2$

Cette expression a été calculée sans tenir

compte des mesures au voisinage du sommet. Dans cette région de fort mélange avec l'environnement, la forme du spectre est modifiée par l'évaporation rapide des petites gouttes. La relation proposée sous-estime alors légèrement les valeurs de la réflectivité.

Avec les autres paramètres (exprimés en microns) on obtient :

$$Z = 5.7 \times 10^{-6} \overline{r}^{4.12}$$
$$Z = 1.3 \times 10^{-6} \overline{r_v}^{4.4}$$
$$Z = 12 \times 10^{-9} r_o^{5.5}$$

En utilisant la valeur 6 pour le coefficient b, cette dernière équation donne l'approximation :

$$Z = 3.1 \times 10^{-9} r_o^{6}$$

Nous avons utilisé la relation obtenue entre Z et M pour essayer de chiffrer le rapport d'entraînement entre le nuage et son environnement. La Figure 6 montre le rapport entre le contenu en eau liquide évalué dans la cellule C à partir des réflectivités radar et le contenu en eau liquide calculé pour une transformation pseudo-adiabatique saturée (Warner 1970). Sous 1500 mètres(région du stratocumulus) ce rapport est supérieur à l'unité. Les réflectivités observées à cet endroit permettent d'envisager la présence de gouttes de précipitation qui expliquerait les fortes valeurs de contenu en eau liquide. La relation entre Z et M qui a été établie dans la cellule C_n à l'état nuageux n'est probablement pas bien adaptée à cette couche. Le rapport d'entraînement peut s'écrire :

$$\mathcal{N} = \frac{1}{M} \frac{dM}{dz} = \frac{b}{R}$$

où R est le rayon moyen du nuage observé.
b = 0.4 permet d'obtenir une altitude correcte du sommet. L'utilisation des quantités d'eau liquide évaluées précédemment conduit à des valeurs de $\mathcal{N}$ et de b qui augmentent avec l'altitude et à une valeur représentative : b = 0.9.

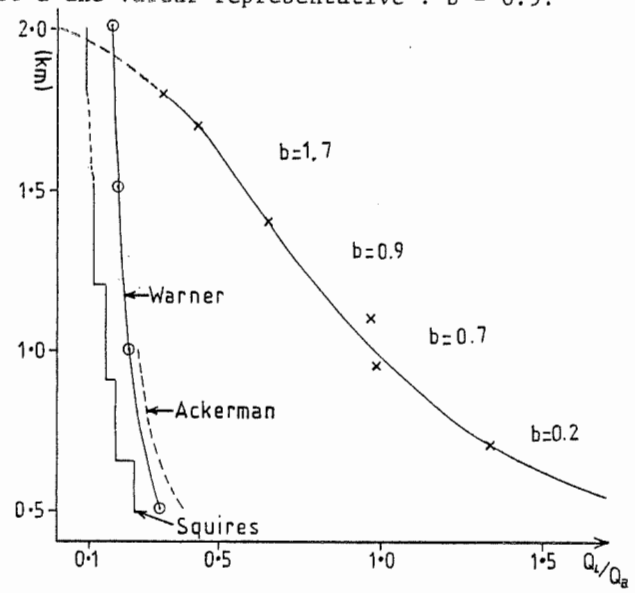

Figure 6 - Rapport du contenu en eau liquide moyen à la valeur adiabatique en fonction de la hauteur au-dessus de la base du nuage.

5 - CONCLUSION

Les nuages étudiés sont de petits nuages chauds pour lesquels aucune précipitation n'a été détectée au sol. La formation successive de cellules dans une direction privilégiée assure leur maintien et contribue à leur déplacement. Des informations sur la répartition verticale du spectre dimensionnel des gouttelettes ont été obtenues grâce à l'utilisation de sondes largables Aquasondes. Les spectres obtenus ont une forme unimodale. Une relation a été établie pour les représenter avec une bonne approximation. La mise en évidence de relations simples entre la réflectivité et des paramètres représentatifs de la structure microphysique du nuage permet l'utilisation quantitative des données radar. Le contenu en eau liquide moyenné par tranche d'altitude et le rapport d'entraînement ont pu ainsi être évalués.

6 - REMERCIEMENTS

Cette étude a été effectuée dans le cadre de l'Action Complémentaire Coordonnée (A.C.C.) Modification Scientifique du Temps de la Délégation Générale à la Recherche Scientifique et Technique (D.G.R.S.T.). Les données du radar 8 mm nous ont été communiquées par l'IOPG. Les radio-sondages ont été effectués par les Services du Centre Météorologique Régional de Bordeaux-Mérignac.

7 - BIBLIOGRAPHIE

ATLAS D.- 1954 - The estimation of clouds parameters by radar. - Journal of Meteorology, 11, 309-317.

BOROVIKOV A.M., GAIVORONSKII, ZAK, KOSTAREV, MAZIN, MINERVIN, KHRAGIAN, SIMETER - 1963 - Cloud physics p. 65 - Transl. by Israel Program f. Scientific Translation. Us Dept. Commerce, Washington, D.C.

CHALON J-P, J.C. FANKHAUSER, P.J. ECCLES - 1976. Structure of an evolving hailstorm, Part I : General characteristics and cellular structure Monthly Weather Review, 104, 564-575.

CHALON J-P, M. ANNE, J-L CHAMPEAUX, R. DELAITRE, G. DESPAUX, X. HENRION, A. MASSON, R.ROUMIGUIERES, H. SAUVAGEOT, G. SENNEQUIER - 1979 - Etude de la physique des précipitations dans les nuages chauds : campagne Aquasonde (Captieux 1978) Note technique de l'EERM N°22 nouvelle série. Direction de la Météorologie - Paris FRANCE.

KLAUS V et J-L CHAMPEAUX - 1977 - l'Aquasonde. La Météorologie VIème Série N°10 Septembre 1977.

KNOLLENBERG R.G. - 1970. The optical Array : an alternative to scattering or extinction for airborne particule size determination. J. Appl. Meteor, 9, 86-103.

MARWITZ J.D. - 1972 - The structure and motion of severe hailstorms Part II : Multicell storms J. Appl. Meteor., 11, 180-188

SQUIRES P. and C.A. GILLESPIE - 1952. A cloud-droplet sampler for use on aircraft. Quart. J. Roy. Meteor. Soc., 78, 387-393.

WARNER J. - 1970 - On steady state one-dimensionnal models of cumulus convection. J. Atmos. Sci., 27, 1035-10.

EVOLUTION OF THE DROPLET SPECTRUM IN COLORADO CUMULUS CONGESTUS

James E. Dye

National Center for Atmospheric Research*
Boulder, Colorado 80307 USA

1. Introduction

The evolution of the cloud droplet spectrum has been a topic of cloud physics research for many years. The early numerical investigations, such as those of Howell (1949) and Mordy (1959), as well as the more recent ones of Warner (1969b) and Fitzgerald (1974) using adiabatic parcel models, predict a narrowing of the droplet distribution with time due to the radial growth rate being inversely proportional to the drop radius. In contrast, many observations, for example Warner (1969a), frequently show the droplet spectrum to be bimodal. Most of the more recent numerical investigations have attempted to explain the cause of this bimodality and broadening of the distribution (Warner, 1973; Mason and Jonas, 1974; Lee and Pruppacher, 1977). Previous measurements have not differentiated between measurements made in mixed regions and those made in regions where the air had ascended adiabatically from cloud base. If the mixing process is indeed responsible for broadening of the spectrum, differences in the distribution should exist between these two regions.

The observations upon which most of the past work has been based have relied largely on measurements utilizing impaction devices and usually on spot samples. Within recent years new instruments--most notably the Particle Measuring Systems (PMS) scattering devices--have allowed continuous measurement of the droplet spectrum to be made. While the new devices are not devoid of error and must be carefully calibrated, many more measurements can be made and, if used judiciously, can further our understanding of the evolution of the droplet spectrum.

The PMS Forward Scattering Spectrometer Probe (FSSP) was used on the NCAR/NOAA sailplane during the 1976 and 1978 field seasons of the Convective Storms Division of NCAR. During these seasons the sailplane was used to spiral in the updrafts of growing cumulus towers and thus, provides a quasi-Lagrangian measurement of the droplet size distribution as it changes with altitude. Although the measurements are deliberately biased towards updrafts, regions of downdraft and interfaces between the updrafts and downdrafts are frequently encountered. Studies by Heymsfield, Johnson and Dye (1978), using the sailplane's temperature, updraft, and liquid water content measurements, have shown that adiabatic regions may exist in many of the clouds investigated by the sailplane. As discussed in the above work, the consistency shown in the independent measurements give a high degree of confidence that adiabatic regions exist. Of the measurements mentioned, the temperature proved to be the most reliable. The equivalent potential temperature (θ_e) derived from the temperature measurement can be used to differentiate between regions which are unmixed and those which are mixed. By using θ_e to identify unmixed and mixed regions and examining the droplet distribution measurements in these regions as the sailplane ascends in the cloud, it is possible to follow the evolution of the droplet spectrum in both the mixed and unmixed regions of the cloud. It is the purpose of this paper to present some results of a study of the cloud droplet evolution using the sailplane data.

2. Measurements

Before going into the results of the measurements it seems appropriate to briefly discuss the reliability of the FSSP measurements, in view of some of the uncertainties which have arisen about the instrument. A number of laboratory evaluations of the FSSP mounted on the sailplane have been performed. The probe has been calibrated for sizing accuracy using water drops of known size as well as by the use of glass beads. The results of this size calibration were reported by Cannon (1978) and sizing accuracy for the measurements reported herein is believed to be ±10%. The total sampling area of the probe was also determined using the experimental setup described by Cannon and agrees well with that determined by PMS. The fraction of droplets accepted by the velocity averaging circuit of the probe was found to average about 40% during the 1978 field season and this value was assumed for the 1976 data. Coincidence errors in the 1976 data arising from the electronic dead time of the instrument were generally less than 30% at the flight speed of the sailplane, and concentration measurements have been corrected for this error using the technique described by Cooper (1978). The concentrations are now felt to be accurate to ±20%. Work is currently underway to evaluate how badly the FSSP distorts the shape of the real droplet spectrum. It is expected that the results will be similar to those reported by Cooper (1978). Specifically that for narrow spectra with standard deviations less than 2 μm, there is some spreading of the spectrum, but that the instrument output does respond to and reflect real changes in the shape of the distribution.

The measurements presented in this paper are primarily those from the 1976 field season.

* The National Center for Atmospheric Research is sponsored by the National Science Foundation.

The sailplane generally penetrated the side of a growing cumulus congestus at about 1 km above base (cloud bases in NE Colorado are typically +5°C and at 4.5 km MSL) and then ascended in the updraft a kilometer or two before leaving the cloud. Cloud depths ranged from 3 to 8 km. Updraft strengths in many of the clouds were commonly 5 to 10 m s^{-1} with peaks of 15 to 20 m s^{-1}. For more details of cloud characteristics see Heymsfield, Johnson and Dye (1978). The FSSP measurements presented in this paper are those from regions free of ice particles as determined by the Cannon cloud particle camera.

3. Results

The results presented below are divided into categories of unmixed and mixed regions. The unmixed regions are those regions for which the equivalent potential temperature (θ_e) was within 1°K of the cloud base θ_e. (The cloud base value of θ_e in most cases was determined by direct measurement of the cloud base by one of the NCAR Queen Airs.) The mixed category contains measurements in regions where θ_e is at least 1°K less than the cloud base value.

Figures 1A and B show the mean cloud droplet diameter as a function of altitude above cloud base for the 1976 cases for both unmixed and mixed regions. Figure 1A also shows the mean diameter predicted from a diffusional growth model in which a parcel of air ascends adiabatically without additional activation of droplets above cloud base. The updraft strength is assumed to be constant at 2 m s^{-1}. A typical northeast Colorado CCN spectrum of $N = 900\ S^{0.54}$ reported by Rogers and Vali (1978) was used for activation of the initial cloud droplet distribution. The calculations were run for cloud base temperatures of 0, 3, and 7°C and cloud base updraft of 2 m s^{-1}. The resulting droplet concentrations were 874, 924, and 965 cm^{-3} progressing from the warmest to the coldest cloud base temperature.

From Fig. 1A we see that in general, in the unmixed regions, the evolution of the mean droplet diameter does follow that predicted from the adiabatic ascent model. Each of the different days has a different cloud base temperature and activated droplet concentration at cloud base, which results in the scatter seen in Fig. 1A. But by examining the points for individual days we see that they follow the shape of the predicted curves. As expected, the measurements in the mixed regions also approach the mean diameters expected from the adiabatic model, but there are also many smaller values caused by erosion of the distribution.

The cloud droplet concentrations for the 1976 data set are plotted as a function of altitude above cloud base in Figs. 2A and B. There is a lot of scatter in the observations and no systematic trend as a function of altitude. The mean values were 800 and 600 cm^{-3} in the unmixed and mixed regions respectively.

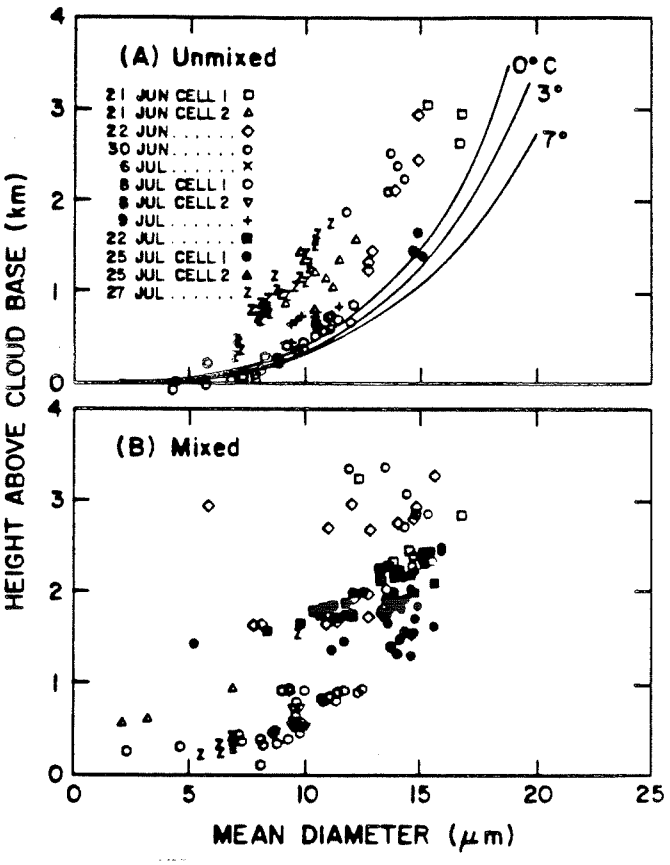

Fig. 1. FSSP measurements of the mean droplet diameter plotted as a function of altitude above cloud base in A) unmixed and B) mixed regions of Colorado cumulus congestus. Values predicted from a parcel model (see text) are shown for different cloud base temperatures.

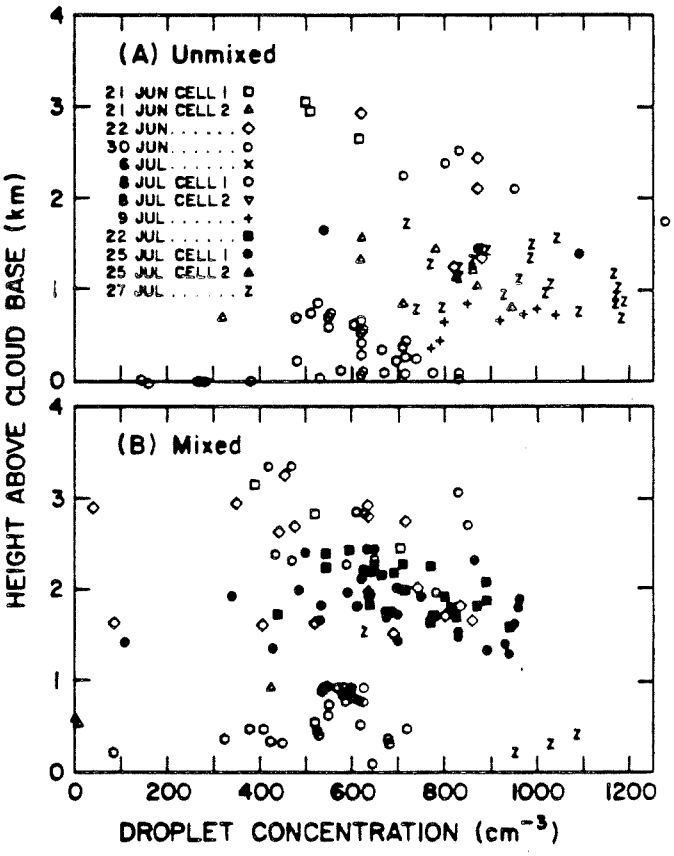

Fig. 2. FSSP measurements of cloud droplet concentration plotted as a function of altitude above cloud base in A) unmixed and B) mixed regions of Colorado cumulus congestus.

The measurements of the dispersion (the standard deviation of the droplet diameter divided by the mean diameter) for this same set of data are shown in Figs. 3A and B. The measurements in the unmixed regions show considerable scatter with a mean value of about 0.26. The measurements from 1 to 3 km above cloud base suggest a slight decrease of dispersion above cloud base, as do measurements from individual days. The measurements in the mixed regions show more scatter than the unmixed regions and both larger and smaller values of dispersion. The larger values are probably a result of the broadening of the spectrum due to the mixing process. A comparison of Fig. 3B with Fig. 2B shows that the few scattered values less than 0.1 probably occurred as a result of evaporation and erosion of most of the droplets in the regions in which those measurements were made.

4. Discussion

Comparison of the observations made by the sailplane in unmixed regions of cumulus congestus clouds of northeast Colorado with results predicted from numerical studies of cloud droplet evolution in an adiabatic parcel model show agreement between predicted and observed values of mean diameter. The measurements of droplet concentration from the entire season were too scattered to determine if the expected decrease in concentration due to expansion of the parcel agreed with observations; and measurements in any one cloud extended over too short an altitude range to attempt to verify this for individual clouds. The scatter in the droplet concentration data results from climatological variations in cloud base temperature, updrafts and CCN spectra.

The dispersion of the droplet spectrum observed in unmixed regions is larger than that predicted from models of adiabatic ascent. For example, Warner (1969b) calculates dispersion of 0.05 after only 200 meters above base in his adiabatic model. When he simulates the effects of turbulence by a random walk process the dispersion is somewhat larger for some cases but still remains between 0.05 and 0.1. Clark (1974) considers the effects of turbulence on the droplet spectrum in a more sophisticated manner, but after a few hundred meters above base the dispersion is still less than 0.1 even for the highest degree of turbulence which he considered.

As mentioned previously the FSSP does create artificial spreading of the spectrum. The degree to which this occurs is being examined but has not been established for the probe mounted on the sailplane. It seems unlikely that the spreading of the spectrum by the FSSP is sufficient to account for the difference between the predicted and observed dispersions.

Other measurements were made in northeast Colorado during 1976 and 1978 by the University of Wyoming using soot-coated impactor slides. For slides exposed in updrafts, the dispersions ranged from 0.12 to 0.32 with a mean of 0.18 (Vali, private communication).

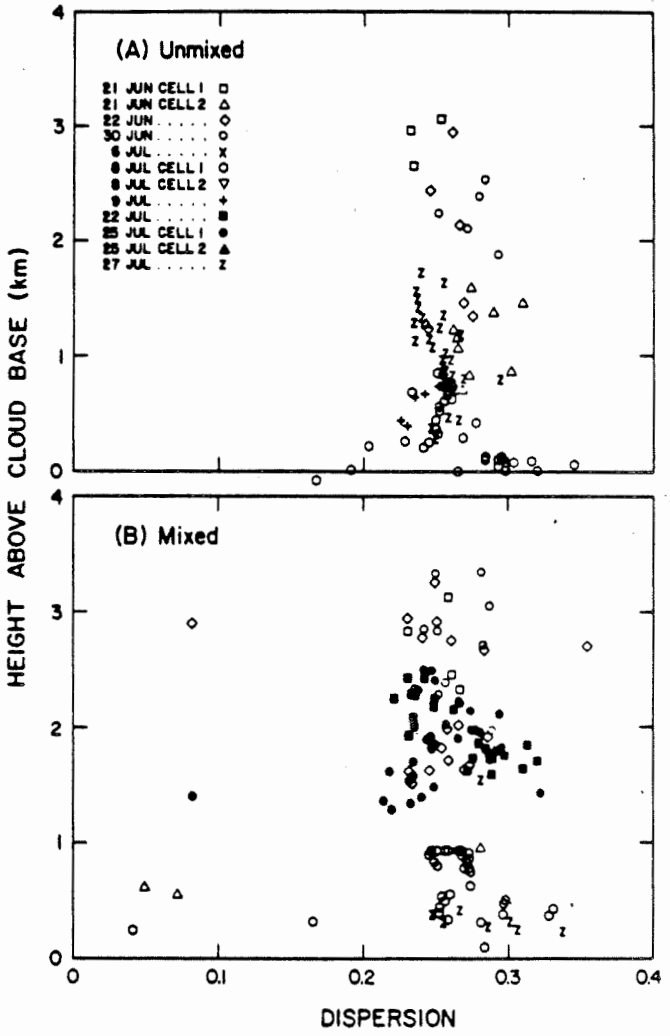

Fig. 3. FSSP measurements of the dispersion of the cloud droplet distribution plotted as a function of altitude above cloud base in A) unmixed and B) mixed regions of Colorado cumulus congestus.

These measurements are based on 17 samples which were taken within the first 1 km above cloud base. The values of dispersion given by these results are smaller than the values shown in Fig. 3A but are larger than those predicted in the adiabatic parcel models.

This information, combined with the measurements of the sailplane in the unmixed cores, suggest that even in the unmixed (i.e., adiabatic) regions of the cloud the droplet distribution is more disperse than that predicted from adiabatic parcel models. Additional research is needed to examine this point further.

5. Acknowledgements

The author gratefully acknowledges the help of Dr. W. Hall in running the adiabatic parcel model. He also would like to thank the many people involved in the collection and analysis of the sailplane data, particularly Dr. A. Heymsfield.

6. References

Cannon, T. W., and W. W. Grotewold, 1978: An improved droplet generator. *Preprints, Conference on Cloud Physics and Atmospheric Electricity,* Issaquah, Amer. Meteor. Soc., 57-59.

Clark, T. L., 1974: On modelling nucleation and condensation theory in Eulerian spatial domain. *J. Atmos. Sci., 31 (8),* 2099-2117.

Cooper, W. A., 1978: Cloud physics investigations by the University of Wyoming in HIPLEX 1977. Report No. AS119, Department of Atmospheric Science, University of Wyoming, Laramie, Wyoming, 320 pp.

Fitzgerald, J. W., 1974: Effect of aerosol composition on cloud droplet size distribution. *J. Atmos. Sci., 31 (6),* 1358-1367.

Heymsfield, A. J., P. N. Johnson and J. E. Dye, 1978: Observations of moist adiabatic ascent in northeast Colorado cumulus congestus clouds. *J. Atmos. Sci., 35 (9),* 1689-1703.

Howell, W. E., 1949: The growth of cloud drops in uniformly cooled air. *J. Meteor., 6,* 134-149.

Lee, I. Y., and H. R. Pruppacher, 1977: A comparative study on the growth of cloud drops by condensation using an air parcel model with and without entrainment. *Pure and Appl. Geophys., 115,* 523.

Mason, B. J., and P. R. Jonas, 1974: The evolution of droplet spectra and large droplets by condensation in cumulus clouds. *Quart. J. Roy. Meteor. Soc., 100,* 23-38.

Mordy, W. A., 1959: Computations of the growth by condensation of a population of cloud droplets. *Tellus, 11,* 16-44.

Rogers, D. C., and G. Vali, 1978: Summer climatology of aerosols and nuclei in the central High Plains of the U.S. *Preprints, Conference on Cloud Physics and Atmospheric Electricity,* Issaquah, Amer. Meteor. Soc., 25-30.

Warner, J., 1969a: The microstructure of cumulus cloud. Part I. General features of the droplet spectrum. *J. Atmos. Sci., 26 (5),* 1049-1059.

_____, 1969b: The microstructure of cumulus cloud. Part II. The effect on droplet size distribution of the cloud nucleus spectrum and updraft velocity. *J. Atmos. Sci., 26 (6),* 1272-1282.

_____, 1973: The microstructure of cumulus cloud: Part IV. The effect on the droplet spectrum of mixing between cloud and environment. *J. Atmos. Sci., 30,* 256-261.

A NUMERICAL METHOD FOR INTEGRATING THE KINETIC EQUATION OF COALESCENCE AND BREAKUP OF CLOUD DROPLETS

I. M. ENUKASHVILY

Dept. for Research and Development Israel Meteorological Service Bet-Dagan ISRAEL

1. Introduction

The approximation of the number density function n(x,t) of cloud droplets between droplets mass grid points $x=x_k$ is the main problem in the numerical integrating of the coalescence and breakup kinetic equation. In Berry's (Berry, 1967; Beheng, 1978) approximation of n(x,t) neither the number concentration nor the liquid water content of cloud droplets are conserved. In Bleck's (Bleck, 1970; Danielsen et al, 1972; Soong, 1974) method it is impossible to estimate the error of the approximate numerical solution and an assumption is made that in each separate droplets packet all droplets are spread over the whole mass interval (x_k, x_{k+1}). This Bleck's uniform distribution hypothesis gives as a result a significant increase of the conversion velocity from cloud droplets to rain drops for real coalescence kernel.

2. The governing equations and computation method

In this study an extension of Bleck's method and of the method of moments (Golovin,1963; Enukashvily, 1964 a,b) is developed. Each separate droplets mass interval $(x_k, x_{k+1})(x_{k+1}=2x_k)$ is considered as a cloud droplets packet with its own number concentration, liquid water content and other moments. The unknown number density function $n_k(x,t)$ in each droplets packet is represented by an expansion in orthogonal polynomials with given weighting function

$$n_k(z,t)=w_k(z,t)\sum_{i=0}^{\infty} a_{ik}(t)\, P_{ik}(z), \quad (1)$$

where:

$z=x/x_k$ represents the nondimensional mass of cloud droplets in the packet (x_k, x_{k+1});

$w_k(z,t)$ - weighting function;

$P_{ik}(z)$ - are polynomials, orthogonal in the range (1,2) with $w_k(z,t)$;

$a_{ik}(t)$ - are the expansion coefficients, which describe the deviation of $n_k(z,t)$ from $w_k(z,t)$.

These expansion coefficients are expressed as a linear combinations of the number density function moments. In this way droplets number concentration, liquid water content and other moments are conserved in each separate droplets packet and the problem of solving the kinetic equation is replaced by one of solving a following set of coupled differential equations for the number density function moments

$$\frac{dM_k^m(t)}{dt} = -\sum_{i=1}^{J} A_{i,k}^m + \sum_{i=1}^{k-1} A_{i,k-1,k}^m + \sum_{i=1}^{k-1} A_{i,k,k}^m - B_k^m + \sum_{i=k}^{J} B_{i,k}^m \quad , \quad (2)$$

where:

$$M_k^m(t) = x_k^m \int_1^2 z^m n_k(z,t)\,dz, \quad (3)$$

J - the total number of droplets packets;

$A^m_{i,k}$; $A^m_{i,k-1,k}$; $A^m_{i,k,k}$ - are the coalescence double integrals;

B^m_k; $B^m_{i,k}$ - are breakup integrals.

The conservation relations between coalescence double integrals are derived.

The computations of the coalescence and breakup double integrals require the values of number density function in each separate droplets packet. Therefore approximating $n_k(z,t)$ by means of first m terms of the expansion (1) and substituting this approximation in the coalescence and breakup double integrals, and also replacing the expansion coefficients $a_{ik}(t)$ by means of linear combinations of moments, we obtain from (2) a finite set of differential equations to compute the first m moments of the $n_k(z,t)$. Note that the convergence of (1) may be quite different for different weighting functions. The most appropriate choice for $w_k(z,t)$, i.e. the one which will yield the most rapid convergence, is a weighting function,which is as close to the $n_k(z,t)$as is possible. Of course if $w_k(z,t)$ is exactly $n_k(z,t)$, there is only one term in expansion (1). It is obviously that Bleck's method is obtained from (2) by including the first one term in (1), that is by assuming

$a_{0k}(t) \neq 0$ and $a_{1k}(t)=a_{2k}(t)=.....=0$

3.Numerical computations and concluding remarks

The method is tested against the existing analytic solutions of the coalescence equation. Numerical results are obtained when for the weighting function the Bleck's uniform distribution hypothesis for $n_k(z,t)$ and the Golovin's (1963) asymptotic solution of the coalescence equation is taken. A comparison between numerical results computed by using the zero approximation (Bleck's method), which includes the one first term in (1) and by using the first approximation, which includes the first two terms in the expansion(1) is made. The results of numerical computations indicate:

a) If the chosen $w_k(z,t)$ is close to $n_k(z, t)$, the difference between numerical results computed by Bleck's method and by using the first approximation of (1) is sufficiently small.
b) If the chosen $w_k(z,t)$ is not close to $n_k(z,t)$, the first approximation of(1) gives the numerical results, which are close to the analytic solutions for the Golovin's (1963)kernel even for 60 min.
c) For Long's (1974) kernel the difference between numerical results computed by using the first approximation of (1) with weighting functions $w_k(z, t)=1$ and $w_k(z,t)= z^{-3/2}$ is not large and therefore these numerical results may be considered as sufficiently correct approximative numerical solution of the coalescence equation for Long's kernel.
d) For practical computation of the coalescence and breakup processes in numerical modeling of clouds and precipitation the use of the first approximations of (1) requires considerable computer time. The weighting functions of the form z^{-c} (c=constant) were therefore tested also. It is shown that the zero approximation of (1) with $w_k(z,t)=z^{-3}$ gives reasonable results for Golovin's kernel (Bleck ,1970); For Long's (1974) kernel the reasonable results may be obtained by using zero approximation of (1) with $w_k(z,t)=z^{-4.8}$.
e) The quasilinear approximations of $n_k(z,t)$ which includes two first terms of (1), in comparison with Berrys six point interpolation, give reasonable results, which are close to the existing analytic solutions.

4.References

Beheng,K.D.1978: Numerical simulation of graupel. J. Atmos.Sci.35, No.4

Berry,E.X.1967: Cloud droplets growth by collection. J.Atmos.Sci. 24,688-701

Bleck,R. 1970: A fast approximative method for integrating the stochastic coalescence equation. J. Geophys. Res. 75, 5165-5171

Danielsen, E.F., R.Bleck and D.A.Morris, 1972: Hail growth by stochastic collection in a cumulus model. J. Atmos. Sci. 29, 135-155

Enukashvily, I.M. 1964a : On the solution of the kinetic equation of coagulation. Izv.Akad.Nauk SSSR, Ser. Geofiz. No. 10,944

Enukashvily, I.M. 1964b :On the problem of the kinetic theory of gravitational coagulation in spatially heterogeneous clouds. Izv. Akad. Nauk SSSR, Ser. Geofiz. No.11,1043

Golovin, A.M.1963: The solution of the coagulation equation for cloud droplets in arising air currents. Izv. Akad. Nauk SSSR, ser. Geofiz. No. 5, 783

Long, A.B. 1974 : Solutions for the droplet collection equation for polynomial kernels. J.Atmos. Sci. 31, No. 4, 1040

Soong, S.T. 1974: Numerical simulation of warm rain development in an axisymmetric cloud model. J. Atmos. Sci. 31 , No.5, 1262-1285

MICROPHYSICAL STRUCTURE OF DRIZZLE INITIATING CONVECTIVE CLOUD

M.FUJIWARA, and I.ICHIMURA,
Meteorological Research Institute,
Tokyo,
K.ISONO
Nagoya University,
Nagoya, Japan

1. Measurement

The droplet sampler has MgO coated cylinder with a spiral strip to obtain a continuous record through 2,142 or 1,071 m of path in cloud with airplane speed 63 m/s. The exposure time is 0.023 or 0.012 sec, and sweeping volume, 0.44x0.64x1,470 mm^3 per sec. The collection efficiency was assumed after Langmuir and Blodgett(1948) for cylinder. Calibration coefficient for MgO was assumed to be constant 0.80 after May(1950) and Mason(1971).

After 3 days of an out-break from China, low cumuli or strato-cumuli developed underneath a weakened inversion and covered the Miyako-jima island (N 25,E 125). No clouds were observed above them. The cloud base stayed at 1,070 m while the towering top changed from 1,980 to 2,700 m. Locally a few dark virgas appeared through which airplane encountered weak drizzle rain, but no evidence of it reaching the ground.

Cloud skeches are shown in Fig.1. After 1st penetration (10:23:00) the cloud tower has decayed very first. Cloud water contents (calculated from the drop data) and concentrations are shown in Fig.2.

In the afternoon, 1st penetration was made during the cloud top grew from 2,400 to 2,400 m. Second penetration was made 12 min later, just before the top decayed to 2,380 m, 3rd penetration, 11 min later, just before the top decayed to 2,320 m.

On 24th, most cloud became fair-weather cu. type. Penetrations were made about middle part of cloud.

2. Results (a) Cloud water content and drop concentration

As shown in Fig.2, the point values of water content and droplet concentration vary remarkably in space. Such violent variation extends to the center part of cloud tower, the variation with down to meter scale of intervals.

Extreme large amounts of cloud water reaching 10 gr/m^3 as point values were observed in the 1st penetration (mature stage), 10:23:10-14, while the average value was 2.94 gr/m^3. Such extreme values were observed also in the afternoon. Those are both in a cloud tower in growing or mature stage. In the afternoon, the average concentration for each penetration was 4.86, 1.49,or 0.93 gr/m^3, respectively, with the cloud evolution. The data from the fair-weather cu. show reasonable values to our knowledges.

(b) Size distributions of droplet

In Fig.3, part of sequence of mass spectra of droplet from the frame no. 1001 to 1500, which was selected from that of mature stage for that the microphysical variation with larger scale is predominant. Since each histogram was pasted so as to save pages, the zones of concentrated base lines mean less cloud water. Following along the frame no. systematic variation with some ten's meter scale (each frame is in 30 cm interval in cloud) is found. Cloud volume of high water content (L-volume) and that of low water content (N-volume) exist side by side.

Although not illustrated here, such specific volume has distinguishably low and high concentrations, respectively, contrary to the water content. In the particular stage of the cloud development, the microphysical property is rather homogeneous within the individual specific volume.

Although the sequence of histograms is disturbed due to the sampling size, the multimodal or monomodal feature of the spectrum can be followed:

(1) The maximum peak values of the water content achieved when the multimodal becomes monomodal at center part of L-volumes.
(2) The multimodal is common in the marginal region of L-volume.
(3) In transient region from N-volume to L-volume, small drops (10μm order) have disappeared.
(4) One transient region of larger scale (from 1170 to 1250) involved L- and N-volumes of smaller scale, say 2-5 m, alternatively.

It is inferred from above evidences that some diffusional and collisional processes in the boundary region between the specific different cloud volumes might played significant role for the drop growth, since the violent microphysical variation extends to the center part of cloud.

3. References

Langmuir,I.and Blodgett,K.B. 1946: A mathematical investigation of water droplet trajectories,U.S.Army Air Forces Tech. Rep. No.5418

May,K. R.1950:The measurement of airborne droplets by the magnesium oxcide method, J.Sci.Instru.,22,p 187

Mason,B.J. 1971:Physics of cloud, Oxf. Univ.Press,p 111

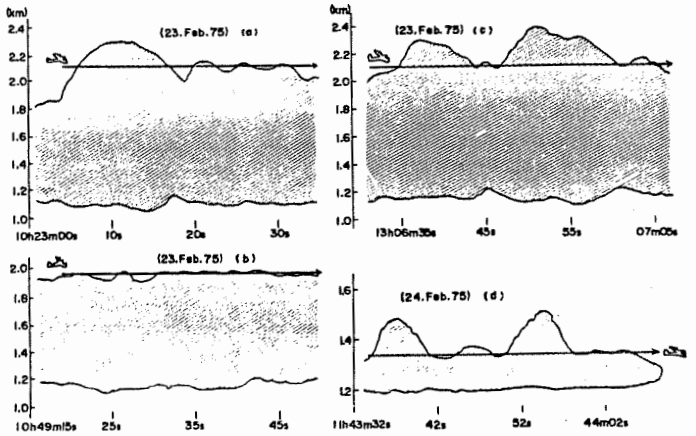

Fig. 1

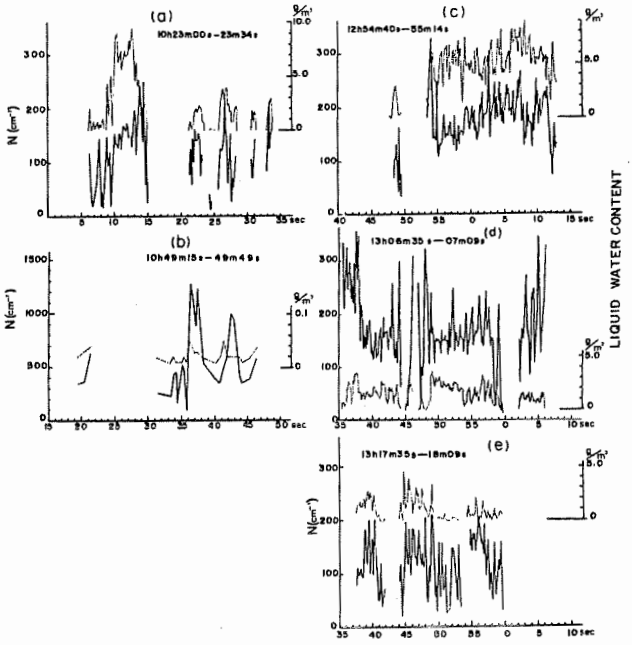

Fig. 2

Fig. 3

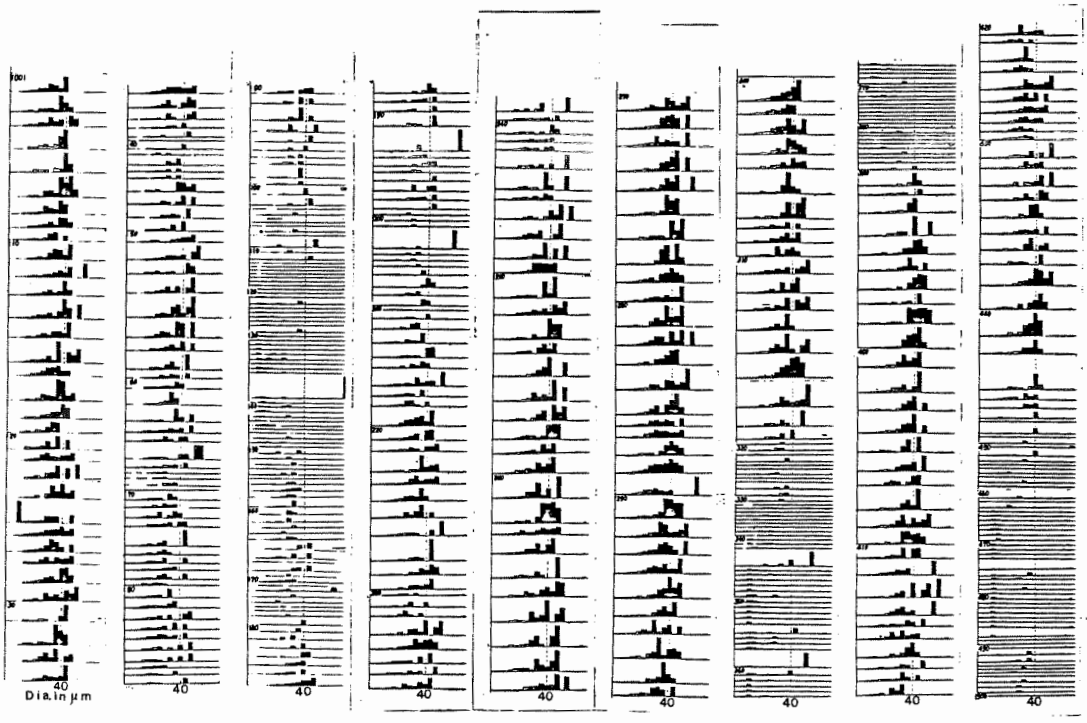

CUMULUS AND STRATOCUMULUS MICROSTRUCTURE FROM IN SITU MEASUREMENTS

J.F. GAYET and M. BAIN

L.A.M.P., University of Clermont-Fd, FRANCE

1. Introduction

The 1979 spring field program of the L.A.M.P. included a study of the microstructure of the icing clouds. It was carried out from the Valladolid airport in an area in the north-west of Spain (Fig. 1) during the SSP3 of the Precipitation Enhancement Project (P.E.P.) of W.M.O. from March 27th to April 4th. As part of that program, the University of Clermont II operated an instrumented DC 7 research aircraft. Approximately 390 cloud penetrations on 8 different days were performed. 90 % were realized at negative temperatures, 36 % were of cumuliform clouds and 64 % of stratiform clouds.

The first part of the paper describes the results of a microstructure statistical study for the two cold cloud types.

The second part shows a relation between the cloud microstructure and the icing rate which is applied to give the intensity of icing conditions in terms of meteorological parameters and can be applied to the growth of graupel.

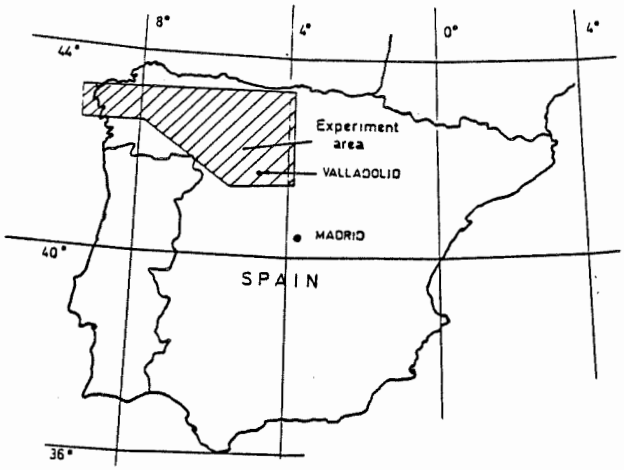

Figure 1

2. Cloud physics instrumentation

The available instrumentation was as follows :

. Three Particle Measuring System probes, FSSP ($3 < D < 45$ µm), 1 D-C ($20 < D < 300$ µm) and 1 D-P ($300 < D < 4500$ µm),

. a Total Water Content probe (TWC - General Eastern 1848),

. a Johnson-Williams cloud liquid water content meter (particle diameter $< \sim 50$ µm),

. usual thermodynamic devices,

. a 3 cm PPI radar.

The instrumentation was complemented with a doppler radar and inertial platform for the dynamical and navigation parameters. The mounting location of the different probes can be seen on fig. 2.

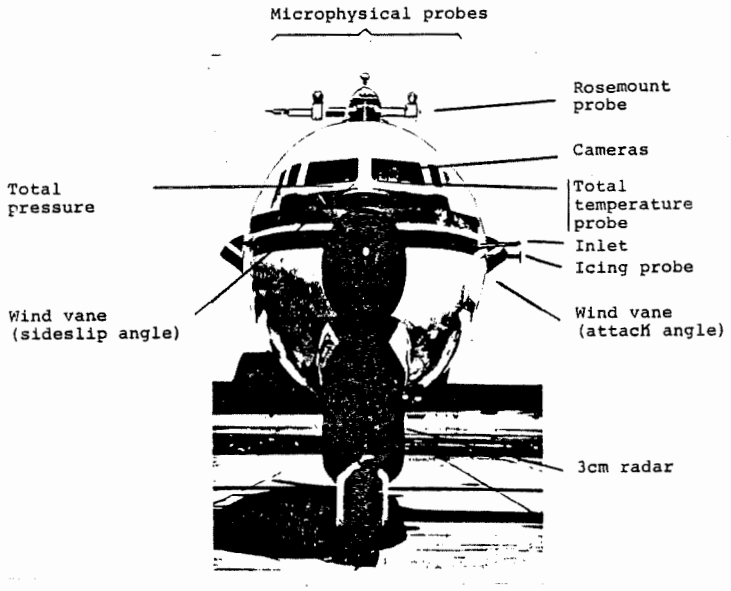

Figure 2

Spatial resolution of tape recorded data was $\sim$ 100 m for all the parameters. A detailed description of the DC 7 instrumentation has been given in a previous paper (Gayet et al. 1979, a-b).

The PMS 1D probe's data presented here have not been corrected in spite of the problems affecting the PMS devices. Isaac et al. (1977) suggest that the 1 D-C size and count particles with an unknown accuracy for the 3 first classes, whereas the first 1 D-P channel can be corrected by a factor which is a function of particle size distribution. In the same way, Brenguier et al. (1980) show that the FSSP undercounts the particles. The undercounting depends on the concentration but also on the droplet size distribution. The PMS 1-D data do not permit the determination of the ice/liquid phase of cloud particles.

3. Global comparison of the microstructure of cumulus and stratocumulus clouds

3.1 Data processing

The results presented below concern microphysical parameters averaged over the cloud penetration. We call penetration, a cloud length greater than $\sim$ 1000 m (10 discrete measurements) which is defined by an average LWC

LWC > 10^{-2} g/m^3. With these criteria the median penetration length was 4800 m, and 84 % of the penetration lengths were between 1000 and 8000 m. Fig. 3 shows an histogram of the temperature at the penetration level. The mean value is found to be at - 9°C and 14 % of the penetrations were carried out at temperatures below - 16°C.

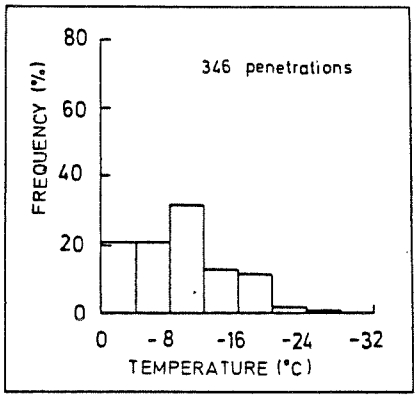

Figure 3

The mean level of cloud penetrations was 2800 MSL. (Most of the clouds, which have been investigated above 60 % over the Duero basin rising ∿ 800 M.s.l). Two microstructure cloud types are described : the cumuliform clouds including cumulus congestus and cumulonimbus which were characterized by a thickness up to 3500 m during the experiment, Nimbostratus, stratus, stratocumulus and altocumulus, all in the stratiform category in which the maximum thickness of the noticed cloud was ∿ 1500 m. The clouds containing large particles (or hydrometeors - diameter > 300 µm) have been differentiated, the lower average concentration limit given by the 1D-P specifications being ∿ 2 x 10^{-2} l^{-1}. The temperature range of cloud traverses and the preliminary results from Vali (1979) seem to indicate that these hydrometeors are more often ice particles.

3.2 Results

We simultaneously present the results concerning cumuliform and stratiform clouds. Figs. 4 to 7 respectively display the histograms of the cloud water content (LWC - g/m^3) from J.W probe, the median volume diameter (*) (Do - µm) and the cloud droplet concentration (Cc - cm^{-3}) from FSSP and the hydrometeor concentration (CH - l^{-1}) from 1D-P probe. Suscript (a) denotes cumuliform clouds, whereas (b) denotes stratiform clouds.

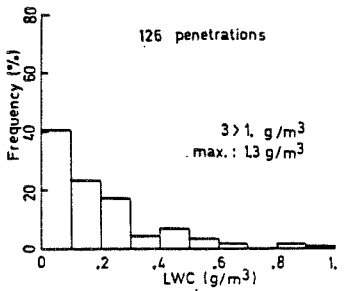

Fig. 4(a)

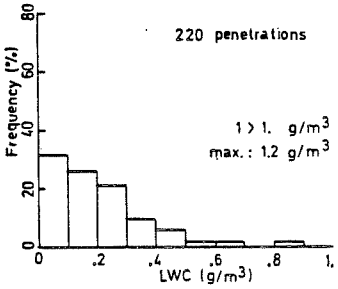

Fig. 4(b)

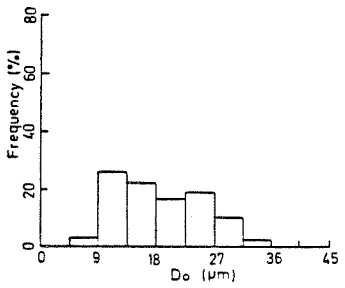

Fig. 5(a)

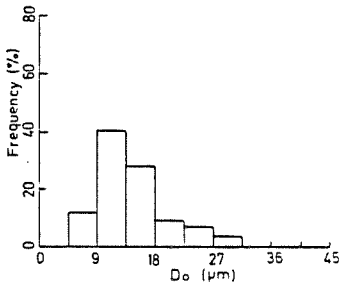

Fig. 5(b)

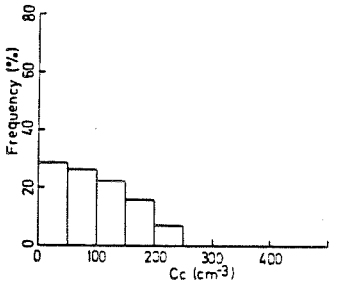

Fig. 6(a)

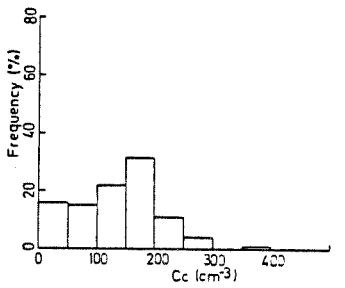

Fig. 6(b)

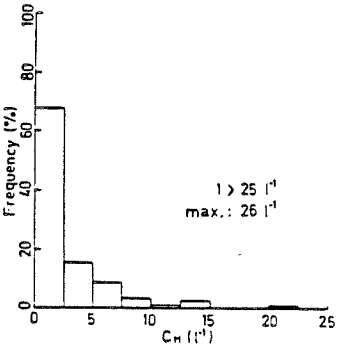

Fig. 7(a)

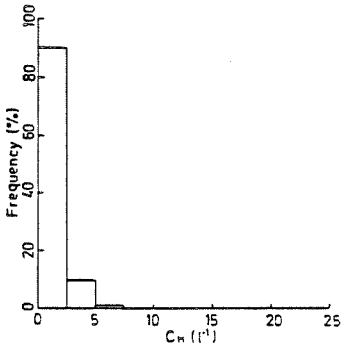

Fig. 7(b)

Table 1 summarizes the mean values (M.V.), the standard deviations (S.D.) of the above mentioned parameters plus the concentration of particles > 70 µm (l^{-1}) and the condensed water content (LWCR - g/m^3) from the TWC probe by substracting the vapor water content computed from the filtered dew point temperature.

Figs. 4 to 7 and table 1 show noticeable differences between the two cloud types. For a same LWC value of cloud liquid water content (∿ 0.23 g/m^3), the median volume diameter is greater (18.5 µm) for cumuliform clouds than for the other cloud type (14.6 µm). These diameter differences are balanced by the droplet concentrations : 94 cm^{-3} against 136 cm^{-3} respectively. Because of the proximity of the experiment area (fig. 1) from the sea and the above mentioned characteristics, the clouds examined can be considered as being maritime.

On the other hand, table 1 shows great differences between the two cloud types for the hydrometeor concentrations and the concentrations of particles > 70 µm. The cumuliform

---

(*) The median volume diameter (Do) is defined by the diameter for which the mass of particles < Do is equal to the mass of particles > Do.

Probes	J - W		F S S P				1 D-P		1 D-C 1 D-P		TWC	
	LWC (g/m^3)		Do(μm)		Cc (cm^{-3})		C_H (l^{-1})		C_{70} (l^{-1})		LWCR g/m^3	
	M.V.	S.D.	M.V.	S.D.	M.V.	S.D.	M.V.	S.D.	M.V.	S.D.	M.V.	S.D.
Cum. clouds	0.23	0.23	18.5	6.7	94	66	2.8	4.0	27.8	53.0	0.6	0.5
Strat. clouds	0.22	0.18	14.6	5.2	136	72	0.8	1.2	6.1	11.6	0.5	0.4

Table 1

clouds have a $C_H \sim 3.5$ times as great (2.8 against 0.8 l^{-1}) and a $C_{70} \sim 4.5$ times as great (27.8 against 6.1 l^{-1}) as that of stratiform clouds. Fig. 8 indicates the percentage of cumuliform and stratiform clouds containing hydrometeors as a function of hydrometeors concentration. 92 % of cumuliform clouds contain more than 0.02 l^{-1} hydrometeor concentration against 67 % for stratiform clouds. No stratiform clouds have a mean value > 6 l^{-1}, and only 5 % of cumulus clouds have a concentration > 10 l^{-1}.

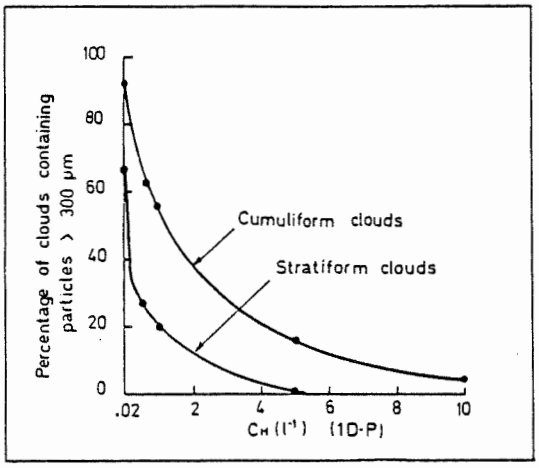

Figure 8

Our cumulus cloud results can be compared with those of Isaac and Schemenauer's ones (1979). These authors had performed many cumulus penetrations over Alaska, using a similar instrumentation and in the same temperature range. They classified the sampled clouds as continental and found median penetration averages of LWC, of concentrations of particles > 70 μm and 350 μm to be 0.3 g/m^3, 0.9 l^{-1} and 0.015 l^{-1} respectively. Although they performed penetrations only within 300 m of the cloud top, comparisons can be made and indicate greater hydrometeor concentrations over Spain.

4. Cloud microstructure and icing conditions

4.1 Icing intensity as a function of liquid water content and median volume diameter

The intensity can be related to the rate of accretion of ice on a cylinder (Lewis, 1947). If no "run-back" occurs on the cylinder and provided there is no sticking of ice crystals, the rate of accretion is given by the following relation : Rw = V∞.LWC.Ew (1), where V∞ is the free-stream velocity (m/s), LWC is the liquid water content (g/m^3) and Ew the water catch efficiency (Rw : g/m^2/s). Ew depends upon several parameters : those characteristic of the air (density and viscosity), those related to the ice collector (diameter and stream velocity) and those related to the cloud (density of water and droplet diameter).

During the experiments described above, an icing probe was filmed every 12 s with a 16 mm camera. The rate of ice accretion (Ra - mm^2/s) of the cross section of ice on the cylinder (Ø = 25.4 mm) has been obtained from the slides. The preliminary measurements of Ra versus the cloud liquid water content (JW probe) for a stratocumulus cloud (flight 10 - March 31) with a small hydrometeor concentration (< 1 l^{-1}) are depicted in Fig. 9.

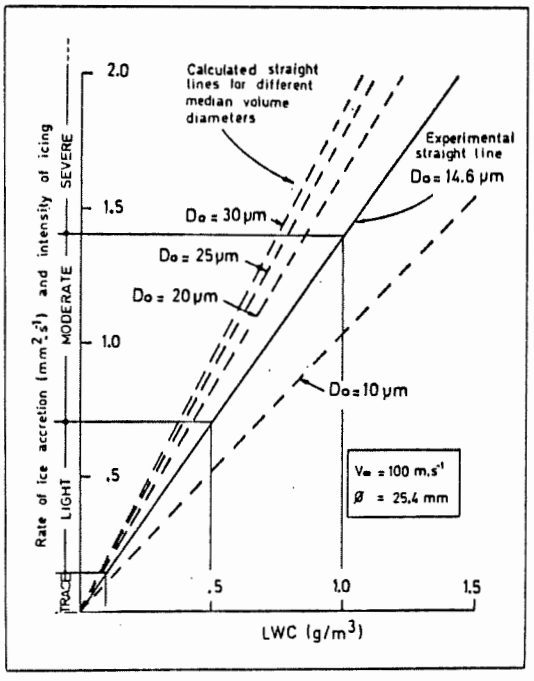

Figure 9

Ra being related to Rw (from ice density and accretional surface area) the ice accretion rate has been computed, using the relation (1) and the Cansdale and Mc Naughtan's formulation (1977) to obtain the data for a nominal speed and an average median volume diameter in stratiform clouds (100 m/s and 14.6 μm). The straight line corresponds to the best fit of data sets. (correlation : ∿ 0.9). The dashed lines on fig. 9 correspond to calculated relations for

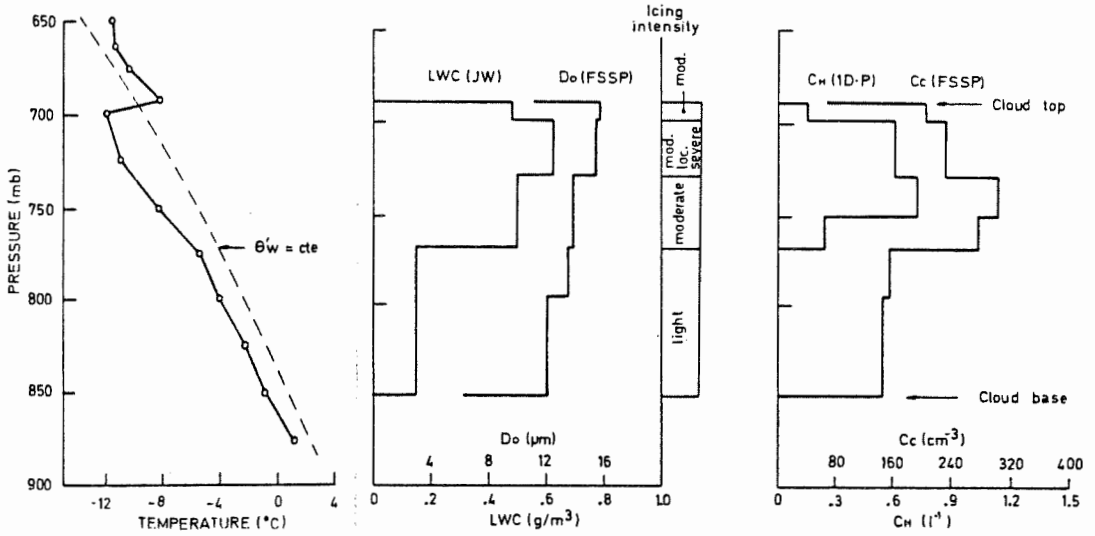

Figure 10

different median volume diameters. The icing intensity recommended by Lewis (1947) and translated in terms of ice accretion rate (Ra) have been also reproduced in Fig. 9. Table 2 gives the icing intensities, the corresponding values of Ra and the ranges of LWC for a median volume diameter of 14.6 μm.

Intensities of icing	Rate of ice accretion (mm^2/s)	Liquid water content (g/m^3)
Trace	0.0 - 0.14	0.0 - 0.1
Light	0.14 - 0.70	0.1 - 0.5
Moderate	0.70 - 1.40	0.5 - 1.0
Severe	1.40 or more	1.0 or more

Table 2

4.2 Icing intensity as a function of altitude in a stratocumulus

This variation has been studied for the flight 10 (from 11h22 to 11h50) at different levels. The cloud thickness was ∿ 1500 m. Fig. 10 shows vertical profiles of mean values of the liquid water content, median volume diameter, hydrometeors concentration, cloud particles concentration and temperature. This figure reveals that the maximum concentrations (0.7 l^{-1} and 300 cm^{-3}) are at ∿ 740 mb. The maximum of liquid water content (0.6 g/m^3) is located beneath the cloud top and the median volume diameter increases (from 12 μm to 15.6 μm) from the base to the cloud top. Using Fig. 9 and the cloud microstructure characteristics, the icing intensity profile has been calculated and is shown in Fig. 10. The more intense icing zone (moderate, locally severe) is found in a cloud thickness of ∿ 350 m below the cloud top and at a temperature of - 11°C. This zone must correspond to that of maximum graupel growth rate.

5. Conclusions

The paper describes general microstructure of cumuliform and stratiform clouds over Spain from 350 cloud penetrations on 8 different days in spring 1979. Noticeable differences occur between the two types of clouds, not on mean values of the cloud liquid water content, but on droplet spectra characteristics and on the occurrence of hydrometeors concentrations.

The icing intensity is related to the liquid water content and the median volume diameter. It was found larger near the top of stratocumulus.

6. Acknowledgements

We are indebted to Prof. R.G. Soulage for his advice and scientific assistance. Thanks are due to the LAMP technical staff, DC7-CEV crews and our colleagues of the Universities of Madrid and Valladolid.

This research was supported by the Direction des Recherches Etudes et Techniques and the Direction Générale de la Recherche Scientifique et Technique.

7. References

Brenguier, J.L. et al., 1980 : "Accuracy and limitation of some cloud physics instruments", Preprints, VIII Conference on Cloud Physics, Clermont-Fd.

Cansdale, J.T. and Mc Naughtan, 1977 : "Calculation of surface temperature and ice accretion rate in a mixed water droplet ice crystal cloud", R.A.E., TR 77090.

Gayet, J.F. and Friedlander, M., 1979 : "The DC 7 research aircraft of the 'Centre d'Essais en vol de Brétigny', W.M.O., PEP report no. 13

Gayet, J.F., 1979 : "Cloud microphysical parameters obtained with the DC 7 aircraft, W.M.O. PEP report no. 13.

Isaac, G.A. et al., 1977 : "Preliminary tests of a cumulus cloud seeding technique, J. Appl. Meteor., 16, pp. 949-958.

Isaac, G.A. and Schemenauer, R.S., 1979 : "Large particles in supercooled regions of Northern Canadian cumulus clouds, J. Appl. Meteor., 18, pp. 1056-1065.

Lewis, W., 1947 : "A flight investigation of the meteorological conditions conductive to the formation of ice on airplanes", NACA TN 1393.

Vali, G., 1979 : "Report of the Ninth Session of the EC panel on weather modification / CAS Working Group on Cloud Physics and Weather Modification, W.M.O.

SHAPE OF RAINDROP SIZE DISTRIBUTIONS SIMULTANEOUSLY OBSERVED AT THREE ALTITUDES

E.G. Gori (†) and J. Joss (T)

(†)- Istituto di Fisica dell'Atmosfera, Consiglio Nazionale delle Ricerche. 00144 Roma - ITALY
(T)- Osservatorio Ticinese, Centrale Meteorologica Svizzera. 6605 Locarno Monti - SWITZERLAND

1. INTRODUCTION

The evolution of precipitation particles has been investigated by means of very different methods during the past 30 years. Hardy (1963) used numerical procedures to combine drop size distributions (DSD's) of rain observed at the ground with the computed changes as the raindrops fall,thus deducing the DSD at the melting level. Ohtake (1969) compared a few distributions of melted aggregate snowflakes and of raindrops sampled simultaneously at two altitudes along a mountain slope by means of filter paper. From these observations he deduced changes occurring in the melting layer. Battan (1977) investigated DSD in rain by means of a zenith pointing Doppler radar,making observation of the reflectivities and Doppler spectra of showers which exhibited a bright-band.

Two major difficulties arise when trying to measure the evolution and growth of precipitation particles in nature. The main difficulty lies in the large natural variability of precipitation and,related to that,the amount of work involved to receive a statistically meaningful sample before the meteorological situation has changed. The second difficulty is encountered when comparing distributions measured at different stations. For that we need a measure to describe the shape. Then we are able to use statistical methods for treating the data and filtering out unwanted noise,e.g. due to the cellular structure of precipitation.

The disdrometers used in this experiment allow to get statistically meaningful samples at 1 min intervals,continuously and unattended at three different altitudes. The parameters, briefly covered in Sec.3,solve the second problem by allowing to measure and compare the shape.

2. OBSERVATIONS

The rough data were collected by means of automatic meteorological field stations,equipped with the electromechanical disdrometer RD-69 and placed along the slope of the Mount Cardada (Fig.1) at altitudes of 225, 370, 1015 metres above sea level (respectively called L, M and H stations). The continuous widespread precipitation,recorded at the three stations, lasted from 1226 to 2349,Sept.28,1974: 684 min of continuous rain.

A zenith-pointing radar,at the M station, exhibits long periods of uniform echo patterns and a marked bright-band above 1600 metres. The relative humidity,80% at the beginning of the rainfall,exceeded 95% in every station after three hours. The wind,observed at M station,was

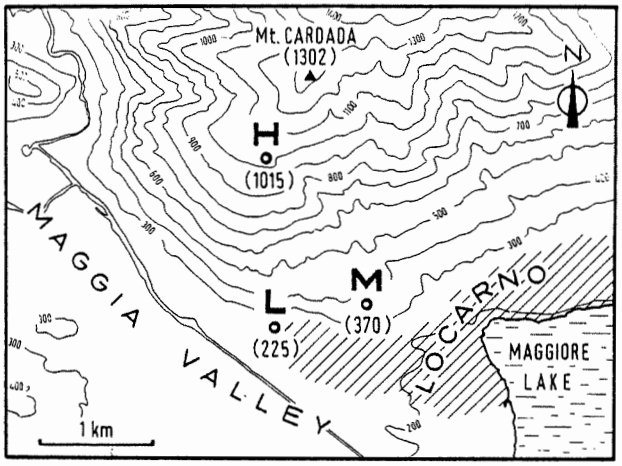

FIGURE 1. Locations of three observation sites on Mount Cardada: L, M and H stations;near Locarno, South of Switzerland.

weak and rarely reached 3 m sec^{-1}. The disdrometers of the H, M and L stations recorded the raindrops on a sampling area of 50 cm^2 in 20 classes of drop-sizes,between 0.3 and 5 mm diameter. The sampling process was continuous and during the storm for each station a total of 684 samples were obtained,each one accumulated during one minute.

3. DSD's PARAMETERS

Following Joss and Gori (1976 and 1978), three sets of parameters were used to describe the DSD in rain,where N(D) is the drop concentration per unit volume and unit diameter and D is the diameter.

3.1 Integral Parameters

σ ($mm^2 m^{-3}$) :optical extinction coefficient

W ($mm^3 m^{-3}$) :liquid water content

R ($mm\ hr^{-1}$) :rain intensity

$R\hat{}$ ($mm^4 m^{-3}$)$=\Sigma N(D)D^4$:related to rain intensity

Z ($mm^6 m^{-3}$) :radar reflectivity factor

3.2 Maximum Contribution Diameters

$D(\sigma)$, D(W), $D(R\hat{})$, D(Z) (mm) :maximum contribution diameters respectively to four σ, W, $R\hat{}$ and Z parameters. For example the maximum contribution diameter D(Z) is the drop size of an exponential DSD with largest contribution to Z as defined by eq.(1):

(1) $D(Z)(mm)= \int_0^\infty N(D)D^6 dD \ / \ \int_0^\infty N(D)D^5 dD.$

3.3 Shape Factors

$S(W\sigma)$, $S(R\hat{}W)$, $S(ZR\hat{})$, $S(Z\sigma)$ (--):shape factors which describe the shape (curvature) of the DSD over the region of the drops which most contribute to the integral parameters specified in

parenthesis. The shape factor $S(Z\sigma)$, as example, is defined by the following equation:

$$(2)\quad S(Z\sigma)=\frac{\left\{\frac{D(Z)-D(\sigma)}{D(Z)+D(\sigma)}\right\}_{\text{observed}}}{\left\{\frac{D(Z)-D(\sigma)}{D(Z)+D(\sigma)}\right\}_{\text{exponential,20 classes}}}$$

$S(Z\sigma)\sim 0$ means quasi monodispersed shape
$S(Z\sigma)< 1$ " toward monodispersed shape
$S(Z\sigma)= 1$ " exponential shape
$S(Z\sigma)> 1$ " more of the very small and/or very large drops than in an exponential DSD.

4. SHAPE OF DSD's OBSERVED AT H, M AND L STATIONS

Using the data reduction process described by Joss and Gori,(1978),examples of the shapes of different sampling periods are shown in Fig.2. If during the whole storm all the drops in each drop class of this rain are added,we

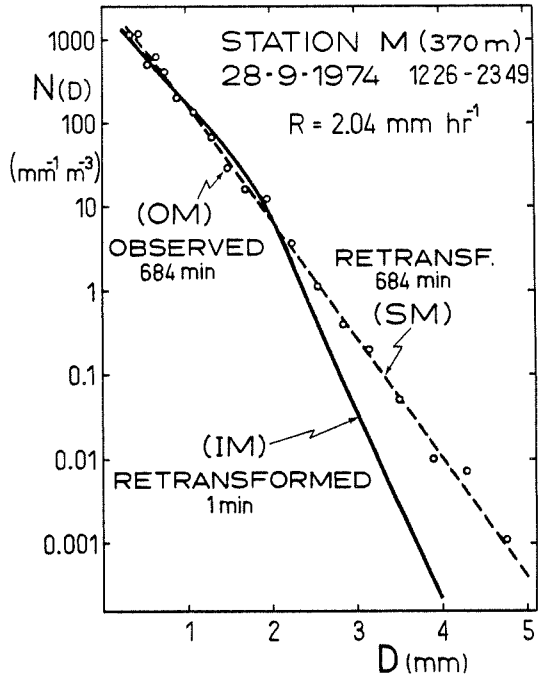

FIGURE 2. Average "instant" distribution (IM) of 684 1-min distributions together with the single sum-distribution (OM) during the same 684 mins, and the quasi-exponential retransformed distribution (SM) of best fit.

find the dots (OM) in Fig.2; the parameters of this distribution are given in Tab.1. These results are in excellent agreement with the quasi-exponential retransformed distribution (SM) of best fit,calculated by means of the following equation,(see also Joss and Gori,1978):

$$(3)\quad N(D)= N_o \exp(-\Lambda D) \;/\; (1-C(X_o-\Lambda D)^2)$$

The following procedure was used in order to derive the average "instant" distribution (IM) in Fig.2:

- parameters of 684 individual 1-min samples were calculated;
- the average of each parameter was calculated; shown as OBS(1') in Tab.1;
- the retransformation of the average parameters to a distribution N(D) of best fit (see (IM) in Fig.2) was calculated by choosing X_o and C in equation (3) such that the parameters

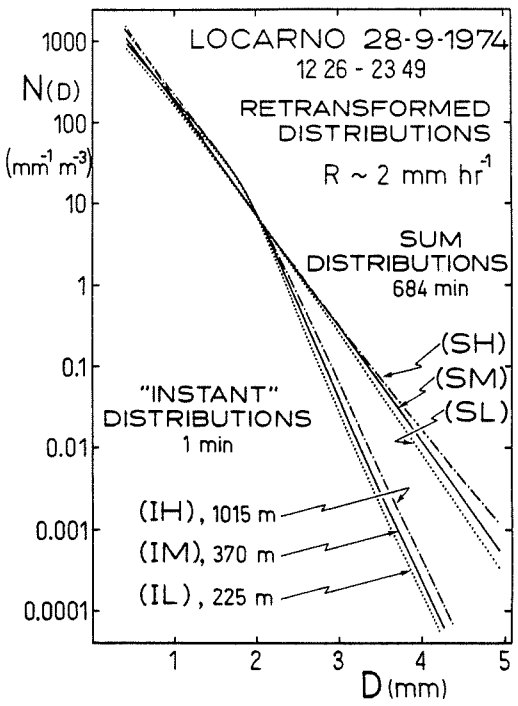

FIGURE 3. Average "instant" distributions (IH), (IM), (IL) of 684 1-min distributions together with the quasi-exponential sum-distributions (SH), (SM), (SL) of drops accumulated during the 684 min at H, M, L stations.

defined in Sec.3 of the retransformed distribution agreed best with the parameters of the observed distributions (for details see Joss and Gori,1978).

The same process,applied to observed distributions at H and L stations leads to the "instant" distributions (IH) and (IL) and those accumulated during the entire precipitation (SH) and (SL),shown in Fig.3. The parameters are given in Tab.1.

The distributions plotted in Fig.3 show that:

A) "Instant" distributions are very different from sum-distributions in spite of the fact that both cover exactly the same data.

B) Distributions recorded at different altitudes are systematically different,the lower station showing a stronger tendency towards monodispersity.

C) The influence of the length of the sampling interval (A) is stronger than that of the altitude (B).

The changes in altitude may be explained by drop collision during falling,by windsorting

	H		M		L	
	Upper	Lower	Upper	Lower	Upper	Lower
$S(W\sigma)$	1.016	1.000	.914	.899	.868	.855
$S(R\hat{}W)$	.908	.889	.814	.798	.772	.756
$S(ZR\hat{})$	.732	.709	.670	.655	.640	.626
$S(Z\sigma)$	.864	.850	.790	.777	.753	.740

TABLE 2. Confidence limits of the average shape factors of the "instant" distributions recorded on 28 Sept. at H, M and L stations. Upper and Lower values represent: Average $\pm \pm Sx/\sqrt{n}$, where n=684; the average shape factors are shown in Tab.1 as OBS(1').

STATION and ALTITUDE	CURVE Figs. 2 + 3	PARAMETERS σ	W	R	Z	S(Wσ)	S(R^W)	S(ZR^)	S(Zσ)	RETRANSFORMED PARAMETERS Λ	N_o	C	X_o	TYPE
H 1015 m	--	213	137	2.22	975	1.07	1.08	1.03	1.05					OBS(684')
	SH	217	139	2.22	970	1.01	1.05	1.08	1.05	3.12	3640	-.007	8	RETR(684')
	--	218	141	2.22	718	1.01	.90	.72	.86					OBS(1')
	IH	219	142	2.22	713	.97	.87	.76	.86	4.05	23600	.061	8	RETR(1')
M 370 m	OM	182	123	2.04	908	.99	.99	.95	.98					OBS(684')
	SM	181	123	2.04	909	.99	.98	.97	.98	3.14	3950	.004	5	RETR(684')
	--	185	126	2.04	675	.91	.81	.66	.78					OBS(1')
	IM	183	126	2.04	674	.94	.80	.66	.79	4.05	25200	.125	7.5	RETR(1')
L 225 m	--	159	110	1.82	791	.94	.93	.92	.93					OBS(684')
	SL	157	109	1.82	794	.96	.93	.91	.94	3.00	3040	.019	3.5	RETR(684')
	--	162	111	1.82	597	.86	.76	.63	.75					OBS(1')
	IL	159	111	1.82	600	.93	.76	.62	.76	4.05	23500	.159	7.3	RETR(1')

TABLE 1. Parameters pertinent to DSD's shown in Fig.2 and Fig.3; RETR and OBS stand for Retansformed and Observed.

and orographic influences. Due to the high relative humidity of 95% evaporation brings little influence in this case, but may be significant otherwise.

The limits of confidence of the average shape factor for the "instant" DSD's plotted in Fig.3 are shown in Tab.2. This shows, for all the shape factors, that these are significant differences between the stations. The test indicates for all stations a significance level of better than 0.5%.

5. CHANGES OF SHAPE DURING PRECIPITATION

In order to investigate the changes during the entire precipitation, we subdivided the sequences of 684 shape parameters of "instant" DSD's into 12 contiguous sequences of 57 values. Then the 12 averages of "instant" shape parameters S(Zσ) for the H, M and L stations were calculated and shown in Fig.4. The correlation

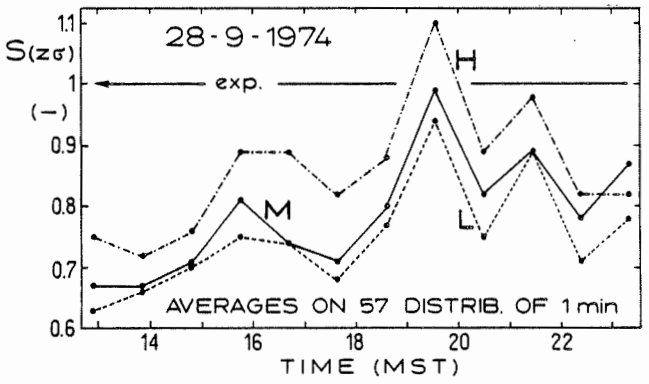

FIGURE 4. Variations of the shape factor S(Zσ), for the average of 57 "instant" shape factors, during the entire precipitation, at H, M and L stations.

		L ↔ M	M ↔ H	L ↔ H
1	C (57 "instant")	0.96	0.89	0.93
2	C ("instant")	0.70	0.62	0.59
3	Δt ("instant"),(min)	1.6	3.0	3.2

TABLE 3. Correlation coefficient C for the three pairs of stations and the equivalent time difference Δt in the autocorrelation function of S(Zσ).

coefficient between the 12 average shapes measured at different altitudes are shown in Tab.3 together with the correlation coefficient for the 684 "instant" shapes. The latter ones are smaller due to small scale variations of the precipitation. The last line in Tab.3 indicates the time Δt needed in the autocorrelation function to decay to the value of the corresponding instant crosscorrelation coefficient in the line 2 of Tab.3.

6. INFLUENCE OF THE SAMPLING PERIOD ON THE SHAPE

In order to examine how the DSD shapes observed at H, M and L stations depend on the sampling period during which the distributions were accumulated, we analyzed the three sequences of 684 1-min samples with the procedure described by Joss and Gori, (1978). The results are partially shown in Fig.5 for the shape factor S(Zσ), reflecting the average shape of the distributions. We find that the difference Δ in shape between different altitudes is roughly independent of the sampling duration. In other words, the way in which the shape approximates the exponential one as the sampling duration is increased is, at first approximation, independent of the sampling altitude.

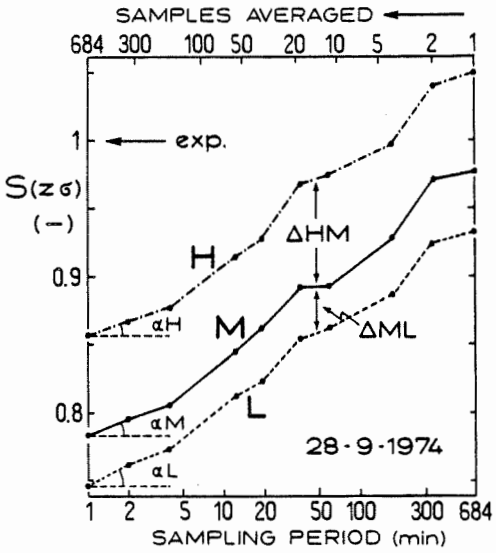

FIGURE 5. Variation of the shape factors as a function of the sampling period for 684 mins of continuous widespread rain (Sept.28, 1974) observed at H, M and L stations.

As pointed out by Joss and Gori,(1978),the angle α in Fig.5 is a measure of the autocorrelation coefficient CA. The smaller α,the higher is CA between samples ($\alpha=0° \rightarrow CA=1$; $\alpha=90° \rightarrow CA=0$).

At the lowest station L,α is highest (100%),at M (94%) and at H lowest (83% of αL). This means that samples at station H are better correlated in time than lower down. The changes are proportional rather to the differences in altitude and not to the horizontal distances between the stations,which are roughly equal ($D_{H-M} \sim D_{L-M}$). This suggests that the changes are due to the different altitude rather than to the horizontal distance. The higher correlation above means that changes at higher altitude occur more slowly and are less pronounced.

7. CONCLUSIONS

The analyses of the DSD's recorded at three altitudes on a mountain slope suggest the following conclusions:

7.1 Major shape changes occur simultaneous at the three altitudes reflecting changes in weather conditions (Fig.4).

7.2 "Instant" distributions deviate strongly from exponential ones,(Fig.3),at all altitudes.

7.3 Distributions at lower altitude are slightly more monodisperse than higher up, (Fig.3 and Tab.1.).

7.4 Exponential distributions are found at every altitude when many "instant" distributions from different conditions are summed,(Fig.3 and Fig.5).

7.5 Shapes at the same time and different altitude show very similar variations (Fig.4). The crosscorrelation coefficient for the two extreme stations,800 m apart in altitude,is the same as the autocorrelation coefficient for any station with a delay $\Delta t \sim 3$ minutes,(Tab.3).

7.6 At the higher altitude the autocorrelation function for a given Δt is also higher, indicating that changes occur more slowly, (Sec.6).

7.7 The experiment does not answer the question of what fraction of the observed significant changes are due to orographic influence and what would be measured in the free atmosphere in a flat country.

ACKNOWLEDGMENT

The authors wish to tank R.Cavalli and H.P.Roesli for their helpful suggestions and criticisms,and are grateful to M.B.Baker for her helpful comments.

REFERENCES

Battan, L.J.,1977: Rain resulting from melting ice particles. J.Appl.Meteor.,16,595-604.

Hardy, K.R.,1963: The development of raindrop size distribution and implications related to the physics of precipitation. J.Atmos. Sci.,20, 299-312.

Joss, J. and E.G.Gori,1976: The parametrization of raindrop size distributions. Riv.Ital. Geofis.,3, 275-283.

------ and ------, 1978: Shapes of raindrop size distributions. J.Appl.Meteor.,17, 1054-1061.

Ohtake, T.,1969: Observations of size distributions of hydrometeors through the melting layer. J.Atmos.Sci.,26, 545-557.

THERMAL, MICROPHYSICAL AND CHEMICAL CONDITIONS IN AN URBAN ENVIRONMENT

L.T. Khemani, G.A. Momin, M.S. Naik, A. Mary Selvam
and Bh.V. Ramana Murty

Indian Institute of Tropical Meteorology, Poona 411 005, India.

1. INTRODUCTION

A study of the rainfall records for the period 1901-1969 in the urban industrial city of Bombay (18° 51'N, 72° 49'E, 11 m ASL) suggested significant increases in rainfall in the downwind region by about 15 per cent during the period of industrialisation (Khemani and Ramana Murty, 1973). The physical reasons for the observed increases in rainfall could not be investigated immediately for lack of the necessary data in the region. For the above research field observational programmes were carried out during 1972, 1973 and 1974 and extensive surface and aircraft observations were made. The results of the study are presented below.

2. LOCATION OF MEASUREMENTS

The locations of the places of measurements are shown in Figure 1. Solid strips in the figure denote the regions of major industrial establishments which were commissioned during the period 1950-1960 (Khemani and Ramana Murty, 1973). The major industries include textiles, fertilizers, chemicals, oil refinery, thermal power generation etc. The population of Bombay city is about 6 million. The meteorological conditions in the region during different seasons were described elsewhere (Mary Selvam et al., 1980).

3.0 MEASUREMENTS

3.1 Surface

Atmospheric trace gases (sulphur dioxide, oxides of nitrogen, and ammonia), total particulates, total hygroscopic and non-hygroscopic nuclei and chemical composition of rain water (chloride, sulphate, nitrate, ammonium, sodium, potassium and calcium) were measured. The location of different measurements and average values of the parameters are given in Tables 1 and 2. The details of the methods of measurements and the techniques of analysis were described elsewhere (Khemani and Ramana Murty, 1968; Khemani et al., 1976).

3.2 Aircraft

Measurements using a DC-3 aircraft were made at about 3000 ft ASL (cloud base level is about 2000 ft ASL). The parameters measured were (i) sulphur dioxide, (ii) ammonia, (iii) giant size hygroscopic and non-hygroscopic nuclei, (iv) cloud condensation nuclei (CCN) at 0.1 per cent supersaturation, (v) cloud droplet size distribution, (vi) liquid water content and (vii) air temperature. The details of measurements of the parameters at (i) and (ii) and (iii) to (vii) were respectively described (Khemani et al., 1976) and (Mary Selvam et al., 1978).

4.0 RESULTS AND DISCUSSION

4.1 Surface Observations

The mean values of hygroscopic and non-hygroscopic nuclei, (ii) total particulate concentration, (iii) sulphur dioxide and oxides of nitrogen obtained from the measurements made at Alibag (non-urban), Colaba (partially-urban) and Kalyan (urban) regions are given in Table 1.

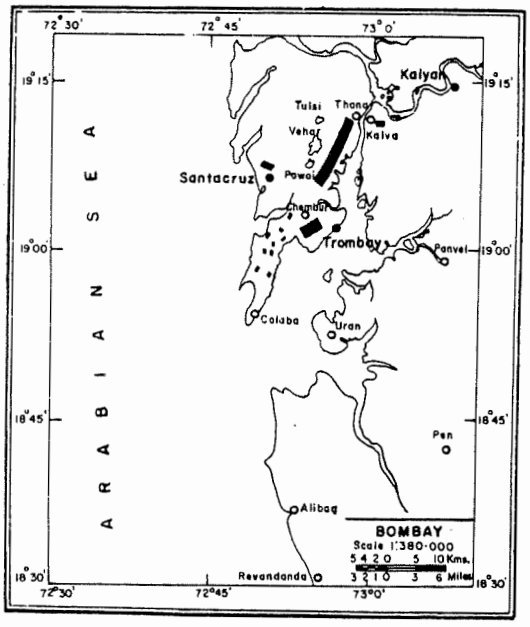

Figure 1 : Location of the places of measurements. Solid strips denote regions of major industrial complexes.

Table 1 : Average concentrations of different parameters at the places of observation

Month 1972	Hygroscopic nuclei (l^{-1})	Non-hygroscopic nuclei (l^{-1})	Total particulates (Cm^{-3})	SO_2 ($\mu g\ m^{-3}$)	NO_x ($\mu g\ m^{-3}$)
		ALIBAG (NON-URBAN)			
Feb.	134	36	84	1.6	3.6
Apr.	353	50	51	3.8	5.4
Sept.	152	34	106	5.4	3.8
Average	213	40	80	3.6	4.3
		COLABA (PARTIALLY-URBAN)			
Feb.	168	57	99	7.4	13.6
Apr.	313	62	77	6.5	8.5
Sept.	129	51	105	14.7	8.8
Average	203	57	94	9.5	10.3
		KALYAN (URBAN)			
Feb.	17	93	195	73.5	26.5
Apr.	51	142	195	22.4	10.8
Sept.	79	262	138	10.6	7.4
Average	50	166	176	35.5	14.9

Table 2 : Average concentrations of different chemical constituents (mg l^{-1}) in rain water samples collected at different places during the summer monsoon seasons (June-September) of 1972 and 1973. The rainfall recorded at the three places is also given.

Year	Rainfall in mm	Cl^-	SO_4^{--}	NO_3^-	NH_4^+	Na^+	K^+	Ca^{++}	Cl/Na	SO_4/Cl
				ALIBAG (NON-URBAN)						
1972	1240	11.85	2.59	0.40	0.16	8.45	1.08	4.16	1.40	0.22
1973	1947	6.70	2.29	0.35	0.21	5.52	0.30	2.18	1.21	0.34
				COLABA (PARTIALLY-URBAN)						
1972	1476	9.05	4.12	0.64	0.27	6.98	1.01	3.05	1.30	0.46
1973	1849	7.38	4.50	0.68	0.31	7.84	0.57	2.42	0.94	0.61
				KALYAN (URBAN)						
1972	1548	4.51	6.98	0.64	0.34	3.42	0.50	2.82	1.32	1.56
1973	2521	2.17	6.30	1.60	0.31	2.21	0.24	1.75	0.98	2.90

The concentration of the total hygroscopic nuclei was maximum at Colaba which is located on the coast (observational site was located on the sea shore) and minimum at Kalyan which is located at about 60 km away from the coast. The concentrations of the total particulates and the total non-hygroscopic nuclei were maximum at Kalyan. The concentrations of sulphur dioxide and oxides of nitrogen were also found to be maximum at Kalyan. The above observations are consistent since a large number of industrial complexes are located in the region.

The results of the chemical composition of rain water samples collected at Alibag, Colaba and Kalyan are shown in Table 2. The concentrations of chloride and sodium were maximum at Alibag (coast) and minimum at Kalyan. The ratio values of chloride to sodium also showed the same trend. The concentrations of sulphate, nitrate and ammonium were minimum at Alibag (non-urban). The ratio values of sulphate to chloride also showed a similar trend.

The above results are consistent as in the case of those shown in Table 1.

4.2 Aircraft Observations

The concentrations of (i) sulphur dioxide, (ii) ammonia, (iii) giant size hygroscopic and non-hygroscopic nuclei, (iv) total particulates, (v) CCN, (vi) cloud droplet concentration, (vii) computed liquid water (LWC) and (viii) air temperature obtained from the observations made over the Arabian sea (50 km off the coast at Santacruz, Figure 1) and Kalyan (urban) regions are shown in Table 3. The cloud droplet size distributions for sea and Kalyan are shown in Figure 2. The values of all the parameters at Kalyan are significantly higher than those for the sea. The results are consistent and are in agreement with those of other studies (Mary Selvam et al., 1976; 1978; Eagen et al., 1974; Dytch, 1975; Carrera, 1975).

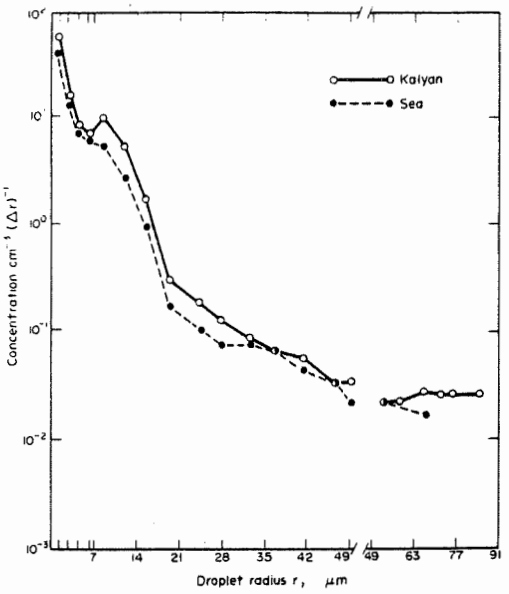

Figure 2 : Droplet spectra in clouds in the Kalyan (urban) and Arabian sea (non-urban) regions.

Table 3 : Average concentrations of different parameters obtained from the observations made over the Arabian sea and Kalyan regions during September 1974.

Giant condensation nuclei		Total Particulates	SO_2	NH_3	CCN	Cloud droplet con.	LWC	Air temp.
Hygroscopic (l^{-1})	Non-hygroscopic (l^{-1})	(Cm^{-3})	($\mu g\ m^{-3}$)	($\mu g\ m^{-3}$)	(Cm^{-3})	(Cm^{-3})	(gm^{-3})	(°C)
		ARABIAN SEA (NON-URBAN)						
15	16	81	3.1	5.8	265	72	0.15	20.0
		KALYAN (URBAN)						
23	46	116	14.6	29.6	478	103	0.24	20.9

4.3 Urban Influence on Cloud Microstructure and Rainfall

The urban influences on the cloud microstructure have been investigated in the recent studies (Mary Selvam et al., 1976; 1978; Dytch, 1975; Hindman et al., 1977). Also, the concentrations of large and giant size condensation nuclei were found to increase in the downwind region of a paper mill (Hindman et al., 1977). Further it was observed that the concentration of cloud drops of diameter greater than 30 μm were more in clouds forming in the plume of the paper mill than those in clouds forming outside the plume region. These observations are in agreement with the results of the present study. The higher concentrations of sulphur dioxide and ammonia found in the downwind regions of the industrial complexes at Bombay could be responsible for the higher concentrations of CCN observed in the region. The excess CCN could be due to the formation of ammonium sulphate particles through the gas-to-particle conversion by photo-chemical reactions (Vohra et al., 1970). The higher concentrations of larger cloud drops found in the clouds forming in the Kalyan (urban) region can help rain development through accelerated coalescence process. Further the warmer temperatures (about 1°C) observed at cloud base levels in the Kalyan (urban) region than those observed in the upwind (sea) would further contribute to enhance the coalescence growth of cloud drops leading to enhancement in rainfall.

The thermal, microphysical and chemical conditions in the urban environment in the Bombay region are thus consistent with the 15 per cent increase in rainfall observed during the period of industrialisation (Khemani and Ramana Murty, 1973).

5.0 CONCLUSIONS

A study of the thermal, microphysical and chemical conditions in the urban environment in the Bombay region suggested the following :

i) The air temperature at the cloud base level in the urban environment was higher by about 1°C than that in the upwind region.

ii) The concentrations of sulphur dioxide, ammonia and oxides of nitrogen were significantly higher in the urban (downwind) environment than in the non-urban (upwind) environment.

iii) The concentrations of sulphate, ammonium and nitrate in the rain water samples collected in the urban region (Kalyan) were significantly higher than those in the non-urban region (Alibag).

iv) The concentrations of giant size hygroscopic and non-hygroscopic nuclei, total particulates, CCN, cloud droplet concentration and concentration of larger cloud drops were significantly higher in the urban environment than in the non-urban environment.

v) The integrated effect of the thermal, microphysical and chemical conditions in the urban environment in the Bombay region appears to be responsible for the 15 per cent increase in rainfall noticed during the period of industrialisation in the region.

ACKNOWLEDGEMENT

The authors are grateful to Dr. A.S.R. Murty for his valuable suggestions while preparing the manuscript. They are also thankful to Shri P.M. Bhanage, for typing the manuscript.

REFERENCES

Carrera, J.N., 1975 : Urban influences on cloud microstructure downwind from St. Louis,Missouri : Upper Level Observations, J. Rech. Atmos., 9, 157-165.

Dytch, H.E., 1975 : Urban influence on cloud microstructure downwind from St. Louis, Missouri : Lower Level Observations, J. Rech. Atmos., 9, 145-156.

Eagen, R.C., P.V. Hobbs, and L.F. Radke, 1974 : Particle emissions from a large kraft paper mill and their effects on the microstructure of warm clouds, J. Appl. Meteor., 13, 535-552.

Hindman, E.E. II, P.V. Hobbs and L.F. Radke, 1977 : Cloud condensation nuclei from a paper mill Part I : Measured effects on clouds, J. Appl. Meteor., 7, 745-752.

Khemani, L.T. and Bh.V. Ramana Murty, 1968 : Chemical composition of rain water and rain characteristics at Delhi, Tellus, 20, 284-292.

Khemani, L.T. and Bh.V. Ramana Murty, 1973 : Rainfall variations in an urban industrial region, J. Appl. Meteor., 12, 187-194.

Khemani, L.T., G.A. Momin and Bh.V. Ramana Murty, 1976 : Atmospheric pollutants and rainfall, Ind. Jour. Radio and Space Phys., 5, 75-79.

Mary Selvam, A., A.S. Ramachandra Murty, R. Vijayakumar and Bh.V. Ramana Murty, 1976 : Electrical and microphysical measurements in the environment of a thermal station, Atmos. Environ., 10, 957-962.

Mary Selvam, A., A.S. Ramachandra Murty, S.K. Paul, R. Vijayakumar and Bh.V. Ramana Murty, 1978 : Airborne electrical and microphysical measurements in clouds in maritime and urban environments, Atmos. Environ., 12, 1097-1101.

Mary Selvam, A. et al., 1980 : Some thermodynamical and microphysical aspects of monsoon clouds, Proc. Indian Academy Sciences (submitted).

Vohra, K.G., K.N. Vasudevan and P.V.N. Nair, 1970 : The mechanisms of nuclei-forming reactions in the atmosphere, J. Geophys. Res., 75, 2951-2960.

AIRCRAFT MEASUREMENT OF MOUNTAIN WAVE CLOUD

H.R. Larsen and G.W. Fisher

New Zealand Meteorological Service
Wellington, NEW ZEALAND.

1. INTRODUCTION

Mountain wave clouds are a relatively common feature of the New Zealand sky. The waves are formed by an approximately north-south mountain chain down the length of the country lying across the strong westerly Southern Hemisphere middle latitude airflow. It is presumed that in the simplest cases the clouds will be formed of air parcels essentially following the wave streamlines and will be free of the effects of entrainment of air at the cloud boundaries, vertical mixing within the cloud and, for stationary waves, of time variability. They therefore offer an excellent natural laboratory in which the evolution of cloud droplet spectra can be studied in isolation from these effects. In addition, because there appears to be little information on the structure of such clouds, they are of interest in themselves: for example their shape relative to the airflow streamlines, the effect of their formation on these streamlines and the nature of the humidity and temperature gradients giving them their characteristic layered form. Cloud physics instrumentation is therefore being fitted to a sailplane to investigate the microphysics and motion fields within these clouds.

2. INSTRUMENTATION

The sailplane being used is an all metal BLANIK L13 high performance two seater. The choice of a sailplane rather than a powered aircraft has conferred a number of advantages in the placement and ease of mounting of equipment. It has also given low airspeed for high resolution measurements, at the expense of restrictions on the weight and power consumption of equipment carried.

All data is recorded on board in digital form on magnetic tape cassettes. To simplify analysis it is available, on replay, in standard computer compatible ASCII format. The SSE 'PACIFIC' Data Acquisition System* (DAS) used is a dual-microprocessor based unit with 12 bit resolution, scanning all sensors every 0.5 seconds (although faster scan rates can be used). It includes a high speed BCD decoder/accumulator interface suitable for recording droplet spectra.

The sensors on the aircraft are listed in Table 1. External sensors are mounted in a package on an outrigger, 0.75m above the fuselage and 2.5m back from the nose (Fig.1). At the top of the package is the FSSP-100 droplet spectrometer. To cover the full droplet size range of interest with a single FSSP, it is alternately switched between its most sensitive (0.5 to 8 μm) and least sensitive (2 to 47 μm) ranges by the DAS on successive data scans (i.e. every 0.5 seconds) to give two complementary sets of interleaved spectra.

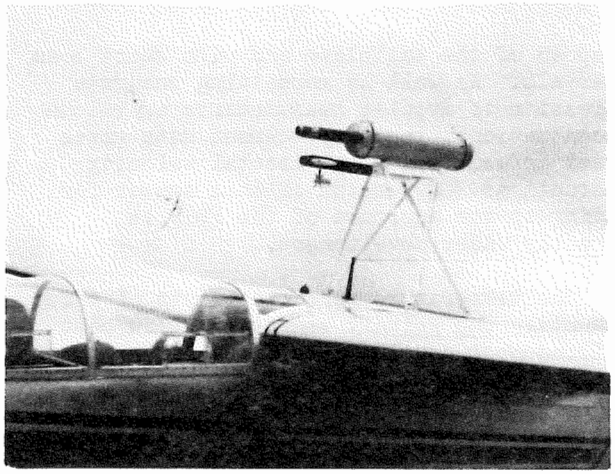

Figure 1. The external instrument package mounted on its outrigger above the aircraft. The reverse flow housing for the temperature sensor projects down from the lower black probe.

Below the FSSP is a probe carrying the sensors for air displacement, temperature, angle of incidence and true vertical. The first of these, the vortex shedding displacement sensor, gives a direct total of cloud air run between data scans. The more traditional use of a simple airspeed measurement to estimate distance travelled leads to errors in the presence of horizontal inhomogeneities, particularly at the low

*Solid State Equipment Ltd, Lower Hutt, N.Z.

Table 1. Sensors mounted on the BLANIK sailplane ZK-GHT for wave cloud studies.

Parameter	Sensor Type	Manufacturer/Type	Range	Resolution	Accuracy	Distance Constant
Pressure	Capacative	Rosemount 1241	-300 to 9100m	1.3m	0.25%	1m
Pressure rate of change	Variometer	Altriss (N.Z.)	+10 to -10ms^{-1}	0.01ms^{-1}	0.3ms^{-1}	1m
Temperature	Semiconductor	Analog Devices AD590	-55 to +150°C	0.02°C	0.1°C	100m
	Cu-Con thermocouple A	N.Z. Met. Service	± 5°C	0.1°C	0.1°C	2m
	Cu-Con thermocouple B	N.Z. Met. Service	±5°C	0.1°C	0.1°C	2m
*Humidity	Capacative	Vaisala	10 to 95% RH	1% RH	?	?
Cloud drop size	Light scattering	Particle Measuring Systems FSSP-100	0.5 to 8 µm 2 to 47µm	0.5 µm 3 µm		
Air displacement	Vortex shedding	J-Tec VA220(modified)	1 to 60ms^{-1}	0.01m	2%	0.01m
Air Speed (IAS)	Differential pressure	Rosemount 1221D	15 to 65ms^{-1}	0.03ms^{-1}	10%	1m
Angle of incidence	Vane/transformer	N.Z. Met. Service	-7° to +12°	0.002°	0.2°	3m
Vertical reference	Gyroscope	Ferranti FH11/E1	-45° to +45°	0.1°	0.1°	2m
*Horizontal position	DME	King 62A(modified)	0 to 170km	17m	17m	17m
Ice concentration	Black Rod	N.Z. Met Service		ice/no ice		
Vertical reference	Pendulum	N.Z. Met. Service	-45° to +45°	0.1°	0.5°	10m

*To be fitted October 1980

airspeed of the sailplane and with short scan intervals. As well as permitting accurate expression of droplet measurements as volume concentrations, the displacement data gives direct information on horizontal velocity fluctuations. A version of this sensor for fitting to the aperture of the FSSP is currently under development.

The temperature sensor consists of three elements. The primary sensor is a low cost semiconductor device which offers high precision but slow response. Bonded to its base are the reference junctions of two short, fine gauge thermocouples whose active junctions give the high frequency component of any temperature changes. The small dynamic range of the thermocouple outputs allows simple local amplification while a comparison of their outputs allows correction for any droplet impactions. In practice very few droplet impactions on the thermocouples have been observed. The sensors are mounted in a reverse flow housing (Rodi and Spyers-Duran, 1972).

The vertical component of the air velocity relative to the aircraft is computed using data from the incidence vane (giving the angle of the airflow relative to the probe), the true vertical sensor (giving angle of the probe to the vertical) and the air displacement sensor. The absolute updraft can then be found using this component and the pressure rate of change.

3. RESULTS

The clouds being studied are between 3,000 and 10,000m in height above sea level, over the low lying Wairarapa region some 50km east of Wellington. Between the Wairarapa plains and the Wellington coast are the Tararuas, a continuous mountain range 1,000 to 1,500m high and approximately 20km wide.

A number of features of interest are already apparent in the data obtained from an initial flight through lenticular cloud on 18 December 1979. These clouds were superficially of a simple form, with smooth boundaries and no external evidence of convective or turbulent overturning.

The results in Fig.2 are for a penetration directly into the upwind boundary of a cloud. They show a very rapid initial growth of the droplets. Within 2 seconds or 70m of the boundary (as determined from the first detection of droplets over 0.5 µm diameter) the mean droplet diameter had reached 8 µm, while beyond this point it increased only slowly. The 70m corresponds to a little under 5 seconds of growth time (the speed relative to the (stationary) cloud boundary is 35ms^{-1}, normal component of the air speed is 20ms^{-1}, wind speed is 15ms^{-1}). The occurrence of very fast growth rates and subsequent formation of a uniform narrow distribution was predicted for lenticular clouds by Howell (1949), although

his calculations of droplet growth do not cover updraft velocities as high as those observed in the present case. The more sophisticated later calculations of the initial evolution of spectra (e.g. Mason and Chien, 1962, Lee and Pruppacher, 1977) are also for lower updraft rates.

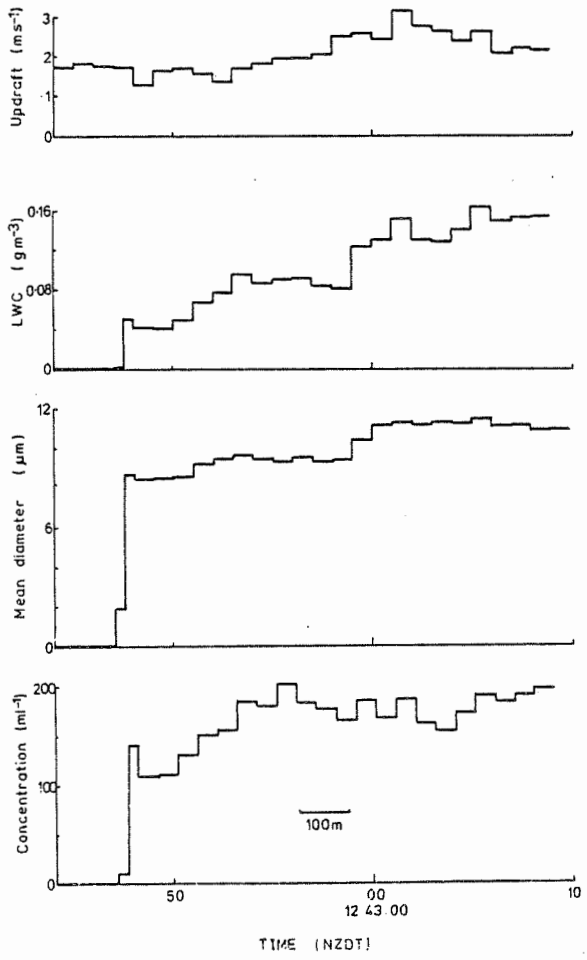

Figure 2. Data for a penetration directly into a lenticular cloud leading edge. Cloud pass A, 18 December 1979, altitude 5800m.

The liquid water content calculated from the FSSP data is also shown in Fig.2 and has the steady increase expected in the rising air of the wave. There is also the expected evidence of an initial delay of some seconds in the conversion of vapour to liquid at the front of the cloud.

Within the cloud the narrowness of the droplet distribution and the uniformity of the droplet concentration (Fig.3) are apparent. The characteristics are quite different to those observed in other cloud types (e.g. Warner 1969, Corbin et al.1977). For comparison, the droplet spectra from a typical non raining cumulus of comparable liquid water content are shown in Fig.4.

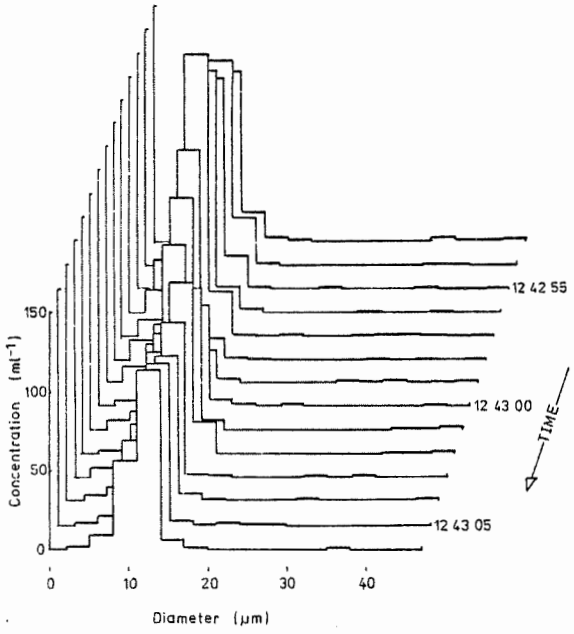

Figure 3. Time sequence of droplet spectra observed within a lenticular cloud. Cloud pass A, 18 December 1979.

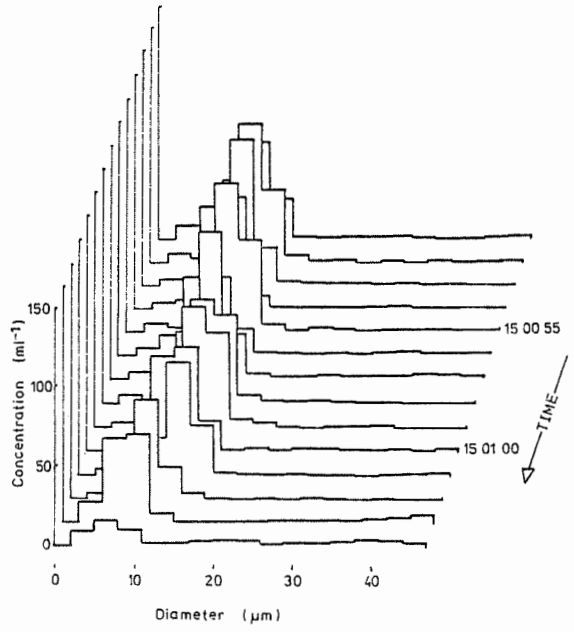

Figure 4. Time sequence of droplet spectra observed in a non-precipitating cumulus cloud. Cloud pass A, 11 September 1979, altitude 830m.

(Note, however, that the cumulus was observed on a different date at a different location and at a significantly lower altitude.) The spectra are compared in Table 2.

Table 2. Comparison of the characteristics of the droplet distributions found in a lenticular and a cumulus cloud. Quantities shown relate, in both cases, to 10 samples from a 200m section of cloud. N is the total droplet concentration and σ_N its standard deviation, $\bar{\mu}$ is the mean droplet diameter and $\sigma_{\bar{\mu}}$ its standard deviation, $\overline{\sigma_\mu}$ is the mean of the standard deviation of the individual spectra, and LWC is the liquid water content calculated from the droplet distributions.

Cloud Type	N	σ_N	$\bar{\mu}$	$\sigma_{\bar{\mu}}$	$\overline{\sigma_\mu}$	LWC
	ml^{-1}	ml^{-1}	μm	μm	μm	gm^{-3}
Ac lent	189	6	11.2	0.3	2.4	0.16
Cumulus	107	54	13.3	2.3	8.1	0.32

4. DISCUSSION

The droplet spectra we have measured to date differ from those presented by Cannon and Sartor (1970) for a large Colorado wave cloud. A small selection of droplet distributions they obtained on Formvar slides show a very broad distribution with low particle concentration. We speculate that their data was obtained well downwind of the cloud leading edge and that their clouds were not as simple as ours but had considerable convective overturning within them.

In this example of a cloud formed by uniform rapid lifting of the air, apparently without entrainment or vertical mixing, a very narrow drop size distribution is produced with a high degree of homogeneity in drop concentration within the cloud. The relative lack of complexity in the processes establishing this drop population should permit a straightforward comparison with theoretical models. If these results are confirmed by later measurements, particularly on lenticular clouds with lower updraft velocities, they will complement the measurements on other, more complex cloud types.

Rogers and Vali (1978) have identified the need for observations clarifying the initial evolution of droplet spectra, and the difficulty of making such observations. The preliminary results described here indicate that the measurements of lenticular clouds using the instrumented sailplane may provide a useful contribution to the solution of this problem.

5. ACKNOWLEDGEMENTS

We are grateful to our pilot, Max Stevens, and to the Wellington Gliding Club who have made the sailplane available to us, for their assistance.

6. REFERENCES

Cannon, T.W. and Sartor, J.D., 1970: 'Some comparison measurements of cloud droplet and particle distributions in clouds using airborne sensors.' Conference on Cloud Physics, Fort Collins, 1970. pp 11-12.

Corbin, R.G., Latham, J., Mill, C., Smith, M.H., Stromberg, I.M., 1977: 'Inhomogeneities in the water properties of fogs and clouds.' Nature 267 pp 32-33.

Howell, W.E., 1949: 'The growth of cloud drops in uniformly cooled air.' J. Meteor. 6 pp 134-149.

Lee, I.Y. and Pruppacher, H.R., 1977: 'A comparative study on the growth of cloud drops by condensation using an air parcel model with and without entrainment.' Pageoph. 115 pp 523-545.

Mason, B.J. and Chien, C.W., 1962: 'Cloud droplet growth by condensation in cumulus.' Quart. J. Roy. Meteor. Soc. 88 pp 136-142.

Rodi, A.R. and Spyers-Duran, P.A., 1972: 'Analysis of time response of airborne temperature sensors.' J. Appl. Meteor. 11 pp 554-556.

Rogers, R.R. and Vali, G., 1978: 'Recent developments in meteorological physics.' Physics Report 48 (see p 119).

Squires, P., 1952: 'The growth of cloud drops by condensation. I. General characteristics.' Aust. J. Sci. Res. 5 pp 59-86.

Warner, J., 1969: 'The microstructure of cumulus cloud. Part I. General features of the droplet spectrum.' J. Atmos. Sci. 26 pp 1049-1059.

RAINDROP BREAKUP : THE ENERGY OF DISRUPTURE

Yean Lee

Stone & Webster Engineering Corporation
Boston, Massachusetts, USA

A. Nelson Dingle

The University of Michigan
Ann Arbor, Michigan, USA

1. INTRODUCTION

It has long been observed that raindrops oscillate, rotate, become distorted, and disintegrate, as they fall through the atmosphere. It has also been realized that coalescence and breakup are important mechanisms in the conversion of warm cloud to rain. The energy associated with each of these processes and its relation to the drop growth and breakup mechanisms are less well known. In this study an analysis is made of the exchanges and transformations of energy in the collision process and a simple model is derived to distinguish the conditions for drop coalescence from those for breakup.

2. ANALYSIS

Laboratory studies of raindrops in collision indicate that many identifiable processes may follow collision (e.g., Spengler and Gokhale, 1973). It is our present aim to determine criteria for distinguishing between the two general cases of collision with coalescence and collision with disrupture. We assume that in all of the possible cases, momentum, mass, and energy are conserved. For simplicity, we envisage a direct "head on" and completely inelastic collision, i.e., one that involves at least momentary coalescence of the two colliding drops. We further assume no effects of electric charges or of internal circulations

The Kinetic Energy Change

The conservation of momentum gives

$$M_\ell V_\ell + M_s V_s = (M_\ell + M_s) V_c$$

where M and V are the mass and speed and the subscripts ℓ, s and c represent large, small and coalesced drops, respectively. The speed of the coalesced drop is therefore

$$V_c = \frac{M_\ell V_\ell + M_s V_s}{(M_\ell + M_s)}$$

and its kinetic energy

$$E_k = \frac{1}{2}(M_\ell + M_s) V_c^2 = \frac{1}{2} \frac{(M_\ell V_\ell + M_s V_s)^2}{(M_\ell + M_s)}$$

immediately after collision. Because the collision is inelastic, kinetic energy is not conserved, and we obtain

$$\Delta E_k = \frac{1}{2} M_\ell V_\ell^2 + \frac{1}{2} M_s V_s^2 - \frac{1}{2}(M_\ell + M_s) V_c^2$$

$$= \frac{1}{2} \frac{(M_\ell M_s)}{M_\ell + M_s} (V_\ell - V_s)^2 \qquad (1)$$

Where ΔE_k is the kinetic energy release realized upon collision and initial coalescence. This term is always positive, and represents energy that must be dissipated either to heat or to work.

Oscillational Energy

Freely falling raindrops possess a natural frequency of oscillation determined by their size and surface tension. According to Lamb (1932), the natural frequency, f, of oscillation of a raindrop can be estimated by means of

$$f = (8\sigma/3\pi M)^{1/2} \qquad (2)$$

where σ is the surface tension.

Raindrops with radii larger than a certain size are subject to deformation and tend to become hydrodynamically unstable. Both experiment and theory indicate that a drop with radius less than 1 mm is nearly spherical with little distortion (Pruppacher and Pitter, 1971). As the drop size increases, the deformation becomes more prominent, and the drop shapes vary from prolate to oblate ellipsoids. Beard (1976) found an empirical expression relating the equivalent spherical diameter (d_o) to the so-called projected (maximum) diameter (d_m) as a result of wind tunnel studies. The expression is

$$\frac{d_m}{d_o} = 0.973 + 0.027\, d_o$$

for d_o in mm.

We know that as long as the amplitude of the drop deformation remains in the proportional (elastic) region, the mechanical vibrations are well-approximated by simple harmonic motion. A raindrop vibrating with natural frequency f and amplitude A may assume such a motion. If we accept this assumption, and further assume that the amplitude of an oscillating drop follows Beard's (1976) formulation, i.e., $A = d_m/d_o - 1$, we can estimate the oscillational energy prior to collision as follows.

$$E_o = \frac{1}{2} KA^2 \tag{3}$$

where K is a constant, since $\omega^2 = K/M$, and $\omega = 2\pi f$. Substituting Eq. (2) in Eq. (3), we have

$$E_o = \frac{16\pi\sigma}{3} A^2 \tag{4}$$

for a 5-mm diameter drop, E_o is 0.14 erg, and it decreases rapidly as drop size decreases.

Rotational Energy

When a raindrop moves through the air, unbalanced external torques cause the drop to rotate. In terms of energy, we may write

$$E_r = \frac{1}{2} I \omega_r^2$$

where I is the moment of inertia and ω_r the angular velocity. For a spherical drop of radius r and mass M, $I = 2/5(Mr^2)$. If we assume r = 0.25 cm, $\omega_r = 30$/sec, then $E_r = 1$ erg, and this may be taken as a rough estimate indicative that the amount of energy in this form is also small prior to collision. In "head-on" collisions, no torque is available, hence E_r after collision is also small for the present case.

Surface Energy Change

The surface energy of a spherical drop is $4\pi R^2\sigma$. As long as the drop is not excessively distorted, this remains a reasonable estimate of its surface energy. To estimate the change of surface energy, ΔE_s, produced by the coalescence of two drops, we assume that each drop may be represented by an equivalent sphere, and hence

$$\Delta E_s = 4\pi\sigma\{(r_\ell^2 + r_s^2) - R_c^2\} \tag{5}$$

Breakup Energy

Numerous mechanisms of drop breakup have been proposed in the literature. Gunn (1949) assumed that the drops are broken up by aerodynamic forces. Gordon (1959) suggested that drops disintegrate because of the deformation. Komabayasi, et al., (1964), using Lamb's theory (1932), attributed drop breakup to the capillary-gravity waves. More recently, Pruppacher and Pitter (1971) suggested that in direct collision of drops the oscillation may lead to a breakup. List (1976) emphasized that breakup is induced by collision.

In the process of drop breakup, the surface energy of the system increases from an original unified-mass state to the final multiple-drop state. Thus a basic increase of surface energy I from an intermediate unstable state to the final multi-drop state. The requirement that such an instability must be created before disintegration can occur may be regarded as a potential barrier to the disintegration (Fig. 1).

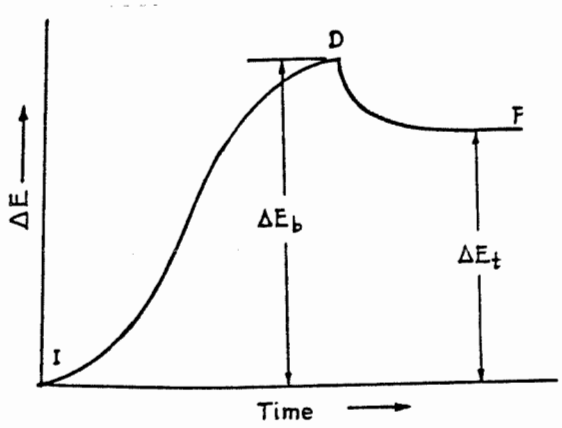

Fig. 1. Energy relationships in the collision-coalescence-breakup sequence

If we consider I to represent the initial undisturbed state of a single spherical drop, F to represent the final undisturbed state of the same water mass after breakup, and C to represent the critical distorted state just prior to breakup, the energy relationships may be envisaged as in Fig. 1. We designate the ordinate of the critical point in this figure ΔE_b, the critical energy required for breakup. If a drop collision releases energy at least equal to ΔE_b, disintegration will occur, if it releases less than this amount of energy, the initial coalescence of the two colliding drops will remain stable.

The analytical specification of ΔE_b depends upon numerous details of each particular collision. To develop an estimate of the minimum value of ΔE_b required for breakup, we assume that it may be approximated by the surface energy difference between the final state (F, Fig. 1) and the initial state (I, Fig. 1) for the case of breakup into n drops of equal size. Then

$$\Delta E_t = 4\pi\sigma r^2(n^{1/3}-1) \tag{6}$$

As a lower limit estimate for ΔE_b, we shall use ΔE_t with $n = 2$.

3. THE ENERGY OF DISRUPTURE

It is perhaps useful to envision the process of drop collision in three stages: (1) a quasi-unstable state as the two drops make contact and the momentum-energy exchanges are initiated, (2) a stage in which the two water masses either bounce apart or coalesce, and (3) a stage following initial coalescence in which the released energy either produces disrupture of the coalesced water mass or becomes absorbed as rotational and oscillational energy and heat within the coalesced drop.

The energy balance may be written

$$Q = \Delta E_k + \Delta E_s + \Delta E_o + \Delta E_r \qquad (7)$$

As indicated above, ΔE_o and ΔE_r are of small magnitude, so that (7) may be reduced to

$$Q \simeq \Delta E_k + \Delta E_s \qquad (8)$$

upon initial coalescence.

We now adopt the term "energy of disrupture" to describe Q, and we propose the following hypotheses:

(a) If $Q < \Delta E_b$, the drops coalesce and Q is dissipated as heat.

(b) If $Q \geq \Delta E_b$, the drops coalesce initially but breakup occurs contributing to surface energy and dissipating any residual energy as oscillational and rotational energy and heat.

4. RESULTS AND DISCUSSION

Values of E_k, E_s and E_o are shown in Figure 2 for drops of 0.01 cm to 0.58 cm in diameter. These curves span 8 orders of magnitude on the energy scale, and E_o is clearly negligible relative to E_k and E_s in freely falling single drops. Thus the source of breakup energy following head-on collisions must be mainly E_k and E_s.

Sample computations have been made for five large drop sizes: D_ℓ = 0.5, 0.38, 0.30, 0.20 and 0.18 cm colliding with small drops in the range 0.01 cm $\leq D_s \leq$ 0.37 cm using the limiting criteria:

$$D_s \leq D_\ell, \text{ and}$$

$$D_c = (D_\ell^3 + D_s^3)^{1/3} \leq 0.58 \text{ cm}$$

Values of ΔE_k, ΔE_s, Q and ΔE_b for D_ℓ = 0.5 cm colliding with the entire range of small drops are shown graphically in Fig. 3.

The intersections of the Q and ΔE_b curves show that for direct collision with drops of diameter D_ℓ = 0.5 cm,

(a) small drops of diameter up to $D_s \simeq$ 0.065 cm will coalesce permanently with the large drop;

(b) small drops in the range 0.065 cm $\leq D_s \leq$ 0.375 cm upon initial coalescence will provide disruption energy, Q, greater than ΔE_t and the coalesced water mass will break up; and

(c) small drops larger than D_s = 0.375 cm will coalesce permanently with the larger drop

provided only that the hypotheses (a) and (b) stated above are correct.

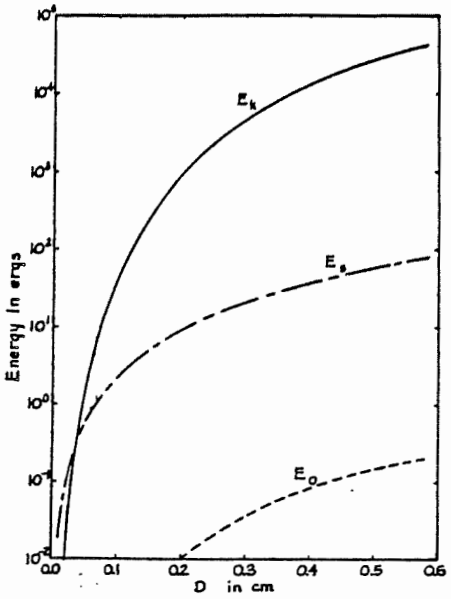

Fig. 2. Variation of the kinetic, surface, and oscillational energy terms with drop diameter.

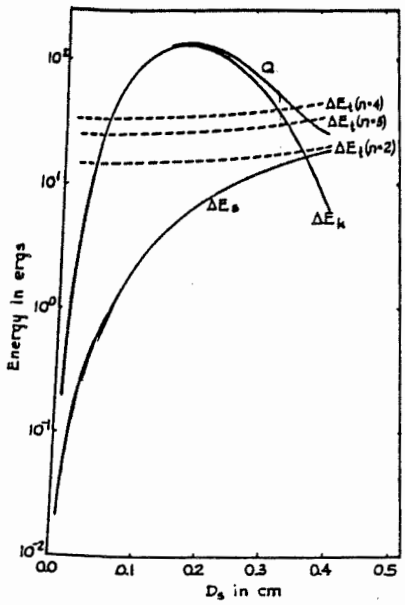

Fig. 3. Kinetic energy change, ΔE_k, surface energy change, ΔE_s, disruption energy, Q, and breakup threshold energy, ΔE_t, as functions of the small drop diameter for a large drop of 0.5 mm diameter.

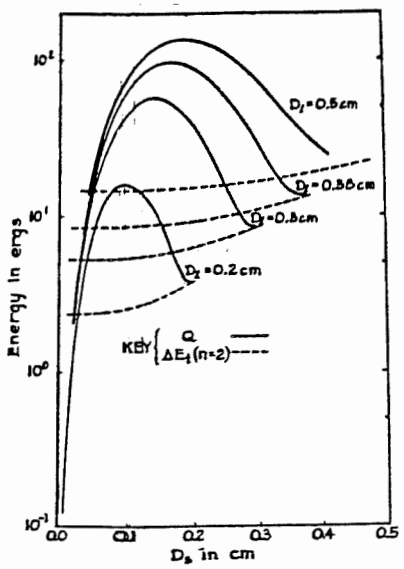

Fig. 4. Disrupture energy, Q, and threshold breakup energy E_b, for drops of diameter D_L = 0.2, 0.3, 0.38, and 0.5 cm as functions of small drop size.

The results from computations for four values of D are shown in Fig. 4. Here the energy of disrupture, Q, and the threshold breakup energy, ΔE , are shown for each case.

Spengler and Gokhale (1973) present a family of somewhat similar curves derived from their concept of "relative kinetic energy" defined to be $1/2\ M_s(V_\ell - V_s)^2$. Although this expression does not occur in the energy balance system, their approximate threshold of 15 ergs for breakup of the coalesced mass of an 0.5 cm and an 0.38 cm drop is within the range of 12 to 33 ergs which we find for the disrupture threshold for such collisions.

Correspondence to the results of McTaggart-Cowan and List (1975) is indicated by computing the maximum numbers of equal-sized fragments that may result from each sample collision. As many as 54 fragments could be produced by a collision between an 0.38 cm and an 0.17 cm drop according to this very simple model. It is of course evident that the head-on collisions with which we are here concerned correspond to the disk-type breakups observed by McTaggart-Cowan and List (1975).

5. CONCLUSIONS

A study based upon the various forms of energy involved in raindrop coalescence and breakup leads to the following conclusions.

(1) The changes of kinetic energy ΔE_k and surface energy ΔE_s are crucial terms in the energy balance system of colliding raindrops. The oscillational energy and rotational energy are approximately four and two orders of magnitude less than the kinetic energy, respectively

(2) A physical model which enables discrimination between the conditions for permanent coalescence and those for breakup is developed. The model invokes a balance of energy and leads to the concepts of energy of disrupture and breakup threshold energy. It is suggested that breakup will occur if the disrupture energy exceeds the breakup threshold energy. Otherwise, permanent coalescence is expected.

(3) Certain two-drop collisions are capable of producing more than 50 equal fragments upon breakup.

(4) Prediction of the drop size spectra produced by raindrop collisions is under study as an extension of the present analysis.

REFERENCES

Beard, K.V., 1976: Terminal Velocity and Shape of Cloud and Precipitation Drop Aloft., J. Atmos. Sci., 33, 851-863.

Gordon, G.D., 1959: Mechanism and Speed of Breakup of Drops, J. Appl. Phys., 30, 11, 1759-1761.

Gunn, R., 1949: Mechanical Resonance in Freely Falling Drops, J. Geophys. Res., 54, 383-385.

Komabayasi, M., T. Gonda, and K. Isono, 1964: Lifetime of Water Drops before Breaking and Size Distribution of Fragment Drops, J. Meteor. Soc. Japan, Ser. 2, 42, 330-340.

Lamb, H., 1932: Hydrodynamics, 6th ed., New York, Dover, 738 pp.

List, R. and J.R. Gillespie, 1976: Evolution of Raindrops Spectra with Collision-Induced Breakup, J. Atmos. Sci., 33, 2007-2013.

McTaggart-Cowan, J.D., and R. List, 1975. Collision and breakup of water drops at terminal velocity. J. Atmos. Sci. 32, 1401-1411

Park, R.W., 1970: Behavior of water drops colliding in humid nitrogen. Ph.D. Thesis Department of Chemical Engineering, University of Wisconsin, Madison, 589 pp.

Pruppacher, H.R. and R.L. Pitter, 1971: A semi-empirical determination of the shape of cloud and raindrops. J. Atmos. Sci., 28, 86-94.

Spengler, J.D. and N.R. Gokhale, 1973: Drop impactions. J. Appl. Meteor., 12, 316-321.

EXPERIMENTS AND MODELS ON COALESCENCE AND BREAKUP OF RAINDROPS

ROLAND LIST, T.B. LOW*, N. DONALDSON AND E. FREIRE
Department of Physics, University of Toronto, TORONTO M5S 1A7, CANADA
*Present affiliation: MEP Company, Downsview, Ontario
and

J.R. GILLESPIE
Atmospheric Environment Service, DOWNSVIEW, Ontario, CANADA

1. INTRODUCTION

Experiments by McTaggart-Cowan and List (1975a and b) on the breakup of colliding water drops (ML for short) produced the first sound basis for the modelling of the evolution of raindrop spectra in nature. Those experiments were carried out under conditions of free fall at terminal velocity for each drop of five size pairs. Impact occured at angles of up to 9^{o} from the vertical. These deviations from zero were shown to have no effect on the outcome of the experiments. The purpose of the experiments was to establish whether drops collide and breakup or whether they just coalesce and contribute to growth. Observations showed, with one exception, that the colliding drop pairs broke up in three different configurations: filament (or neck), sheet and disk. The fragment numbers increased substantially from filament to disk. Only one bag breakup was observed and seems to be unimportant. The following pair sizes (diameters in mm)were studied: (4.6;1.8), (4.6;1.0), (3.6;1.8), (3.6;1.0) and (3.0;1.0). The experiments with each drop pair were repeated at least a hundred times in order to get statistically meaningful, average fragment size distributions. Drop breakup was studied at laboratory pressure.

One may question the original selection of sizes because they may seem large in hindsight. However, in the late sixties, when the experiments were started, the accepted view was that drops would breakup because of aerodynamic instabilities, at drop sizes of ~6mm. No substantial information was available at that time on the importance of collisions. Thus, the above listed selections seemed to be in the sensitive area where coalescence and breakup are replacing each other.

The ML drop sizes turned out to be on the large side and left a considerable gap between the region of breakup and the region where it is normally assumed that coalescence dominates. The implications of the ML work could not be recognized without the modelling of the evolution of raindrop spectra with particle ensembles where both coalescence and breakup were included. This led to the rainshaft models by List and Gillespie (1976) and Gillespie and List (1978).

These authors parameterized the fragment size distributions of ML by interpolation in the breakup and extrapolation in the coalescence region. The model was one-dimensional and represented an infinitely wide rainshaft with a source of rain at the top 2km level. In a first version the rain was supplied steadily at different rainfall rates with drop sizes as represented by a Marshall-Palmer distribution (MP for short) and followed to the ground. In a second model, the temporal equilibrium drop distribution was established for a layer in which the rain falling out at the bottom was fed back in the top. The major results were quite surprising and can be given as follows:

1) The drop size distribution conserved the MP character.
2) Single peak or double peak (non-MP) distributions changed into MP with time.
3) Within a few kilometers of fall the drop size distributions approached an equilibrium distribution - which was only a function of rainfall rate.
4) The peaks in the mass distribution were around sizes of 2-2.5mm, with very few particles around 4-5mm.
5) In terms of warm rain (i.e. no ice in the clouds) this means that only relatively small drops can be expected for wide-spread, continuous precipitation.

The last result seemed supported by observations. However, there was the question about cold rain (involving the ice phase) in which many large drops fall. Explanations may lie in a drop stabilization by ice remnants during part of the fall from the melting level. Other contributing factors could also be the time and space variations within a given rainfall. The question now is whether the experiments and the added parameterization are representing processes in clouds.

2. EXPERIMENTS ON BREAKUP AND PARAMETERIZATION

The importance of drop breakup for the modelling of rain warranted an extension of the data base by studying more drop pairs with sizes [mm] (1.8;0.395), (4.0;0.395), (4.4;0.395), (1.8;-0.715), (1.8;1.0), and, for testing the overlap: with ML, (3.0;1.0) (Low, 1977). These ranges were made possible by increasing the experimental sensitivity of droplet detection from 0.5mm to 40um and finally led to a disappearance of the sharp cutoffs in the size distributions at 0.5mm observed by Gillespie (1977).

The new results confirmed the three breakup configurations found by ML, and again the pattern observed was that a large fragment, corresponding to the initial large drop, is produced by each collision. For filament breakup a fragment corresponding to the smaller drop of the interacting pair is also clearly detecta-

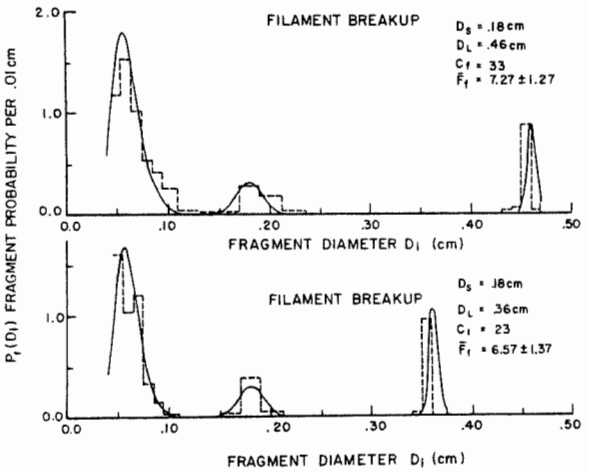

Figure 1. Fragment probability per 0.01cm size interval for a fragment of size D_i, for filament configuration; dashed lines for experimental data, solid lines for the fitted probability density function; the original drop pair is characterized by the large drop diameter D_L and that of the small drop D_S; C_f and F_f are the number of collisions and the average fragment numbers per collision, respectively.

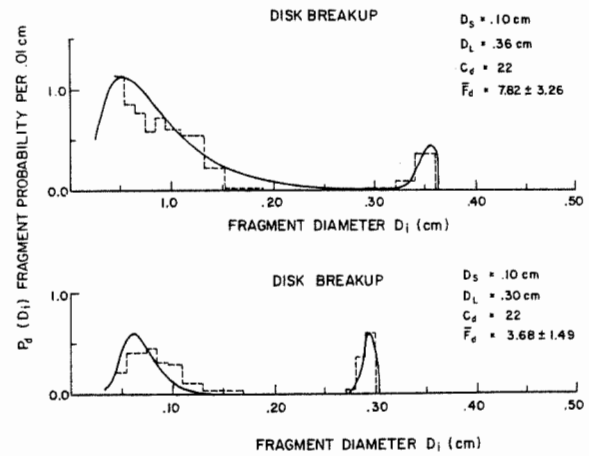

Figure 2. Fragment probability per diameter interval for disk breakup.

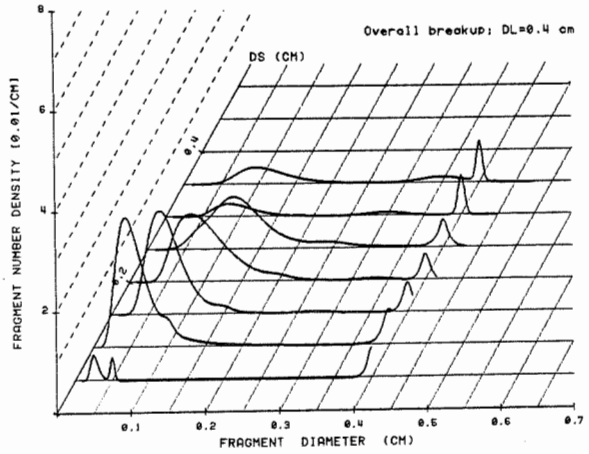

Figure 3. Fragment size distributions for overall breakup for large drops D_L=4mm, colliding with smaller drops of diameters $0.5 \leq D_S \leq 3.5$mm. The peaks on the right side represent remnants of the large drops. The remnants of the small drops can also be recognized, while the peaks to the left represent smaller fragments.

ble. This can occur with sheets, but in cases where the smaller drop is small, the corresponding fragment may disappear in the multitude of the smaller fragments. In the disk breakup the smaller drop is not reflected in any specific fragment. Typical results are shown in Figures 1 and 2.

Low (1977) found an analytical description of the data in the form of normal and log-normal distributions which covered the whole range of the experiments. This approximation is plotted as solid curves in Figures 1 and 2. In order to get overall distributions however, the fractional occurence of filament, sheet and disk breakup also needed parameterization. The result of this procedure is displayed in Figure 3 for drop pairs where the large drop diameter, D_L, is 4mm. The small drop size, D_S, is varied in steps of 0.5mm. Increasing D_S from 0.5mm shows how the remnants of the small drops first appear as a separate peak, then show up as a "shoulder" to the small fragment peak and later turn up again as a separate, wide bump. The small fragments peak around D_S=1.0mm. The cutoff for some of the peaks for the large fragments is caused by mass conservation, which does not allow any fragment with a size exceeding the sum of the two original drop masses.

The parameterization describes by interpolation the fragment spectra of any drop pairs. This means that the surface in 3-space of Figure 3 is extended into 4-space by a variation of D_L.

How often does breakup occur? This question was answered by looking at the fraction of all the collisions which resulted in coalescence. Figure 4 gives these probabilities, with the conditions for which collisions always result in breakup, and for which, for example, 50% of collisions result in coalescence and 50% in breakup (curve labeled 0.5).

There is one more point to be looked into before any rain modelling is possible. We need to make assumptions about collisions for drop pairs with sizes below 0.5mm. In absence of adequate data the average fragment numbers were extrapolated; linking known data to the new results by a "match-up" function (Low, 1977). The overall situation is illustrated in Figure 5, which also shows some of the approximations by Gillespie (1977). Another aspect was the extrapolation to large drop pair behavior, with the assumption that nearly equally sized, large drops would coalesce. The importance of this assumption will be discussed later.

With these parameterizations of experiments and some additional assumptions (as specified above), it is now possible to calculate the 4913 breakup and 545 coalescence coefficients of the type described by List and Gillespie (1976) and which form the coalescence and breakup matrix. Fortunately only 2601 of all the terms remain non-zero. They form the basis for the modelling of the evolution of raindrop spectra.

3. THE RAIN SHAFT MODEL

The calculations involving the new experimental data were carried out within the same bounds of the shaft model by Gillespie and List (1978) (i.e. 1-dimensional dependence of z and steady state). The equation controlling the evolution of the raindrop spectrum is the kinetic equation:

$$\frac{\partial n(m)}{\partial t} + \nabla \cdot n(m)\vec{V}_T(m) = C(m) + B(m), \qquad (1)$$

where n(m) is the number density in the mass interval m to m+dm, $V_T(m)$ is the drop's terminal velocity as calculated with the formula by Best (the drops are assumed to always be at terminal speed, even after collision and breakup), C(m) is the rate of production by coalescence of drops with mass between m and m+dm, and B(m) is the rate of creation of drops in the m category due to breakup. Both C and B consist of two terms, one deals with the positive contribution by which an m-drop is created either by coalscence of two smaller drops or by breakup involving at least one larger drop, while the second term deals with the losses of m-drops either because they coalesce and fall into a bigger category or because they are involved in breakup and fall into other (normally smaller) size bins (Gillespie and List, 1978).

In steady state equation 1 reduces to:

$$\frac{\partial n}{\partial z} + V_T^{-1}(C - B - n\frac{\partial V_T}{\partial z}). \qquad (2)$$

By giving the model a MP spectrum at the 2km level for example, this equation is integrated downward to find the drop spectrum as a function of height.

Figure 6 shows the evolution of two spectra, starting MP at the 2km level with two different rainfall rates. The resulting spectra at the ground (0km) show a distinct departure from MP. Four specific points can to be made:

1) After some fall the spectra do not conserve their MP character.
2) There are a great many small drops to be found near the ground with sizes smaller than 1mm.
3) While their concentration is very low, the large drops (D_L=5mm) are not depleted as expected. There is a particle diameter beyond which the concentration is even higher then at the 2km level.
4) The existence of equilibrium distributions, as previously observed, is not established and needs further tests by modelling.

For comparison the Gillespie-List (1978) data are also shown. The difference between the new and old results is caused by the use of the new data set which includes regions where coalescence is dominant. Different assumptions about the outcome of collisions of large drops with nearly equal mass must have also had an effect.

Since rainfall rate is conserved, the model

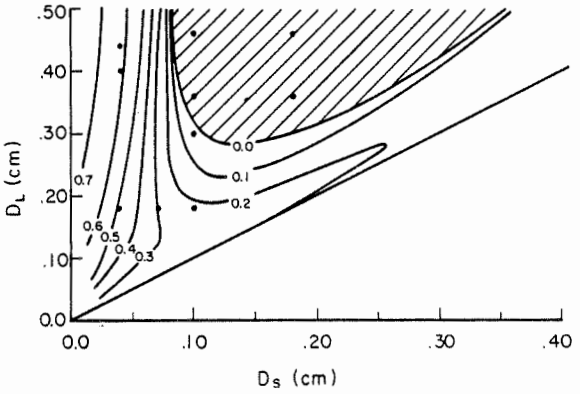

Figure 4. Values for coalescence efficiency E for colliding drop combinations; the dots represent the measuring points; the diagonal line has E=0.19.

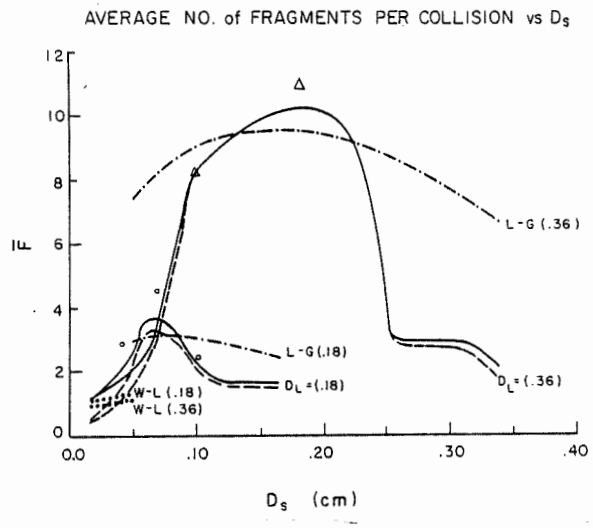

Figure 5. Average number of fragments per collision for drop pairs with D_L=0.36 and 0.18cm; solid lines for overall fragments, dashed lines for breakup only; values from List and Gillespie (1976) and Whelpdale and List (1971) for comparison.

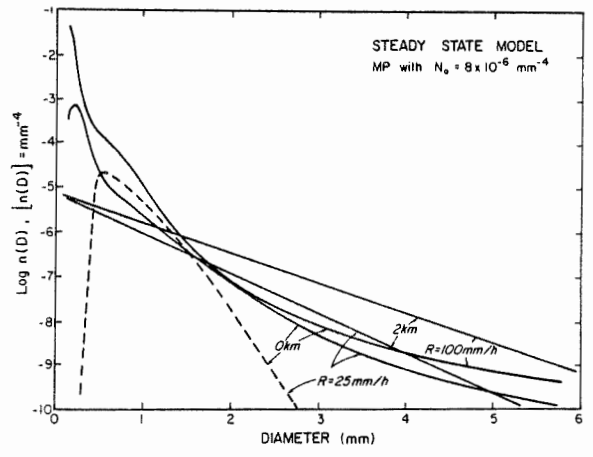

Figure 6. Evolution of a rain drop spectrum in a one-dimensional shaft model, starting from Marshall-Palmer at the 2km level, for two rainfall rates; dashed line from Gillespie (1977). Note the high number concentration of small drops as they develop during the fall.

was also tested in this respect: it gave a change of only 0.007% over the 2km fall distance.

In the evolution of the liquid water content per size interval more water is concentrated in the size-region below 1.5mm. The evolution of the rainfall rate per drop size interval is given in Figure 7. It shows that the small drops with diameters below 1.5mm dominate again and produce most of the precipitation at the ground.

Figure 8 represents the total liquid water content (or mass density) as a function of height for three rainfall rates. A sorting effect is particularly evident for the curve for 100mm/h. The increase can be explaned by considering two factors: the first is the convergence of mass density due to the velocity convergence (accounting for 8%), the second is the concentration increase by the breakup and coalescence processes which caused the shift to smaller drops with smaller fall speeds. This vertical change in rainfall rate is given by:

$$\frac{\partial R}{\partial z} = \frac{\partial}{\partial z}\sum_i (m_i V_i) = \sum_i \left(m_i \frac{\partial V_i}{\partial z} + V_i \frac{\partial m_i}{\partial z}\right) \qquad (3)$$

The sums are taken over all the mass bins.

4. CONCLUSIONS

The extension of the experimental data base on coalescence and breakup of rain-sized drops and its parameterization, as well as the addition of some arguments about events involving large, nearly equally sized drops, results in a slower evolution of spectra (as compared to Gillespie and List (1978)) and to distributions which are no longer Marshall-Palmer. In particular, the new model produces large numbers of small drops in a region where it was hitherto assumed that they are depleted through collection by larger drops.

The following aspects need study and clarification by experiment: the details of the collision/breakup process in general and in particular for nearly equal-sized drops; and the pressure dependence of these mechanisms. From the numerical modelling point of view, sensitivity to different assumptions, time dependence and the introduction of warm-rain microphysics into two-dimensional cloud models have high priority.

ACKNOWLEDGEMENTS. This study was sponsored by the Canadian Atmospheric Environment Service, the National Scientific and Engineering Research Council of Canada, and the US National Oceanic and Atmospheric Administration, Department of Commerce, through its National Severe Storms Laboratory, Norman, Oklahoma.

REFERENCES

Gillespie, J.R., 1977: Numerical modelling of the evolution of drop size distributions in rain. Ph.D. thesis, University of Toronto, pp.147.

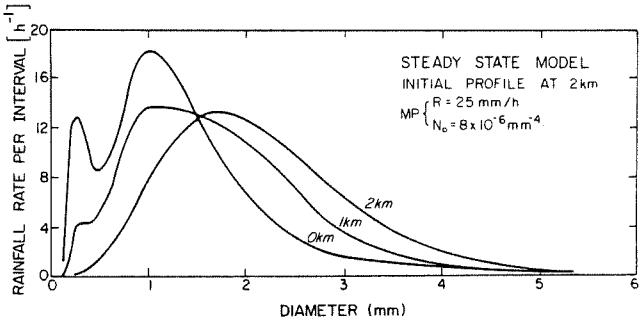

Figure 7. Rainfall rates in the different size intervals; starting from a Marshall-Palmer distribution at the 2km level.

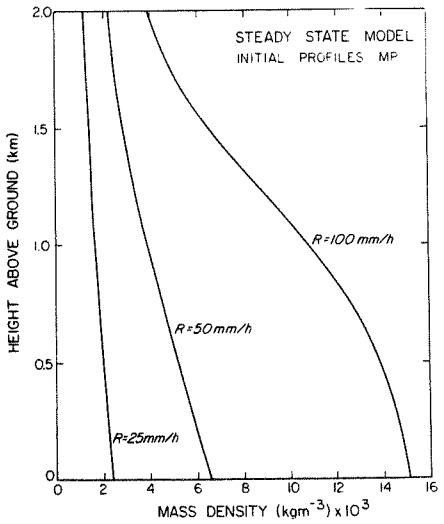

Figure 8. Liquid water content (or mass density) evolution as the rain, characterized by different rainfall rates, approaches the ground; increases are due to lowering of fall velocities and shift of the water substance to smaller drops which fall slower; the effect is more pronounced for high rainfall rates with more collison/breakups.

Gillespie, J.R., and R. List, 1978: Effects of collision-induced breakup on drop size distributions in steady-state rainshafts. Pure Appl. Geophys., 117, 4, 599-626.

List, R., and J.R. Gillespie, 1976: Evolution of raindrop spectra with collision-induced breakup. J. Atmos. Sci., 33, 2007-2013.

Low, T.B.,1977: Products of interacting raindrops, experiments and parameterization. Ph.D. thesis, University of Toronto, pp.230.

McTaggart-Cowan, J.D., and R. List, 1975a: An acceleration system for water drops. J. Atmos. Sci., 32, 1395-1400.

--------- ------, 1975b: Collision and breakup of water drops at terminal velocity. J. Atmos. Sci., 32, 1401-1411.

Whelpdale, D.M., and R. List, 1971: The coalescence process in raindrop growth. J. Geophys. Res., 76 2836-2856.

(For more detailed literature revue see referenes in above mentioned papers.)

DISSOLUTION OF GASES IN RAIN

A. K. Mukherjee

Meteorological Office
Pune, INDIA

Introduction

For several years considerable effort has been devoted to the analysis of removal of atmospheric contaminant by rain. The bulk of the work however has been devoted to aerosol removal, Most authors considered trace gases to be totally soluble in rain and hence considered washout of gas from the theory of irreversible washout usually applied to aerosols. Noted exception is Postma (1970) who in his excellent paper on'Effect of solubilities of gases on their scavenging by raindrops' demonstrated that the total solubility approach to gas scavenging is not appropriate.

Hales (1972) gave a theory of gas scavenging by rain. He pointed out the follow-important processes in this connection.

1. Washout rate of a gas will be lowered as the precipitation becomes saturated with the pollutant gas in question.

2. A falling raindrop may become super-satured (in gas concentration) with respect to the ambient atmosphere and a desorption of pollutants may occur.

From these it follows that the reversible nature of gas washout necessitates knowledge of spatial distribution of conventration of the pollutant gas in the atmosphere prior to the assessment of washout rates. The absorption - desorption phenomenon introduces a possibility of redistribution of precipitation. Considering these, Hales gave a generalised theory of gas scavenging to provide a fundamental basis for gas washout analysis.

Hales' approach has got the following limitations -

1. The gas is supposed to be removed by raindrop only after it has fully grown. The removal of gas from air even at the stage of formation of cloud droplets has not been taken into account.

2. A general theory of removal of gas should not only attempt to calculate the removal of gaseous pollutants but should also be applicable in the case of dissolution of constituent soluble gases of air.

In the present paper an attempt has been made to remove the above limitations. Whereas Hales tried to develop his theory on the basis of diffusion of pollutant in gas phase followed by the diffusion of dissolved gas in liquid phase, the present approach is from the concept of gaseous molecules striking the cloud (or rain) drops. It may be stated here that a number of micro-physical phenomena involving liquid phase should emerge in a total treatment of removal of gas by rain or cloud. Particularly important is possible chemical reaction in the liquid. But this has not been dealt with here. Whereas this has not been ignored, the process has not been followed. Thus, the present approach may be treated as a first attempt in the direction of removal of gases by cloud and raindrops from the considerations of kinetic theory of gases purely on a physical basis.

2. Derivation of the basic equations :

The first question is - how any soluble gas can enter into rain water. From the consideration of airflow round a spherical obstacle, it can be shown that the gas molecules will be deflected around the cloud particles and hence should not come in contact with them. Hence they will not be dissolved by sweeping action of moving cloud particles of rain drops. They can only dissolve when the gas molecules hit the cloud droplet (or rain drop) because of the random translatory motion of the molecules.

Let us assume that a droplet is growing in favourable conditions. At the same time it is capturing some of the molecules of a soluble gas. Let r be the radius of the droplet and m_r be its mass. The rate of growth of cloud droplet by condensation of water vapour on it is given by

$$\frac{dm_r}{dt} = 4\pi D r (\rho - \rho_r) \quad \text{---- (1)}$$

where D is the molecular diffusion coefficient of water vapour, ρ_r the water vapour density at the surface of the droplet and ρ that of the ambient air.

Rate of dissolution of a soluble gas on a droplet of radius r is proportional to the area $4\pi r^2$ and the mass of gas mole-

cules striking unit area per unit time of the droplet denoted by μ. Rate of dissolution of the gas will then be given by

$$\frac{dS_r}{dt} = A\mu 4\pi r^2 \quad \text{..... (2)}$$

where S_r is the mass of gas dissolved and A is the fraction of gas captured by the droplet. It is a fraction with value quite low for slowly soluble gas and may be assumed to be nearer unity for very highly soluble gas like ammonia. Again we know

$$m_r = \frac{4}{3}\pi r^3 \quad \text{..... (3)}$$

Assuming the density of water as unity the concentration of the dissolved gas in the droplet is given by

$$C_r = S_r/m_r \quad \text{..... (4)}$$

From these equations we get

$$\frac{dC_r}{dr} = \frac{d}{dr}\left(\frac{S_r}{m_r}\right) = \frac{1}{m_r}\frac{dS_r}{dr} - \frac{S_r}{m_r^2}\frac{dm_r}{dr}$$

$$= \frac{1}{m_r}\left\{\left(\frac{dS_r}{dt}\Big/\frac{dm_r}{dt}\right) - \frac{S_r}{m_r}\right\}\frac{dm_r}{dr}$$

From equations (1) to (4) we get

$$\frac{dC_r}{dr} = \frac{3A\mu}{D(\rho-\rho_r)} - \frac{3C_r}{r} \quad \text{..... (5)}$$

Thus we get the rate of change of concentration of dissolved gas with the size of the drop. Now let us consider the rate of change of concentration with time.

$$\frac{dC_r}{dt} = \frac{d}{dt}\left(\frac{S_r}{m_r}\right) = \frac{1}{m_r}\frac{dS_r}{dt} - \frac{S_r}{m_r^2}\frac{dm_r}{dt}$$

$$= \frac{3A\mu}{r} - \frac{3C_r D(\rho-\rho_r)}{r^2} \quad \text{..... (6)}$$

Now let us consider the significance of the term A. This is the fraction of gas captured by the drop. For this we can assume that

$$A = a(C_s - C_r) \quad \text{..... (7)}$$

where a can be assumed to be constant at constant temperature provided there is no chemical reaction in the liquid phase other than the reversible reaction of the dissolved gas and water. C_s is the solubility of the gas in water and is constant at constant temperature and partical pressure. Thus equations (5) and (6) becomes

$$\frac{dC_r}{dr} = \frac{3a\mu(C_s - C_r)}{D(\rho-\rho_r)} - \frac{3C_r}{r}$$

$$= \frac{3a\mu C_s}{D(\rho-\rho_r)} - \frac{3a\mu C_r}{D(\rho-\rho_r)} - \frac{3C_r}{r} \quad \text{..... (8)}$$

$$\frac{dC_r}{dt} = \frac{3a\mu C_s}{r} - \frac{3C_r}{r}\left\{a\mu + \frac{D(\rho-\rho_r)}{r}\right\} \quad \text{..... (9)}$$

By expressing the concentration in mole fractions 'X' we may write

$$\frac{dX_r}{dr} = \frac{3a\mu X_s}{D(\rho-\rho_r)} - \frac{3a\mu X_r}{D(\rho-\rho_r)} - \frac{3X_r}{r} \quad \text{..... (10)}$$

$$\frac{dX_r}{dt} = \frac{3a\mu X_s}{r} - \frac{3X_r}{r}\left\{a\mu + \frac{D(\rho-\rho_r)}{r}\right\} \quad \text{..... (11)}$$

Using Henry's law we may write

$$X_s = H \cdot y \quad \text{..... (12)}$$

where y is mole fraction gas in gaseous phase, and H is a constant. Substituting this in equations (10)and (11) we get

$$\frac{dX_r}{dr} = \frac{3a\mu Hy}{D(\rho-\rho_r)} - \frac{3a\mu X_r}{D(\rho-\rho_r)} - \frac{3X_r}{r} \quad \text{..... (13)}$$

$$\frac{dX_r}{dt} = \frac{3a\mu Hy}{r} - \frac{3X_r}{r}\left\{a\mu + \frac{D(\rho-\rho_r)}{r}\right\} \quad \text{..... (14)}$$

Thus these two equations give us the variation of concentration of dissolved gas in cloud and raindrops with respect to the concentration of the gas in ambient air. It may be pointed out that although the term y directly expresses the concentration, the term μ is indirectly connected with concentration of gas.

3. Special Cases

Let us now consider the influence of each factor in the equations :

3.1 Dependence of solubility of gas :

In equations (8) and (9) we find that rate of dissolution of gas is directly related to the solubility of the gas. This gives an interesting information about the ambient temperature. The solubility of a gas decreases rapidly with increase in temperature. Thus the lower the ambient temperature, the greater is the rate of dissolution. In case of a raindrop further growth by diffusion can be neglected. In that case, equation (9) gives us a clearer picture of connection of concentration with solubility of gas in rain. Again in this condition if $C_r \to 0$ as in the case when raindrops enter into a polluted area containing soluble gases,

$$\frac{dC_r}{dt} \simeq \frac{3a\mu C_s}{r} \quad \text{..... (15)}$$

which means that rate of change of concentration is directly proportional to the solubility in the initial stage of dissolution of gas by rain.

3.2 Dependence on degree of supersaturation :

As degree of supersaturation increases $(\rho - \rho_r)$ increases. Equation (5) indi-

cates that when $(\rho-\rho_r)$ is low, the rate of dissolution in the cloud droplets is more. In case $(\rho-\rho_r)$ is low and r is big as in case of raindrops, we may neglect $3c_r/r$ in equation (5) at least when c_r is small. In that case the rate of dissolution of the gas becomes almost inversely proportional to the supersaturation of course within the limit of equation (7). Again equation (6) indicates that under conditions of higher supersaturation the rate of dissolution is lower and vice-versa.

In case $(\rho-\rho_r)$ becomes zero, there will be no growth of the drop according to equation (1). Then

$$\frac{dc_r}{dt} = -\frac{d(c_s-c_r)}{dt} = \frac{3a\mu(c_s-c_r)}{r} \quad \ldots (16)$$

or (Cs - Cr) will decrease exponentially with time.

During the initial stage of cloud growth in presence of the gas, we may take r to be very small and $(\rho-\rho_r)$ of quite high value so that (from equation 5)

$$\frac{dc_r}{dr} \simeq -\frac{3c_r}{r} \quad \ldots\ldots (17)$$

This means smaller drops should become more concentrated than the bigger drops in the initial stage of cloud growth. This is otherwise understandable since smaller drops have bigger surface to volume ratio than the bigger drops.

In case $(\rho-\rho_r)$ becomes negative, i.e. when the raindrop moves in an unsaturated environment, equation (6) indicates that the concentration of gas will increase with lapse of time. But this is not very simple, since the size of the drop will also change due to evaporation. Looking at equation (5) we find that the radius of the drop is decreasing and hence as the particle becomes smaller the concentration would increase.

3.3 Variation of concentration of gas :

A raindrop may pass through a highly polluted area and then to an area which is practically unpolluted. While passing through polluted area the raindrop dissolves the pollutant gas as per equation (15). But when it goes to the unpolluted area, we may have $y \simeq 0$ and $\mu \simeq 0$. Then

$$\frac{dx_r}{dt} = -\frac{3x_r D(\rho-\rho_r)}{r^2} \quad \ldots (18)$$

which means the gas will be desorped, a condition mentioned earlier.

A complication comes when $(\rho-\rho_r)$ becomes negative. In such a case dx_r/dt will be positive as per equation (18) which means that the water of the drop will evaporate to increase X_r. We should, therefore, consider this process from a different angle. From equation (2) we have

$$\frac{ds_r}{dt} = A\mu 4\pi r^2 = a(c_s-c_r)\mu 4\pi r^2 \quad \ldots (19)$$

But $\lim y \to 0, c_s \to 0$ as per Henry's law,

Hence $$\frac{ds_r}{dt} = -a c_r \mu 4\pi r^2 \quad \ldots (20)$$

Whereas equation (18) can be used for a supersaturated environment only and presents complications for saturated and unsaturated environments, equation (19) is of general applicability. For a general statement we may write that if the concentration of environmental gas is so low that the saturation concentration, at the existing partial pressure is less than Cr then the raindrop or cloud droplet would desorp. Thus a raindrop may serve as a carrier of gaseous pollutants and serve to redistribute.

4. Removal of carbon dioxide by monsoon rain water :

Cloud particles and raindrops form in air where carbon dioxide is a natural ingradient. Barrett and Brodin (1955) pointed out that all natural water should contain dissolved carbon dioxide and at 25°C rain water should have pH = 5.7. This value is arrived at considering the dissolved carbon dioxide to be in equilibrium with the atmospheric gas. Or, in other words, any rainwater showing pH greater than 5.7 should be regarded as alkaline. This view has been accepted by WMO (1978). But Mukherjee (1957, 1964, 1978) has repeatedly shown that pH of rain water measured at Calcutta (an inland station), Bombay (a coastal station) and over the sea on board a research vessel 400 km. away from the nearest land the pH is always between 6.0 and 7.0. This indicates that carbon dioxide may not be fully dissolved. The above equations can be used to understand why it is so. The arguments are as follows.

(1) In the tropics the temperature of the cloud droplets and the raindrops should be higher than that in extratropics. Thus the value of c_s is lower and as per equations (8), (9) and (15) the rate of dissolution of carbon dioxide should be low.

Even if we assume that the life of cloud droplet is long enough to dissolve carbon dioxide fully, when they combine and fall they come down to environment of higher temperature. The value of c_s decreases with rise in temperature. Thus if the rain drop falls to the surface of environmental temperature 30°C and attain equilibrium at that temperature, it would be unsaturated when brought to 25°C (in the laboratory) and hence the pH may be shown as greater than 5.7.

(2) In the condition of summer monsoon in India, the air is saturated upto 500 mb. In that case $(\rho-\rho_r)$ is likely to be greater than at other places. Equations (5) and

(6) show that rate of dissolution of carbon dioxide should be slower with higher values of $(\rho - \rho_r)$. Moreover according to equation (1) the growth of the droplet is faster. Thus carbon dioxide may not come into equilibrium by the time cloud droplets mature and combine to form raindrops and subsequently fall.

In most of the places, the subcloud layer may be unsaturated. As per arguments in 3.2 it can be shown that the concentration of dissolved gas would increase. In the sub-cloud layers during the summer monsoon in India air is fully saturated. This would not help the increase in concentration of the gas.

Summarising we get that in summer monsoon condition the rate of increase in concentration during growing stage of cloud particles is slow and again due to absence of evaporation of the drops in subcloud layer the concentration does not increase. Moreover, the process of cloud formation may be very fast and hence the life of water droplet in air may be short. Net result is that in the condition of summer monsoon the rainwater may not have dissolved carbon dioxide in equilibrium with the atmospheric gas.

In the equations (8) and (9) the term 'a' depends on chemical composition of the raindrop and also on the chemical composition of the contaminants. In trying to explain the pH observations, this has not been taken into consideration. There may be other explanations for the observations that pH in monsoon rain water is greater than 5.7. The one given in this paper is from physical considerations only.

References.

Barrett, E. and Brodin, G., (1955) : The Acidity of Scandinavian Precipitation, Tellus, 7 (2), 251-257.

Hales, J.M. (1972) : Fundamentals of the Theory of Gas Scavenging by Rain, Atmos. Environ. 6 (9), 635-659.

Mukherjee, A.K. (1957) : Hydrogen Ion Concentration of Monsoon Rain Water at Calcutta, Indian Jour.Met.Geophys.8(2), 321-325.

Mukherjee, A.K. (1964) : Acidity of Monsoon Rain Water, Indian Jour.Met.Geophys.15 (2), 267-271.

Mukherjee, A.K. (1978) : pH of Monsoon Rain water over sea, Indian Jour.Met.Geophys. 29 (4), 749.

Postma, A.K. (1970) : Effect of Solubilities of gases on their Scavenging by Raindrops, Precipitation Scavenging (1970) Edited by R.J.Engelmann and W. G.N.Sliner, Co-ord. 247-256.

World Meteorological Organisation (1978) International Operations Handbook for Measurement of Background Atmospheric Pollution, 44.

THE SHAPE OF RAINDROP SPECTRA FOR DIFFERENT SITUATIONS AND AVERAGING PERIODS

V. G. Plank, R. O. Berthel and L. V. Delgado

Air Force Geophysics Laboratory
Bedford, Massachusetts U.S.A.

1. INTRODUCTION

Joss and Gori (1978) have presented ground-based disdrometer data for widespread and thunderstorm rain which indicate that the shape of the raindrop size distribution spectra is exponential for "long" averaging periods (32 to 512 minutes) but that it departs from exponential (toward monodispersity) when the averaging periods become smaller, approaching a 1 minute, or "instant", period. They also found that the departures from exponential were more pronounced at small rainfall rates than at larger rates.

Considerable rain data have been acquired in the the last several years by the cloud physics MC-130E aircraft of the Air Force Geophysics Laboratory (AFGL). These data were acquired using a one dimensional optical array spectrometer, described by Knollenberg (1970, 1972) and produced by Particle Measuring Systems (PMS), Inc., Boulder Colorado.

Rain data of this kind were selected for four different situations of aircraft flight. Two were situations of widespread rain of moderate to heavy intensity which were sampled near Talladega, Alabama on 23 February 1977 and between Little Rock, Arkansas and Memphis, Tennessee on 2 March 1978. The other two were situations of showery rain of light to moderate intensity that were sampled near Wallops Island, Virginia, on 22 March 1977, and near the Kwajalein Atoll, in the Marshall Islands, on 27-28 June 1977. Other additional rain situations are also being investigated but the analysis of these have not been completed as of the date of this abstract.

The data for the four cited rain situations were analyzed in a manner permitting comparisons with the findings of Joss and Gori. A non-dimensional plotting technique, described by Sekhon and Srivastava (1970) was used to ascertain the shape of the raindrop spectra. The aircraft data for each situation were first analyzed and plotted for the basic resolution time of the PMS instruments (the 1 second buffer accumulation time). The 1 second data were next combined and averaged over longer sampling periods, 5, 10, 50, 100 and 500 seconds, respectively, limited by the total flight time of the aircraft sampling. The data for each averaging period were also separated into two categories of liquid water content which were (1) smaller than the average of the total data set and (2) larger than the average of the total data set.

2. THE DETERMINATION OF SPECTRAL SHAPE

The exponential relation describing the size distribution of raindrops is given by, (Marshall and Palmer, 1948),

$$N = N_o e^{-\Lambda D}, \text{ No. cm}^{-4} \qquad (1)$$

where N is the number concentration of the raindrops (per diameter bandwidth) and D is the drop diameter.

The liquid water content of such distribution, integrated from $D = 0$ to $D = \infty$, is

$$W = \frac{\pi}{6} \rho_w \int_0^\infty N D^3 \, dD \qquad (2)$$

or, from equation 1,

$$W_\infty = \frac{\pi \rho_w N_o \Gamma(4)}{6 \Lambda^4} \text{ g cm}^{-3} \qquad (3)$$

The median volume diameter of the distribution is

$$D_o = \frac{\alpha}{\Lambda} \text{ cm} \qquad (4)$$

where, for integration from $D = 0$ to $D = \infty$, $\alpha = 3.67$ (Atlas, 1953).

Sekhon and Srivastava (1970) have pointed out that equations 3 and 4 may be used to write equation 1 in the non-dimensional form

$$\frac{\rho_w N D_o^4}{W_\infty} = \frac{\alpha^4}{\pi} e^{-\alpha D / D_o} \qquad (5)$$

They further note that a plot of $\rho_w N D_o^4 / W_\infty$ versus D/D_o on semi-logarithmic paper will yield a straight line of slope α and intercept α^4 / π. For the Atlas value of α, the intercept is 57.7. A plot of this equation is shown in Fig 1, labeled $n=o$.

Spectral shapes other than exponential may also be recognized on a diagram of the Fig 1 type. For example, one family of curves for which the equations of N, W_∞ and D_o can be written and plotted non-dimensionally is the family of "moments of exponentials" for which

$$N = N_n D^n e^{-\Lambda n D} \qquad (6)$$

$$W_\infty = \frac{\pi}{6} \rho_w N_n \int_0^\infty D^{3+n} e^{-\Lambda_n D} dD , \quad (7)$$

from equations 2 and 6, or

$$W = \frac{\pi}{6} \rho_w N_n \frac{\Gamma(4+n)}{\Lambda_n^{4+n}} , \quad (8)$$

when integrated. Additionally,

$$\Lambda_n = \frac{\alpha}{D_0} \quad (9)$$

where

$$\alpha = 3.67 + n . \quad (10)$$

From equations 6, 8, 9 and 10

$$\frac{\rho_w N D_0^4}{W_\infty} = \frac{6(3.67+n)^{4+n}}{\Gamma(4+n)\pi} \left(\frac{D}{D_0}\right)^n e^{-(3.67+n) D/D_0} \quad (11)$$

Plots of this equation for n values of 1, 10, 10^2 and 10^3, also for -1, -2 and -3, are shown in Fig 1. It is seen that, with the increasing positive values, the spectral shape is tending more and more toward monodispersed. With the negative values, the spectral shape becomes concave upward, relative to the simple exponential for n=o.

When size distribution information is obtained instrumentally, the data are truncated at some minimum size, dictated by the sensitivity of the instrument, and they may also be instrumentally truncated at some maximum size. Moreover, there are physical size limits that govern the largest size drops that will exist in any given situation (for example, the breakup size). Instrumental data are also classified data, in that the number concentration information is obtained for definite size classes of the hydrometeors.

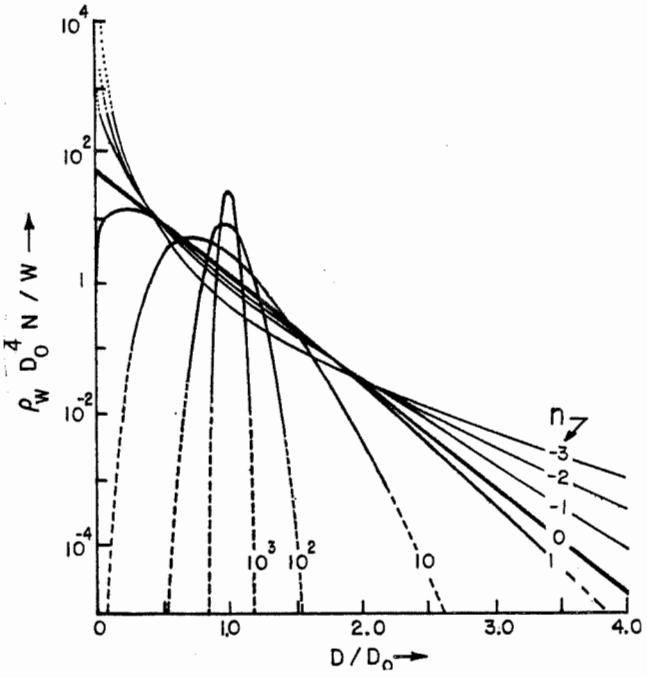

Fig 1. Spectral shapes plotted from Equation 11.

It is beyond the scope of this abstract to consider and illustrate the various ways that truncation and classification cause modification of the spectral shapes relative to those shown as examples in Fig 1. Suffice it to say that unless the lower and/or upper diameter truncation is very severe the spectral shapes will not differ markedly from those for no truncation. Classification of the data causes departures from "the comparable continuous-distribution-function values" but these departures, too, are rather small, providing that the number of size channels used for counting exceeds 10, or so. Another effect with classification occurs because the threshold number count in any given channel with the 1DP instrument is 1 count per second. This means that, in the nondimensional plots of the aircraft spectra, no points will be plotted in the lower portion of the diagram, where, in Fig 1, the curves are dashed.

3. THE AIRCRAFT DATA AND AVERAGING METHODS.

Four rain situations were selected for analysis and discussion herein, as cited previously in the introduction. The aircraft PMS data for these situations were acquired with a one-dimensional particle array spectrometer having a wide angle probe. This so-called 1DP instrument was designed to sample precipitation size particles. In rain, the instrument provides size distribution information for fifteen counting channels of nominal width equal to 300 μm over a diameter size range from 202 μm to 4660 μm. The actual widths of the channels vary somewhat from nominal for reasons discussed by Knollenberg (1975). The accurate widths are known, however, and were used in all computations leading to the non-dimensionalized spectra.

The sampling volume of the 1DP probe for an indicated airspeed of 150 kts (77.2 m s^{-1}, which was held constant for all sampling passes) is variable for the different size channels from about .05 to .13 m^3 s^{-1}. The average or nominal value for all channels is approximately .1 m^3 s^{-1}. The sampling volume also varies somewhat depending on the particular altitude-temperature relationships between indicated and true air speed, by about five percent, relative to nominal. The buffer accumulation time of the instrument, which establishes the minimum sampling resolution, is one second.

Computations and non-dimensional plotting were first accomplished, for the four rain situations mentioned, for the spectral data of 1 second resolution. (These were channel number-count data normalized per cm^3 of volume per cm bandwidth.) The mean liquid water content was computed for the entire flight period through rain for each of the days. These periods were from 2222 to 2246 GMT for the widespread rain of 23 February 1977 near Talladega, Alabama, from 2037 to 2103 GMT

for the widespread rain of 2 March 1978, between Little Rock, Arkansas and Memphis, Tennessee, from 1413 to 1419 GMT for the showery rain of 22 March 1977 near Wallops Island, Virginia, and from 2313 GMT, 27 June 1977, to 0115 GMT, 28 June 1977, for the showery rain near the Kwajalein Atoll in the Marshall Islands.

From knowledge of the mean liquid water content value for the flight period, the one second spectral data could be separated into two liquid water content categories, of samples having individual values greater than the mean and less than the mean. Non-dimensional computations and plotting were accomplished separately for each category.

The plots of these data for 23 February and 22 March 1977 are shown in the upper diagrams of Figs 2 and 3. (There is insufficient space in this abstract to also illustrate the plots for 2 March 78 and 27 June 1977. But, we will comment about these situations later.) The left hand diagrams of Figs 2 and 3 show the data for less than average water content; the right hand diagrams show the data for greater than average water content.

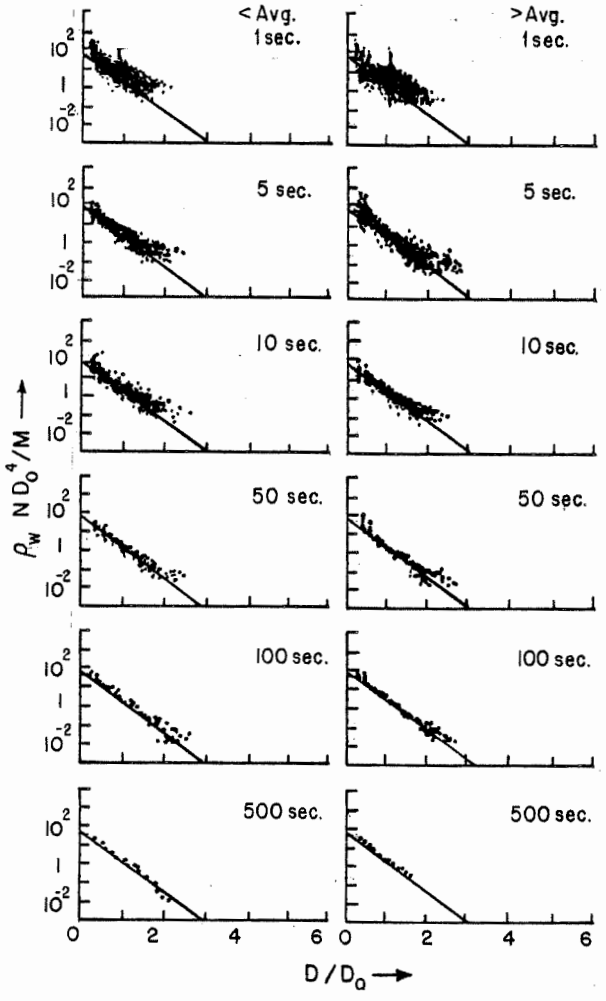

Fig 2. Non dimensional spectra as a function of averaging interval for rain flight of 2 March 1977 near Talladega, Alabama Samples with less than average water content are shown at left. Those with greater than average content are shown at right.

The number count data were next summed and averaged for successive five second intervals of flight and the mean liquid water content for these "5 second data" was determined and data categorization and plotting were accomplished for the "below mean" and "above mean" spectra. These plots are the second diagrams from the top in Figs 2 and 3.

Likewise, the data were summed, averaged, categorized and plotted for successive flight intervals of 10, 50, 100 and 500 seconds, limited by the total sampling time of the aircraft in the given situations. These plots are also shown in Figs 2 and 3.

4. DISCUSSION

The non-dimensionalized data for the widespread rain situation near Talladega, Alabama, of Fig 2, reveal fairly regular behavior relative to the exponential reference line of Sekhon and Srivastava. There is appreciable dispersion of the data for the one second samples which decreases with increased averaging interval. In the one second samples there is also a "spike" of data points near $D/D_0 = 1.0$. This spike is associated with spectra that are monodispersed (all raindrops contained in one

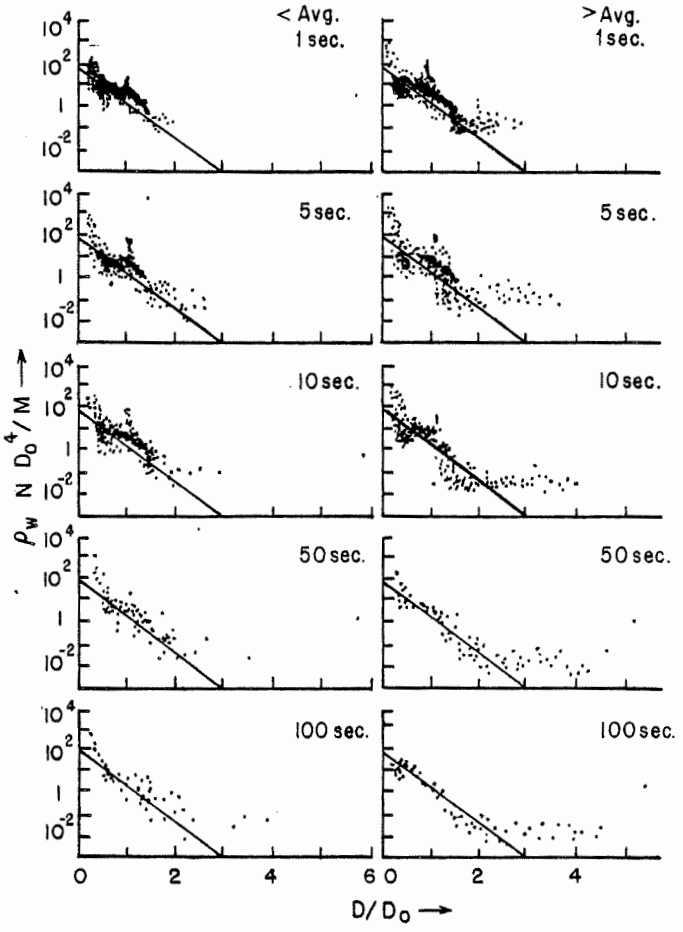

Fig 3. Non-dimensional spectra as a function of averaging interval for rain flight of 22 March 1977 near Wallops Island Virginia, with same format as Fig 2.

single size channel) or with spectra that have a pronounced predominance of liquid water content in a single channel. With averaging, it is seen that the dispersion and features of the one second spectra are rather quickly modified to near exponential. It is also seen that there are few appreciable differences between the spectral plots for the small water content samples as opposed to those for the large water samples.

In contrast to these rather regularly behaved data of Fig 2, the spectra plots of Fig 3, for the showery rain sampled near Wallops Island, Virginia, reveal considerable differences of shape. At one second resolution, the data for both the small and large water contents show a data spike near $D/D_0 = 1.0$ and a definite concavity downward relative to the exponential. Also, numerous of the data points for large D/D_0 occur well above the exponential line. With averaging, the spectral shape does become closer to exponential but even at the longest averaging time of 100 seconds there is considerable departure from exponential in the large D/D_0 portion of the spectrum. It can be seen that the maximum D/D_0 values for this showery rain are appreciably larger than for the widespread Alabama rain.

It may be mentioned, without illustration, that the non-dimensional spectra for the widespread rain situation of 2 March 1978 from Little Rock and Memphis fall "in between" the ones illustrated in Figs 2 and 3. For small D/D_0, the data points adhere reasonably close to the exponential line. But, for large D/D_0, most points fall well above the line. There is little difference, on 2 March 1978, between the spectra of small and large water content. The spectra for the showery rain of 27-28 June 1977, at Kwajalein, reveal very similar characteristics to the showery rain at Wallops, of Fig 3. The Kwajalein data likewise show no appreciable differences between the small and large water content samples.

Thus, to summarize our tentative findings for the four rain situations we have investigated to date, there appears to be shape differences between showery type rain and widespread rain. However, within any one of our four situations, there are no apparent differences for the spectra of small water content as opposed to those of large water content.

For both rain types, the spectra tend to become more exponential with longer averaging intervals. This tendency is very apparent for the widespread rain of Fig 2. However, the tendency is only a very general one in the cases of our other three situations.

Hence, our investigations thus far verify the Joss and Gori (1978) finding that the shape of rain spectra become more exponential with averaging period but we do not note appreciable differences associated with the water content of the samples. We observe that, with showery rain, the samples at one second resolution contain many spectra which have a predominant water content in a single size channel or that have a "peaked shape" (characteristics akin to the Joss-Gori" tendency toward monodispersity"). With averaging, these monodispersed features are rapidly "smoothed out", toward exponential, except for the large D/D_0 points which continue to exceed the exponential even at the longest averaging period. With widespread rain, the tendency from monodispersed toward exponential is not as pronounced.

One possible explanation for our apparent differences relative to Joss and Gori concerning widespread rain may be that our rain data were acquired at cloud level or just below cloud base whereas their data were acquired at the surface level. Many of the smallest rain drops, in a given rain situation, might conceivably evaporate, in whole or part, between a saturated cloud level and a possibly less-than-saturated surface level. Such occurrence would be consistent with our tentative findings as well as with theirs.

The authors wish to acknowledge that the non-dimensional plotting technique was first developed at AFGL by Dr. Robert M. Cunningham, with the assistance of Mr. Morton Glass, AFGL and personnel of Digital Programming Services, Inc., Waltham, Massachusetts.

5. REFERENCES

Atlas, D., 1953: Optical extinction by rainfall. J. Meteor. 10, 486-488.

Joss, J. and E. G. Gori, 1978: Shapes of raindrop size distributions. J. Appl. Meteor., 17, 1054-1061.

Knollenberg, R. G., 1970: The optical array: an alternative to extinction and scattering for particle size measurements. J. Appl. Meteor., 9, 86-103.

Knollenberg, R. G., 1972: Comparative liquid water content measurements of conventional instruments with an optical array spectrometer J. Appl. Meteor., 11, 501-508.

Knollenberg, R. G., 1975: The response of optical array spectrometers to ice and snow; a study of probe size to crystal mass relationships. AFCRL-TR-75-0494, 70 pp. [NTIS No. ADA020276].

Marshall, J. S., and W. McK. Palmer, 1948: The distribution of raindrops with size. J. Meteor., 5, 165-166.

Sekhon, R. S., and R. C. Srivastava, 1970: Snow size spectra and radar reflectivity. J. Atmos. Sci., 27, 299-307.

TURBULENCE EFFECT ON WARM CLOUD MICROSTRUCTURE

II-3.14

K.I. Vasilieva, V.M. Merkulovich, A.S.Stepanov

USSR State Commettee for Hydrology, Meteorology & Control of Natural Environment
Moscow, USSR

Stochastic condensation equations have been obtained for an arbitrary ratio of vapour phase relaxation time and turbulence Lagrangean time scale. An analysis is given of droplet spectrum behaviour under local perturbations of liquid water cloud medium thermohydrodynamics. Numerical modeling results of cloud microstructure under local variations are presented accounting for the condensation and coagulation processes.

When describing turbulized cloud microstructure analyzed are, as a rule, two alternative cases: relative water vapour excess time scale τ is much shorter than the integral Lagrangean turbulence time scale $\mathcal{T}_L$ [1-2] and $\tau \to \mathcal{T}_L$ [3-4]. The first case is typical of the cloud middle part and the second one - of the cloud base and top. Such an approach permits to simplify the derivation of stochastic condensation equations but does not give a possibility to carry out physical and mathematical modeling of the whole cloud life (from its formation to dissipation).

Assume that the following conditions are valid: 1) typical space-time scales of fluctuating parameters variations exist; 2) the scales are much smaller than the corresponding space-time variation scales of parameters averaged over turbulence realizations; 3) the velocity field correlation function can be presented as $\langle v_i'(t)\, v_j'(t_1)\rangle = (1/\mathcal{T}_L)\kappa_{ij}\, \exp(-|t-t_1|/\mathcal{T}_L)$; 4) non-adiabaticity of fluctuations is described by the Burgers approach [4], i.e. by introducing the time scale for pulsation dissipation $\mathcal{T}_L$.

With the method used in [1, 4] one can obtain an equation of stochastic condensation for an arbitrary ratio of τ and $\mathcal{T}_L$:

$$\frac{d}{dt}\frac{f}{\rho} + \frac{\partial}{\partial S}\dot{S}\frac{f}{\rho} - \frac{1}{2}\frac{\partial}{\partial x_i}\kappa_{ij}\left[\frac{\partial}{\partial x_j} + \frac{\partial}{\partial S}A_j\right]\frac{f}{\rho} - \frac{1}{2}\kappa_{ij}\frac{\partial}{\partial S}A_i\left[\frac{t_o+2\tau}{t_o}\frac{\partial}{\partial x_j} + \frac{\partial}{\partial S}A_j\frac{t_o+\tau}{t_o-\tau}\right]\frac{f}{\rho} = 0. \qquad (1)$$

$$\frac{d\theta}{dt} - \frac{1}{2}\frac{\partial}{\partial x_i}\kappa_{ij}\left(\frac{\nu_j}{\gamma_2} + \frac{2\eta_j\tau}{t_o}\right) - \frac{L}{2c_p}\frac{\rho_w}{\rho}\overline{R\dot{S}f} + \frac{1}{4}\kappa_{ij}\rho_w\frac{L}{c_p}\left[\frac{t_o+2\tau}{t_o}\overline{A_i R\frac{\partial}{\partial x_j}\frac{f}{\rho}} + \frac{\tau+t_o}{\tau-t_o}\overline{RA_i\frac{\partial}{\partial S}A_j\frac{f}{\rho}}\right] = 0 \qquad (2)$$

$$\hat{K}\left(\theta + \frac{L}{c_p}\frac{c}{\rho}\right) = 0.$$

$$\hat{K} \equiv \frac{d}{dt} - \frac{\partial}{\partial x_i}\kappa_{ij}\frac{\partial}{\partial x_j} \qquad (3)$$

where f - drop size and hygroscopic substance fraction distribution function; θ - potential temperature; c, m - vapour density and saturated vapour density above clean water surface; ρ - liquid water content; ρ, ρ_w - air and water densities; R, S - drop radius and surface values; κ_{ij}, $\mathcal{D}$ - turbulence and molecular diffusion coefficients for water vapour; F - a correction for drop growth rate $\dot{S}$ due to surface tension and hygroscopic substances effect; L, c_p - condensation latent heat and specific heat for air at constant pressure; T - temperature.

In equations (1)-(3) the following notation is used:

$$\tilde{F} = \overline{FRf}/\overline{Rf}; \quad \gamma_1 = 1 + \frac{L}{c_p T}\frac{c}{\rho} + \frac{L}{c_p\rho}\frac{\partial m}{\partial T}(1+F); \quad \gamma_2 = \gamma_1\overline{Rf}/\overline{Rf}; \quad \vec{\nu} = \frac{\partial}{\partial\vec{x}}\left(\frac{L}{c_p}\frac{c}{\rho} + \theta\right); \quad t_o = 2\tau + \gamma_2\mathcal{T}_L$$
$$\vec{\eta} = \frac{\partial\theta}{\partial\vec{x}} - \frac{1}{\gamma_2}\vec{\nu}; \qquad \tau = \left[4\pi\mathcal{D}\overline{Rf}\right]^{-1}$$
$$\vec{A} \quad \frac{8\pi\mathcal{D}\tau\mathcal{T}_L\rho}{t_o\rho_w} \quad \frac{c_p}{L}\gamma_1\vec{\eta} \qquad (4)$$

In all the cases of repeated use of indeces summing-up is assumed, the line above means integrating over drop and equivalent hygroscopic nucleus sizes. For asymptotic cases when $\tau \ll \mathcal{T}_L$ and $\tau \gg \mathcal{T}_L$ of the equations may have the form obtained in [1, 2, 4].

The analysis of Eqs. (1)-(3) with $\tau \ll \mathcal{T}_L$ has shown that turbulent mixing leads to drop spectrum broadening when even a single pseudo-potential temperature gradient or humidity gradient, or drop concentration gradient, or hygroscopic substances dissolved in cloud water gradient are non-zero. If, for example, non-zero is only the vertical gradient of salt specific content

(μ) in cloud water, and when the initial Gaussian perturbation μ is localized in the region of size a , then the drop size distribution variance behaviour is as follows [5]. At first the variance as a function of distance from the perturbation center has the form of a bimodal curve. At $t = t_0$ the modes coincide in the perturbation center. At $t \ll a^2/\kappa$ the variance increases as $t^{1/2}$ attains maximum and then falls to the initial value as $t^{1/4}$. The time, when the variance achieves and exceeds some given value, depends on meteorological conditions and perturbation parameters.

As this takes place drop spectrum asymmetry at $t < t_0$ decreases with time near the perturbation spectrum and increases away from it. Beginning with the moment t_0 the asymmetry increases in the whole volume.

A more detailed study of thermohydrodynamics effect on cloud microstructure has been carried out by numerical modeling. Let a warm cloud be horizontally homogeneous, a 450-m layer away from the cloud top and base being studied. Assume now the initial drop size distribution be described by the exponent [1] at the effect of salts on drop growth rate being negligible. Let the drop size distribution vary with time only due to stochastic condensation and gravitational coagulation. At the initial instant the local perturbation $\tilde{\theta}$ with the magnitude of -7°C is preset for the cloud layer center. To solve this problem is interesting first of all because it will make it possible to determine natural heterogeneity effect on the cloud medium. On the other hand, the introduction of seeding agents (a mostly used weather modification method) always causes "temperature spots" occurrence, the influence of which on cloud microstructure had not been studied in detail yet.

The above problem has been solved numerically by the explicit scheme with the following parameter values: $K = 4.5 \frac{m^2}{c}$, drop concentration $N = 500$ cm^{-3}, the layer base temperature $T_0 = 283$°K, specific liquid water content $q_w = 0.00834$. At the lower and upper cloud layers the drop size distribution was chosen stationary [1] . Minimum drop size R considered by the scheme was 0.5 μm. The account made for smaller drops could complicate the calculation scheme chosen. The distribution function truncation at point R_0 leads to appearance of drop specific concentration "computational gradient causing additional broadening of distribution. The evaluations made have shown [6] that this distribution broadening rate is about 1 μm/h. Maximum radius $R_N = 456.3$ μm.

The calculation results have shown that due to cooling a cold zone of 30 m diameter is formed (see Fig. 1a). In this zone a sharp increase of humidity P , mean drop radius R and concentration N occur (Fig. 1b). The distribution function variance (Fig. 1c) decreases at first, then increases, the variance as a function of distance of the perturbation center for $t \leq 5$ min being a bimodal one. The coincidence of the modes does not take place as in case of perturbation μ . But one of the modes for 30 min $\geq t \geq 5$ min becomes small. For

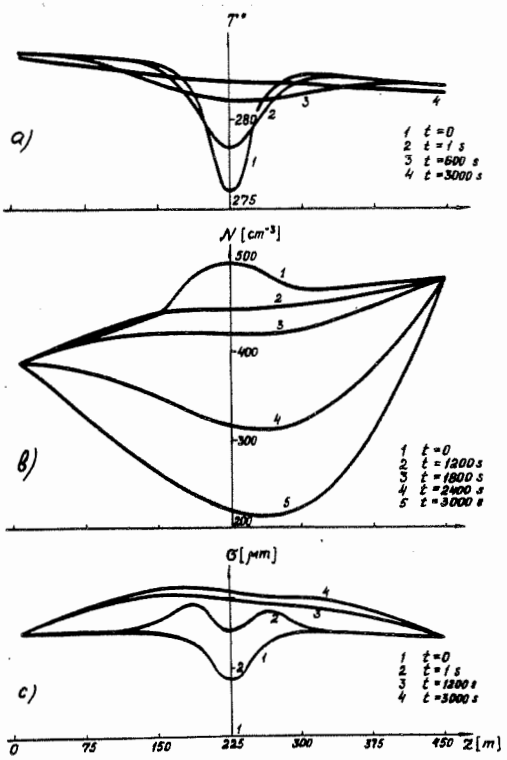

Fig. 1. Temperature (a), drop concentration (b), distribution variance (c) dependences on distance from disturbance center for various periods of time.

$t >$ 30 min the second mode becomes noticeable again, though it is formed at a more distant level from the perturbation center than at $t \leq$ 5 min. Such variance behaviour is due to coagulation process. Intensive variations of concentration and dispersion at $t \leq$ 15 min are mainly caused by turbulence.

Temperature space and time variations are shown in Fig. 1a. The temperature changes rather intensively during first 10 - 15 min. A decrease of the temperature gradient causes a decrease of all microphysical parameters variation intensity (Fig. 1a). It should be noted that at $\bar{R} \leq 10$ μm, $G/\bar{R} \leq 0.3$ and $P \leq 1$ g^{-3} the gravitational coagulation process at first ($t \approx 30$ min) is slow. For longer times coagulation intensity increases rapidly, that may be caused by rather large drops appearing in the system. The coagulation process effect

on fine drop part of the drop size distribution becomes more pronounced after the second maximum of the function $f(R,z,t)R^3$. The curve describing variance for $t > 30$ min space variation becomes bimodal. In this case it is connected with the coagulation process due to which the concentration gradient is formed and variance grows.

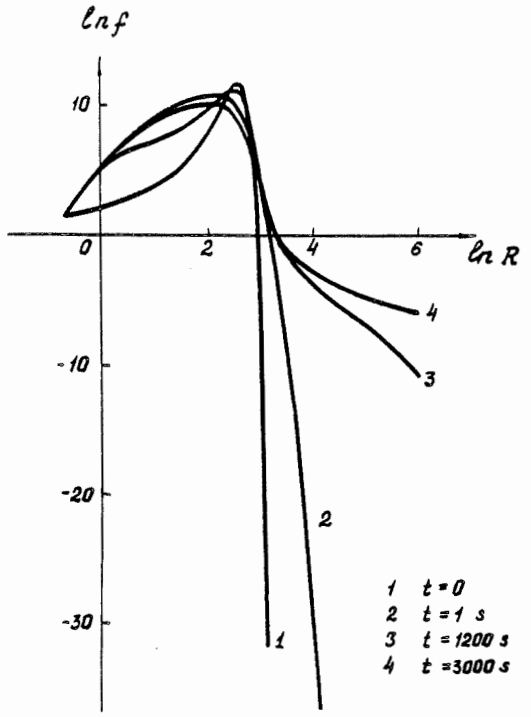

Fig. 2. Drop size distribution at 225 m for various periods of time.

Fig. 2 shows the cloud drop distribution variation with time at z=225 m, i.e. in the center of the cold zone. An increase of the fine drop fraction and the mean radius decrease observed for $t \leq 15$ min are caused by turbulence. A subsequent decrease of these parameters are governed by coagulation.

On the base of the data obtained the integral characteristics have been found: concentration and liquid water content of the drops with the radii more than 100 and 250 μm. If, in view of [7], it is assumed that a cloud is a precipitation one, when the concentration and liquid water content of the corresponding drop size exceeds 1500 m^{-3} and 0.005 g^{-3}, then in the given cloud layer drizzle is formed during 35 min at the levels above 3200 m.

REFERENCES

1. Stepanov S.S. Condensation growth of cloud drops in the turbulent atmosphere. 1975, Izv. Akademii Nauk SSSR. Ser. FAO, v.11, No.1, 27-42.
2. Voloshchuk V.M., Sedunov Yu.S. The kinetics equation of the droplet spectrum evolution in a turbulent medium at the condensation stage of cloud development. 1977, Meteorologiya i hydrologiya, No.3, 3-14.
3. Buykov M.V., Dehtyar M.I. 1968. On the theory of stratiform cloudiness. P.I. General equations. Trudy UkrNIGMI, vyp. 70, 3-20.
4. Stepanov A.S. 1979. Turbulence effect on cloud microstructure at condensation. A theory of stochastic condensation. Hydrometeoizdat, L., 15-29.
5. Merkulovich V.M., Stepanov A.S. 1977. The effects of the hygroscopicity and surface tension on the cloud droplet condensation growth in the turbulent medium. Izv. Akademii Nauk SSSR, v.13, No. 2, 163-171.
6. Stepanov A.S. 1976. On the influence of turbulence on the spectrum of cloud droplets size at condensation. Izv. Akademii Nauk SSSR, Ser. FAO, v.12, No.3, 281-292.
7. Voit F.Ya., Kornienko E.E., Husid S.R. 1972. Some peculiarities of precipitation formation process in cumulus clouds, Trudy UkrNIGMI, vyp. 118.p.61-80.

The Rainrates and Drop Spectra Associated With Different Precipitation Types

Harry C. Vaughan and Gary R. White
Iowa State University
Ames, Iowa U.S.A.

Introduction

Examination of drop spectra from different rain regimes indicate they have unique characteristics, (Strantz, 1971). Our radar echo rain intensity measurements were mapped for a warm shower, Figure 1a, and an air mass thunderstorm, Figure 1b, and each shows distinctly different internal structure of the precipitation intensity and complexity. The work presented here is divided into two parts: first, a description of theoretical upper limits of rain rates computed from a hypothetical mono-dispersed rain, and second: statistical characteristics of actual drop spectra from different rain regimes and their differing characteristics.

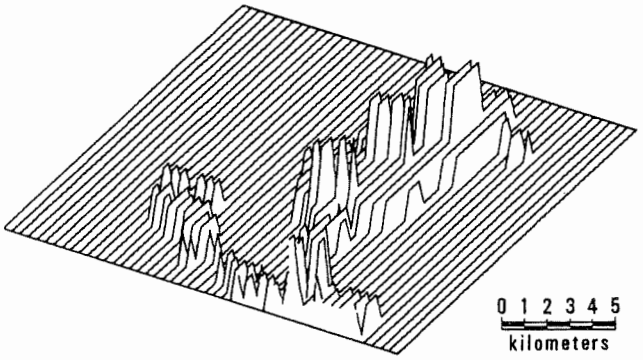

Figure 1a. Three-dimensional radar rain intensity map of nocturnal, 2332 CST, air mass shower, July 9, 1975. The vertical scale expanded tenfold, level 1-0.1 mm hr^{-1}, level 2-0.3 mm hr^{-1}.

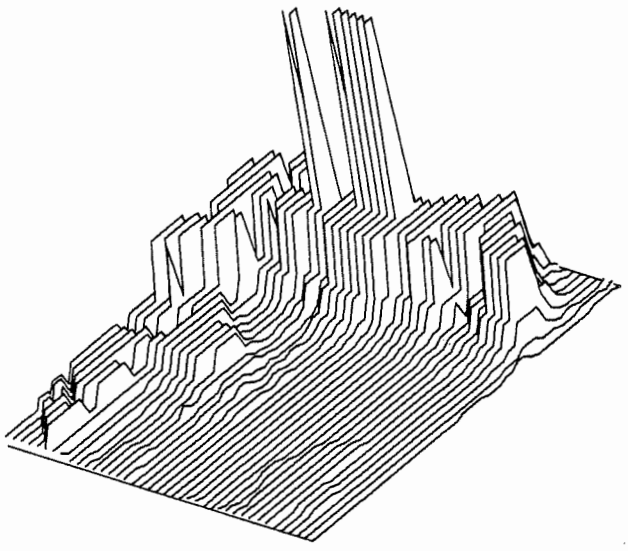

Figure 1b. Three-dimensional radar rain intensity map of early evening, 1901 CST, air mass thunder shower. Level 1-0.1 mm hr^{-1} lower left, level 2-0.3 mm hr^{-1}, level 3-1.0 mm hr^{-1}, level 4-3.0 mm hr^{-1} and level 5-10 mm hr^{-1}.

The objective of the research was to obtain a better understanding of the limits in rain rates from specific types of rain regimes.

Hypothetical Drop Spectra

A review of a number of drop spectra measurements from both mid-continent and tropical drop populations consistently show less than one drop cm^{-2} sec^{-1}, irrespective of the type of precipitation. For concenience, a one drop cm^{-2} sec^{-1}, population was chosen and a hypothetical mono-dispersed rain rate computed for a range of 0.5 to 5 mm diameter drops. The resulting rain rates, Table 1, were then used to compute a modified Marshall-Palmer distribution, where the parameter N_o was computed from the rain rate using the Waldvogel technique, (Waldvogel, 1974). As might be expected, values of W became excessive for drops greater than 2 mm diameter as taken from the primary, hypothetical mono-dispersed, computation. This is not intended to imply that rain rates for short periods may not exceed 150 mm hr^{-1}, only that sustained precipitation approaches an upper limit near this value when averaged over a reasonable period, say 1 hour, Figure 2. The first spectral distribution very nearly describes a stratus drizzle. With no convection such a rain may closely resemble a mono-dispersed spectra with a spectral width of 0.3 mm. The remaining distributions will be discussed in the next section.

Selected Drop Spectra From Mid-Continent and Tropical Rains

Drop spectra measurements from different rain regimes used here have been made by both an electro-mechanical drop spectrometer and dye paper, where each stain diameter was measured to 0.1 mm diameter and the computed drop diameters placed in 0.1 mm increment categories. Minute by minute drop spectra were compared from selected rain regimes. By categorizing rain regimes in regard to the environment under which precipitation developed and grew, it was found the mean drop diameter and standard deviation of the samples tended to remain within defined bounds, Figure 3. Five synoptic and subsynoptic categories were chosen and are described in Table 2. With the possible exception of category I and some aspects of III the spectra distributions are generally exponential with a negative slope. Category I under the simplest conditions of tropical (warm) showers may, for short periods, generate a mono-dispersed spectra with a spectral width of 0.3 mm and nearly symmetrical shape. This is attributed to a nearly homogeneous environment, where all of the drops experience identical growth opportunity. As the conditions become more complex, the drop growth remains within the maximum growth region layer and the spectral range increases.

What is suggested here is that an approximate upper limit may be represented by recomputing rain rates, from the hypothetical drop density used previously, and the mean drop diameter from each category. These values are

given in column 6 of Table 2. Mason-Andrews (1960) suggested no single rainfall intensity-liquid water content relationship could be developed. The present authors agree. This may be in a large part because of general geographical conditions which restrict the development of a single universal emperical description of the precipitation process. The samples cited here were from geographically pure regions, either central Iowa, a simple prairie, or eastern Puerto Rico, a pure maritime environment. In both environments the spectral distribution was quite uniform from one shower to the next. As might be expected from Figure 1a sampling beneath specific locations from similar showers generally provide a spectra unique to that physical location from shower to shower. The assumption made here is that the upper limit of rainfall is governed by activity related to specific synoptic or sub-synoptic scale events. One problem not addressed in these calculations is a decrease in drop population as the mean drop diameter increases. Here we have maintained a single population irrespective of rain rates.

Literature

Strantz, R. Typen der Regentropfenspektren. Meteorol. Rdsch. 24, Heft 1 (1971).

Waldvogel, A. The No Jump of Raindrop Spectra. J.Atmos. Sci. 31:5 (1974).

Mason, B. J. and J. B. Andrews. Drop-size distributions from various types of rain. Quart. J. Roy. Met. Soc. 86:346-353 (1960).

Table I

$\bar{D}$	Computed Rain Rate mm Hr^{-1}	W grams m^{-3}	Computed N_o	Computed Lambda
0.5	2.4	144.8	4,244	3.09
1.0	18.8	1,134.2	8,429	2.19
1.5	63.6	3,836.9	12,654	1.79
2.0	150.8	9,097.7	17,873	1.55
2.5	294.5	17,767.1	21,091	1.39
3.0	508.9	30,701.0	25,310	1.27
3.5	807.8	48,734.0	29,524	1.17
4.0	1,206.4	72,781.9	33,747	1.09
4.5	1,717.6	103,622.6	37,965	1.03
5.0	2,347.6	141,630.4	42,133	0.98

Table II

Category	Synoptic Situation	Cloud Type	Precipitation Type	Mean Drop Diameter $\bar{D}$	Computed Rain rate mm/hr
I	warm over running	stratus	drizzle light rain	0.63	5.23
II	pre-frontal (cold)	cumulus	showers thunder showers	1.73	92.60
III	pre-frontal (warm)	stratus strato-cumulus	drizzle rain	0.82	10.39
IV	non-frontal tropical	cumulus	rain	0.83	10.76
V	air mass	cumulus	showers rain	0.73	7.33

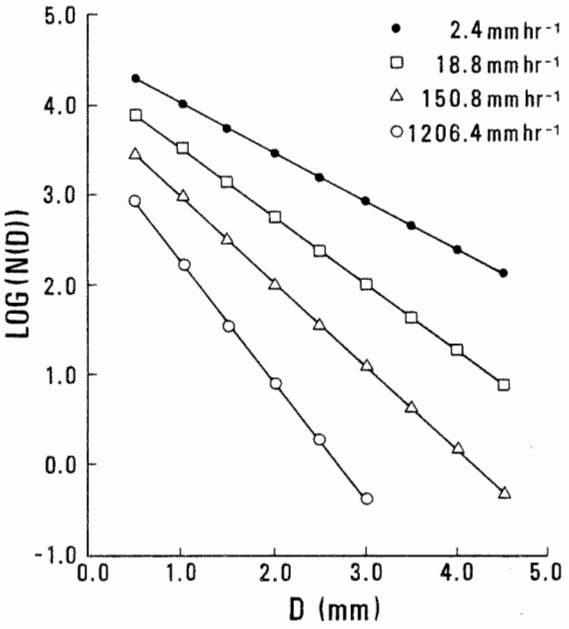

Figure 2. Hypothetical drop distribution computed from four rain rates.

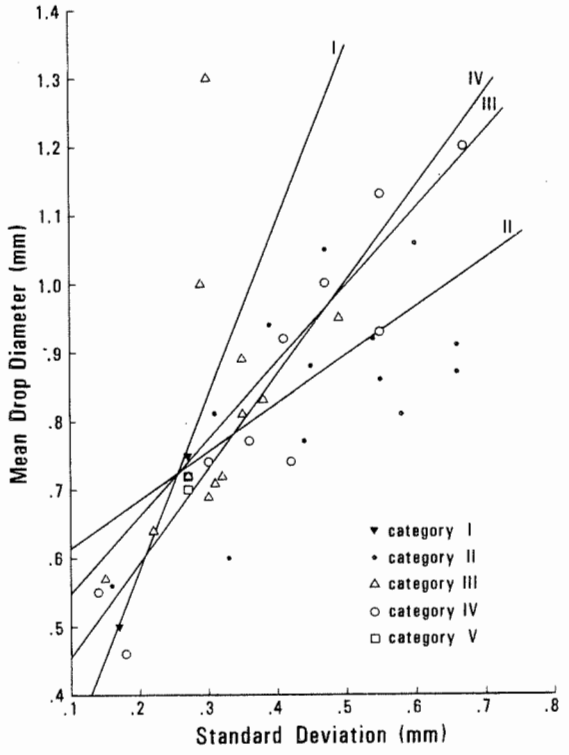

Figure 3. Example of observed mean drop diameter $\bar{D}$ and standard deviation for five categories as defined in Table II.

CLOUD DROPLET DISTRUBUTIONS IN WINTERTIME ROCKY MOUNTAIN CLOUDS

P. A. WALSH

Department of Atmospheric Science
Colorado State University
Fort Collins, Colorado U.S.A.

I. Introduction

Winter clouds over the high plains and mountains of Colorado and southeastern Wyoming are of interest to people both in and out of the atmospheric sciences community. The snowfall from such clouds has a year around impact on the economy by influencing both winter recreation and summer agriculture. The importance of the clouds has been recognized by meteorologists. Research in the areas of cloud physics, weather modification and numerical modeling has been ongoing for a number of years.

During the winter seasons 1974-1977, a survey of cloud droplet distributions was made in a number of winter cloud types using an optical sensing probe and an impaction sampler. In addition to droplet measurements, state parameters and ice crystal data were obtained. The research was the first extensive use of an automated optical probe as a primary sampler in cold, mixed-phase clouds. The value of the survey was enhanced by the basic microphysical nature of the measurements, the combination of state of the art optical sensing and a traditional impaction technique, the continuity of instrumentation throughout the study and the variety of the winter clouds examined. Prior to this study information on cloud droplet distributions in Rocky Mountain winter clouds had been based on non-continuous impaction sampler data, laboratory simulations and/or extrapolations from research done in coastal, summer or warm (>0°C) clouds.

II. Instrumentation

The Axial Scattering Spectrometer Probe (ASSP), designed by Partical Measuring Systems, Inc. (PMS), is an optical scattering probe which samples and sizes cloud droplets continuously and records the information on magnetic tape. Droplets are sized into 15 size classes by measuring the amount of light scattered into the collecting optics during droplet interaction with a focused laser beam. The probe has four selectable bin widths (0.5, 1.0, 2.0, and 3.0 μm) to cover the full range 0.5-45.0 μm. The primary size range is 2-30 μm with a 2 μm resolution.

The Wyoming cloud gun is a single-shot impaction sampler with an advanced timing mechanism accurate to 0.1 millisecond. Droplets are impacted onto a soot-covered glass surface for an accurately measured length of time. Analysis of the impaction craters, which includes consideration of the exposure time, air speed at the impaction time and collection efficiencies results in a description of the cloud droplet spectrum and concentration.

A laboratory calibration was done prior to the field observations to permit intercomparisons of subsequent droplet measurements. In contrast to PMS factory calibration with glass beads, a monodisperse water droplet spray was used for the tests. The two samplers were compared over a range of 8-38 μm diameter to a laboratory standard. The cloud gun impaction sampler agreed well with the laboratory

TABLE 1. SUMMARY OF CASE STUDIES

CLOUD TYPE	$\bar{d}$ (μm)	d_{max} (μm)	$\sigma/\bar{d}$	CONC (cm^{-3})	LWC ($g\ m^{-3}$)	GROWTH TIME (sec)	ICE CRYSTALS ($liter^{-1}$)	PRECIP
Non-convective Cap Clouds	8.0	16	.25	100-300	0.05-0.20	500-1000	1-5	NO
Upslope-Frontal System	7.5	22	.35	100	0.05	200-2000	1-10	YES
Convective Cap Cloud	7.0	16	.25	125	0.04	300	0.1-1	NO
Small Winter Cumulus Clouds	7.3	16	.25	100	0.03	300-1000	10-70	YES
Orographic Storms								YES
Leading Edge	8-10	22	.18	50-300	0.10-0.20	<350	1-10	
Convection	10-14	30	.40	250	0.40	350-600	10-30	
Over Mountains	13-18	>40	.40	250-300	0.50-0.80	>1000	50-100	

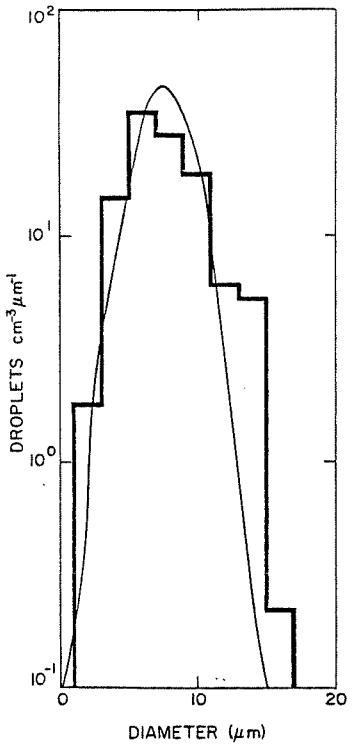

ASSP
$\bar{d}$ 7.6 μm
$\sigma_{observed}$ 2.7 μm
σ_{real} 2.0 μm
CONC 220 cm^{-3}
LWC .071 g m^{-3}

Figure 1. Droplet spectrum observed in a non-convective, non-precipitating cap cloud. Histogram indicates observed spectrum, smooth curve shows approximation to the real spectrum after application of the calibration correction.

standard and calibration curves were developed to account for systematic errors in the ASSP data.

III. Results

A summary of the cloud droplet spectra observed in five winter cloud types is presented in Table 1. After correcting the ASSP data according to calibration results, the spectra were fitted to Gaussian (or normal) distributions and characterized by the arithmetic mean, $\bar{d}$ and the arithmetic standard deviation, σ.

A 'typical' spectrum observed at some stage of all of the study clouds including the orographic storm had a mean diameter <10 μm and a narrow range of droplet sizes. Droplets >15 μm in diameter were rare and those ≥20 μm were noted in only a few instances. Droplet concentrations were generally <300 cm^{-3} and liquid water contents were typically <0.10 g m^{-3}. An actual droplet distribution, observed in a non-precipitating cap cloud, is presented in Figure 1. The spectrum is very similar to that described for the 'typical' case. Droplet concentrations and liquid water contents throughout the research were lower than those observed in visually similar continental air mass clouds by MacCready and Takeuchi, 1968 and Breed et al., 1976.

Three of the five cloud types studied were observed to produce precipitation. In high plains winter clouds precipitation is formed by an ice phase (Bergeron) process. Ice growth may result either from a diffusion process or an accretion (riming) mechanism. The two non-precipitating cloud types were characterized by small, narrow droplet spectra (like that in Figure 1) and low ice crystal concentrations. Short in-cloud growth times were not sufficient to produce precipitation size particles by diffusion and the combination of small crystals and small droplets has been determined to be inefficient for accretional growth. (Pitter and Pruppacher, 1974; Schlamp et al., 1975.)

A comparison between a cloud gun sample and the ASSP is shown in Figure 2. Longer in-cloud growth times led to the development of a slightly broader droplet spectra. Cloud droplets 15-20 μm in diameter in concentrations >0.1 cm^{-3} were observed. Droplets in this size range have low collection efficiencies and were observed as light rime on large dendritic snowflakes falling from the upslope-frontal cloud.(Walsh,1980)

Cloud droplet spectra observed in the small winter cumuli were unable to develop large droplets or broad distributions despite long in-cloud growth times. Competition for vapor was dominated by the diffusional growth of a high concentration of ice crystals. Droplet distributions varied little from the 'typical' spectrum through the entire lifetime of the precipitating cells.

Characteristics of observed cloud droplet spectra echoed the complexity of the extensive orographic storms. Three distinct liquid water regions within the storms were identified by Marwitz et al., 1976.

The development of cloud droplet distributions at the leading edge was very similar to the sequence observed in simple cap clouds. Observations agreed well with calculations by Howell, 1949 on the growth of droplet spectra in uniformly cooled air and indicated that

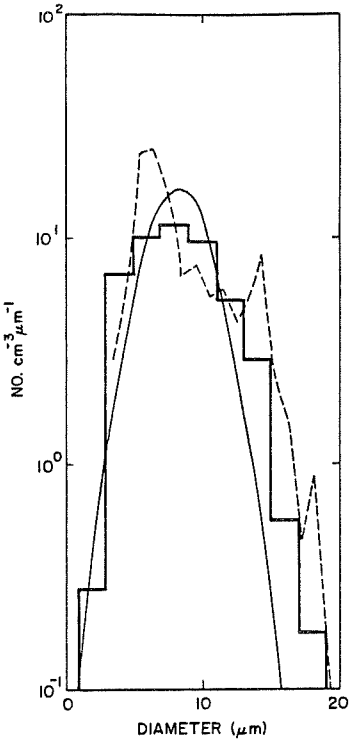

ASSP $\bar{d}$ 8.3 μm
σ_o 3.1 μm
σ_r 2.3 μm
CONC 94.4 cm^{-3}
LWC .041 g m^{-3}

Cloud Gun Sample
$\bar{d}$ 8.7 μm
σ 3.4 μm
CONC 126.0 cm^{-3}
LWC .066 g m^{-3}

Figure 2. Comparison between the ASSP (histogram), corrected ASSP (smooth curve) and a cloud gun sample (dotted line) in the upslope-frontal cloud.

entrainment and turbulence had a minimal effect on the smooth orographic formation process. Longer parcel transit times resulted in larger droplets and broader droplet distributions until at some distance from the leading edge the diffusional growth of ice became the dominant process and caused the glaciation of the liquid region.

Approximately 15 km upwind of the mountain barrier cloud droplets were observed in a convective region embedded in the extensive glaciated layer cloud. Updraft velocities of 3-5 m sec^{-1} appeared to be related to the development of a confluence zone near the surface. The spectra in the convective region were broad with mean diameters of 10-13 μm. Droplet concentrations averaged 250 cm^{-3} while droplets 15-20 μm in diameter were observed in concentrations >1.0 cm^{-3}. Liquid water contents averaged about 0.4 g m^{-3}. A peak value of 1.0 g m^{-3} was noted. The presence of large cloud droplets has been linked to the efficiency of many ice multiplication mechanisms, especially the Hallett-Mossop mechanism (Hallett and Mossop, 1974). Although large droplets were present in adequate concentrations, temperatures were much colder than the optimal interval of -3 to -8 °C. Conditions suitable for the Hallett-Mossop mechanism were not observed in any of the winter cloud types studied.

Figure 3 shows a bimodal droplet distribution which was observed in a liquid water region over and slightly upwind of the mountain barrier. The cloud gun data showed peaks at 12 μm and 21 μm diameter and significant concentrations of droplets >30 μm diameter. The ASSP failed to resolve the bimodal structure but did detect a very broad spectra and the presence of the large droplets. Droplets 20-30 μm in diameter probably grew by condensation over a period of 30 minutes, but the presence of droplets >40 μm implied that a coalescence process was active in this region. Calculations of condensation growth rates suggested that the origin of some of the droplets was the embedded convective region and others were the product of uninterrupted condensational growth in the general orographic flow. Observations of graupel and heavily rimed aggregates at surface stations and the presence of heavily rimed crystals along the flight path were consistent with the presence of significant concentrations of large droplets and emphasized the dominance of accretional growth in the formation of precipitation.

The observations and analysis described above are examples of the usefulness of cloud droplet data in assessing the origin and development of study clouds and characteristics of active precipitation formation mechanisms.

IV. Acknowledgements

This paper presents an incomplete summary of the author's M.S. thesis research which was done at the University of Wyoming. The research was supported by the Meteorology Program, Atmospheric Science Section, National Science Foundation Grant ATM75-02515. A continuation of this work is currently being funded by NSF Grant ATM78-19261,01 at Colorado State University.

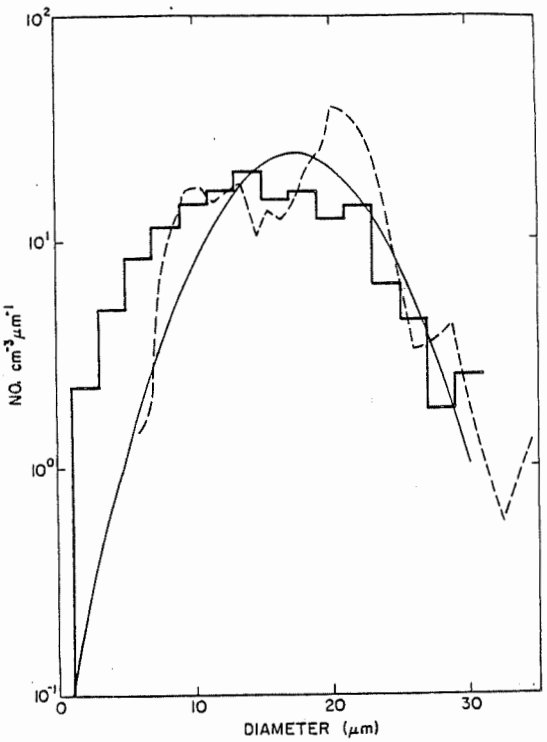

Figure 3. Comparison between the ASSP (observed and corrected) and cloud gun sample observed in an orographic storm. Cloud gun shows a strongly bimodal droplet spectrum. (Key in Figure 2)

ASSP (observed)	(corrected)	Cloud Gun Slide
$\bar{d}$ 15.1 μm	$\bar{d}$ 17.4 μm	$\bar{d}$ 18.5 μm
σ 6.2 μm	σ 5.0 μm	σ 6.3 μm
LWC 0.84 g m^{-3}	CONC 310 cm^{-3}	LWC 1.7 g m^{-3}
		CONC 375 cm^{-3}

V. References

Breed, D. Q., L. O. Grant, and J. E. Dye, 1976: Cloud droplet distribution in high elevation continental cumuli. Preprints, International Conference on Cloud Physics, Boulder, Colorado, pages 658-664.

Hallett, J. and S. C. Mossop, 1974: Production of secondary ice particles during the riming process. Nature, 249, pages 26-28.

Howell, W. E., 1949: The growth of cloud drops in uniformly cooled air. Journal of Meteorology, 6, pages 134-149.

MacCready, P. B., Jr., and D. M. Takeuchi, 1968: Precipitation initiation mechanisms and droplet characteristics of some convective cloud cores. Journal of Applied Meteorology, 7, pages 591-602.

Marwitz, J. D., W. A. Cooper, and C. P. R. Saunders, 1976; Structure and seedability of San Juan storms. Final report to the Division of Atmospheric Water Resources Management, Bureau of Reclamation, Department of the Interior. Contract No. 14-06-D-6801, July 1, 1974 - August 31, 1976. 329 pages.

Pitter, R. L. and H. R. Pruppacher, 1974: A numerical investigation of collision efficiencies of simple ice plates colliding with supercooled water drops. Journal of the Atmospheric Sciences, 31, pages 551-559.

Schlamp, R. J., H. R. Pruppacher and A. E. Hamielec, 1975: A numerical investigation of the efficiency with which simple columnar ice crystals collide with supercooled water drops. Journal of the Atmospheric Sciences, 32, pages 2330-2337.

Walsh, P. A., 1977: Cloud droplet measurements in wintertime clouds, M. S. Thesis, Department of Atmospheric Science, University of Wyoming, Laramie, Wyoming. 170 pages.

Walsh, P. A., 1980: Seedability and precipitation efficiency of an upslope-frontal storm. Submitted to the Third WMO Scientific Conference on Weather Modification, Clermont-Ferrand, France.

II.4 - Population de Cristaux de Glace et Flocons de Neige

Ice Crystals Population and Snowflakes

ICE PARTICLES IN CLEAR AIR

A. A. Barnes, Jr.

Air Force Geophysics Laboratory
Bedford UNITED STATES

INTRODUCTION

The precipitation of ice particles from clear air has been noted by observers in polar regions. Hogan (1975) reported that ice crystal precipitation at the South Pole (2800 m) was observed at the surface only when cirrus clouds were present at higher altitudes. He found that ice crystal precipitation was relatively common and sometimes achieved a depth of 3 mm within a few hours under calm conditions. Surface temperatures ranged from -30°C to -40°C. He distinguished two categories of ice crystals; diamond dust, consisting of crystals with maximum dimension of approximately 100 microns or less, and larger columns similar to those reported in cirrus at similar temperatures by Jiusto and Weickmann (1973). Single columns up to 1.3 mm in length were observed by Hogan, but fragil combinations (referred to as prism bundles by Jiusto and Weickmann) were also observed.

On 29 March 1974 at a surface temperature of -22.3°C, Ohtake and Holmgren (1974) found ice crystals falling from cloudless skies over Alaska with a maximum concentration of 9.6×10^4 crystals/m^3 for particles larger than 25 microns. The concentratons were derived from fall velocities based on measurements by Kajikawas (1973) and Jayaweera and Cottis (1969).

Between 14 December 1974 and 28 January 1975 at the South Pole, Ohtake (1976) observed ice crystal falls on both cloudless and cloudy days. The maximum concentration was $8.7 \times 10^4/m^3$. The larger columns were 1 mm long and 0.2 mm in diameter, similar to Hogan's findings, and were noted on cloudy days. These crystals were thought to originate in Ci or Cs before passing through a layer of As. On days without any visible clouds smaller crystals with average diameters of 60 microns were observed. In January and February 1975 at the South Pole Kikuchi and Hogan (1979) found that ice crystals formed by spontaneous nucleation in the free atmosphere. An increase in number concentration was correlated with the appearance of cirrus clouds. The crystals were usually columns, but occasionally more than half were plate type. At temperatures around -35°C, plates larger than 200 microns prevailed.

Observations in Northern Alaska (Ohtake, et al, 1978) reconfirmed that ice crystals frequently fall from clear skies. The maximum concentration was about 100 crystals per liter ($10^5/m^3$) at -25°C. Crystals ranged from 30 to 300 microns in diameter. Ice crystals were observed up to 900 meters using a PMS cloud probe on an airplane, but no particles were detected at 1000 meters altitude. The aircraft observations indicated that the moisture source was from the towns of Barrow and Browerville, Alaska in this case. Open leads in the ice were shown to be moisture sources in other cases. These moisture sources are far removed at the South Pole indicating other moisture sources for the ice crystals.

AIRCRAFT OBSERVATIONS

We have occasionally observed ice crystals in clear air at heights up to 10 km using the snow stick on the C-130. In the last few years we have detected ice particles in clear air with the PMS instruments on the MC-130 and on the Learjet 36 and have labeled the phenomena sub-visible cirrus.

The largest particles recorded by the 1-D cloud probe in cloudless skies have been around 200 microns. On the other hand particles as large as 2200 microns have been detected by the 1-D precipitation probe when flying between 7 and 9 km altitude, in clear air, but underneath cirrus clouds. Generally, the maximum concentrations in cloudless skies have been 10^4 counts/m^3 for particles larger than 2 microns. The counts have become as large as $10^5/m^3$ in clear air under cirrus clouds.

The frequency of encounter of these particles in clear air is difficult to ascertain. On two flights of the C-130 between Ohio and California using the 1-D cloud probe as a detector, sub-visible cirrus was encountered in 15% of the clear air on one flight and in 80% of the clear air on another.

The Lear has detected sub-visible cirrus up to 13.7 km over the United States and over the Kwajalein Atoll in the Marshall Islands. The maximum size of the particles becomes smaller at these higher altitudes, and detection is by the PMS axially scattering probe which has limitations in determining size of ice particles.

Because of the darker sky background at higher altitudes, thin cirrus which is not visible from the ground can be seen above the Lear when flying at high altitude. This is particularly true at Kwajalein where the tropopause is above 16 km.

On 22 August 1978 the Lear encountered sub-visible cirrus for 62 minutes over Kansas at altitudes between 10.3 and 13.2 km. The peaks of the size spectra were at four microns in two runs and were at or below two microns in the other three runs. Total particle count ranged from $5 \times 10^4/m^3$ to $10^3/m^3$ which was the lower detectable limit. Most of the counts were made by the ASSP, but counts were recorded in the lowest channel of the 1-D precipitation probe (~200 microns) in all five runs. Extropolation of the ASSP curves intersected the first channel of the precipitation probe close to the channel's detection level. This implied that these data points could be real rather than electronic noise in the 1-D precipitation probe.

In order to verify that particles greater than 100 microns existed in sub-visible cirrus, the PMS 2-D precipitation probe on the C-130 was modified to provide additional information on the time between the larger, infrequently encountered ice crystals. The initial test of the modification was made on 2 February 1980 on a track from Wright-Patterson AFB, Ohio to Chicago, Illinois to west of Madison, Wisconsin. During a forty minute period when the C-130 was between 5.5 and 6.0 km altitude at -17°C in clear air with no clouds overhead the 2-D recorded a number of particles. The average rate of detection was approximately 2 per minute or $.14/m^3$ for particles larger than roughly 100 microns and 1 per minute or $6 \times 10^{-2}/m^3$ for particles larger than 300 microns. These 2-D records lend credence to those occasional counts noted in the lower channels of the 1-D precipitation probes. These stray counts had previously been considered as a residual noise problem in the electronic circuits of the 1-Ds in both the C-130 and the Lear.

On other flights in sub-visible cirrus visual observations of the larger ice crystals as seen on the snow stick were in the 200-300 micron range. These size particles were also detected by the 1-D precipitation probe while many smaller particles were detected by the ASSP in the 2-30 micron range. Occasionally, as mentioned above, particles with diameters of 1000 microns or larger were detected but these larger particles were associated with visible cirrus above the aircraft.

The descriptions of the polar, clear sky ice crystal falls are not very different than the descriptions of the ice crystals detected by aircraft in sub-visible cirrus. The major amount of moisture must come from within the atmosphere since there are no ice leads or anthropogenic sources at these altitudes with the exception of aircraft exhaust. This indicates that lifting motions are the major cause of the sub-visible cirrus.

CONCLUSIONS

PMS particle detectors on a C-130 and on a Lear 36 have recorded cirrus particles in sub-visible cirrus while visibilities were generally in excess of 100 km. Particles on the snow stick were usually in the 200-300 micron range, but occasional particles with diameters in excess of 1000 microns were detected. The PMS equipment confirmed these observations and also showed a large number of particles in the 2-30 micron range. Particles larger than 1000 microns were associated with cirrus clouds above the aircraft.

The wide spread occurrence of sub-visible cirrus seems to be associated with natural atmospheric causes. Since aircraft exhaust is a minor contributor to the moisture at cirrus levels, wide spread lifting motions and the naturally available water vapor are considered to be the progenitors of sub-visible cirrus.

REFERENCES

Hogan, A. W., 1975: Summer ice crystal precipitation at the South Pole, J. Appl. Meteor., 14, No. 2, 246-249.

Jayaweera, K. O. L. F., and R. F. Cottis, 1969: Fall velocities of platelike and columnar ice crystals, Quart. J. Roy. Meteor. Soc., 95, 703-709.

Jiusto, J. E., and H. K. Weickmann, 1973: Types of snowfall, Bull. Amer. Meteor. Soc., 54, No. 11, 1148-1162.

Kajikawa, M., 1973: Laboratory measurement of falling velocity of individual ice crystals, J. Meteor. Soc. Japan, 51, 263-272.

Kikuchi, K., and A. W. Hogan, 1979: Properties of diamond dust type ice crystals observed in summer season at Amundsen-Scott South Pole Station, Antarctica, J. Meteor. Soc. Japan, 57, No. 2, 180-190.

Ohtake, T., 1976: Ice crystals in the Antarctic atmosphere, Proc. International Conf. Cloud Physics, 26-30 July 1976, Boulder, 484-487.

Ohtake, T., and B. E. Holmgren, 1974: Ice crystals from a cloudless sky, Proc. Conf. Cloud Physics, 21-24 October 1974, Tucson, 317-320.

Ohtake, T., K. O. L. F. Jayaweera and K. Sakurai, 1978: Formation mechanism of ice crystals in the cloudless atmosphere. Proc. Conf. Cloud Physics and Atmos. Electricity, 31 July - 4 August 1978, 122-125.

A NUMERICAL STUDY ON ICE PARTICLE MULTIPLICATION BY ACCRETION

K.D. Beheng

Institut für Meteorologie und Geophysik
Universität Frankfurt/M., FRG

1. INTRODUCTION

Observations show that the microphysical characteristics of glaciating maritime clouds differ significantly at the beginning and at the end of glaciation. In the beginning large liquid raindrops occur in concentration of about 1 l^{-1} and ice particles in concentration of the order of 10^{-1} l^{-1}. After completion of glaciation large raindrops still exist and the concentration of regular ice crystals as well as of other ice particles, as e.g. graupel, is increased by one to three orders of magnitude (Koenig, 1963; Hallett et al., 1978).

To account for short conversion times (all water to all ice) and for the occurrence of large amounts of regular ice crystals it is suggested (Hallett and Mossop, 1974) that as a result of riming growth of ice particles ice splinters are produced the concentration of which depends on the accreted mass leading to quick transformation rates in that large supercooled drops are converted to ice particles by collision with ice splinters.

2. MATHEMATICAL AND PHYSICAL TREATMENT

At first the microphysics of glaciating maritime convective clouds are schematically outlined as to be simulated. Starting with a maritime cloud droplet size distribution (liquid water content: 1 g m^{-3}; mean radius: $\bar{r}_o = 14$ μm) coagulation of liquid droplets leads after some time to large liquid raindrops. The time in which the concentration of large raindrops with radii $r \geq r^*$ (r^*: critical large drop radius) increases to 1 l^{-1} is called coagulation time t_c. At that time "primary" hexagonal ice crystal plates are assumed to be present in a given concentration. By accretion they grow to "primary" graupel. As claimed by the ice splinter hypothesis ice splinters are produced in a concentration which is related to the accreted mass. In the present paper ice splinters are assumed to have no mass and no fall velocity. Once ice splinters are present they may collide with supercooled large raindrops with radii $r \geq r^*$ and let them freeze assuming that one ice splinter will let freeze one large raindrop. The frozen drop may accrete cloud droplets too, subsequently forming a "secondary" graupel producing ice splinters on his own and so leading to a chain reaction of splinter production. Because more ice splinters are produced than "consumed" by collisions with large raindrops the remaining ice splinters are assumed to grow by sublimation to large "secondary" ice crystals.

To summarize the origin and interaction of the various cloud particles we have (1) liquid cloud droplets and when coagulation proceeds large raindrops, (2) primary hexagonal ice crystals, for example originated from ice nuclei, (3) primary graupel, formed by accretion of cloud droplets on primary ice crystals, (4) frozen drops or secondary graupel resp., formed by collisions of ice splinters with large drops and by accretion of cloud droplets on frozen drops resp. and (5) ice splinters the concentration of which is increased by riming and decreased by incorporation in freezing drops.

The interaction processes mentioned above are described by stochastic collection equations (Berry, 1967; Beheng, 1978) extended by an equation corresponding to secondary graupel production and interaction as well as by an equation describing the splinter balance. The interaction processes of various cloud particles are taken into consideration by different collision efficiencies (CE), fall velocities (FV) and mass-size-relationships (MSR). The CE and FV of coagulation and interaction between hexagonal ice crystals and droplets are the same as in Beheng (loc. cit.). Riming growth of primary and secondary graupel resp. is represented by CE of Beard and Grover (1974) and FV as well as MSR (primary graupel ≡ lump graupel 1; secondary graupel ≡ lump graupel 3) by Locatelli and Hobbs (1974). For ice splinter interaction considering the assumption made above the collection kernel is independent of the ice splinter's size and fall velocity. CE is set equal to 1. Note that different values of CE and MSR for the graupel particles as in Beheng (loc.cit.) are used.

3. RESULTS

The effects of various (1) primary ice crystal concentrations N_{pi}, (2) radii of large raindrops r^* and (3) ice splinter production rates α on the microphysical evolution are investigated. The size distribution of the primary ice crystals (a Gaussian distribution function) is varied only by the concentration N_{pi} while the mean ice crystal axis $\bar{a}_i$ = 205 µm and the standard deviation σ = 2,0 is held fixed.

The results are shown in terms of time variation of (1) the decrease of LWC due to accretion and freezing, (2) the radii of the graupel characterized by the mode of the corresponding size distributions $\bar{r}_p$ and $\bar{r}_s$ (subscript "p" for primary and "s" for secondary graupel) and (3) the concentration of ice splinters or secondary ice crystals resp. N_{si} and of secondary graupel N_{sg}. The concentration of primary ice crystals N_{pi} is assumed to be identical to that of primary graupel N_{pg} and is assumed to be constant in time.

In Fig. 1 the time dependent variation of LWC, $\bar{r}_p$, $\bar{r}_s$, N_{si} and N_{sg} is shown varying the primary ice crystal concentration N_{pi} = 2,5 X 10^{-3} to 2,5 X 10^{-6} cm^{-3} with r^* = 178 µm and α = 350 per milligram accreted mass (mg AM) held fixed. While for the larger N_{pi} the decrease of LWC begins at once, for the smaller N_{pi} the decrease starts not before a certain time has elapsed (in the following called dead time t_d -see below-). The slope of decreasing LWC is steep and changes only moderatly with varied N_{pi}. In case of large N_{pi} the concentration of secondary graupel N_{sg} as well as of secondary ice crystals N_{si} increases by one order of magnitude exceeding the concentration of primary ice crystals by one (for the larger) and by three (for the smaller N_{pi}) orders of magnitude at the end of the glaciation. Due to the large concentrations of primary and secondary ice crystals the size of primary and secondary graupel is small and nearly constant in time with maximum values of $\bar{r}_g \approx 300$ µm and $\bar{r}_s \approx 550$ µm. In both cases the size of secondary graupel is larger than of the primary graupel indicating that despite the decreasing LWC coagulation can produce large drops which by freezing become large frozen drops and subsequently secondary graupel. Note that even with a very small N_{pi} the LWC decreases by 80 percent in a time of about 350 s after the dead time has elapsed; the dead time t_d is the time interval between the end of the coagulation time and the time at which the LWC has decreased by 10 percent.

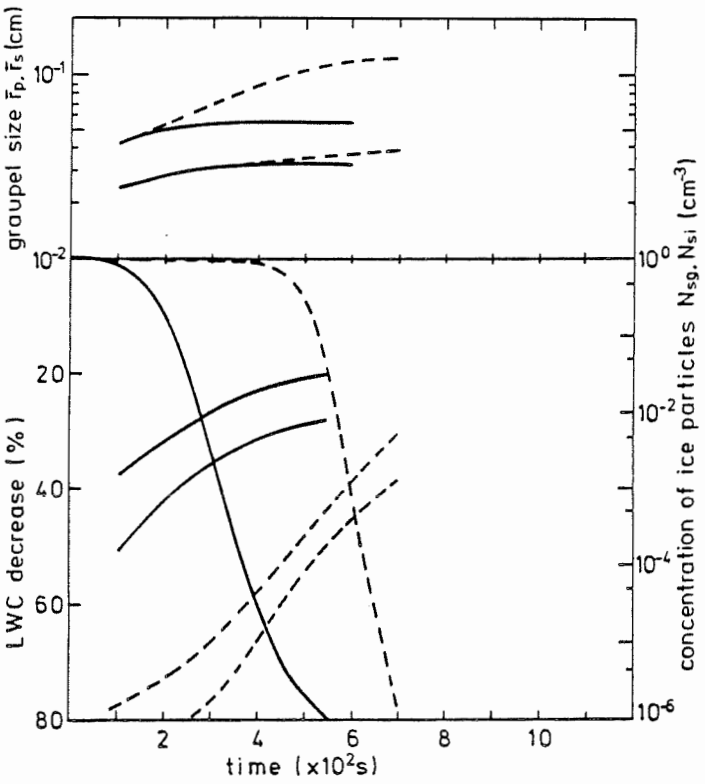

Fig. 1

Time-dependent variation of [lower part] liquid water content (LWC), concentration of secondary graupel N_{sg} (lower curve) and of secondary ice crystals N_{si} (upper curve) and [upper part] of the size of primary graupel $\bar{r}_p$ (lower curve) and of secondary graupel $\bar{r}_s$ (upper curve) as function of primary ice crystal concentration N_{pi} = 2,5 X 10^{-3} cm^{-3} (———) and N_{pi} = 2,5 X 10^{-6} cm^{-3} (- - - -) with α = 350 splinters per mg AM and r^* = 178 µm held fixed. For interpretation see text.

Now we turn to the effect of the radii of "large" drops r^* (Fig. 2). Large can mean drops of diameter either of 100, 250 or 500 µm due to the point of view of the observer or to the detection limit of the sampling device. The influence is tested with an extremely small radius value r^* = 56 µm and with a reasonable value r^* = 178 µm, and N_{pi} = 2,5 X 10^{-6} cm^{-3} and α = 350 per mg AM held fixed. By changing r^* the the coagulation time increases strongly; for r^* = 56 µm t_c = 550 s, for r^* = 178 µm t_c = 1050 s. We see that the dead time t_d is five minutes shorter for r^* = 178 µm than for r^* = 56 µm indicating that by freezing of "large" drops more mass is converted to ice than in case of "small" large drops. In both cases the slope of the decreasing LWC is nearly equal just as the concentration of secondary graupel and ice crystals. For r^* = 178 µm the size of secondary graupel is much larger than

of primary graupel while for $r^* = 56$ µm the opposite is valid. In both cases the final sizes of the smaller or larger graupel resp. differ not very significantly.

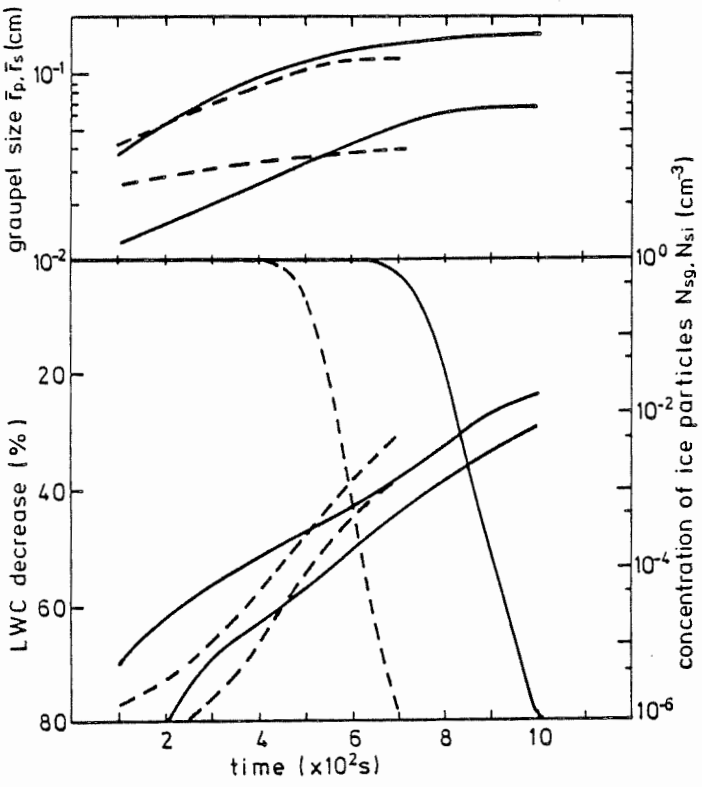

Fig. 2

Time-dependent variation of the same parameters as in Fig. 1 but now as a function of large drop radius $r^* = 56$ µm (———) and $r^* = 178$ µm (– – – –) with $N_{pi} = 2{,}5 \times 10^{-6}$ cm^{-3} and $\alpha = 350$ splinters per mg AM. For interpretation see text.

The most interesting parameter seems to be the ice splinter production rate α. The production rate α is changed from 350 to 50 per mg AM with $N_{pi} = 2{,}5 \times 10^{-5}$ cm^{-3} and $r^* = 178$ µm held fixed (Fig. 3). We note that with decreasing α the dead time increases and the slope of decreasing LWC decreases. As expected high production rates result in high concentration of secondary graupel and ice crystals whereas by decreasing α the concentration of both secondary graupel and ice particles decreases by an order of magnitude. The size of the primary graupel $\bar{r}_p$ remains nearly constant whereas the size of secondary graupel $\bar{r}_s$ increases with decreasing α, an effect just shown in Fig. 1 as a result of decreasing N_{pi} but here caused by the smaller secondary ice crystal concentration. But it seems important to note that with an only small N_{pi} the LWC decreases completely in reasonable times after the dead time has elapsed.

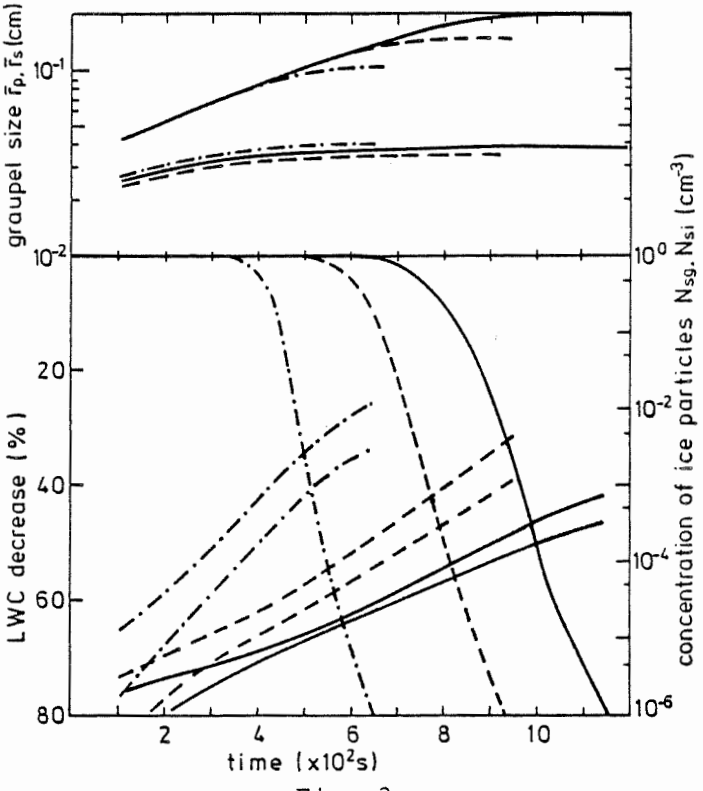

Fig. 3

Time-dependent variation of the same parameters as in Fig. 1 but now as a function of splinter production rate $\alpha = 350$ (–·–·–·), $\alpha = 100$ (– – – –) and $\alpha = 50$ (———) splinters per mg AM with $N_{pi} = 2{,}5 \times 10^{-5}$ cm^{-3} and $r^* = 178$ µm held fixed. For interpretation see text.

While so far microphysical paramters have been discussed as the concentrations and sizes of cloud particles now attention is focussed on time scales involved in the glaciation process. We split the total time from the start of glaciation in three parts: (1) the coagulation time t_c, (2) the dead time t_d, both defined above, and (3) finally the glaciation time t_g, i.e. the time of decreasing LWC by 10 to 70 percent of the start value. The sum of the three time intervals $t_c + t_d + t_g = t_\Sigma$ is called "inherent" microphysical time (IMT). If we choose $\alpha = 50$, 100 and 350 splinters per mg AM, $N_{pi} = 2{,}5 \times 10^{-3}$ and $2{,}5 \times 10^{-5}$ cm^{-3} and $r^* = 56$ and 178 µm 12 case studies result, the characteristic time intervals t_d, t_g and t_Σ of which are displayed in Fig. 4. We note that the small primary ice crystal concentration N_{pi} (indicated by hatching) leads to dead times t_d double as long as the larger N_{pi}. Reducing the ice splinter production rate α shows the same effect as reducing N_{pi}.

The influence of changing N_{pi}, α and the large drop radius r* on the glaciation time t_g and IMT is not very significant although small N_{pi} and small result in somewhat longer IMT's. Surprisingly the glaciation times t_g are shorter than 9 minutes, more than 50 percent of all cases (N=12) shorter than 6 minutes with no marked influence of any parameter investigated.

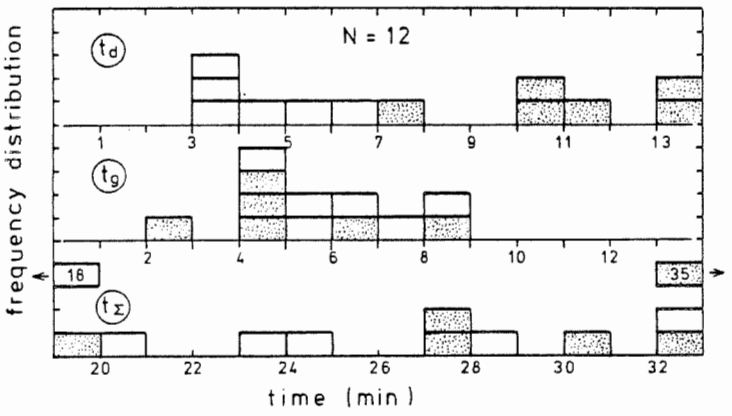

Fig. 4

Frequency distribution (N=12) of dead times t_d, glaciation times t_g and "inherent" microphysical times t_Σ. Hatching indicates primary ice crystal concentration $N_{pi} = 2{,}5 \times 10^{-5}$ cm^{-3}.

Finally some findings are compiled. At the end of glaciation the multiplication factor of ice crystals as relation between primary and secondary ice crystal concentration amounts to 10 to 10^3. The concentrations and radii of secondary graupel resp. range from 5×10^{-4} to 1×10^{-2} cm^{-3} and 600 to 2000 µm resp.. The concentrations of secondary ice crystals vary between 1×10^{-3} and 5×10^{-2} cm^{-3}, the radii of primary graupel between 300 and 2000 µm. Considering that the concentration of large drops decreases only slightly during glaciation (results not shown) and that the glaciation times are shorter than 9 minutes all these values reported are consistent with observational data.

4. CONCLUSIONS

The results of numerical simulations of the microphysical behaviour of glaciating maritime clouds show that proceeding from realistic initial conditions all microphysical characteristics as size and concentration of ice particles and large liquid drops as well as the characteristic time scales agree well with observations. It seems that the microphysical conditions before initiation of glaciation, e.g. the warm phase development by coagulation, determine crucially the glaciation process even if the ice splinter production rate is small and the primary ice crystals concentration is comparable to the ice nuclei concentration.

5. REFERENCES

Beard, K.V. and S.N. Grover, 1974: Numer. collision efficiencies for small raindrops colliding with micron size particles. J.Atmos.Sci. 31, 543-550

Beheng, K.D., 1978: Numerical simulation of graupel development. J.Atmos. Sci. 35, 683-689

Berry, E.X., 1967: Cloud droplet growth by collection. J.Atmos.Sci. 24, 688-701

Hallett, J. and S.C. Mossop, 1974: Production of secondary ice particles during the riming process. Nature 249, 26-28

Hallett, J., R. Sax, D. Lamb and A.S. Murty, 1978: Aircraft measurements of ice in Florida cumuli. Quart. J. Roy.Meteor. Soc. 104, 631-651

Koenig, L.R., 1963: The glaciating behaviour of small cumolonimbus clouds. J.Atmos.Sci. 20, 29-47

Locatelli, J.D. and Hobbs, P.V., 1974: Fall speeds and masses of solid precipitation particles. J. Geophys. Res. 79, 2185-2197

ICE CRYSTAL CONCENTRATIONS IN ISOLATED CUMULUS CLOUDS OF MONTANA

Todd A. Cerni and William A. Cooper
University of Wyoming
Laramie, Wyoming U.S.A.

1. INTRODUCTION

For the past three years, the University of Wyoming has operated an instrumented aircraft in the summer (May-July) field season of the High Plains Cooperative Program (HIPLEX) conducted on the high plains of eastern Montana, U.S.A. The experimental project area, some 300 km in diameter, is situated on a semi-arid, gently sloping plain with mountains to the west and southwest. The mean elevation of the project area is 800 m, the latitude 45°N, the mean annual temperature is 7°C and the mean annual precipitation is 350 mm, most of which occurs in the summer in the form of convective showers and thunderstorms. The climate is decidedly continental.

2. CLOUD PHYSICS INSTRUMENTATION

During the 1979 field season of HIPLEX the University of Wyoming operated a model 200 T Beechcraft Super King Air, instrumented aircraft. It is certified for operation to 9.5 km MSL, has a maximum cruising speed of 140 m/s and a typical operating speed, for cloud physics work, of 100 m/s. An extensive list of primary and derived, state and cloud physics parameters are available for display to the crew and are recorded on magnetic tape. These are summarized in Cooper (1978a). A brief description of those instruments which were most important for the present analysis will be given here:

a) Cloud drop size distribution and concentration were measured with a forward-scattering spectrometer probe (FSSP) similar to that described by Knollenberg (1976). In its normal operating mode, the drop size distribution is measured for the range 3 μm to 31 μm with 2 μm resolution in size and 0.1 sec (10 m) resolution in space. All drops greater than 30 μm diameter are placed in the last size bin.

b) Ice crystal concentration, size distribution and habit identification are available from a combination of three sampling devices. A 2D cloud and 2D precipitation probe (Knollenberg, 1976) record the two dimensional shadow of all particles passing through their sample aperture. The cloud probe has a range of 25 to 800 μm, with 25 μm resolution and a sampling rate of 5 ℓ/s at 100 m/s. The precipitation probe has a range of 200 to 6400 μm, with a 200 μm resolution and a sampling rate of 170 ℓ/s at 100 m/s. Field trials indicate that the practical minimum detectable size of the cloud probe is slightly larger than 25 μm. The 2D images are all processed by computer to reject artifacts due to streakers (water shedding off the deiced upstream edge of the probe and across the sample aperture), splashing of large drops and small objects which may trigger the recording circuitry but cast a shadow of diameter less than one element of resolution. In addition, the aircraft carries a decelerator sampler in which oil-coated slides are exposed to an airstream moving at 1/11 of the aircraft speed. The hydrometer samples are then preserved in chilled silicone oil and photographed under a microscope. Water drops can easily be distinguished from ice crystals for diameters greater than 25 μm. Comparisons between ice crystal concentrations measured with the 2D cloud probe and oil coated slides show a ratio (2D/slide) between 2:1 and 1:1 (Cooper, 1978b). The computer processed 2D cloud probe images, aided by manual processing of the oil-coated slides and viewing of all 2D images, was used to determine the ice concentration in each of the sample clouds.

3. ISOLATED CUMULUS CLOUDS OF EASTERN MONTANA

The clouds for this study were carefully selected for the purpose of investigating ice concentrations in the tops of cumulus clouds which were primarily the result of nucleation. To this end, five criteria were established to qualify clouds as part of the investigation.

a) From photographic evidence, aircraft crew voice notes and aircraft vertical velocity measurements, the cloud must not be subsiding at the time of penetration.

b) No radar echo must be detected by the aircraft radar (∿ 15 dBZ threshold) prior to penetration.

c) From photographic evidence, aircraft crew voice notes and ice crystal size and habit determinations, it must be clear that the cloud is not being contaminated by ice crystals eminating from another cloud.

d) From either photogrammetric determinations or direct measurements by a second project aircraft (Lear jet), a measurement of cloud top temperature must be available.

3) Aircraft penetration must be made within 500 m of cloud top.

Originally, 103 clouds from the 1979 field season were considered for this study. Of those, 65 passed the first 4 selection criteria and 45 passed all 5 criteria. Based on comparisons

between photogrametric determinations and direct measurements by the Lear jet, the r.m.s. error of cloud top temperature for the 45 clouds estimated as ±0.6°C.

The frequency distributions of cloud top temperature and cloud base temperature for the sample are shown in Figures 1 and 2, respectively. The mean cloud base temperature of the sample is +4.3°C and is a representative average for eastern Montana clouds for the months of June and July. The average cloud top temperature for the sample is -13.7°C, and represents nothing more than the typical flight level at which the aircraft was operated in an effort to discover the temperature threshold for the creation of ice.

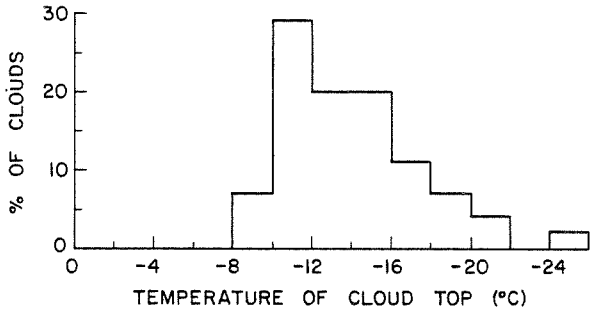

Figure 1 Distribution of cloud top temperature for the 45 selected clouds.

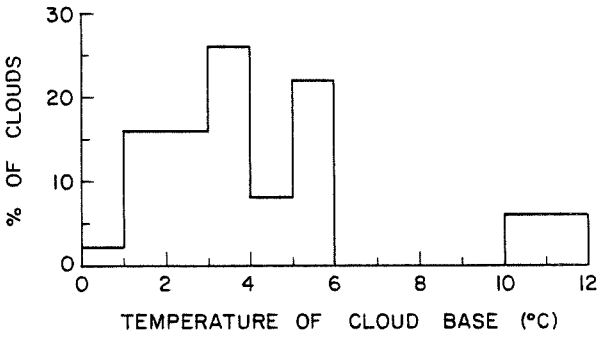

Figure 2 Distribution of cloud base temperature for the 45 selected clouds.

The frequency distribution of pass averaged liquid water content and cloud drop concentration is displayed in Figures 3 and 4, respectively. The mean liquid water content is .54 g/m^3 and is somewhat above average as compared to the mean of all cumulus penetrations for the 1979 season. The broad nature of the distribution is due to both the large variance in cloud base temperatures of the sample and to the variance in the amount of entrainment found for different clouds on the same day. The mean drop concentration is 370 cm^{-3} and reflects the continental nature of the clouds. It should be mentioned that a correlation between amount of entrainment and drop concentration has been noted for these clouds. Hence pass averaged drop concentrations may well be higher, closer to cloud base and 100 m averages of drop concentration in the wettest portion of a cloud always exceeds the pass averaged values.

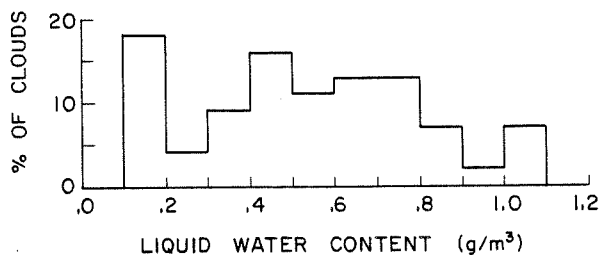

Figure 3 Distribution of pass averaged liquid water content, as measured with a Johnson-Williams devise, for the 45 selected clouds.

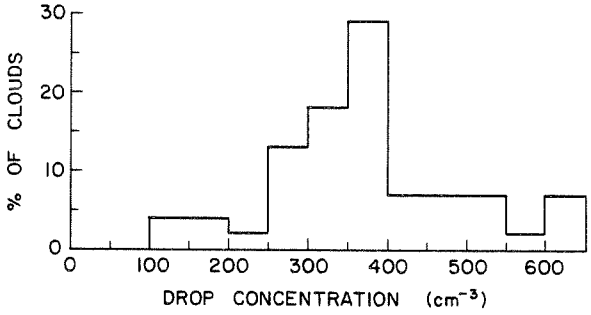

Figure 4 Distribution of pass averaged cloud drop concentrations, as measured with an FSSP, for the 45 selected clouds.

4. ICE CRYSTAL CONCENTRATIONS

Ice nuclei measurements have traditionally shown a very strong dependence of concentration on temperature (Bigg and Stevenson, 1970). However ice crystal concentrations in cumulus clouds have commonly exceeded the concentration of ice nuclei which might be activated at the summit temperatures of such clouds (Mossop et al., 1972). This descrepancy has given support for various ice multiplication mechanisms (Mossop et al., 1972). This cloud sample has been carefully selected according to the aformentioned criteria such as to minimize the probability of ice multiplication being active and maximize the probability that the ice cyrstals detected were the result of nucleation near cloud top. It was hoped that such a sample would show a correlation between ice crystal concentration and cloud top temperature.

Figure 5 shows the pass averaged ice crystal concentrations versus cloud top temperature for all clouds in the sample. The lower limit for detection of ice crystals in these clouds was about 0.1/ℓ and those clouds which were found to contain no ice were plotted on the x axis (.05/ℓ) of the graph. The correlation between summit temperature and ice crystal concentration is .06, hence the correlation is very small. The threshold cloud top temperature for the appearance of ice was found to be -10°C.

Although ice crystal concentration is poorly correlated with summit temperature, there appears to be a strong correlation between the % of

clouds containing ice and summit temperature. Table 1 displays the results of dividing the sample into 5 temperature bins and averaging the points shown in Figure 5.

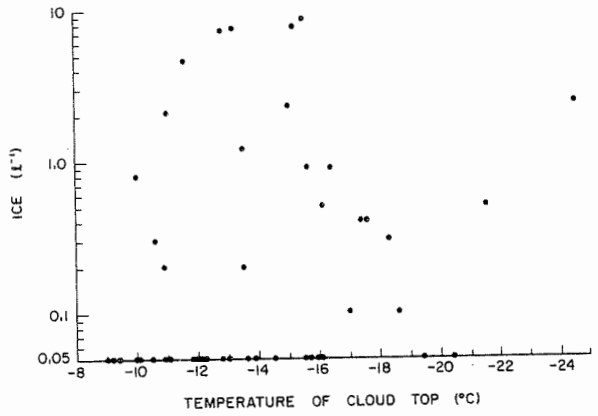

Figure 5 Pass averaged ice crystal concentration versus cloud top temperature for the 45 clouds.

TABLE 1

Cloud top temperature	Number of clouds	% of clouds with ice	% of clouds with ice > 1/ℓ	Average ice concentration per cloud
- 8 to - 9.9°C	3	0	0	0.0
-10 to -11.9°C	13	38	15	0.6
-12 to -13.9°C	9	44	33	1.8
-14 to -15.9°C	9	44	33	2.2
< -15.9°C	11	82	9	0.5
all	45	49	20	1.1

The average concentrations of ice found in cumulus cloud tops in eastern Montana far exeeeds the average concentrations of ice found in unmixed updraft cores in northeastern Colorado cumulus congestus by Heymsfield et al., (1979). They found mean concentration of ice cyrstals, in the size range of 100-400 μm, less than or equal to 0.2 ℓ^{-1} at all penetration temperatures between 0°C and -21°C. Their mean for all penetrations was only 0.02 ℓ^{-1}. There are similarities between the cumulus clouds of these two regions, especially with regards the dominance of the ice phase precipitation mechanism (Cooper, 1978b). The conclusion to be drawn from this comparison is that cumulus cloud tops and not unmixed updraft cores serve as a primary region for the creation of ice. Twomey (1958) gave 1/ℓ as the minimum concentration of ice or large particles required to initiate the precipitation process. On this basis, 20% of all the clouds and 33% of the clouds with summit temperatures of -12°C to -16°C contained sufficient ice crystal concentrations to initiate the precipitation process.

Figure 6 displays the % of clouds with ice for maritime cumulus in Tasmania as reported by Mossop et al, (1970), for 44 continental cumulus near Yellowknife, NWT, Canada as reported by Isaac and Schemenauer (1979) and for the present sample. The points representing the present sample are plotted at the average summit temperature for all clouds within a temperature bin and show a correlation coefficient of 0.93 for the linear regression fit shown. The agreement with Isaac and Schemenaur (1979) and the value of the correlation coefficent is striking. However two points must be made. The 44 cumulus cloud sampled near Yellowknife, NWT and the 45 cumulus clouds of eastern Montana bear some resemblence. The mean cloud base temperatures and cloud drop concentrations are very similar. The latter clouds have significantly higher liquid water content which is probably a reflection of the fact that they were deeper and penetrated farther above cloud base. An important observation regarding the high correlation coefficient is the fact that it is primarily produced by the the lowest and highest temperature points. The three middle points, which represent 31 clouds, indicate rather similar ice crystal concentrations for summit temperatures between -10°C and -16°C. This feature is significant and is not reflected in the data of Isaac and Schemenauer (1979).

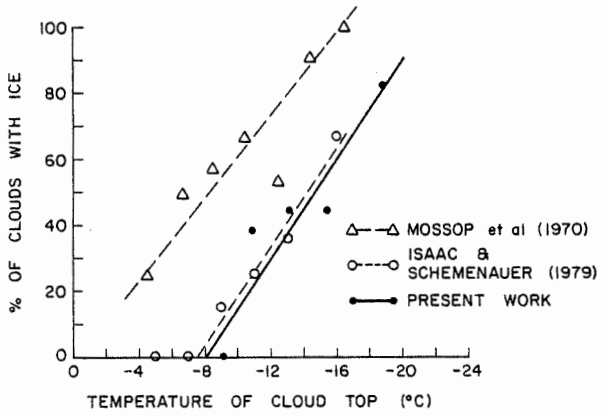

Figure 6 A comparison of maritime cumului in Tasmania, (Mossop et al, 1970) continental cumului near Yellowknife N.W.T., Canada (Isaac and Schemenauer, 1979) and the data displayed in Table 1.

5. CHARACTERISTICS OF CLOUDS CONTAINING ICE

During the HIPLEX field seasons of 1978 and 1979, it became clear that clouds with summit temperatures in the approximate range of -10°C to -16°C achieved much higher ice crystal concentrations on post-frontal days than on other days. On post-frontal days, it also appeared that cumulus clouds had larger mean drop diameters. The general synoptic characteristic of post-frontal days was the existance of ample low level moisture and low level instability to support vigorous convection, but that the convection was capped by a synoptic scale, subsidence inversion which created a very dry, stable layer somewhere between the -8°C to -15°C level. Clouds with tops to only -10°C to 14°C would produce precipitation with much greater frequency on post-frontal days than on other days.

One possible expalnation for these enhanced ice crystal concentrations is the creation of ice through the evaporative cooling of cloud tops as they penetrate the dry, stable layer. Mossop et al. (1968) and Young (1974) have also discussed this possibility. It was observed

that the cloud tops could experience 1-2°C evaporative cooling and become negatively buoyant as dry air was apparently entrained and mixed with cloudy air. Calculations indicate that evaporating drops may suffer as much as 4-6°C cooling, provided they are large enough to survive the rapid evaporation and fall back into the cloud top before completely disappearing. The nucleation mode must then be either contact or emersion. Work by Cooper (1979) suggests that contact nucleation is the most active mode of nucleation for airborne aerosol samples collected in the HIPLEX area.

Figure 7 shows that the existence of large cloud drops and a dry environment near cloud top clearly increase the probability of ice in clouds whose summit temperatures are between -10°C and -16°C. Points falling outside the box indicated by the dashed lines represent clouds which either lack 40/ℓ or more of large drops or are growing through on environment with less than a 10°C dew point depression. Such clouds have a 7% (1/15) frequency of occurrancy of any ice. Clouds represented by points within the box have 75% (12/16) frequency of occurrance of some ice. All 8 clouds with 1.0/ℓ or more ice are represented by points within the box. It should be noted that the penetration levels for 27 of the 31 clouds represented in Figure 7 were at temperatures colder -8°C, the upper temperature limit prescribed by Mossop et al (1972) for ice crystal multiplication in cumulus clouds. Also, none of the clouds had yet achieved significant precipitation development as evidence by lack of a radar echo. Hence, the data of Figure 7 provides support for the aforementioned connection between ice crystal nucleation and post-frontal conditions in eastern Montana cumulus clouds.

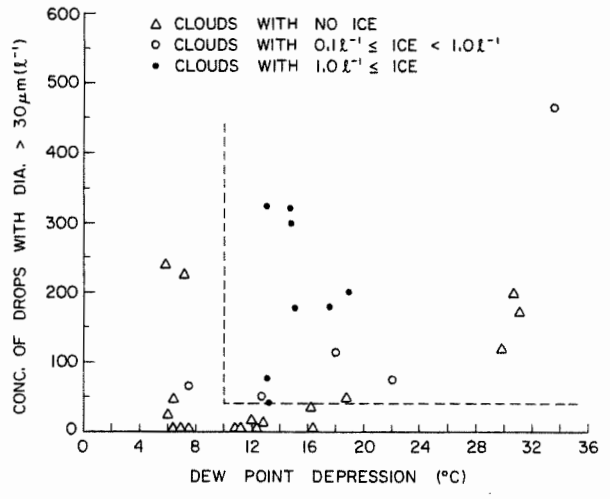

Figure 7 Clouds (31), with summit temperature between -10 C and -16 C, plotted with regards to their pass averaged ice crystal concentration, pass averaged concentration of drops greater than 30 μm diameter and dew point depression of cloud environment at the aircraft penetration level.

6. ACKNOWLEDGEMENTS

This research was sponsored by the U.S. Water and Power Resources Services under contract 7-07-83-V0001. This research would not have been possible without the combined efforts of the scientists, pilots and staff of the HIPLEX field program and the University of Wyoming.

7. REFERENCES

Bigg, E. K. and C. M. Stevenson, 1970. Comparisons of concentrations of ice nuclei in different parts of the world. J. de Rech. Atmos., 4, p. 41.

Cooper, W. A., 1978a. Cloud physics investigations by the University of Wyoming in HIPLEX 1977. University of Wyoming Report No. AS119, p. 3.

Cooper, W. A., 1978b. Precipitation mechanisms in summer-time storms in the Montana HIPLEX area. Preprints, Conf. on Cloud Physics and Atmos. Elec., Issaquah, Wash., p. 347.

Cooper, W. A., 1980. A method of detecting contact ice nuclei using filter samples. Preprints, The Eighth Intern. Conf. on Cloud Physics, Clermont-Ferrand, France.

Heymsfield, A. J., C. A. Knight and J. E. Dye, 1979. Ice initiation in unmixed updraft cores in northeast Colorado cumulus congestus clouds. J. Atmos. Sci., 36, p. 2216.

Isaac, G. A. and R. S. Schemenauer, 1979. Large particles in supercooled regions of northern Canadian cumulus clouds. J. Appl. Meteor., 18, p. 1056.

Knollenberg, R. G., 1976. Three new instruments for cloud physics measurements. Preprints, Intern. Conf. on Cloud Physics, Boulder, Colo., p. 554.

Mossop, S. C., R. E. Rushin and K. J. Heffernan, 1968. Glaciation of a cumulus at approximately -4°C. J. Atmos. Sci., 25, p. 889.

Mossop, S. C., A. Ono and E. R. Wishart, 1970. Ice particles in maritime clouds near Tasmania. Quart. J. Roy. Meteor. Soc., 96, p. 487.

Mossop, S. C., R. E. Cottis and B. M. Bartlett, 1972. Ice crystal concentrations in cumulus and stratocumulus clouds. Quart. J. Roy. Meteor. Soc., 98, p. 105.

Twomey, S., 1958. Quantitative aspects of seeding rates for use in supercooled clouds. Bull. Obs. Puy de Dome, 2, p. 33.

Young, K. C., 1974. The role of contact nucleation in ice phase initiation in clouds. J. Atmos. Sci., 31, p. 768.

GEOGRAPHICAL VARIABILITY OF ICE PHASE EVOLUTION IN SUPERCOOLED CLOUDS

J. Hallett, D. Lamb and R.I. Sax*

Desert Research Institute
Reno, Nevada, U.S.A.

*Joseph Oat Corporation
Camden, New Jersey, U.S.A.

A necessary prerequisite to understanding the ice phase evolution in convective or other clouds is an appreciation of the evolution of the supercooled water content both in the form of cloud droplets and rain drops. This is predicated by the development of the cloud drop spectrum, the detailed evolution of which is related initially to the CCN spectra of the entering air, and ultimately to the detail of the cloud top mixing process, Chai & Telford (1979). The evolution of the ice phase essentially follows one of three classifications depending on the prior evolution of the supercooled water spectrum. In type I, there is a one-to-one relation between an ice nucleus and an ice crystal, the numbers of ice crystals nucleated increasing with altitude and decreasing temperature, to be later redistributed throughout the cloud by vertical mixing process. In type II, a secondary ice generation process occurs during the growth of graupel in the temperature region -3°C to -8°C. The efficiency of this process is dependent on the presence of droplets diameter $\phi \lesssim 13$ μm in concentration $\gtrsim 100$ cm^{-3}, and droplets $\phi \gtrsim 25$ μm in concentration $\gtrsim 1$ cm^{-3}, Mossop (1978 a.). These secondary crystals grow from the vapor, rime and in turn produce more graupel particles and more secondary particles. These graupel particles are the initial fallout; as the cloud evolves vapor grown crystals become more evident. In type III, supercooled rain drops have evolved by coalescence from the cloud drops and are frozen by hydrodynamic capture of the small (100 μm) vapor grown secondary particles; these in turn become graupel particles and produce more secondary ice particles by growth in the -3 to -8°C region. Both processes II and III give an approximate exponential increase of ice particle concentration while cloud conditions persist, with III being a faster process, (Lamb et al. this conference).

The type III process has been associated with warm base convective clouds growing in regions of abundant cloud nuclei, such as the Florida Peninsula or Missouri. The type II process has been associated with situations where supercooled rain drops have failed to form, yet the upper tail of the drop spectrum ($\phi > 25$ μm) has evolved. This occurs in more maritime situations, with cooler cloud bases or less vigorous convective and more stratiform situations, where the drop spectrum has had time to undergo greater evolution through mixing. Maritime clouds off Tasmania, convective clouds over Soccoro, New Mexico and warmer cloud base temperature Colorado summer convective clouds gives examples of this process. The type I process with absence of secondary ice production, operates in cool base continental convective clouds and in more stable systems in cyclonic storms. Colorado summer convective cloud with cool base < 4°C are examples of this process.

Absence of secondary ice production can similarly be attributed to a lack of smaller cloud droplets $\lesssim 13$ μm, a situation most likely under conditions of extremely clean air, where all particles become active as cloud nuclei. Thus, trade wind cumuli well away from nuclei sources as in Hawaii, and in ocean hurricane situations, might be expected to depend only on primary ice nucleation.

A geographical classification of situations into these different types must assess the likelihood of evolution of the liquid phase to give the concentrations of the liquid phases approximating to columns A, B, C of Table I.

TABLE I

Classifications of Systems for Secondary Ice Evolution Associated With Graupel Growth At Temperatures -3 to -8°C.

TYPE	A Cloud Drops $\phi \lesssim 13$ μm	B Cloud Drops $\phi \gtrsim 25$ μm	C Cloud Drops $\phi \gtrsim 500$ μm	CONDITIONS
I a.	none	100	few ℓ^{-1}	no secondary ice
I b.	500	none	none	
II	500	10	none	secondary ice; slow evolution (20 minutes)
III	500	50	10 ℓ^{-1}	secondary ice; fast evolution (5 minutes)

These concentrations are to be related to three principal parameters;
first: the cloud base temperature specifies the amount of moisture made available for drop growth in the critical levels, Mossop,1978 b.
second: the detail of the cloud condensation nucleus spectrum, giving the initial drop size distribution in the air ascending from cloud base
third: the detail of the mixing process as the cloud top penetrates further into its environment. The modifications of the cloud drop spectrum through this mixing and the eventual development through coalescence to precipitation sized drops to be carried to and above the secondary ice production zone. Included with these considerations is the overall time scale of the cloud evolution. A cumulus cloud is in general shorter than stratiform cloud whose persistance can lead more efficiently to a broader drop spectrum.

From these general considerations, the secondary ice classification can be assigned as in Table II.

TABLE II

Tentative Assignment of Secondary Ice Generation Type According to Specific Meteorological Situation From Various Studies.

LOCATION	CLOUD BASE TEMPERATURE	-3 to -8°C, Number of Drops $\phi > 25$ µm Drops Present (X)	$\phi < 13$ µm Absent (0)	$\phi > 500$ µm	TYPE MOST (LESS) LIKELY
Florida (summer convection)	22°C	X	X	X	III
Hallett et al. 1978					
Missouri (summer convection)	20°C	X	X	X	III
Koenig, 1963					
Colorado (summer convection)	4°C	0	X	0	I
	12°C	X	X	0	II
Heymsfield et al. 1979					
Hallett 1975					
Caucasus (summer thunderstorm)	10-13°C	X	X	(?)	(II) III
Sulakvelidze 1967					
Sierra (winter frontal, orographic clouds)	+5°C	X	X	(X?)	II (III)
Hallett 1980					
Tasmania (convective, winter)	+5°C	X	(X)	(X)	II (III)
Mossop et al. 1972					
New Mexico summer convection with mountain recycling.	+4°C	X	X	0	II
Gaskell & Wagner, 1980					
Israel winter continental cumuli	+5°C	0	X	0	I
Gagin, 1975					
Hawaii, development to deep convection	20°C	X	0	X	I
Twomey & Squires, 1959					
Montana (summer convection)	0°C	0	X	0	I

REFERENCES

Baker,M.B., Latham,J. 1979. The evolution of droplet spectra & the rate of production of embryonic rain drops in small cumulus clouds. J.Atmos.Sci., 36, 1612-1615.

Mossop,S.C. 1978 a. The influence of drop size distribution on the production of secondary ice particles during graupel growth. Roy.Met.Soc.Quart.Journ., 104, 323-330.

Mossop,S.C. 1978 b. Some factors governing ice particle multiplication in cumulus clouds. J.Atmos.Sci., 35, 2033-2037.

Telford,J. & Chai,S. 1979. A new aspect of condensation theory - Pageoph Vol. 117 in press.

ACKNOWLEDGEMENT

This work was supported in part by a grant from the National Science Foundation, Washington D.C., Grant No. (ATM 77-07995).

OBSERVATIONS OF SNOW SIZE SPECTRA IN FRONTAL CLOUDS: DEVIATIONS FROM THE MARSHALL-PALMER FORM

Paul H. Herzegh
The Center for the Environment and Man, Inc.
Hartford, CT USA
and
Peter V. Hobbs
Department of Atmospheric Sciences
University of Washington
Seattle, WA USA

1. INTRODUCTION

Marshall and Palmer (1948) were the first to use an exponential relationship between concentration and diameter to describe the size spectra of raindrops. Their relation took the form

$$N(D) = N_o \exp(-\lambda D) \qquad (1)$$

where $N(D)dD$ is the concentration of drops in the diameter range D to $D+dD$ and N_o and λ are empirical parameters. Since that time, exponential relations such as (1) have been widely used to describe rain, snow and hail size spectra (Gunn and Marshall, 1958, Sekhon and Srivastava, 1970; Federer and Waldvogel, 1975). However, more recent studies have shown that in many situations, particle size spectra do not follow an exponential form. For example, Houze, *et al.* (1979) found that 76% of the snow size spectra which they observed in frontal clouds contained significant deviations from the exponential form for diameters ≤ 2 mm.

In this paper we examine the forms of the snow size spectra which were observed in three cold-frontal precipitation systems using measurements collected as part of the University of Washington's CYCLES (Cyclonic Extratropical Storms) Project. Radar measurements were obtained from the National Center for Atmospheric Research (NCAR) CP-3 radar (wavelength 5.45 cm), which was located 45 km south of Seattle, WA during January 1976 and on the Pacific coast at Ocean Shores, WA during December 1976. Airborne measurements were obtained from the University of Washington's B-23 and NCAR's Sabreliner. Particle-size spectra were measured aboard the aircraft by Particle Measuring Systems (PMS) cloud and precipitation probes.

2. MESOSCALE AND SYNOPTIC SETTINGS

On 26 January 1976, radar and aircraft observations were obtained in a mesoscale rainband associated with a cold surge aloft, slightly ahead of an upper-level cold front. On 22 January 1976, measurements were made in a wide cold-frontal rainband and in a region of lighter, spotty precipitation behind it. On 8 December 1976, radar and aircraft measurements were made in a widespread area of cloud and precipitation associated with the trailing portion of a cold front aloft.

3. INTERNAL STRUCTURE AND VERTICAL AIR MOTIONS IN THE PRECIPITATION SYSTEMS

The NCAR radar was routinely operated in the vertically-pointing mode as precipitation areas passed over the radar site. The resulting measurements yielded detailed time-height sections of radar reflectivity factor (Z) which can be roughly interpreted as cross-sections along the mean wind direction, which ranged from about 245° to 260°.

a. Precipitation structure

Three general characteristics which emerged from the time-height sections of Z are exemplified in Fig. 1a. First, note that Z generally increased downward above the 0°C level. This is a normal consequence of the growth of falling precipitation particles in cloud. Second is the layer of high Z values (the bright band) which appears just below the 0°C level in Fig. 1a. The bright band results from the increased radar backscattering of melting snowflakes bearing a thin film of liquid water and indicates that snowflakes were the dominant particle forms above the 0° C level. Third is the occurrence of nearly-vertical precipitation shafts (shaded in Fig. 1a) which are associated with embedded convection. Individual shafts ranged from about 3 to 10 km in width.

b. Vertical air motions

The vertical air velocity (W) in snow over the CP-3 radar was deduced from the relationship

$$W = V_D - V_P \qquad (2)$$

where V_D is the mean vertical Doppler velocity of particles at a specific height above the radar, and V_P is the mean reflectivity-weighted terminal velocity of the particles. The quantity V_D was estimated from measurements of Z as described by Herzegh and Hobbs (1980). Due to spatial variabilities in types and size spectra of snow particles, values of W derived from (2) may be in error by up to ± 0.30 m s^{-1} .

The pattern of vertical air motions in the cold-surge rainband (Fig. 1b) was reminiscent of that associated with mid-latitude squall lines, which contain young, vigorous convective cells in their leading portions and older, dissipating cells to the rear. A region of deep convection was located ahead of the cold-surge surface observed. Like the cold-surge rainband, the wide cold-frontal rainband contained updrafts above and ahead of the cold-frontal surface and downdrafts beneath it. However, aircraft observations of icing, cloud structure, and turbulence indicate that the vigorous convection in this system was mainly confined to the region above 5 km altitude. The convective cells present, which are termed generating cells because of the precipitation trails generated within them,

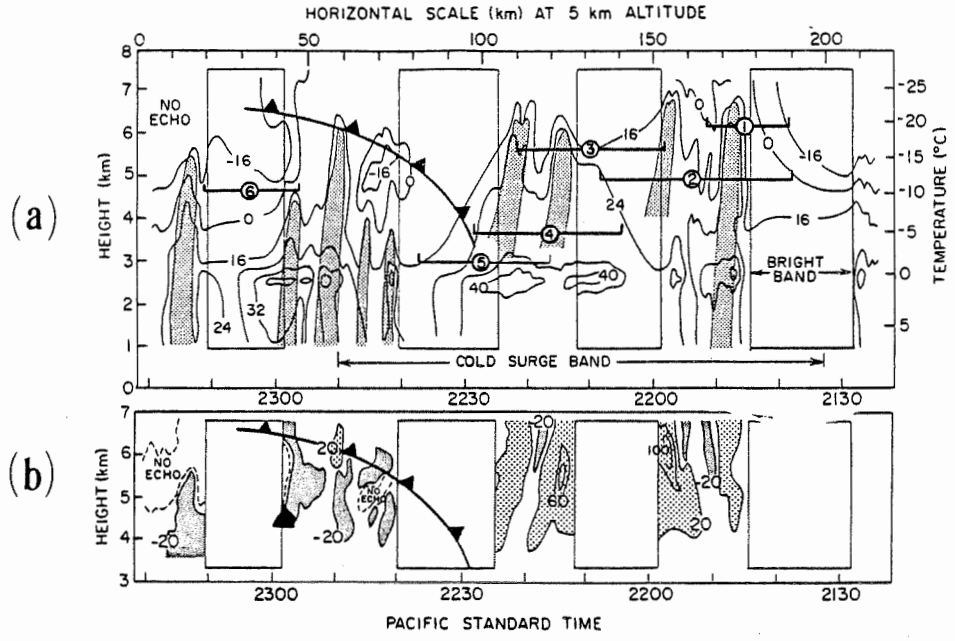

Figure 1. Time-height sections through a cold-surge rainband on 26 January 1976: (a) radar reflectivity factor (dBZ) with precipitation shafts shaded, (b) vertical air velocity (cm s^{-1}). Rectangles enclose regions where data are missing. In (a) aaircraft flight tracks are numbered 1-6. In (b) light shading is for updrafts ≥ 20 cm s^{-1}, dark shading is for downdrafts ≥ 20 cm s^{-1} and contour interval is 40 cm s^{-1}.

contained updrafts as strong as 1.2 m s^{-1} . Radar measurements in the region of the overhanging cold front aloft revealed an irregular pattern of vertical air motions in which most updrafts were located above the cold-frontal surface and most downdrafts were located below it.

c. Summary of cloud environments observed

The general characteristics of the precipitation systems discussed above are summarized by the five cloud environments described in columns 1-5 of Table 1. These environments differed from one another mainly through the role of convection in each. The least convective environments observed were the regions of stratiform cloud associated with the cold fronts aloft on 8 December and 22 January 1976 (lines 1 and 2, Table 1). Moderate convection in the form of shallow generating cells was present in the the upper portions of the cloud systems observed on these two days (lines 3 and 4, Table 1). Strong, deep convection was found in the warm-sector rainband observed on 26 January 1976 (line 5, Table 1).

4. MEASUREMENTS OF SNOW SIZE SPECTRA

Measurements over 5-sec intervals by the PMS Probes yielded average snow size spectra corresponding to a 0.7 km path length. The spectra observed were categorized according to the degree to which they were exponential in form for diameters from 0.3 to 3.12 mm. The categories defined were:

1) Exponential (having no major deviations from the exponential form);
2) Super-exponential (having an excess of particles ≤ 2 mm in diameter);
3) Sub-exponential (having a deficit of particles ≤ 2 mm in diameter);
4) Non-exponential (having other deviations from the exponential form).

Each spectrum type is illustrated in Fig. 2.

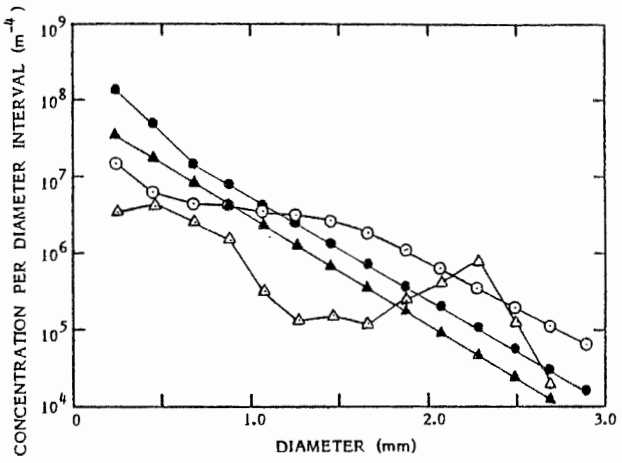

Fig. 2. Examples of sub-exponential (⊙), exponential (▲), super-exponential (●), and non-exponential (△) snow size spectra. Note deviations from exponential form for diameters 2 mm in sub-exponential and super-exponential spectra.

The results of the above analysis, summarized in columns 6-10 of Table 1, reveal several correlations between spectrum type and cloud environment. Stratiform clouds (lines 1 and 2, Table 1) were marked by high proportions of sub-exponential spectra (up to 87%) and much lower fractions of exponential and super-exponential spectra. However, as the degree of convective activity increased (from top to bottom in Table 1), the fractions of sub-exponential spectra decreased, reaching a minimum of 7% in the deep convective environment, where 80% of the spectra observed were exponential or super-exponential.

These observations indicate that the snow size spectra in stratiform environments are, in general, depleted of particles in the diameter range 0.3 to 2 mm. The deepest depletion is observed in the diameter range 0.5 to 1 mm. Although a full understanding of these observations is not yet possible, our data do suggest a

TABLE 1. Summary of observations of cloud environment characteristics and corresponding snow size spectrum types.

Cloud Environment	Lapse Rate	Date	Altitude (km)	Average Wind Shear (10^{-2} m^{-1})	Total No. of Spectra	Sub-Exponential Spectra (%)	Exponential Spectra (%)	Super-Exponential Spectra (%)	Non-Exponential Spectra (%)
TYPE 1: Stratiform cloud	Stable	8 Dec 76	4.0 - 5.2	1.34	38	87	0	0	13
TYPE 2: Stratiform cloud with well-defined precipitation trails	Stable	22 Jan 76	2.4 - 4.8	0.85	59	76	14	0	10
TYPE 3: Weak generating cells embedded in stratiform cloud	Moist Adiabatic	8 Dec 76	5.2 - 6.4	0.71	50	72	20	2	6
TYPE 4: Vigorous generating cells embedded in stratiform cloud	Moist Adiabatic	22 Jan 76	4.8 - 7.3	0.32	63	32	56	6	6
TYPE 5: Deep convective cells	Moist Adiabatic	22 Jan 76	3.0 - 6.2	0.13	70	7	49	31	13

qualitative explanation involving the formation of aggregate snowflakes, the dominant precipitation particle type in the cloud environments described in Table 1. The fact that most component crystals collected by aggregate snowflakes are between 0.1 and 1.5 mm in diameter indicates that the process of aggregation itself will result in some depletion of in-cloud particle concentrations over a diameter range similar to that in which depletion is actually observed. Conversely, processes such as particle fragmentation (Vardiman, 1978), the riming-splintering ice multiplication mechanism described by Hallett and Mossop (1974) and droplet freezing, whose roles in frontal clouds have been discussed by Hobbs, *et al.* (1980) and Herzegh and Hobbs (1980), can supplement the concentrations of small ice particles in clouds. Thus, the degree of particle depletion observed may reflect the balance between aggregation and these supplementary processes. Accordingly, the vigorous activity expected of supplementary processes in convective environments, where strong turbulence and cloud liquid water are common, could account for the formation of super-exponential rather than sub-exponential spectra there. In addition, vertical changes in the horizontal wind speed may contribute to the observed depletion of particles in the 0.3 to 2 mm diameter range by separating fast-falling particles from slow-falling ones. Such a mechanism could effectively sort particles which are 0.3 to 3 mm in diameter, due to rapid changes of fallspeed with diameter in this size range. As shown by Column 5 of Table 1, the average vertical shear of the horizontal wind decreased from a maximum of 1.34×10^{-2} m^{-1} in the stratiform environment, where sub-exponential spectra dominated, to a minimum of 1.31×10^{-3} m^{-1} in the deep convective environment, where very few sub-exponential spectra were observed.

5. QUANTITATIVE EFFECTS OF OBSERVED SNOW SIZE SPECTRUM DEVIATIONS

The depletion and enhancement of the concentrations of particles ≤ 2 mm in diameter described in § 3 can influence the functional relationships among precipitation rate (R), precipitation mass content (M), and radar reflectivity factor (Z), and thus may account for some of the uncertainty in estimates of R and M which are based on measurements of Z.

The magnitude of this uncertainty was assessed by examining values of the parameters

$$R^* = R/R_o \quad \text{and} \quad M^* = M/M_o$$

where R and M apply to the observed spectrum and R* and M* are the precipitation rate and precipitation mass content, respectively, of a corresponding hypothetical spectrum of equal slope and radar reflectivity factor, but lacking any deviation from the exponential form. Thus, R* and M* indicate quantitatively how the observed spectrum deviations affect precipitation rate and precipitation mass content. The deficit of small particles in sub-exponential spectra leads to values of R* and M* which are < 1, while the excess of small particles in super-exponential spectra leads to values > 1.

The histograms in Fig. 3 show the frequency of occurrence of values of R* for each of the 5 environments described in Table 1. Corresponding values of M* are not shown since they have been found to closely follow the relationship

$$M^* = R^{*1.22} .$$

In stratiform cloud (Type 1 environment) R* ranged from 0.3 to 0.8, indicating that the precipitation rates associated with the sub-exponential spectra observed there ranged from about 30 to 80% of those which would be associated with exponential spectra of equal radar reflectivity factor. The mean values of 0.5 for R* and 0.4 for M* shown in Fig. 3 for this environment suggest that in similar environments, radar estimates of R which assume that the snow size spectra within the radar beam follow the exponential form are likely to be low by about 50%, while corresponding estimates of M are likely to be low by about 60%. Similar radar estimates of R and M in stratiform cloud containing weak generating cells (Type 3 environment) are, on the average, likely to be low by about 30%, while no systematic error is indicated for estimates of R and M in convective regions, where snow size spectra are dominantly exponential and super-exponential in form.

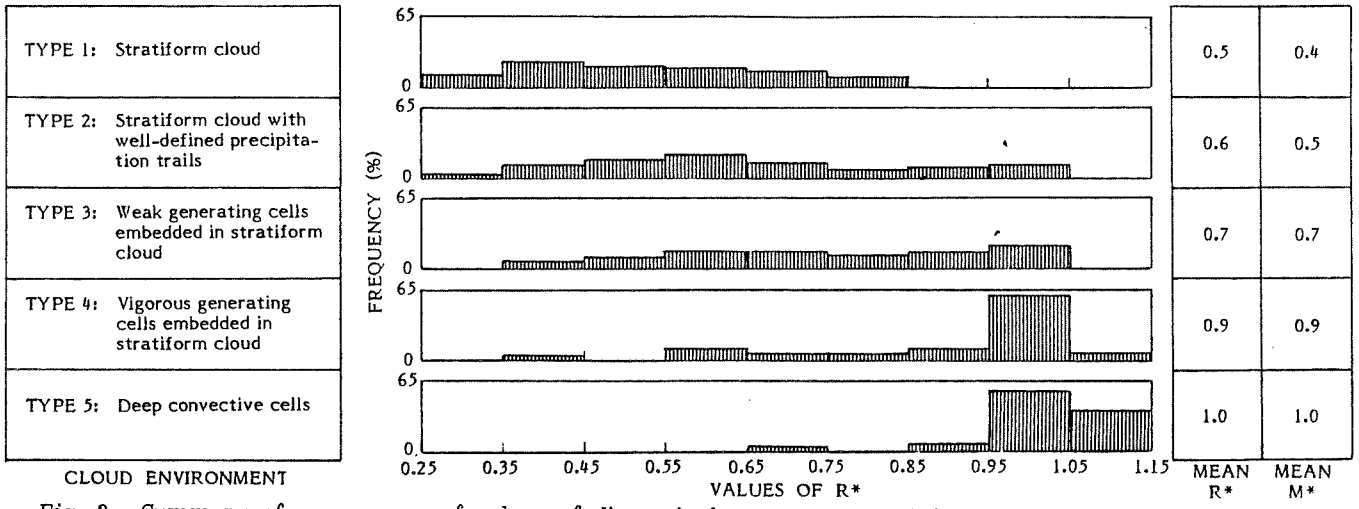

Fig. 3. Summary of occurrence of values of dimensionless parameters R amd M*. Cloud environments are described at left; histograms in center give frequency of occurrence of values of R* for each environment; mean values of R* and M* for each environment are shown at right.*

6. SUMMARY AND CONCLUSIONS

Snow size spectra measured aloft in clouds associated with three frontal systems were categorized according to the degree to which they were exponential in form for diameters from 0.3 to 3.12 mm. Several correlations between spectrum type and cloud environmental characteristics were revealed. Stratiform clouds were marked by high proportions (up to 87%) of sub-exponential spectra and much lower fractions of exponential and super-exponential spectra. As the degree of convective activity increased, fractions of sub-exponential spectra decreased, reaching a minimum of 7% in an environment of deep convection, where 80% of the spectra observed where exponential or super-exponential.

Different spectrum types observed are believed to reflect different states of balance among processes which produce small ice particles in cloud (such as fragmentation, droplet freezing, and ice multiplication by the riming-splintering mechanism) and those which can remove small particles (such as aggregation and particle size-sorting). However, a complete understanding of roles played by these processes in the development of sub- and super-exponential spectra will require additional field studies and detailed microphysical modeling efforts.

The depletion of small particles associated with sub-exponential spectra was found to contribute significantly to the uncertainty of radar estimates of R and M in snow. In stratiform cloud, radar estimates of R which assume that the snow size spectra within the radar beam follow the exponential form are likely to be low by about 50%, while corresponding estimates of M are likely to be low by 60%. In convective areas, these errors diminish to near zero. Thus, in frontal clouds, where convective bands are frequently embedded in widespread stratiform precipitation, it appears that radar estimates of snowfall could be significantly improved by taking into account correction factors based on observed errors such as those described above. Further examination of errors such as these in mid-latitude snowfall is warranted.

Acknowledgments: We thank the members of NCAR's Atmospheric Technology Division, who operated the CP-3 radar and Sabreliner, and members of the University of Washington's Cloud Physics Group for their help in collecting data.

This analysis was supported by the Atmospheric Research Section, National Science Foundation (NSF) under Grant ATM77-22327 and by the Charles E. Culpeper Foundation, Inc. The CYCLES Project is supported by the Atmospheric Research Section, NSF, under Grants ATM74-14726-A02 and ATM77-01344; the Air Force Office of Scientific Research (Contract F49620-77-C-0057); the Environmental Research Laboratories of the National Oceanic and Atmospheric Administration (Grants 04-7-022-44023 and-44033); and the U.S. Army Research Office (DAAG 29-79-C-0005). Computing support was provided by NCAR, which is sponsored by NSF.

References

Federer, B. and A. Waldvogel, 1975: Hail and raindrop size distributions from a Swiss multicell storm. J. Appl. Meteor., 14, 91-97.

Gunn, K.L. S. and J.S. Marshall, 1958: The distribution with size of aggregate snowflakes. J. Meteor., 15, 452-466.

Hallett, J. and S.C. Mossop, 1974: Production of secondary ice particles during the riming process. Nature, 249, 26-28.

Herzegh, P.H. and P.V. Hobbs, 1980: The mesoscale and microscale structure and organization of clouds and precipitation in mid-latitude cyclones. II: Warm-frontal clouds. J. Atmos. Sci., (in press).

Hobbs, P.V., T.J. Matejka, P.H. Herzegh, and R. A. Houze, Jr., 1980: The mesoscale and microscale structure and organization of clouds and precipitation in mid-latitude cyclones. I: A case study of a cold front. J. Atmo. Sci., (in press).

Houze, R.A., Jr., P.V. Hobbs, P.H. Herzegh, and D.B. Parsons, 1979: Size distributions of precipitation particles in frontal clouds. J. Atmos. Sci., 36, 156-162.

Marshall, J.S. and W.McK. Palmer, 1948: The distribution of raindrops with size. J. Meteor., 5, 165-66.

Sekhon, R.S. and R.C. Srivastava, 1970: Snow size spectra and rada reflectivity. J. Atmos. Sci., 27, 229-307.

Vardiman, L., 1978: The generation of secondary ice particles in clouds by crystal-crystal collision. J. Atmos. Sci., 35, 2168-2180.

MICROPHYSICS OF COASTAL FOG AND STRATUS

James G. Hudson

Desert Research Institute
University of Nevada System
Reno, Nevada, U.S.A.

1. INTRODUCTION

Variations in the microstructure of convective type clouds have been attributed to systematic differences in the concentration of CCN (Squires, 1958), which depend upon air mass origin (Twomey and Wojciechowski, 1969). Several studies have shown the relationship between CCN concentrations and drop concentrations in convective clouds.

Variations in the microstructure of fog have also been reported (e.g. May, 1961; Garland, 1971). However, it has not been possible to actually match fog drop and CCN concentrations because the observed CCN concentrations are almost always higher than the concentrations of drops in fog or stratus (e.g. Low, 1975; Goodman, 1977). This is because fogs and stratus form at low supersaturations, which cannot be reliably duplicated in diffusion type cloud chambers (Twomey, 1967: Sinnarwalla and Alofs, 1973; Hudson and Squires, 1976).

One of the major purposes of this study was to actually measure the effective supersaturation in fog by simultaneously measuring both the nuclei of fog condensation and the fog drop concentration. In so doing, it would then be possible to see to what extent fog microstructure is actually determined by the aerosol.

2. APPARATUS

The measurement of CCN can be extended to lower values of supersaturation by using the isothermal haze chamber (IHC) first described by Laktionov (1972). IHC's have been described by Hudson (1976, 1978) and Alofs (1978). The basic operating principle of the IHC relates to the fact that the equilibrium size of a haze droplet, r_o, at 100% R.H. (supersaturation = 0) is uniquely related to the critical supersaturation, S_c, of the nucleus. At T = 20°C the relationship is:

$$r_o = \frac{4.1 \times 10^{-6}}{S_c} \qquad (1)$$

where r is in centimeters and S_c is in percent.

The Desert Research Institute (DRI) IHC is a device which subjects sample aerosol to 100% relative humidity for 100 to 200 seconds. In most cases, this is enough time to allow the drops to attain their equilibrium sizes at which time they are counted and sized by an optical particle counter (OPC - Royco 225). The size is then related to the critical supersaturation S_c so that an N vs. S_c curve can be drawn (such as Figure 1).

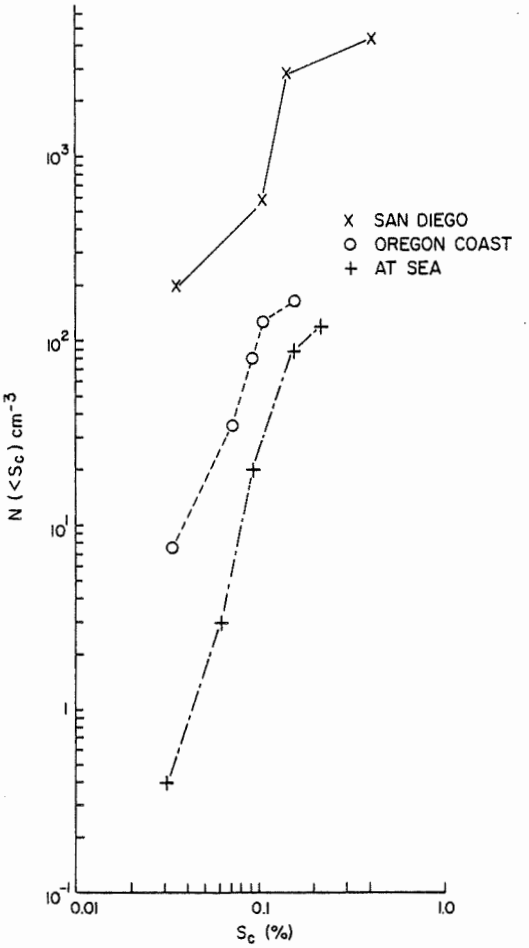

Figure 1. Typical fog condensation nucleus (FCN) spectra at three locations. X = San Diego, 27 Dec. 1975; 0 = Yaquina Head, 26 July 1977; + = R.V. Wecoma (30 km off Oregon coast) 29 July 1977.

The DRI IHC was built along the same lines as the continuous flow diffusion (CFD) chamber (Hudson and Squires, 1976), in that the sample occupies only a small volume of the cloud chamber which is made up mostly of particle-free filtered air. This instrument has been more fully described by Hudson (1976). Results from the DRI CFD and IHC were usually continuously monitored and were found to be consistent as exhibited in Figure 2.

3. FIELD OPERATION

Measurements were made at three coastal locations: (1) the Naval Ocean Systems Center at Pt. Loma, San Diego, CA; (2) Trinidad Head in northern CA; and (3) Yaquina Head on the central Oregon coast. Another set of

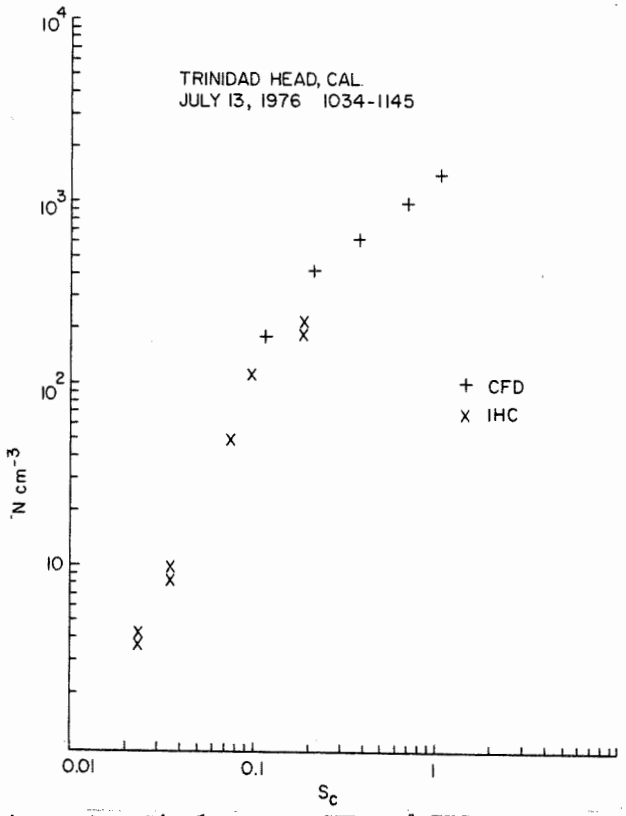

Figure 2. Simultaneous CFD and IHC measurements.

measurements was made at San Nicholas Island (90 km off the California coast from Pt. Mugu; 110 km southwest of Los Angeles). At these locations, a CFD and an IHC were operated from within a shelter. The optical bench of one Royco OPC was placed on the roof of the trailer in order to monitor ambient aerosol (fog when it occurred). A fifth set of measurements was made from the R.V. Wecoma at a distance of about 30 km from the Oregon coast. Some additional measurements were made from an aircraft off the southern California coast. In this case, a PMS OPC was used to measure the cloud drop spectrum.

4. RESULTS

Figure 3 shows fog with numerous drops while Figure 4 shows very few drops. The San Diego data (Fig. 3) does not show much of a distinction between unactivated haze drops and activated cloud drops but the fogs measured at sea do show a very clear distinction between haze and cloud drops. The levelness of the cumulative distribution shows that a tiny proportion of the drops are between 0.4 μm and 2.0 μm radius. The absence of drops in this size range is presumably due to the fact that the drops which would have equilibrium haze sizes in this range have become activated and have grown to larger sizes. Small drops (those grown on nuclei with higher Sc's) remain small because they are unactivated. Intermediate distributions were found at all locations.

These differences in fog microstructure may be explained by examining Fig. 1 which shows typical FCN and CCN distributions at these sites. These data clearly demonstrate the direct relationship between particle concentrations and fog drop concentrations.

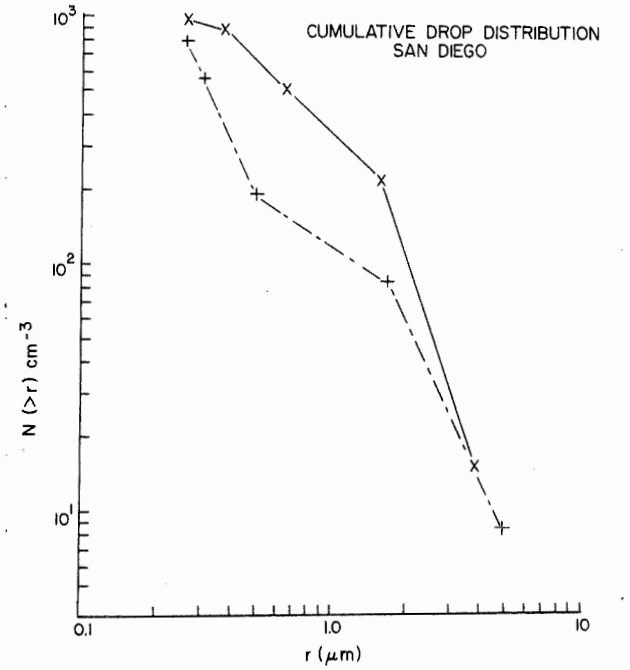

Figure 3. Cumulative number of drops greater than the threshold sizes vs. radius. This data was taken at the Naval Oceans System Center, Pt. Loma, San Diego, CA. + = 0100 h PDT, 8 Oct 1976; X = 0205 h PST, 27 Dec 1975.

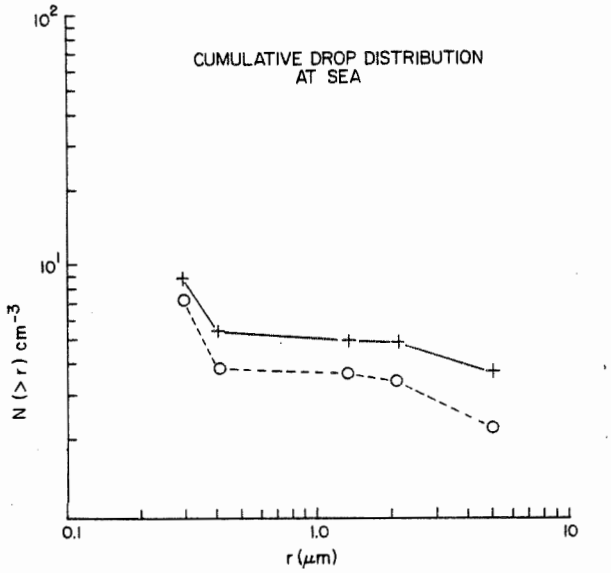

Figure 4. Same as Fig. 3. Data taken onboard the R.V. Wecoma at about 30 km from the Oregon coast at Newport. + = 0830-0840 h, 0 = 0843-0901 h, PDT, 29 July 1977.

Table 1 summarizes some of the nucleus spectra collected at the various sites. The slope of the FCN distribution is usually much higher than that for the CCN distribution.

Figure 5 shows an example of simultaneous drop size distributions in fog and in the IHC. Since the IHC operates at 100% R.H., this represents the equilibrium drop distribution in the ambient air at 100% R.H. The FCN concentration can be derived by using equation (1). By combining these data, it is possible to associate nucleus concentrations for specific Sc's with drop concentrations. First, it is necessary to assume that larger drops are formed on larger

Table 1. Characteristics of the CCN and FCN Distributions

Location/Time	Air Mass Type	CCN C 1%	CCN K 1-0.2%	FCN N S=0.04%	FCN K 0.2-0.04%	Visibility at 100% R.H.
San Diego, 7/7/76 1152-1130	Cont.	1400	0.7	18	2	2,800 m
Trinidad, 7/13/76 1034-1145	Cont.	1300	0.85	11	2	5,000 m
Yaquina, 9/30/77 1237-1314	Maritime	230	0.2	25	1	6,000 m
San Diego, 10/14/76 1144-1248	Polluted	2500	0.7	250	∿ 0.7	420 m
San Diego, 12/26/75 2309-2324	Polluted	--	--	180	2	380 m
Yaquina, 7/26/77 1719-1852	Cont.-Mar. Modified	2000	2	11	2	10,000 m
Trinidad, 7/15/76 1750-0800		--	--	12	2.3	5,000 m
San Diego, 6/26/76 0641-0646				35	2.1	1,600 m
Yaquina, 7/26/77 0221-0225				25	1.2	5,000 m
Wecoma, 7/29/77 0830-0840				0.8	3.3	20,000 m
San Diego, 12/27/75 0340-0353				90	∿ 1.5	600 m
San Diego, 12/27/75 0030-0040				115	∿ 2.8	800 m
San Nicholas Island 5/28/78 - 1200	Poll-Mar. Modified	3600	1.5	∿ 2	∿ 3.5	7,600 m

nuclei (those with lower Sc's); then a one-to-one correspondence can be made between Sc and r where N(<Sc) from the IHC is matched with N(>r) from OPC measurements of fog.

If the ambient air were exactly saturated, then the number vs. size distribution in the IHC should match that for the OPC on ambient aerosol. If the ambient environment is supersaturated (at S_m), then some of the larger nuclei (those with $S_c < S_m$) should grow beyond their r_o sizes and should, in fact, exceed their critical sizes, r_c. In that case, the concentration of large drops should be greater in ambient air than in the IHC. The third curve in Fig. 5 is strictly an artificial device which takes the IHC data and moves the sizes from r_o to r_c (multiplying r_o by $\sqrt{3}$). This does not represent any real distribution because drops cannot remain in equilibrium at their critical radii unless the ambient supersaturation exactly matches their Sc. Obviously this is impossible for a distribution of nuclei. However, this curve is useful because its intersection with the ambient distribution indicates the level of the effective supersaturation in the fog. Above this size, there are more drops in the ambient distribution because they have had the opportunity to grow beyond their critical size. At smaller sizes, the artificial distribution equals or surpasses the ambient drop distribution because these drops are unable to grow beyond their critical sizes. Thus, the Sc corresponding to the r_c at the intersection of these curves yields the effective supersaturation in the fog.

Several examples from the various surface sites yielded effective supersaturations between 0.06% and 0.11%. Aircraft measurements in

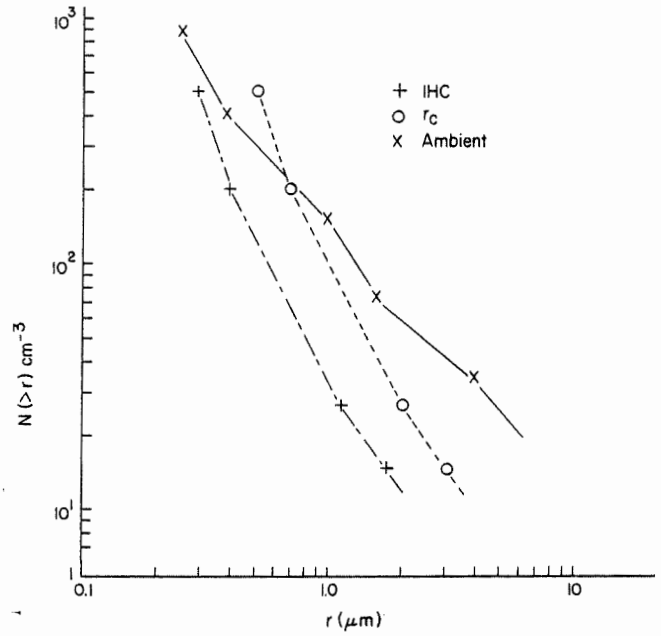

Figure 5. Similar to Fig. 3. Data from San Diego, 0641-0646 PDT, 26 June 1976. X = direct aerosol, + = simultaneous cumulative drop distribution in the IHC, 0 - takes the IHC curve and moves the sizes from r_o to r_c ($r_c = 3\ r_o$). This curve does not represent any real drop distribution but is only used to determine the effective supersaturation in the fog which was 0.10%. Visibility calculated from the drop distribution = 300 m. Visibility measured simultaneously by an MRI visiometer = 160-300 m. Effective supersaturation 0.10%.

stratus off the southern California coast displayed higher supersaturation between 0.2 and 0.3%. In a few cases at the San Diego site there was no intersection between the ambient drop curve and the N vs r_c curve (at least up to the sizes which could be measured). This would indicate that the "fog" was not supersaturated even though the visibility was measured to be less than 100 meters.

Potentially low visiiblities (<1 km - Table1) in saturated air (R.H. = 100%) were possible only in "polluted" regimes where there were high FCN concentrations such as that often observed at the San Diego site. However, none of the data collected here supports the contention that fog type visibilities can exist in substantially subsaturated air because even the highest FCN concentration yielded a visibility of 2 km at 99% R.H.

Figure 6 shows a composite of diurnal averages at San Nicholas Island for three components of the aerosol CN, CCN, and FCN. All three aerosol components show a mid-day peak in concentration which hints at photochemical particle production. Furthermore, the fact that the smallest but most numerous particles show the largest variations is in keeping with the hypothesis of particle production. The increase of daytime over nighttime concentrations was about 50% for CN, 30% for CCN and 10% for FCN. The aerosol at SNI was subject to the influence of various air masses - maritime, continental and polluted - as the concentration showed a great deal of day-to-day and even hour-to-hour variation.

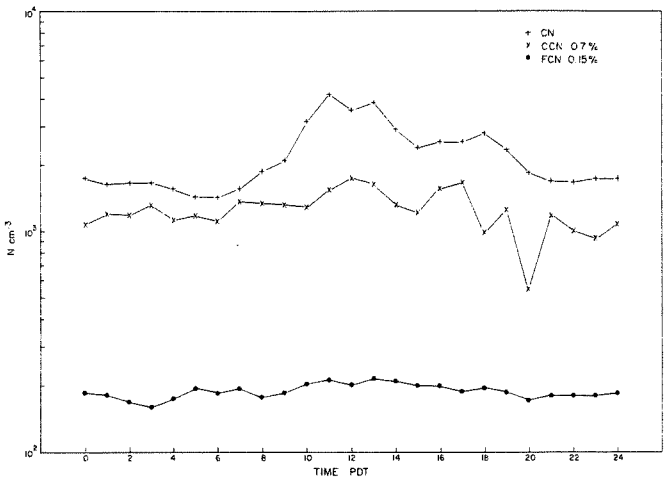

Figure 6. Composite diurnal averages of aerosol concentration at San Nicholas Island for May 14-31, 1978. Each point represents the average value at a particular hour for the entire period. + = condensation nuclei (CN or Aitken nuclei; X = cloud condensation nuclei (CCN) (S_c = 0.7%); • = fog condensation nuclei (FCN) (0.15% S_c).

Figure 7 illustrates the frequency distribution of four aerosol components, showing that all components vary over about an order of magnitude. The diurnal variation especially for CN seemed to be superimposed upon the secular variations due to air mass origin (wind direction). In fact a diurnal CN plot for cases only with westerly wind direction (the maritime direction)showed only a slightly less pronounced mid-day peak concentration (4 K cm^{-3} instead of 6 K cm^{-3}). In fact, four out of five days which had maritime wind fetches also displayed distinct mid-day peaks in concentration.

5. CONCLUSIONS

Wide variations in fog microstructures have been shown to be due to variations in FCN concentrations. It has been shown that, like CCN concentrations, FCN concentrations are also higher in continental and polluted air. CCN and FCN concentrations can vary by two orders of magnitude. This variability is apparently responsible for the systematic variation in fog microstructure between fogs formed in maritime, continental, and "polluted" air masses, with FCN and drop concentrations increasing respectively. These simultaneous FCN and drop size distributions have shown an effective fog supersaturation of between 0.06% and 0.11%. However, drop distributions in continental air (or "polluted" air) show that in fog there is often not a clear distinction between unactivated haze drops and activated drops as is thought to be the case for convective type clouds. Thus, unactivated haze drops can play an important role in fog visibility impairment.

6. ACKNOWLEDGEMENTS

This research was sponsored by the Office of Naval Research, Contract N-00014-75-C-0527. Much of the equipment was obtained by the National Science Foundation under Grant DES-73-0631.

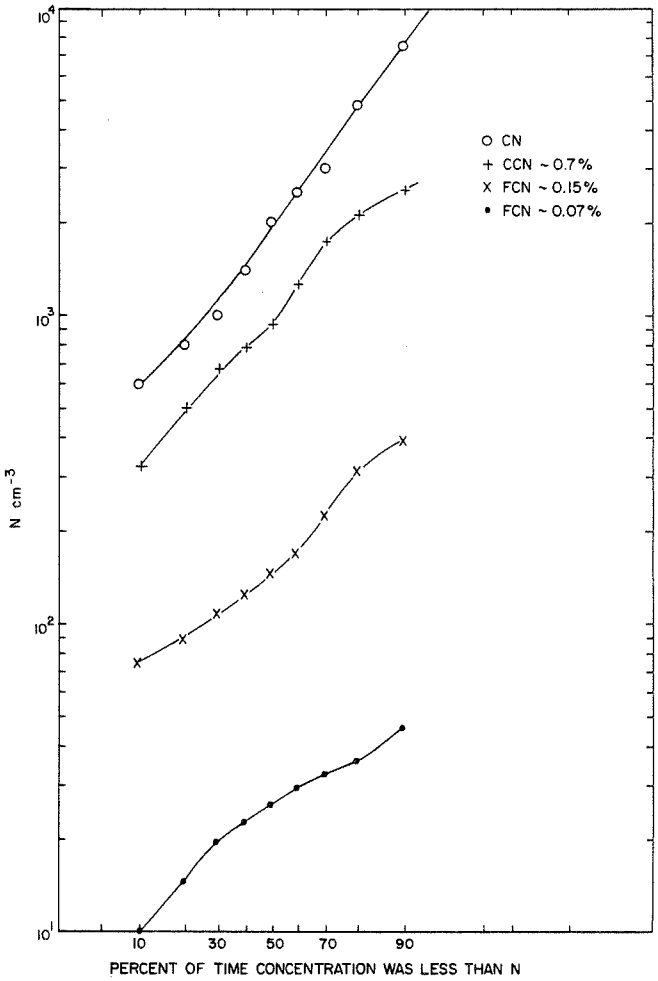

Figure 7. Frequency distribution of various aerosol components at San Nicholas Island, May 14-31, 1978.

7. REFERENCES

Alofs, D.J., 1978: Performance of a dual-range cloud nucleus counter. J. Appl. Meteor., 17, 1286-1297.

Fitzgerald, J.W., 1972: A study of the initial phase of cloud droplet growth by condensation. Comparison between theory and observation. Dissertation for Ph.D. in the Geophysical Sciences, Univ. of Chicago, pub. as Tech. Note 44 of the Univ. of Chicago, Cloud Physics Lab, June.

Garland, J.A., 1971: Some fog droplet size distributions obtained by an impaction method. Quart. J.R. Met. Soc., 97, 483-494.

Goodman, J., 1977: The microstructure of Calif. coastal fog and stratus. J. Appl. Meteor., 16, 1056-1067.

Hudson, J.G. and P. Squires, 1976: An improved continuous flow diffusion cloud chamber. J. Appl. Meteor., 15, 776-782.

Jiusto, J.E., 1966: Maritime concentration of condensation nuclei. J. Rech. Atmos., 2, 245-250.

Kocmond, W.C., et al., 1969: A review of project fog drops "Progress of NASA Research on Warm Fog Properties and Modification Concepts," NASA SP-212.

Laktionov, A.G., 1972: A constant-temperature method of determining the concentrations of cloud condensation nuclei. Atmos. Oceanic Phys., 8, 382-385.

Low, R.D.H., 1975: Microphysical and meteorological measurements of fog and supersaturation. Tellus, XXVII, 5, 507-513.

May, K.R., 1961: Fog-droplet sampling using a modified impactor technique. Quart. J.R. Met. Soc., 87, 535-548.

Sinnarwalla, A.M., and D.J. Alofs, 1973: A cloud nucleus counter with long available growth time. J. Appl. Meteor., 12,831-835.

Squires, P., 1958: The microstructure and colloidal stability of warm clouds. Part I: The relation between structure and stability. Part II: The causes of the variations in microstructure. Tellus, 10, 256-271.

Twomey, S., and P. Squires, 1959: The influence of cloud nucleus population on the microstructure and stability of convective clouds. Tellus, 11, 408-411.

Twomey, S., 1967: Remarks on the photographic counting of nuclei. J. Rech. Atmos., 3, 85-90.

Twomey, S. and J. Warner, 1967: Comparison of measurements of cloud droplets and cloud nuclei. J. Atmos. Sci., 24, 702-703.

Twomey, S. and T.A. Wojciechowski, 1969: Observations of the geographical variations of cloud nuclei. J. Atmos. Sci., 26, 684-688.

Vernon W. Keller* and Robert I. Sax**
NOAA (NHEML)
Coral Gables, Florida, USA

1. INTRODUCTION

The rime-splintering hypothesis for secondary ice production, advanced by Hallett and Mossop (1974), is based upon the concept that accretion of a population of small and large cloud droplets by graupel particles present within a narrow temperature range (-3°C to -8°C) leads to the formation of crystalline ice which can later serve as centers for new graupel. Implicit in the hypothesis is the importance of the cloud's updraft structure in governing the timing of the ice production by controlling the flux of graupel particles through the critical temperature zone.

This paper presents a case study of an unseeded isolated cumulus tower which rapidly produced large numbers of small ice crystals within its active updraft region. Until the present study, maximum concentrations of ice crystals observed near -10°C in the updraft regions near the tops of unseeded Florida cumuli were generally only a few per liter. The microphysical characteristics of this case study cloud, particularly the evolution of the spatial distribution and habit of the crystalline ice relative to the updraft are shown to be consistent with a rime-splintering hypothesis for secondary ice production.

2. OBSERVATIONS

The case study (August 15, 1978 Cloud 3) presented here involves an isolated deep (base + 22°C) cloud located in the southern most portion of a cluster of clouds centered just off the west shore of the Florida peninsula near Naples. This cluster of clouds was associated with the west coast sea breeze and during this particular afternoon was the only cluster of clouds to be found anywhere over South Florida. This cloud was penetrated a total of seven times at the -13°C sampling level, 6.7 km (22k ft), by the NOAA RF42 WP-3D aircraft. During the first four penetrations the cloud was in a dissipating state, but, by the time of the fifth penetration, a new tower was actively growing through the remains of the older cell. Following pass 7 the cloud continued growing very rapidly such that further passes could not have been performed without jeopardizing the safety of both the aircraft and crew.

*Present Affiliation:

NASA
Marshall Space Flight Center, Alabama

**Present Affiliation:

Joseph Oat Corporation
Camden, New Jersey

Figure 1 shows a plan view of the penetration sequence relative to Cloud 3 (August 15, 1978). Each of the seven cloud passes is numbered and North is indicated with an arrow. Figure 2 shows plots for the initial cloud pass of total ice particle concentration (derived from an optical scattering device) and formvar replica - deduced concentrations of both graupel and vapor grown ice crystals. On this pass all crystalline ice had major axis diameters greater than 100 μm. The ERT ice particle counter is the commercial version of the University of Washington's instrument (Turner and Radke, 1973). Also indicated on Fig. 2 are regions of the cloud where the vertical wind (W) is less than 0 m s^{-1} and less than negative 6 m s^{-1}. In pass 3/1 a downdraft existed at the sampling level over the entire expanse of the cloud. The cloud was in a dissipating state with a cloud top height, deduced from nose film photogrammetric measurements, of 12.8 km (42k ft). The cloud was nearly pinched off in the middle. It contained a moderate amount of ice nearly all of which was in the form of graupel. The small amount of supercooled water present was in the form of small raindrops. These observations are typical of those found in dissipating cumulus clouds in the South Florida environment.

The cloud continued to dissipate for passes 3/2, 3/3, and 3/4. However, just prior to pass 3/5 a new cloud bubble grew through the -13°C flight level in the midst of the dissipating tower. Figure 3 shows plots for pass 3/5 of vapor grown ice crystal concentration and total graupel concentration deduced from a frame by frame (resolution ~ 0.02s) analysis of the formvar replications. Also indicated on Fig. 3 are portions of the pass where the vertical updraft was greater than 4 m s^{-1}. The main point here is the presence of many small ice crystals in the active updraft region of the cloud. The concentration of small ice crystals ($d \leq 100$ μm) approached 900 ℓ^{-1}. This far exceeds maximum concentrations previously observed in unseeded South Florida cumuli and even approaches the maximum concentrations (1300 ℓ^{-1}) observed in South Florida clouds massively seeded with silver iodide, (Sax et. al., 1979).

Figures 4 and 5 are photographs of formvar replica from pass 3/5. Figure 4, taken from a portion of the replica frame corresponding to a time of 2124:31 GMT, shows seven vapor grown ice crystals. Five of these crystals were replicated such that only their basal faces are observable. They appear as hexagons with inscribed six pointed stars. It is difficult to determine if they are really

plates as they appear or equiaxed columns as viewed end-on. The other two crystals in Fig. 4 are shown enlarged in Fig. 5. They are definitely equiaxed columns and the one in the upper part of Fig. 5 shows hollowed prism faces. All seven of these ice crystals have major axis diameters less than 100 μm. In fact, the 100 μm diameter class distinction criteria was chosen for this cloud pass to allow discrimination between these type crystals, which we believe originated from a secondary ice multiplication process lower in the cloud, and large stellar crystals (not shown), which we believe grew for substantial time periods at or near the flight level. Figure 6 shows plots for pass 3/6 of formvar replica - deduced ice crystal concentrations and graupel concentrations along with ERT ice particle concentrations. Maximum formvar ice crystal concentrations on this pass did not exceed 275 ℓ^{-1} but the ice crystals were larger than the majority of those detected on pass 3/5. In fact, ice crystals with $d > 100$ μm were found in about the same concentrations on this pass as ice crystals with $d \leq 100$ μm. The major point to observe in Fig. 6 is that the greater part of the ice on pass 3/6 was located in the downdraft regions, consistent with our previous experience, rather than in the updraft region as in pass 3/5.

3. DISCUSSION

The occurrence of abundant numbers of small ice crystals (900 ℓ^{-1}) in pass 3/5 of an unseeded cumulus cloud is interpreted to be direct evidence for a secondary ice multiplication mechanism operative in the Florida atmospheric environment. We suggest that the observations in this study are consistent with the Hallett - Mossop hypothesis for secondary ice production. Graupel particles ($d > 300$ μm) ranging in concentration from 50 ℓ^{-1} (pass 3/1) to 15 ℓ^{-1} (pass 3/4) fell through the flight level (-13°C) into the hypothesized generation zone (-3°C to -8°C) for a period of at least seven minutes. Supercooled water droplets ($d > 150$ μm) ranging in concentrations from 15 ℓ^{-1} (pass 3/1) to 10 ℓ^{-1} (pass 3/4) passed downward through the flight level during this same time period. Other studies, Sax and Keller (1980) and Hallett et. al. (1978), have shown that large amounts of supercooled cloud water in the form of both small cloud droplets and cloud droplets having diameters greater than 25 μm, (conditions hypothesized as necessary for the Hallett - Mossop secondary ice production mechanism to be effective) always exist in the region -3°C to -8°C of actively growing summertime cumuli in Southern Florida. Thus, the new bubble (pass 3/5) vigorously growing upwards through the remains of the dissipating older tower certainly had contained within it the particulate criteria for the Hallett - Mossop ice multiplication mechanism to operate.

The generation zone (-3°C to -8°C) in this case corresponded to an altitude of between 5.3 km (17.5k ft) and 5.9 km (19.5k ft). If one assumes ice splinter particles of negligible size were produced in the generation zone and were immediately carried upward to the -13°C (6.7km) sampling level with an average velocity of 10 m s^{-1}, growing the whole time from the vapor at increasingly colder temperatures, then the calculated time interval between splinter production in the generation zone and collection of vapor grown ice crystals on formvar replica at the -13°C flight level ranges between 75 and 140 seconds. Average crystal diameter axial growth rates along both the 'a' and 'c' axes for small vapor grown ice crystals in a supercooled water cloud over this temperature range (-3°C to -13°C) are roughly 0.5 μm s^{-1}, Ryan et. al. (1976). (Recall that the basic habit of ice crystals is primarily a function of temperature with prisms occurring from -3°C to -8°C, more or less equiaxed crystals from -8°C to -11°C, and plates from -11°C to well below -15°C.) Using these reasonable assumptions, one can calculate that the vapor grown ice crystals collected at the 6.7 km (22k ft) flight level should have had major axis diameters ranging from 35 μm to 70 μm. This is consistent with the observations of pass 3/5 that the majority (everything but stellars) of the ice crystals had major axis diameters less than 100 μm. Crystals in passes 3/6 and 3/7 were in general larger than those observed in pass 3/5 because of the additional time for growth in regions of lower updrafts.

We postulate that maximum graupel ($d > 300$ μm) concentrations were high (140 ℓ^{-1}) in pass 3/5 and increased slightly more (to 150 ℓ^{-1}) in passes 3/6 and 3/7 because ice splinters were being continuously captured by large supercooled droplets in the manner predicted by Hallett et. al. (1978), who showed that the probability of a splinter being caught by a supercooled drop is roughly independent of the size of the drop in the range 0.1 to 1.0 mm. Splinters are considered here as either 'splinters' produced directly during the riming process or from cloud droplets (in which case the frozen droplets may be thought of as second generation 'splinters').

The importance of cloud pulsation growth dynamics on the microphysics cannot be overemphasized. In this case the dissipating cloud provided a large flux of graupel throughout the hypothesized generation zone of the new cloud bubble. If ice multiplication proceeded according to the Hallett - Mossop hypothesis, it is reasonable to assume that following the initial production of prolific numbers of splinters, the strong updraft velocity evident in a portion of pass 3/6 (Fig. 6) carried the majority of the secondary particles and the graupel aloft; away from the generation zone. The positive feedback aspect of the multiplication mechanism was broken and by the time of pass 3/6, the strong updraft region of the tower was relatively ice - free. In this situation the ice multiplication mechanism would be repressed until the updraft again weakened or graupel particles grew sufficiently large to allow them to fall back into the generation zone.

4. CONCLUSION

The presence of enormous quantities of small crystalline ice particles within an active updraft near the top of an isolated Florida cumulus cloud at -13°C argues persuasively for the occurrence of secondary ice production. The observations presented in this case study point to a rime-splintering generation mechanism operating within a region 1 km or so below the flight level, consistent with the multiplication hypothesis advanced by Hallett and Mossop (1974). It is shown, though, that the ice production is very much dependent upon the evolution of the updraft. In this case, the tower grew through the remains of a previously existing cloud and a downwards flux of graupel occurred in the generation zone at the proper time for the new updraft to be infused with the products of the multiplication mechanism. We suspect that such circumstances though not typical, are not infrequent within an evolving population of cumuli. The opportunity to sample such a sequence of microphysical events, however, is probably rare considering the very narrow time windows involved.

5. REFERENCES

Hallett, J., and S. C. Mossop, 1974: Production of secondary ice particles during the riming process. Nature, 249, 26-28.

Hallett, J., R. I. Sax, D. Lamb and A. S. R. Murty, 1978: Aircraft measurements of ice in Florida cumuli. Q. J. Roy. Met. Soc., 104, 631-651.

Ryan, B. F., E. R. Wishart, and D. E. Shaw, 1976: The growth rates and densities of ice crystals between -3°C and -21°C. J. Atmos. Sci., 33, 842-850.

Sax, R. I., and V. W. Keller, 1980: Water - ice and water - updraft relationships near -10°C within populations of Florida cumuli. (Accepted for publication in J. Appl. Meteor.).

Sax, R. I., J. Thomas, and M. Bonebrake, 1979: Ice evolution within seeded and nonseeded Florida cumuli. J. Appl. Meteor., 18, 203-214.

Turner, F. M., and L. F. Radke, 1973: The design and evaluation of an airborne optical ice particle counter. J. Appl. Meteor., 12, 1309-1318.

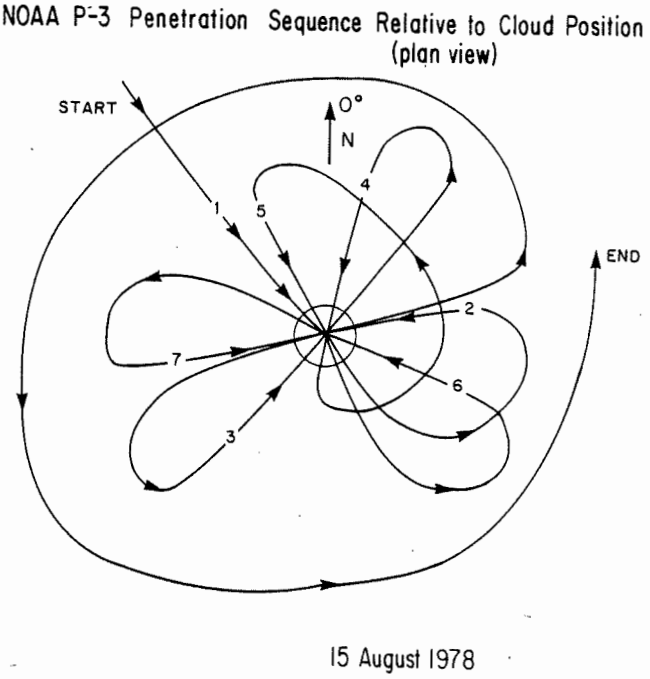

FIGURE 1

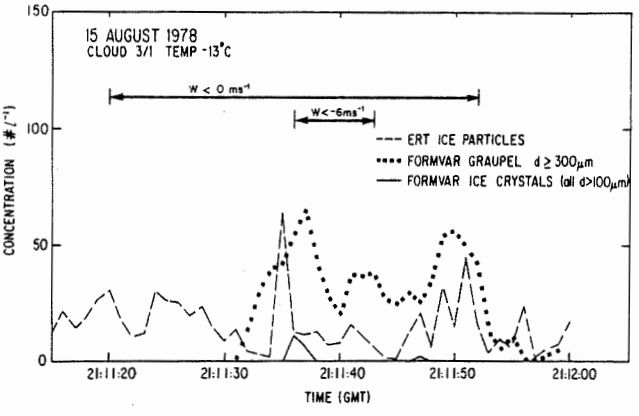

FIGURE 2

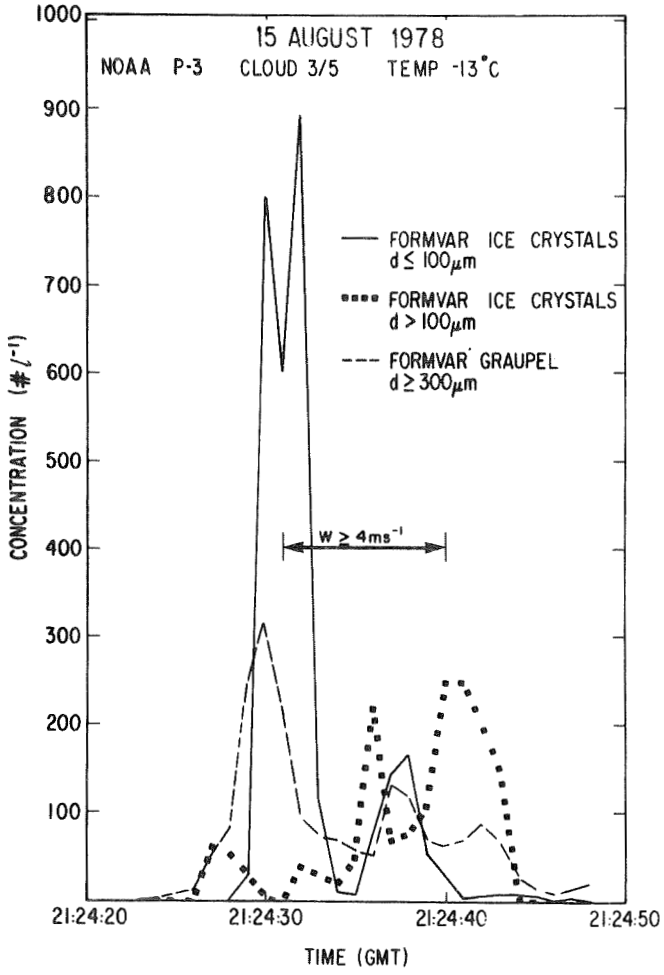

FIGURE 3

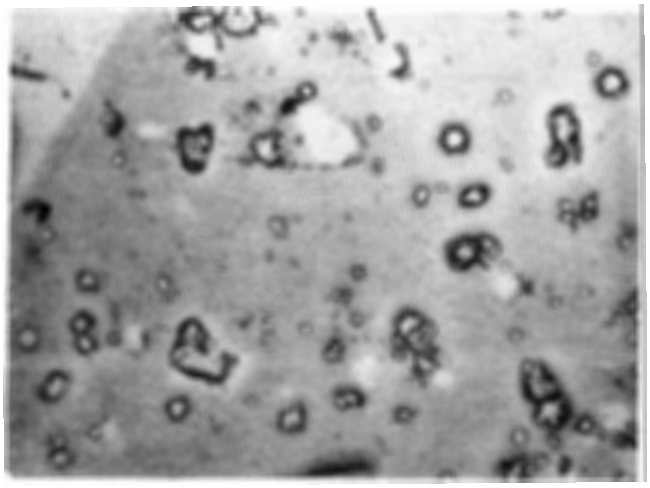

FIGURE 4

150 μm

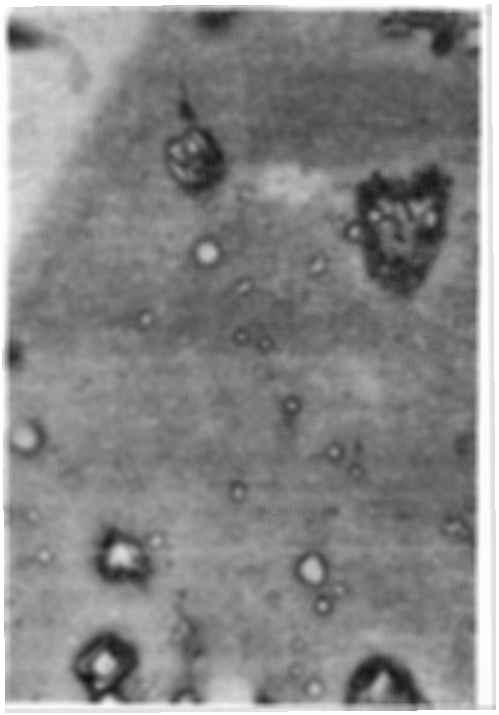

FIGURE 5

75 μm

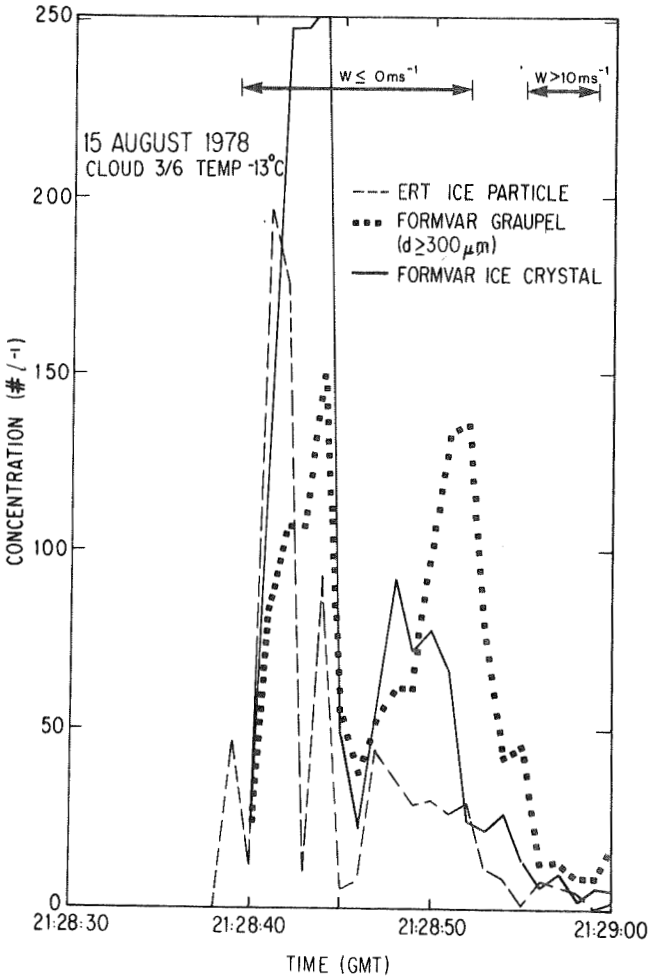

FIGURE 6

OPTICAL PROPERTIES OF THE CLOUD CRYSTAL MEDIUM

V.V.Kuznetsov, N.K.Nikiforova, L.N.Pavlova, A.G.Petrushin, O.A.Volkovitsky

The USSR State Committee for Hydrometeorology
and Control of Natural Environment, Moscow, USSR

The solution of many problems in physics of atmosphere, such as radiative exchange or visibility forecast in severe weather conditions is based on the optical cloud medium models. In spite of numerous publications on optical properties of ice crystal clouds in the last decade, no appropriate optical models of this widespread type of atmospheric aerosols have been developed. Models of ice spheres and cylinders have been used until recently to calculate the optical properties of ice crystal clouds, however, these models did not provide the description of some specific properties of light scattering by crystals revealed from the experiments. It should be noted that almost all the experimental data have been obtained in the laboratory, as it is difficult to carry out optical experiments in the natural ice crystal clouds. Most experimental studies, beginning from Huffman [1], deal with the phase scattering function (indicatrix) of visible radiation. It was difficult to conclude on the application of the above ice cloud models for calculating phase scattering functions, since there was a great discrepancy in measurement results obtained by different authors, particularly in the vicinity of the 90° scattering angle.

The known measurement results of spectral radiation extinction by crystal cloud medium within the range of 0.5-25 μm obtained from the laboratory and field (up to 12 μm) experiments have some differences. When measuring mainly plate-shaped crystals with the sizes of 40-200 μm in the laboratory, extinction minima were observed in the vicinity of the 2.8 and 10.3 μm wavelengths. In the field experiments (with crystals having the shape of needles, their sizes unknown), nearly neutral spectral extinction was observed.

This paper presents some results of the theoretical and experimental studies of visible radiation scattering and spectral extinction by ice nonspherical particles that have been recently performed by the authors. Experiments were made in a cold chamber 100 m^3 in volume where a cloud medium was generated with the crystals of particular shape, plate-shaped ones having a diameter up to 200 μm and thickness about 10 μm [2], and columnar ones with the length up to 200 μm and diameter about 40 μm.

I. Visible radiation scattering

Phase scattering function was measured in a horizontal scattering plane for the horizontal propagation of radiation beam with the wavelength of 0.63 μm. Phase scattering function measuring time was 10 s within the range of scattering angles from 10 to 170°. Simultaneously, the measurements were carried out on the coefficients of directed light scattering at the angles of 10° and ~180° and on the depolarization of a backscattering signal $D = I_{\perp}(\pi) / I_{\parallel}(\pi)$. When comparing the relative phase scattering functions $f(\theta) = I(\theta) / I(10^\circ)$, obtained under different conditions it was found that the presence of spherical particles in a mixed cloud medium ($0.03 \leq D < 0.4$) has much greater effect on the angular distribution of scattered radiation than a variation in crystal size and shape in ice crystal medium ($D_{\pi} \geq 0.4$). The average measured results for the crystals of different shape and size are given in Fig.1. The dispersion of the values $f(\theta)$ does not exceed ±30%. It should be noted that the phase scattering function calculated for ice cylinders [3] underestimates $f(\theta)$ in the vicinity of the 90° angles, does not describe the scattering maxima in the vicinity of halo angles, and significantly understimates the backscattering.

We have studied the light scattering by a hexagonal prism which is much larger in length than in diameter, using the approximate methods of geometrical optics and diffraction. As a result, the expressions were obtained for calculating a normalized phase scattering function for prisms in different directions Θ. Fig. 1 shows the calculated results of the phase scattering function for the assembly of prisms of different sizes, their long axes being randomly oriented in the plane of incident radiation propagation. Curve I shows the light scattering in the plane of prism orientation and curve 2 the scattering in the orthogonal plane. It is evident that the prefered prism orientation resulted in light scattering asymmetry. The intensity of light scattering at

the angle $\Theta=90°$ in the plane of prism orientation is about twice as much as that in the orthogonal plane. This result agrees with the previous experimental data [2]. Halos corresponding to the 22° and 46° angles occur in different scattering planes. The calculated phase scattering functions for prisms are in satisfactory aggreement with the experimental data in the range of $\Theta=20$–$170°$. The underestimation of the calculated values for $\Theta \simeq 180°$ appears to be the result of neglecting the effect of surface waves, etc. As the variation in crystal shape, size and orientation does not result sufficient change of phase scattering function within this range of scattering angles (except halo angles), the following approximated expression was proposed for calculating normalized phase scattering functions

$$I(\Theta)=\frac{T_o\left(\frac{\pi}{2}-\frac{\Theta}{2}\right)}{1+T_o\left(\frac{\pi}{2}-\frac{\Theta}{2}\right)}\left[\frac{3}{4}+\frac{1}{4}T_o\left(\frac{\pi}{2}-\frac{\Theta}{2}\right)\right],$$

where $T_o\left(\frac{\pi}{2}-\frac{\Theta}{2}\right)$ - is the Frensel reflection coefficient.

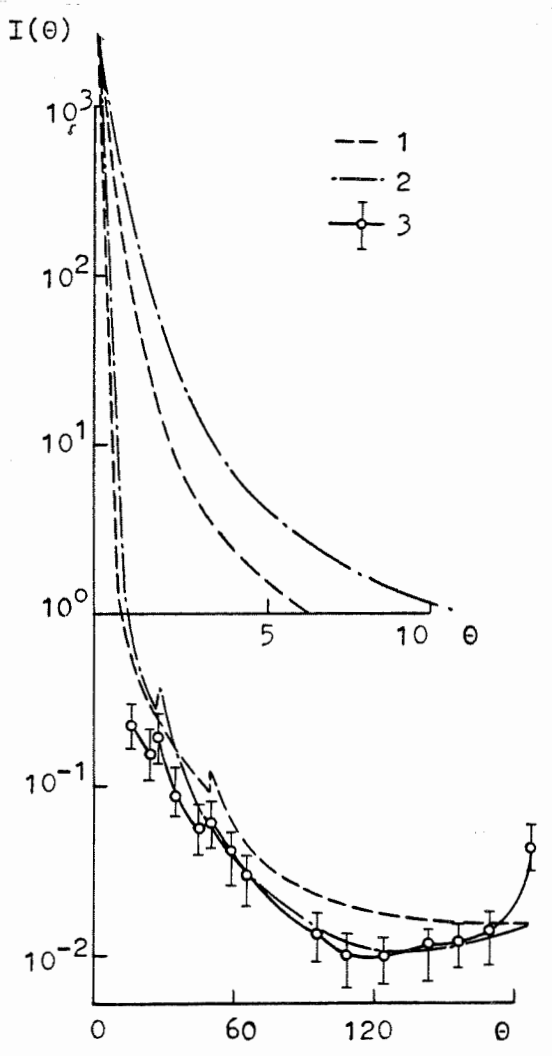

Fig. 1. Phase scattering functions of radiation with $\lambda = 0.63\,\mu$m: 1,2 - calculated; 3 - measured.

2. Spectral extinction of infrared radiation by ice particles of different shapes

To study the effect of particle shape and size on radiation extinction, experimental studies were made within the wavelength ranges from 2.5 to 3.5 μm and 8 to 12 μm (where the minima were observed), and the values of extinction efficiency factor $K_e(\lambda)$ were calculated for ice spheres, cylinders and plates within the wavelength range 8 to 12 μm. Fig. 2 shows the results of experimental determination of $K_e(\lambda)$ for the crystals of various shapes: plates with half-thickness $\bar{\Delta}_\rho \simeq 4.5 \div 5\,\mu$m, columns with $\bar{r} \simeq 10\,\mu$m ($\pm 5\,\mu$m) and prisms with $\bar{\ell} \simeq 2\bar{r} \simeq 5\,\mu$m (in Fig. 2a).

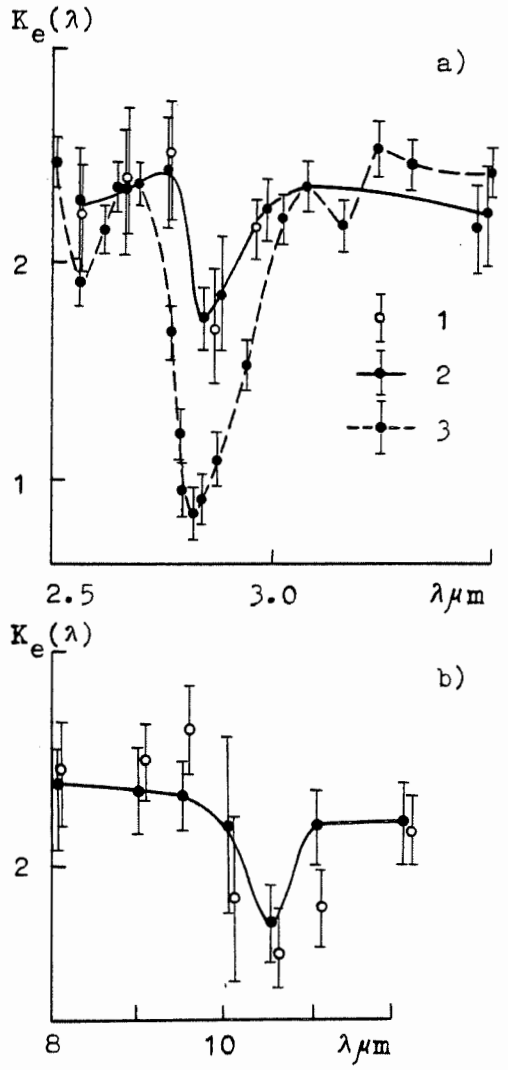

Fig. 2. Spectral radiation extinction by crystal medium: 1 - plates; 2 - columns; 3 - prisms.

The experimental data suggest that crystal shape does not exert a significant effect on the efficiency of radiation extinction within the wavelength ranges studied. Variation in the mean characteristic size of

particles appears to have more significant effect than their shape. However, it has not been possible to obtain any quantitative results for the experimental data because of their great dispersion.

The calculated results of $K_e(\lambda)$ for ice spheres, cylinders and plates of the same characteristic size $r_s = r_c = \Delta\rho = 5\mu$ m (the radii of spheres and cylinders, and the half-thickness of plates) are presented in Fig. 3.

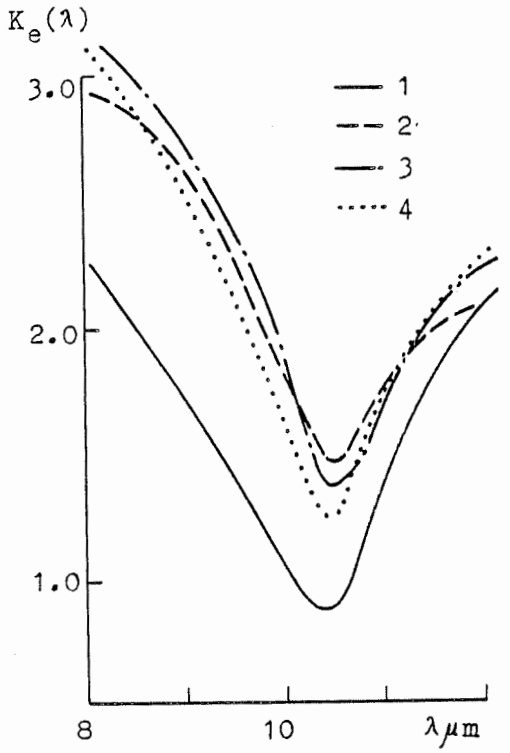

Fig. 3. Dependence of extinction efficiency factor on wavelength for ice particles of various shapes: 1 - sphere $r_s = 5\mu$ m; 2 - plate $\Delta\rho = 5\mu$ m; 3 - cylinder $r_c = 5\mu$ m; 4 - sphere $r_s = 7\mu$ m.

The axis of incident radiation forms an angle $\alpha = 0 \div 80°$ with the normal to the major axes of cylinder and plate. The calculations show that the values of $K_e(\lambda)$ for cylinders and plates differ insignificantly. The values of $K_e(\lambda)$ for spheres are considerably smaller than those for cylinders and plates. It should be noted that the calculated values of $K_e(\lambda)$ for the ice spheres with radius $\bar{r}_s = \Delta\rho/\cos\alpha$ rather closely agree with those for cylinders and plates within this range of λ (curve 4 in Fig.3 for $\bar{r}_s = 7\mu$ m). It is interesting to note that the calculated dependence $K_e(\lambda)$ for the plates with $\Delta\rho = 5\mu$ m, when using the values of complex refractive index m from /4/, is in good agreement with the experimental data in Fig. 2b within the range of $\lambda = 9 \div 12\mu$ m.

3. Conclusions

1. Phase scattering function of visible radiation in crystal cloud medium depends insignificantly on the shape, size and orientation of crystals in the range of scattering angles 10 to 170°.

2. The expressions are obtained for calculating the phase function of radiation scattering by ice prisms which adequately describe the experimental data.

3. It is shown that infrared radiation extinction by the ice particles having the form of plates and cylinders (columns) of the same characteristic size differs insignificantly. Increase in particle size results in increasing values of $K_e(\lambda)$ in the minima at $\lambda \simeq 2.8$ and 10.3μ m.

4. The experimental data of $K_e(\lambda)$ for $\lambda = 9 \div 12\mu$ m are in a satisfactory agreement with the calculated ones with the values of m taken from [4].

References

1. Huffman P.J., Thursby W.R. 1969. Light scattering by ice crystals. J.Atmos.Sci., vol.26, No.5, p.1073-1077.
2. Nikiforova N.K., Pavlova L.N., Petrushin A.G., Snykov V.P., Volkovitsky O.A. 1977. Aerodynamic and optical properties of ice crystals. J.Aerosol.Sci., vol.8, No.3, p.243-250.
3. Liou K.-N. 1972. Light scattering by ice clouds in the visible and infrared. J.Atmos.Sci., vol.29, No.3, p.524-526.
4. Schaaf I.W., Williams D. 1973. Optical constants of ice in the infrared. J.Opt.Soc.Amer., vol.63, No.6, p.726-732.

ON THE INITIATION OF REGENERATIVE ICE PRODUCTION IN DEEP CUMULI

D.Lamb, J.Hallett, and R.I.Sax*

Desert Research Institute
Reno, Nevada, U.S.A.

*Joseph Oat Corporation
Camden, New Jersey, U.S.A.

I. INTRODUCTION

Observations of ice evolution in deep natural cumulus and cumulus congestus clouds have provided evidence for the rapid glaciation of supercooled clouds at temperatures often greater than -10°C (Koenig, 1963, 1968; Mossop et al., 1968, 1970, 1972; Hallett et al., 1978). Conditions conducive to such effective glaciation have been associated with the presence of large drops (supercooled "rain" in concentrations in excess of 1 ℓ^{-1}), weak or pulsating updrafts, and high ratios of ice particle to ice nucleus concentrations (previous references plus Mossop, 1972).

It has been common among the various workers to attribute such glaciation behavior to some sort of "ice multiplication" process. Without detailing the history of the various hypotheses, we note here simply that secondary ice particles ("splinters") can apparently be generated during the accretional riming of large graupel (Hallett and Mossop, 1974), at least within a restricted temperature range (-3 to -8°C), by some as yet undetermined mechanism (Mossop, 1976). The obvious inferrence of such secondary ice generation taking place in natural clouds containing substantial concentrations (> 1 ℓ^{-1}) of supercooled rain drops ($\sim$ 1 mm diameter) is the creation of a microphysical setting in which splinters and graupel particles (from the freezing of the rain drops) build up simultaneously in exponential fashion by regenerative feedback.

The evolution of ice in clouds conducive to regenerative processes has been studied numerically by several workers (e.g., Koenig, 1977; Chisnell and Latham, 1976), but explicit attention was not given to the initiation of the ice phase from primary nucleation events. Hallett et al. (1978) showed favorable comparisons between calculated and observed time scales for glaciation, provided the regenerative glaciation model began with an initial concentration of "proto-ice". The origin of the primary ice was not discussed, nor the additional time required for the primary nucleation events to establish such initial ice concentrations, a potentially serious consideration given the relatively warm temperatures at which the primary nucleation must take place. Here, we extend the earlier work and show that high concentrations of ice can build up in reasonable times in an initially ice-free cloud when the primary nucleation events are supplemented by the simultaneous generation of secondary ice.

II. MECHANISMS INVOLVED IN ICE PRODUCTION

In a related context Lamb et al.(1980) described a simple conceptual model based on the set of microphysical interactions depicted in Fig. 1.

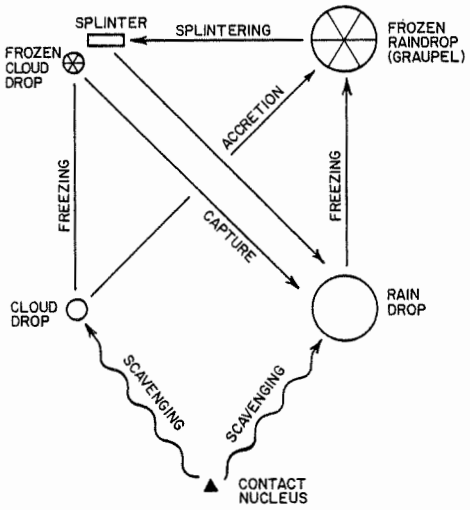

Figure 1. Schematic representation of the various cloud particle interactions.

Although this other work also included depositional nucleation as a means of forming primary ice, it was shown that the slower and, therefore, more conservative process is contact nucleation. Restricting ourselves to the Brownian scavenging of contact nuclei by, respectively, the small supercooled cloud drops (having no fallspeed) and the large supercooled rain drops (having appreciable fallspeed), we see from Fig. 1 that such primary nucleation events will generally lead to the production of "graupel" either directly by the contact freezing of rain drops or indirectly

by the collisional capture of the frozen cloud drops. Once rain drops freeze and begin to accrete cloud water, a small but finite fraction of the accretional events may lead to the liberation of a secondary ice particle ("splinter"). Such secondary ice adds to the general population of small ice particles that can be aerodynamically captured by the supercooled rain drops. This triangular pathway in the upper right portion of Fig. 1 constitutes the regenerative feedback mechanism responsible for the exponential increase in the concentrations of large graupel particles and splinters calculated by Hallett et al. (1978).

In order to be realistically conservative in this quantitative treatment we have intentionally kept the concentration of contact nuclei low (10^{-4} ℓ^{-1}; c.f., Koenig, 1977) and have restricted the capture efficiency of the small ice particles by the rain drops to 0.1 (c.f., Chisnell and Latham, 1976). Although influences of the dynamical structure of a cloud on the microphysical rates are recognized as important in the real atmosphere, they are not included here for the sake of clarity and brevity.

III. RESULTS

As one expects from the use of a contact nucleus concentration as low as 10^{-4} ℓ^{-1}, ice cannot build up at any reasonable rate by primary nucleation events alone, as shown in Fig. 2.

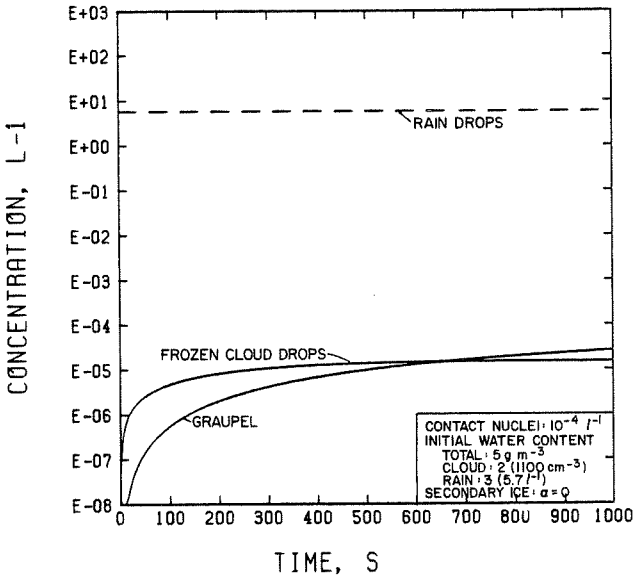

Figure 2. The restricted build-up of ice in the absence of secondary ice formation.

After 10^3 s less than one in 10^5 rain drops has been converted to a graupel particle, even allowing for the indirect process of freezing rain drops by the capture of frozen cloud drops (Fig. 1).

In sharp contrast to this highly restricted build-up of ice, Fig. 3 shows the evolution of ice after the generation of secondary ice has been included in the calculations, the generation rate being proportional to the fraction α of cloud drops larger than 25 μm in diameter that generate 1 splinter.

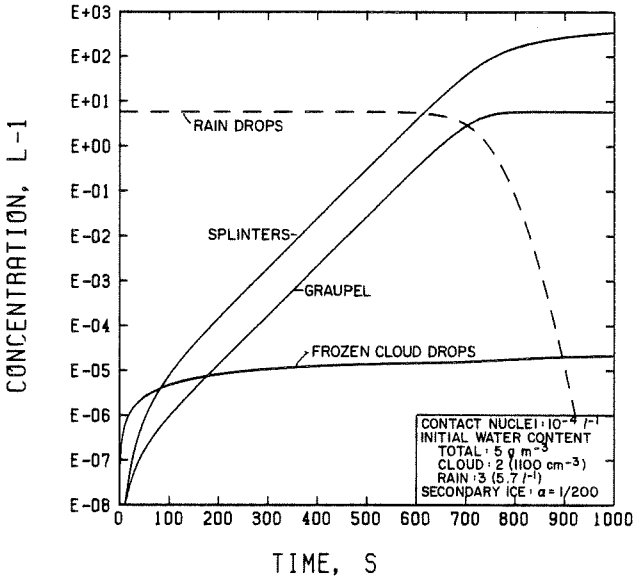

Figure 3. The evolution of ice in the presence of secondary ice production.

Now, except during the earliest stages (to about 100 s, during which capture of the frozen cloud drops are the primary means of nucleating rain drops), graupel builds up exponentially in response to the simultaneous generation of secondary ice (splinters) and the freezing of the rain drops. The relative importance of the various mechanistic pathways to the formation of the graupel particles at various stages in the evolution is shown in Fig. 4. In essence, it is the capture of the splinters by the supercooled rain drops, followed by their freezing to form new splinter-generating particles which dominates the glaciation. The primary nucleation, weak as it is alone, needs only to get the regenerative process initiated.

In this treatment we have defined the

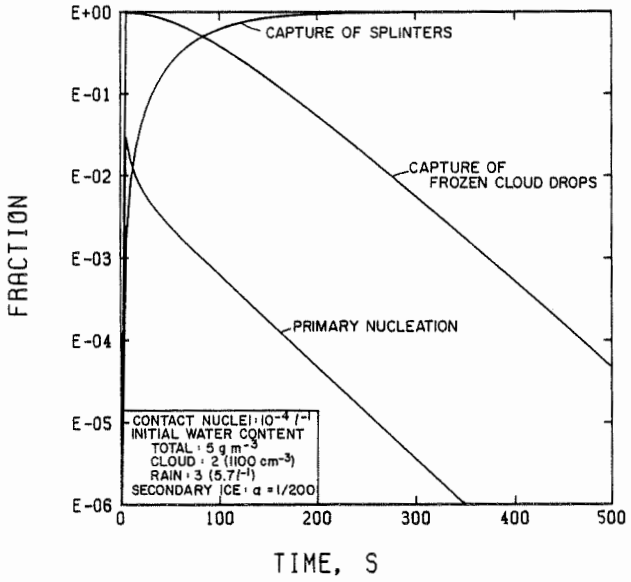

Figure 4. The relative importance of the three main pathways for generating graupel from supercooled rain. "Fraction" refers to the ratios of the rates of rain nucleation by the respective pathways to the total rate of graupel formation.

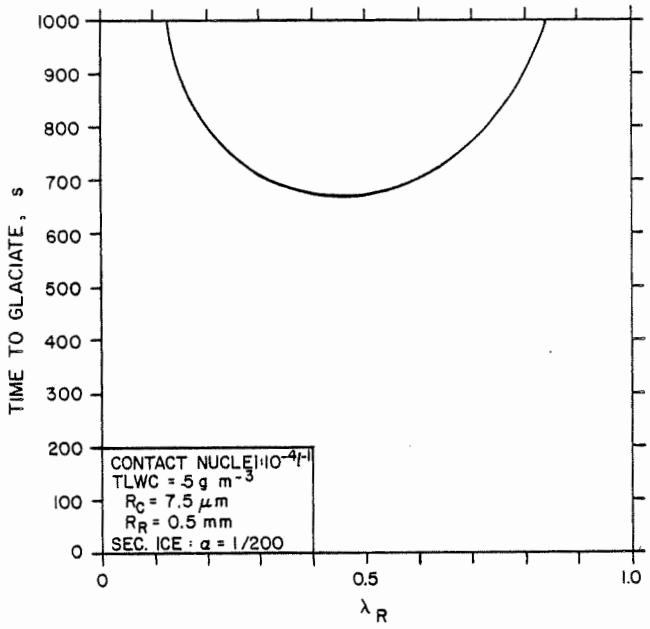

Figure 5. The dependence of glaciation time (time at which the concentrations of graupel and rain are equal) on the fraction λ_R of the total initial liquid water content existing in the form of rain.

time to achieve "complete" glaciation as the length of time for the concentration of large graupel particles to build up to the decreasing concentration of remaining rain drops (dashed line in Fig. 3). Since the mechanism quantitatively most responsible for the initiation of the regenerative ice processes is the two-stage process involving the capture of frozen cloud drops by rain drops, both ends of the drop spectrum are required. This is demonstrated readily in Fig. 5, a plot of the "glaciation time" as λ_R, the fraction of the initial liquid water content (5 g m^{-3}) that constitutes the rain water, is varied from 0 (cloud water only) to 1 (rain water only). A minimum is clearly visible near λ_R = 0.45, an indication that an additional requirement for reasonably rapid glaciation to take place in natural cumuli is the simultaneous presence of both cloud and rain water. This has obvious implications to the glaciation of extreme cloud forms, those of strictly continental origin and those of purely maritime origin.

IV. SUMMARY AND CONCLUSIONS

By means of a simple conceptual model of glaciation microphysics, it has been shown that secondary ice production can lead to powerful ice regeneration processes which quickly dominate the glaciation of an initially ice-free cloud once initiated by the freezing of cloud drops which are subsequently captured by supercooled rain drops. If significant concentrations of both cloud and rain drops are present, even low concentrations ($\sim 10^{-4}$ ℓ^{-1}) of natural contact nuclei can lead to the short glaciation times observed when the primary nucleation and regenerative processes occur simultaneously.

ACKNOWLEDGEMENTS

The authors acknowledge the partial support of this work by the Atmospheric Sciences Division of the U.S. National Science Foundation (Grant No. ATM 77-07995) and the use of the NCAR software packages which generated the computer graphics.

REFERENCES

Chisnell,R.F. and Latham,J., 1976. Ice particle multiplication in cumulus clouds. Quart.J.Roy.Meteor.Soc., 102, 133-156.

Hallett,J. and Mossop,S.C., 1974. Production of seondary ice particles during the riming process. Nature, 249, 26-28.

Hallett,J., Sax,R.I., Lamb,D. and Ramachandra Murty,A.S., 1978. Aircraft measurements of ice in Florida cumuli. Quart.J.Roy.Meteor.Soc., 104, 631-651.

Koenig,L.R., 1963. The glaciating behavior of small cumulonimbus clouds. J.Atmos. Sci., 20, 29-47.

Koenig,L.R., 1968. Some observations suggesting ice multiplication in the atmosphere. J.Atmos.Sci., 25, 460-463.

Koenig,L.R., 1977. The rime-splintering hypothesis of cumulus glaciation examined using a field-of-flow cloud model. Quart.J.Roy.Meteor.Soc., 103, 585-606.

Lamb,D., Sax,R.I., Hallett,J., 1980. Limitations on the rates and magnitudes of latent heat released in seeded cumuli. Proceedings of the Third WMO Scientific Conference on Weather Modification (Clermont-Ferrand, France, 21-25 July 1980).

Mossop,S.C., 1972. The role of ice nucleus measurements in studies of ice particle formation in natural clouds. J.de Rech.Atmos., 6, 377-389.

Mossop,S.C., 1976. Production of secondary ice particles during the growth of graupel by riming. Quart.J.Roy.Meteor. Soc., 102, 45-57.

Mossop,S.C., Cottis,R.E. and Bartlett,B.M., 1972. Ice crystal concentrations in cumulus and stratocumulus clouds. Quart. J.Roy.Meteor.Soc., 98, 105-123.

Mossop,S.C., Ono,A. and Wishart,E.R., 1970. Ice particles in maritime clouds near Tasmania. Quart.J.Roy.Meteor.Soc., 96, 487-508.

Mossop,S.C., Ruskin,R.E. and Heffernan,K.J., 1968. Glaciation of a cumulus at approximately -4°C. J.Atmos.Sci., 25, 889-899.

FORMATION MECHANISM OF ICE CRYSTAL PRECIPITATION IN THE ANTARCTIC ATMOSPHERE

Takeshi Ohtake and Masayuki Inoue

Geophysical Institute
University of Alaska
Fairbanks, Alaska USA

1. INTRODUCTION

In the central antarctic area, ice crystals have frequently been observed precipitating from clear skies. The entire formation mechanism for these ice crystals has never been described, in spite of extensive observations. Studies on the ice crystals regarding occurrence, shapes, sizes, concentration and chemical composition of nuclei related to weather phenomena such as wind direction, moisture trajectory, cloud situation, temperature and humidity profiles were carried out. Concentrations of ice nuclei effective at water saturation and sub-water saturation environments were also measured. In this paper, possible formation mechanisms of the ice crystals in the antarctic atmosphere are proposed on the basis of the observations described above.

2. OBSERVATIONS

The ice-crystal concentration was continuously recorded by an acoustic sensor (for ice-crystal counts) and an ice-crystal replicator. The concentration varied widely, by as much as 2 orders of magnitude in 10 to 60 minutes. The maximum concentration observed was 100 crystals per liter of air. The changes in concentration were used to correlate ice-crystal events with cloudiness and cloud forms (using an all-sky, slow-motion movie camera), wind direction, and upper air conditions, such as humidity and temperature aloft, including specially detailed radiosonde readings with dry ice calibration.

On 59 days between June 11 and August 23, 1977, precipitating ice crystals were collected on slide glass plates coated with oil and photographed under low temperature conditions. The surface temperatures were between -39.4° and -71.4°C.

The ice crystals at the South Pole formed in basically five different kinds.

2.1 Assembled bullet crystals

This type of ice crystal is most common and also the largest (about 1 mm or larger) of all observed at the South Pole in summer and winter as an example shown in Figure 1. Columnar crystals with complex inner structures were not unusual precipitating at the same time. Since those crystals are large they are the major contributor to the snow accumulation throughout a year.

The assembled bullet crystals were associated with incursions of moist upper air ($\sim$500 mb level in summer and 600 mb level in winter) at temperatures between -40° and -55°C, and often coincided with a high cirrus or cirrostratus cloud layer at 2000 to 4500 m above ground level (AGL).

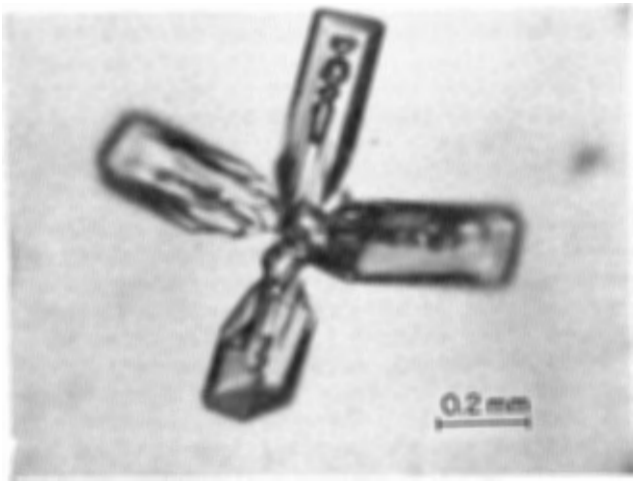

Figure 1. Assembled bullet ice crystals collected on 16 July, 1977. Surface temperature was -59.2°C. These crystals are from high cirrus clouds.

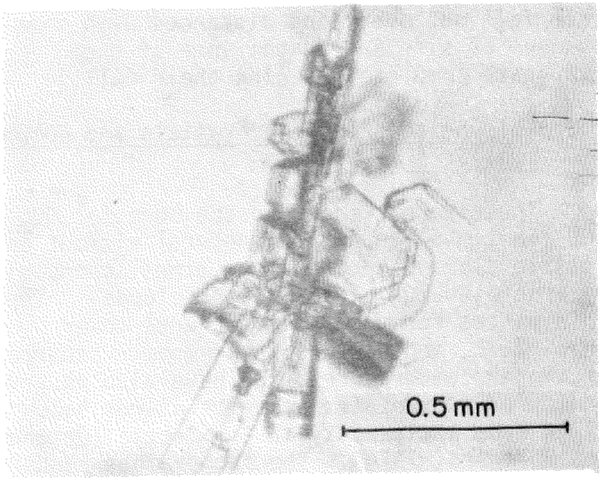

Figure 2. Combined side plane crystals collected 10 July, 1977. These crystals are usually from middle clouds such as altostratus and altocumulus.

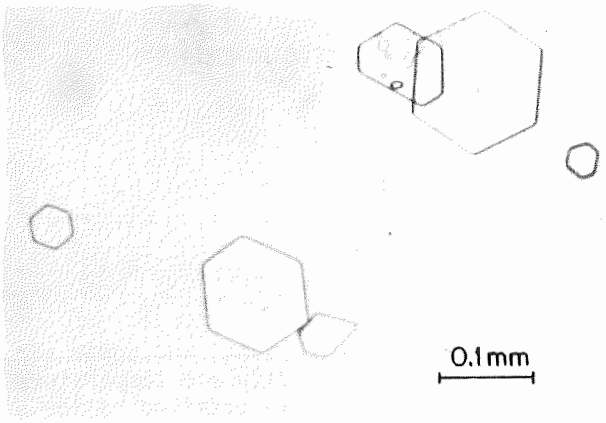

Figure 3. Plate crystals from clear sky on 8 December, 1977. (The highest temperature aloft was -27.7°C).

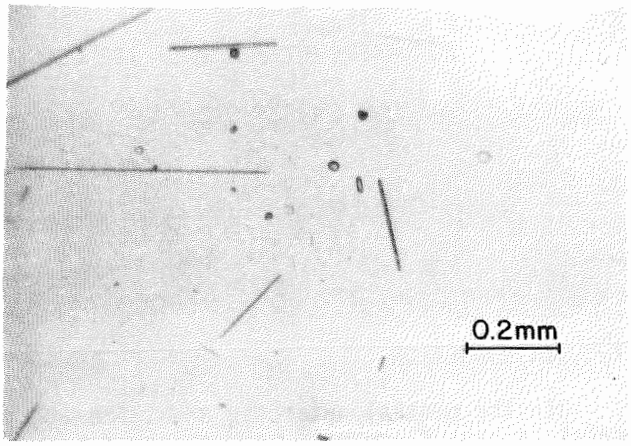

Figure 4. Pencil-shaped ice crystals. Sampling data is missing.

2.2 Combined ice crystals in form of side planes, bullets and columns

These crystals were observed with moist upper air (~670 mb level) at temperatures between -30° and -45°C, and were found in association with altostratus cloud layers in 700-2000 m AGL broken or overcast sky. Figure 2 shows an example of side plane crystals. They were about 1 mm in size but play a lesser role in the Antarctic mass balance because of their lower frequency of occurrence.

It is noticed that the manners of both types of ice crystal precipitations in winter were observed consistently throughout a year at the South Pole. When both high and low cloud layers were found to have a high moisture content, the first and second type of crystals occurred simultaneously. The temperature-humidity conditions characterized by the crystal shapes seem to be agreed well to the conditions extended from Magono and Lee's (1966). Ice crystals from both high and middle clouds form and grow in the clouds, then fall out over long distances with some changes of size and shape; some of them evaporate completely during their fall.

2.3 Thin hexagonal plate crystals and columns smaller than 0.2 mm

These were created in the lowest 1,000 m AGL (mostly a few hundred meters) without any visible cloud layer, but sometimes accompanied by fractostratus clouds (water clouds). These thin plates formed at temperatures lower than -25°C, and none of their growth occurred at higher temperatures. We have also observed growth of such plates at temperatures below -22°C from a clear sky in the Arctic (Ohtake and Holmgren, 1974). The temperature range for formation of thin hexagonal plates does not agree with the generally accepted range reported by Kobayashi (1958) and Magono and Lee (1966) of -10° to -18°C. Further studies are needed to explain this discrepancy. Figure 3 shows these ice crystals.

Even in winter, these crystals were mostly observed under clear skies with a slight wind 2 - 5 meters per second from the grid north. Such crystals in winter seemed to fall only from clear skies (One should bear in mind the difficulty of observing clouds in darkness). Because of small masses, these crystals do not substantially contribute to snow accumulation in Antarctica but offer an interesting cloud physics topic.

2.4 Pencil and triangular-shaped crystals

These crystals formed near the surface, under clear skies, with northeasterly winds at 1 - 6 m per sec, and during extremely low temperatures of -50°C or below at the lowest part of the atmosphere. The pencil crystals had well defined basal planes (c) and very long prismatic faces (a); the maximum ratio of the c/a axes was 200. (Figure 4 shows some examples of pencil ice crystals.) Triangular crystals and pencil crystals occurred under similar conditions. Some triangle crystals are shown in Figure 5. Examination of these crystals by electron microscope revealed no detectable nucleus at magnification of 20,000 times. This result confirms that these crystals were formed by homogeneous nucleation at temperatures below -40°C.

2.5 Block and polyhedral ice crystals

These crystals (about 0.02 mm in size) were observed in winter under clear skies with northerly wind of 5 m per second and at temperatures of approximately -58°C. (See Figure 6 for example.) The polyhedrons were mostly 20 faceted, occurring with many thin plates (which are described in 2.3) at sizes of about 0.02 mm. Their shapes and formation conditions are similar to Fairbanks' ice fog crystals (Ohtake, 1970). The complex shape are probably due to non-uniform growth conditions under the extremely low temperatures.

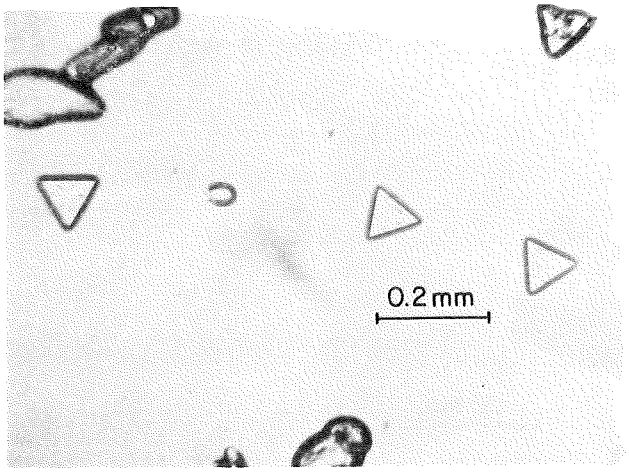

Figure 5. Triangle-shaped ice crystals on 18 July, 1977.

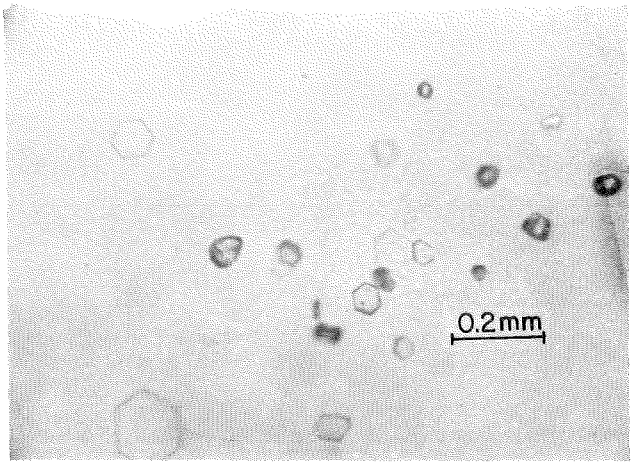

Figure 6. Block-shaped ice crystals and thin plate crystals precipitated from clear sky on 15 July, 1977 at temperature of -56.1°C.

3. MECHANISM OF CLEAR SKY ICE CRYSTAL PRECIPITATION

The kind of ice crystals mentioned in 2.3 is the most complicated and has the most interesting formation mechanism. Ice crystals are usually formed at a relative humidity of 100 percent, which is also the critical humidity for cloud formation in the atmosphere. So these ice crystals usually should be formed within a cloud. We observed that most of the cases of clear-sky ice crystal precipitation were found in layers corresponding to measurements of humidities higher than ice saturation. Humidity measurements obtained from radiosonde observations (RAOB's) were corrected for surface pressure ($\sim$700 mb) since the ground calibration procedure assumed 1000 mb. However, since very large numbers of these ice crystals were observed in the antarctic cloudless atmosphere, one may advance the possibility of deposition nucleation, i.e., water vapor deposition directly onto nuclei under sub-water saturation (or ice saturation) conditions. To examine this possibility, an experiment was performed at the South Pole during the 1977-1978 austral summer. When aerosols, which may become ice nuclei, were collected on hydrophobic membrane filters and exposed to water vapor at -25°C, ice crystals did not form on the aerosols unless the water vapor concentration was larger than the water saturation value. Nevertheless, ice crystals sometimes precipitate from the cloudless sub-ice saturated sky. Values of humidity in the upper air obtained by NWS at South Pole were frequently calibrated by clear sky seeding of dry ice. A piece of dry ice hanging down from a radiosonde makes streaks of ice clouds when the humidity is greater than ice saturation.

During the 1976-77 and 1977-78 austral summer field seasons, ice-crystal replication revealed that many ice crystals were in the form of stepped columns by the freezing of water droplets (Magono et al., 1976). An example of stepped column crystals is shown in Figure 7. Ice-crystal precipitations were associated occasionally with fractostratus clouds or a high, humid, cloudless layer. In both cases, such a humid layer existed approximately 100 meters to 500 meters high, and the wind in the layer always was directed between 300° and 50° from the Greenwich Meridian.

From the trajectory analyses using 700-, 500-, and 400-milibar isoheight maps, the moisture and nuclei for the ice crystals observed at South Pole were transported from the Weddell Sea after traveling more than 7 days toward the Antarctic Plateau (Ohtake, 1976). The nuclei of individual ice crystals replicated at Pole Station were analyzed by means of an X-ray energy spectrometer during 1975-1976; about 50 percent of the summer ice crystals contained sodium, magnesium, sulfur, and chlorine, which are major components of sea salt from the ocean (Ohtake, in press).

Similarly to the mechanism for the arctic ice-crystal formation (Ohtake et al., 1978), the clear-sky ice crystals at the South Pole may result from the freezing of low-level stratus cloud droplets, which form by slightly uprising and cooling warm air transported from the Weddell Sea along the slight slope toward the Antarctic Plateau. The patchy stratus clouds are sometimes beyond sight from Pole Station, although many times such ice crystals may occur with the stratus clouds or fog banks upwind from the South Pole Station.

There may be plenty of hygroscopic in the lower antarctic atmosphere as Hogan (personal communication) found at the South Pole in 1978. Those particles may be sulfuric compound because sulfur "S" was found in many ice crystals (Ohtake, in press). It is possible to form water droplets on these hygroscopic particles in sub-water saturation environments and to follow their subsequent freezing.

Acknowledgements: The authors are indebted to Dr. T. Yogi and Mr. S. Barnard for their observations of ice cyrstals in winters at the South Pole and to Mr. A. Fountain and Mr. Chi-Fan Shih for their help in data processing. This material is based upon work supported by

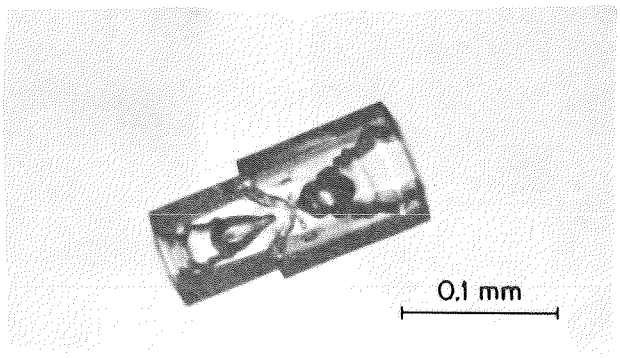

Figure 7. A stepped column crystals collected on 13 December, 1976. This crystal was presumed to be formed by freezing of water droplet.

Division of Polar Programs, National Science Foundation under Grants DPP 74-04037 and DPP 76-23114.

REFERENCES

Kobayashi, T., 1958. The growth of snow crystals at low saturations. *Philosophical Magazine,* 6:1363-1370.

Magono, C., S. Fujita, and T. Taniguchi, 1976. Shapes of single ice crystals originated from frozen cloud droplets, *Preprints of International Conference on Cloud Physics,* 26-30 July, 1976, Boulder, Colorado. pp. 103-106.

Magono, C., and C. W. Lee, 1966. Meteorological classification of natural snow crystals. *Journal of the Faculty of Science,* Hokkaido University Series 7, Geophysics, 2: 321-365.

Ohtake, T., 1970. Studies on ice fog, Office of Air Programs, Publication No. APTD-0626, Environmental Protection Agency, Research Triangle Park, NC 27711, 177 pp.

Ohtake, T., 1976. Source of nuclei of atmospheric ice crystals at the South Pole, *Antartic Jour. of U.S.,* 11, 148-149.

Ohtake, T., In press. X-ray analyses of nuclei in individual fog droplets and ice crystals, *Proceedings of 9th International Conference on Atmospheric Aerosols, Condensation and Ice Nuclei,* University College, Galway, Ireland, 21-27 September 1977.

Ohtake, T., and B. E. Holmgren, 1974. Ice crystals from a cloudless sky, *Preprints of Conference on Cloud Physics,* Tucson, Arizona, 21-24 October 1974. 317-320.

Ohtake, T., K. Jayaweera, and K. Sakurai, 1978. Formation mechanism of ice crystals in the cloudless atmosphere, *Preprints of Conference on Cloud Physics and Atmospheric Electricity,* 31 July-4 August 1978, Issaquah, Washington, pp. 122-125.

UNIQUE CLOUD MICROPHYSICAL DATA DERIVED FROM ATMOSPHERIC OPTICAL PHENOMENA: EXAMPLES OF PASSIVE REMOTE SENSING STUDIES

Kenneth Sassen

Dept. of Meteorology, University of Utah
Salt Lake City, Utah, USA

Explanations for the presence of optical phenomena in the atmosphere have traditionally challenged some of the most formidable minds of science. In more recent times, these historical speculations have been replaced by more exact theoretical simulations of the manner in which hydrometeors scatter sunlight. As a result, there remain few types of optical displays which can not be satisfactorily explained by models utilizing hydrometeors with specified size, or shape and orientation (see, e.g. Tricker, 1970).

We would like to point out that this knowledge of the causes of optical phenomena is a powerful tool for cloud microphysical studies which is hardly exploited to its full extent. Occurrences of optical phenomena in the atmosphere, albeit relatively uncommon, can provide the means to determine the characteristics of a large population of undisturbed hydrometeors, often under conditions where direct *in situ* measurements would be difficult or impossible to obtain. Hence, through a passive remote sensing approach involving the analysis of photographic observations of optical displays, unique cloud microphysical information can be gathered from the ground, and this data can be used to increase our understanding of important cloud processes. Through the use of a microdensitometer, an instrument which converts the density of a photographic image to quantitative measurements, quite precise data can be generated. As examples of the type of information which can be recovered using this approach, summarized below are the findings from two studies, one each concerned with cloud droplets and ice crystals present in the atmosphere.

Initial Contrail Formation

The formation and persistence of aircraft condensation trails is a problem of considerable complexity. Particularly with regard to the *initial* contrail formation, cloud droplet-ice crystal growth predictions as well as *in situ* measurements would be quite difficult to obtain. Fortunately, contrails are occasionally observed to generate the iridescence phenomenon as the aircraft passes within ~30° of the sun, so that a passive remote sensing method is available to study the process of initial contrail formation. As described in Sassen (1979), the diffraction-corona theory can be applied to iridescence observations to determine cloud droplet sizes, providing estimates of droplet growth rates in the forming contrail.

Figure 1 shows the results of such an analysis of photographs of a contrail which displayed iridescence while forming and which later persisted as an ice cloud. It can be seen that, with reasonable assumptions of aircraft height and speed, cloud droplet diameters can be derived as a function of the distance behind the aircraft, or approximate growth time. We find droplet radius growth rates of ~1-3 $\mu m\ s^{-1}$ as the contrail is forming, indicating that the contrail environment is initially highly supersaturated. Moreover, there is evidence that the cloud droplets began freezing (at an environmental temperature of -40°C) soon after achieving a diameter of ~3 μm, or after about 2 seconds total contrail lifetime.

Ice Crystal Fall Attitudes

Knowledge of the falling behavior of ice crystals has been derived primarily from model experiments performed to simulate atmospheric conditions in the laboratory tank. In the real atmosphere, such information can be obtained through observations of various optical phenomena which require the presence of uniformly arrayed ice crystals, if it is possible to concurrently sample the size and type of particles present. The light pillar, a nocturnal man-made analog of the sun pillar which is observed during light snowfall or ice fog, provides the best opportunity for relating crystal fall attitudes to crystal characteristics.

Figure 2 illustrates the information which can be gained through photographic observations of light pillars in combination with ice crystal size data. Shown is the relationship between the Reynolds number (Re) corresponding to the modal crystal diameter present and the half-width divergence angle of the pillar which is simply related to the approximate maximum crystal wobble angle from the horizontal plane. These results yield general agreement with the model experiment predictions for stable fall ($1.0<Re<100$), but further show that crystals with $Re\tilde{}10$ display the most perfect alignment. Moreover, the distribution of reflected light intensity horizontally across the pillars is typically Gaussian in character, demonstrating that the ice crystals are distributed normally from the horizontal plane. These findings can be accounted for by the response of the ice crystals to turbulence-induced fall attitude pertibations, a destablizing force not reproduced in the laboratory tank simulations.

References

Sassen, K., 1979: Iridescence in an aircraft contrail. *J. Opt. Soc. Am.*, 69, 1080-1083.

Tricker, R. A. R., 1970: *Introduction to Meteorological Optics*, American Elsevier, New York.

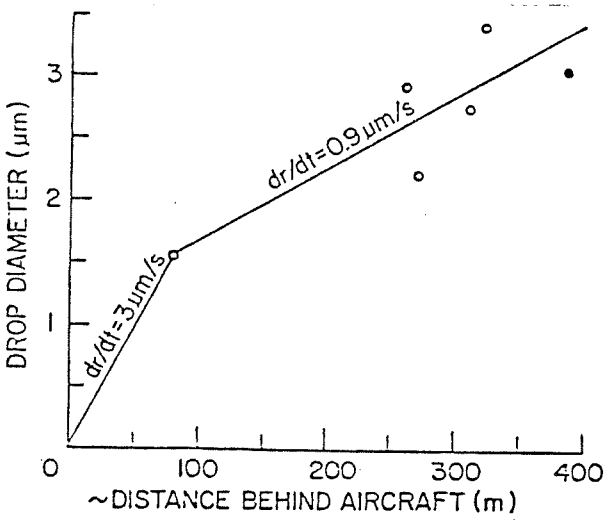

Figure 1. Cloud droplet growth rates in a forming contrail as derived from iridescence observations.

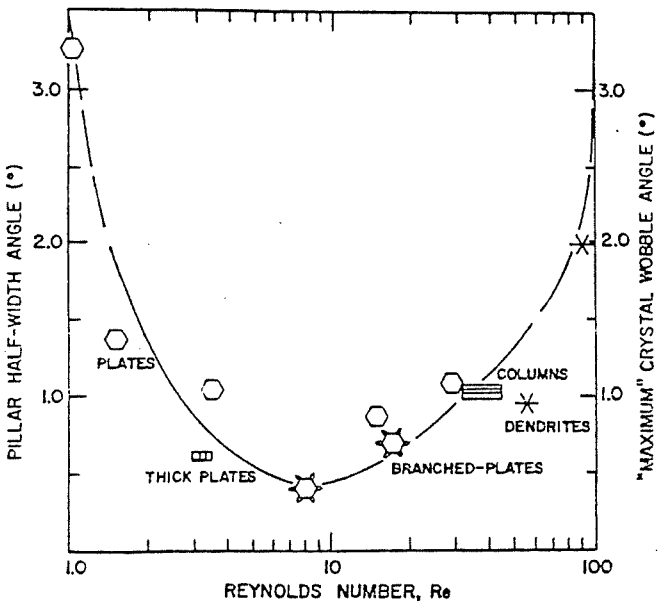

Figure 2. The angular deviations from the horizontal plane of various ice crystals producing light pillar displays.

ICE MULTIPLICATION BY RIME BREAKUP

Gabor Vali
University of Wyoming
Laramie, WY, U.S.A.

Introduction

The origins of ice particles in clouds of different kinds is gradually becoming clarified, but there are still many remaining questions. The problem has two basic aspects: that of identifying processes which contribute to the populations of ice particles in clouds, and that of establishing the realms of activity for each process.

Perhaps the most important point which became established over recent years is that there are primary and secondary processes of ice generation; those which involve nucleation of ice, and those which rely on the pre-existence of other ice particles. In this paper, a brief account will be given of observations which are suggestive of a secondary process of ice generation (multiplication) via the breakup of rime.

Fragmentation of crystals due to collisions has been examined already as a possible multiplication process, by Vardiman (1972), by Hobbs and Farber (1972) and by Jiusto and Weickmann (1973). These authors considered primarily the consequences of collisions of vapor-grown ice crystals. The process to be described in this paper is similar to that discussed in the papers cited above, with the difference that the breakup of rime accreted on crystals is considered here instead of the fragmentation of vapor-grown crystals themselves.

Observations

The observations relating to rime breakup have been made in the course of studies of cloud composition by instrumented aircraft. The principal data sources are: 1) In-situ shadow images of hydrometeors, and 2) Photographs of ice particles collected on slides. The shadow images are produced by a 2-D probe (Particle Measuring Systems, Boulder, Colorado), are recorded on magnetic tape, and are reproduced on paper after the flight. Resolution in these images is about 25 um, and the minimum size of particle reliably detected is about twice that value. Meaningful comments about particle shapes are possible for images exceeding about 150 μm in size. The sampling rate of the instrument is near 50 liters per kilometer of flight path. The ice particle collections are made on oil-coated slides, in a decelerator which reduces particle impact speeds to about 7 m/s. The sampling rate of the slides is nearly the same as that of the 2-D probe; exposure times of the slides are varied according to the particle concentration, to yield a large sample but without overlap of particles on the slides. The slides are stored cold until photographed at 12X magnification after the flight. The resulting photographs have a usable resolution of around 5 μm. Because of the high resolution, and because of the generally good quality of the photographs, the nature of ice particles can be deduced quite accurately from these samples. The main shortcomings of the technique is the occasional fracturing and splattering of particles which occurs even at the reduced impaction velocity.

Using the two techniques of observation described above, in conjunction with other data on state parameters, air motions and cloud droplet populations, relatively complete descriptions of cloud composition are possible, giving a good basis for examining the manifestations of hydrometeor growth processes. Because of the rapid motion of the aircraft through the clouds, it is much more difficult to obtain information on the temporal evolution of a given population of hydrometeors. For these reasons the description of the rime breakup process can be given mainly in terms of the characteristics which accompany it, but without good data on the time rates involved.

The observations relating to rime breakup were made in moderately convective clouds of mid-latitude, continental character. Temperatures at the tops of the clouds were generally between -12° and -20°C. The concentrations and mean sizes of cloud droplets were in the ranges 500-1000 cm^{-3} and 8-15 μm respectively. With such relatively cold temperatures and small cloud droplets, rime grows with a filamentary structure of low density. It is not entirely clear whether conditions other than temperature and drop size are also required for such filamentary growth of rime; it is conceivable, for example, that electrical charges of specific distributions might also play a role. The nature of the filamentary rime is clearly revealed by the slide collections; the rime consists of long strands of droplets and of cones of very small spread. The shadow images also show that rime branches protrude out from the larger particles and the outlines of the particles are highly convoluted.

Almost invariably, when conditions exist

such as those described above, the concentration of ice particles reaches 30-100 per liter, and sometimes more. These concentration values are derived from the 2-D data and therefore reflect the concentration of particles greater than 50 μm. Overall concentrations might be even higher. On the other hand, based on the slide data it can be concluded that of the total concentration only a small fraction, maybe 1-10 per liter, are recognizably vapor-grown crystals in their entirety or as part of a larger rime (graupel) particle. The majority of particles appear to consist of rime only, without any vapor-grown crystals or crystal fragments in them. The vapor-grown crystals which are found are often surprisingly free of rime over most of their surface, even when found as part of, or attached to graupel particles. The habits of the crystals appear to be well related to the cloud top temperatures according to the known dependence of crystal type on growth temperature, with water-saturated conditions.

The size distributions of the particle populations are close to exponential, under the type of conditions when rime breakup seems to be occurring. An example of such a size distribution is shown in Fig. 1. The sizes of the vapor-grown crystals are generally spread over a relatively narrow range, for example 200-800 um.

These observations are consistent with the explanation that the fragmentation of filamentary, low-density rime is the process leading to the high ice particle concentrations. Mechanisms which might be involved in producing the fragmentation are collisions between particles, and the sublimation of narrow connecting points in the rime if the particles traverse subsaturated regions. Collisions are almost certainly the major contributors to causing breakup. It is easy to envisage how collisions could lead to numerous fragments of rime, given the filamentary character of the rime and hence the existence of weak points in the structure. The splattering of the rime on the sampling slides provides a somewhat exaggerated but not totally unrealistic indication of how fragile these rime structures are. The fact that the size distributions are exponential is also suggestive of a dispersion process being involved in the production of powders of solid materials.

Implications

The evidence seems fairly strong that the process of rime breakup described in this paper is a mechanism of secondary ice generation which can lead to significant increases in the concentrations of ice particles in clouds. The conditions under which the process operates are known from the observations in rough detail; the ranges of conditions under which the process operates and the dependence of the efficiency of the process on the various parameters are not yet known. Neither are the data comprehensive enough to deduce the rate of evolution of particle concentrations or sizes. Being tied to the nature of the rime which is accreted on ice crystals, understanding of the details of the dependence of rime structure on environmental parameters will be necessary, before the details of the breakup phenomenon can be clarified. Some parameterization of the process might be possible, for use in numerical cloud models, and such calculations then might give some measure of the impact of the breakup process on precipitation production. It seems likely that the breakup process results in more rapid development of precipitation, because the majority of the rime fragments produced in the breakup are of precipitable sizes and they continue to grow rapidly by further riming, provided that the cloud water is not depleted entirely.

References

Hobbs P.V. and R.J. Farber, 1972: J. Rech. Atm., 6, 245

Jiusto J.E. and H.K. Weichmann, 1973: Bull. Amer. Meteor. Soc., 54, 1148

Vardiman L., 1972: Atmos. Sci. Paper No. 191, Colo. St. Univ.

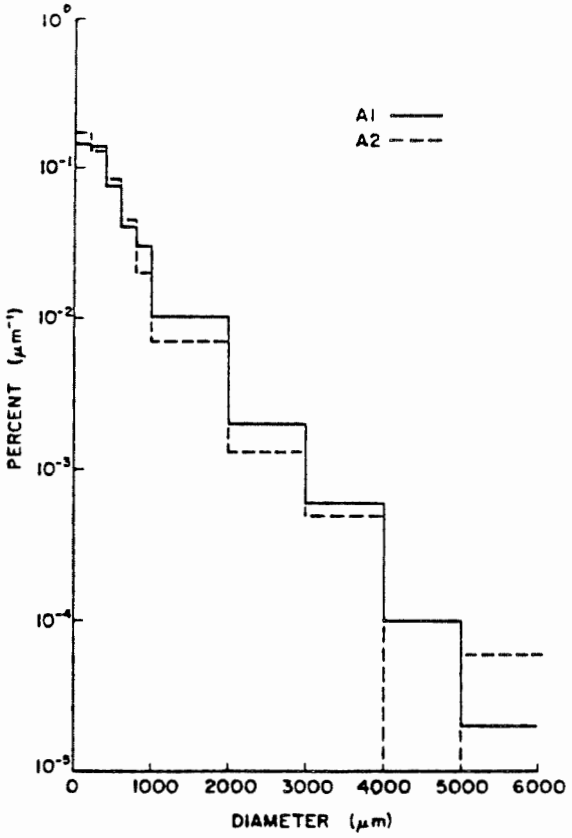

Figure 1. Size distributions of ice particles observed in Cu med. on 26 June 1976 in Wyoming. The two different distributions refer to two consecutive passes through the same cloud, six minutes apart. Derived from 2-D probe data.

ELECTRICAL EFFECTS ON THE ROTATIONAL DYNAMICS OF ICE CRYSTALS

A. J. Weinheimer and A. A. Few, Jr.
Department of Space Physics and Astronomy
Rice University
Houston, Texas, UNITED STATES

In recent years, there have been a number of observations indicating that thunderstorm electric fields cause alignment of ice crystals present in the clouds (Hendry and McCormick, 1976; Cox and Arnold, 1979; Watson et al., 1979). These observations include depolarization of radio waves by the anisotropic crystal orientations, as well as rapid changes in this depolarization coincident with lightning flashes and the attendant field changes. These rapid changes are presumably a result of rapid changes in the degree of ice crystal alignment and also the direction of the alignment. These changes typically occur over times of a few tenths of a second or less. Prior to these measurements, Vonnegut (1965) had observed rapid changes in the optical brightness of thunderclouds illuminated by the sun. These rapid changes, which occurred in less than a second, were coincident with lightning flashes.

In addition to the rapid changes, the radio frequency observations indicate gradual changes in ice crystal orientations occurring over times ranging from 15 seconds to a few minutes. These times are comparable to times required for the electric field to build up inside some clouds, suggesting that the gradual field build-up is reflected in gradual alignment changes.

This paper discusses an analysis of the rotational dynamics of ice crystals when subject to the torques exerted by the electric field and by the air. The columnar and plate-like crystals are approximated as conducting and dielectric, prolate and oblate spheroids; and estimates are made of the torques exerted on these spheroids. Also, characteristic times for the crystal rotation are determined. The possible significance of the electrical alignment is then briefly discussed.

The ice crystals may be treated as either conducting or dielectric spheroids depending on the characteristic rotation time involved in any particular case. For example, if the rotational motion is slow enough that free charge has sufficient time to redistribute itself in response to the changing crystal orientation, the crystal surface may be treated as an equipotential. If, however, the rotational motion is somewhat faster, but still on a time scale greater than the dielectric relaxation time of ice, the crystal may be treated as a dielectric. In most cases of interest, the dielectric relaxation time represents the ultimate limit to how fast a crystal may rotate under the influence of an electrical torque.

At any rate, for both columnar and plate-like crystals, the electrical torque is of the form,

$$T_E = 4\pi\,\varepsilon_o\,E^2\,a^3\,f(k,\varepsilon_r)\cos\theta\,\sin\theta$$

where E is the electric field, a is the equatorial radius of the equivalent spheroid, θ is the angle between the field and the crystal's axis of rotation, and f is a function of the crystal's axis ratio k and its relative permittivity ε_r. The equation of motion of a crystal subject to only this torque (neglecting the aerodynamic torques for the moment) is equivalent to that for a pendulum. As a result, crystals will tend to oscillate like pendulums in response to a field change.

At low Reynolds numbers, the inertial terms in the Navier-Stokes equation for the air flow may be neglected. This Stokes flow assumption leads to a drag torque proportional to the spheroid's angular velocity ω:

$$T_s = 8\pi\mu\omega a^3 g(k)$$

where μ is the viscosity of the air and g is a function of the axis ratio k. Within this low Reynolds number approximation there is no torque which tends to orient the crystals (with three perpendicular planes of symmetry) in any particular direction. Combining this drag torque with the electrical torque yields, for the smaller (lower Reynolds number) crystals, a damped pendulum type of motion for which various characteristic times may be defined depending on whether the motion is overdamped or underdamped. In all cases, complete alignment with the field ultimately results for these small crystals. A lower limit on crystal size for this type of motion is due to the disorienting effects of Brownian motion. The upper limit is, for columns, a diameter on the order of 10 μ and, for plates, a diameter on the order of 100 μ, though there may be some variation of these upper limits with the axis ratio.

At higher Reynolds numbers, the observations that disks and cylinders tend to fall with preferred orientations indicates that there is an aerodynamic torque which must be overcome by the electrical torque if there is to be electric field alignment of ice crystals. We approximate this aerodynamic torque by using an ideal fluid (nonviscous) approach. Although such an approach is certainly inadequate to treat a number of the flow features for ice crystals (it predicts zero drag), our analysis

indicates that it may be of some use in predicting torques. We find that it consistently overestimates the real torque and by a factor which, though variable, is typically between 2 and 8. This is no small amount of uncertainty, but since the electrical torques of interest vary over many orders of magnitude, a factor of 2 to 8 is not overwhelmingly large in comparison. Also, the fact that the fluid torque appears always to be an upper limit enables us to be certain of the predominance of electrical torques when the ideal aerodynamic torque is less than or equal to the electrical torque. The expression for this ideal fluid (potential flow) torque is the following:

$$T_p = M' U^2 h(k) \cos\phi \sin\phi$$

where M' is the mass of the air displaced by the spheroid, U is its velocity, h is a function of the axis ratio k, and ϕ is the angle between the vertical and the spheroid's axis of symmetry. So for the larger crystals we compare this torque to the electrical to determine whether complete electric field alignment may take place. Even if complete alignment does not occur, alignment with the horizontal component of the field may be possible for the axes of columns constrained by the air flow to lie in the horizontal plane. Drag torques have not yet been incorporated into the analysis for these higher Reynolds numbers.

We have performed the above described analysis of the rotational dynamics for a spectrum of ice crystal sizes and axis ratios and also electric field strengths. Though our results are much more detailed in our paper, we may summarize them briefly and qualitatively as follows. It is found that for relatively strong fields of 100 kV/m, practically all crystals with axes whose lengths differ by as little as a factor of 2 (or more) will be at least partially aligned. For moderate fields of 10 kV/m, a substantial amount of alignment exists, and for fields even as small as 1 kV/m there may be some alignment for sufficiently nonspherical crystals of the right sizes.

References

Cox, D. C., and H. W. Arnold, 1979: Observations of rapid changes in the orientation and degree of alignment of ice particles along an earth-space radio propagation path. J. Geophys. Res., 84, 5003-5010.

Hendry, A., and G. C. McCormick, 1976: Radar observations of the alignment of precipitation particles by electrostatic fields in thunderstorms. J. Geophys. Res., 81, 5353-5357.

Vonnegut, B., 1965: Orientation of ice crystals in the electric field of a thunderstorm. Weather, 20, 310-312.

Watson, P. A., N. J. McEwan, A. W. Dissanayake, and D. P. Haworth, 1979: Attenuation and cross-polarization measurements at 20 GHz using the ATS-6 satellite with simultaneous radar observations. IEEE Trans. on Antennas and Propagation, AP-27, 11-17.

DIFFERENT SIZE DISTRIBUTIONS OF SNOW BASED ON METEOROLOGICAL SITUATIONS

T.Yagi and H.Uyeda

National Research Center for Disaster Prevention
Tsukuba Science City, JAPAN

1. Introduction

Heavy snowfalls in the districts along the coast of the Sea of Japan are mainly caused in connection with cold air outbreaks from the continental polar air mass. In this winter monsoon condition, the Sea of Japan plays an important role for the heavy snowfalls. The cold air is supplied a great deal of water vapour from the warm sea surface and heated in its lower layer during the travel over the Sea of Japan leaving the Continent. The process results an increase of the atmospheric instability, and hence violent convective activities are caused and durable heavy snowfalls are realized.

The districts along the coast also experience snowfalls caused by a passage of a cyclone, especially in so-called warm winter. This type of snowfalls is specified by a relatively small amount of precipitation and a short duration. In many cases, stratiform clouds are responsible for the snowfalls.

These different meteorological situations are expected to materialize some different size distributions of snow, and the ensuing discrepancy in the relationship of the radar reflectivity factor Z to the precipitation rate R.

The direct purpose of the present research is to obtain the Z-R relationships for snow in the region of Niigata Prefecture, one of the most snowy regions among the coastal districts. For prevention and preparedness against the serious snow disaster, a weather radar would be a powerful means to obtain information on snowfall area and intensity on a real time basis. Then the Z-R relationship is essential for the measurement by radar.

For rain, a great number of measurements of the Z-R relationship have been reported (Battan, 1973) and compiled with regard to the rainfall types (Fujiwara, 1965). However, only a few reports for snow are available up to date (Imai et al., 1955; Gunn and Marshall, 1958; Fujiwara et al., 1972; Yoshida, 1975; Kajikawa and Kiba, 1978; Harimaya, 1978). The authors have tried to make observations in 1978 and 1979. In the former year heavy snowfalls were predominant under the winter monsoon, whereas in the next year snowfalls were mainly brought on by cyclones. This preliminary paper clarifies the different characteristics of size distribution of snow particles observed in the two years and discusses the discrepancy in the Z-R relationship between both years.

2. Methods of observation and analysis

For calculation of the Z-R relationship of snow particles, a space size distribution must be known in terms of the diameter of the water drop formed on melting of the snow particles, assuming any break-up does not occur. In order to provide this, the filter paper method was introduced as follows: A horizontal sheet of brushed velvet (26 cm × 36 cm) was exposed to snowfall on the ground. After exposure, the velvet was taken inside a shelter, then the snow particles on the velvet were photographed and melted into water drops in a heated and humidified box. The melted drop did not wet the velvet. A filter paper dusted with water-blue dye was laid on the velvet and the drops were absorbed.

From the previous calibration of the filter paper, the diameter D of the drop to which the snow particles melted could be readily measured. If a large snowflake melts into several drops, all spots arising from the original snowflakes were totalized with the aid of the photograph of the snowflake and the diameter of the snowflake was taken as the diameter of the circular area according to the total number and area of spots. The diameters of melted snow particles were measured every 0.2 mm. Thus the horizontal distribution was obtained. The conversion of the horizontal distribution to the corresponding distribution in space N_D were made by using the measurements of the terminal speed V of snowflakes (Kajikawa, 1974) and graupel particles (Kajikawa, 1975).

The radar reflectivity factor Z ($mm^6\ m^{-3}$) is given by

$$Z=\int_0^{D_{max}} N_D D^6 dD, \qquad (1)$$

and the precipitation rate R ($mm\ hr^{-1}$) by

$$R=\frac{\pi}{6}\int_0^{D_{max}} V N_D D^3 dD, \qquad (2)$$

where D_{max} is the maximum diameter of the melted snow particles. Using Z and R defined above, the Z-R relationship was determined empirically as

$$Z=BR^{\beta}, \qquad (3)$$

where B and β are constants and depend on precipitation types.

3. Results

The observation was carried out in Nagaoka (20 km from the Sea of Japan), Niigata Prefecture, on 25 January to 1 February in 1978 and 27 January to 4 February in 1979. The number of effective data obtained was 106 in 1978 and 58 in 1979. The data for each year were analyzed with respect to snowflakes and graupel particles.

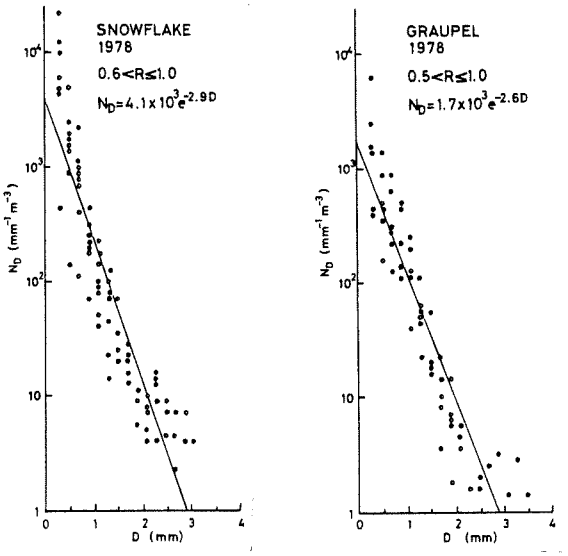

Fig.1 A size distribution for snowflakes.
Fig.2 A size distribution for graupel particles.

3.1 Size distribution

Generally, the size distribution for snow particles fits well to an exponential of the form

$$N_D=N_0\exp(-\Lambda D), \qquad (4)$$

as found for rain by Marshall and Palmer(1948). Examples of the size distribution for snowflakes and graupel particles are shown in Figs.1 and 2, respectively. The distribution for snowflakes under a precipitation rate between 0.6 and 1.0 mm hr^{-1} was expressed by $N_D=4.1\times10^3\exp(-2.9D)$. In the case of graupel particles for a precipitation rate between 0.5 and 1.0 mm hr^{-1}, corresponding equation was $N_D=1.7\times10^3\exp(-2.6D)$.

To specify the characteristics of size distributions observed, the particular value of N_0 and Λ for every value of R was taken into account. So all data for the types of snow particles obtained in an individual year were classified into several groups for precipitation rate, and values of N_0 and Λ were computed for each class which had an averaged precipitation rate. Then the dependences of N_0 and Λ upon R were obtained. Attempts for such averaging are to reveal a systematic change of size distribution with rate of snowfall for several samples of snow obtained on different days.

Results in 1978. The number of data for snowflakes was 68 in 1978, and they were classified into 8 categories depending upon precipitation rate. Fig.3 shows plots of N_0 and Λ against the average precipitation rate. The solid line is a regression curve for 8 points. The N_0 value increased ($N_0=3.7\times10^3R^{0.57}$) as the precipitation rate increased. The Λ value decreased ($\Lambda=2.6R^{-0.10}$) as the precipitation rate increased. Namely, the characteristics for 1978 snowflakes were that the distribution became broader and the number of particles increased on the whole as the precipitation rate increased.

In the case of the 1978 graupel particles with 38 data and 7 categories of precipitation rate, as seen in Fig.4, the N_0 value increased ($N_0=3.6\times10^3R^{0.98}$) and the Λ value decreased only a little ($\Lambda=2.9R^{-0.002}$) as the precipitation rate increased. This resulted in almost no change in the pattern of distribution and the total increased number of particles is attributed to the increase of the precipitation rate.

Results in 1979. In the case of snowflakes which had 36 data and 7 categories of precipitation rate, a remarkable decrease of the N_0 value with increasing R value is demonstrated in Fig.5, where $N_0=1.5\times10^3R^{-0.38}$ and $\Lambda=2.0R^{-0.34}$. The snowflake characteristics for 1979 were in contrast to that of 1978, that is, the number of smaller particles decreased with increasing precipitation rate and the distribution became much broader due to a notable increase of larger snowflakes also with increasing precipitation rate.

In the case of the graupel particles for 1979, 22 data and 4 categories of precipitation rate are illustrated in Fig.6, where $N_0=9.7\times10^2R^{-0.01}$ and $\Lambda=2.2R^{-0.20}$. There were almost no change in N_0 and a decrease in Λ, which were also in contrast to the 1978 graupel case. Namely, the increase of precipitation rate was due to the increase of the larger graupel particles in the case of 1979.

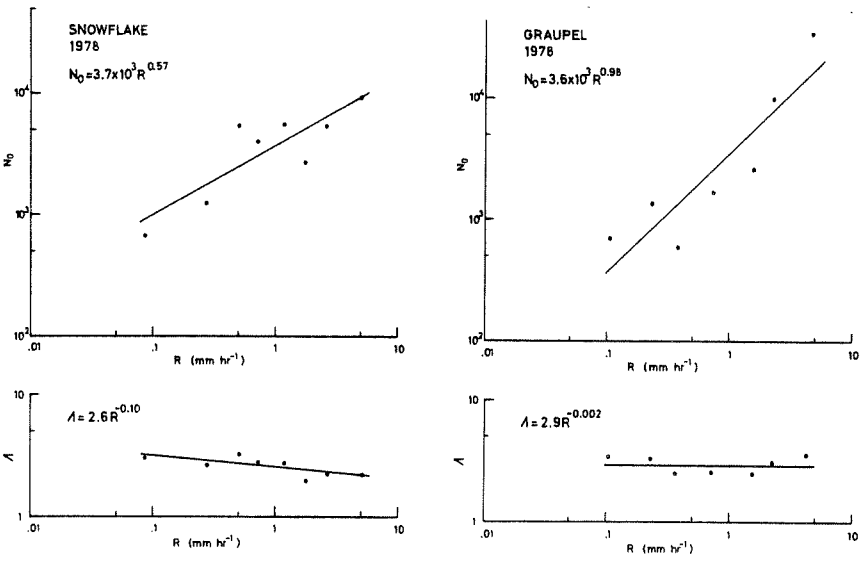

Fig.3 Size distributions for snowflakes observed in 1978, in terms of N_0 & Λ vs. R (for equation $N_D=N_0\exp(-\Lambda D)$).
Fig.4 Same as Fig.3, but for graupel particles observed in 1978.

3.2 Z-R relationship

Using Equation 1 and 2, the radar reflectivity factor Z and the precipitation rate R were reduced from the size distribution data obtained. Then the relationship between Z and R were computed in the form of Equation 3 as follows:

Results in 1978. The Z-R relationship for snowflakes in 1978 was $Z=1200R^{1.3}$. The range of precipitation rate in this case was 0.013 to 11 mm hr^{-1}. The case for graupel particles was $Z=650R^{1.1}$ and the range of precipitation rate varied from 0.058 through 8.1 mm hr^{-1}.

Results in 1979. The relationship of Z to R for snowflakes was $Z=2600R^{1.8}$ and the precipitation rate ranged from 0.031 to 4.3 mm hr^{-1}. This result indicates

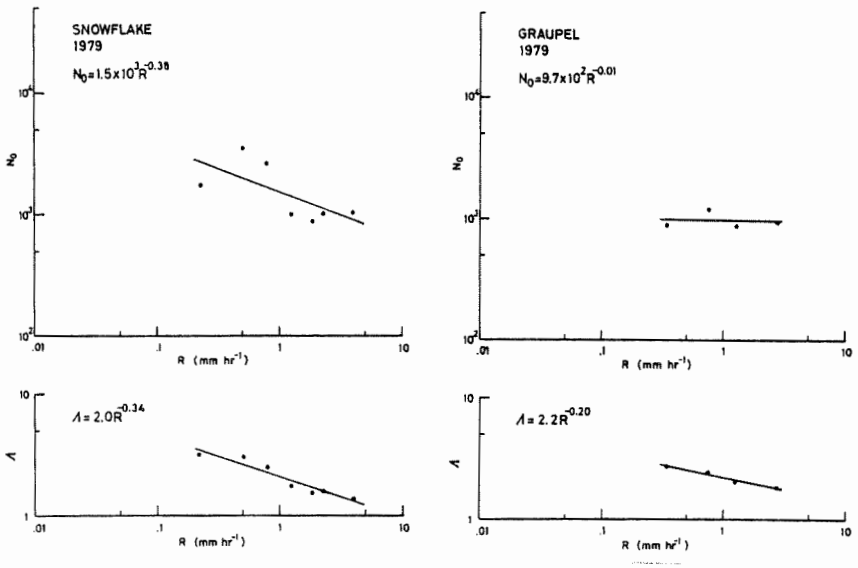

Fig.5 Same as Fig.3, but for snowflakes observed in 1979.
Fig.6 Same as Fig.3, but for graupel particles observed in 1979.

greater B and β values in 1979 compared to those for 1978. For the case of graupel particles, the Z-R relationship was $Z=960R^{1.6}$ with a range of 0.13 to 3.7 mm hr^{-1} in precipitation rate. Also the greater B and β value in this case is significant when compared to the result for the 1978 graupel event.

4. Discussion

All results described in the former section are outlined in Table 1, including the water content M (g m^{-3}) and the median volume diameter D_0 (mm) which were reduced for snowflakes and graupel particles in each year. In this section a difference between meteorological conditions of snowfall is discussed with respect to the size distribution and Z-R relationship.

First, in the case of snowflakes, the observed results show that the Z-R relationship in 1978 was $Z=1200R^{1.3}$ and that in 1979 $Z=2600R^{1.8}$. A discrepancy in the relationship between the results for both years could be attributed to a difference in the size distributions, as a result of the meteorological situation peculiar to the observation period of each year. The data in 1978 was mainly obtained under the so-called heavy snowfalls during a strong winter monsoon. On the other hand the majority of the data obtained in 1979 was for snowfalls related to extratropical cyclones which passed over the observation point. In the 1979 winter, the strong monsoon as usual did not occur; it was a warm winter in 1979. This difference in weather conditions between both winters would appear in the form of size distribution as follows:

For 1979 snowflakes where cyclonic conditions prevailed, the value of N_0 in Equation 4 decreased with increasing precipitation rate and the value of Λ also showed a distinct decrease. An explanation for such a trend could be that the number of small snowflakes or snow crystals decreased relative to that of the larger snowflakes which increased due to processes of accretion and coagulation as the precipitation rate increased. These characteristics of size distribution were the same as the results of Gunn and Marshall (1958) obtained from observations for snowflakes from stratiform clouds. And such similarity in size distribution would result in a relatively good coincidence in the Z-R relationship, that is, $Z=2600R^{1.8}$ by the present authors and $Z=2000R^{2.0}$ by Gunn and Marshall (1958).

For the snowflakes in 1978 formed under strong monsoon conditions, the N_0 value showed a remarkable increase and the Λ value gently decreased with increasing precipitation rate. This may indicate that the number of larger snowflakes increased, but still smaller particles existed and grew abundant in number as the precipitation rate increased. Namely, a very distinctive feature in size distribution for snowflakes in 1978 was that numerous small particles fell with larger-size snowflakes at the higher precipitation rate. Due to the existence of numerous small particles in 1978 the median volume diameter in 1978 was small in comparison with that in 1979, and also the water content in 1978 was large in comparison with that in 1979 because of a lower fall velocity of small particles. These features would be reflected in the 1978 Z-R relationship, $Z=1200R^{1.3}$, i.e., smaller B and β values than those in 1979. It is also considered that the features in size distribution observed under heavy snowfalls was related to a constant supply of water vapour from the warm Sea of Japan to the cold atmosphere during the strong winter monsoon season.

Next, in the case of graupel particles, the observed results show that $Z=650R^{1.1}$ in 1978, and $Z=960R^{1.6}$ in 1979. The characteristics in size distribution were an increase of N_0 and constancy of Λ in 1978, and the constancy of N_0 and a decrease of Λ in 1979, respectively with increasing precipitation rate. In 1978, numerous powder snow particles fell with graupel particles, then such size distributions as men-

Table 1 Precipitation factors for snowflakes and graupel particles observed in 1978 and 1979; precipitation rate R in mm hr^{-1}, N_0 and Λ values in size distribution $N_D=N_0\exp(-\Lambda D)$, water content M in g m^{-3}, median volume diameter D_0 in mm, and B and β values in Z-R relationship $Z=BR^{\beta}$.

	year	data	R	N_0	Λ	M	D_0	B	β
Snowflake	1978	68	0.013-11	$3.7\times10^3R^{0.57}$	$2.6R^{-0.10}$	$0.23R^{0.95}$	$0.9R^{0.11}$	1200	1.3
	1979	36	0.031-4.3	$1.5\times10^3R^{-0.38}$	$2.0R^{-0.34}$	$0.20R^{0.82}$	$1.3R^{0.41}$	2600	1.8
Graupel	1978	38	0.058-8.1	$3.6\times10^3R^{0.98}$	$2.9R^{-0.002}$	$0.15R^{0.89}$	$1.0R^{0.02}$	650	1.1
	1979	22	0.13-3.7	$9.7\times10^2R^{-0.01}$	$2.2R^{-0.20}$	$0.11R^{0.84}$	$1.3R^{0.24}$	960	1.6

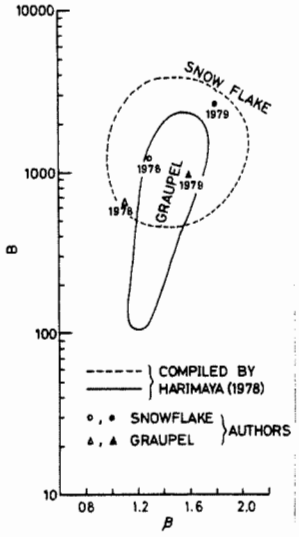

Fig.7 The domains of B and β values in the equation of $Z=BR^{\beta}$ for snowflakes and graupel particles compiled by Harimaya (1978), and the present authors' results superimposed on the same B-β plane.

tioned above were resulted. So the B and β values in 1978 were smaller than those in 1979, similar to the case of snowflakes. This follows that the precipitation rate R in heavy snowfalls under winter monsoon conditions is larger than that in snowfalls related to a cyclone, under the same radar reflectivity factor Z.

Finally, a comparison between the present results and other observers' for the Z-R relationship is attempted. Harimaya (1978) drew two domains for snowflakes and graupel particles on the B-β plane, based on his measurements and those of several workers (Imai et al., 1955; Gunn and Marshall, 1958; Fujiwara et al., 1972; Yoshida, 1975), as seen in Fig.7. In this figure the Z-R relationship for snowflakes is indicated by the broken line and those of graupel particles by the solid line. As the present authors' results are superimposed on the same figure, then it can be said that they are included in respective domains. This is good in a way, because Harimaya's compilation was designed to include, possibly, the observational results for various conditions of weather. However, it should be noted that the observed data available now including the present authors' are still insufficient to classify the Z-R relationship with respect to meteorological situations of snowy weather.

5. Summary and conclusions

Observation of size distribution for snowflakes and graupel particles were made in Nagaoka, 20 km from the Sea of Japan, in January to February, in 1978 and 1979. The data in 1978 were obtained mainly in heavy snowfalls when winter monsoon conditions were prevalent, whereas those in 1979 were obtained under extratropical-cyclonic conditions. Such a difference in meteorological situations gave discrepancy between the size distribution of snowflakes and graupel particles for two years.

In the case of snowflakes, in 1978 the size distribution grew slightly broader with a distinct increase of smaller particles as the precipitation rate increased, and in 1979 the size distribution became remarkably broad with a distinct decrease in the smaller particles as the precipitation rate increased. In the case of graupel particles, the significant feature in size distributions was the same as in the case of snowflakes; the existence of numerous smaller particles was very remarkable in 1978 under the higher precipitation rate.

Based on such differences in size distribution, it can be stated that the precipitation rate R in heavy snowfalls under winter monsoon conditions are larger than that in snowfalls related to a cyclone, under same radar reflectivity factor Z.

Acknowledgements: The authors are indebted to Mr. H. Seino, National Research Center for Disaster Prevention (Present affiliation; Kyushu National Agricultural Experiment Station), for his contribution in the 1978 observation and data analysis. This work was partially supported by the Special Fund for the Promoting of Multiministerial Research Project under the jurisdiction of the Science and Technology Agency, entitled, "Studies on watch-system of snow coverage for snow removal of highway networks and precipitation process in heavy snowfalls".

References

Battan, L. J., 1973: Radar observation of the atmosphere., 84-113, The University of Chicago Press.

Fujiwara, M., 1965: Raindrop-size distribution from individual storms., J. Atmos. Sci., Vol.22, No.5, 585-591.

————, T. Yanase and K. Takahashi, 1972: Relationships between radar reflectivity Z and the rainfall intensity R on snowflake and graupel., Tenki, Vol.19, No.1, 31-36.

Gunn, K. L. S. and J. S. Marshall, 1958: The distribution with size of aggregate snowflakes., J. Meteor., Vol.15, No.5, 452-461.

Harimaya, T., 1978: Observation of size distribution of graupel and snow flake., J. Fac. Sci., Hokkaido Univ., Ser.VII, Vol.5, No.3, 67-77.

Imai, I., M. Fujiwara, I. Ichimura and Y. Toyama, 1955: Radar reflectivity of falling snow., Papers Meteor. Geophys., Vol.6, No.2, 130-139.

Kajikawa, M., 1974: Measurement of falling velocity of snow flakes., Res. Rep. Akita Tec. Col., No.9, 83-87.

————, 1975: Measurement of falling velocity of individual graupel particles., J. Meteor. Soc. Japan, Vol.53, No.6, 476-481.

———— and K. Kiba, 1978: Observation of size distribution of graupel particles., Tenki, Vol.25, No.5, 390-398.

Marshall, J. S. and W. M. Palmer, 1948: The distribution of raindrops with size., J. Meteor., Vol.5, No.2, 165-166.

Yoshida, T., 1975: The relation between radar reflectivity and snowfall intensity by kerosene-soaked filter paper method., J. Meteor. Res., Vol.27, No.3, 107-111.

EFFECTS OF COALESCENCE IN A MELTING LAYER ON TWO-WAVELENGTH MICROWAVE BACKSCATTERING

T.Yokoyama and H.Tanaka

Water Research Institute, Nagoya University
Nagoya, JAPAN

1. Introduction

A wide variety of behaviors of falling snowflakes in the melting layer, especially coalescence and breakup processes, have so far been investigated by many workers: Gunn and Marshall (1958), Lhermitte and Atlas(1963), Ohtake(1969), Takeda and Fujiyoshi(1978) and so on. In spite of their efforts, understanding of the roles of the melting layer for rainfall mechanism are still far from complete since there are many uncertain parameters such as complex refractive index, drag coefficient and shape deformation of a melting snowflakes.

Radar observation using two wavelengths can avoid such uncertainties as are involved in one-wavelength observation. In this paper, dependence of backscattering cross-section, and hence radar reflectivity factors, on wavelength obtained by observation is compared with that obtained by non-coalescence and non-breakup model of the melting layer. Discrepancies between them can be explained by introducing coalescence process into the present model.

2. Non-coalescence and non-breakup model of the melting layer

Firstly we shall propose a model of the melting layer which is more sophisticated than that of Ekpenyong and Srivastava(1970). Radar reflectivity factors based on the model will be compared with the observational results. This model includes the following assumptions: (1) coalescence and breakup of particles never occur, (2) melting snowflakes are described by two concentric spheres with water and snow, (3) precipitation rate is equal at all levels and is steady. Ekpenyong and Srivastava(1970) assumed in their calculation of microwave scattering that the relation between melting rate and backscattering cross-section was decided uniquely independent of particle diameters. According to Mie scattering theory of Aden and Kerker(1951), however, this assumption is not always applicable to large concentric spheres like melting snowflakes. Our calculation of backscattering cross-section is exact based on the theory of Aden and Kerker(1951).

Fig.1 shows the vertical profiles of radar reflectivity factor for different wavelevgths when precipitation rate is 2mm/hr. We can find that the differences of radar reflectivity factor for three wavelengths (except a millimeter wavelength) are rather small if non-coalescence and non-breakup model is used. Fig.2 shows the increments of radar reflectivity factor from 0°C level to the peak of bright band, i.e., the upper part of the melting layer, for two wavelengths(3.21cm and 5.6cm) for a wide range of precipitation rates. It can be seen that the increments of radar reflectivity factor of 5.6cm wavelength are slightly larger than those of 3.21cm wavelength. The decrements from the peak of bright band to rain level, i.e., the lower part of the melting layer, for two wavelengths are demonstrated in Fig.3. The decrements of 5.6cm wavelength are larger than those of 3.21cm wavelength especially when the precitation rate is high.

3. Observation of the melting layer by two wavelength radars

Observations of the precipitation from stratiform cloud associated with a Baiu front were made by means of two radars of which wavelengths are 3.2cm and 5.6cm during the period from 26 June to 1 July, 1979 at the Kashima branch of the Radio Research Laboratories facing on the Pacific Ocean. Fig.4 shows time-hight cross-section of radar reflectivity factor and time variation of the precipitation rate measured on the ground during the period of 22.20 to 23.30(JST) on 27 June. Bright band is clearly found just below 5km level. The vertical profiles of radar reflectivity factor were obtained along precipitation streaks.

In Fig.5, the increments of radar reflectivity factor in the upper part of the melting layer for two wavelengths are shown. It is clear that the increments of 5.6cm wavelength are much larger than those of 3.2cm wavelength. Comparison of the decrements of radar reflectivity factor for two wavelengths in the lower part of the melting layer is demonstrated in Fig.6. In this case the discrepancies between the decrements for two wavelengths are not remarkable.

4. Comparison between model calculation and observation

The upper part of the melting layer

From Fig.2 and Fig.5, it should be noted that the increments corresponding to 5.6cm wavelength are larger than those corresponding to 3.2cm wavelength for both model calculation and observation. Especially this tendency is more remarkable for observation than for model calculation. In order to examine the reason for such discrepancies of the tendencies between model calculation and observation, we tried to carry out a calculation using simple coalescence model in which particles are monodispersive. The result of calculation shows that only the changes of particle size by coalescence lead to large difference between the increments for two wavelengths. Changes of other parameters such as falling velosity, complex refractive index of snow and way of

melting do not cause such large discrepancies.

The lower part of the melting layer

From Fig.3 and Fig.6, the discrepancies of the decrements of radar reflectivity factor are rather small between model calculation and observation. In order to check the result in more detail,we made some calculations based on the simple coalescence-breakup model changing a couple of parameters such as falling velocity, complex refractive index and way of melting. The results demonstrate that change of radar reflectivity factor caused by coalescence and breakup have the same tendency as that caused by changing parameters above mentioned. Therefore we can not discriminate whether size change of particles is effective or not in this region.

5. Conclusions

From the results obtained by model calculation and observation above mentioned,the following conclusions about coalescence and breakup processes occuring in the melting layer are obtained.

(1) It is confirmed that coalescence of the melting snowflakes is predominant in the upper part of the melting layer. This conclusion from two-wavelength method is more persuasible than that from traditional method,but we can only conclude qualitatively at present.

(2) In the lower part of the melting layer, we can not clarify which process is predominant,coalescence and breakup. To get more detailed informations in this part of the melting layer,we must select a more suitable pair of wavelengths.

Acknowledgements

The authors wish to thank Dr.K.Nakamura and Mr.J.Awaka,the Kashima Branch of the Radio Research Laboratories,for affording facilities to use 5.6cm radar.

References

Aden,A.L.,and M.Kerker, 1951: Scattering of electromagnetic waves by two concentric spheres. J.Appl.Phys., 22, 1242-1246.

Ekpenyong,B.E.,and R.C.Srivastava, 1970: Radar characteristics of the melting layer--a theoretical study. Tech.Note No.16,Lab.Atmos.Probing, University of Chicago, 34pp.

Gunn,K.L.S.,and J.S.Marshall, 1958: The distribution with size of aggregate snowflakes. J.Meteor., 15, 452-461.

Lhermitte,R.M.,and D.Atlas, 1963: Doppler fall speed and particle growth in stratiform precipitation. Proc.Tenth Wea.Radar Conf. Boston Amer.Meteor.Soc., 297-302.

Ohtake,T., 1969: Observation of size distributions of hydrometeors through the melting layer. J.Atmos.Sci., 26, 545-557.

Takeda,T.,and Y.Fujiyoshi, 1978: Microphysical processes around melting layer in precipitating clouds as observed by vertical pointing radar. J.Meteor.Soc. Japan, 56, 293-303.

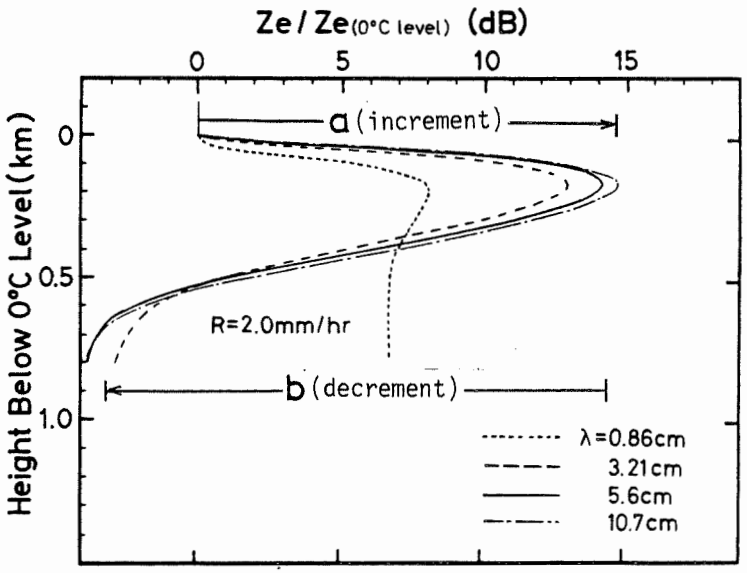

Fig.1 Vertical profiles of radar reflectivity factor for various wavelengths(0.86cm,3.21cm,5.6cm,10.7cm) obtained by using non-coalescence and non-breakup model of the melting layer. Abscissa is Ze normalized by 0°C level value. Parameters 'a' and 'b' in this figure indicate an increment of Ze in the upper part of the melting layer and a decrement in the lower part,respectively.

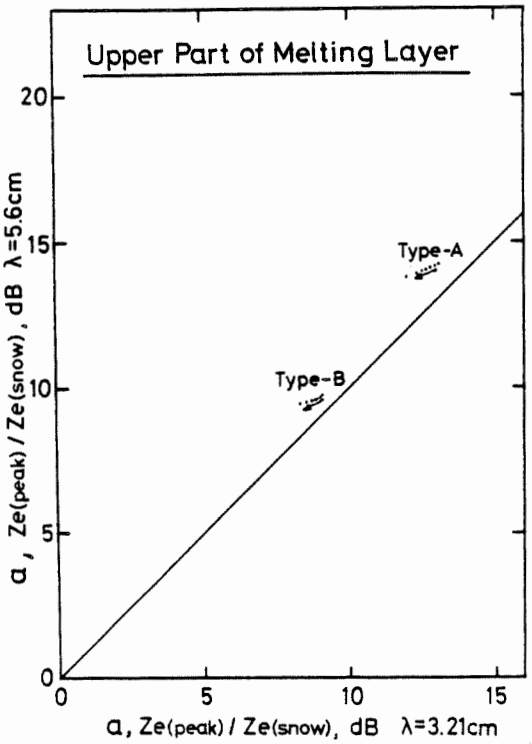

Fig.2 Comparison of increments of radar reflectivity factor calcurated using non-coalescence and non-breakup model for 3.21cm wavelength(abscissa) and 5.6cm(ordinate) in the upper part of the melting layer. Type-A and Type-B indicate snow types classified by snow density. The density of Type-A and Type-B snow are 0.05 and 0.20,respectively. Each point along arrow corresponds to 0.5,1,2,4,8,16 and 32mm/hr precipitation rate.

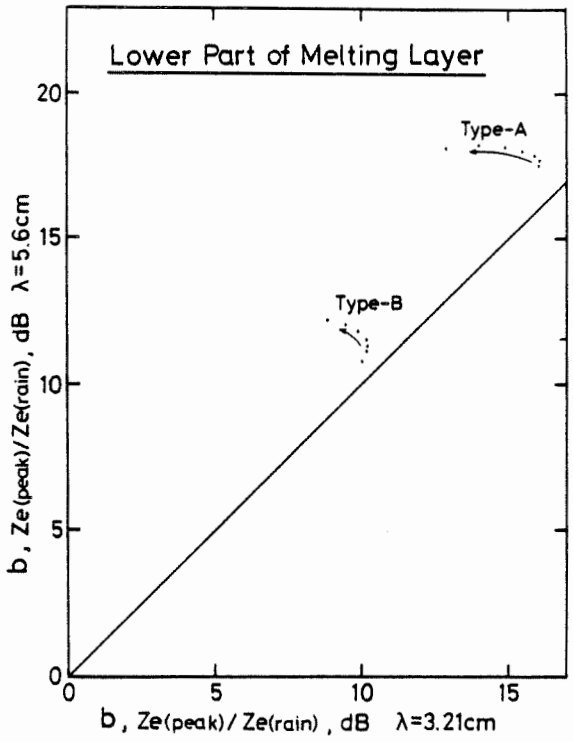

Fig.3 Same as Fig.2 but for decrements of radar reflectivity factor for 3.21cm and 5.6cm wavelength in the lower part of the melting layer derived by model calculation.

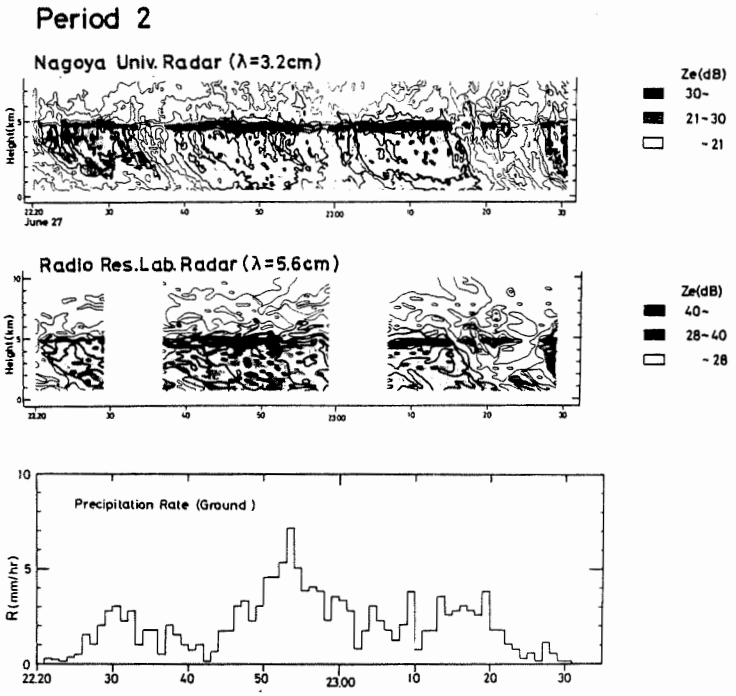

Fig.4 Time-height cross-section of radar reflectivity factor(upper:3.2cm, middle:5.6cm) and time variation of the precipitation rate measured on the ground(lower figure) with a high response rain gauge at Period-2 —— from 22.20 to 23.30 (JST) on 27 June,1979.

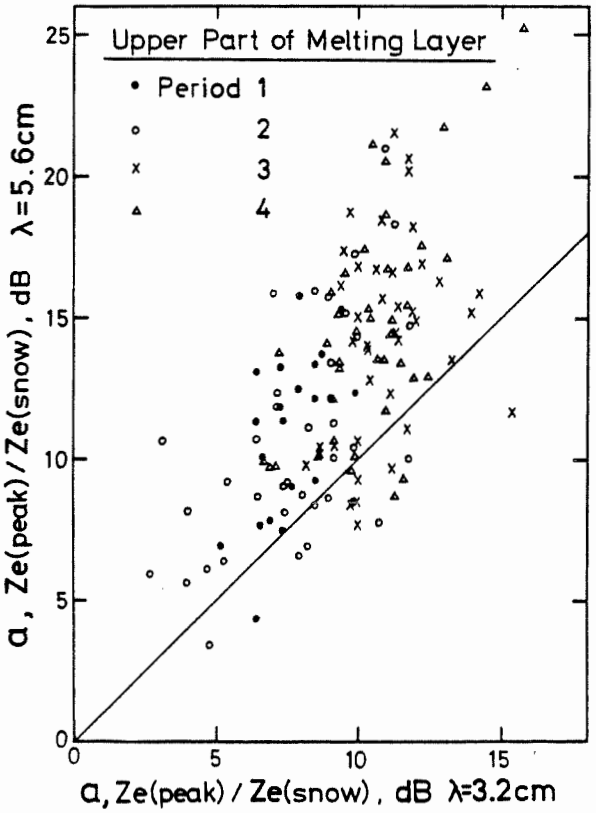

Fig.5 Comparison of increments of radar reflectivity factor for 3.2cm wavelength(abscissa) and 5.6cm (ordinate) in the upper part of the melting layer obtained from radar observations, throughout four periods.

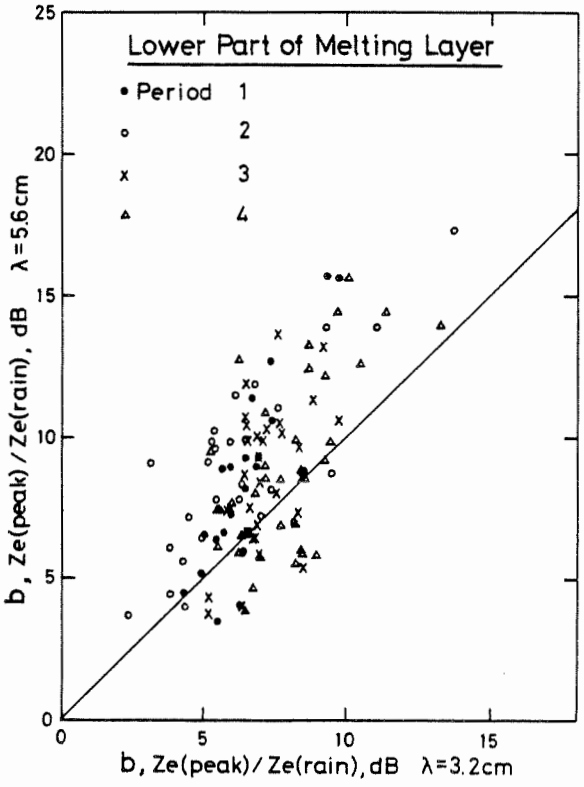

Fig.6 Same as Fig.5 but for decrements of radar reflectivity factor in the lower part of the melting layer.

II.5 - Grêlons

Hailstones

THE ORIGIN OF HAILSTONE EMBRYOS DEDUCED FROM ISOTOPE MEASUREMENTS

B. Federer, B. Thalmann, A. Oesch, N. Brichet, A. Waldvogel

Atmospheric Physics ETH
Zurich SWITZERLAND

J. Jouzel, L. Merlivat

Département de Recherche et Analyse
CEN-Saclay FRANCE

1. INTRODUCTION

One of the fundamental questions in hail formation is the temperature of the origin of hailstone embryos. It is possible to derive these by means of isotopic measurements from hailstones collected on the ground, if, firstly, the relative enrichment of HDO and $H_2{}^{18}O$ in the hydrometeors from which hailstones are grown, and its decrease with height can be estimated reliably. Secondly, the isotope content of the vapor feeding the cloud at cloud base (R_o) and the degree of its change during the growth time of the hailstones should be known accurately. The 1D-steady state model presented by Jouzel et al. (this conference) gives more realistic profiles of the isotope content of hailstones R_H than the previously used adiabatic models. In the new model the assumption that the D-content in the hail layers is essentially that of the accreted cloud droplets was dropped and the interactions of 5 water species have been taken into account. Concerning the second problem the isotope content of subcloud vapour was measured during two summer seasons to assess the value of the traditional R_o-determination and to obtain a measure of the variability of R_o during a hailday. With these new tools a refined interpretation of the growth history of 33 hailstones fallen on 3 days is presented. The size of the stones, collected from the ground or quenched directly in the chilled hexane of the hail collector, ranged from 11 to 46 mm and the frequency of graupel or frozen drop embryos in all stones collected on those days is given in Table 1.

2. DETERMINATION OF R_o, THE ISOTOPE-CONTENT OF VAPOR AT CLOUD BASE.

The R_o value is usually determined from the extreme values of D, ^{18}O measured in hailstones and by attributing those to growth temperatures of -35C and 0C for example. In this way the relationship between the D content of the condensed phase R_c and R_o is obtained. Since in the new model the deuterium content of hail R_H results from the interaction of 5 water species, no analytical relation exists between the isotope content of the hailstone layers R_H and R_o. Therefore a trial and error method has been employed: First a reasonable R_o is estimated using the adiabatic assumption. The model is then run yielding an approximate R_H-profile. The D-concentration corresponding to a specific extreme temperature or, better, identified from crystallographic analysis (no large crystals at T_c < -24C, no small crystals at T_c > -15C), is compared with the result of this first approximation*. New approximations of R_o are obtained by shifting the theoretical profile to coincide with an increasing number of temperature reference points. The final R_o value then yields the optimum R_H-profile as well as the D-profile of the entrained vapor R_e by using the average decrease dR_e/dz = 0.0039 ppm/m (Ehhalt, 1974). In this method it must be assumed that the isotope content of subcloud vapor is reasonably constant both vertically and horizontally.

*Crystal size in the growth layers was inferred from off-center thin sections.

	graupel %	frozen drop %	not classified	total number	temperature at CCL (°C)
August 6, 1977	37	49	14	35	6.7
July 14, 1978	38	52	10	239	11.2
August 6, 1978	28	63	9	430	9.3

Table 1: Embryo classification for the 3 storms. Total number of stones and percentage of the embryo types are given. The cloud base (CCL) temperatures are also tabulated.

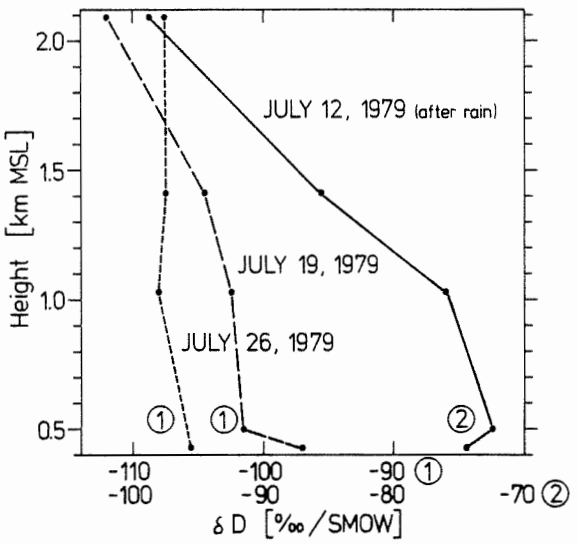

Fig. 1. Three measured deuterium profiles of water vapor in clear air as a function of altitude. Note the different scale on the abscissa for July 12, 1979 which represents a typical gradient after a rain shower.

This has been checked in an experiment with up to 5 stations, sampling simultaneously in and near the experimental area at altitudes between 430 and 2100 m MSL in typical prestorm conditions. The 3 most important results of a total of 153 vapor measurements on 29 days can be summarized as follows: 1) The D-content of vapor at any one sampling station typically varied by less than 1 ppm within 2 hours (maximum 1.8 ppm at station Neuenkirch probably due to the wet ground). 2) The horizontal variability was surprisingly large, typically 2 ppm and up to 3.5 ppm. This casts doubt on the value of measurements in narrow valleys which might be subject to a very local circulation. The mean relations, obtained on all sampling days are:
$\delta D = 7.6\ \delta^{18}O + 3.4$ for Emmen (425 m MSL) 1978 and
$\delta D = 6.7\ \delta^{18}O - 7.0$ for Emmen 1979.
Feldmoos 1979 (30 km to the SE, 805 m MSL) yielded
$\delta D = 7.1\ \delta^{18}O - 2.1$. The relation for Pilatus (2100 m MSL) resembles most closely the theoretical relation: $\delta D = 7.9\ \delta^{18}O + 9.7$. 3) The vertical concentration-gradients are small in cloudless situations but up to 3 ppm (for D) after rain (see Fig. 1).

In conclusion, for the R_o-determination we use the direct vapor measurements of the lowest atmospheric layer, measured in the plain. If none are available, we choose the crystallographic method which gives the smallest intervals for the possible R_o's. A comparison of the two independent methods results in almost the same R_o's. This gives considerable confidence in the correctness of R_o and therefore in the model-calculated absolute temperature scales.

3. APPLICATIONS TO EMBRYOS

3.1 Isotope-content

In Fig. 2 we have plotted the isotope concentrations of the hailstone embryos analysed on August 6, 1977, August 6, 1978 and July 14, 1978 in a $\delta D - \delta^{18}O$ diagram. The relation $\delta D = 8.5\ \delta^{18}O$ + const., valid for equilibrium conditions, is drawn for comparison through the "coldest" ice sample for each day, where equilibrium conditions are most likely to prevail. Any deviation from the equilibrium line is due to kinetic effects from condensation-evaporation processes which are characterized by a slope 3.5 in the above relation (Jouzel and Merlivat, this conference). Fig. 2 shows that the range of δD for the embryos is about 22 ‰ on August 6, 1977 and 1978 and about 32 ‰ on July 14, 1978 which is comparable to the range reported by Roos et al. (1977) for his South African embryos.

Most of the embryos lie close to the equilibrium line and within the measurement uncertainty. If the ice samples from the entire stones are plotted in a similar diagram (not shown), the warmer, clear layers with large crystals tend to show a pronounced evaporation effect; these layers must have been grown in the wet régime. As expected the graupel embryos are closer to the $D - {}^{18}O$ equilibrium line than the frozen drop embryos. The latter are generally warmer and show signs of evaporation, especially at the higher isotope contents. This indicates that the drops were evaporating slightly prior to their freezing. This is because they were warmer than the environment, a situation to be

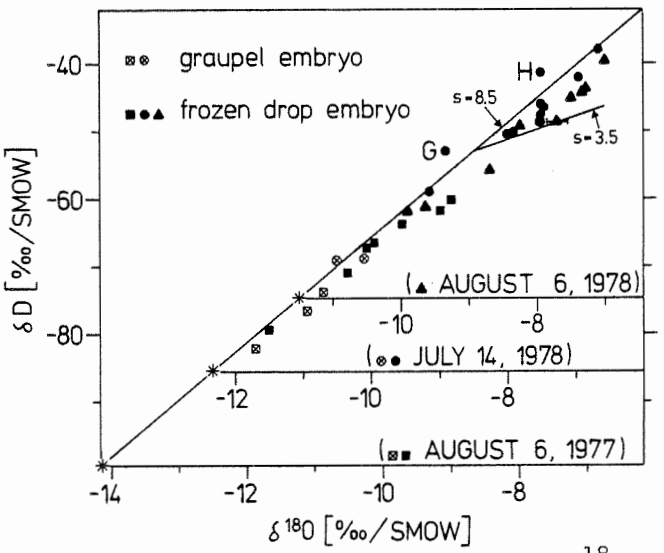

Fig. 2. Plot of the deuterium content vs. ^{18}O - concentration of the 33 analysed hailstone embryos. The equilibrium line with slope 8.5 is plotted through the 3 points (asteriks) representing the coldest ice sample of the day. The non-equilibrium line with slope 3.5 through a selected point is used to correct the measured isotope values for evaporation effects as suggested by Bailey et al. (1969). The error bar indicates the standard deviation of the ^{18}O measurement.

expected with millimeter-sized drops ascending in a moderate updraft and growing by coalescence. On the other hand two frozen drop embryos, designated by letters in Fig. 2, are lying to the left of the equilibrium line for July 14, 1978 which indicates that condensation was occurring on the cold drops prior to their freezing. This and the fact that graupel are generally poorer in isotopes, but drop embryos do not show any substantial evaporation, raises the question whether the drop embryos G and H were merely melted and recirculated graupel, a possibility indicated by workers in Colorado. This problem will be addressed in the next section.

3.2 Recirculation

In order to show that it is unlikely that the frozen drop embryos on July 14, 1978 were merely melted graupel, we assume that a graupel grown to a size of 3 mm diameter from an ice crystal nucleated somewhere between the -10 and -15°C-isotherms, would have a D-content between R_i and R_c at the -25°-isotherm (point A in Fig. 3). Suppose now that this graupel falls out of the updraft and is transported below the 0°-isotherm in weak downdrafts as indicated for instance by the closed loop circulation by Dye et al. (1978). The melting time of the graupel to produce a drop of $r \tilde{=} 1$ mm would be about 100 seconds in a cloud of $T_c \geq +2°C$ (Drake and Mason, 1966), whereas the isotopic relaxation time t_a for the same drop is of the order of 400 s (Stewart, 1975). The situation is schematically depicted in Fig. 3 at the +2°C-isotherm,

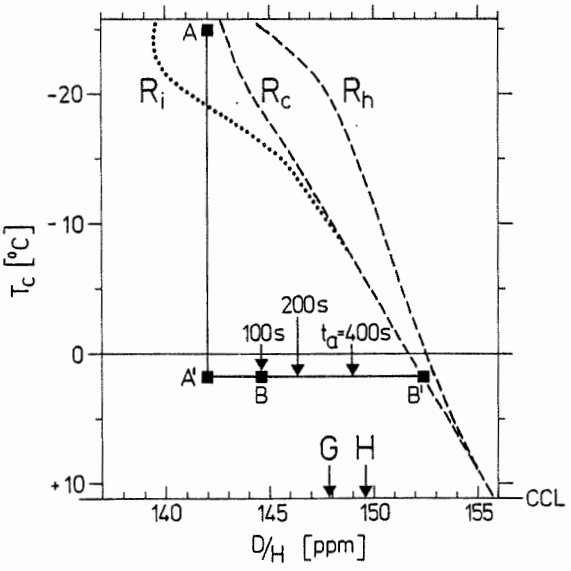

Fig. 3. Deuterium content of cloud water R_c, cloud ice R_i and hydrometeor water R_h as a function of cloud temperature T_c. The time for a drop of radius r = 1 mm to approach isotopic equilibrium is indicated at the + 2°C-isotherm. The drop would reach the relaxation time t_a only after 400 s and would have a D-content of 149.0 ppm. The graupel particle with an assumed diameter of 3 mm starts to melt at A' for 100 s (point B).

where it is shown that the D-content of the drop is always considerably smaller than the one of the water species surrounding it (point B'), unless the drop is kept in balance for an unrealistically long time period. If the drop then started to ascend again in the strong updraft from point B, interacting with cloud droplets only (no breakup), it is unlikely that it would reach D-contents of 147.9 and 149.6 ppm as measured in embryos G and H respectively. It is clear that there are many arbitrary assumptions in this reasoning and each case would have to be calculated separately with varying updraft speeds and LWC's. But the fact that the D-content of all embryos identified as graupel is at least 2 ppm lower than that of the drop embryos and the observation that the two embryos exhibiting condensation have D-contents lying in the range of those for the frozen drop embryos (showing evaporation), leads us to conclude that most embryos were probably grown by coalescence.

4. APPLICATION TO TRAJECTORIES

The application of the new isotopic model to the D-profiles of the entire hailstones yields a range of growth temperatures which is much narrower than those obtained earlier with the adiabatic model (Fig. 4). In Fig. 4a the δD-profiles are shown together with the bubble structure of 3 stones of August 6, 1977. From the profile of stone G for example, a rapid upward motion beginning at a radius of r = 11 mm and spanning the whole δD-range of 18 °/oo could be inferred. Incidentally this rapid upward motion is accompanied by the formation of a clear layer, a fact observed in most published isotope analyses of hailstones and already described by Federer et al. (1978). This ascent is seen to be much less dramatic in Fig. 4b where the 3 stones oscillate in a temperature range of merely 8°C during their entire growth. This means that both embryo and hailstone growth take place in a nearly balanced state and that changes in opacity are not due to large changes in cloud temperature but rather to changes in LWC, ice content and/or drop spectra.

The narrowing of the temperature range of hailstone trajectories due to the use of the more realistic model also changes the earlier calculations of maximum updraft speeds u. Since the determination of u is critically dependent on the altitude change of the stone with radius dz/dr, the earlier excessive speeds of up to 80 m/s would be corrected down to considerably lower values in the present approach.

The amplitudes of the recirculation of large stones which extended over several kilometers in the earlier model are now reduced considerably. Hailstone recirculation is present in only 9 of the 25 stones from which we obtained radial D-profiles. Interestingly, the 3 hailstones with graupel embryos (1 C-type) from the same site on August 6, 1977 show recirculation, whereas the 4 with frozen drop embryos (2A and 2C-type) do not. Crystallographic analysis of the rest of the analysed ensemble (see Table 1) points in the same

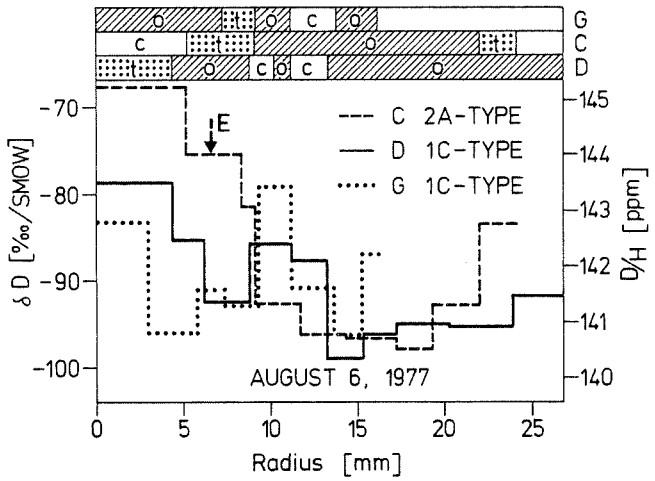

Fig. 4a. Deuterium content δD vs. radius of 3 hailstones from Aug. 6, 1977 with bar indications of bubblyness: opaque, transparent and clear ice.

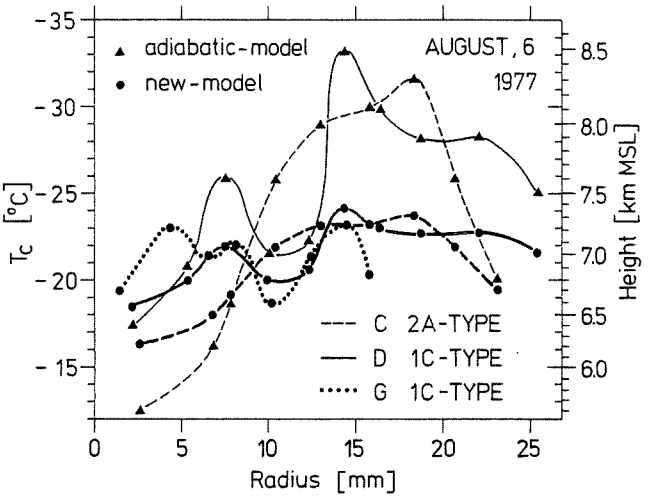

Fig. 4b. Comparison of trajectories of the hailstones in Fig. 4a calculated with the adiabatic (triangles) and the new model (circles).

direction. This is consistent with the graupel originating at a generally colder level than drop embryos and therefore the greater necessity for the graupel to recirculate in order to become large.

5. CONCLUSIONS

The interpretation of the growth history of hailstones and their embryos has been refined with the use of a model which takes into account the interaction of 5 water species, entrainment and fallout. Furthermore the variability of the isotope content of subcloud air (R_o) assumed to be constant during the growth time of hailstones, has been investigated by direct measurements.

The following conclusions were obtained from this preliminary data set:

1) The directly determined R_o-values are very similar to the ones from the independent crystallographic method. This gives considerable confidence in the latter which is used in conjunction with Macklin's composite diagram (no large crystals at $T_c \leq -24^oC$ and no small crystals at $T_c \geq -15^oC$). Simultaneous R_o-measurements on the ground show a significant horizontal gradient but a much smaller vertical gradient, both dependent on the local weather condition.

2) The application of the new isotopic model results in a much narrower temperature range for the trajectories indicating that hailstone growth takes place in a nearly balanced state. As the main advantage the new model eliminates some contradictions in the adiabatic model like growth temperatures $>0^o$ and excessive updraft speeds.

3) In most of the hailstone trajectories investigated, no pronounced recirculation of the stones was detected. This is in contrast to results obtained with earlier isotope interpretations which supported the recycling hypothesis.

4) The simultaneous measurement of D and ^{18}O on the same sample allows to correct for condensation-evaporation effects during hailstone growth. Evaporation effects for D of up to 1 ppm ($\delta D = 6^o/oo$) are observed in accordance with the laboratory measurements of Bailey et al. (1969).

5) A theoretical comparison of the melting time of a typical graupel with the isotopic relaxation time of the drop produced leads us to conclude that the frozen drops observed were not merely graupel melted below the 0^oC-isotherm and recirculated.

6. REFERENCES

Bailey, I.H., J.R. Hulston, W.C. Macklin and J.R. Stewart, 1969: On the isotopic composition of hailstones. J. Atmos. Sci., 26, 689-694.

Drake, J.C. and B.J. Mason, 1966: The melting of small ice spheres and cones. Quart. J. Roy. Meteor. Soc. 92, 500-509.

Dye, J.E., L.J. Miller, B.E. Martner and Z. Levin, 1978: Growth and recirculation of precipitation in an evolving convective storm. Preprints Conf. on Cloud Physics, Issaquah, Washington, 528-533.

Ehhalt, D.H., 1974: Vertical profiles of HTO, HDO and H_2O in the troposphere. NCAR Tech. Note No. 101.

Federer, B., J. Jouzel and A. Waldvogel, 1978: Hailstone trajectories determined from crystallography, deuterium content and radar backscattering. Pageoph 116, 112-129.

Roos, D.v.d.S., H. Schooling and J.C. Vogel, 1977: Deuterium in hailstones collected on 29 November 1972. Quart. J. Roy. Meteor. Soc. 103, 751-768.

Stewart, M.K., 1975: Stable isotope fractionation due to evaporation and isotopic exchange of falling waterdrops: Applications to atmospheric processes and evaporation of lakes. J. Geophys. Res. 80, 1133-1146.

GRAUPEL EMBRYOS

T. Harimaya

Department of Geophysics, Hokkaido University
Sapporo, JAPAN

1. Introduction

For discussions of the formation mechanism of graupel in clouds, it is necessary to clarify what graupel embryos are. Harimaya (1976, 1977) observed graupel particles by the thin section method and the direct method in which graupel particles are disassembled and showed that both snow crystals and frozen drops can become graupel embryos. The result was verified experimentally by Pflaum et al. (1978) who succeeded in growing graupel particles from frozen drop embryos and graupel particles from model snow crystal embryos using a vertical wind tunnel.

Since it has been clearly shown that both snow crystals and frozen drops are the graupel embryos, the question that follows are the conditions which determine whether the snow crystals or the frozen drops become the graupel embryos. This study of embryos can yield significant information about the clouds which produce them. In order to study the graupel embryos under different meteorological conditions, an observation in central Japan was carried out in addition to the previous observations in northern Japan. In this paper, the relationship between embryo type and meteorological condition will be described using the results. Then, based on the relationship, the regional characteristic in embryo type also will be described.

2. Observation of graupel embryo

In order to clarify what the graupel embryos are, the author examined the graupel particles by the thin section method and direct disassembling method of the graupel particles under a microscope. Thin sections in parallel to their growth direction through their centers were made. If graupel particles grow from snow crystals or frozen drops, it will be expected that they have the vertical section of snow crystals or frozen drops at their top as embryos. The thin sections of graupel particles were examined under a polarization microscope. This optical system can easily detect the c-axis of thin sections under a sensitive color plate, that is to say, when the color is yellow the c-axis is directed from top to bottom and when the color is blue the c-axis is directed from right to left.

Fig.1 shows a thin section of a graupel particle with a vertical section of a snow crystal at its top. Based on the shape, the yellow straight line at its top is considered to be the vertical section of a snow crystal. In addition, since the color is yellow, its c-axis is directed from top to bottom. Accordingly the straight line is the vertical section of a plane snow crystal.

Fig.2 shows a graupel particle with sections of two frozen drops at its top. Sizes of spherical parts at its top are 200 μm and 165 μm in diameter, respectively. Based on their shapes, it is considered that they are frozen drops.

By the thin section method, the sections of snow crystals and frozen drops were found at the top of graupel particles. Next, graupel particles were examined by the direct method in order to confirm that both snow crystals and frozen drops are embryos. Graupel particles were carefully disassembled under a microscope. However, it was difficult to identify a snow crystal or a frozen drop as an embryo of a graupel particle, because we had not developed observational techniques by which a snow crystal embryo or a frozen drop embryo could be picked out with certainty from the graupel parti-

Fig.1 Microphotograph of a thin section of a graupel particle with a snow crystal at the top. The yellow straight line is the vertical section of a snow crystal.

cle. The author has succeeded in several cases as shown in Fig.3. Fig.3 shows a snow crystal of dendritic type picked out from a hexagonal graupel, a snow crystal of dendritic type picked out from a conelike graupel and a frozen drop picked out from a conelike graupel, respectively. From the observational results described above, it was confirmed that both snow crystals and frozen drops can become graupel embryos.

3. Relationship between embryo type and meteorological conditions

The temperature at the cloud base and thickness of mixed clouds were calculated from aerological data in order to examine the relationship between embryo type and meteorological conditions. Based on observations which were made in northern Japan and central Japan during the winter season using snow crystal sondes (Magono and Tazawa, 1966; Magono and Lee, 1973; Taniguchi and Magono, 1978), there were cloud droplets only in the parts warmer than -20 °C in snow clouds. Therefore, in this calculation the thickness of mixed clouds was defined to be the thickness between the cloud base and -20 °C level if the cloud top is higher than -20 °C level. Fig.4 shows the meteorological conditions at the time when each embryo was observed. The ordinate and abscissa show the thickness of mixed clouds and temperature at cloud base, respectively. Frozen drop embryos belong to the upper region above boundary A and snow crystal embryos belong to the lower region below boundary B. While there are frozen drop embryos and snow crystal embryos in the region between boundary A and boundary B, it is seen that embryos change from snow crystals to frozen drops, as the temperature at cloud base is warmer and as the thickness of mixed clouds is thicker.

Next, we must examine whether there are large cloud droplets in snow clouds under the meteorological condition on the upper right corner in Fig.4. Based on the observational results using snow crystal sondes (Taniguchi and Magono, 1978), it appears that snow clouds sometimes contain large cloud droplets larger than 100 μm in diameter. The temperature at the cloud base and thickness of mixed clouds at the time when cloud droplets were observed by snow crystal sondes (Magono and Tazawa, 1966; Magono and Lee, 1973; Taniguchi and Magono, 1978) were calculated from aerological data. It is shown in Fig.5 that these values are added in Fig.4. The small open circles and large open circles show the cases with only small cloud droplets and with large cloud droplets, respectively.

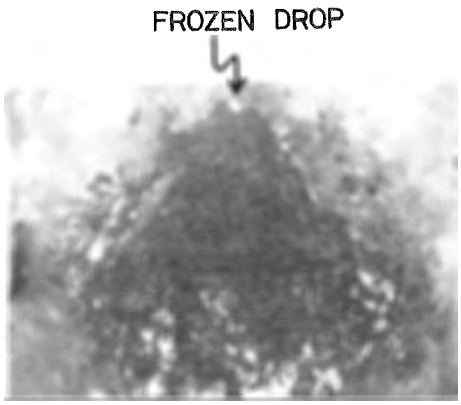

Fig.2 Microphotograph of a thin section of a graupel particle with two frozen drops at the top.

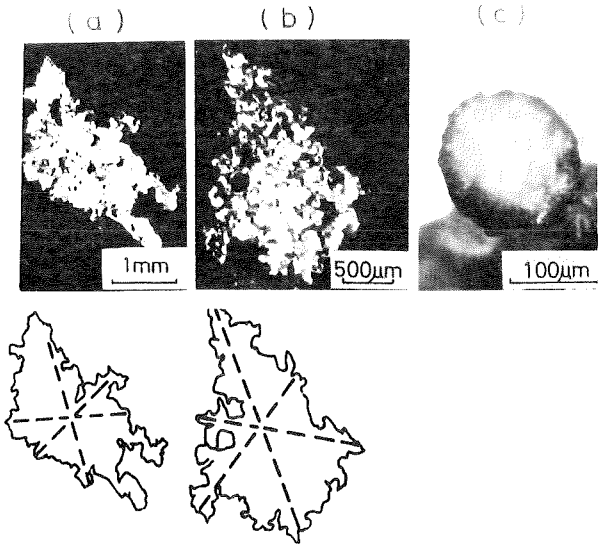

Fig.3 Snow crystal embryos (a, b) and a frozen drop embryo (c) picked out from graupel particles.

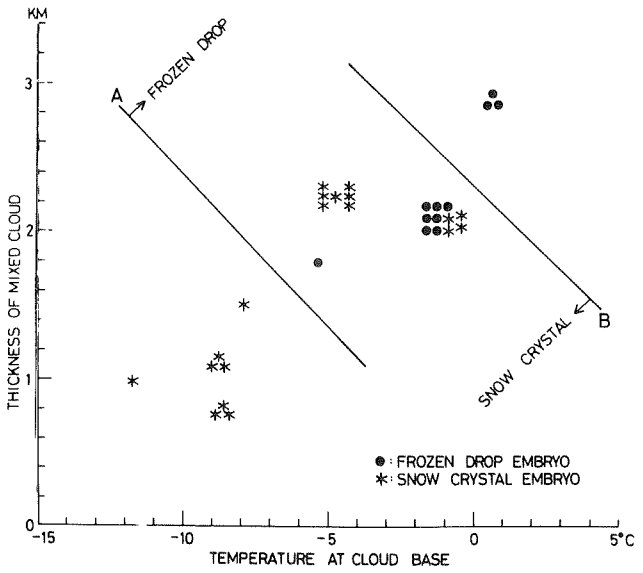

Fig.4 Relationship between embryo type and meteorological conditions.

It is seen that small cloud droplets and large cloud droplets are situated at the lower left corner and at upper right corner respectively, that is to say, large cloud droplets are situated at the region in which the temperature at the cloud base is warmer and the thickness of mixed clouds is greater. Since warmer temperatures at the cloud base provides a higher liquid water content, the meteorological condition corresponding to upper right corner is suitable for liquid coalescence owing to a higher liquid water content and greater thickness of mixed clouds (e.g. Singleton and Smith, 1960). Therefore, it is reasonable that large cloud droplets are situated at the upper right corner in Fig.5. In this figure frozen drop embryos are situated in the region in which large cloud droplets belong. Therefore, it is considered that warmer temperature at the cloud base and greater thickness of mixed clouds contribute to the formation of large cloud droplets, then the large cloud droplets transform into frozen drops and grow into graupel particles. This interpretation is reasonable under the liquid coalescence process in supercooled clouds without a melted layer.

4. Regional characteristic in embryo type

In the previous section it was shown that embryo type was classified by use of the temperature at the cloud base and thickness of mixed clouds. On the other hand, it is well known that graupel particles often precipitate on the western shore of northern Japan and central Japan during the winter season. As the meteorological condition in central Japan is different from that in northern Japan, it may be expected that the predominant embryos in each region are different. Sapporo and Wajima were selected as representative observation points of northern Japan and central Japan respectively, because aerological observations are carried out at both points. Statistical analysis was made using only the aerological data at the time when graupel particles precipitate for one hour before and after the aerological observation time. The temperature at the cloud base and thickness of mixed clouds at the time were calculated from the adopted aerological data (1967/68～1976/77). These value are shown in Fig.6 in the same manner as shown in Fig.4. As the region occupied by frozen drop embryos could not be distinguished from the region occupied by snow crystal embryos using a boundary line in Fig.4, the middle line between boundary lines A and B may be adopted as the boundary line between both regions. The boundary line is indicated by a solid line in Fig.6. It is seen that snow crystals are superior to frozen drops as embryos in Sapporo while frozen drops are superior to snow crystals as embryos in Wajima. This result shows that the predominant embryo type in Sapporo is different from that in Wajima and suggests that the precipitation mechanism may be different for each region.

5. Conclusions

Some workers claim snow crystals as the candidate of graupel embryos while others state that frozen drops are the graupel embryos. But, in this paper

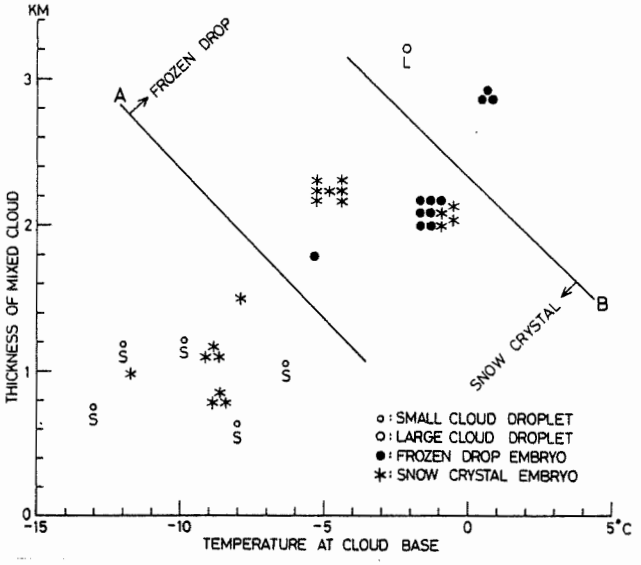

Fig.5 Relationship between cloud droplet type and meteorological conditions.

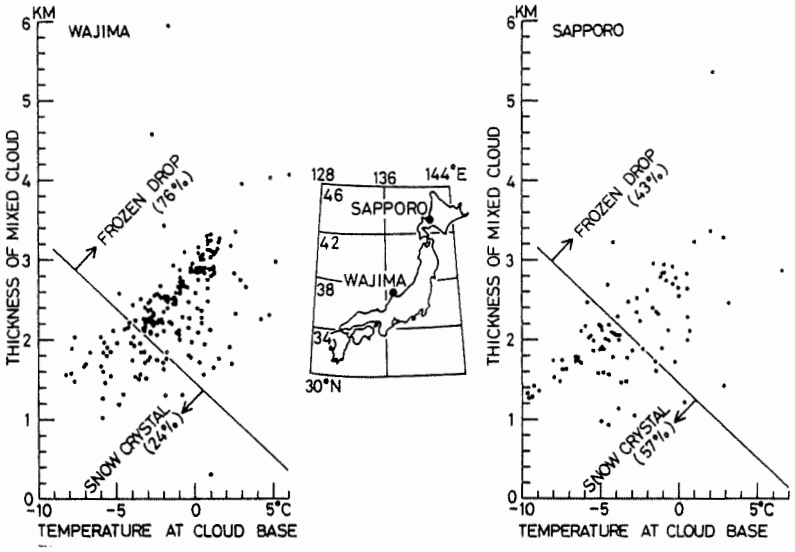

Fig.6 Regional characteristics in embryo type.

it was shown by thin section method and direct method that both snow crystals and frozen drops can become graupel embryos.

By parameters of the temperature at the cloud base and thickness of mixed clouds, it was determined whether snow crystals or frozen drops are predominant as graupel embryos. It was seen in the diagram that embryos change from snow crystals to frozen drops, as the temperature at the cloud base is warmer and as the thickness of mixed clouds is greater. If the observational results of cloud droplets are plotted on the diagram of graupel embryos, frozen drop embryos are situated in the region in which large cloud droplets belong. Therefore, it is considered that the warmer temperature at the cloud base and greater thickness of mixed clouds contribute to the formation of large cloud droplets, then the large cloud droplets transform into frozen drops and grow into graupel particles.

The embryo type in northern Japan and central Japan was investigated statistically using the relationship between the embryo type and meteorological conditions mentioned above. As a result, it was clearly shown that snow crystal embryos are predominant in northern Japan while frozen drop embryos are predominant in central Japan. This suggests that the precipitation mechanism may be different for each region.

Acknowledgments

The author wishes to express his hearty thanks to Prof. C. Magono, Hokkaido University, for his encouragement and discussion throughout this study. The expense of this work was defrayed by scientific research funds from the Ministry of Education, Science and Culture of Japan.

References

Harimaya, T., 1976: The embryo and formation of graupel. J. Meteor. Soc. Japan, 54, 42-51.

Harimaya, T., 1977: The internal structure and embryo of graupel. J. Fac. Sci., Hokkaido Univ., Ser.VII, 5, 29-38.

Magono, C., and C.W. Lee, 1973: The vertical structure of snow clouds, as revealed by "snow crystal sondes", Part II. J. Meteor. Soc. Japan, 51, 176-190.

Magono, C., and S. Tazawa, 1966: Design of "snow crystal sondes". J. Atmos. Sci., 23, 618-625.

Pflaum, J.C., J.J. Martin and H.R. Pruppacher, 1978: A wind tunnel investigation of the hydrodynamic behaviour of growing, freely falling graupel. Quart. J. Roy. Meteor. Soc., 104, 179-187.

Singleton, F., and D.J. Smith, 1960: Some observations of drop-size distributions in low layer clouds. Quart. J. Roy. Meteor. Soc., 86, 454-467.

Taniguchi, T., and C. Magono, 1978: Observations of the electric charge and snow crystals in winter thunderclouds using sondes. Paper presented at the meeting of the Meteor. Soc. Japan held in Sendai.

A NUMERICAL CLOUD MODEL TO INTERPRET THE ISOTOPE CONTENT OF HAILSTONES

J. JOUZEL [2], N. BRICHET [1], B. THALMANN [1], B. FEDERER [1]

(1) Atmospheric physic, ETH, 8093 ZURICH (Switzerland)
(2) D.P.C./SPP/SP, CEN/Saclay, BP n° 2, 91190 GIF S/YVETTE (France)

To interpret isotopic results relative to hailstones in terms of trajectories, it is necessary to calculate the isotopic content of the condensed water which participates in the hailstone growth. Only a limited work has been done in this field assuming adiabatic ascent of air parcels without removal of precipitation and mixing of surrounding air (Jouzel et al., 1975). The main problem with adiabatic models is they are too simplistic without entrainment and fallout. This led to obvious contradictions. Roos et al. (1977) found it impossible to reconcile the moist adiabatic model with the large range of D-concentrations observed for three storms occuring on one day. Jouzel et al. (1975) have given six very stringest conditions for the applicability of the adiabatic M.N.R. model and it is highly questionable whether these are ever met in a hailstorm. Our present purpose is to derive an isotopic model base or a more realistic cloud model. As a basis, we use the steady state model described by J.H. Hirsch (1971) which takes into account entrainment of outside air, precipitation fallout and interactions between water vapor, cloud water, hydrometeor water cloud ice and large ice particles.

I - The cloud model.

The moisture balance equation necessary to derive the isotopic model are those described in the Hirsch report (1971), with slight modifications in respect of the freezing and mixing processes. Figure 1 shows the different mixing ratios versus cloud temperature for the storm which occured in the NAPF region (Switzerland) on July 14, 1978, Q_c, Q_n, Q_i and Q_g representing respectively cloud water, hydrometeor water, cloud ice and large ice particles.

The water balance throughout the depth of the cloud is

$$\frac{dQc}{dz}+\frac{dQi}{dz}+\frac{dQh}{dz}+\frac{dQg}{dz}+\frac{dq}{dz}=-\mu(q+Qc+Qi+Qg+Qh+qe)-Fh-Fg \qquad (1)$$

where Z is the altitude, q and q_e, the mixing ratios of the water vapor in the cloud and in the environment respectively and μ the entrainment rate. F_h and F_g correspond to the loss of hydrometeor water and large ice particles by precipitation fallout.

II - The isotopic model.

The isotopic fractionation is due to differences existing between the saturation vapor pressures and the molecular diffusivities in

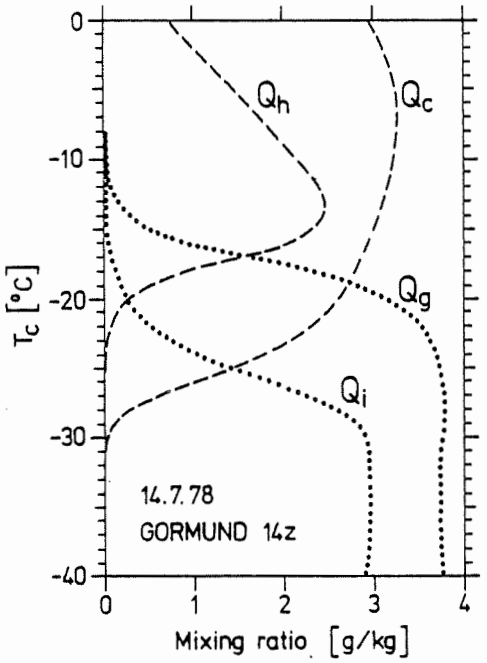

Fig. 1 - Cloud model (14/7/1978)

air of the $H_2{}^{16}O$, HDO and $H_2{}^{18}O$ molecules giving rise respectively to an equilibrium and a kinetic effect. These two effects occur at the liquid-vapor or solid-vapor phase changes and primarly affects the cloud droplets and ice crystals formation. However, owing to the ininteractions between the different phases, it is necessary to follow the isotopic evolution of all these phases during the parcel ascent. For this purpose, we define the following quantities :

- R_v, R_c, R_h, R_i and R_g are the isotopic contents of the vapor, cloud droplets, hydrometeors, cloud ice and graupels respectively. We take this denomination, both for the D/H and $^{18}O/^{16}O$ ratios, the proposed equations being valuable for the two isotopic species.

- q', Q'_c, Q'_h, Q'_i, Q'_g, F'_n, F'_g are the isotopic mixing ratios defined as $q' = j\, q\, R_v$ as so on, j being a coefficient equal to 2 x 19/18 for deuterium and 20/18 for oxygen 18. We will establish the equations giving the derivative functions (versus Z) of the isotopic mixing ratios of each phase present in the cloud.

Vapor phase - dq'/dZ is derived from the definition of q' as :

$$1/j\ dq'/dz = R_v\ dq/dz + q\ dR_v/dz \qquad (2)$$

Cloud droplets - The isotopic relaxation time of cloud droplets is sufficiently low in order that this phase is in isotopic equilibrium with water vapor whatever is the updraft speed (Jouzel et al., 1975). The equation $R_c = \alpha R_v$, α

being the fractionation coefficient is always verified and we deduce that :

$$\frac{1}{j}\frac{dQc}{dz} = \alpha R_v \frac{dQc}{dz} + \alpha Qc \frac{dR_v}{dz} + Qc R_v \frac{d\alpha}{dz} \quad (3)$$

Cloud ice. The isotopic behaviour of cloud ice has not yet been studied when water vapor, cloud ice and cloud droplets coexist. In that case, there is a supersaturation over ice and a kinetic isotopic effect occurs. Let us consider an ice particle of mass m, with no appreciable fallspeed, its growth can be described by :

$$\frac{dm}{dt} = (q - q_{si})\, d\, A \quad (4)$$

where t is the time, q_s the saturation mixing ratio relative to ice, d, the molecular diffusivity of water vapor in air and A, a coefficient depending of the form of the ice crystal, of the air pressure and of the air temperature. The corresponding isotopic equation is :

$$\frac{1}{j}\frac{dm'}{dt} = \left(q R_v - q_{si}\frac{R_s}{\alpha_i}\right) d' A \quad (5)$$

m' and d' are the mass and the molecular diffusivity of the isotopic species, α_i the isotopic fractionation coefficient for the solid-vapor phase change. R_s is the isotopic content in the ice surface. As there is no isotope homogeneisation in the ice, R_s is also the isotopic content of the new water vapor deposited and is equal to 1/j dm'/dm. It results that $R_s = \alpha_{ci} R_v$, α_{ci} taking account of both equilibrium and kinetic effects and being defined as :

$$\alpha_{ci} = \left[\frac{d}{d'}\left(1 - \frac{q_{si}}{q}\right) + \frac{1}{\alpha_i}\frac{q_{si}}{q}\right]^{-1} \quad (6)$$

At the cloud scale, this fractionation is very similar and only affects the new deposited water vapor at the exclusion of the already formed cloud ice and dQ'_i/dZ is consequently given by

$$\frac{1}{j}\frac{dQ'_i}{dz} = -\frac{Qi\alpha_{ci}R_v}{Qi+Qc}\frac{dq}{dz} - \frac{\mu Qi}{Qi+Qc}(qR_v - qeRe) + \alpha R_v\left(\frac{\Delta Qc}{\Delta z}\right)_f - Ri(\mu Qi + Rig) \quad (7)$$

Re is the water vapor isotopic content outside the cloud at the altitude Z.

$\left(\frac{\Delta Qc}{\Delta z}\right)_f$ corresponds to formation of cloud ice by freezing of cloud water and R_{ig} to conversion and accretion to graupel.

Hydrometeor water. A complete equation giving the isotopic content of a single drop growing from water vapor and cloud droplets has been previously derived by Jouzel et al. (1975). It can be easily extended to a population of drops which is, in the Hirsch model, supposed to follow a Marshall-Palmer distribution as :

$$\frac{1}{j}\frac{dQ'h}{dz} = V' + \alpha R_v R_{ch} - R_h(R_{hg} + \mu Q_h + F_h) \quad (8)$$

v' is an isotopic exchange term. Assuming that the drops are in thermal equilibrium, v' is equal to :

$$V' = \frac{8\pi N_0 d'q(R_v - R_h/\alpha)}{V_{th}} \int_0^{\infty} f' r e^{-2\lambda r} dr \quad (9)$$

r and V_{th} are the drop radius and the mass weighted mean velocity. No (number of drops) and λ are related to the mean volumic radius r_h and to the mixing ratio, Q_h, by $\lambda = \frac{1.835}{r_h}$ and $No = \frac{\lambda^4 Qh}{\pi \rho l}$ ρl being the liquid water density. f' is the ventilation coefficient.

Ice particles. None of the processes leading to ice particles formation is accompanied by isotopic fractionation and dQ'_g/dZ is directly derived

$$\frac{1}{J}\frac{dQ'_g}{dz} = Ri\, Rig + Rh\, Rhg + \alpha R_v Rcg - Rg(Fg + \mu Qg) \quad (10)$$

R_{hg} and R_{cg} correspond to formation of ice particles from hydrometeors and cloud droplets.

Isotopic content of the different cloud water species. The water balance existing throughout the cloud for the isotopic species is the same as for $H_2{}^{16}O$.

$$\frac{dQc'}{dz} + \frac{dQi'}{dz} + \frac{dQh'}{dz} + \frac{dQg'}{dz} + \frac{dq'}{dz} = -\mu(q + Qc + Qi + Qg + Qh - qe) - F'_h - F'_g \quad (11)$$

We obtain the expression of dR_V/dZ, introducing in this equation the different isotopic mixing ratio terms previously defined

$$\frac{dR_v}{dz}(q + \alpha Qc) = \quad (12)$$
$$\frac{\mu Qc}{Qi+Qc}\left(qe(R_e - \alpha R_v) + qR_v(\alpha - 1)\right) - V' - R_v\left(\frac{dq}{dz}\left(1 - \frac{\alpha_{ci}Qi + \alpha Qc}{Qi + Qc}\right) + Qc\frac{d\alpha}{dz}\right)$$

This is the basic relation of the new isotopic model, allowing to follow the isotopic content of the water vapor in a cloud.

This equation is a very general one, valuable whatever is the cloud model since the terms specific to the cloud phases interactions are excluded. Neglecting the ice phase formation (Qi = 0), the entrainment (s = 0) and the hydrometeor-water vapor exchange (V = 0), equation 12 becomes identical to that proposed by Merlivat and Jouzel (1979) to study isotopic transfer at a global scale. Then, it includes the Rayleigh distillation formula for $Q_c = 0$ and if all the cloud water is kept, its integration leads to the relation used in a close system (MNR model).

We use equation 12 to calculate ΔRv. For the condensed phases, the change in isotopic mixing ratios ΔQ' from level i to j can be expressed as : $\frac{1}{j}\Delta Q' = R^i \Delta Q - Q^j \Delta R \quad (13)$

Injecting 13 in 3, 7, 8 and 10 yields an equation for ΔR_c, ΔR_i, ΔR_h and ΔR_g. The step by step procedure to solve for the isotopic content at each height interval is described in detail in the annual report of Grossversuch IV (Cloud physics group, E.T.H., 1980). The isotopic profile of hail, R_H, is finally obtained by averaging

$$R_H = \frac{Ec\,Qc\,Rc + Ei\,Qi\,Ri + Eh\,Qh\,Rh + Eg\,Qg\,Rg}{Ec\,Qc + Ei\,Qi + Eh\,Qh + Eg\,Qg} \quad (14)$$

where $E_c = 0.8$, $E_h = 0.8$, $E_i = 0.1$ and $E_g = 0.001$ were taken as best estimates in the first application of the model.

We take the following values for the physical parameters involved in the previous equations. α are deduced from Majoube's experiments (1971 a, 1971 b). We use for d the formula proposed by Musil (1970) and take $d'/d = 0.9755$ and 0.9723 for the $HDO - H_2{}^{16}O$ and $H_2{}^{18}O - H_2{}^{16}O$ couples respectively (Merlivat, 1978). The ventilation coefficient for hydrometeors is that derived by

Stewart (1975). Since the isotopic exchange processes are most pronounced in the liquid phase, the height profiles of the isotopic contents are very sensitive to the relative distribution of liquid and ice i.e. to the freezing function f(T). Instead of a linear function as used by Hirsch, a B 166 (1953) freezing process seems more appropriate for cloud droplets (d < 100μ)

$$f(T) = 1 - ae^{-bT_s} \qquad (15)$$

where T_s is the temperature of supercooling and a et b are constants.

As an illustration of the results, the deuterium values versus temperature for the july 14 hailstorm is shown on figure 2. In addition, we have reported the curve deduced from the MNR model (Jouzel et al. 1975). The deuterium content outside the cloud, R_e, is taken from Ehhalt's (1974) mean profile, and is supposed equal to 142.1 ppm at the cloud base. In that particular case, the isotopic exchange term, V', has been calculated using a monodisperse population with drop radius r_n.

The curve for isotope concentration in hailstones, R_H, can be seen to deviate substantially from the adiabatic curve R_{MNR}, used in previous works. Down to a temperature of - 18° C, R_H is around 1.5 ppm richer and then decreases considerably poorer than R_{MNR}. The richer start is due to the presence of hydrometeor water which is not in equilibrium with the water vapor. This, of course, affects the vapor which is less depleted in isotopes so that R_c is also richer in this region. The situation changes soon after ice begins to form. The kinetic effect of vapor deposition is seen in the "bump" on R_i at T_c = - 23° C. The bump in R_h at T_c =-30° C is due to rapid disappearance of cloud water which has a major influence on R_H through equation 15.

It is clear that from a cloud physics point of view, the new model is still unrealistic because the particles interactions are all parameterized according to Kessier's (1969) scheme. The next step in the development of this model will therefore be to drop the parameterizations. But as shown in figure 2, it is an important stepforward compared to the model previously used.

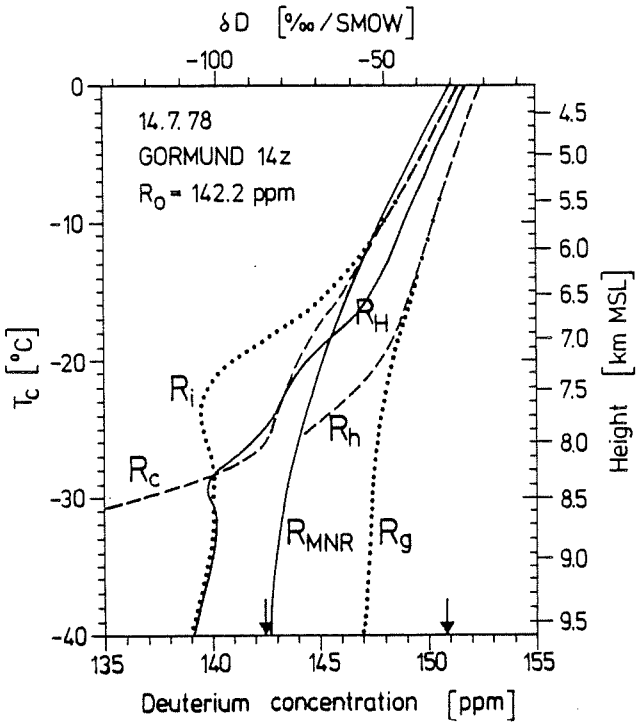

Fig. 2 - Isotopic model (14/7/1978)

REFERENCES.

E.K. BIGG (1953), The supercooling of water. Proc. Phys. soc. B 66, 688

D.H. EHHALT (1974), Vertical profiles of HTO, HDO and H_2O in the troposphere, NCAR TN/STR-100

J.H. HIRSH (1971), Computing modeling of cumulus clouds during project cloud catcher, Report 71-7, South Dakota, School of mines and technology.

E. KESSLER (1969), On the distribution and continuity of water substance in atmospheric circulations Meteor, Hongr., 10, n° 32, 84 PP

J. JOUZEL, L. MERLIVAT and E. ROTH (1975), Isotopic study of hail, J. Geophys. Res., December 20, Vol. 80, n° 36.

M. MAJOUBE (1971 a) Fractionnement en ^{18}O en la glace et la vapeur d'eau. Journal de Chimie Physique, 68, n° 4.

M. MAJOUBE (1971 b) Fractionnement en ^{18}O et en deutérium entre l'eau et sa vapeur. Journal de Chimie Physique, 68, n° 10.

L. MERLIVAT (1978), Molecular diffusivities of $H_2{}^{16}O$, $HD^{16}O$ and $H_2{}^{18}O$ in gases, Journal of Chemical Physics, 69, n° 6

L. MERLIVAT and J. JOUZEL (1979), Global climatic interpretation of the deuterium-oxygen 18 relationship for precipitation, J. Geophys. Res., Vol. 84, n°8.

D.J. MUSIL (1970), Computer modelling of hailstones growth in feeder clouds, J.A.S. Vol. 27

D.V.D.S. ROOS, H. SCHOOLING and J.P. VOGEL, Deuterium in hailstones collected on 29 November 1972, QJRMS Vol. 103, n° 438.

M.K. STEWART, (1975), Stable isotope fractionation due to evaporation and isotopic exchange of falling waterdrops : Applications to atmospheric processes and evaporation of lakes, J. Geophys. Res., Vol. 80, n° 9.

GROWTH REGIME OF HAILSTONES AS DEDUCED FROM SIMULTANEOUS DEUTERIUM AND OXYGEN 18 MEASUREMENTS.

J. JOUZEL, L. MERLIVAT

CEN/Saclay - DPC/SPP/SP - B.P. n° 2, 91190 GIF S/YVETTE (France)

The behaviour of the HDO and $H_2{}^{18}O$ molecules are very similar during the cloud water condensation processes which occur very slowly close to liquid-vapor equilibrium. It results that the δD and $\delta^{18}O$ contents of the precipitation are generally linked by a linear relationship with a slope close to 8 (Daansgard - 1964). In the case of evaporation, an additional kinetic effect due to the differences between the molecular diffusivities in air of the three isotopic species ($H_2{}^{16}O$, HDO and $H_2{}^{18}O$) has to be taken into account.

During hailstone growth, the evaporation takes place from the liquid phase when the surface temperature is 0°C (wet growth). An isotopic enrichment of the collected water due to this mechanism has been predicted and experimentally demonstrated in an icing tunnel by Bailey et al. (1969). The first objective of this work was to determine if this enrichment effect was observed on natural hailstones.

I - Experimental results.

The distinction between kinetic and equilibrium fractionation effects is made possible through the analysis of both isotopes, deuterium and oxygen 18. For this purpose we have taken advantage of a new mass spectrometer allowing D and ^{18}O determinations the same sample, with a size of about 20 mg of water. A very detailed study of both isotopes repartition has been carried out on five large hailstones, three of them formed in the Massif Central region (France) during a 1971 storm and the other two during the Alberta storm (Canada) previously studied by Jouzel et al. (1975)

We present the results relative to one of the french hailstones (Yssendon, with a mean diameter equal to 9 cm) in a classical D-^{18}O diagram (figure 1), these parameters being expressed in the δ notation. The precisions on individual points are equal respectively to 0.5 and 0.15 ‰ for δD and $\delta^{18}O$. To interpret these data in terms of a possible kinetic isotopic enrichment, it is necessary to know the δD-$\delta^{18}O$ relationship in the collected cloud water. To this end, we have applied the classical MNR model corresponding to the curve 1 (Jouzel et al. 1975), the isotopic water content at the cloud base being deduced, assuming that evaporation and consequently kinetic fractionation are negligible for the poorer opaque layer formed in the dry growth regime at low temperature (around - 30° C). Recently, Jouzel et al. (This conference), have proposed a more realistic isotopic model which substantially deviates from the MNR one, as long as one isotope is concerned. However Merlivat and Jouzel (1979) have shown that the δD-$\delta^{18}O$ relationship keeps very general and the interpretation of the data presented on figure 1 does not greetly depend on the isotopic cloud model used.

Figure 1 clearly shows a general shift of the hailstone samples towards relatively higher ^{18}O values as expected when evaporation occurs. This effect is maximum for clear layers and relatively weak fot the opaque ones. The opaque embryo appears unaffected.

This shift is observed in all the studied hailstones but this example is the most covincing to demonstrate the existence of a kinetic isotopic effect during natural hailstones growth.

II - Theoretical aspect.

- Wet growth regime. The mass balance equation of the liquid film surrounding the hailstone, $\frac{d\mu_L}{dt}$ (t being the time) can be written

$$\frac{d\mu_L}{dt} = \frac{d\mu_H}{dt} - \frac{d\mu_f}{dt} - \frac{d\mu_e}{dt} - \frac{d\mu_s}{dt} \qquad (1)$$

The liquid film grows by captation of cloud water, $\frac{d\mu_H}{dt}$, and is reduced by freezing, $\frac{d\mu_f}{dt}$, evaporation, $\frac{d\mu_e}{dt}$ (owing to the difference between surface hailstone temperature, t_s equal to 0° C and the air temperature t_a), and shedding $\frac{d\mu_s}{dt}$ as pointed out by Carras and Macklin (1973) and List (1977). We define the corresponding isotopic masses, $\frac{d\mu'_L}{dt}$, $\frac{d\mu'_H}{dt}$, $\frac{d\mu'_f}{dt}$, $\frac{d\mu'_e}{dt}$, $\frac{d\mu'_s}{dt}$ taking this denomination for both the HDO or $H_2{}^{18}O$ molecules, the proposed equation being valuable for the two isotopic species. The isotopic contents R_L and R_H are respectively equal to $\frac{1}{j}\frac{\mu'_L}{\mu_L}$ and $\frac{1}{j}\frac{\mu'_H}{\mu_H}$, j being a coefficient equal to $\frac{19}{18}$ for deuterium and $\frac{20}{18}$ for oxygen 18. The isotopic mass balance equation is given by :

$$\frac{d\mu'_L}{dt} = \frac{d\mu'_H}{dt} - \frac{d\mu'_f}{dt} - \frac{d\mu'_e}{dt} - \frac{d\mu'_s}{dt} \qquad (2)$$

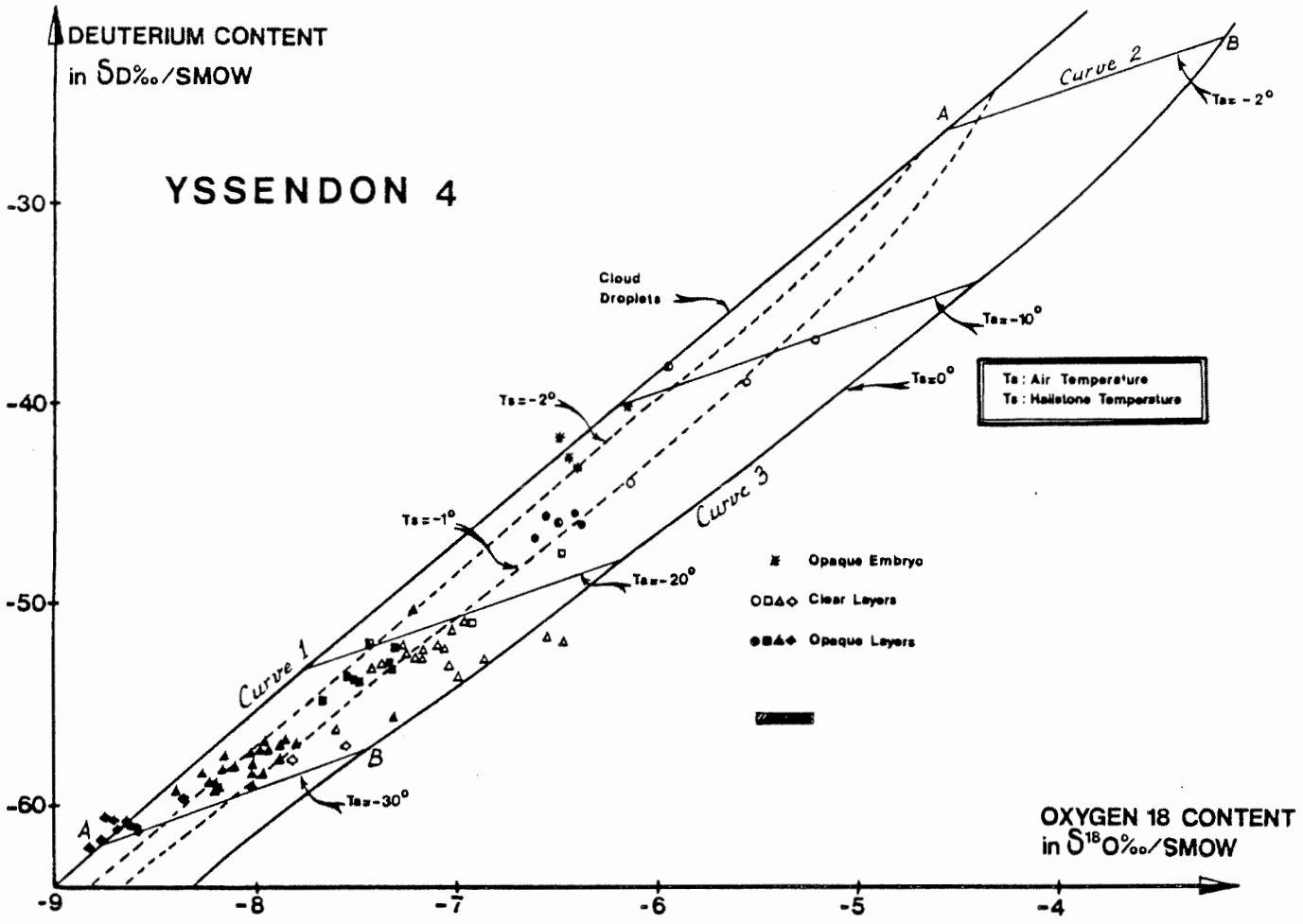

Figure 1 - D-^{18}O diagram. Experimental and theoretical results.

Only freezing and evaporation give rise to isotopic fractionation. It results :

$$\mu_L \frac{dR_L}{dt} = (R_H - R_L)\frac{d\mu_H}{dt} + (1-\alpha_s)\frac{d\mu_f}{dt} + \frac{d\mu_e}{dt} - \frac{1}{j}\frac{d\mu'_e}{dt} \quad (3)$$

α_s being the isotopic fractionation coefficient relative to the liquid-solid phase change.

We use the growth and thermodynamic equations proposed by Mason (1971). In particular, the evaporation rate is given by :

$$\frac{d\mu_e}{dt} = 2\pi L_v R d(\rho_s - \rho_e) Sh \quad (4)$$

L_v being the latent heat of vaporization, d, the coefficient of molecular diffusivity of water vapor in air, R, the hailstone radius, ρ_s and ρ_e, the vapor density at the surface of the sphere and in the remote environment and Sh, the Sherwood number. The corresponding isotopic equation is

$$\frac{1}{j}\frac{d\mu'_e}{dt} = 2\pi L'_v R d'\left(\rho_s \frac{R_L}{\alpha} - \rho_e R_v\right) Sh' \quad (5)$$

α is the isotopic fractionation coefficient relative to the liquid-vapor phase change, R_v the isotopic content of the vapor, d'^v and L'_v, the molecular diffusivity and the latent heat of vaporization of the isotopic species and Sh' the isotopic Sherwood number. Equations 3, 4 and 5 allow to derive the isotopic content of a liquid film surrounding a hailstone. This has been donewith (figure 1) the cloud data relative to the Massif Central storm, the cloud water isotopic content being deduced from the MNR model (curve 1). We take $d'/d = 0.9755$ and 0.9723 for the HDO-$H_2{}^{16}O$ and $H_2{}^{18}O$-$H_2{}^{16}O$ couples respectively (Merlivat - 1978).

Firstly, we have studied the behaviour of a growing liquid film up to a maximum thickness, e_M, at different cloud temperatures. When e_M is reached the water in excess is lost, this corresponding to the shedding process. The D and ^{18}O contents evolve along the curves 2, which are practically straight lines of slope about 3.5, from A (isotopic equilibrium) to an asymptotique value B representing the maximum possible enrichment. This last value is independent of the maximum thickness e_M. In addition, we have drawn the envelope of all the calculated maximum enrichments (curve 3), allowing to define an area (between curves 1 and 3), in which all the representative points of a liquid film are theoretically expected.

Dry growth - During dry growth, col-

lected water is rapidly frozen by conduction into the stone (Bailey et al., 1969), preventing such important evaporation as during wet growth. However a low evaporation takes place during the freezing time t_f of the droplets and it is easily demonstrated that the resulting enrichment E_s is equal to $E_o \cdot t_f/t_o$, E_o and t_o being the enrichment and the freezing time when the surface temperature is equal to 0° C. Using the results of Macklin and Payne (1967), this enrichment has been calculated for different values of the hailstone surface temperature, t_s. This effect is weak for t_s = - 1° C and t_s = - 2° C (figure 1) and becomes negligible when the hailstone surface temperature is lower than - 2° C.

III - Interpretation of experimental results.

- Growth regims.

We finally obtain a diagram in terms of our temperature, t_a, and surface hailstone temperature, t_s (figure 1). Experimentally, the maximum possible enrichment is observed only for the clear layer samples represented by triangles and the effect is slightly smaller for the three other clear layers. However, the clear samples are very generally formed at hailstone surface temperature higher than - 1° C, thus confirming the wet growth regime of formation. On the other hand, we observe that all the opaque samples correspond to surface temperature lower than - 1° C. Nevertheless, if we except the opaque embryo and the poorer opaque leyer taken as reference, a small enrichment is displayed showing that the three other opaque layers have been effectively formed in the dry growth regime but at relatively high surface temperature (around - 2° C). The absence of any enrichment effect for the opaque embryo clearly indicates that the Yssendon 4 hailstone has been formed starting from a graupel.

- Trajectories.

Before interpreting the results in terms of trajectories, it is necessary, owing to the enrichment effect, to determine the isotopic content of the water at the moment of collection. This value corresponds, in a $D-^{18}O$ diagram, to the intersection of the curve relative to the cloud droplets (curve 1) with a straight line of slope 3.5 passing by the representative point of each sample. Using this procedure and the MNR model for cloud droplets, we have deduced the trajectories of the five studied hailstones. The curves relative to two of them, Yssendon 4 and Alberta E (formed during the Alberta storm of 1971, August 7) are shown on figures 2 and 3. In each case, we have represented the initial trajectory obtained without considering the enrichment effect and the corrected trajectory calculated applying the above described procedure.

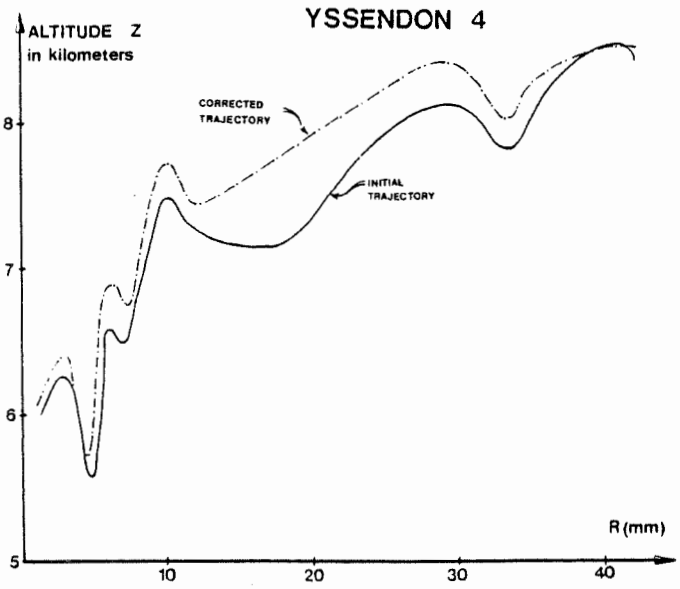

Fig. 2 - Trajectories deduced for the Yssendon 4 hailstone.

After the formation of the graupel embryo (up to r = 5 mm), the Yssendon 4 trajectory is composed of a unique ascent from 5.5 to 8.5 km, a noticeable point being the absence of growth during the descent to the ground. The two other Massif Central hailstones, with size up to 85 mm, present similar single up and down trajectories showing that these three hailstones were likely formed in a supercell storm. Unfortunately, no radar data are available to confirm this assumption. The correction due to isotopic enrichment does not appear very important (less than 0.5 km) and in any case, does not greatly modify the informations possibly deduced from such curves relative to the updraft speeds or to the growth regimes (Jouzel et al., 1975).

The more complicated story of the Alberta hailstones is very well confirmed with succession of upward and downward movements (figure 3). A stricking feature, clearly observed for the first time, is the systematic occurence of wet growth during ascents and dry growth during descents (except for the outer clear layer formed during the last descent to the ground). It is interesting to notice that the clear layer from 7 to 12 mm develops in the wet growth regime over a large range of temperatures.

If we had interpreted all these isotopic data using the new model proposed by Jouzel et al. (this conference) it clearly results a decrease of the amplitude of the trajectories but the qualitative conclusions drawn stay unchanged. In addition of the classical informations about trajectories, we have

shown that simultaneous D and ^{18}O determinations, allow us to demonstrate, for the first time, an isotopic enrichment due to evaporation in natural hailstones and to deduce information about the growth regime of the stones.

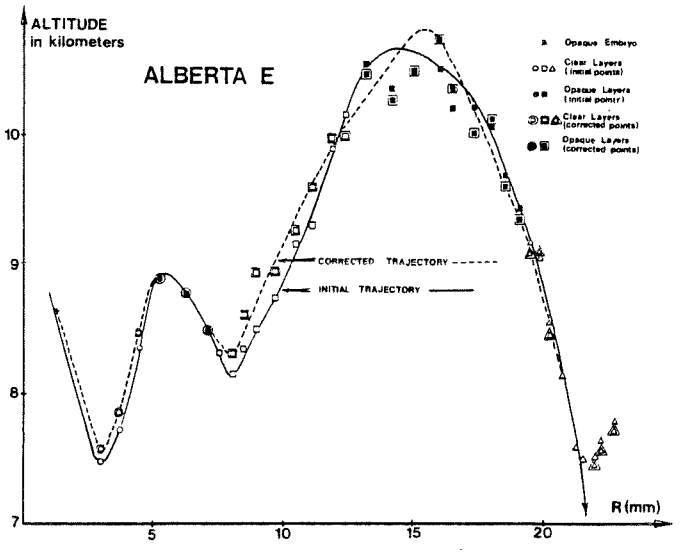

Fig. 3 - Trajectories deduced for the Alberta E hailstone.

Acknoledgments : This work received a financial support of the G.N.E.F.A. (Groupement National d'études des fléaux atmosphériques). We tank P. ADMIRAT, P. DUVAL and S. ZAIR, for their collaboration to this work. We are very grateful to M. LELU who carried out isotopic measurements and to R. CHIRON for his technical assistance.

REFERENCES.

H. BAILEY, J.R. HULSTON, W.C. MACKLIN and J.R. STEWART (1969), On the isotopic composition of hailstones, J.A.S., Vol. 26

J.M. CARRAS and W.C. MACKLIN (1973), The shedding of accreted water during hailstone growth, Quart. J.R. Met. Soc. Vol. 99.

W. DAANGARD (1964), Stable isotopes in precipitation, Tellus, Vol. 16, n° 4

J. JOUZEL, L. MERLIVAT and E. ROTH, (1975), Isotopic study of hail, J. Geophys. Res., Vol. 80, n° 36

J. JOUZEL, N. BRICHET, B. THALMANN and B. FEDERER (1980), A numerical cloud model to interpret the isotope content of hailstones, VIII Int. Conference on cloud Physics, Clermont-Ferrand.

R. LIST, (1977), Ice accretions on structures, Journal of Glaciology, vol. 19, n° 81.

W.C. MACKLIN and G.S. PAYNE (1967), A theoretical study of the ice accretion process, Quart. J.R. Met. Soc. n° 93.

L. MERLIVAT (1978), Molecular diffusivities of $H_2{}^{16}O$, $HD^{16}O$ and $H_2{}^{18}O$ in gases, Journal of Chemical Physics, vol. 69, n° 6.

L. MERLIVAT and J. JOUZEL (1979), Global climatic interpretation of the deuterium-oxygen 18 relationship for precipitation, J. Geophys. Res., Vol 84, n° 8.

OBSERVATIONS OF THE FREE-FALL BEHAVIOR OF CONELIKE GRAUPEL PARTICLES

M. Kajikawa
Department of Earth Science, Akita University, Akita, JAPAN

1. Introduction

It is considered that a knowledge of the free-fall behavior of graupel particles is necessary for the study of their growth and hailstone embryos.

Magono (1953) found in the first place that an oblique position of the axis of rotational symmetry was the stable fall mode for the conelike graupel particles. Zikmunda and Vali (1972) and Kajikawa (1975) also observed that the axis of symmetry oscillated around the vertical with the base down orientation.

Recently, Kajikawa (1977) observed the free-fall modes of conelike graupel particles ranging from 0.8 to 8.3 mm in size using the stroboscopic photographs and summarized as follows. Those particles under 1 mm in size fell with the stable attitude of base down orientation. Over this size, the axis of symmetry of them oscillated around the vertical. When the size exceeded about 3.5 mm, those particles tumbled during free-fall, in general. Pflaum et al. (1978) studied the hydrodynamic behavior of artificial graupel particles. They observed the spinning, helical and various oscillating motions and the simple straight fall with fixed orientations, but no tumbling motions because the size of particles was smaller than 3 mm.

On the other hand, the model experiment of fall mode for conelike particles was performed by List (1959), Jayaweera and Mason (1965), Goldburg and Florsheim (1966) and List and Schemenauer (1971). In those experiments, the relationship between characteristic fall modes and Reynolds number or the apex angle of conelike models was discussed in detail.

The purpose of this study is to observe the free-fall behavior of conelike graupel particles in detail by means of a stereoscopic camera system and to clarify the conditions of various factors affecting the fall modes of them. The observation was carried out at Akita, 10 m a.s.l., during the winter of 1978.

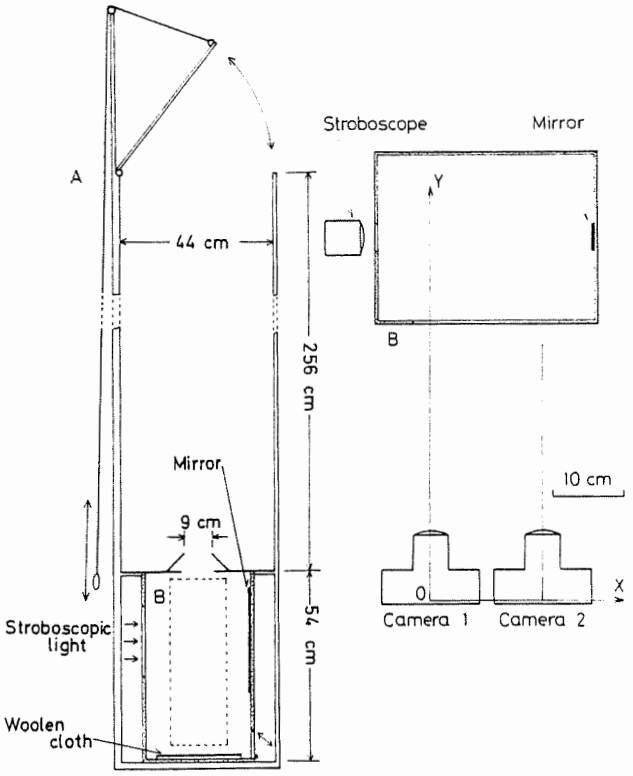

Fig.1 Apparatus, stereoscopic camera system and co-ordinate axes.

2. Method of observation

The apparatus and stereoscopic camera system used in this observation are shown in Fig.1. This apparatus is made of two parts, a metal tower (A) and a wooden box (B) for the observation of free-fall behavior. The tower is provided with a movable cover on the top, which is exposed in open air.

After passing through the tower, some graupel particles fall at terminal velocity into the observation box. The number of particles was controlled by a slit (9x4 cm). The lower parts of this box and tower were made airtight to keep the air in them stable. The falling particles illuminated by stroboscopic light were photographed through a front glass of the box using the stereoscopic camera system. The optical axes of two cameras were horizontal and parallel, with the base line of 16 cm. The optical center of camera 1 was chosen as a origin (0) of the rectangular coordinate system (X,Y and Z) in space.

Individual graupel particles corresponding to the trajectories in photographs were sampled on a woolen cloth. After the particles were caught, the cloth was taken out from the box and then the particles were photographed by a close up camera, so as to measure the size and apex angle of conelike graupel.

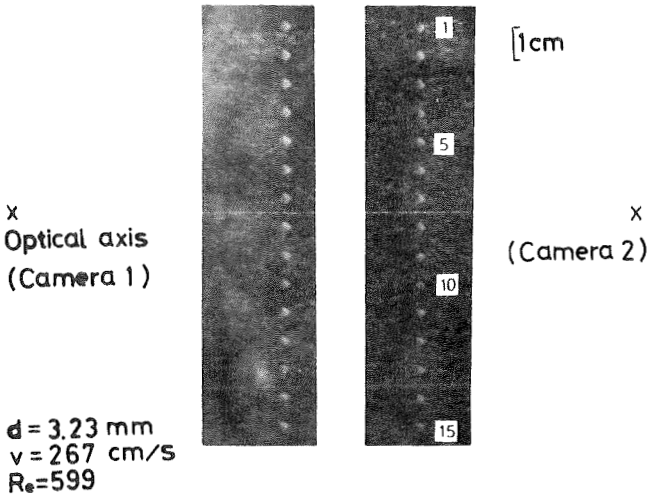

Fig.2 A example (Case 1) of stereoscopic photographs at 1/300 sec intervals. d is the base diameter of circular cone, v the falling velocity and Re the Reynolds number.

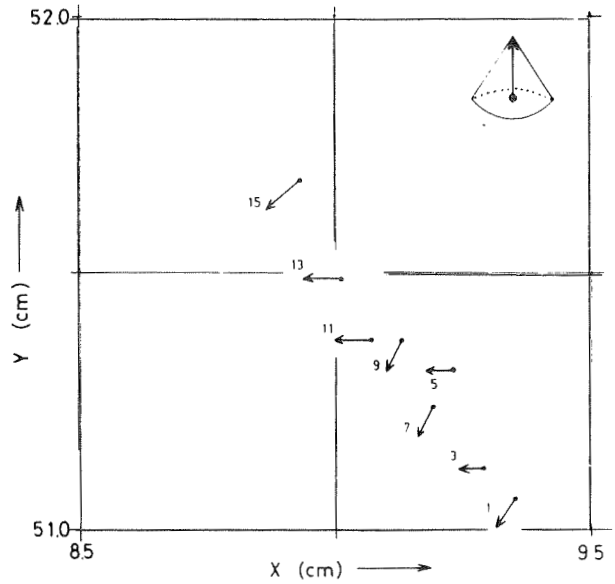

Fig.3 Horizontal movement of the conelike graupel (Case 1). Thick arrows are the axes of rotational symmetry.

3. Results and considerations

3.1. Analysis of free-fall behavior of conelike graupel particles by stereophotographic method

One example of pairs of stereoscopic photographs is shown in Fig.2. The angular oscillation of axis of rotational symmetry can be seen from this figure. Fig.3 is the projection of falling motion on horizontal plane. The coordinates of apex and center of circular cone were calculated from the corresponding points on the pair of photographs. In this figure, arrows and number indicate the positions of axis of conelike graupel taken in time interval 1/150 sec, corresponding to the photographs of Fig.2. So the length of arrows changed slightly, this fall mode was the spinning motion of apex. The period of this motion is about 0.03 sec.

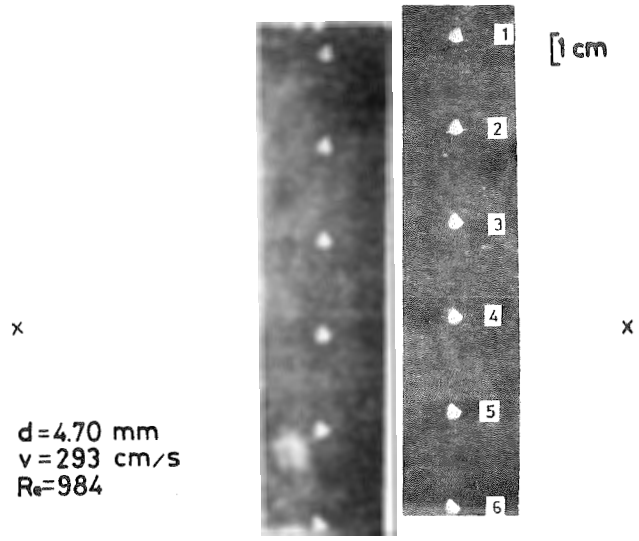

Fig.4 Stereoscopic photographs of Case 2, taken with time interval of 1/100 sec.

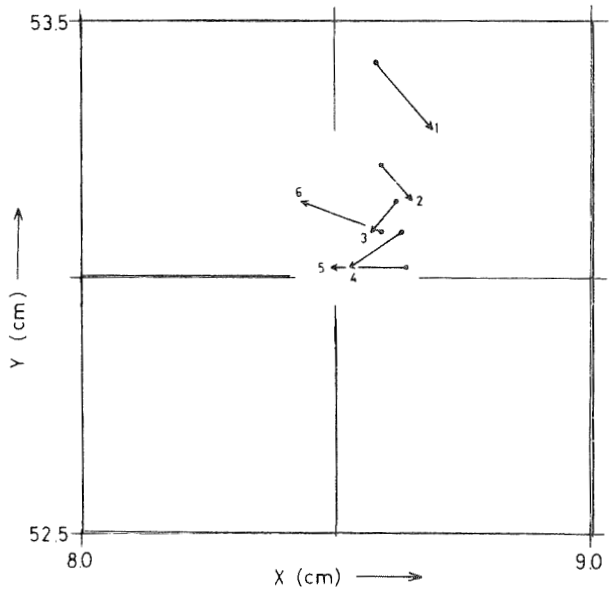

Fig.5 Horizontal movement of the conelike graupel (Case 2).

The other example of pairs of photographs is shown in Fig.4. Fig.5 is the projection of falling motion of conelike graupel (Case 2) on horizontal plane. It is considered from this figure that the change of length of arrows and the spinning motion of apex were appeared clearly. Although this graupel does not indicate the tumbling motion in this photographs, it seems that soon after this motion comes in succession, because of the large Reynolds number.

3.2. Classification of free-fall mode of conelike graupel particles

According to the results of present and previous observation (Kajikawa, 1977), the fall modes of conelike graupel particles were classified into the three main types, in the same manner as given by the model experiment of List and

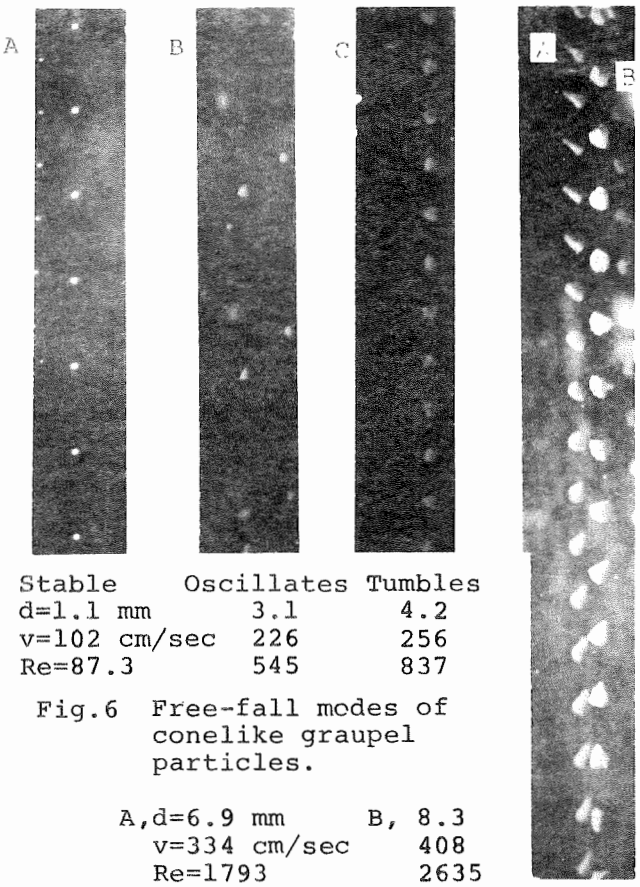

Stable	Oscillates	Tumbles
d=1.1 mm	3.1	4.2
v=102 cm/sec	226	256
Re=87.3	545	837

Fig.6 Free-fall modes of conelike graupel particles.

A,d=6.9 mm B, 8.3
v=334 cm/sec 408
Re=1793 2635

Fig.7 Examples of the imperfect tumbling motion.

Schemenauer (1971). The first is a stable motion with base down orientation and vertical direction of fall (Fig.6A). The axis of rotational symmetry (axis of conelike graupel) was slightly oblique in almost cases, as being pointed out by Magono (1953).

The second type is a oscillating motion of the axis of conelike graupel with base down orientation. It can be seen that this type is split up into the following two groups , the simple reciprocating motion (Fig.6B) and the spinning motion of apex (Fig.2). During this oscillating motion, the angular displacement to either sides of the fall direction is smaller than 90°.

The third type is a tumbling motion with rotation of axis of conelike graupel. It can be considered that this type is divided into the folloeing two groups . In the perfect tumbling motion (Fig.6C), the apex down position (to take the downward direction completely) is taken during fall. On the other hand, in the imperfect tumbling motion (Fig.7), the apex down position is not seen during fall, but the angular displacement to either sides of fall direction by the spinning motion of apex is larger than 90°

3.3. Relationship between the fall mode and Reynolds number

Fig.8 is the relationship between the fall modes and Reynolds number. For convenience, the observational results were divided into two groups according to the air temperature when each graupel particles were observed. The mean density of graupel particles was 0.42 g/cm^3 and 0.23 g/cm^3 in the condition of $T \geq 0.5$ °C and $T < 0.5$ °C, respectively (Kajikawa, 1977).

It can be seen from Fig.8 that the distinct difference in fall modes is appeared as Re increases. This observational result confirms that of model experiments by many researchers, in general tendency. However, the oscillating motion starts at smaller Re (about 100) in this observation than that of model experiments (about 300, in the experiment of List and Schemenauer, 1971). The tumbling motion starts at Re of about 800 in the model experiments, on the other hand this fall mode starts at Re of about 700 in this observation. It is considered that the main reason of those discrepancies between the model experiments and observation is due to the surface roughness and nonsymmetry of natural conelike graupel.

The imperfect tumbling motion is observed even in the base diameter of 8.3 mm as seen in Fig.7. This confirms that the conelike embryo corresponding to a few thousands of Re is seen the inside of hail stones as analysed by Magono and Gotoh (1972), provided that the hail stones of lump type grew from the conelike graupel particles. It can be considered that the conelike graupel particles showed the perfect tumbling motion change into lump type particles in the process of their growth, but the particles falling with the imperfect tumbling motion

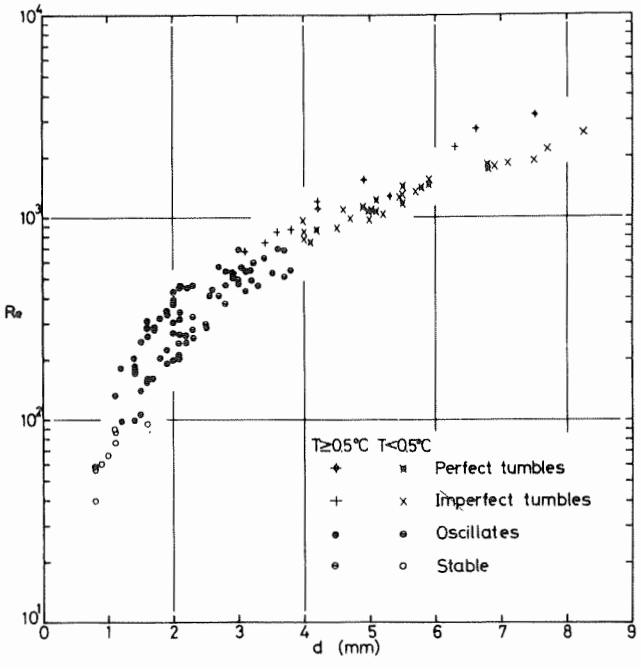

Fig.8 Relationship between the fall modes and Re. T and d are air temperature and base diameter.

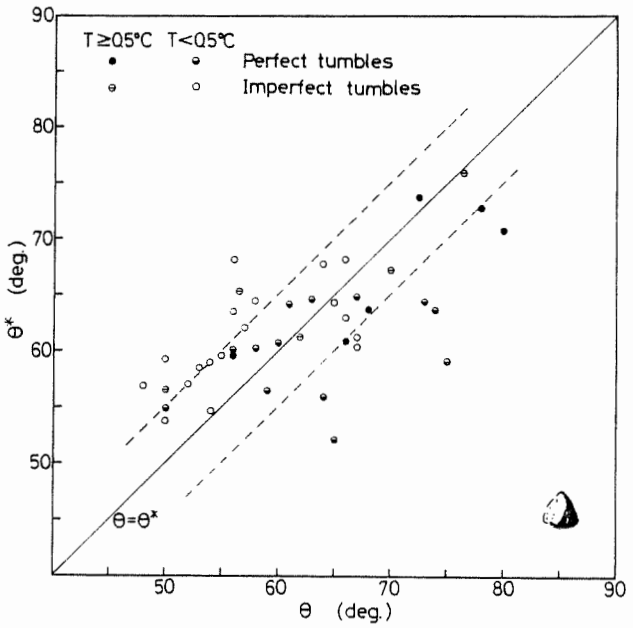

Fig.9 Relationship between the apex angle (θ) and θ* defined by Jayaweera and Mason (1965).

do not change into the lump type easily.

3.4. Relationship between the tumbling motion and apex angle

Fig.9 is the relationship between the apex angle (θ) and θ* defined by Jayaweera and Mason (1965). They found by model experiment that the cones of base radius (r) with spherical cap of height (h) fell with base down orientation if $\theta < \theta^*$, and with base up orientation if $\theta > \theta^*$, where

$$\theta^* = 0.68\frac{h}{r} + \frac{\pi}{4}$$

provided $0.2 < h/r < 1.0$. It may be considered that the conelike graupel in the region of $\theta > \theta^*$ has a tendency of fall with the perfect tumbling motion, on the other hand it shows the imperfect tumbling motion in the region of $\theta < \theta^*$, at Re above 700. Although the uncertainty of ±5° (broken lines in Fig.9) is existent, the tendency descrived above can be seen in this figure. The uncertainty is due to the ununiformity of density at the inside of natural graupel particles and the error of measurement of apex angle.

4. Concluding remarks

The free-fall behavior of conelike graupel particles was observed by means of stereophotographs. For Re < 100, which is corresponding to d (size)< 1 mm, the particles fell with stable attitude of base down orientation. Over this Re the particles oscillated with base down orientation. When Re exceeded about 700, which is corresponding to d of about 3.5 mm, the particles tumbled in free-fall.

However, the imperfect tumbling motion as seen in Fig.7 was ovserved even in large particles. It is considered that the occurence of this motion is concerned with the apex angle and the ununiformity of density at the inside of particles.

Acknowledgment

The author wishes to thank Prof. C.Magono and Dr. T.Harimaya, Hokkaido University, for useful discussions.

References

Goldburg, A. and B.H.Florsheim,1966: Transition and Strouhal number for the incompressible wake of various bodies. Phys. Fluids, 9, 45-50.

Jayaweera, K.O.L.F. and B.J.Mason,1965: The behavior of freely falling cylinders and cones in a viscous liquid. J. Fluid Mech., 22, 709-720.

Kajikawa, M.,1975: Measurement of falling velocity of individual graupel particles. J. Meteor. Soc. Japan, 53, 476-481.

Kajikawa, M.,1977: Observation of fall attitude of conelike graupel particles. Memoirs Fac. Edu. Akita Univ. (Natural Sci.), 27, 78-85.

List, R.,1959: Zur Aerodynamik von Hagelkornern. Z. Angew. Math. Phys., 10, 143-159.

List, R. and R.S.Schemenauer,1971: Free-fall behavior of planar snow crystals, conical graupel and small hail. J. Atmos. Sci., 28, 110-115.

Magono, C.,1953: On the growth of snow flake and graupel. Sci. Rep. Yokohama Nat. Uni. Sec.1,2, 18-40.

Magono, C. and H.Gotoh,1972: On the conversion from a conelike graupel to a hail stone of lump type. Proc. Autumnal Meeting of Meteor. Soc. Japan, Niigata,22,67 (in Japanese).

Pflaum, J.C., J.J.Martin and H.R.Pruppacher,1978: A wind tunnel investigation of the hydrodynamic behaviour of growing, freely falling graupel. Quart. J. R. Met. Soc., 104, 179-187.

Zikmunda, J. and G.Vali,1972: Fall patterns and fall velocities of rimed ice crystals. J. Atmos. Sci., 29, 1334-1347.

PATTERNS OF HAILSTONE EMBRYO TYPE IN ALBERTA HAILSTORMS

Nancy C. Knight

National Center for Atmospheric Research*
Boulder, Colorado 80307 USA

Marianne English

Alberta Research Council
Edmonton, Alberta, Canada T6G 1K8

One of the basic reasons for investigating hailstones has been to look for systematic changes in the hailstone structures that reflect something about preferred hailstone trajectories. All simple models such as those which have been postulated by Browning and Foote (1976), Young (1977), and English (1973) predict something about hailstone trajectories. In Browning's model, for example, the largest hailstones grow at the edge of a weak echo region and should fall first followed by the smaller ones and by rain. Young illustrates similar size sorting effects and English suggests that the largest hailstones have the lowest trajectories. Some of these predictions can be checked by getting time-resolved collections and by examining the hailstones.

The Alberta Hail Program is a good opportunity to make these kinds of checks because of the existence of a dense volunteer observer network and good radar data. The members of the volunteer network have provided hailfall data and have collected hailstones in the past and were asked to do so again during July 1979. In addition to these collections, time-resolved, sequential samples were also obtained using a mobile vehicle directed from the operations center. On two days during this period, 7 and 21 July 1979, organized, isolated storms passed over the operational area and the data presented here were obtained.

The first of the storms occurred on 7 July. Figure 1 illustrates the resulting hailswath. All reports received from the volunteer network are represented by dots in the figure and the outer contour encloses all of the reports of hail. The shaded areas indicate hail sizes estimated by the observers to be greater than approximately 24 mm in largest dimension. Figure 2 repeats the hailswath and gives the location of the samples collected and examined, the percentage of frozen drop embryos observed in the hailstones, and the maximum hailstone size in each sample. Figures 3 and 4 give the same information for the storm on 21 July. As is shown in Figs. 2 and 4, the largest hailstones and the largest percentage of frozen drop embryos tend to occur on the southern edge of the hailswath with the smaller stones and larger percentages of graupel embryos tending to be observed on the northern edge.

As has been reported (Knight and Knight, 1978), hailstones with maximum dimensions larger than 25 mm tend to have a greater percentage of frozen drop embryos and the tendency is illustrated here in Fig. 5 for the storm on 21 July. The results from the storm on 7 July with a smaller sample size showed the same tendency.

A vertical cross section of the radar echo of the storm on 21 July at the time that the largest number of the samples were obtained is shown in Fig. 6. This section is taken along a line which is approximately the direction of motion of precipitation particles with respect to the storm as determined by studying the motion of small-scale reflectivity maxima (Barge and Bergwall, 1976). The location of the samples, the percentage of frozen drop embryos, and the size of the largest stone is also given and they show that the sample closest to the updraft contains both the largest stone and 100% drop embryos with the percentage of frozen drop embryos and the maximum size of the stones tending to decrease with distance from the updraft. Unfortunately, the sample size is small for the sample closest to the updraft, containing only two hailstones. The sample immediately next to it contained only six stones of which two had unidentifiable embryos. The total number of hailstones in all of the represented samples was 62. Although only one vertical cross section is shown, others from both storms also show similar results. The larger hailstones and the larger percentages of frozen drop embryos were found closest to the updraft and in general, the size and percentage of frozen drop embryos declined with distance from it.

Although it is difficult to draw firm conclusions from these results because of the small size of some of the most critical samples, it seems apparent that in both storms a tendency could be demonstrated in which the hailstones falling closest to the updraft had predominantly frozen drop embryos and those falling furthest from the updraft had graupel embryos. The larger stones had a larger percentage of frozen drop embryos. A total of 810 stones were examined for the two storms and this tendency for the larger stones to have frozen drop embryos was very apparent.

English (1973) modelled the growth of large hail in Alberta hailstorms and found that the

* The National Center for Atmospheric Research is sponsored by the National Science Foundation.

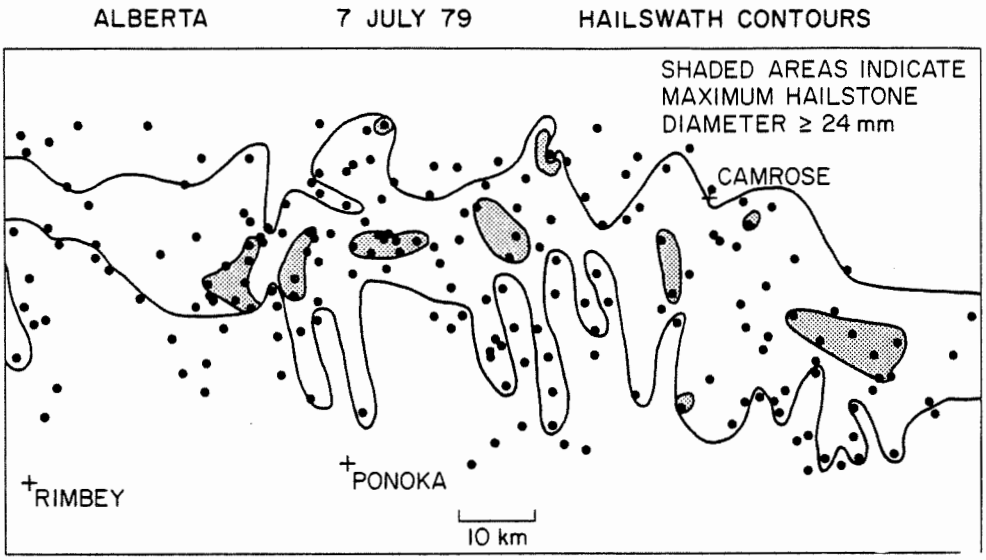

Fig. 1. Hailswath, 7 July 1979. Shaded areas indicate hail sizes estimated by observers to be equal or greater than approximately 24 mm in longest dimension.

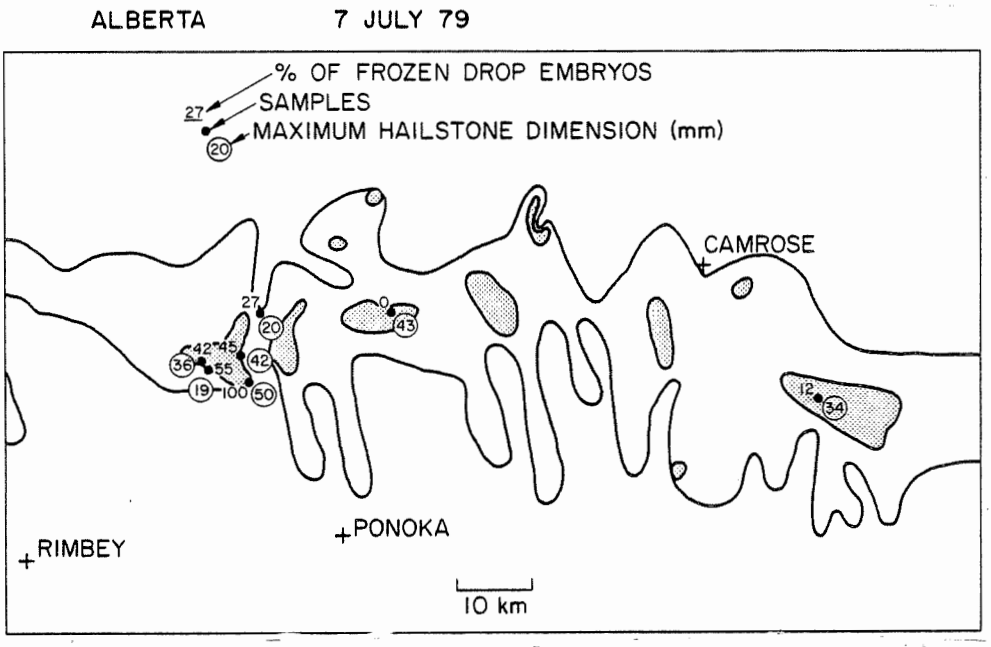

Fig. 2. Same as Fig. 1 and showing location of samples, percent of frozen drop embryos and maximum hailstone size in sample.

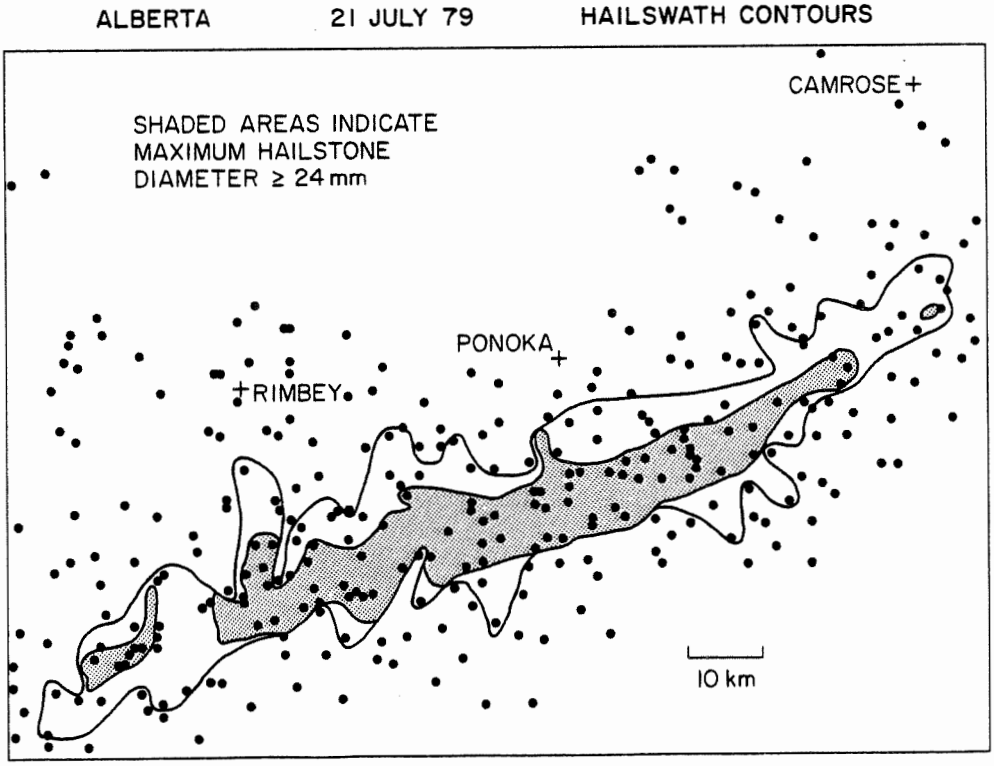

Fig. 3. Hailswath, 21 July 1979. Shaded areas same as Fig. 1.

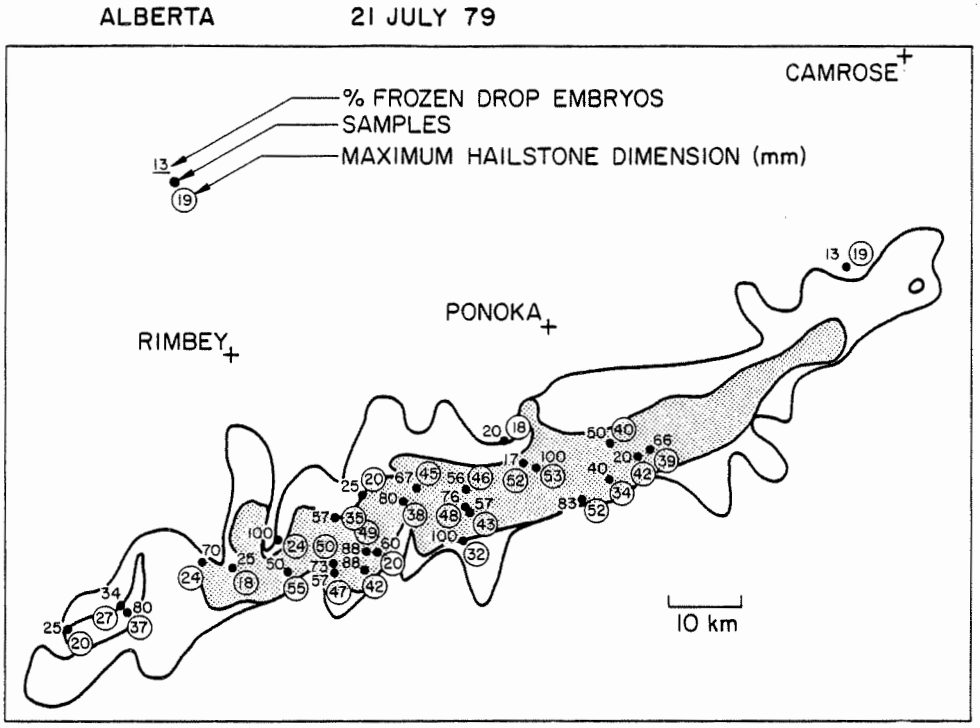

Fig. 4. Same as Fig. 3 and showing location of samples, percent of frozen drop embryos, and maximum hailstone size.

largest hailstones tended to follow the lowest trajectory and fell out closest to the updraft. Embryos that resulted in large hail tended to grow just enough so that their fall speed remained close to that of the updraft as they ascended slowly in and over the updraft. Embryos that resulted in small hail tended to rise rapidly into upper parts of the cloud where little growth was possible and finally fell out far away from the updraft region. Possible trajectories of hailstones in storms such as the two reported here are illustrated in Fig. 7, a represention of the hail growth process in these types of storms. If frozen drop embryos and graupel embryos follow different trajectories, the frozen drop embryos must have some initial advantage either in size, point of injection into the main updraft, or in time. The fall speed of drop embryos is likely to be higher than that of comparably sized graupel because of their greater density, which, other things being equal, would lead to lower trajectories.

The results obtained from the hailstone studies in these two storms seem to confirm the model suggested by English as well as that of Browning and Foote. It is interesting to note, however, that the time-resolved sequential samples from these storms which covered periods of about fifteen minutes in both cases, show the larger hailstones falling approximately half way through the hailfall period and no pronounced change in embryo type during the entire sampling period. These samples, however, were from the north side of the hailswaths.

The trajectories illustrated in Fig. 7 also suggest implications for seeding for the mitigation of hail in that, if the embryos do follow these trajectories, the graupel embryos cannot compete effectively with the frozen drops and if the goal in seeding hailstorms is to reduce the size of the hailstones produced by the storm, the methods used must produce frozen drop embryos of the right size and in the right location to compete with the natural embryos that produce the largest hail.

At present it is impossible to determine the origin of frozen drop embryos from evidence given in hailstone thin-sections. They may be produced by a coalescence process, especially if large, insoluble particles are present

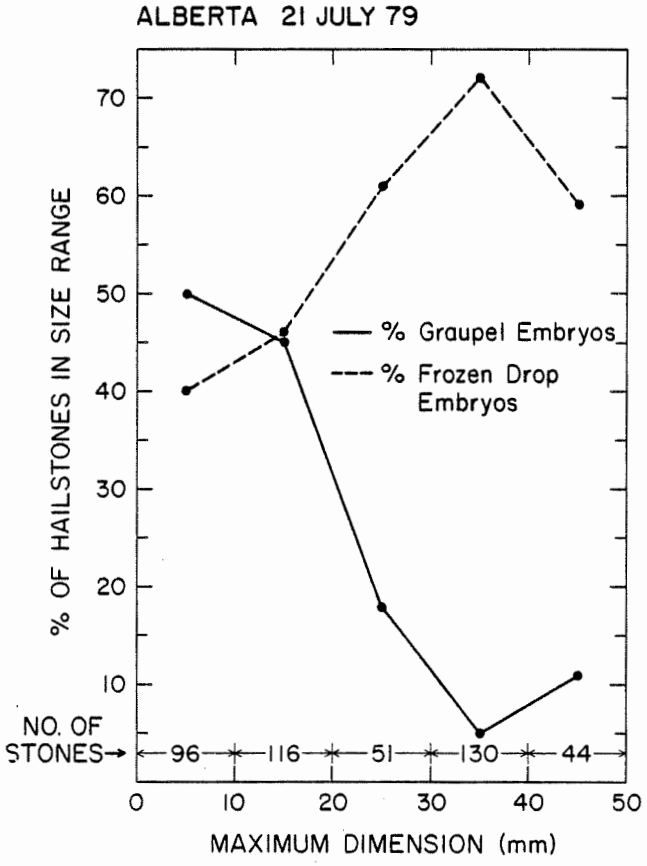

Fig. 5. Percentage of different embryo type with hailstone size.

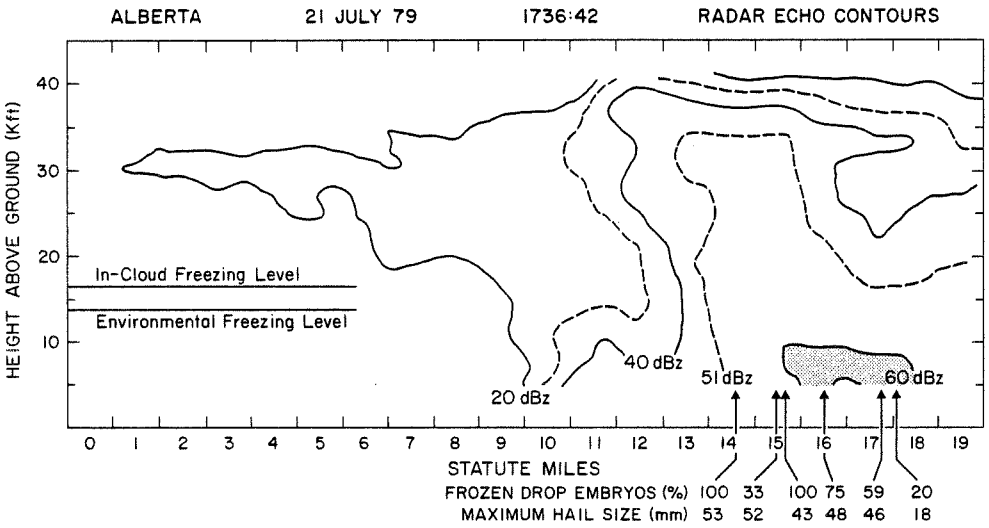

Fig. 6. Vertical cross section of the radar echo of the storm on 21 July at the time that the largest number of samples was obtained. The section is taken along a line which is approximately the direction of motion of precipitation particles with repsect to the storm as determined by studying the small-scale reflectivity maxima (Barge and Bergwall, 1976).

(Rosinski *et al.*, 1979), or shedding from growing hailstones. In areas such as NE Colo. where the primary precipitation formation process is known to be through the ice phase, it is more likely that they are produced by graupel falling below the melting level, melting and refreezing. Results of investigations of the embryos of Alberta hailstones conducted by one of the present authors (NK) prior to the 1979 hail season showed 80% graupel embryos and it is likely that the ice process often predominates in Alberta as well. Both of the storms discussed had associated feeder clouds that merged with the main storm and vertical cross sections of the radar echo show particles falling through the melting level in the feeder clouds.

The two storms reported here were similar in many respects. They occurred over adjacent areas and travelled in approximately the same direction, both lasting for periods in excess of four hours. The cloud base temperature was approximately +7°C in both storms and they had similar radar structures and produced large hail. The storm on 21 July produced a much larger proportion of frozen drop embryos than did the one on 7 July. At present there is no explanation for the difference in percentages of embryo type in the two storms although it is possible that it may lie in the much smaller number of samples obtained from the first storm.

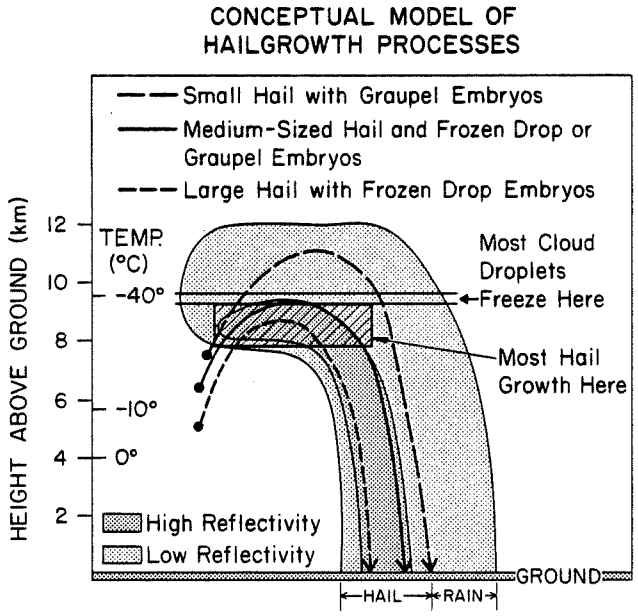

Fig. 7. Conceptual model of hailstone trajectories.

Acknowledgments: The first author gratefully acknowledges the contributions of Dr. Charles A. Knight. Many thanks are due to all involved in the collection of the hail samples from staff of the Alberta Research Council and the Alberta Weather Modification Board to the farmers of Alberta.. Special thanks are due to Ford Bergwall of the Alberta Research Council for determining the direction of motion of precipitation particles with respect to the storm for the two storms. The project was (partially) funded by the Alberta Weather Modification board.

References

Barge, B. L., and F. Bergwall, 1976: Fine scale structure of convective storms associated with hail production. Report 76-2, Atmospheric Sciences Division, Alberta Research Council, Edmonton, Alberta. In two volumes.

Browning, K. A., and G. B. Foote, 1976: Airflow and hail growth in supercell storms and some implications for hail suppression. *Quart J. Roy. Meteor. Soc., 102,* 499-533.

English, M., 1973: Alberta hailstorms, Part II: Growth of large hail in the storm. *Meteor. Monogr., 14(36),* 37-98.

Knight, N. C., and C. A. Knight, 1978: South African Lowveld hailstone embryos. *Preprints, Conf. on Cl. Phys. and Atmos. Elec., Issaquah, Amer. Meteor. Soc., 194-197.*

Rosinski, J., C. A. Knight, C. T. Nagamoto, G. M. Morgan and N. C. Knight, 1979: Further studies of large, water-insoluble particles within hailstones. *J. Atmos. Sci., 36,* 882-891.

Young, K. C., 1977: "A numerical examination of some hail suppression concepts," in *Hail: A Review of Hail Science and Hail Suppression. Meteor. Monogr., 16(38),* 195-214.

EFFECTS OF THE GROWTH CONDITIONS UPON THE CRYSTAL ORIENTATION IN ARTIFICIAL AND NATURAL HAILSTONES

L.Levi[+], F.Prodi, L.Lubart

Servicio Meteorológico Nacional, Buenos Aires, ARGENTINA

FISBAT-CNR, Rep. Nubi e Precipitazioni, Bologna, ITALY

1. Introduction

Crystallographic orientation distributions have been obtained and analyzed to infer the hailstone growth conditions in the cloud, and comparisons have been made of the peaks found in these distributions with those observed in cylindrical deposits accreted in known wind tunnel conditions (Knight and Knight, 1968; Aufdermaur et al, 1963; Levi and Aufdermaur, 1970; Macklin and Rye, 1974; Levi et al, 1974; Macklin et al, 1976). However there are some disagreements about the results found by different authors in artificial accretions. In addition it is necessary to define to what extent the results obtained from cylinders accreted around a fixed rotation axis may be applied to natural hailstones.

In the present work the crystal orientation in cylindrical accretions and in natural hailstones is studied. The frequency distributions are obtained, not only of the angle φ between the crystal c-axis and the growth direction, but also of its component angles η and ϑ between the growth direction and the projections of the c-axis onto the plane of the section and onto the plane normal to it through the radius. In fact, remarkable differences are found between the η and ϑ distributions which should be taken into account when the significance of the peaks of the $f(\varphi)$ curves is discussed.

2. Artificial accretions

Cylindrical accretions were grown in dry regime using an icing wind tunnel, under the same conditions described by Levi and Prodi (1978): wind speed U = 29 m sec^{-1}, mean droplet volume diameter d = 17 μm. All deposits except one were grown in dry regime (deposit temperature $T_d < 0°C$). Plastic replicas of the cylinder cross sections were prepared for crystallographic analysis.

The $f(\eta)$, $f(\vartheta)$ and $f(\varphi)$ distributions were obtained, as indicated by Macklin and Rye (1974), by analyzing 150-300 crystals per sample and by counting their number in intervals, 4° in width, centered on each whole degree from 2° to 88°. Some examples of the results obtained for the $f(\varphi)$ curves are given in Fig.1. Typical $f(\varphi)$ distributions at air temperature T_a = -15°C, for dry and wet deposits, with their main peaks at $\varphi < 5°$ and $\varphi > 70°$ respectively, are shown in Fig.1a. The curves in Fig.1b and in Fig.1c show that at $T_a < -20°C$ the main peaks in the distributions shift towards larger angles. At T_a = -21°C (Fig.1b) no pronounced maxima are found at T_d = -2°C, but, at T_d = -6°C and -11°C peaks at $\varphi \sim 30°$ and $35° > \varphi > 50°$ respectively may be observed. At T_a = -27°C

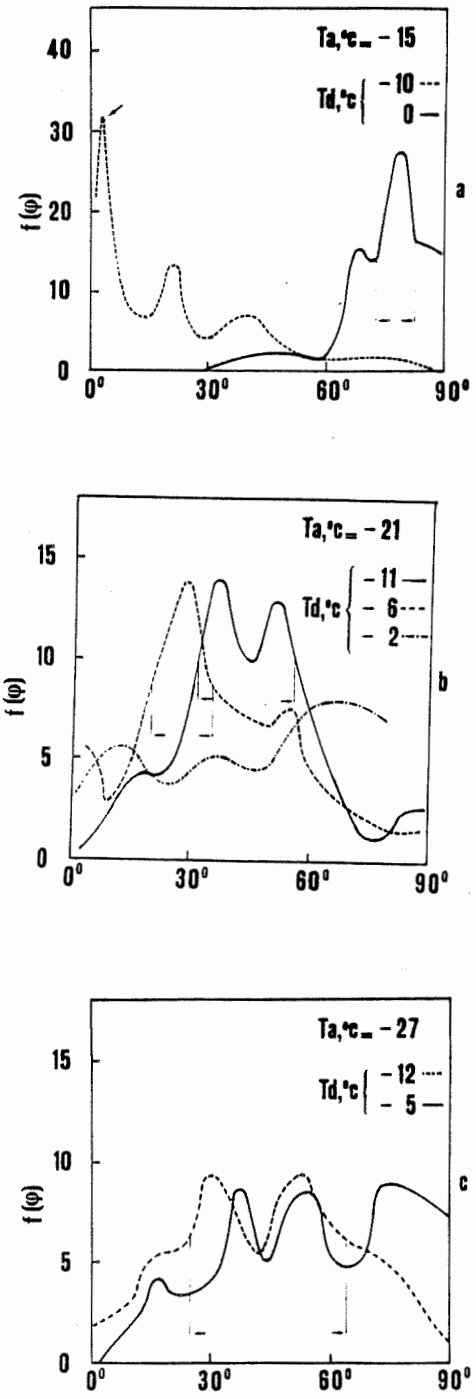

Fig.1 Distributions of $f(\varphi)$ in artificial accretions. Peaks with significance > 0.99 are indicated by interval bars and arrows.

[+]Consejo Nacional de Investigaciones Científicas y Técnicas and Comisión Nacional de Energía Atómica, Argentina.

peaks are found in the interval $30° < \varphi < 50°$ both at $T_d = -12°C$ and $T_d = -5°C$, but, at the latter value of T_d, the curve also presents a maximum at $\varphi \sim 75°$. The features of the curves corresponding to $T_a = -21°C$, $T_d = -2°C$, and $T_a = -27°C$, $T_d = -5°C$ probably indicate the coexistence of crystals nucleated both in dry and wet regimes. Notice that, at $T_a = -27°C$, accretion would occur close to the dry-wet limit, even at $T_d = -5°C$.

Rye and Macklin (1973) tested the significance of the peaks in the $f(\varphi)$ distributions by assuming that the c-axis orientation is axially symmetric with respect to the radial direction, i.e. that the random distribution is represented by a sinusoidal curve. When this assumption is valid, the $f(\eta)$ and $f(\vartheta)$ distributions should be statistically equivalent.

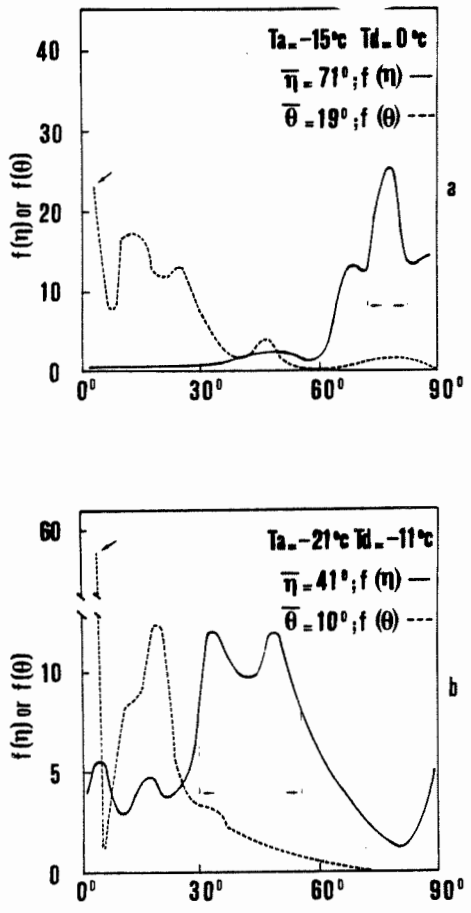

Fig.2 Distributions of $f(\eta)$ and $f(\vartheta)$ for artificial accretions

However it is shown in Fig.2 that, for cylindrical accretions, a systematic difference is obtained between these distributions. There are sharp peaks at small angles in all $f(\vartheta)$ distributions, independently of the growth conditions, whereas the $f(\eta)$ curves are quite similar to those corrsponding to $f(\varphi)$, the position of the peaks being related to the air and deposit temperatures. This behaviour is evident even in the wet growth deposit (Fig.2a), for which the peaks in the $f(\eta)$ and $f(\vartheta)$ distributions are in opposite positions.

Due to the difference between $f(\eta)$ and $f(\vartheta)$ the sinusoidal random distribution for φ should be replaced by the constant $f_r = N\Delta\varphi / 90°$ (where N is the number of the analyzed crystals and $\Delta\varphi$ is the 4° width interval). Taking into account this behaviour, f_r has been used to test, by the binomial statistics, the significance of peaks for the $f(\varphi)$ as well as for the $f(\eta)$ and $f(\vartheta)$ curves.

Note that all curves, except one curve in Fig.1b, present significant peaks which, for η and φ, vary with T_a and T_d. At low temperatures ($T_d = -11°C$ in Fig.1b and both curves in Fig.1c) there are sometimes two such peaks, approximately symmetric with respect to $\varphi \sim 40$-$45°$. These may be considered as a part of one complex maximum which is significant despite its width.

3. Natural hailstones

The crystallographic orientation was studied in several layers of ten oblate hailstones produced by two hailstorms, that occurred at Mendoza city on January 29,1976(Hailstones A) and at Rivadavia (Mendoza) on December 22,1976(Hailstones B and C).According to the radar data the top of the cloud in the latter storm reached about 17 Km and the life time of the cell was about ½h. The stones were 3-4 cm in maximum diameter, with a ratio of minor to major axes ranging from 0.6 to 0.8. After storage during a few weeks in a deep freezer at a temperature of about -20°C, they were cut through the equatorial plane, and replicas of their etched surfaces were prepared for analysis.

From the replicas the mean crystal section $\bar{\sigma}$ was measured and, for some layers, the frequency distributions $f(\eta)$, $f(\vartheta)$ and $f(\varphi)$ were determined. Table 1 summarizes the results, by giving the values of $\bar{\eta}, \bar{\vartheta}, \bar{\varphi}$ and the corresponding $\bar{\sigma}$. As it is seen, it is always $\bar{\vartheta} \leq \bar{\eta}$, with $\vartheta < \bar{\eta}$ in 80% of the cases and $\vartheta = \bar{\eta}$ in 20%.

TABLE 1

Values of $\bar{\eta}, \bar{\vartheta}, \bar{\varphi}$ and $\bar{\sigma}$ for different hailstone layers

Hailstone	Layer	$\bar{\eta}$	$\bar{\vartheta}$	$\bar{\varphi}$	$\bar{\sigma}$, mm^2
B6	1	40	20	46	0.4
	2	27	20	37	1.5
	3	48	20	54	0.3
B8	4	31	23	46	2.0
C2	1b	24	21	36	0.3
	3	29	25	42	1.2
C5	4	50	36	63	2.4
C6	2	15	15	23	2.4
	3	32	19	40	1.9
C8	1	44	34	59	0.1
	2	34	35	51	0.5
	3	45	36	63	2.0
C9	2	14	13	22	1.2
	3	45	19	52	3.8
A7	1b	19	12	24	1.0
	2	36	20	44	3.4
A4	1	27	27	41	0.4
	2	25	18	33	4.2
A2	2	39	20	46	3.5

It results that usually the c-axis orientation is not rotationally symmetric even for natural hailstones. However, the comparison of the

values of $\bar{\eta}$ and $\bar{\theta}$ given in Fig2 for artificial accretions with those in Table 1 shows that, in the latter case, the effect is less pronounced and it varies from one sample to another. This different behaviour, which could be interpreted in terms of the non fixed rotation axis of the hailstones, indicates that the $f(\eta)$ and $f(\vartheta)$ distributions must be tested before discussing the $f(\varphi)$ distributions. Actually, when $f(\eta) \sim f(\vartheta)$ the random distribution to be considered could approximate to the sinusoidal curve, and a function of the type $h(\varphi) = f(\varphi)/N \operatorname{sen}\varphi$ (see Rye and Mackin,1973) should be used to discuss the hailstone growth conditions.

A few examples of the distributions $f(\eta)$, $f(\vartheta)$ and $f(\varphi)$ for natural hailstones are given in Figs 3,4 and 5. Fig.3a is a typical case of similar $f(\eta)$ and $f(\vartheta)$ distributions. The corresponding $f(\varphi)$ curve given in Fig 3b presents a broad maximum in the interval 10-20°. However the curve may not be discussed by direct comparison with those for artificial accretions in Fig.1, since, due to the similarity of the $f(\eta)$ and $f(\vartheta)$ distributions, the orientation of the c-axes must be considered rotationally symmetric with respect to the radial direction. Due to this characteristic, the "zero angle peak" shown by the $h(\varphi)$ curve, given in the same figure, may be considered evidence of dry growth at rather high air temperature. Since the ice was clear and $\bar{\sigma} \sim 1$ mm^2, it would result $T_a = -15$°C and T_d just below 0°C (Levi and Aufdermaur,1970; Levi and Prodi,1978).

The frequency distributions in Fig.4 indicate a higher disorder of the crystal orientation and a larger difference between the $f(\eta)$ and $f(\vartheta)$ curves. Since the ice was clear, i.e. T_d remained near 0°C, the evident maximum of both $f(\varphi)$ and $h(\varphi)$ curves near $\varphi = 20°$ may be related to a decrease of T_a with respect to the previous layer, possibly due to the fact that the hailstone was carried by the updraft towards higher cloud levels where $-15 > T_a > -18$°C.

Figs.5a and 5b show an example where the $f(\eta)$ and $f(\vartheta)$ distributions are markedly different. In this case the $f(\eta)$ curve slightly oscillates about a nearly constant value. On the contrary the $f(\vartheta)$ curve presents a significant peak near 0°C. Thus the sinusoidal random distribution of φ would not be applied and the zero angle peak of the $h(\varphi)$ curve, shown in Fig.5b, may not be considered evidence of dry growth. Therefore the large disorder shown in the same figure by the $f(\varphi)$ curve, with $\bar{\varphi} \sim 50°$, indicates that growth probably occurred in wet or limit wet regime.

The frequency distributions given in Figs. 3,4 and 5 may be considered representative of the behaviour observed for the studied hailstones (Table 1). Among the analyzed layers a few presented the characteristics of Fig.3 (C6 layer2; C2 layer 1b; C9 layer 2; A7 layer 1b). In several cases frequency distributions were found, more similar to those in Fig 4 (B8 layer 4; C2 layer 3; B6 layer 2). Finally, for most hailstone layers characterized by $\bar{\varphi} \gtrsim 50°$ the frequency distributions showed similarities with those in Fig.5 (for instance C5 layer4; C8 layer3; C9 layer3).

It is interesting to observe, however, that $f(\varphi)$ curves typical of spongy growth, with peaks at $\varphi > 70°$ (as shown for instance in Fig.1),

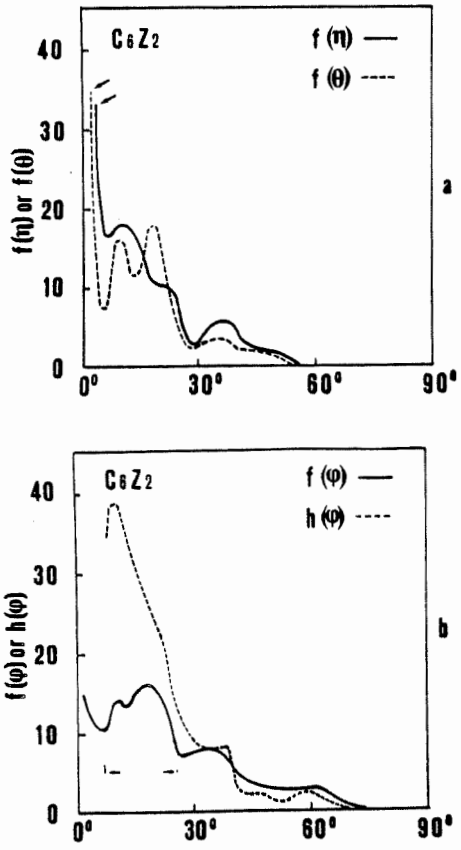

Fig.3 Frequency distributions for hailstone C6; layer 2.

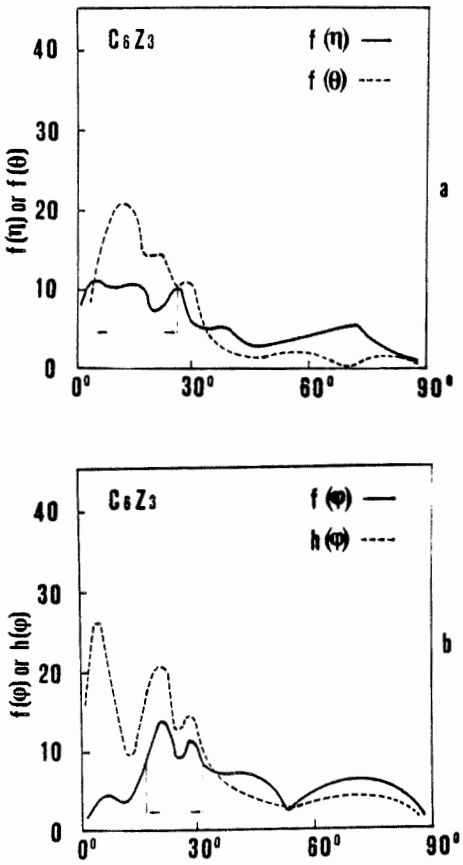

Fig.4 Frequency distributions for hailstone C6, layer 3.

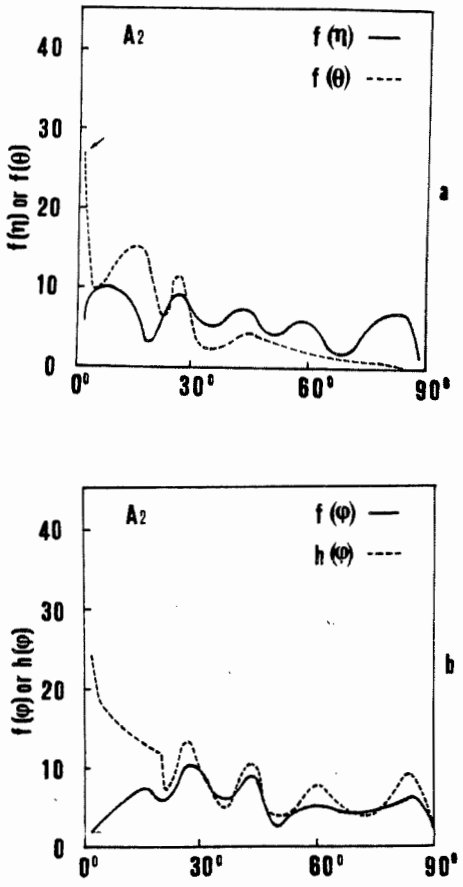

Fig.5. Frequency distributions for hailstone A2 layer 2.

could not be found for the natural hailstones analyzed here.

In spite of this, the hailstone thin sections presented in several cases large air cavities, frequently distributed as rings at small distance from the embryo, that could be considered evidence of liquid water ejected during spongy growth. For instance hailstone C9 showed a bubble ring between the dry growth layer 2 and the layer 3 which presented frequency distributions similar to those in Fig.5.

It may be concluded that the analyzed hailstones presented layers grown in dry, wet and spongy regime. On the other hand, the values obtained for $\bar{\sigma}$, which were, in several layers, of the order of 1 mm^2 or more (Table 1), and observations of the ice opacity indicate that growth was mainly taking place at $T_a > -25°C$ and that even when dry growth was established, T_d remained rather near 0°C.

It may be interesting to observe that, according to the one dimensional Hirsh model(1971) applied with the radiosoundings data of Dec.22, 1976, the transition from liquid hydrometeors to groupels would have occurred at the cloud level between 7.4 and 8.4 Km, where the cloud temperature varied from-16.5 to -23.5°C, i.e. in about the same temperature interval found from the hailstone analysis.

4. Conclusions

a) In artificial accretions the $f(\eta)$ and $f(\vartheta)$ curves are quite different from each other. The $f(\vartheta)$ curves present peaks near 0°in all the experimental conditions tested. This behaviour should be related to the fixed rotation axis of the growing deposit.

b) The $f(\eta)$ and $f(\varphi)$ curves present peaks which depend both on T_a and T_d The dependence on T_d is especially evident at $T_a \sim -20°C$. For $T_a < -25°C$ the peak position is mainly determined by T_a.

c) In oblate hailstones, cut through their equatorial plane, the $f(\varphi)$ curves present also peaks near 0°, though the effect is less pronounced than in artificial accretions.

d) The peak position of the $f(\eta)$ and $f(\varphi)$ curves may be used to determine T_a and T_d in natural hailstones. The samples analyzed in the present work, showing no defined peak in their distributions, were grown near the dry-wet limit. Therefore they did not display the wide range of growth conditions needed to extensively test this criterium.

5. Acknowledgments

The authors are thankful to M.V.Carrilho for preparation of the frequency distribution program, to A.Malossini for technical help and to M.E.Saluzzi for providing informations about the storm.

References

Aufdermaur A.N.,R.List,W.C.Mayes and M.R.de Quervain,1963:Kristallachsenlagen in Hagelkörnern. Z.Angew.Math.Phys.14,574-589

Carras J.N. and W.C.Macklin,1975: The opacity of accreted ice. Quart.J.Roy.Met.Soc. 101,203-206.

Hirsch J.H.,1971: Computer modeling of cumulus clouds during project cloud catcher. Inst.Atm.Sci. South Dakota School of Mines and Techn.Report 71-7,61pp.

Knight C.A. and N.C.Knight,1968:Spongy hailstone growth criteria.I Orientation fabrics. J.Atmos.Sci.25,445-452.

Levi L. and A.N.Aufdermaur,1970: Crystallographic orientation and crystal size in cylindrical accretion of ice. J.Atmos.Sci. 27,443-452

Levi L.,E.M.Achaval and L.Lubart,1974: Structure of ice grown from droplet accretion and solidification process.J.Crystal Growth, 22,303-310.

Levi L. and F.Prodi,1978: Crystal size in ice grown by droplet accretion.J.Atmos.Sc. 35,2181-2189

Macklin W.C. and P.J.Rye,1974: Crystallographic orientation distribution in accreted ice.J.Atmos.Sc, 31,849-852

Macklin W.C.,J.N.Carras and P.J.Rye,1976: The interpretation of the crystalline and air bubble structure of hailstones. Quart.J. Roy.Met.Soc,102,25-44

Rye P.J. and W.C.Macklin,1973:Interpretation of crystallographic orientations in accreted ice. J.Atmos.Sc, 30,1421-1426.

CYLINDER ICING, PART I: DEPENDENCE OF NET COLLECTION RATE AND SPONGINESS ON ROTATION RATE

ROLAND LIST, G.B. LESINS AND P.I. JOE
Department of Physics, University of Toronto,
TORONTO, CANADA M5S 1A7

1. INTRODUCTION

The growth by the accretion of supercooled water droplets onto on object (a cylinder, a hailsone, etc.) is dependent on cloud properties such as air temperature,liquid water content, size distribution of water droplets and air density. In addition, the shape of the iced object, its size and surface features together determine the aerodynamics and thus also affect the growth process.

One of the most important parameters determining ice growth is the net collection efficiency E_{net}(List,1978/79). If E_{net} were known as a function of all the cloud and icing object parameters then ice accretion rates could be predicted. This paper reports measured values of E_{net} and ice fractions of spongy deposits on rotating cylinders and relates them to the heat and mass flux. The effect of rotation on the growth rate and ice fraction of the deposit is also examined.

2. THE EXPERIMENT

The icing experiments were performed in a closed circuit wind tunnel at the University of Toronto. The air velocity in the vertical measuring section could be varied from 9 to 18 ms^{-1}. The entire wind tunnel was set up in a walk-in cold room whose temperature could be set as low as $-28^{o}C$. An additional cooling unit was located within the tunnel to compensate for compressible and frictional heating and allowed the tunnel air to reach a minimum temperature of $-24^{o}C$. Further details of the wind tunnel can be found in Murray and List (1972).

The plexiglass measuring section (Figure 1) was 48cm high, expanding from a cross-section of 15 by 15cm to 21 by 21cm at the top. Attached to the bottom of this section was an aluminum mount which supported a horizontal plexiglass cylinder (23cm long and 1.90cm diameter) which rotated at set speeds between 0.5 to 35Hz.

Water was injected into the airstream through an atomizing nozzle, 1.8m below the measuring section, into a tunnel part where the airspeed was 10 times slower than above. Before injection, the water was filtered and deionized. The nozzle was kept at a temperature just above $0^{o}C$ to allow maximum adjustment of the droplet temperature to that of the surrounding air (normally to within less than 10% of the original temperature difference). The size distribution of the droplets could be controlled to some extent by the air flow through the nozzle. The mean volume diameter of the droplets could be varied from 90um to 150um. The liquid water content, W_f, was varied from $2gm^{-3}$ to $40gm^{-3}$ by adjusting the water flow through the nozzle.

The values for W_f were measured using a Knollenberg 2-D Cloud Droplet Optical Array Spectrometer configured for laboratory use. An independent technique was also applied to measure W_f. This consisted of collecting the water droplets onto an aluminum slab (4.76cm by 1.90cm) which was initially cooled to $-196^{o}C$ in liquid nitrogen. Due to the relatively large droplets the collision efficiency could safely be assumed to be one, and since no bouncing was observed the collection efficiency was also one. The final uncertainty in W_f is $\pm$10%. Analysis of the icing had to be confined to the centre 2-4cm of the cylinder and wind tunnel since W_f decreased towards the tunnel walls.

The environmental parameters that were set at the start of each experiment (no pressure variation was possible) were air temperature, liquid water content, air velocity, cylinder rotation rate and mean volume diameter of the supercooled droplets in the airflow. The rotating cylinder was subjected to icing for a known amount of time. All cylinders had an initial diameter of 1.90cm and were normally not allowed to grow more than 0.5cm in radius. The surface temperature of the cylinder was monitored by an infrared radiometric microscope to determine whether the ice deposit was "wet" ($0^{o}C$) or "dry" ($\leq 0^{o}C$).

At the completion of an icing experiment the cylinder was removed from the tunnel, photographed, weighed and then a sample of the ice deposit (2 to 20g) was removed and placed in a 50ml calorimeter in order to determine the ice fraction in the possibly spongy deposit. The calorimetric check was unnecessary whenever the ice deposit was dry. The error in I is $\pm$8%.

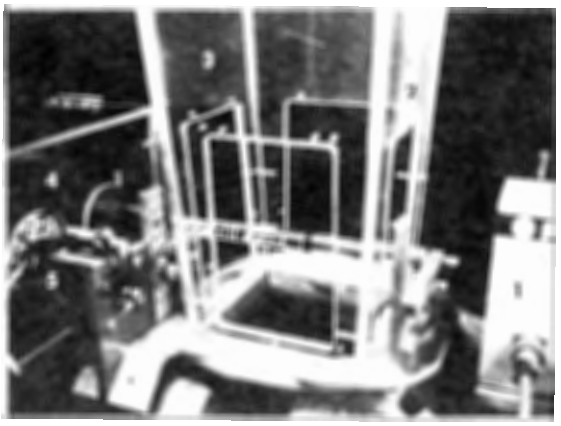

Figure 1. View of the measuring section of the wind tunnel, with the air flow upwards. 1 Laser for Knollenberg Droplet Spectrometer, 2. Slot for radiometric microscope viewing, 3. Tunnel walls, 4. Knollenberg analyser, 5. Motor for cylinder rotation, 6. Plexiglass cylinder before icing.

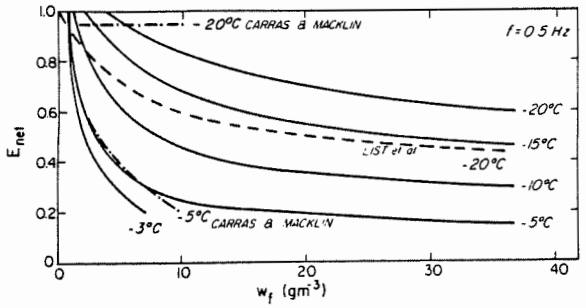

Figure 2. Experimental results for the net collection efficiency, E_{net}, versus liquid water content, W_f, for 5 air temperatures, at a rotation rate of 0.5Hz, an air velocity of 18ms^{-1}, and a mean volume diameter of water droplets of 90um (solid lines). Results from Carras and Macklin (1973) are shown after being adjusted for speed by the velocity dependence given by List et al.(1976). Data from List et al. (1976) is also shown. The lower values of E_{net} may also be caused by the observed bouncing, not just shedding.

The net collection efficiency, E_{net}, is defined as the fraction of the initially collected water droplets, which permanently accretes onto the cylinder. It can be calculated by using the definition and the observation that the collection efficiency E=1 by measuring the final diameter of the iced cylinder, D, from the photograph.This leads to:

$$E_{net} = \frac{(D - D_i)\pi\,[\rho_w - I(\rho_w - \rho_i)]}{2\,t\,V\,W_f}\,, \qquad (2.1)$$

where D_i is the initial cylinder diameter, ρ_w and ρ_i are the densities of water and ice respectively, at 0°C, I is the ice fraction in deposit, t is the icing time, V is the air velocity and W_f is the liquid water content. Error analysis of Equation 2.1 yields an uncertainty of ±15% for E_{net}.

3. NET COLLECTION EFFICIENCY AND ICE FRACTION

A series of icing experiments were performed with cylinders (diameter 1.9cm) at an air velocity of 18ms^{-1}, over a range of liquid water contents, W_f from 2 to 40gm^{-3} and air temperature, t_a between -2 and -20°C and cylinder rotation rate of 0.5 ± 0.2Hz and a mean volume diameter of the incoming supercooled droplets of 90um. Measurements of E_{net} and the ice fraction I were taken in order to determine the different heat transfer terms. E_{net} decreased consistently with increasing W_f and increasing t_a (Figure 2).It was observed to decrease with increasing W_f, but not below limiting values. At temperatures higher than -5°C the net collection efficiency drops off very quickly and , for higher liquid water contents, assumes values below 20%. However, no dependence of I on t_a was observed in the range $-4^{o} \leq t_a \leq -16^{o}$(Figure 3). While

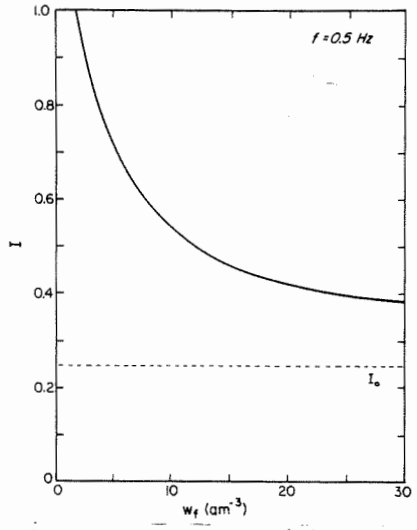

Figure 3. Ice fraction (I) dependence on liquid water content, W_f. Data was averaged over the temperature range $-4^{o}=t_a=-16^{o}$C, where the variation of I was less than its uncertainty of ±8%. I_o (=25%) is the asymptote for high W_f according to the curve fit. The lowest measured value for I was 33%.

some dependence on t_a could be expected it was not resolved within the ±8% error in I. For temperatures warmer than -4°C the ice fraction seemed to increase slightly.

Parametric equations were sought to describe the experimental results for E_{net} and I. The best least square fits for the stated temperature range and E=1 are given by:

$$E_{net} = E_o + \frac{1 - E_o}{1 + K_E(W_f - W_E)}, \qquad (3.1)$$

and

$$I = I_o + \frac{1 - I_o}{1 + K_I(W_f - W_I)}\,, \qquad (3.2)$$

where: $E_o = 0.0165 - 0.0206t_a$, [-],
$K_E = -0.122 - 3.79t_a^{-1}$, [m^{3}g^{-1}],
$W_E = 1.29 + 0.147t_a + 0.0128t_a^2$,
$I_o = 0.25$, [-],
$K_I = 0.1798$, [g^{-1}m^3]
$W_I = 2.0$, [gm^{-3}].

4. HEAT TRANSFER ASPECTS OF SHEDDING AND ROUGHNESS

The process of heat transfer by conduction and convection, Q_{CC}*, evaporation, condensation or sublimation, Q_{ESC}*, droplet accretion and losses, Q_{CP}*, and freezing, Q_F*, are parts of the total heat flux and sinks for icing cylinders. In quasi-equilibrium their sum is zero. Ludlam (1951) was one of the first to derive the equation for riming cylinders. List (1962) expanded it for spongy ice growth and later (1977) included losses of accreted water by shedding etc.

Under present consideration are the roughness

factor, θ, for the terms Q_{CC}^* and Q_{ESC}^* and possible contributions due to the properties of the shed water (supercooling, t_s, or ice fraction, I_s) as expressed in:

$$Q_{CP}^* = -VD[E_{net} W_f C_w (t_d - t_a) + (E - E_{net}) W_f (C_w (t_s - t_a) - I_s L_f)]. \quad (4.1)$$

where D is the cylinder diameter, C_w the specific heat of water, L_f the latent heat of freezing, and the subscripts for temperature, t, are s for shed water, a for ambient air, and d for deposit.

To assess the effects of 0 and the shed water a percentage heat flux residual R* is calculated according to:

$$R^* = 100 \frac{(Q_F^* + Q_{CC}^* + Q_{ESC}^* + Q_{CP}^*)}{|Q_F^*| + |Q_{CC}^*| + |Q_{ESC}^*| + |Q_{CP}^*|}. \quad (4.2)$$

assuming that all the swept out water droplets are accreted, that no roughness effect has to be taken into account and that the shed water contains no ice and has a temperature of 0°C. Any R*=0 will mean that the assumptions need to be revised, that effects occur which have to be associated with the new terms in the theory (their sum or difference).

This residual R* was found to be zero for $W_f \approx 13 gm^{-3}$ and was a relatively weak function of temperature. R* becomes negative for $W_f \geq 13 gm^{-3}$ reaching about -20% at $W_f = 40 gm^{-3}$. A negative value for R* means that the theory with parameters chosen as discribed above is predicting too much cooling at the cylinder's surface. For $W_f \leq 13 gm^{-3}$ R* becomes positive, predicting insufficient cooling, and increases to 30% for $W_f \leq 4 gm^{-3}$ and $t_a \geq -3°C$. This larger deviation for warm temperatures and low liquid water contents occurs in a region where E_{net} is a rapidly varying function and hence larger systematic deviations could result.

Systematic errors in the measurements of E_{net} and I could explain the non-zero value for R* only in the region $10 gm^{-3} \lesssim W_f \lesssim 20 gm^{-3}$. Thus, the general validity of the assumptions is questionable. If the shed water were supercooled to some degree at the moment of shedding, then the cylinder will lose less heat than originally assumed. This alone could correct R* for W=13 gm^{-3}. For such values a thicker water skin develops on the cylinder's surface which undergoes frequent disruption producing shed water. This results in a shorter residence time for the temporarily accreted water which, as a consequence, may remain supercooled to some degree.

For $W_f \leq 13$ gm^{-3} the "insufficient" cooling can be improved by increasing the value of the surface roughness factor, 0, from one. At low W_f, when the ice is less spongy, rough elements several millimeters in height are quite frequent and will induce enhanced convective and evaporative cooling.

W_f ↑ \ t_a(°C)	-2	-4	-6	-8	-10	-12	-14	-16	-18	-20
4	2.5	2.1	1.9	1.7	1.6	1.5	1.4	1.3	1.2	1.1
8	1.9	1.6	1.5	1.4	1.4	1.3	1.3	1.3	1.2	1.1
12	1.5	1.3	1.2	1.1	1.1	1.1	1.0	1.0	0	-1
16	1.2	0	0	-1	-1	-2	-3	-4	-6	-9
20	0	0	-1	-2	-3	-4	-5	-7	-10	-13
24	0	-1	-2	-3	-4	-5	-7	-9	-12	-15
28	0	-1	-2	-3	-4	-6	-8	-10	-13	-17
32	0	-1	-2	-3	-5	-6	-8	-11	-14	-17

Table 1. Values for the roughness factor 0 or the temperature of the shed water, t_s(°C), in order to balance the heat flux (i.e. R*=0) are listed for different air temperatures, t_a, and liquid water content, $W_f[gm^{-3}]$. The values less than or equal to zero are for shed water temperature while values greater than or equal to one are for the roughness factor.

Table 1 shows the calculated values for t_s (values less than or equal to zero are in °C with θ=1) and for θ (values greater than one with t_s=0°C). Reasonable values for t_s ($\approx t_a$) are predicted as are the values for θ except for $W_f \leq 4 gm^{-3}$ and $t_a \geq -3°C$ where the values for E_{net} and I are less accurate. It should be added that R*=0 could also be explained by the difference of two terms which compensate each other in various degrees over the whole parameter range.

5. THE EFFECTS OF ROTATION ON ICING

The net collection efficiency, ice fraction and total mass growth rate, M_T, were measured as a function of the cylinder rotation rate, f, for $W_f = 5 gm^{-3}$, $V = 18 ms^{-1}$ and d=90um. M_T is the total increase in mass of the cylinder divided by the time of the experiment. It was calculated to give an estimate of the growth efficiency at higher rotation rates where meaningful E_{net} calculations were impossible due to the formation of spikes on the cylinder.

Figures 4 and 5 show that E_{net} and I undergo rapid variations with rotation rate, even at low f. From f=0.5 to 7Hz at -5°C and f=0.5 to 3Hz at -10°C, the ice fraction decreases from about 0.75 to 0.4 at -5°C and to 0.5 at -10°C. In this region E_{net} increases just sufficiently to maintain the same heat balance; the total amount of ice formed, as given by the product $E_{net} \times I$, is roughly independent of f. The trade-off effect between E_{net} and I can only be determined experimentally. This variation in I appears to be associated with the characteristics of the water skin.

For f=0.5Hz there was a substantial bulge of water (up to 3mm) near the flow separation lines on the cylinder where nearly all the shed water originates. As the rotation rate was increased up to the value where I was a minimum the bulge in the water skin became smaller and the water skin was more uniform in thickness. This allowed more of the accreted water to be trapped by the ice matrix of the deposit, thereby reducing the

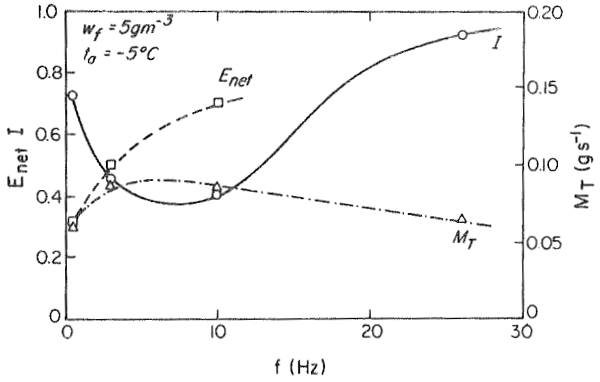

Figure 4. Ice growth, represented by the net colloection efficiency, the ice fraction and the total mass growth rate M_T, as function of cylinder rotation rate, f, for an air velocity of $18ms^{-1}$, a liquid water content of $5gm^{-3}$ and an air temperature of -5^oC. The ice fraction reaches a minimum of 36% at 7Hz.

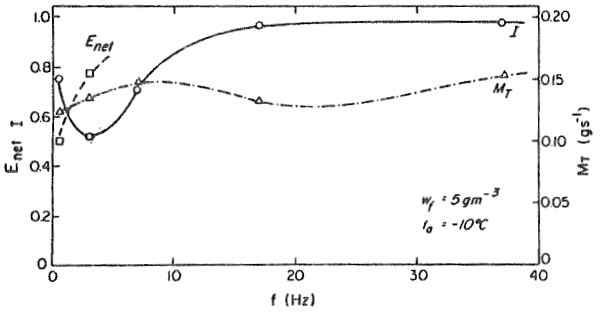

Figure 5. Same as Figure 4 but for an air temperature of -10^oC. The minimum ice fraction of 52% occurs at f=3Hz.

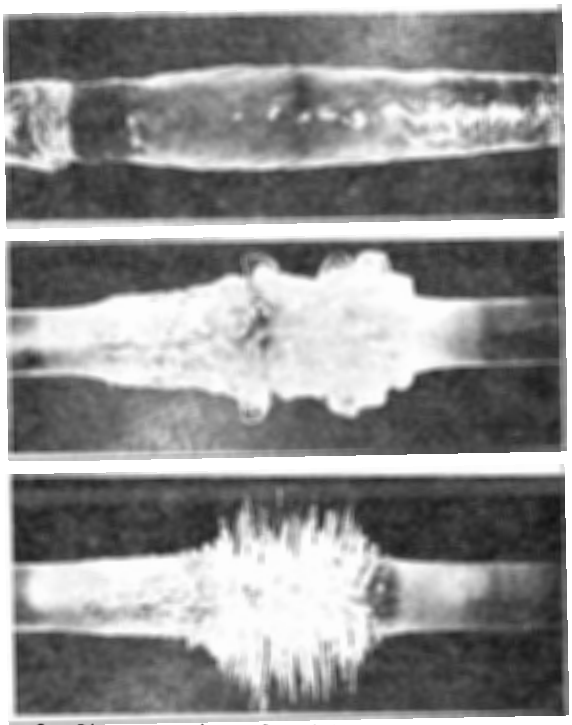

Figure 6. Photographs of cylinders iced at a velocity of $18ms^{-1}$, a liquid water content of $5gm^{-3}$ and an air temperature of -10^oC. The rotation rates from above were 0.5, 7, and 37Hz, respectively. The diameter of the un-iced cylinder part visible in the two lower photographs was 1.9cm.

shedding and hence increasing E_{net} and the growth rate.

As f was increased beyond the minimum point in I the cylinder's surface became increasingly rough. The shallow ridges and knobs transformed into large fairly rounded lobes of up to 1cm in size. If f went beyond about 15Hz, then conically shaped spikes formed. Even higher rotation rates produced longer, thinner and sharper spikes (Figure 6).

Figures 4 and 5 reveal that the ice fraction approaches the value one for large f as the liquid water on the cylinder is being spun off by the centrifugal forces. Also at high rotation rates the lobes and spikes will promote increased convective cooling. Such enhancements can only be determined experimentally.

6. CONCLUSIONS

1.) Icing of rotating (up to 35Hz) cylinders (diameter 1.9cm) in a cross flow containing supercooled water droplets over the ranges of air temperature from -2^o to -20^oC and of liquid water content from 2 to $40gm^{-3}$ showed that the net collection efficiency and the ice fraction varied from 10 to 100% and 33 to 100% respectively, with asymptotic values found at high W_f, as also represented by empirical formulas. While the net collection efficiency was found to be temperature dependent, the ice fraction in the deposit was not.

2.) There are strong indications that a roughness factor and non-zero temperature and ice content of shed or otherwise lost water needs to be considered. The size of the effects should be measured independent from each other.

3.) Variation of the cylinder rotation lead to higher ice fractions both at low and high rotation rates with substantially lower values in between. Even at relatively high temperatures where great sponginess is expected, hard ice was observed.

4.) Extending the results to hailstone growth implies that the ice growth rates and the characteristics of deposits are affected considerably by rotational behavior, i.e. aerodynamics. In this light, the chances to interpret hailstone growth on the basis of their structure are very remote.

ACKNOWLEDGEMENTS. The work reported here was sponsored by the National Research Council of Canada.

The references are listed in Part II.

CYLINDER ICING, PART II: INSTANTANEOUS CONVERSION OF CLOUD WATER INTO RAINDROPS

ROLAND LIST, P.I. JOE AND G.B. LESINS
Department of Physics, University of Toronto,
TORONTO, CANADA M5S 1A7

1. INTRODUCTION

Artificial hail growth experiments by the University of Toronto Cloud Physics group in 1972 and 1974 (List, 1977, List et al., 1976, Joe et al., 1976) and those by Carras and Macklin (1973) demonstrated the presence of substantial water loss mechanisms during wet growth. These losses not only represent a decrease in the net collection efficiency of the hailstones (defined as the ratio of the water mass that permanently accretes on the hailstone to that which collides with it), they also result in an instantaneous conversion of cloud droplets into rain drops. The purpose of this paper is to study these losses as a function of icing conditions. From previous experience it was felt that icing of rotating horizontal cylinders in a vertical airstream with supercooled droplets should be studied first since their symmetry is simpler than that of spheroids or other three-dimensional bodies.

2. THE EXPERIMENT

The basic setup for the icing experiments was described in Part I (List et al., 1980). Additionally, facilities for photographing the experiments were also available. These included a 35mm motorized Nikon System, a Panasonic video system, a Bolex 16mm movie and a high speed Hycam camera. Illumination was provided by either two flood lamps used for the movies or two General Radio Strobolumes (model 1540 P1) units which could be triggered by the 35mm camera system or operated independently.

A series of experiments were recorded on video tape in which the parameters of liquid water content, W_f, and air temperature, t_a, were varied between $9.3 gm^{-3}$ and $41.8 gm^{-3}$ and -5^oC to -18^oC, respectively. The cylinder diameter, D, was 1.9cm and its rotation rate was 0.5Hz. The tunnel velocity, V_T, was 18m/s. The cylinder was oriented parallel to the axis of the camera lens. Illumination was provided by the strobes which were set to flash at a rate of 60Hz. The flash duration was 10us. The camera lens was a Canon TV zoom lens (17mm to 102mm) and provided a magnification of 2.8 on the video monitor.

3. DESCRIPTION OF THE SHEDDING

For the icing conditions used in this investigation, the ice deposits were relatively smooth (Figure 6, top, Part I). The shedding originated from an accumulation of water near the flow separation points of the cylinder (Figure 1), it occurred in the form of drops, but sheets and filaments, which also broke into drops, could also be seen. The water skin on the side of the cylinder moving with the air stream was carried by the ice substrate, with additional assistance by the air stress, to the opposite side where it accumulated, and was prevented from further movement by aerodynamic forces. This behaviour was also observed in the experiments of Roos and Pum (1974).

Under special conditions (either high W_f or low V_T) an additional but smaller bulge developed from which shedding also materialized. This bulge occurred on the side of the cylinder moving with the air stream, as there was insufficient friction between the water skin and the underlying substrate to counteract the Bernoulli forces. This bulge generally occurs farther away from the stagnation point (line) than the primary one.

A periodic movement of the primary bulge was observed. The shedding in the form of drops occurred more or less continuously, but it was not sufficient to completely offset the accumulation of the accreted water. As the bulge increased in mass it moved toward the front stagnation point under the force of gravity, with a limit of about 80^o from the stagnation point. There, more spectacular forms of shedding occured in the form of sheets (Figure 2) or filaments (Figure 3). These formations then broke up to form some of the larger drops observed. Afterwards, the bulge decreased in size, moved away from the stagnation point to about 100^o, and the process repeated itself.

Mechanical forces between the underlying spongy ice and the water skin are mainly responsible for transporting the accreted water. The air stress, surface tension and air pressure at the water/air boundary essentially determine the formation of the bulges and the shedding.

Most of the shed material (90%) was carried into the wake by the air flow.

4. SHEDDING RATES

The shed drops were counted in different size categories from the video monitor. This gave the number of shed drops per frame per category, f_i. The count was done for a constant volume with a width, W, of 3.2cm, a height, H, of 2.5cm and a depth, DOF, of 4.3cm, centered 3cm above the top of the cylinder. Over 4,500 frames were counted from six hours of video recordings.

The number of drops per frame was converted to a number production rate of shed drops per unit cylinder length by correcting for the fact that the drops had not reached terminal velocity immediately after shedding. Since small drops reach terminal speed in a shorter distance than large drops, this effect meant that the large

reach terminal speed in a shorter distance than large drops, this effect meant that the large drops were overcounted relative to the small ones. This led to the introduction of a velocity adjustment factor f_v, assuming that the extra residence time is proportional to the terminal velocity.

It was further assumed that the sample counted is representative of the real spectrum and differs only by a scaling factor f_T. Further, the losses by splashing were supposed to be small compared to the shedding. Any errors in these assumptions do not affect the final result as long as they are systematic and a multiplicative correction is appropriate.

The total mass production rate, S, per unit cylinder length, for drops with diameter d_i, a terminal velocity, v_{ti}, and a water density, ρ_w, is given by:

$$S = \frac{f_f \sum_i (\pi/6)\, d_i^3\, \rho_w\, f_i (V_T - v_{ti})}{\mathrm{DOF}\ H}, \qquad (4.1)$$

where $f_f = f_T f_v$. Equation 4.1 requires SI units with m, kg and s.

The non-dimensional scaling factor f_f can only be determined empirically. Therefore, it implicitly contains a correction for possible systematic errors in the assumptions.

From the bulk determination of the water losses (List et al., 1980) the shedding can also be expressed by:

$$S = (1-E_{net})\, W_f\, V_T\, D\ . \qquad (4.2)$$

A least squares fit yields f_f=62. The number production rate of shed drops in the i^{th} category per unit bin interval per unit cylinder length is given by:

$$n_i = \frac{f_f f_i\, (V_T - v_{ti})}{\mathrm{DOF}\ H}\ . \qquad (4.3)$$

A remarkable feature of the relations of number production rate, n(d), versus shed drop diameter (Figures 4a,b,c) is the uniformity among the curves. These curves are Gaussian in nature, with a peak at a drop diameter d=1.22mm, with a half width of about 0.7mm. This suggests a curve fit using a Gamma function:

$$n(d) = \frac{A}{pq\Gamma(q)}\, e^{-(d-d_0)/q}\, (d-d_0)^{(p-1)}. \qquad (4.4)$$

Of the four parameters (p,q,d_0,A) only one is not determined. The lowest size class is d_0(=0.5mm), the peak is located at $d_0+q(p-1)$ =1.22mm. Mass flux conservation determines A according to:

$$(1-E_{net}) W_f V_T D = \int_{d_0}^{\infty} n(d)(\pi/6)\, d^3 \rho_w\, dd, \qquad (4.5)$$

or, by integrating:

Figure 1: The Water skin before eruption: t_a=-5°C, W_f=10gm^{-3}, V_T=9m/s, f=0.5Hz, counterclockwise, D=1.9cm, magnification 2.75.

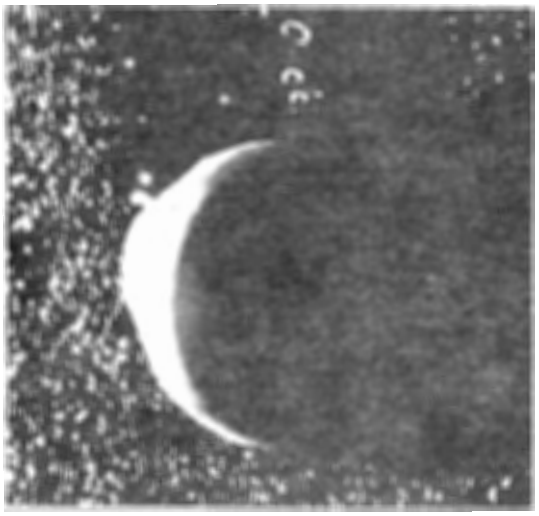

Figure 2: Shed drops in the wake: t_a=-10°C, W_f=18mg^{-3}, V_T=18m/s, f=0.5Hz, counterclockwise. D=1.9cm. magnification 2.0.

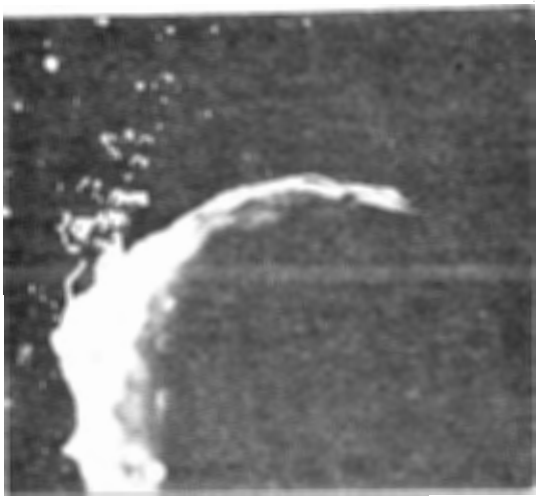

Figure 3: Disruption of the water skin in the form of a sheet breaking up into drops; t_a=-5°C, W_f=18gm^{-3}, V_T=18m/s, f=0.5Hz, counterclockwise, D=1.9cm, magnification 2.0.

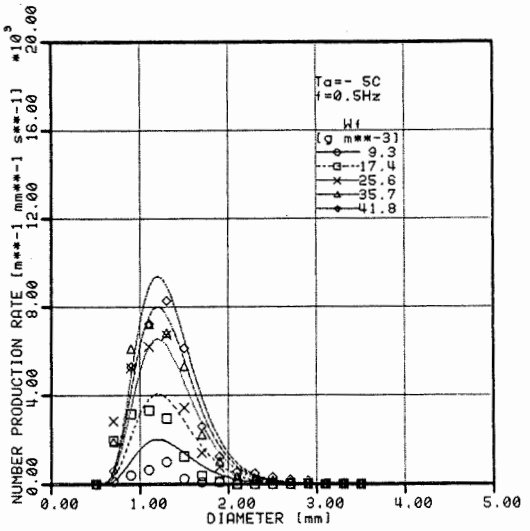

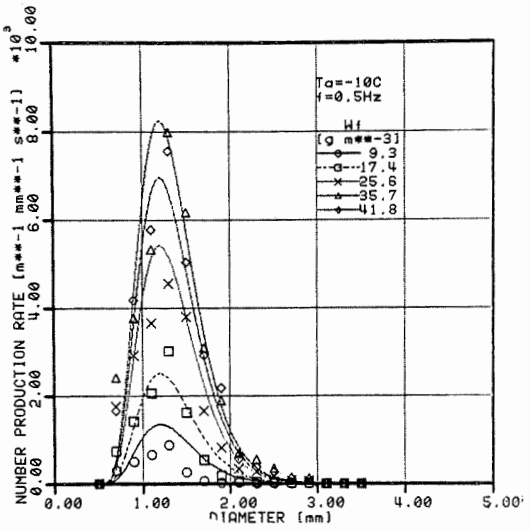

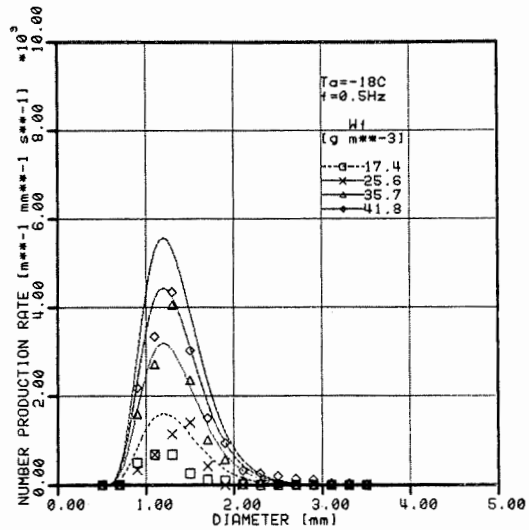

Figures 4a, b and c: Number production rate per meter of cylinder length and mm-drop diameter interval, as function of the diameter of the shed drops; for different liquid water contents, one rotation rate, and a given air temperature.

$$A = \frac{(1-E_{net})\, W_f\, V_T\, D}{\rho_w\, d_v^3}\,, \qquad (4.6)$$

where the mean volume diameter of the shed drops is given by:

$$d_v = [p(p+1)(p+2)q^3+3d_0p(p+1)q^2 + 3d_0^3pq+d_0^3]^{1/3} \qquad (4.7)$$

Thus there are four parameters and three equations. The last parameter p (or q) can be determined by a best fit to the data. The results are p=8, q=0.103, d_0=0.5mm, $\bar{d}_v$=1.4mm The physical interpretation is that A is the total production rate of shed drops by the cylinder per unit cylinder length.

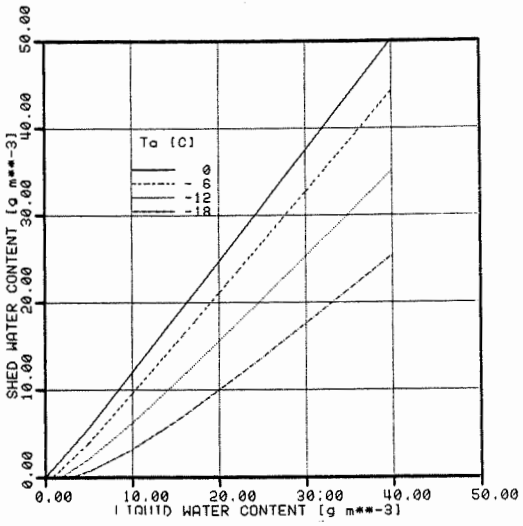

Figure 5: Relation of (shed) water contents in wake and liquid water content in swept out cloud, assumming that the shed drops have a size equal to the mean volume diameter (1.4mm) and their terminal velocity is equal to 4.9m/s. A line with a slope greater than one means that the shed water content above the cylinder is greater than that below.

5. LIQUID WATER CONTENT OF SHED DROPS

The liquid water content represented by the shed drops can be estimated if all the shed water moves at the terminal velocity of the mean volume diameter. Conservation of mass flux gives:

$$W_{fshed} = (1-E_{net})\, W_f \frac{V_T}{V_T-v_t} = 1.37(1-E_{net})\, W_f\,. \qquad (5.1)$$

where $v_t(\bar{d}_v)$=4.9m/s according to the paper by Pruppacher and Klett (1975).

It can be seen from this equation that if E_{net} is smaller than 0.27, the shedding can increase the water content above the cylinder even though there is an associated decrease of the mass flux. Plots of W_{fshed} versus W_f (Figure 5 and Figure 2, Part I) show that this situation may be expected whenever shedding occurs at temperatures warmer than about -8°C and liquid water contents greater

han $5gm^{-3}$. The curve for $0^{o}C$ has an assumed $E_{net}=0$ and the cloud water striking the cylinder is immediately converted to "rain" water.

The results, extrapolated to hailstone growth give support to the concept of the water accumulation zone in thunderstorms expressd by Sulakvelidze et al. (1967). These authors claimed that liquid water contents up to 30 gm^{-3} were found in the form of large drops above the region of hail growth. More recently, Federer and Walvogel (1978) have also shown evidence for a big drop zone as postulated by Voronov (1973). In this case, the large drop zones were not associated with large liquid water contents.

6. CONCLUSIONS

Experiments on the icing of slowly rotating rotating (0.5Hz) cylinders (diameter 1.9cm) at air temperatures of -5, -10 and $-18^{o}C$, with relative air speeds of 18m/s and liquid water contents between 9 and $42gm^{-3}$ showed that:

1. Icing cylinders (but also hailstones) are efficient and instantaneous converters of cloud droplets to rain drops through shedding and other losses of already accreted water.

2. The shedding mechanism is dependent on the air flow around the cylinder, the heat and mass transfer (which helps to determine the freezing rate), the cylinder rotation, and the mobility of the water skin within the air pressure field at the cylinder's surface.

3. The observed shed drops had sizes between 0.4 and 3.6mm. Their production rate can be parameterized using a Gamma function, with the peak of the spectrum at a diameter of 1.22mm and the mean volume diameter at 1.4mm.

4. It was shown in Part I that net collection efficiencies are very often much lower than 50% at liquid water contents which are reasonable from the point of view of atmospheric icing.

5. The liquid water content above the cylinder (i.e. on the "down"stream-side) may be larger than that below due to the lower absolute vertical velocity of the large drops as compared to the cloud droplets (which move essentially at the speed of the air). This factor is particularly important at warmer temperatures close to the freezing point (warmer than $-10^{o}C$).

6. Extrapolating to growing hailstones it can also be expected that large drops with similar size spectra are shed by rotating or gyrating hydrometeors. These drops can then form a zone of big drops in a hailstorm above the hail growth region.

ACKNOWLEDGEMENTS. This work was sponsored by the National Science and Engineering Council of Canada.

REFERENCES FOR PARTS I AND II

Carras, J.N., and W.C. Macklin, 1973: The shedding of accreted water during hailstone growth. Quart. J. Roy. Meteor. Soc.,99, 639-648.

Federer, B. and A. Walvogel, 1978: Time-resolved hailstone analyses and radar structure of Swiss storms. Quart. J. Roy. Meteor. Soc., 104, 69-90.

Joe, P.I., R. List, P.R. Kry, M.R. de Quervain, P.Y.K. Lui, P.W. Stagg, J.D. McTaggart-Cowan, E.P. Lozowski, M.C. Steiner, J. von Niederhausern, R.E. Stewart, E. Freire, and G. Lesins, 1976: Loss of accreted water from growing hailstones. Proceedings VIIth Intern. Conf. Cloud Physics, July 26-30, Boulder, Colorado, 264-269.

List, R., 1962: Zur Thermodynamik von Schwammeisansaetzen an langsam rotierenden Zylindern. Winterbericht, Eidg. Institut fuer Schnee- und Lawinenforschung, 25, 106-109.

------, 1977: Ice accretions on structures. J. Glaciology, 81, 451-465.

------, 1979: The cloud physics dilemma. Rivista Italiana Geofisica Scienze Affini, 5, Bossolasco-Anniversary issue, 131-138.

------, P.I. Joe, G. Lesins, P.R. Kry, M.R. de Quervain, J.D. McTaggart-Cowan, P.W. Stagg, E.P. Lozowski, E. Freire, R.E. Stewart, C.G. List, M.C. Steiner, J. von Niederhausern, 1976: On the variation of the collection efficiency of icing cylinders, Proceedings VIIth Intern. Conf. Cloud Physics, July 26-30, Boulder, Colorado, 233-239.

------, G.B. Lesins, P.I. Joe, 1980: Cylinder icing, Part I: Dependence of net collection rate and sponginess rotation rate, Proceedings VIII Intern. Conf. Cloud Physics, July 21-25, Clermont-Ferrand.

Ludlam, F.H., 1951: The heat economy of a rimed cylinder. Quart. J. Roy. Meteor. Soc., 77, 663-666.

Murray, W.A., and R. List, 1972: Freezing of water drops freely suspended in a vertical wind tunnel. J. Glaciology, 11, 415-429.

Pruppacher, H.R. and J.D. Klett, 1978; The microphysics of clouds and precipitation, D. Reidel Publishing Co., Dordreult, Holland.

Roos, D.S., and H.-D.R. Pum, 1974: Sponginess in ice grown by accretion. Quart. J. Roy. Meteor. Soc., 100, 640-657.

Sulakvelidze, G.K., N.Sh. Bibilashvili and V.F. Lapcheva, 1967: Formation of precipitation and modification of hail processes. Gichrometeoizdat, Leningrad, 1965, Israel Program Scientific Translations, Jerusalem.

Voronov, G.S., 1973: Some results of radar investigations of convective cloud evolution. Meteorologia i Gidrologia, 6, 46-55.

A STUDY OF THE INITIAL STAGE OF THE ACCRETION PROCESS

O.B.Nasello (x), L.Levi (xx), E.M.de Achával and E.A.Ceppi (x)

Instituto de Física de la Atmósfera
Servicio Meteorológico Nacional
Buenos Aires – ARGENTINA

1. INTRODUCTION

The crystal structure of supercooled droplets frozen after impinging at low speed on an ice substrate has been studied by several authors in order to obtain information which could be useful for the interpretation of the structure of wind tunnel ice accretions and of natural hailstones.

Hallett (1964) and Rye and Macklin (1975) studied the phenomenon on substrates with different orientations. Rye and Macklin showed that, for a given droplet temperature, T_a, and a substrate orientation the droplets froze, with very few exceptions, following the substrate orientation down to a transition substrate temperature T_s^*, where a droplet has a high probability ($P > 0.5$) of haying a crystallographic orientation different from that of the substrate. They observed that, the values of T_s^* depend on T_a as well as on the substrate orientation and suggested that, a correspondence could exist between the values of T_s^* and the substrate temperature range, for which crystals forming wind tunnel ice accretions were observed to change from large to small sizes.

Levi et al. (1980) noted that, T_a and T_s played a similar role in the studied phenomenon, so that, for constant T_s a transition air temperature T_a^* could also be defined. They consequently carried out a series of experiments where droplets of 75 μm and 135 μm diameter were made to collide, at their terminal fall speed, with a prismatic or a basal substrate. They studied P as a function of $T = T_a = T_s$ and found values of T^* which depend on the droplet diameters and on the substrate orientation. Furthermore, these authors observed that, for $T < T^*$ new crystals were formed in a few droplets and that, among these, the prevailing orientations were with their c-axes at small angle to the substrate surface, both for the basal and prismatic substrate. For $T > T^*$ the droplets became polycrystalline and their orientations could not be revealed. As a complement to these experiments, a few accretions without ventilation were also grown by the same authors. It was found that, at $T_a = -7^oC$ and $T_s = -3^oC$, accretions about 5 mm thick followed the substrate orientation, whether basal or prismatic, with the exception of a few small crystals imbedded in the prevailing single crystal. These were mainly oriented at random and their total cross section was less than 5 o/o of the accretion surface.

Levi et al. concluded that the behaviour observed for single droplets colliding at low speed with the ice substrate, is in accordance with the results obtained for ice accretions grown without ventilation. However, these results may not be used to explain the very different structure shown by dry growth wind tunnel accretions. Actually, the latter usually consist of crystals growing with their c-axis at large angle to the accretion surface. This orientation is established along the first droplet layers, regardless of the nature of the substrate and, when this is ice, of its orientation, even at T_a and T_s values well above the transition temperatures (Levi and Aufdermaur, 1970).

Considering that these results could be related to the higher speed of the droplet collisions with the substrate, in the present work new experiments were carried out, where droplets were made to collide at 10 m/sec with prismatic and basal ice surfaces. The crystal structure of single and overlapping droplets, frozen on the substrate, was analysed. As a complement, a few experiments without ventilation were also performed.

2. EXPERIMENTAL

The experiments were carried out in a vertical square section cold room, 160 cm high and 30 cm side.

Two droplet generators were used, a spray nozzle giving a droplet spectrum of 84 ± 30 μm medium volume diameter and a vibrating needle device (Mason et al.,1963), which provided several streams of approximately uniform droplets, ranging from 50 μm to 200 μm diameter.

For experiments without ventilation, droplets of destilled water, generated near the top of the cold room, were received on an ice substrate placed about 10 cm above the cold room bottom.

Experiments with ventilation were performed in a small wind tunnel, 5 cm diameter, assembled in the cold room. Fig.1 shows the general layout of the apparatus. The droplets falling in the precooling section at a speed of about 1 m/sec reached, within 3 o/o, the surrounding air temperature. In the working section, air was drawn at 10 m/sec speed. The air inlet was roughly exponential to reduce turbulence.

When ventilation was not introduced, the cold room temperature could be decreased down to -30^oC but with the tunnel in operation, the minimun air temperature in the precooling zone was -15^oC, as, in these conditions some heat exchange with the surrounding air could not be avoided.

(x) Instituto de Matemática, Astronomía y Física — Universidad Nacional de Córdoba and Consejo Nacional de Investigaciones Científicas y Técnicas (CONICET).

(xx) Comisión Nacional de Energía Atómica — Fellow of the CONICET.

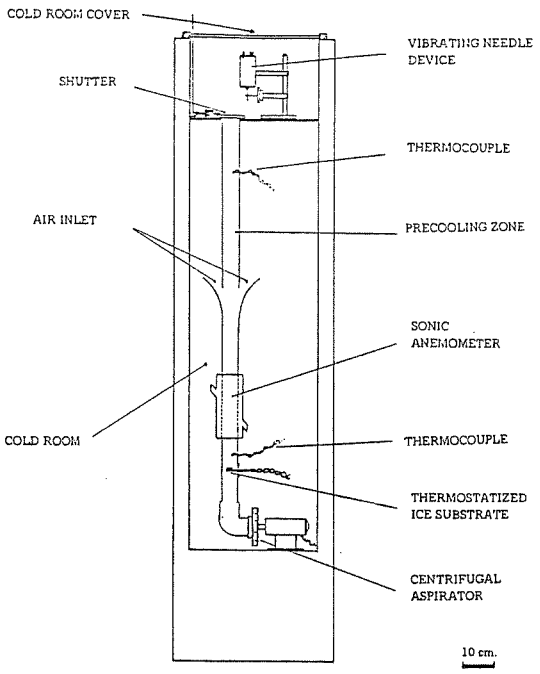

Figure 1: Schematic wind tunnel arrangement.

Before beginning the experiments, the cold room cover was briefly opened and the vibrating needle device, with the reservoir filled with destilled water at 0°C, was introduced in the upper cold room compartment. After checking that, one of the droplet streams was directed toward the tunnel mouth, the shutter was opened from the outside and the experiment was initiated. It was not possible, during this operation, to select the most convenient droplet stream, so that the experiments were not all performed with the same droplet diameter.

The ice substrate was, for the experiments performed both with and without ventilation, an ice sheet 2 to 5 mm thick and 1.5 cm wide, cut from a single crystal, so that basal or prism surfaces were obtained. A small electronically controlled heater was used to keep the substrate temperature at the desired value.

The crystal structure of the frozen drops was revealed by using two succesive layers of 2 o/o and 4 o/o solutions of formvar in 1–2 Dichloroethane and allowing them to dry under controlled conditions of humidity and temperature. The replicas obtained in this way showed thermal pits and grain boundary grooves formed by selective evaporation of the ice substrate, as well as, chemical pits formed by the etching effects of the formvar solution. These chemical pits gave important information in the present case, where the orientation of tiny new crystals, formed in frozen droplets, ussually could not be revealed by rather large thermal pits. Actually, striations parallel to the [000$\bar{1}$] direction were formed by chemical etching on approximately prism faces, while hexagonal pits appeared on planes almost normal to the c-axis. A wide range of differents features were observed on surfaces other than the above mentioned, not all allowing for the identification of the plane.

3. RESULTS

3.1 Prismatic Substrate

a) Crystal Structure of Single Frozen Droplets

The air and substrate temperature T_a, T_S, corresponding to wind tunnel experiments where single frozen droplets could be analysed separately, are given in Table 1. On the third line of the table, N represents the number of droplets which could be observed. Table 1 shows that, in most cases, the temperature conditions which may exist when accretions grow in wind tunnels were simulated by keeping $T_S > T_a$.

TABLE 1

T_a (°C)	−3.5	−6.5	−10.0	−11.5	−12.5	−13.0	−14.5
T_S (°C)	−8.5	−11.5	−6.5	−11.0	−6.5	−4.5	−6.5
N	>100	50	>100	>100	30	>100	50

The analysis of the crystal structure of frozen droplets showed that these usually followed the substrate orientation. Only for the experiment corresponding to T_S= -6.5°C and T_a = - 10°C, two droplets were frozen as new crystals, their c-axes nearly normal to the substrate surface.

It may be concluded that, for T_a > - 15°C and different values of T_S, droplets with diameter D ⩽ 200 μm, that freeze separately on a prismatic substrate, have a very low probability of inducing the formation of new crystals, even at the impact velocity of about 10 m/sec used in the present experiments. Since the (T_a, T_S) pairs used were in all cases higher than the transition temperatures found for droplets of similar diameters, frozen on similar ice substrates without ventilation, (Rye and Macklin, 1975 and Levi et al., 1980), it may be concluded that in the present conditions, the larger impact speed did not substantially change the droplet freezing behaviour.

b) Crystal Structure of Overlapping Droplets

The values of T_a and T_S, for experiments performed on a prismatic substrate by injecting droplets in the tunnel during 3 minutes are given in Table 2.

TABLE 2

T_a (°C)	−9.0	−9.0	−9.0	−11.0	−11.5	−13.5
T_S (°C)	−2.5	−4.5	−6.5	−11.0	− 4.5	− 4.5

It may be noted that in this case the temperature T_a ranged in the narrow interval of −9°C to −13.5°C, while T_S varied from −2.5°C down to −11°C.

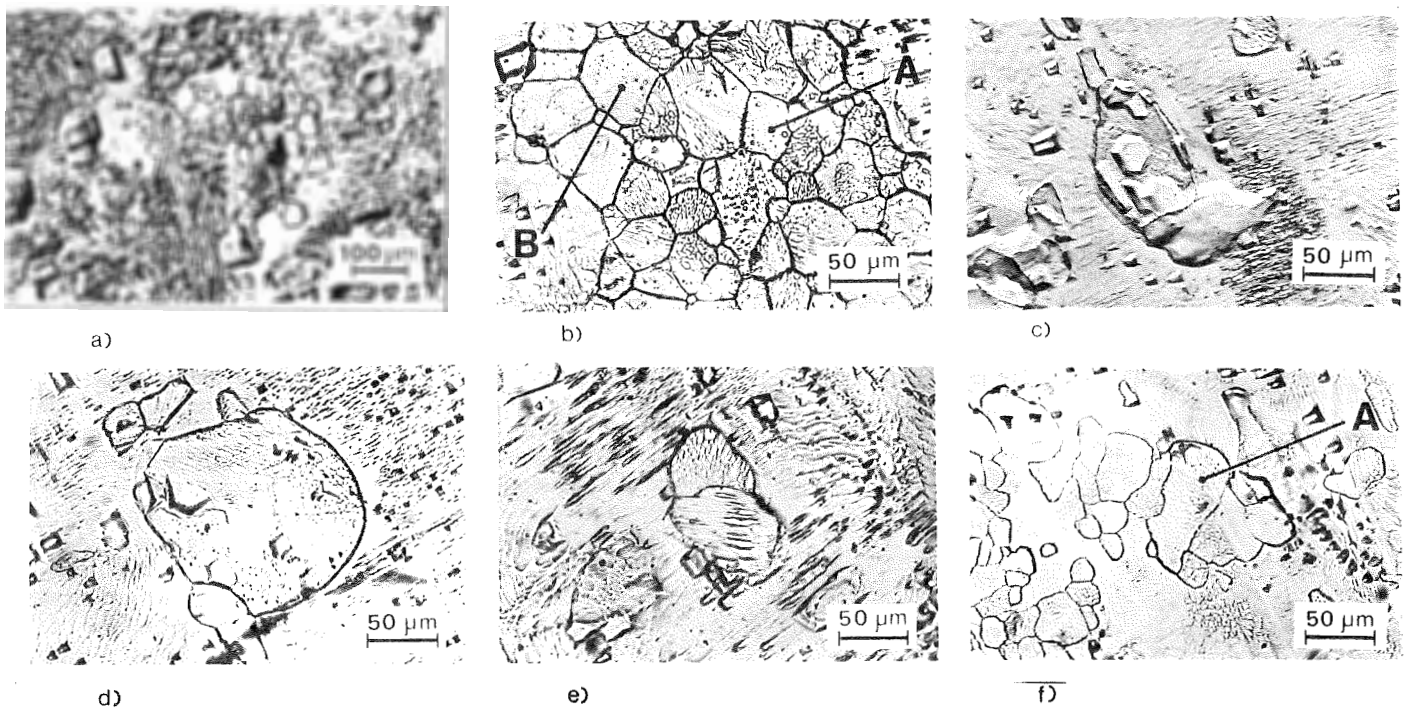

Figure 2: Polycrystalline structures in droplets frozen on the prismatic substrate. A, B basal crystals. a) and b) $T_a = -9^oC$, $T_s = -4.5^oC$; c) $T_a = -11.5^oC$, $T_s = -4.5^oC$; d) $T_a = -9^oC$, $T_s = -2.5^oC$; e) $T_a = -11^oC$, $T_s = -11^oC$; f) $T_a = -11.5^oC$, $T_s = -4,5^oC$.

For the injection time used, the droplets impinging on the substrate could overlap or freeze superimposed to each other, forming a nearly continuous layer on limited zones of the substrate. In these conditions, crystals with new orientations, usually a few microns in size, were observed throughout the studied temperature range. Some examples of the results obtained are given in Fig. 2.

Fig. 2a shows a very polycrystalline structure, apparently formed in two overlapping droplets, surrounds by an area that presents the substrate orientation. Fig. 2b shows another polycrystalline structure formed in a droplet layer frozen on the prismatic substrate. The chemical pits, appearing on most crystals, suggest a tendency of the crystals c-axes to be inclined to the substrate surface. Some crystals, such as those marked A and B, present a nearly basal orientations. Fig. 2c and 2d are examples of new crystals with a nearly basal orientation, clearly shown by the hexagonal thermal pits. In the Fig. 2e other orientations appear, one of them with its c-axis parallel to the substrate surface, but at large angle to the substrate c-axis. Fig. 2f was obtained from an experiment where $T_a \cong T_s \cong -11^oC$; in this case the substrate appeared slightly rough, probably because it was covered by a nearly continuous droplet layer, however, the grain boundaries of some new crystals may be clearly seen.

A few experiments were also carried out on the prismatic substrate, without ventilation at (T_a, T_s) : (−19°C, −3°C), (−19°C, −4°C) and (−23°C, −6°C). In these cases it was found that, by operating the spreading nozzle during about 3 minutes, the ice substrate appeared covered by a continuous layer of partially superimposed droplets, the orientations of which always followed that of the substrate. These results, considered together with those previously obtained by Levi et al. (1980) for thin accretions grown without ventilation, indicate that the formation of the polycrystalline structures shown in Fig. 2, do not occur when droplets collide at low speed with a prismatic substrate, even though they may interact during the freezing process.

3.2 Basal Substrate

The conditions for the experiments performed using basal substrate are given in Table 3.

TABLE 3

T_a(°C)	−5.0	−8.5	−10.5	−11.0	−11.5	−11.5	−12.5
T_s(°C)	−6.5	−4.5	−3.5	−4.5	−11.0	−11.0	−13.0

On this substrate the experiments where single or overlapping droplets were studied gave similar results, showing that, the droplets followed the substrate orientation. Exceptionally, a few small isolated crystals with different orientations were observed. It is interesting to note that this behaviour was also followed by droplets of 200 μm diameter, even at the minimum temperature used in the present experiments, i.e. $T \cong T_a \cong T_s = -13^oC$. This temperature is lower than the transition temperature corresponding to droplets of this size colliding at low speed with this substrate orientation. According to Levi et al. (1980), this temperature would be $T = -11^oC$.

To confirm the fact that an increase in the impact velocity of droplets with the substrate results in an increase of the probability that the droplets follow the basal substrate orientation, two experiments at $T_a = T_s = -13^oC$ were performed, using the same droplet spectrum, both with and without ventilation. It was found that all the droplets colliding at 10 m/sec with the substrate followed the substrate orientation, whereas the droplets impinging at their free fall speed were polycrystalline. This different behaviour is shown in Fig. 3a and b respectivelly. It may be seen that several new crystals were formed in the droplet of Fig. 3b, while the droplet in the Fig. 3a is more spread and oriented as the substrate.

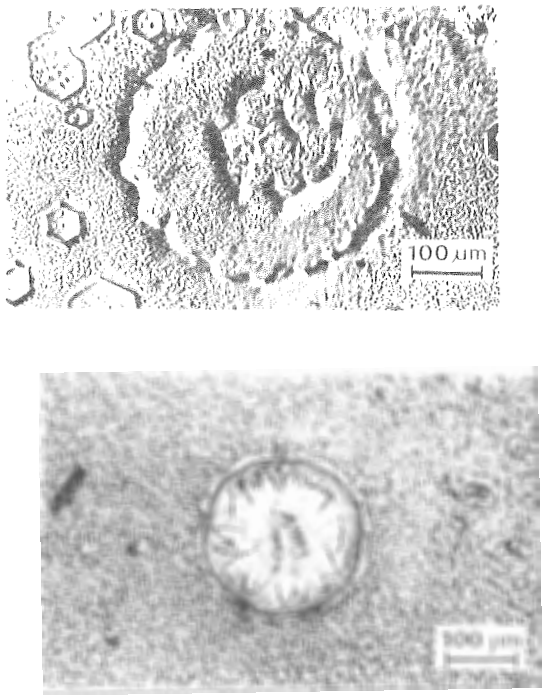

Figure 3: Crystal structure of droplets of 200 µm diameter frozen on the basal substrate at $T_a \cong T_s \cong -13^oC$ a) impact droplet speed: 10 m/sec; b) Terminal free fall collision.

4. DISCUSSION AND CONCLUSIONS

The freezing process for droplets colliding at low speed with ice substrates has been previously discussed by Hallett (1964) and Levi et al. (1980). According to Levi et al. approximately basal dendrites, following a prismatic substrate orientation, would rapidly grow outwards in the supercooled droplet, hindering the development of those new crystals which could be assumed to have the largest nucleation probability, i.e. those oriented with their c-axes normal to the substrate c-axis. On the contrary, a basal substrate could only advance slower in the droplets, since the process consists, in this case, of the succesive growth of ice layers parallel to the substrate surface. Consecuently, any new crystal nucleated with its c-axis parallel to the surface i.e. normal to the substrate c-axis, would have a large chance to develop in the droplets by dendrites growth. Due to these mechanisms the transition temperature for a prismatic substrate would be lower than for a basal one.

The present results obtained for droplets colliding at 10 m/sec with an ice substrate may now be considered to indicate that some steps of the freezing process are modified by the increase of the impact speed. This different behaviour could possibly be related to the fact that the water layer, formed by the droplets that spread on the substrate would became thinner with the increase of the impact speed. Actually, in this case, it could be assumed that short dendrites, approximately normal to the substrate surface, could not favourably compete with laterally advancing crystals, which would determined a nearly complete solidification of the thin water layer.

Thus, on the prismatic substrate, new embryos could develop and determine the formation of the observed polycrystalline structures. On the contrary, in the case of the basal substrate, the epitaxial layer as it advances on the substrate may be assumed to hinder the development of any new crystals.

It must be noted, however, that the polycrystalline structures found on the prismatic substrate were only observed when many droplets froze, partially superimposed, after impinging on the substrate at 10 m/sec. In order to explain this behaviour, it could be assumed that, under the said conditions, the droplet spreading would increase, not only due to the impact velocity, but also due to a possible change in the microstructure of the substrate surface. This change could be associated with local temperature variations or with the presence of a liquid film on the surface of the newly frozen droplets.

The present results may now be applied to explain the structure of dry regime wind tunnel accretions grown at air temperatures near those of the present experiments ($T_a \cong -10^oC$, Levi and Aufdermaur, 1970). Actually, when these accretions begin on a non conveniently oriented ice substrate (for instance on a prism surface), new orientations may be formed inmediately in agreement with the results in Fig. 2. This figure shows that, among these orientations, some crystals are formed with their c-axis approximately normal to the surface. Now, according to the results in Fig. 3, this special orientation would tend to continue in successive droplets, probably advancing laterally at the same time (Rye and Macklin, 1973). Due to this process, after the formation of a few droplet layers, crystals with their c-axes approximately radial (basal orientation) would prevail in the cylindrical accretions forming large grains, because, new crystals rarely form once the preferential orientation is established.

It may be interesting to note that, for droplet impact speeds ranging from a few cm/sec to 10 m/sec, substantial variations in the accretion structure may be expected to occur. This fact should be taken into account when the structure of small hailstone embryos, that may collide at relatively low speeds with the droplets, is studied.

Acknowledgement

The authors are indebted to J.M.Caranti for fundamental contributions in designing the wind tunnel. O.B.Nasello, L.Levi and E.A.Ceppi are gratefully to the CONICET for the finantial support.

REFERENCES

HALLET, J., 1964: Experimental studies of the crystallization of supercooled water. J.Atmos.Sci. 21, 671-677.

LEVI, L. and AUFDERMAUR, A.N., 1970: Crystallographic orientation and crystal size in cylindrical accretions of ice. J.Atmos.Sci. 27, 443-452.

LEVI, L., NASELLO, O.B. and ACHAVAL, E.M. de, 1980: Crystal structure of droplets frozen on an ice substrate. J.Crystal Growth. In press.

MASON, B.J., JAYARATNE, O.W. and WOODS, J.D., 1963: An improved vibrating capillary device for producing uniform water droplets of 15 to 500 µm radius. J.Scient.Instrum. 40.

RYE, P.J. and MACKLIN, W.C., 1973: Interpretation of crystallographic orientations in accreted ice. J.Atmos. Sci. 27, 1421-1426.

RYE, P.J. and MACKLIN, W.C., 1975: Crystal size in accreted ice. Quart.J.R.Met.Soc. 101, 207-215.

HELICOPTER ROTOR BLADE ICING: A NUMERICAL SIMULATION

M.M. Oleskiw and E.P. Lozowski

University of Alberta
Edmonton, CANADA

1. INTRODUCTION

Next to engine intake icing, the icing of the main rotor blade represents the most serious threat to the safe operation of helicopters in supercooled water clouds (Stallabrass and Lozowski, 1978). Ice accretion on the main rotor increases its drag, thereby necessitating an increase in engine power to maintain the same lift and altitude. In addition, asymmetrical shedding of accreted ice can cause imbalance of the rotors, strong vibrations, and severe stresses on the blades and control hub.

The most promising current method of icing control on the main rotor is electro-thermal de-icing, in which the leading edge of the blade is heated in a periodic fashion in order to weaken the adhesive bond between the accumulated ice and the blade, and to allow aerodynamic forces to cause the ice to break away. Because of the limited power available on helicopters for this purpose, the design of such systems needs to be optimized very carefully. Wind tunnel and in-flight testing are absolutely necessary. However, an important adjunct to the experimental testing is computer modelling of the icing and de-icing process. This paper concerns itself with the development of a computer model for airfoil icing. Although developed for the purpose of investigating helicopter rotor icing, the model is of general applicability to two-dimensional airfoils, or in fact to any longitudinally symmetric body. This paper concerns itself principally with the methodology of the model. Because of space limitations, only a selection of results can be presented.

2. METHODOLOGY

The modelling process for airfoil icing can be conveniently broken down into two aspects, first the aerodynamics of the impingement of water droplets on the airfoil, and secondly the thermodynamics of the resulting accretion. In the present paper we deal exclusively with the first aspect. This is sufficient for the investigation of dry accretion; that is, accretion under ambient conditions in which all of the impinging water freezes at the point of impact. The wet accretion process, in which some impacting water remains unfrozen and runs back along the airfoil, will be considered in subsequent papers. Wet accretion on cylinders has been treated by Cansdale and McNaughtan (1977), and by Lozowski et al. (1979).

In our approach towards simulating the dry accretion process, we have broken down the numerical procedure into the following steps:

1. to determine the potential flow field around an airfoil of arbitrary shape.
2. to determine the incompressible velocity field around the airfoil.
3. to calculate the droplet trajectories within the airstream using the steady-state droplet drag coefficient.
4. to derive collision efficiencies for the airfoil as a function of surface position, airspeed, droplet size, and angle of attack.
5. to calculate the spatial distribution of icing during a short time interval assuming dry accretion.
6. to calculate the new airfoil shape as modified by the ice accretion.
7. to repeat steps 1 to 6 as often as desired and thereby determine the growth of the dry accretion as a function of time.
8. to improve the calculations through the incorporation of compressibility effects on the airstream, acceleration effects on the droplet drag, and the effect of the airfoil boundary layer on the droplet trajectories.

In the present paper, we will describe the development of the model up to step four.

3. POTENTIAL FLOW ABOUT AN ARBITRARY AIRFOIL

Several approaches are available for calculating the potential flow about airfoils. While the conformal transformation method of Theodorsen and Garrick (1932) may be adequate for determining the potential flow about the original airfoil section, it would not be expected to give a good estimate of the flow around an airfoil whose shape has been substantially altered by the ice accretion. Hess and Smith (1967) have developed a technique for potential flow estimation, which makes use of a surface distribution of sources, sinks and vortices along the airfoil. This method, however, is expensive to compute and rather sensitive to the specified distribution of airfoil coordinates. The method used in the present study was developed by Kennedy and Marsden (1976). It employs a vorticity distribution along the airfoil surface, coupled with the boundary condition that the stream function is a constant on the surface, in order to obtain the potential flow. For comparable accuracy, this method requires far less computer time than that of Hess and Smith.

In the Kennedy-Marsden method, the airfoil surface is divided into N line segments, S_j,

each with a constant vorticity density $\gamma(S_j)$. The stream function $\psi(x,y)$ at any point external to the airfoil P(x,y) is then given by:

$$\psi(x,y) = y\cos\alpha - x\sin\alpha - \frac{1}{2\pi}\sum_{j=1}^{N}\int_{S_j}\gamma(S_j)\ln r(P,S_j)\,dS_j \quad (1)$$

where α is the angle of attack of the airfoil, and $r(P,S_j)$ is the distance between P and a point on the element S_j. The accuracy of this method was tested by comparing its predicted stream function for a cylinder with the analytical solution. Using fifty surface elements, the stream function error is at most 0.1% near the cylinder, and it falls below 0.01% at distances exceeding about four diameters.

4. THE DROPLET TRAJECTORY EQUATION

Pearcey and Hill (1956) have expressed the complete equation of motion of a droplet in accelerated flow as:

$$\frac{d\bar{X}_d}{dt} = \bar{V}_d \quad (2)$$

$$\frac{d\bar{V}_d}{dt} = \frac{2(\rho_d - \rho_a)}{(2\rho_d + \rho_a)}\vec{g} - \frac{3C_D\,\rho_a}{4r_d(2\rho_d + \rho_a)}|\bar{V}_d-\bar{V}_a|(\bar{V}_d-\bar{V}_a) - \frac{9\rho_a}{(2\rho_d + \rho_a)r_d}\sqrt{\frac{\nu_a}{\pi}}\int_{-\infty}^{t}\frac{d\bar{V}_d}{d\tau}\frac{d\tau}{\sqrt{t-\tau}} \quad (3)$$

where $\bar{X}_d(x_d,y_d)$ is the droplet position vector

$\bar{V}_d(u_d,v_d)$ is the droplet velocity vector

$\bar{g}$ is the gravitational acceleration

C_D is the steady-state droplet drag coefficient

ρ_a is the air density

ρ_d is the droplet density

r_d is the droplet radius

ν_a is the kinematic viscosity of the air

and t is the time

The first term on the right-hand-side of (3) combines the buoyancy of the droplet in air and the gravitational acceleration. The second term is the steady viscous drag, and the third (referred to as the history term) is related to the finite rate of vorticity diffusion from the surface of the droplet in accelerated motion. This equation implicitly incorporates the droplet induced mass, resulting from the momentum it imparts to the air as it accelerates.

The results presented in the present work have been calculated using (3) without the history term. However, based on an analysis by Crowe et al. (1963) we estimate that for the application to rotor blade icing it may be significant. Consequently, we are presently incorporating the history term into the model. This is in contrast to the calculations of Norment (1976). For droplet flow about aircraft fuselages, he found that the history term could be neglected.

5. THE COMPUTATIONAL PROCEDURE FOR TRAJECTORIES

The air velocity components may be calculated at any point along the droplet trajectory by differentiating the stream function using finite differences. This is done with a space increment equal to the diameter of the droplet, which gives essentially an average air velocity over the droplet. Because of the economy with which ψ may be calculated using the Kennedy-Marsden approach, it is evaluated as needed at precise points along the trajectory of the droplet, rather than by interpolating among values of ψ at a fixed array of grid points.

The four component trajectory equations have been numerically integrated using the fourth-order Runge-Kutta-Fehlberg method, which permits the time step to be continuously adjusted for optimum accuracy and speed of computation (Burden et al., 1978; Lapidus and Seinfeld, 1971).

The droplet is taken to impinge upon the airfoil, if any part of it contacts the airfoil surface. Thus close to the airfoil, the finite size of the droplet must be taken into account. This is particularly true for those trajectories just within the envelope of colliding trajectories, where the angle of incidence from the normal to the airfoil surface is large.

6. THE CALCULATION OF COLLISION EFFICIENCIES

Given a series of collision points, the distances along the airfoil surface from the nose to the collision location, L_i, are determined by approximating the surface with at least 200 line segments. The initial release distances Y_i from the dividing streamline are then plotted against the corresponding L_i. A cubic spline curve is used to interpolate between the data points, with the spline constrained to have a zero first derivative at the end points.

Using the coefficients calculated for the spline, the collision efficiency E is calculated as a function of the distance along the airfoil surface from the nose,

$$E(L) = \frac{dY}{dL} \quad (4)$$

7. RESULTS

An example of a series of trajectory calculations for droplets of 20 μm diameter impacting a NACA 0015 airfoil with chord length 0.2127 m, angle of attack 8°, and a free stream velocity of 61 m s^{-1}, is shown in Fig. 1. The envelope of collision trajectories extends 2 % of the chord length back from the nose on the upper surface, and 30% on the lower surface.

In order to compare the predictions of the present model with a standard reference, the collision efficiency for a cylinder of diameter 2.54 cm at a velocity of 30.5 m s^{-1} was calculated. Fig. 2 compares the result (for 20 μm diameter droplets) with the results of Langmuir and Blodgett (1946) as approximated by Lozowski et al. (1979). The present results indicate an overall collision efficiency of 56.4% as opposed to the Langmuir-Blodgett value of 50%, the majority of the difference occurring at relatively small distances from the axis of symmetry of the flow.

Fig. 3 displays the collision efficiency of a NACA 0015 airfoil of length 0.2127 m of a free stream velocity of 61 m s^{-1}. The droplet diameter is again 20 μm, and the angle of attack is 0°. The overall collision efficiency is 40.4%. Fig. 4 is the same as Fig. 3, except that the angle of attack is 8°, which corresponds to the trajectories of Fig. 1. The overall collision efficiency has increased to 52.4%, and the maximum has shifted to about 0.015 chord lengths below the nose.

8. CONCLUSIONS

A numerical model has been developed which calculates the trajectories of droplets in the potential flow field about an airfoil of arbitrary shape. Using the set of resulting collision locations, the airfoil collision efficiency can be determined as a function of airfoil type, surface position, chord length, air speed, angle of attack, and droplet diameter. Preliminary results indicate acceptable agreement with previous work. Efforts are continuing to incorporate a non-steady-state droplet drag coefficient, as well as to extend the study into aspects of the time-dependent accretion processes for helicopter rotor blades.

9. ACKNOWLEDGEMENTS

The authors wish to thank Dr. D.J. Marsden for his enthusiastic advice regarding the adaptation of the surface vorticity method of potential airflow calculation for the present study. Thanks are also due to Mrs. Laura Smith who obligingly typed this manuscript at short notice. This work was supported in its early stages by the National Research Council of Canada. The application to helicopter icing is funded by the U.S. Army Cold Regions Research and Engineering Laboratory under contract DACA89-79-C-0004.

10. REFERENCES

Burden, R.L., J.D. Faires, and A.C. Reynolds, 1978: Numerical Analysis. Prindle, Weber & Schmidt, 579 pp.

Cansdale, J.T. and I.I. McNaughtan, 1977: Calculation of surface temperature and accretion rate in a mixed water droplet/ice crystal cloud. Royal Aircraft Establishment Tech. Report #77090, 24 pp.

Crowe, C.T., J.A. Nicholls, and R.B. Morrison, 1963: Drag coefficients of inert and burning particles accelerating in gas streams. Ninth Symp. on Combustion, Academic Press, 395-405.

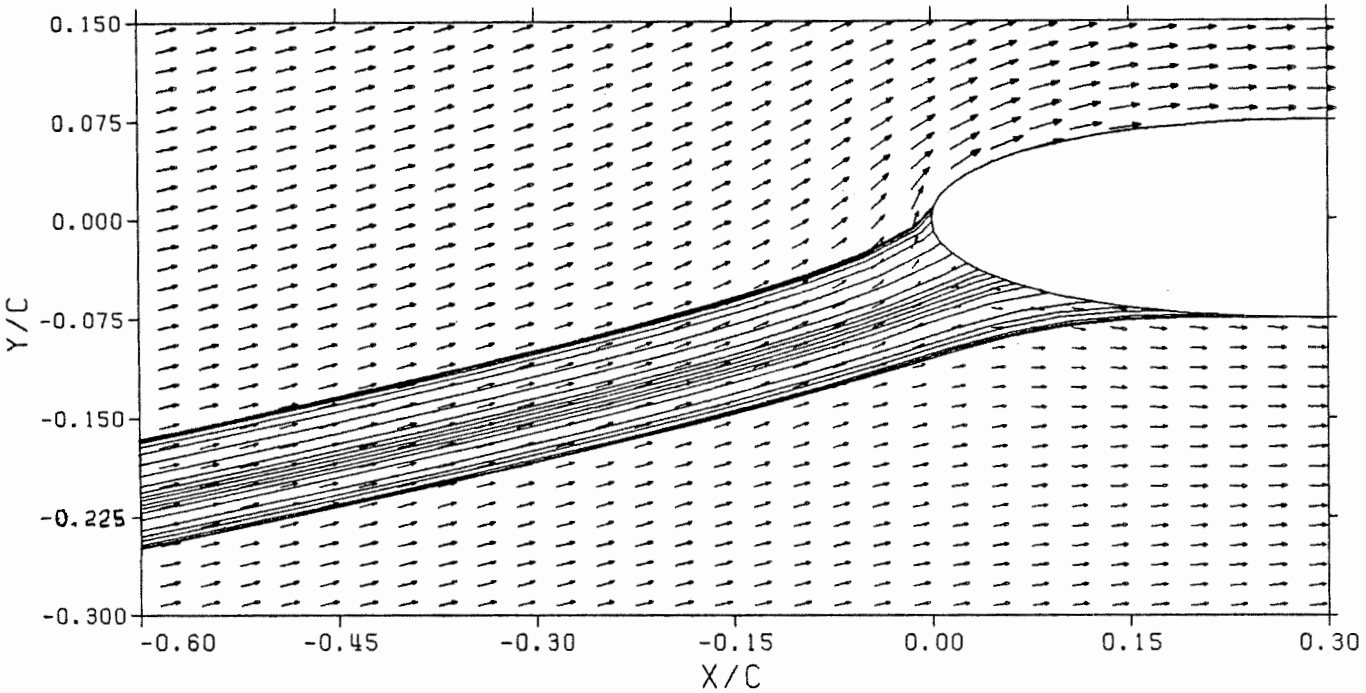

Fig. 1. Droplet trajectories for a NACA 0015 airfoil at 8° attack. Arrows represent air velocity. Conditions in text.

Hess, J.L. and A.M.O. Smith, 1967: Calculation of potential flow about arbitrary bodies. Progress in Aeronautical Sci., 8.

Kennedy, J.L. and D.J. Marsden, 1976: Potential flow velocity distributions on multicomponent airfoil sections. Can. Aero. and Space Jour., 22, 243-256.

Langmuir, I., and K.B. Blodgett, 1946: A mathematical investigation of water droplet trajectories. AAF Tech. Rep. #5418, 47 pp.

Lapidus, L. and J.H. Seinfeld, 1971: Numerical Solution of Ordinary Differential Equations, Academic Press, 299 pp.

Lozowski, E.P., J.R. Stallabrass, and P.F. Hearty, 1979: The icing of an unheated non-rotating cylinder in liquid water droplet-ice crystal clouds. National Research Council of Canada Report LTR-LT-96, 109 pp.

Norment, H.G., 1976: Effects of airplane flowfields on hydrometeor concentration measurements. Proceedings, Int'l. Conf. on Cloud Phys., July 1976, 591-596.

Pearcey, T. and G.W. Hill, 1956: The accelerated motion of droplets and bubbles. Aust. Jour. of Phys., 9, 19-30.

Stallabrass, J.R. and E.P. Lozowski, 1978: Ice shapes on cylinders and rotor blades. Paper presented at NATO Panel X Symp. on Helicopter Icing, London, November, 1978.

Theodorsen, T. and I.E. Garrick, 1932: General potential theory of arbitrary wing sections. NACA Report #452.

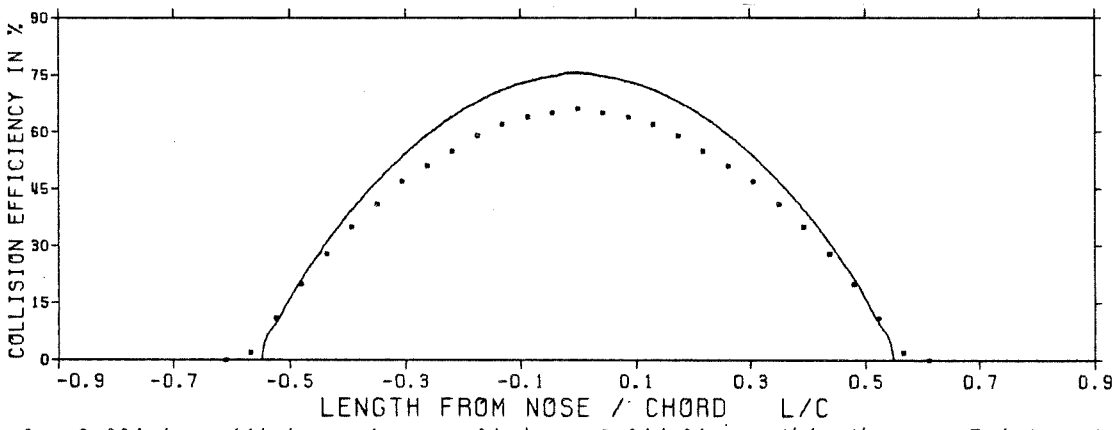

Fig. 2. Collision efficiency for a cylinder. Solid line - this theory. Points - Langmuir and Blodgett. Conditions in text.

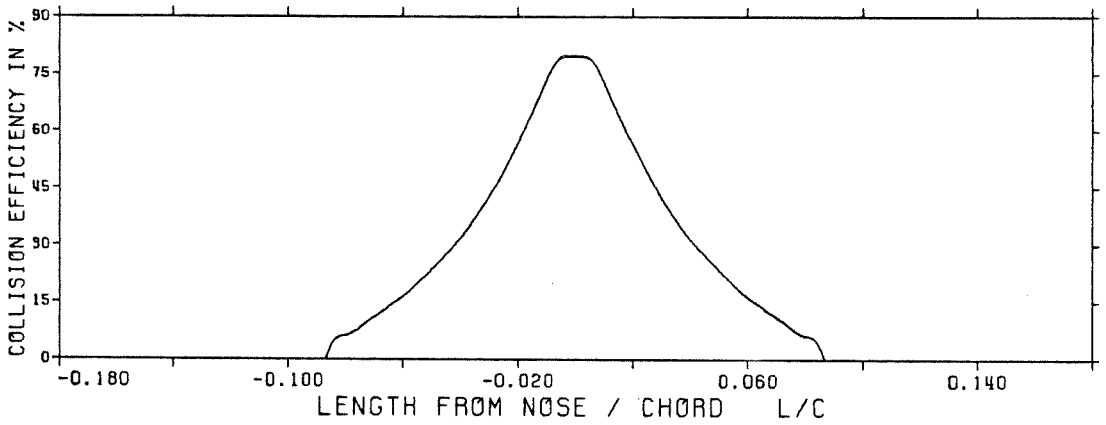

Fig. 3. Collision efficiency for a NACA 0015 airfoil at 0° attack. Conditions in text.

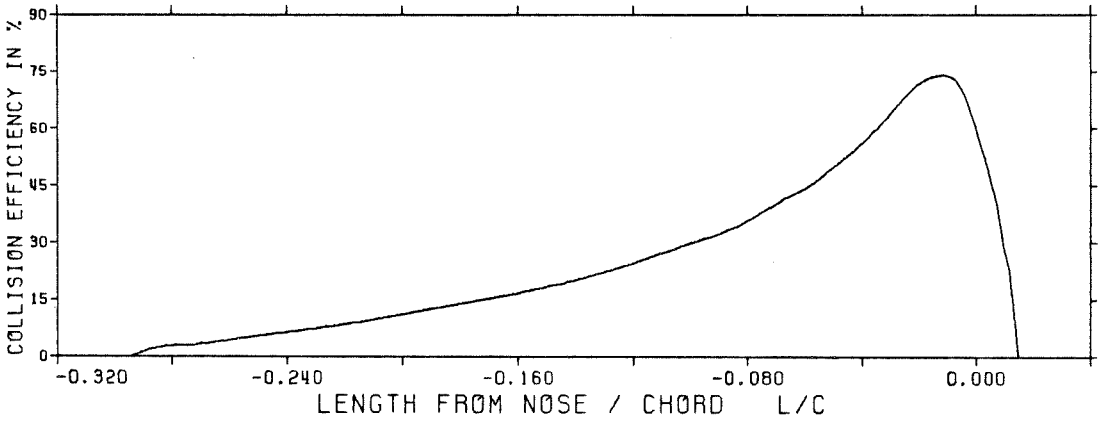

Fig. 4. Collision efficiency for a NACA 0015 airfoil at 8° attack. Conditions in text.

AIR BUBBLE AND CRYSTALLOGRAPHIC CHARACTERISTICS OF FROZEN, SOAKED RIME

J. C. Pflaum and N. C. Knight

National Center for Atmospheric Research*
Boulder, Colorado U.S.A.

1. Introduction

One of the ultimate goals of atmospheric research is to achieve a better understanding of hail formation processes within thunderstorms. Efforts toward this end have included multifaceted field projects combining radar, aircraft penetrations, and ground observations; numerical cloud models; and laboratory investigations of hydrometeor growth. Within this last category, considerable attention has been directed toward analyses of the hailstones themselves since it has long been thought that the complex crystallographic and air bubble patterns found within the stones contain the secret of their formation.

Numerous attempts have been made to reproduce observed hailstone properties within laboratory grown ice accretions (for a review, see Macklin, 1977). While these efforts have provided some insights into hail formation mechanisms, they have fallen short of complete interpretation. The innate difficulties of exactly reproducing atmospheric behavior under laboratory conditions is one explanation for existing inconsistencies. Just as critical, however, is the fact that any attempts at duplicating hailstone structures must be based on some inherent assumptions about how hailstones actually grow in the atmosphere. From density measurements of hailstones collected at the ground and estimates of hydrometeor growth conditions within severe storms, there has been general agreement among the scientific community that hailstones grow mainly by direct accretion of high density (~ 0.9 g cm^{-3}) ice or through freezing of spongy ice acquired during episodes of wet growth. Accordingly, almost all laboratory simulations of hailstone properties have centered around these two growth mechanisms. Recently, Pflaum (1980) has shown that hailstone formation might well proceed through the acquisition of low density rime followed by wet growth soaking and freezing. The present research effort examines the crystallographic and air bubble structures of ice formed in such a manner and compares the findings to actual hailstones.

2. Experimental Technique

The research effort employed a modified version of the experimental design described by Ashworth and Knight (1978). A brief, general description follows, the reader being referred to the above-mentioned article for more specific details.

Cylindrical accretions were grown using a simple icing tunnel located within a temperature controlled walk-in cold room. Air from the room was driven by a centrifugal fan into a water spray housing, through a contraction section and finally through a uniform rectangular tube approximately 1 m in length. The accretions were grown at the end of the rectangular section upon cylindrical styrofoam substrates fitted over a horizontal aluminum rod. The cylinders had an outer diameter of 2 cm and were rotated at a rate of 1 Hz. The deposit temperature was monitored by a thermistor embedded in the styrofoam, flush with the cylindrical surface. Airspeeds could be varied between 0 and 35 m s^{-1} and were usually chosen to match the expected terminal velocity of a hydrometeor of size and density similar to that of the accretion.

A cloud of supercooled water drops was produced by two water sprayers located in the center of the airflow. Variations in droplet sizes and liquid water contents could be produced by varying the air and water pressure leading to the sprayers. The median volume droplet radius ranged from 5 to 20 μm as the air pressure feeding the sprayers was decreased from 40 to 15 psi. By adjusting the water pressure, liquid water contents could be varied between a few tenths and several g cm^{-3}. This enabled low density rime as well as wet growth conditions to be produced over a temperature range of -5 to -30°C. Approximate calculations of thermal and gaseous relaxation times indicated that, in most cases, the cloud had attained equilibrium with the environmental air prior to impaction with the accreting cylinder.

A typical experiment proceeded as follows. The cold room was adjusted to the desired temperature. A cylinder was coated with a thin layer of solid ice to seal the pores of the styrofoam. This prevented any air bubbles, which normally would be trapped in the ice, from escaping through the styrofoam during the riming, soaking, and freezing process. The width of the ice-coated cylinder was measured and the cylinder weighed. The centrifugal fan was turned on and the sprayers activated. The rotating cylinder was placed in position at the far end of the icing tunnel and rime was allowed to grow to a thickness between 0.5 and 1 cm. The cloud was shut off and the rimed cylinder weighed and measured. From the difference between the rimed and unrimed values of weight and thickness, the density of the deposit was determined to ± 0.05 g cm^{-3}. The sprayers were reactivated to produce wet growth conditions and the rimed cylinder was placed back in position. Wet growth was

*The National Center for Atmospheric Research is sponsored by the National Science Foundation.

allowed to proceed until visual inspection indicated that the rime was totally soaked. This was usually at the point when liquid water began to be shed by the accretion. The cloud was shut off and the sample allowed to completely freeze in the airstream.

Thin sections of the accreted ice were prepared by slicing the accretion with a band saw, hand filing a smooth surface, freezing the ice onto a glass slide, and thinning to a desired thickness on a milling machine. Thin sections of 1 mm thickness were photographed to record air bubble structures; thin sections of 100-200 μm thickness were photographed between crossed polaroids to record crystal structures. In addition, a 1 cm thick section of the accretion was annealed for 1 hr and thin sections prepared as above for the purpose of examining recrystallization effects. Experiments were performed at temperatures ranging from -5 to -30°C with rime densities between 0.1 and 0.9 g cm^{-3}. Subsequent wet growth was produced at the same temperature as the initial rime formation as well as at substantially different temperatures.

3. Results

At the time of writing this extended abstract, the acquisition and analysis of data is still in progress. Accordingly, it would be premature to present any quantitative information on air bubble size distributions and concentrations or crystal size variations as functions of initial rime densities and temperatures. These will be available at the time of the conference. It is appropriate, however, to discuss some preliminary general findings on the nature of frozen soaked rime.

Lobe-like protuberances were commonly observed to develop during riming growth. Upon subsequent soaking and freezing, the lobe structures were preserved and distinct air bubble characteristics developed.

Within the lobes themselves, air bubble distributions were broad, with sizes ranging from 1 μm to larger than 100 μm. Many bubbles often appeared with unusual shapes. When the initial rime density was low ($\lesssim$0.25 g cm^{-3}) larger bubbles dominated the distribution and the ice appeared quite transparent. At higher densities ($\gtrsim$0.25 g cm^{-3}) there were large concentrations of tiny air bubbles (1-3 μm) which gave the ice a very opaque appearance.

At the inner edge of the soaked rime portion of the accretion, large amounts of air were often trapped. Depending on the freezing rate, this trapped air appeared as a concentric ring of air bubbles or as large (mm size) air inclusions.

Radial chains of air bubbles were almost always found between adjacent lobes. They were encased in narrow channels of clear ice. Frequently, air inclusions of millimetric dimensions were also found in the lobe boundaries.

These observations are quite consistent with air bubble features of natural hailstones as reported by Browning (1966), Browning et al. (1968), Carte and Kidder (1966), Knight and Knight (1973), Macklin et al. (1970), among others.

The sizes of crystals contained in the final accretion were dictated by the temperature of the initial rime formation. The ambient temperature at which the rime was soaked had no effect on the final crystalline size within the soaked rime portion of the accretion.

When riming and soaking were produced at similar temperatures, crystals grew through the rime lobe boundaries into the wet growth region without structural change. This relates well to the observed property of natural hailstones that crystalline changes occur less frequently than opacity variations.

As was demonstrated by Knight et al. (1978), high density, dry growth ice accretions are subject to substantial recrystallization effects even if maintained at a temperature of 0°C for only a few minutes. In the present work, there was an indication that ice which formed through the soaking and freezing of rime was already substantially recrystallized and exhibited only a minimal response to further annealing. Accordingly, the possibility exists that this type of ice formation can be uniquely identified in natural hailstones by annealing them and observing little or no change in crystal structure. Of course, this requires fresh and properly collected hailstones for a true test. In addition, these efforts need to be coupled with air bubble observations to distinguish such ice from pure wet growth ice, which also seems to be less susceptible to recrystallization.

Photographs supporting the above-mentioned results have been withheld for brevity's sake. They will be available for presentation at the conference.

References

Ashworth, T., and C. A. Knight, 1978: Cylindrical ice accretions as simulations of hail growth: I. Effects of rotation and of mixed clouds. JAS, 35, 1987-1996.

Browning, K. A., 1966: The lobe structure of giant hailstones. QJRMS, 92, 1-14.

_____, J. Hallett, T. W. Harrold, and D. Johnson, 1968: The collection and analysis of freshly fallen hailstones. JAM, 7, 603-612.

Carte, A. E., and R. E. Kidder, 1966: Transvaal hailstones. QJRMS, 92, 382-391.

Knight, C. A., and N. C. Knight, 1973: Quenched spongy hail. JAS, 30, 1665-1671.

_____, T. Ashworth and N. C. Knight, 1978: Cylindrical ice accretions as simulations of hail growth: II. The structure of fresh and annealed accretions. JAS, 35, 1997-2009.

Macklin, W. C., 1977: The characteristics of natural hailstones and their interpretation. Hail: A Review of Hail Science and Hail Suppression, G. B. Foote and C. A. Knight, Eds., Meteor. Monogr., No. 38, 65-87.

_____, L. Merlivat, and C. M. Stevenson, 1970: The analysis of a hailstone. QJRMS, 96, 472-486.

Pflaum, J. C., 1980: Hail formation via microphysical recycling. JAS, 37, 160-173.

HYPERFINE BUBBLE STRUCTURES IN ICE GROWN BY DROPLET ACCRETION

F.Prodi and L.Levi[+]

Laboratorio FISBAT-CNR, Rep.Nubi e Precipitazioni, Bologna, ITALY

1. INTRODUCTION

The bubble structure of ice grown by accretion was investigated by List et al (1972) and by List and Agnew (1973), who established some relations between this structure and the growth conditions. Continuing this line of study, Carras and Macklin (1975a) carried out an extensive analysis of the bubble concentration and size distribution in accreted ice and ice grown from bulk water, and were able to clarify, on the basis of their results, the role of the freezing rate as the main physical factor determining these features.

However, there is no systematic information about specific hyperfine bubble configurations observed both in artificially accreted ice and in natural hailstones. Thus List and Agnew (1973) and Roos and Pum (1974) observed the formation, in cross sections of wind tunnel deposits grown in wet or spongy regimes, of skew fan-like structures, appearing as periodical variations of the ice opacity. According to Roos and Pum this effect was especially pronounced in centrifugated spongy accretions, where the opaque zones presented radial lines and transversal fronts of air bubbles.

For natural hailstones the subject was touched on by Browning (1966) who noted the formation of periodical bubble rings running parallel to the stone surface, and attributed the observed periodicity to the tumbling action of the stone.

In the present work, the hyperfine bubble structure of artificial ice accretions grown in dry, wet and spongy regimes is studied, mostly at low rotation rates to investigate if the air bubble configurations exhibit specific features in this condition. Theoretical estimates of Knight and Knight (1970) and of Kry and List (1974) suggest that the motion of oblate hailstones should be a symmetric gyration about the horizontal, with rotation rates, about the spinning axis, of 2-6 Hz. However slower rotation rates cannot be completely ruled out for natural hailstones, which differ from the smooth spheroids used as models for theoretical calculations, due to their frequently irregular surface.

Examples of bubble rings in natural hailstones are also presented and discussed.

2. EXPERIMENTAL CONDITIONS AND RESULTS

The experiments were performed in a vertical icing wind tunnel already used by Levi and Prodi (1978) and an extensive description of the apparatus and of the experimental conditions may be found there. The wind speed in the working section was 29 m sec^{-1} and droplets of 17 μm mean volume diameter were injected. The water

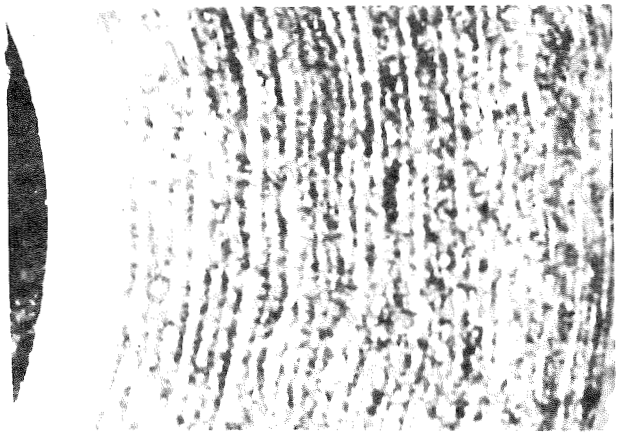

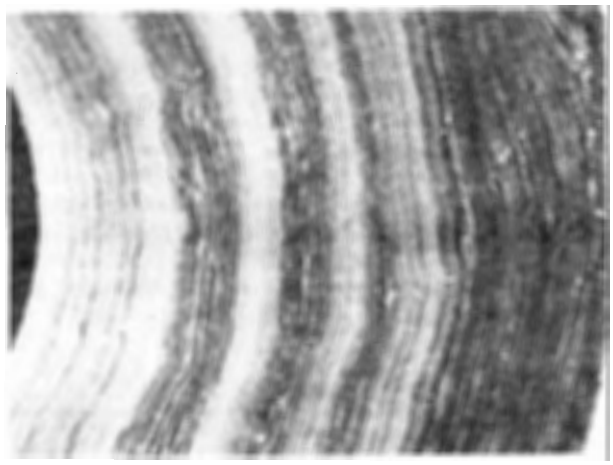

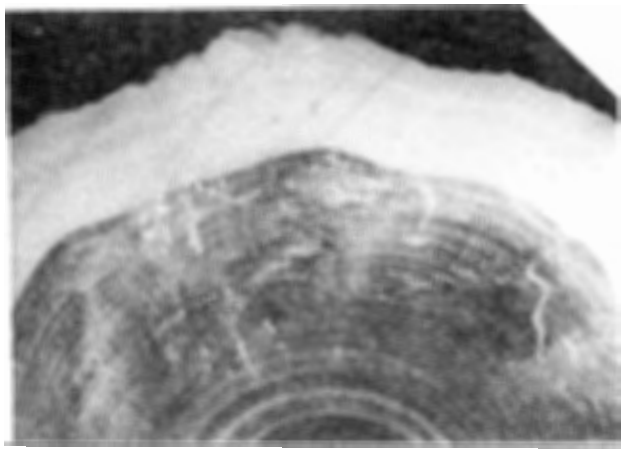

Fig.1. Bubble fronts in dry growth cylindrical deposits: distinct bubble fronts(a); faint bubble fronts (b); distinct bubble fronts and fan-like structure (c).

[+]Consejo Nacional de Investigaciones Científicas y Técnicas and Comisión Nacional de Energía Atómica, Argentina.

content varied from 0.5 to 6 g m^{-3} for the different experiments. The air temperature T_a varied from -10°C to -27°C and the mean deposit temperature T_d from 0°C to -15°C. The accretions were grown at 0.25 Hz in dry regime and mostly at 1 Hz in wet or spongy regime.

a) Dry growth

For proper values of the air and deposit temperatures, T_a and T_d, that will be specified below, the cross sections of the deposits showed bubble fronts, the number of which was equal to the number of rotations. A more careful inspection of the structures revealed that, rather than separate rings, the bubble fronts described a closely wound continuous spiral. Typical examples of bubble fronts are given in Fig 1.

The T_a, T_d conditions favorable to the formation of this type of air bubble fronts are represented in Fig.2. Here, deposits showing distinct bubble fronts (Fig.1a), faint bubble fronts (Fig.1b) and uniform opacity (external layer in Fig.1c) are gathered in separate zones of the T_a, T_d plane. Following Ashworth and Knight (1978) the isopleths of the radial growth rate of cylindrical accretions have also been drawn on the same plane (dashed lines in the figure). It can be observed that the boundaries between adjacent zones are also isopleths of the radial growth rate. There is a wide range of air temperatures where distinct fronts were formed, from T_a =-17°C down to the lowest T_a values used in the experiments (T_a =-27°C). However the formation of such structures is limited to the area of growth rates >0.6 mm min^{-1}, where the difference between T_a and T_d is quite large, T_d being in most cases few degrees only below 0°C. An area follows where faint bubble fronts are formed and the growth rate varies from 0.6 to 0.5 mm min^{-1}; finally, in the area where the growth rate is < 0.5 mm min^{-1}, a uniform ice opacity results. Thus a good correlation is found, as expected, between the appearance of the fronts and the growth rate of the deposits.

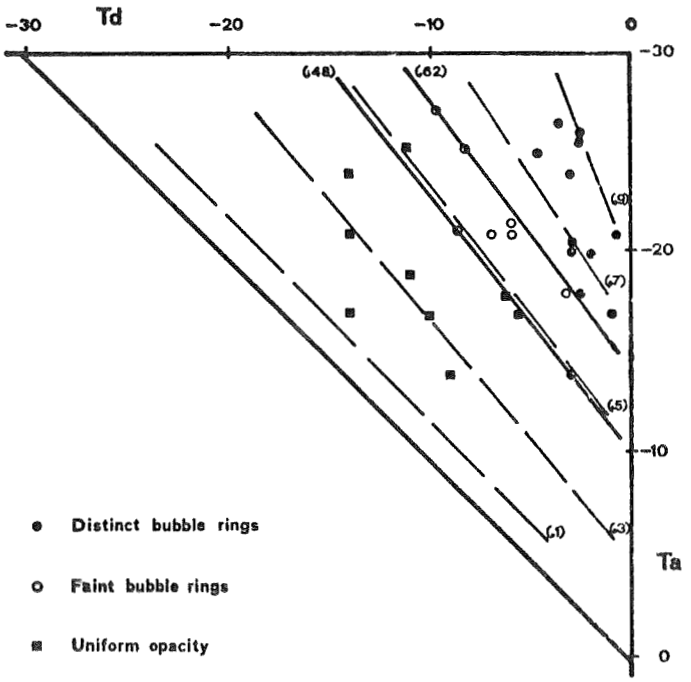

Fig.2. Bubble structure in cylindrical deposits at 0.25 Hz as a function of T_a and T_d. Isopleths of growth rate are also drawn, (mm min^{-1}).

The radial average density of the rings ranged in the present experiments from 4 to 12 per mm, giving a wavelength $80 < \lambda < 250$ μm. When the surface was knobby, the bubble fronts displayed the curvature of the lobes, their relative distance increasing in correspondence to the protuberances and narrowing in the regions between them. Due to the periodicity of lobes this effect frequently determined the fan like structure of the ice sections shown in Fig.1c.

b) Wet and spongy growth

The bubble structure of wet or spongy growth at the low rotation rate of 0.25 Hz was analyzed for a few deposits. It was found that, in this case, bubble fronts were formed but no correspondence could be established between the number of fronts and that of the rotations. For example,

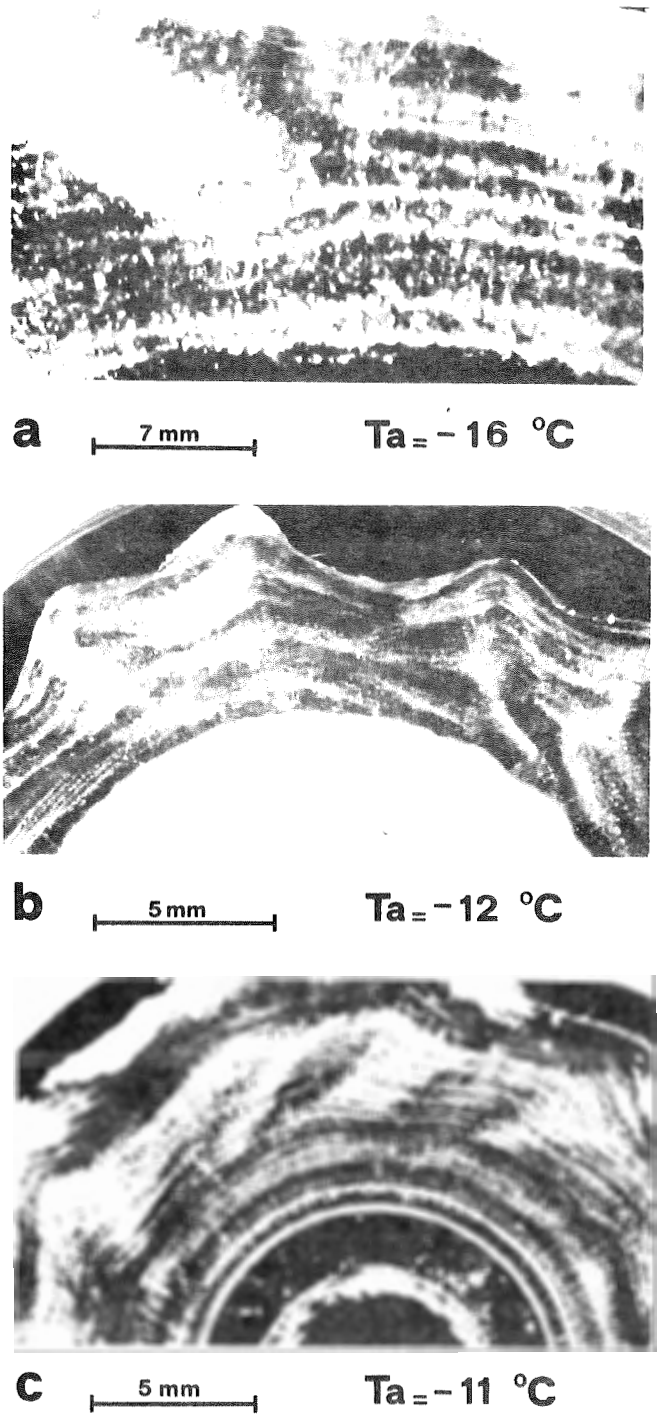

Fig.3. Bubble fronts and lobes in wet and spongy regime: bubble front morphology (a); discontinuous bubble fronts (b); fan-like structure in correspondence of lobes (c).

25 rings were counted in a deposit which experienced 96 rotations, the resulting wavelength being λ = 370 um. Similar wavelengths were obtained when the rotation rate was increased to 1 Hz. The latter speed was used for most wet or spongy growth experiments. These were carried out at air temperatures varying between -10°C and -16°C, i.e. inside the range of cloud temperatures where spongy growth may be expected to occur frequently. As it may be observed in Table 1, in these conditions the wavelength of bubble fronts varied from about 250 to 400 μm, the highest value pertaining to the highest spongyness.

Table 1

Wavelength of bubble fronts in wet and spongy regimes.

T_a, °C	Spongyness ratio	Wavelength, um
-14	0.00	250
-13	0.00	270
-16	0.08	244
-10	0.11	353
-10	0.17	370
-14	----	370^

^Rotation rate 0.25 Hz.

As far as the morphology of bubble fronts is concerned, in spongy growth they are regularly interrupted by radial segments of bubbles (Fig. 3a), which suggests a cellular-like structure, similar to that formed by aggregates of insoluble particles observed by Prodi et al (1980), in spongy accretions grown from droplets containing Ni spherule powder. The fronts are less continuous than in dry growth and they usually increase in thickness in the vicinity of lobes (Fig.3b). In some cases of wet or spongy growth a fan like structure appears, similar to that discussed by Roos and Pum (1974) (Fig.3c).

Fig.3b may also be analyzed to obtain information about the process of lobe generation from the bubble configuration. Here a ring-like structure of bubbles, formed at a small distance from the initiation of the spongy layer, is interrupted by periodic protrusions of bubbly ice. These protuberances correspond to the initiation of lobes which are slightly inclined with respect to the radial direction.

3. DISCUSSION

a) Dry growth

The formation and characteristics of the dry growth bubble rings may be related both to the amount of accreted water per rotation of the deposit, which determines the distance between fronts, and to the periodical variations of the local surface temperature T_s, which affects the ice opacity. For a given value of the rotation rate and of the wind speed, both separation and opacity contrast of rings depend on the growth rate, which is related to the difference between T_a and T_d, as it results from Fig.2 This figure shows that at 0.25 Hz faint bubble rings appear at a growth rate where the accretion occurs far enough from the dry-wet limit to ensure the separate freezing of individual droplets on the whole collecting surface, but at a difference between T_a and T_d large enough to determine non negligible fluctuations of T_s and consequently of the ice opacity.

The opacity of accreted ice has been studied by Carras and Macklin (1975b) as a function of the mean deposit temperature T_d, for cylinders rotating at 0.5 Hz. Their results, applied in the present case by replacing the variable T_d by T_s, justify the formation of faint bubble rings observed here.

On the other hand, when the growth rate is $\gtrsim$ 0.6 mm min^{-1} and the difference between T_a and T_d is near 20°C, the accretion process, which would occur well inside the dry regime on the area A in Fig.4, could become locally wet on area C. Here the droplets, instead of freezing individually would form a continuous liquid film, which would freeze at an increasing rate in the wake and subsequently cool down after its solidification is completed. In this way the high contrast between opaque and transparent layers, in the distinct bubble ring zone of Fig.2 could be due to: 1) the different freezing rate of droplets accreted in dry regime on the surface surrounding point A and of the continuous water film, freezing slowly on the surface zone surrounding C, where T_s approximates 0°C; 2) the increase of the freezing rate of the water film itself, occurring when the latter enters the wake, where it solidifies completely, trapping the excess of dissolved air , previously segregated at the ice-water interface.

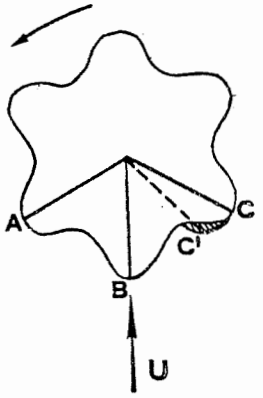

Fig.4. Scheme of a knobby deposit, growing in wet or limit dry-wet regimes.

When, for similar values of T_a and T_d, the rotation rate is increased, locally wet conditions would not be established on C so that mechanism 2) would not operate. Thus, the reason why distinct bubble rings were not observed by previous authors would be the higher rotation rates of their deposits. Since in most cases rotation rates $\gtrsim$ 0.5 Hz were used, the present results also indicate that a reduction to 0.25 Hz would be enough to drastically change the fluctuations of the local growth conditions that determine the periodical variations of the ice opacity.

b) Wet or spongy growth. In their study of spongy growth, Roos and Pum (1974) noted that, since water would never be completely eliminated from the accreted deposit, freezing would be a continuous process, so that the bubble fronts should be formed by a long range segregation mechanism. They noted, however, that the wavelength of the bubble fronts was about half an order of magnitude less than that obtained by Carte (1961) from laboratory experiments. Consequently, Roos and Pum suggested that the observed submillimeter wavelength may be attributed to the inhibiting effect of the ice matrix with respect to the

bubble formation. This mechanism, which could also be applied in the present case, may be considered to coincide with that proposed by Prodi et al(1980) to explain the cellular-like structure shown by aggregates of tracer Ni spherules in accreted spongy ice. On the other hand, the fan-like structure observed here both in spongy and wet regimes could be explained by the asymmetric lobe development due to water accumulating on zone C in Fig.4. Thus, a similar explanation could be given to the formation of fan-like structures in spongy and wet regime and in the dry-wet limit discussed in a).

Finally, it must be noted that the bubble fronts were observed here after total freezing of the deposits, so that their structure could be more convenient for its comparison with the structures in natural hailstones than the bubble configurations observed by Roos and Pum in centrifugated artificial accretions.

4. NATURAL HAILSTONES

An example of natural hailstones showing well defined bubble fronts is shown in Fig.5. Similar features were observed in other hailstones from the same precipitation (Negrar,PoValley, August 27,1971), all of them presenting typical features of wet or spongy growth. In the example of Fig.5 distinct but rather irregular bubble fronts may be observed in layer I. They are distributed at a distance of about 300μm, which coincides with that found in artificial accretions grown in wet or spongy regimes. The fronts become less defined in layer II, where lobes, also typical of the spongy regime, are generated, as it is shown by the presence of bubbly protuberances, and in some cases, by the curvature of the corresponding bubble fronts.

Examples of bubble fronts possibly formed in dry growth have been presented by Browning (1966). In his case the fronts were rather regularly distributed, at a distance which changed from sample to sample, but which could be as low as 200 μm. The assuption that in this case bubble fronts were generated in dry growth conditions coincides with Browning's interpretation of the phenomenon. However it must be noted that, if this interpretation is correct, the rotation speed of the considered hailstones should have been of the same order of magnitude as the one used in the present experiments, i.e. rather low with respect to the stationary rotation rates calculated by Kry and List (1974).

Fig.5. Bubble fronts and lobes in a natural hailstone (Negrar,Po Valley,August 27,1971).

REFERENCES

Ashworth T. and C.A.Knight,1978: Cylindrical ice accretions as simulations of hail growth:I Effects of rotation in mixed clouds. J.Atmos. Sc.35,1987-1995

Browning,K.A.,1966: The lobe structure of giant hailstones. Quart.J.Roy. Met.Soc,92,1-14

Carras,J.N. and W.C.Macklin,1975 a: Air bubbles in accreted ice. Quart.J.Roy.Met.Soc.101, 127-146.

Carras,J.N. and W.C.Macklin,1975b: The opacity of accreted ice. Quart.J.Roy.Met.Soc.101; 203-206

Carte,A.E.,1961:Air bubbles in ice. Proc.Phys. Soc,77,757-768

Knight,C.A. and N.C.Knight,1970: The fall behavior of hailstones.J.Atmos.Sc27,672-681.

Kry,P.R. and R.List,1974: Angular motions of freely falling spheroidal hailstone models. Phys.Fluids,17,1093-1102.

Levi,L.and F.Prodi,1978:Crystal size in ice grown by droplet accretion.J.Atmos.Sc. ,35,2181-2189

List,R.,W.A.Murray and C.Dyck,1972:Air bubbles in hailstones.J.Atmos.Sc,29,916-920

List,R. and T.A.Agnew:Air bubbles in artificial hailstones.J.Atmos.Sc.30,1158-1165

Prodi,F.,C.T.Nagamoto and J.Rosinski,1980:A preliminary study of ice grown by droplet accretion using water-insoluble particles as tracers. J.Appl.Met. in press.

Roos,D.v.d.S. and H.D.R.Pum,1974: Spongyness in ice grown by accretion.Quart.J.Roy.Met.Soc. 100,640-657.

SOME SMALL SCALE VARIATIONS OF HAIL IN SPACE AND TIME

D.v.d.S. Roos

National Physical Research Laboratory CSIR
Pretoria SOUTH AFRICA

1. INTRODUCTION

One of the methods for gaining more knowledge of hail aloft is to relate aspects of hail at ground level to the hail growth environment. This paper deals essentially with a) preliminary results of small scale variations in hailfalls found in a newly established hailpad network and b) small scale variations in space and time in the features of hailstone embryos manifested at ground level.

2. HAILFALL CHARACTERISTICS

CSIR hailpads, which incorporate a cold-rolled aluminium sheet of 0.315 mm thickness as sensor (Roos, 1978), were set up in a network of 200 sq km in Pretoria. A novel technique was applied to infer E, the impact kinetic energy density, not from measurements of individual dents but directly from the total distortion of the sensor (Roos, 1980). It was found that light, medium, heavy and violent hailfall intensities corresponded to $E \leq 10$, $10 < E \leq 100$, $100 < E \leq 1000$ and $E > 1000$ J/sq m, respectively. It was proved possible to estimate the hail mass concentration from E provided that the diameter of the largest hailstone(s) is known.

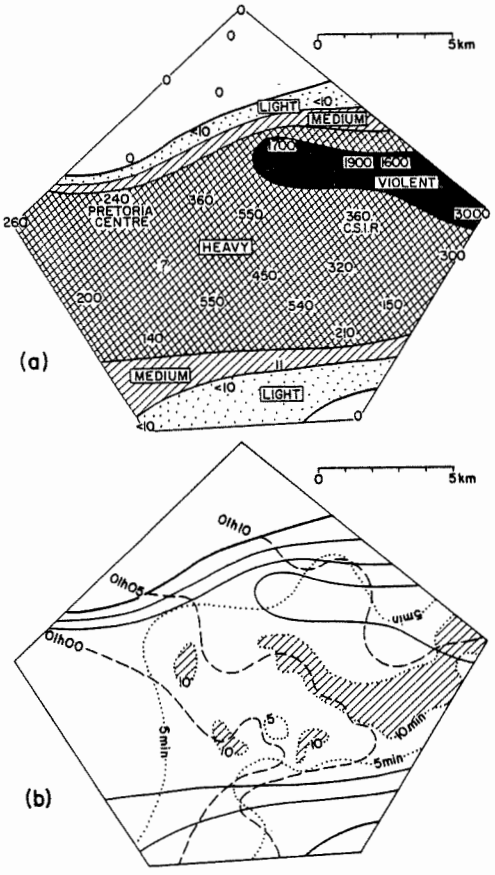

Figure 1. a) Intensities of hailfall on 1979-09-21 in the hailpad network; units are J/sq m. b) Onset times (broken lines) and durations (dotted lines) of hailfall; full lines correspond to a).

Results for hailfalls from two storms are discussed. The first storm hit Pretoria at about 01h00 (SAST) on 1979-09-21 and caused millions of rands worth of damage. E-values for 23 of the then existing 30 field stations are shown in Fig. 1a. Severe hailfalls (with $E > 100$ J/sq m) covered two-thirds of the network and extended over a width of at least 8 km. The corresponding maximum hailstone sizes (exceeding 3 cm in diameter) suggest that a wide-spread updraught reached speeds that generally exceeded 30 m/s at the levels of hailstone growth nearly 10 km MSL (Roos *et al.*, 1977). E-gradients in the vicinity of the "violent" region were found to be very steep. Likewise, hail mass concentrations decreased from ∿10 kg/sq m inside this region to zero over a distance of no more than 2 km.

Onset times and durations of hailfalls were obtained from 160 hail reports of which 70 % claimed an accuracy of 1 min or better and the rest 2 min or better. Evidently the leading edge of the hail was very irregular and moved north-eastwards at about 40 km/h (Fig. 1b). Point hailfalls of at least 5 min occurred mainly in "heavy" and "violent" regions; the longest durations (>10 min) were found in three small (∿1 sq km) and one larger (∿15 sq km) area but these did not correspond to the region of maximum E.

The space and time variations of hailfall features depend on many factors. Consider, e.g., a simple model of a circular hail cell of diameter d km moving through still air at speed v km/h and generating hail homogeneously. The duration of hailfall (min) at a point x km from the locus of the centre of the corresponding hailswath is given by

$$t(x) = 60\ (d/v)\ (1 - 4x^2/d^2)^{\frac{1}{2}},$$

which shows that even for this idealised case, t(x) and hence E will decrease (sinusoidally) with increasing x. The real picture is much more complex: onset times and durations are determined by d, which depends on the expansion and contraction of a non-

circular hail cell, by v, which depends both on the in-cloud air flow pattern and hail cell growth, and by wind drifting of falling hailstones, which depends on the sub-cloud air flow pattern. Other techniques are obviously needed to study these fundamentally important factors.

The number of hailpads within the network was increased from 30 to 72, resulting in one field station per 2.8 sq km. This compares favourably with the figure of one site per 2 sq km that Changnon (1977) considered necessary to measure adequately the area of loss in a region. The denser network was traversed by a storm on 1979-10-21 that left 41 hailpads dented (Fig. 2a). The heaviest hailfalls were <200 J/sq m and they covered no more than one-tenth of the network. In contrast to a finding for the first storm, the width of hailswaths increased with decreasing intensity.

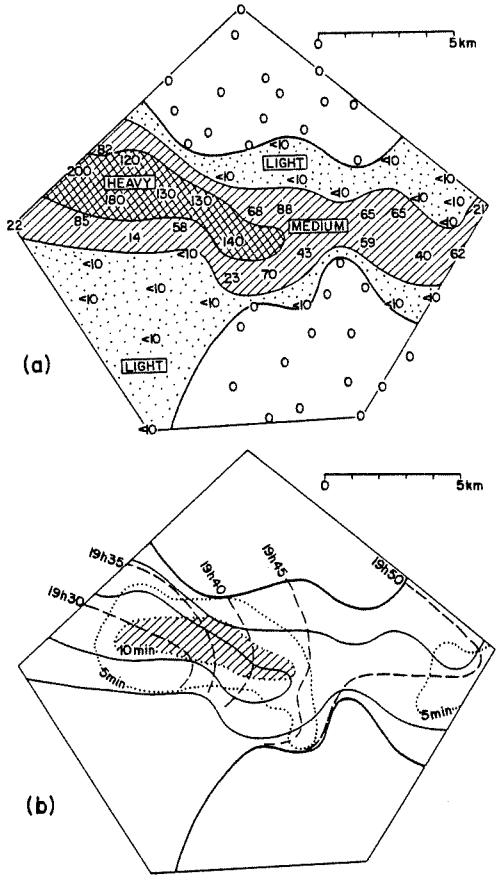

Figure 2. a) Intensities of hailfall on 1979-10-21 in the hailpad network; units are J/sq m. b) Onset times (broken lines) and durations (dotted lines) of hailfall; full lines correspond to a).

According to hailfall times (obtained from 45 hail reports with accuracies similar to those above) the leading edge of the hail, of convex shape, showed a tendency to accellerate while moving eastwards at an average speed of about 20 km/h. Hailfalls lasting for at least 5 min occurred mainly in "medium" and "heavy" regions while the longest durations (>10 min) were, in contrast to before, confined roughly to the region of maximum E. It seems that the durations and intensity patterns of this hailfall may be explained roughly in terms of the equation for t(x) given above.

3. EMBRYO CHARACTERISTICS

Embryos constitute the earliest discernible growth centre in hailstones. Many embryos develop to form damaging hailstones while others may melt to form raindrops. Hence embryo studies have important implications for damaging hail, weather modification and rain formation.

3.1 Classification

Various schemes have been used by different authors for the classification of embryos (Table 1). This is partly because it is impossible to be completely objective in classification and also because there may be differences related to geographical regions, as discussed by Knight and Knight (1978). Unfortunately different classification schemes may have the effect of not revealing actual differences: for example, "glaze" embryos have been considered synonymous to "frozen drops" but indications are that these sets are not identical. Studies of 600 embryos from three storms over three years led to a scheme for classifying embryos as type K1 (conical, milky - often called "conical graupel"), K2 (conical, glassy), S1 (spheroidal, milky), S2 (spheroidal, glassy - Table 1 shows how this type differs from the next) and S3 (spheroidal, glassy - often called "frozen drop")(Fig. 3). This scheme is simple yet comprehensive since information on shape and opacity may be acquired independently as follows: all K's are conical, 1's are milky, S's are spheroidal and 2's and 3's are glassy. In Table 1 the distinguishing features of each embryo type are shown and, where possible, related to the views of other authors.

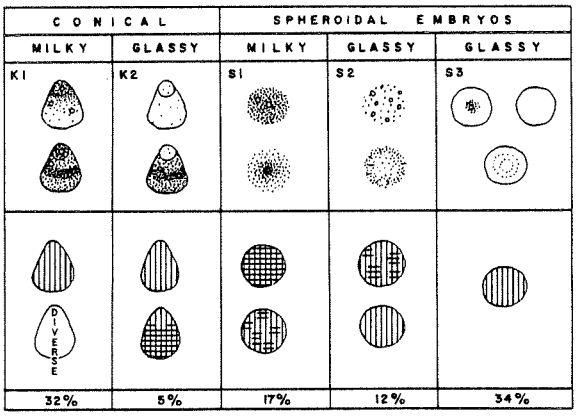

Figure 3. Schematic presentation of features of five embryo types; relative occurrences are shown at the bottom. Small air bubbles are indicated by dots and larger ones by tiny circles, large crystals by hatching and small ones by cross-hatching. "Small" and "large" are quantified in Table 1.

3.2 Occurrence and interpretation

The 600 analysed hailstones were representative of all sizes that had been collected. Practically the same percentages of milky (49 %) and glassy (51 %) embryos were found but there were less K (37 %) than S (63 %) specimens (Fig. 4). Correlations were found between the occurrence of conical shapes and milky ice (and hence between spheroidal shapes and glassy ice) but none of the collections contained more conical than milky embryos. The interpretation of embryo features is mostly qualitative, if not speculative, because the relationship between structure and growth mechanism is not certain. For example, milky ice is associated with rapid freezing (to which a relatively low liquid water content will be conducive) and hence low deposit temperatures, which imply low air temperatures and small crystals. However, among milky embryos, K1 often comprised large crystals. If this implies that water had penetrated a porous substrate and subsequently froze, the K1 embryos concerned may have experienced large height fluctuations in clouds. Evidently then, milky ice does not necessarily indicate growth high in clouds only. On the contrary, similar arguments indicate that glassy ice, i.e. at least 51 % of the embryos examined (Fig. 4b), probably did grow relatively low in clouds.

The relative occurrence of embryo types was found to depend on various factors. Not surprisingly, there were significant differences from storm to storm. The relative occurrence of K-embryos for three storms from the same geographic region (Fig. 4a) were 22, 51 and 48 % while those of milky embryos were 35, 60 and 68 %, respectively. Variations were also found within a given storm. Figure 4c shows how the relative occurrence of embryo types at a specific point varied with arrival time: while 97 % of the specimens that arrived between 15h45 and 15h50

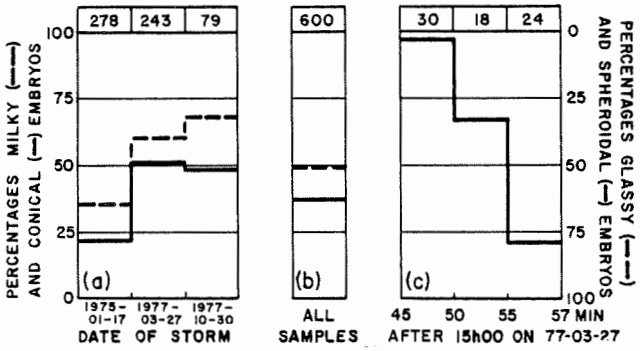

Figure 4. Occurrence of embryos according to shape (full lines) and opacity (broken lines); numbers per interval are shown at the top. The scale on the right increases downwards. a) Data per storm day. b) Totals from a). c) Data for time-resolved samples (graphs coincide).

were conical and milky, this value decreased with time to reach a mere 21 % for the last two min of hailfall. The role that storm stage may play in the relative occurrence of embryo types was demonstrated by specimens collected from different hailstreaks: the envelopes in Fig. 5a show where hail was probably falling at the indicated times. Figure 5b shows that the relative frequency of K-embryos decreased sharply from 55 % (for the early stage of hailstreak 1) to 5 % (for its late stage); correspondingly, milky embryos decreased from 66 to 27 %. Corresponding variations found between the late stage of hailstreak 1 and the adjacent hailstreak 2 were not significant.

Carte and Kidder (1970) found, for 1718 specimens from the Transvaal Highveld, that the relative occurrence of rimed embryos increased with hailstone size. Knight and Knight (1978) found, for 1318 specimens from the Transvaal Lowveld (300 km east of the Highveld), a decrease in the relative occurrence of graupel embryos with hailstone size.

Table 1. Features of the suggested five types of embryos. Where applicable, corresponding classifications of other authors are indicated.

Shape	Type	Opacity: Appearance	Opacity: Bubble features*	Crystal features†	Designations by other authors: Mossop and Kidder (1961)	Carte and Kidder (1970)	Knight and Knight (1976)	Federer *et al.* (1978)
Conical	K1	Milky	Apex: many bubbles, often large ones. Base: either bubbly or bubble free; bubbles sometimes in layers.	Large or small or assorted; large ones elongated in growth direction.	b1, b2	rime	graupel	1C
	K2	Glassy	Apex virtually bubble free. Base: few bubbles, sometimes more and then often layered as in K1.	Mostly large crystals. Also, decreasing from large to small in growth direction.	-	glaze	-	2D?
Spheroidal	S1	Milky	Bubbly, sometimes densest at the centre.	Mostly small; also assorted with large.	a, b3?	rime	spher. bubbly	1A, 1B
	S2	Glassy	Few bubbles, often large; randomly distributed; centre often least dense.	Mostly assortment of large and small; also large, random crystals	-	glaze	-	2B, 2C
	S3	Glassy	Virtually bubble free; bubbles clustered at centre; or bubble rings.	Virtually always large and random; sometimes a single crystal.	c	glaze	frozen drop	2A, 2D

*Diameter of large bubbles ≧100 μm. †Longest dimension of large crystals ≧1 mm.

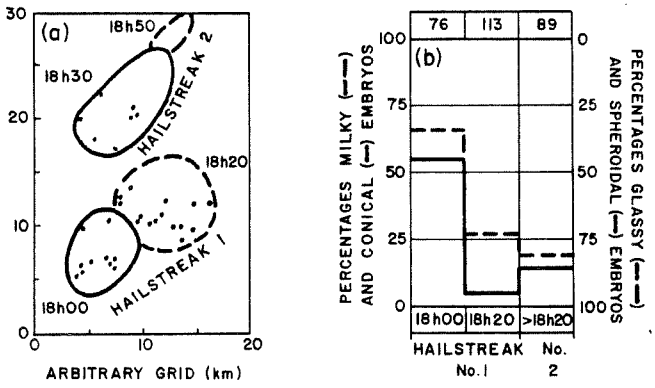

Figure 5. a) Plan presentation of two hailstreaks of 1975-01-17 indicated by isochrones. Dots show points from where samples were analysed. b) Occurrence of embryos according to shape and opacity, per hailstreak. Numbers per interval are shown at the top.

The present Highveld results seem to agree with the Lowveld rather than earlier Highveld results: of the 396 hailstones not exceeding 25 mm in longest dimension, 56 % were milky and 43 % conical while for the 204 larger specimens only 35 % were milky and 26 % conical. Evidently, spheroidal, glassy embryos (which are thought to have grown at relatively low levels and could approximately have been balanced by an increasing updraught) were favoured to develop into large hailstones.

4. CONCLUSIONS

The newly established dense network of hailpads in Pretoria, complemented by hail observers, has revealed small scale variabilities of hailfall similar to those reported by Changnon (1977) and Carte and Held (1978). In particular, the severe September storm ($\bar{E} \approx 560$ J/sq m) showed steep gradients and great variability while the October storm was much less intense ($\bar{E} \approx 45$ J/sq m) and simpler in structure. The intensity of the latter storm was above average for Pretoria and, evidently, also for Illinois where $\bar{E} \approx 2$ J/sq m (Changnon, 1977), but comparable to the average for north-east Colorado where $\bar{E} \approx 50$ J/sq m. The hailpads comprising $\sim$0.3 mm thick sheets of aluminium have proved capable of registering satisfactorily hailfalls ranging in intensity from a few to a few thousand J/sq m and three years of field trials have shown that weathering has no adverse effect. The new technique of measuring the distortion of hail sensors is recommended for further studies of hailfall intensities since it saves much on time, cost and effort.

The classification scheme for hailstone embryos presented above has proved to be straightforward and objective. Large variations were found in the relative occurrence of embryo types in hailstones of all sizes with regard to both arrival time and storm stage, which suggest short term variations in the growth environment of embryos. Variations in the predominant type of embryo in the growth environment may jeopardise the outcome of hail suppression efforts because it is thought that while "frozen drop" embryos may respond favourably to seeding, "graupel" embryos may in fact lead to an increased hail response (summarised by Atlas, 1976). Therefore, basic research on the mechanisms of embryo growth and the environmental conditions that govern them should be intensified. Further studies of embryo occurrence could establish how significant local space-time variations are and whether geographical differences do in fact exist. Evidently, the need for more data on all aspects of hail growth and consolidation of efforts is very real.

ACKNOWLEDGEMENTS

Section 3 was taken from a chapter of the author's Ph.D.-thesis accepted by the University of South Africa, Pretoria. Special thanks are due to voluntary hail observers who collected samples and sent in reports.

REFERENCES

Atlas, D., 1976: The present and future of hail suppression. *Proc. Second W.M.O. Sci. Conf. Wea. Modific.*, Boulder, Colorado, 207-216.

Carte, A.E. and G. Held, 1978: Variability of hailstorms on the South African Plateau. *J. Appl. Meteor.*, 17, 365-373.

Carte, A.E. and R.E. Kidder, 1970: Hailstones from the Pretoria-Witwatersrand area, 1959-1969. *CSIR Res. Rep. 297*, Pretoria, 1-42.

Changnon, S.A., 1977: The scales of hail. *J. Appl. Meteor.*, 16, 626-648.

Federer, B., J. Jouzel and A. Waldvogel, 1978: Hailstone trajectories determined from crystallography, deuterium content and radar backscattering. *Pure Appl. Geophys.*, 116, 112-129.

Knight, C.A. and N.C. Knight, 1976: Hail embryo studies. *Preprints Internat. Conf. Cloud Phys.*, Boulder, Colorado, 222-226.

Knight, N.C. and C.A. Knight, 1978: South African Lowveld hailstone embryos. *Preprints Conf. Cloud Phys. Atmos. Electr.*, Issaquah, Washington, 1-4.

Mossop, S.C. and R.E. Kidder, 1961: Hailstorm at Johannesburg on 9th Nov. 1959, II. Structure of hailstones. *Nubila*, 4, 78-86.

Roos, D.v.d.S., 1978: Hailstone size inferred from dents in cold rolled aluminum sheet. *J. Appl. Meteor.*, 17, 1234-1239.

Roos, D.v.d.S., 1980: Hailfall intensities. Submitted for publication in *S. Afr. J. Sci.*

Roos, D.v.d.S., H. Schooling and J.C. Vogel, 1977: Deuterium in hailstones collected on 29 Nov. 1972. *Quart. J. Roy. Meteor. Soc.*, 103, 751-767.

OBSERVATIONS OF ANOMALOUS LARGE PARTICLES INSIDE COLORADO AND OKLAHOMA THUNDERSTORMS

Paul L. Smith, Jr., Dennis J. Musil, and Douglas C. Jansen

Institute of Atmospheric Sciences
South Dakota School of Mines and Technology
Rapid City, South Dakota 57701

1. INTRODUCTION

An armored T-28 research aircraft (Sand and Schleusener, 1974) was used during the 1970's to investigate the interior characteristics of hailstorms in the Great Plains region of the United States of America. Hydrometeor observations were of particular interest and the aircraft carried an increasingly elaborate array of hydrometeor sensors. Beginning in 1975, this array included an optical hailstone spectrometer that senses particle sizes in the range from about 0.5 to 5 cm. The observed concentrations of particles larger than about 2 cm are much higher than was anticipated on the basis of previous knowledge about hailstone size distributions. The purpose of this paper is to report these T-28 observations and advance a tentative explanation.

2. DESCRIPTION OF THE HAIL SPECTROMETER

The hail spectrometer design is based on the shadowgraph principle described by Knollenberg (1970). It measures the vertical widths of particles (or rather, of the particle shadows) as they pass through its sensing aperture. Theses by Shaw (1974) and Spahn (1976) discuss the detailed design of the instrument. It uses a larger optical array than the instruments developed by Knollenberg, to increase the sampling volume to about 100 m^3 per kilometer of flight path for the smallest particles (the effective sampling volume diminishes somewhat with increasing particle size).

The sampling aperture of the instrument is large enough that some particle coincidences, or near coincidences, are expected. The electronic circuitry is designed to distinguish between separate particles as long as their shadows do not overlap as they pass through the aperture. If the shadows are separated, the instrument can size and count the particles properly. It sorts them into 14 size categories, and the particle counts for each category are recorded digitally for each second of flight. The particles sampled are presumed to be graupel or hail, although large raindrops or snowflakes could register in the smallest size categories.

The nominal flight speed of the T-28 is 100 m s^{-1}, and the area of the sampling aperture of the hail spectrometer is about 0.1 m^2. Thus each 1-sec sample corresponds to a sampling volume of about 10 m^3. An end-element rejection technique used to eliminate erroneous sizing of particles not entirely within the active area also reduces the effective sampling volume somewhat for the larger size categories.

3. SUMMARY OF 1975 OBSERVATIONS

A preliminary report of observations from the hail spectrometer and the other hydrometeor sensors on the T-28 was given at the 1976 International Conference on Cloud Physics (Smith et al., 1976). A more detailed analysis of the hailstone size distributions observed during the 1975 northeast Colorado field season was reported the same year (Spahn and Smith, 1976). No particles larger than a nominal size of 2.5 cm were observed during the 1975 season.

The evidence from the 1975 observations suggested that the hailstone size distributions were exponential in form. However, they had steeper slopes (hence, smaller proportions of large hailstones) than those reported by Douglas (1964) from Alberta. Observations of hailstone size distributions in Switzerland (Federer and Waldvogel, 1975) tended to confirm these general findings. There were, of course, substantial variations in individual size distributions, especially for small sampling volumes; however, distributions for volumes of 50 m^3 or more appeared to conform reasonably well to the exponential function.

4. FIRST OBSERVATIONS OF LARGE PARTICLES: 1976

Particles larger than 2.5 cm were first observed by the hail spectrometer in three 1976 storms in northeast Colorado. The concentrations of particles larger than about 2 cm were found to be much higher than would be expected if one simply extrapolated exponential functions fit to the observations for smaller sizes. Comparison of these aircraft observations with hailstone observations at the ground (Fig. 1) and the pilot's reports did not support the indications of such high concentrations of large hailstones (Miller et al., 1978). Moreover, equivalent radar reflectivity factors estimated from the observed particle size distributions were often much larger than the actual observations and, in some cases, were too large to be plausible.

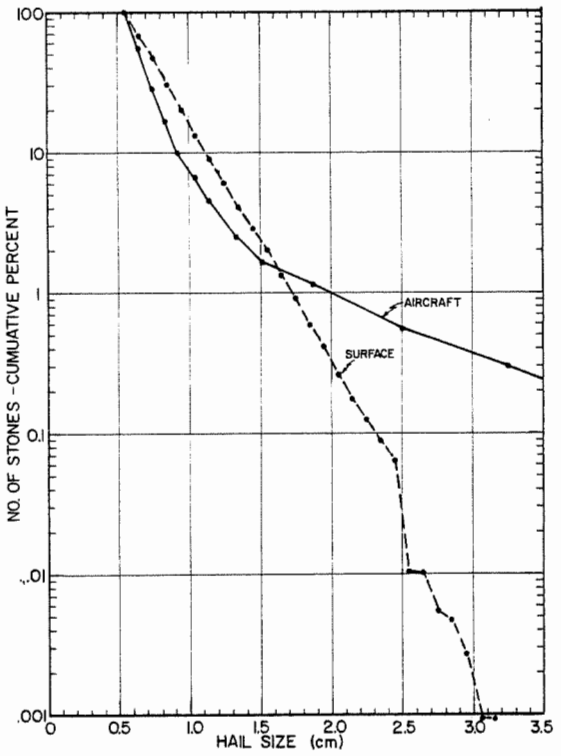

Fig. 1: Cumulative frequency distributions of hailstone sizes observed on 22 June 1976 in northeast Colorado. Ordinate gives percent of hailstones equal to or larger than indicated size. Aircraft data from T-28 hail spectrometer; surface data from NHRE hail pad network. [From Miller et al., 1978]

These comparisons raised doubts about the validity of the hail spectrometer measurements. A variety of possible explanations was suggested; one was that ice fragments breaking off the aircraft structure or the instrument housing were responsible for the indications of large particles. Plans were therefore made to modify the instrument to evaluate some of the possible alternatives.

5. MODIFICATION OF THE HAIL SPECTROMETER

In the initial configuration, 10 size categories were assigned to particles up to about 1.5 cm across, leaving only four categories for larger sizes. The small hailstones were known to be much more numerous, and it was thought important to provide fine resolution in that portion of the size range. The seemingly anomalous observations of the large particles in 1976, however, suggested that changes were in order.

The hail spectrometer electronics were accordingly modified to provide more uniform resolution over the full working range of particle sizes. The criterion adopted in the redesign was that the nominal size for each category should represent a factor two increase in hailstone mass over the next smaller category. Some minor departures from this criterion were made to simplify the electronic logic. The resulting configuration allocated only eight size categories to particles up to about 1.5 cm across, leaving six categories available for larger particles. (An increase in the total number of categories was not practical because of data recording limitations.)

A "slow-particle detector" was also added to the instrument to detect particles moving through the sensing aperture at speeds substantially less than the aircraft's true airspeed. This feature was intended to detect ice fragments that may have broken off or rebounded from the aircraft or instrument structure.

6. LARGE-PARTICLE OBSERVATIONS DURING SESAME '79

The T-28 was not operated in 1977. During the 1978 field season in northeast Colorado, only one mature storm was investigated and it contained hailstones only up to about 1 cm.

The next observations of large particles occurred during the SESAME '79 project in Oklahoma. On several occasions, particles up to the largest size category (nominal size 5.0 cm) were again observed. The general character of the observations was remarkably similar to those in 1976, lending credence to the previous observations.

Figure 2 shows the cumulative particle size distribution for one example from 27 May 1979. The semi-log plot shows the total number concentration $N_L(D)$ of particles with diameters (actually, shadow widths) larger than or equal to the indicated size D. The curve in Fig. 2 and the "aircraft" curve in Fig. 1 are quite similar: nearly linear for particles smaller than about 1.0 cm, with slight curvature above 1 cm and a more pronounced break in slope around 1.5 cm. For the data in Fig. 2, the number concentration of particles larger than 1.5 cm is about 0.7 m^{-3}, and of ones larger than 3 cm about 0.3 m^{-3}.

Shown for comparison in Fig. 2 is the cumulative size distribution according to Douglas' (1964) hailstone size distribution function. The observed concentration of particles larger than 2.5 cm is more than five times the Douglas value, and that of particles larger than 4 cm more than 100 times the Douglas value. There is ample evidence that the Douglas function overestimates the concentrations of large hailstones, as compared to more recent observations at the ground (e.g., Federer and Waldvogel, 1975; or Smith et al., 1975). Thus the T-28 observations from both Oklahoma (1979) and Colorado (1976) indicate concentrations of particles larger than about 2 cm, which are much higher than those suggested by hailstone observations at the ground.

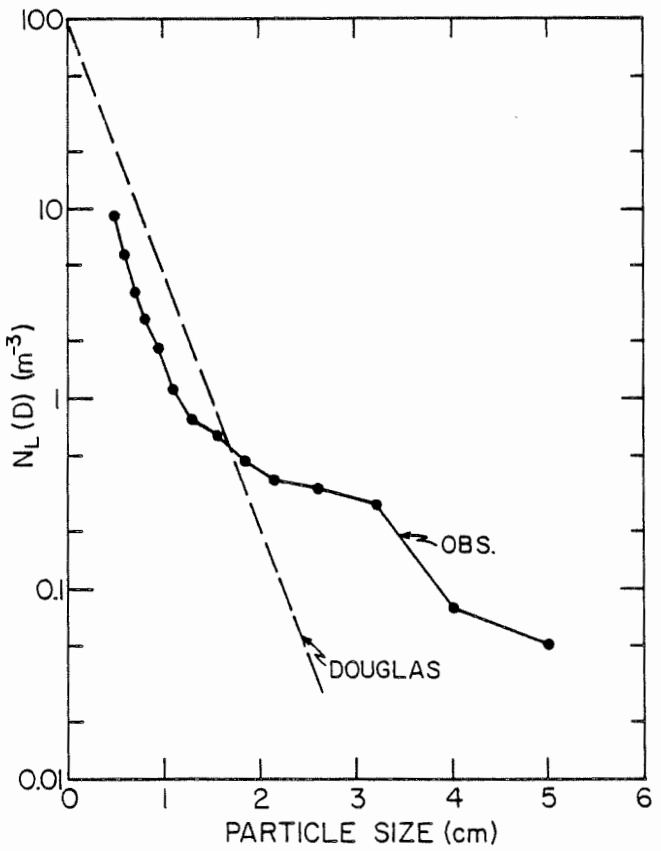

Fig. 2: A particle size distribution measured over a 1-km path in an Oklahoma thunderstorm on 27 May 1979. Ordinate gives number concentration of particles equal to or larger than indicated size. Solid curve shows observed distribution, while dashed line shows Douglas function for same mass concentration (9.5 g/m^3).

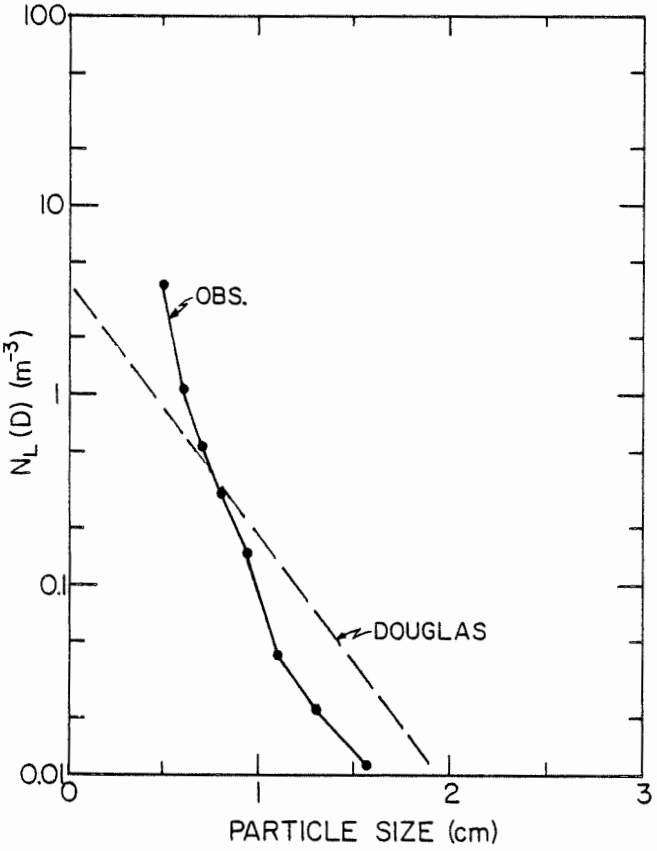

Fig. 3: Similar to Fig. 2, but for a different 1-km path in the same storm where only particles up to about 1.6 cm across were observed. Douglas function shown here is for the observed mass concentration of 0.4 g/m^3.

The total hail mass concentration calculated from the size distribution in Fig. 2 assuming spherical ice particles with densities of 0.92 g cm^{-3} is 9.5 g m^{-3}. While this value is among the largest obtained from the T-28 observations (the maximum to date being about 12 g m^{-3}), it is not unreasonable. However, the equivalent radar reflectivity factor computed from the distribution is in excess of 74 dBz. The corresponding SESAME radar measurements at the time were much smaller.

There was again no supporting evidence of the presence of hailstones of such large sizes. Recordings of the audible hailstone impacts on the T-28 windscreen and the pilot reports do not indicate solid particles as large as several centimeters. The damage to the aircraft during the flight did not suggest encounters with such high concentrations of large solid hailstones. There were no confirming reports of large hailstones at the ground.

When only particles up to about 1.5 cm across are present, size distributions determined from the hail spectrometer data resemble exponential functions more closely (Fig. 3). There is some suggestion of a slight curvature above about 1 cm in Fig. 3, but in most similar cases it is very slight. The concentrations of particles larger than 1 cm or so drop below the Douglas values. Figure 3 shows a concentration of 1.5 cm particles of only 0.01 m^{-3}, more than an order of magnitude less than in Fig. 2.

7. TENTATIVE EXPLANATION OF THE OBSERVATIONS

The large particles indicated by the hail spectrometer are believed to be real. However, the other evidence is incompatible with the presence of high concentrations of large hailstones. The observed radar reflectivity factors, the evidence of hailstone impacts on the aircraft, and the limited available comparisons with corresponding observations at the ground are not consistent with the presence of large solid ice particles. We therefore believe that the particles are giant low-density graupel of some sort. Supporting evidence for such a hypothesis has been obtained from dual-wavelength radar studies in Colorado. The T-28 pilots have also frequently reported seeing large "slush particles" hitting the windscreen.

Such particles would tend to sweep up great amounts of cloud liquid water and should therefore grow very quickly. On the other hand, they do not seem to appear in the precipitation at the ground so they must break up somehow during descent. So far the details of their fate in the clouds remain a mystery.

Other possible explanations for the large particle observations have been evaluated and most have been discounted. The "slow-particle detector" gave positive indications on numerous occasions in Oklahoma. However, they occurred where only small particles were present, as well as where large ones were observed. Moreover, the slow-particle detector sometimes appeared to stay on for more than a minute. The slow-particle indications have been ascribed to probable fogging or wetting of the instrument optics rather than slow-moving ice fragments.

Particle coincidence probabilities were estimated during the initial design of the hail spectrometer (Shaw, 1974) and found to be small. In the actual observations, the concentrations of particles larger than 1.5 cm are less than 1 m^{-3}. The instrument sampling volume is about 10 m^3 s^{-1}, so no more than 10 particles of these sizes are observed per second. At the nominal T-28 flight speed of 100 m s^{-1}, the spacing between large particles therefore averages 10 m or more; that is, at least 200 particle diameters. Coincidence events involving large particles are therefore very unlikely.

To better define the nature of the large particles, plans are now underway to convert the hail spectrometer into a two-dimensional imaging device. In that way the shapes, and therefore the compositions, of the particles can be determined. There is also some hope of photographing one of the particles with the T-28 particle camera (Cannon, 1976). However, its sampling volume is so small that the chance of finding one of the giant particles in the field of view is remote. The largest particle thus far photographed is less than 1.5 cm in diameter.

Acknowledgments. This material is based upon work supported by the Division of Atmospheric Sciences, National Science Foundation, under Grant ATM-7827018. The contributions of G. N. Johnson in the development of the hail spectrometer are gratefully acknowledged.

REFERENCES

Cannon, T. W., 1976: A particle camera for powered aircraft. Preprints Intn'l. Conf. Cloud Physics, Boulder, Amer. Meteor. Soc., 572-575.

Douglas, R. H., 1964: Hail size distribution. Proc. 1964 World Conf. Radio Meteor. (11th Wea. Radar Conf.), Boulder, CO, Amer. Meteor. Soc., 146-149.

Federer, B., and A. Waldvogel, 1975: Hail and raindrop size distributions from a Swiss multicell storm. J. Appl. Meteor., 14, 91-97.

Knollenberg, R. G., 1970: The optical array: an alternative to scattering or extinction for airborne particle size determination. J. Appl. Meteor., 9, 86-103.

Miller, J. R., Jr., D. J. Musil, G. N. Johnson, J. L. Halvorson, and P. L. Smith, Jr., 1978: Airborne versus ground hail sizes. Preprints Conf. Cloud Physics and Atmos. Elec., Issaquah, WA, Amer. Meteor. Soc., 178-181.

Sand, W. R., and R. A. Schleusener, 1974: Development of an armored T-28 aircraft for probing hailstorms. Bull. Amer. Meteor. Soc., 55, No. 9, 1115-1122.

Shaw, W. S., 1974: Development of an airborne optical hailstone disdrometer. Report 74-16, Institute of Atmospheric Sciences, S.D. School of Mines and Technology, Rapid City, South Dakota. 35 pp.

Spahn, J. F., 1976: The airborne hail disdrometer: an analysis of its 1975 performance. Report 76-13, Institute of Atmospheric Sciences, S.D. School of Mines and Technology, Rapid City, South Dakota. 65 pp.

_____, and P. L. Smith, Jr., 1976: Some characteristics of hailstone size distributions inside hailstorms. Preprints 17th Conf. Radar Meteor., Seattle, WA, Amer. Meteor. Soc., 187-191.

Smith, P. L., Jr., D. J. Musil, S. F. Weber, J. F. Spahn, G. N. Johnson, and W. R. Sand, 1976: Raindrop and hailstone size distributions inside hailstorms. Preprints Intn'l. Conf. Cloud Physics, Boulder, CO, Amer. Meteor. Soc., 252-257.

_____, C. G. Myers, and H. D. Orville, 1975: Radar reflectivity factor calculations in numerical cloud models using bulk parameterization of precipitation. J. Appl. Meteor., 14, 1156-1165.

THE AERODYNAMICS OF FREELY FALLING DISKS AND IMPLICATIONS FOR UNDERSTANDING THE FREE FALL MOTIONS OF ATMOSPHERIC PARTICLES.

R.E. STEWART* AND ROLAND LIST
University of Toronto, TORONTO, CANADA M5S 1A7
*Present address: University of Wyoming, Laramie, U.S.A.

1. INTRODUCTION

Before the growth of atmospheric particles such as snow crystals, graupel and hailstones can be explained and predicted, their free-fall motions must be understood. Terminal velocities are just one aspect and it must be recognized that other motions such as rotation and horizontal movement will also affect growth through changes in accretion and mass and heat transfers.

The limitations of wind tunnel experiments were much reduced in the present experiments, where aerodynamic forces and torques could be calculated from changes in position and orientation of freely falling particles as observed with a high speed camera.

In the present experiments with a fall-tower (Stewart et al.,1976) styrofoam and balsa disks with diameters of 2.0-3.1cm were chosen as falling bodies (Stewart, 1977) and released at different angles. The terminal velocities ranged from 1.7 to 3.2ms^{-1} while the Reynolds numbers varied from 2200 to 4450. [Studies in water have shown that this shape falls in an unstable manner for Reynolds numbers above 100 (Willmarth et al., 1964, Stringham et al., 1969, List and Schemenauer, 1971).]

2. EXPERIMENTAL SETUP AND ANALYSIS TECHNIQUES

In order to study the motions of a disk over the 3.25m fall distance, the particles are released from rest and are followed by a horizontally pointing high-speed camera which is driven to fall vertically at a velocity similar to that of the disk being studied so that the disk remains in the camera's field of view (Rentsch, 1975, Stewart et al., 1976). Since the particles are observed through a mirror system their location in space can be determined on the basis of the multiple pictures obtained. The standard deviation of errors in the camera frame are 0.6mm for X, and 0.2 for Y and Z at a distance of 45cm from the film plane.

The orientation of a disk is described by the Euler angles. These angles were calculated in a "trial-and-error" computer program with the aid of colour coded marks placed onto the disks'surfaces. Accuracy is about $\pm$ 3^{o} for each of the Euler angles. Both translational and angular velocities and accelerations were calculated by central finite differencing techniques. The disks were photographed at a frame rate of 200 frames/s using Ektachrome 7242 film.

3. DESCRIPTIONS OF FREE-FALL EXPERIMENTS

The dimensions of the disks were chosen so that a limited study of the dependence of the motions on Reynolds, Re, and non-dimensional moment of inertia, I*, could be made. Re is defined by $Re = DU/\nu$ and I* is defined by $I^* = (\pi/4)(\rho_b/\rho_a)\gamma\,[1/16 + (1/12)\gamma^2]$ where D is the diameter of the disk, U its velocity relative to still air, ν the kinematic viscosity of air, ρ_b and ρ_a the disk and air density respectively, and γ is the disk's thickness-to-diameter ratio.

The disks were made from styrofoam sm(ρ_b= 0.123 g/cm^3) and had the same thickness ratio of 0.275 $\pm$ 0.005, two styrofoam disks of diameters 2.0 and 3.1 cm have the same value of I* (0.43 $\pm$ -0.01),but their terminal velocity Reynolds numbers Re_o [using data for disks falling face-down from Hoerner (1957)] are 2200 and 4100, respectively. A balsa disk of diameter 2.13cm has Re_o=4450 (within 8% of Re_o for the larger styrofoam disk), but I* for the balsa disk (1.53 $\pm$ -0.01) is almost four times that of the styrofoam disks. Experiments with the styrofoam disks will elucidate Re effects, and motions exhibited by the larger styrofoam disk and the balsa disk will point out I*effects.

Approximately 175 experiments were carried out. The styrofoam disks were released from 0^{o}(facedown), 45^{o} and 90^{o} (edge-down) while the release angle was 0^{o} in all drops of the balsa disk.

4. OBSERVED FREE FALL MODES

Only three free-fall modes were observed in all the 175 experiments: oscillation (essentially about a horizontal diameter), rotation about a horizontal diameter, and gyration. Gyration consists of spin about the minor axis which is rotating at a constant or periodically varying angle about the horizontal axis so that the spin axis moves on the surface of a circular or elliptical cone (Kry and List, 1974a,b).

Styrofoam disks released face-down reached or approached an oscillation mode of roughly constant amplitude (Fig.1). The disks fell nearly vertically, although horizontal swinging in the directon perpendicular to the oscillation axis was coupled with the angular oscillations. The fact that the same observatons were made when the release angles were 45^{o} suggests that the final state is independent of release angle up to at least 45^{o}.

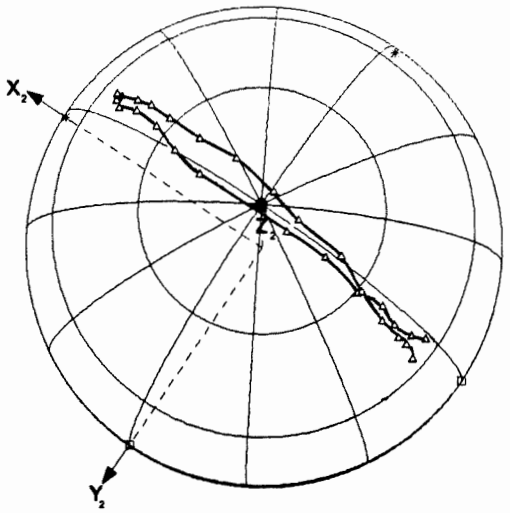

FIG. 1: Orientation of disk which is centered in the middle of the sphere, and where the points are the intersections of the outward normal from the face of the disk with the sphere's surface. Contours not visible from the viewing point are dotted. The space axes coincide with the center of the disk. Time runs clockwise.

5. CHARACTERISTICS OF THE OSCILLATION MODE

The angular and translational characteristics of the oscillations are shown in Table 1. Angular amplitudes increased with Re_o and decreased with I*, oscillation frequencies decreased with increasing Re_o and were relatively independent of I*, whereas the non-dimensional oscillation frequency (defined as the Strouhal number S = nD/U where n is the oscillation frequency) showed the opposite dependence on Re_o and I*. These observations are similar to those made by Willmarth et al.(1964) and Willmarth et al. (1967). Horizontal drift increased with Re_o and I* in agreement with results obtained by Stringham et al. (1969). As shown in the typical results of Fig. 1, oscillations were essentially about a horizontal diameter. The sense of the deviations about a horizontal diameter were opposite to the sense of spin about the minor axis. This can be explained by utilizing a gyroscopic analogy and by noting that the aeordynamic torque will be restoring (Willmarth et al., 1967).

For the styrofoam disks, calculated drag, C_D, lift, C_L, and torque, C_τ, coefficients as functions of attack angle agreed within experimental error with results presented by Hoerner (1957) for stationary disks in a wind tunnel (Stewart,1977). C_D is defined as $C_D = F_D/[(\pi/8)(\rho_a U^2 D^2)]/C_L$. C_L is defined the same except F_L replaces C_D, and C_τ is defined as $C_\tau = \tau/[(\pi/8)\rho_a U^2 D^3]/F_D$ where F_D is the aerodynamic force in the direction opposite to $\vec{U}$, and τ is the aerodynamic torque acting about a diameter. For stationary disks and attack angles $< 45^o$, C_D decreases linearly with attack angle α and C_L and C_τ increase linearly with (Hoerner, 1957). α is defined by $\cos\alpha = \vec{N}.\vec{U}/(NU)$, where N is the outward normal from the positive face of the disk.

TABLE 1: Characteristics of disks oscillating, rotating or gyrating while falling; s: styrofoam, b: balsa, A: oscillation amplitude (deg), n: frequency (Hz), S: Strouhal number, ω'_m: average largest vaue of angular velocity (rad/s), ω_m: average largest value of angular acceleration (rad/s^2), V_{fd}: vertical velocity falling face-down (m/s), V_m: average vertical velocity (m/s), C_{DZ}: average vertical drag coefficient, U_m: horizontal drift velocity (m/s), R_{UV}: fraction of horizontal drift to vertical velocity, R_{pD}: ratio of peak-to-peak horizontal swinging-to-diameter, R_{pV}: ratio of peak-to-peak horizontal velocity fluctuation-to-vertical velocity, R_{ag}: ratio of peak-to-peak horizontal acceleration fluctuation-to-gravity, 0: nutation amplitude (deg), :precession amplitude (deg), f_s: spin frequency about minor axis (Hz), R_{ns}: ratio of nutation/precession to spin frequency.

D	2.0(s)	3.1(s)	2.1(b)
Re_o	2200	4100	4450
I*	0.44	0.42	1.53
Oscillation:			
A	30-35	50-55	20-30
n	4.5	3.3	3.5
S	0.05	0.045	0.023
ω_m'	14	19	5.0
ω_m	350	350-370	100
V_{fd}	1.65	2.01	3.17
V_m	1.79	2.30	3.36
C_{DZ}	0.99	0.88	1.04
U_m	0.025	0.055	0.40
R_{UV}	0.01	0.024	0.12
R_{pD}	0.65	1.10	-
R_{pV}	.26	.36	-
R_{ag}	1.20	1.60	-
Rotation about horizontal:			
n	8.7	7.8	
S	0.106	0.12	
V_{fd}	1.65	2.01	
V_m	1.65	2.01	
C_{DZ}	1.17	1.17	
U_m	0.6	0.55	
R_{UV}	0.35	0.25	
Gyration			
0		65	70
		57	59
n		6.7	10.5
S		0.09	0.066
f_s		1.8	3.0
R_{ns}		3.7	3.5
V_{fd}		2.01	3.17
V_m		2.26	3.30
C_{DZ}		0.91	1.07
U_m		0.35	0.25
R_{UV}		0.15	0.08

The aerodynamic coefficients generally showed some hysteresis with respect to orientation changes. This is shown in Fig. 2 for C_D and C_L. C_D profiles closely followed α changes, but largest values of C_L generally lagged peaks of α by 0.02- 0.05s, and C_L minima sometimes lagged α minima by 0.01-0.02s. These trends suggest that adjustment of the fluid flow lagged behind the continually changing orienta-

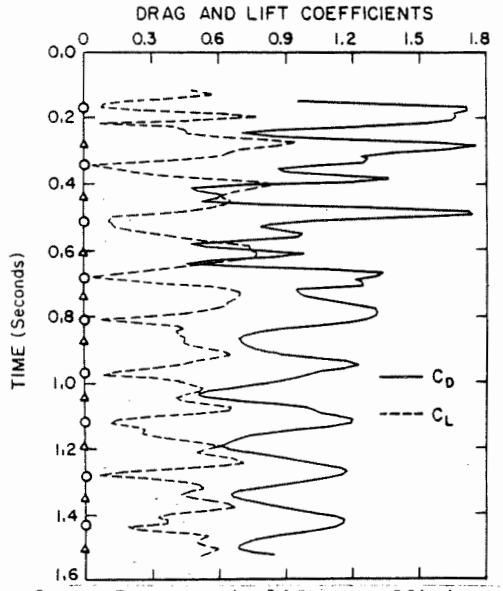

FIG. 2: Drag and lift coefficients as functions of time for the 3.1cm styrofoam disk released face-down. Terminal velocity was reached by 0.5s. Circles and triangles correspond to times when minima and maxima, respectively, occurred in the attack angle.

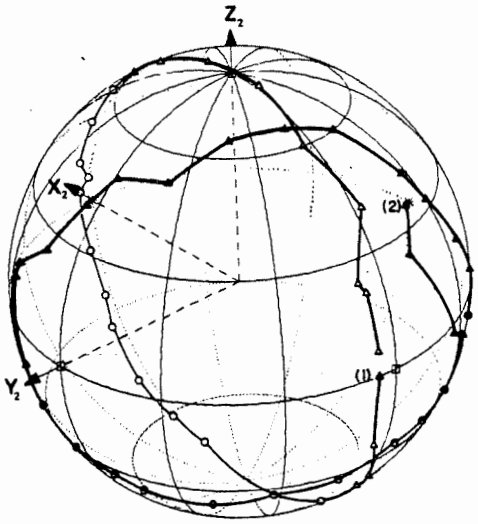

FIG. 3: Orientation of the 3.1cm styrofoam disk after edge-down release showing the first (1) rotational cycle (great circle through the poles)and the last (2) cycle representing gyration (circle around point on equator)of the same experiment. The numbers are located at the starting points of the cycles.

tion. A phase shift also existed in the relation of C to orientation changes. C lead orientation changes by about 0.015s The phase lead of the aerodynamic torque with respect to orientation means that energy was being extracted from the oscillations (Willmarth et al., 1967; Stewart, 1977), the oscillations were being damped.

6. CHARACTERISTICS OF ROTATION ABOUT A HORIZONTAL DIAMETER MODE

Characteristics of the free-fall experiments in which rotation about a horizontal diameter occurred are summarized in Table 1. The rotation frequency decreased with Re_0. Although S was the same within 5%, it should be noted that the rotation frequency of the 3.1cm styrofoam disk fluctuated 10-20% about its average value of 7.8Hz. The horizontal drift was relatively independent of Re_0.The high C_{DZ} values agree with the results of Stringham et al. (1969), who found that the vertical velocities of disks tumbling in water were often close to the values they would have had if they had fallen face-down.

7. CHARACTERISTICS OF THE GYRATION MODE

The 3.1cm styrofoam disk and the balsa disk autogyrated after rotational accelerations began. An example of the change in free-fall mode from rotation about a horizontal diameter to gyration for the 3.1cm disk is shown in Fig. 3. The changes in free-fall mode from oscillations or rotations about a horizontal diameter suggest that these motions became unstable. Statically, any diameter (about which the moment of inertia is least) and the minor axis (about which the moment of inertia is greatest) are stable rotation axes in a torque-free environment (Smart, 1951). However,due to some interaction with the air, the effective moment of inertia about the rotation diameter may become distinguishable from the effective moment of inertia about the diameter perpendicular to the rotation axis. If the effective moment of inertia about the rotation axis increases, and, thus becomes intermediate, such a rotation would be unstable. A small displacement of the angular momentum vector from the rotation diameter would cause the angular momentum to be divided among the principal axes so that spin would begin about the minor axis. The experiments clearly indicated that the instabilities which occurred changed the free-fall mode to gyration.

The experiment in which the 3.1cm styrofoam disk remained rotating about a horizontal diameter but with a fluctuating rotation frequency, supports this interpretation of the evolution of gyration. The fluctuations result from a coupling between the effective moment of inertia and the rotation frequency when there is no component of the angular momentum about axes other than the rotation axis (Stewart, 1977).

Characteristics of the free-fall experiments in which gyration occurred are shown in Table 1. Spin about the minor axis, nutation/precession frequency and average vertical drag coefficient increased with I*, whereas Strouhal number decreased with I*. The ratio of nutation/precession frequency to spin frequency was almost independent of I*.

In all observations, the relative sense of minor axis spin and nutation/precession was the same. Some gyration characteristics exhibited by the disks were simliar to the characteristics predicted for spheroids of axis ratio >0.5 at Re $<10^4$ (Kry and List, 1974b).

One difference between the experimental and predicted results is the relative sense of minor axis spin and nutation/precession. Expermentally, these two quantities were in the same

sense, but the predicted relation is opposite. The distinction may be related to a difference in sense of aerodynamic torque at large attack angles. If the overall features of the torque acting on a cylinder of thickness ratio 1.0 (Willmarth et al.,1967) are applicable to the disks used here, then the torque is acting to align the disk's edge with the flow at these angles. For spheroids, the torque is always restoring.

9. SUMMARY, CONCLUSIONS AND COMMENTS

The primary conclusion from the free-fall experiments is that three distinct modes were observed:
(1) oscillation almost about a horizontal diameter,
(2) rotation about a horizontal diameter,
(3) gyration.
Characteristic translational motions are superimposed on these modes.

Unsteadiness of free-fall motion incresese with Re and I*. The oscillation amplitude increases with Re, and although the oscillation amplitude of a balsa disk is lower than that of a stryofoam disk at the same value of Re, this mode can abruptly change into gyration for balsa disks. This does not occur for styrofoam disks

None of the free-fall motions exhibited by the disks are predictable from wind tunnel measurements which ignore dynamic or non-stationary effects. The phase shifts of the aerodynmic coefficients, the horizontal drifts of the oscillating disks, the change in free-fall mode from oscillation or rotation to gyration, and the constant or decreasing energies of the secondary motions are all manifestations of dynamic effects.

Rotation about a horizontal diameter is unstable if the effective moment of inertia about the rotation diameter becomes intermediate due to air influences. Autogyration was observed for disks with thickness ratio of 0.275 so the effective moment of inertia increases. For disks with thickness ratios greater than 0.87, rotation could become unstable if this effective moment of inertia were able to decrease.

Other shapes may also be able to autogyrate If the effective moment of inertia about the rotation axis increases, oblate spheroids and right cones with apex angles 53^{o} could autogyrate if, respectively,rotation is initially about a major axis or about an axis perpendicular to the symmetry axis. Only if the effective moment of inertia could decrease could prolate spheroids and right cones with apex angles 53^{o} autogyrate.

Gyration may be important for understanding the growth of atmospheric particles. For example, it may be the mechanism responsible for changes in the shape of growing hailstones. Hailstones are typically spheroidal or conical in shape, and small conical particles are often the embryos of these hailstones. Spheroidal hailstones have normaly maintained their shape after the initial conical shape changed. In a vertical icing tunnel, the shapes of growing spheroidal hailstone models were maintained if the models were restricted to gyrate with the relative sense of minor axis spin and nutation/precession opposite (Macklin,1978). If this is the characteristic angular motion of natural spheroidal hailstones, the change from the initial conical shape may have occurred after this particle began to gyrate with opposite senses of spin and nutation/precession. Since conical hailstones maintain the shape of their embryos, this suggests that the growth regimes in clouds and their changes affect the particle dynamics.

In summary, the experiments have shown that distinct free-fall modes occur and that these modes are influenced by aerodynamic effects caused by the motions themselves. Similar modes may occur for other shapes, sizes and densities; one could even speculate that they represent the major modes of free fall and that irregular tumbling doesn't exist.

ACKNOWLEDGEMENTS: These studies were carried out within a program sponsored by the National Research Council of Canada.

REFERENCES

Hoerner, S.F.,1957: Fluid Dynamic Drag, Addison-Wesley.

Kry, P.P. and R. List, 1974a: Aerodynamic torques on rotating oblate spheroids.Phys. Fluids,17, 1087.

------- ------, 1974b: Angular motions of freely falling spheroidal hailstone models. Phys. Fluids,17, 1093.

List, R. and R.S. Schemenauer, 1971: Free fall behavior of planar snow crystals, conical graupel and small hail. Bull.Amer.Met.Soc. 47,110.

List, R., U.Rentsch, A.C.Byram and E.P.Lozowski: On the aerodynamics of spheroidal hailstone models. J.Atmos.Sci.,30,653.

Macklin, W.C., 1977: The characteristics of natural hailstones and their interpretation. In: Hail: A review of hail science and hail suppression. Meteor.Monographs, 16, 38, 65-86, American Meteorological Society, Boston, 1977.

Smart, E.H., 1951: Advanced Dynamics, McMillan and Co. Ltd., London.

Stewart, R.E., 1977: Experimental investigation of the aerodynamics of freely falling disks, PhD thesis, University of Toronto.

---------- , R. List and U.W. Rentsch, 1976: Aerodynamics of freely falling bodies. Proc. Int. Conf. Cloud Phys., Boulder, USA, 258-261.

Stringham, G.E., D.B. Simons and H.P. Guy, 1969: The behavior of large particles falling in quiescent liquids. Geological Survey Professional Paper 562-C,Washington DC,.

Willmarth, W.W., N.E. Hawk and R.K. Harvey, 1964: Steady and unsteady motions and wakes of freely falling disks. Phys. Fluids, 7, 197.

---------, N.E. Hawk, A.J. Galloway and F.W. Ross, 1967: Aerodynamics of oscillating disks and a right-circular cylinder. J. Fluid Mech. 27,177.

ANALYSIS OF THE ECHOES AND THE HAILSTONE MICROSTRUCTURE OF A SUPERCELL HAILSTORM

Songxi Yang, Tangfu Liu, Naihu Gong
Lanzhou Institute of Plateau Atmospheric Physics of the Chinese Academy of Sciences
Lanzhou, Gansu, PEOPLE'S REPUBLIC OF CHINA
Jialiu Xu
Geology and Geography Department of Lanzhou University
Lanzhou, Gansu, PEOPLE'S REPUBLIC OF CHINA

On 4 June, 1976, a meteorological radar* in Pingliang County, Gansu Province tracked and observed a supercell hailstorm from 16:53-20:50 (Beking time). The hailstorm moved into the boundary of Pingliang County from 19:00-20:00 and much hail fell in the vicinity of Qinglong station. At the Qingiong station, total precipitation fron 18:54 to 21:08 was 36.5 mm and hailfall extended from 19:20 to 20:05 with giant hailstones appearing at 19:40-19:46.

The wind velocity under the hailstorm cloud was smaller, symbolizing that the in-flow amount at the lowers was smaller, which might account for the weakening both of updraft and "weak echo region"[1].

1. ECHO STRUCTURE

Fig. 1A-D enumerated the three dimensions echo structures from 18^{29} to 19^{36}. Fig. 1A is a combination of the whole informations of PPI and RHI gathered within the four minutes from 18^{27-31}. There was only one main echo core in the outline of $Z_e=10^{4.6}mm^6m^{-3}$ (46dbZ) with a maximum center as big as $Z_e=10^{5.6}mm^6m^{-3}$ and a top extending 7 Km above ground. It was a lightly hailswath at the position of 340°, 27 Km in horizontal distance. On the cross section of RHI (Fig. 1A), at the most northern side (the back of the moving direction) of the main core's weak echo region. There were two regions of $Z_e=10^{3.6}mm^6m^{-3}$, 2-8 Km above ground. It is estimated that this was resulted from the precipitation particle by passing the northern side of the main core at the middle air of the supercell. If at that time the echo structure was quasistationary, the echo boundary of a certain isoline might be regarded as an envelop of certain particles which would move up and down and would cut through the cross section of RHI (Fig. 1A). Actually it had both the movements. Most of the small particles in the above mentioned two Z_e regions eject from the hailstorm aloft together with the incus outflow. The big particles might fall on the ground to the north of hailstorm through the selection of horizontal wind. They had no chance of entering the foot of updraft and were not grow up to the giant sizes in recycle. The top of the outline of the main core echo $Z_e=10^{4.6}mm^6m^{-3}$ (Fig. 1B) was upwards of 8 Km, the temperature was around -40°C and the bottom had not yet reached the ground. It was inferred that the precipitation and hailstorm particles were well under the way of growth.

In the front part of the main core (Fig. 1B) there was a secondary core echo with a top of outline ($Z_e=10^{4.6}mm^6m^{-3}$) less that 6 Km and a temperature around -25°C. It was a precipitation (shower and small hail) echo touching the ground.

The form of the secondary core was quite peculiar, different from "embryo curtain" as put forward by Browning et. al.[2]. Because in light of a strict condition for existence of embryo curtain, there must be a vault of "boundary weak echo region" between the curtain and the main core. But there was no such a vault. On the other hand, the central of a curtain is more class intensity levels less that those of main cell and does not touch the ground. However, the secondary core was equal in intensity with the main core and presenting a precipitation form of touching the ground. That is to say, in the secondary core, the velocity of updraft which kept balance with the terminal velocity of falling particles was by far faster that those of which gave birth to embryonic curtain, and the precipitation particles were greatly bigger in size than the hail embryoes.

Although the shape of secondary core bore some resemblance to the "feeder cloud" or the "daughter cloud" of multicell hailstorm as analysed by Dennis[3], Musil[4], and Browning[5], yet the secondary core was obsiously different. A top of "feeder cloud" or "daughter cloud" was nearly the same with that of a main cell, while the top of the secondary core was by far lower than the main core: An echo of "feeder cloud" or "daughter cloud" shared with main echo a common environmental condition and a common mechanism for hail growth, making it im-

---

* Type JMA-133D made in Japan, wave length 3.2 cm, beam width 1.3°, pulse duration 2 μ sec, peak pulse power 200 KW, repetition frequency 210 sec^{-1}.

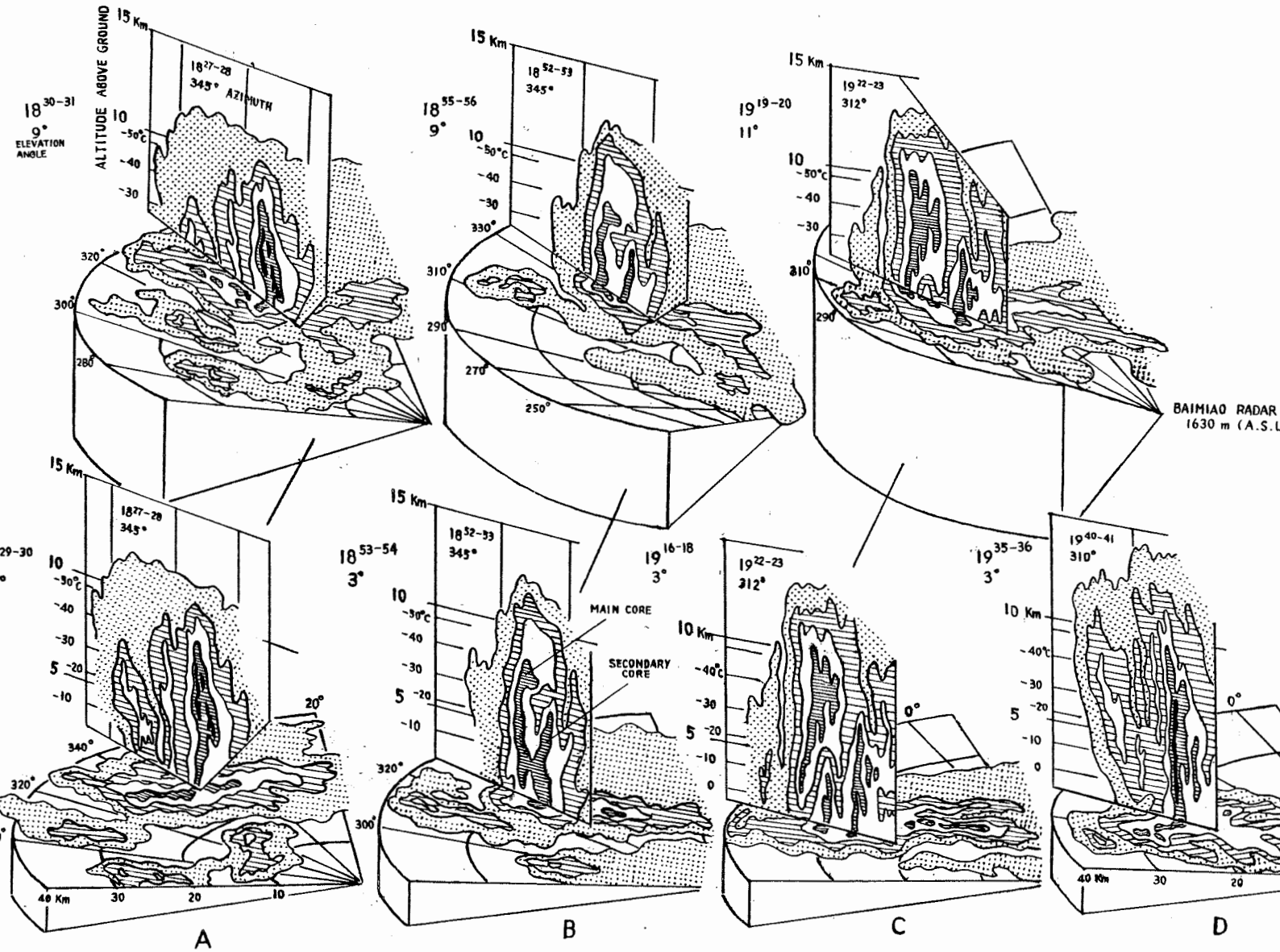

Fig.1 The Three Dimension Structure of the Echoes of the Pimgliang Hailstorm on 4 June 1976.
The Isolines of the Echoes are $Z_e = 0$, 26, 36, 46, 56 dbz from the Outside to the Inside Respectively

possible to give rise to a precipitation under the conditions much lower than the main echo. But the secondary core presented a state of precipitation. From this we may certainly infer that the secondary core might well be a disturbance of updraft at the front part of the supercell under the condition of weak updraft. Because its appearance was in advance of the falling of big hailstones on the ground, it must have played an important role in hailstone growth (Fig. 1B, 1C, the time was from 18^{52} to 19^{23}, the falling of big hailstones began at 19^{24-40} in Qinglong station).

There is still one more interesting thing on Fig.1B which merits our attention: There was a juncture between the two echo cores, whose temperature was $-5^{\circ}C$ — $-10^{\circ}C$. We drew an inference from this that certain precipitation particles or hail embryoes must have been transported to the main core echo through the disturbance motion at the juncture and, in turn, certain hailstones in the main core must have entered the secondary core with the help of the easterly horizontal momentum acquired from the higher layers. In this way they became grew by absorbing the superco led water droplets. The common existence of the two cores must have created favourable conditions for the formation of larger hailstones.

Fig. 1C is the continuation and development of Fig. 1B, which just reflects the main features of the echoes before the appearance of giant hailstones. Fig. 1D is a repetition of Fig. 1A in shape just when giant hailstones fell on the ground but in intensity and altitude it exceeds Fig. 1A.

2. THE MICROSTRUCTURE OF HAILSTONES

1) Hail embryo

We selected 25 hailstones with diameters upwards of 1 cm from those collected on the spot at Qinglong station while it was hailing and analysed the thin section of them which showed that there were five types of hail embryoes. Their code names of the English letters are the same with the document[6] (A-transparent spherical, B-semi-transp. spher. with big air bubbles, C-instransp. spher. full of small air bubbles, D-partly intrasp. in narrow end, cone-shaped and elliptical, E-intransp. cone-shaped or elliptical.), but the proportion of the different types are characterized by the fact that types A and B amounted to 52% (A-32%, B-20%, C-16%, D-16%, E-16%). The diameters of types A and B were 3-13mm, in which most of them were 5-7 mm. Referring to the experiment to freeze water drops performed by Bigg[7], we know that the freezing temperature of water drops 5-7 mm in diameter is about $-19^{\circ}C$. This shows that the hail embryoes which had formed the big water drop slowly frozen, which made us come to the conclusion that the embryo source must have been the middle layers of the cloud with high liquid contents and not too low temperature.

The frequency of the diameter of the hail embryoes is comparatively close to normal distribution, its formula is:

$$f(d_o) = 5.37 \times 10^{-2} \times d_o^{7.5} \times e^{-1.2d_o} \quad (\%)$$

where, d_o is the diameter of embryo (mm), those of $d_o > 6$ mm amount to half of the total.

According to transparency of the ice layers hailstones, we find that there are 1-7 layers in those of 25 selected hailstones. 4-5 layers and 1-2 layers are 45.5 % and 33.6 % respectively.

2) Hailstone shape and relative spectrum

The 139 hailstones on analysis here were collected at Qinglong station at the time of hail shooting; 113 of them were gathered at Caizhuang (3 Km to the southwest of Qinglong station) after the hail shooting.

33 % the 111 collected at Caizhuang were in the shape dry persimmon and those in the shape of spheroid and cerebrum were 23 % and 22 % respectively. Those in the shape of dry persimmon were comparatively oblate, something like plates. The whole contour of cerebrum is semispherical, with an obvious hollow at the bottom and folds on the surface very much like the shallow-hilled irregularities[8]. This type of hailstorms also grew under the condition of comparatively higher liquid water contents or larger supercooled water droplets.

A random sample of 710 hailstones were collected at Caizhuang after hail

shooting, statistics showed that the formula of hailstone relative spectrum is as follow:

$$f(d) = 115 \times e^{-0.125d} \quad (\%) \quad d \geq 6 \text{ mm}$$

where, d is the diameter of a hailstone. The mode number is 6 mm.

REFERENCE

(1) Marwitz, J.D. and E.X. Berry, 1970 "The weak echo region and updrafts of a severe hailstorm". 14th Radar Meteor. Conf. Nov. 17-20, 1970, TUCSON, ARIZONA 43-47

(2) Browning, K.A., and G.B.Foote, 1976 "Air flow and hail growth in supercell storms and some implications for hail suppresion". Quart. J.Roy. Meteor. Soc., 102 499-533

(3) Dennis, A.S., Schock, C.A. and Koscielski, A., 1970, "Characteristics of hailstorms of Western South Dakota" J.Appl. Met., 9, 127-135

(4) Musil, D.J., 1970, "Computer modeling of hailstone growth in feeder clouds" J.Atmos. Sci., 27 474-482

(5) K.A. Browning, J.C. Fankhauser, et.al. 1976 "Synthesis and Implications of Hail Growth and Hail Suppression" Monthly Weather Review 104(5) 603-610

(6) 徐家骝，黄孟容，刘钟灵，段兆吉，1965 “甘肃岷县地区1964年6—7月两次冰雹雹谱、雹切片的分析” 气象学报 35(2)

(7) B.J. Mason THE PHYSICS OF CLOUDS Qxford University Press 1971

(8) Browning, K.A. 1966 "The lobe structure of giant hailstones" Quart. J. Roy. Meteor. Soc., 92,1-14

Imp Sciences . 24 , avenue des Landais - 63170 - Aubière . Dépôt Légal .

3e trimestre 1980